Controlling handedness of triarylamine trisamide assemblies by means of circularly polarized light or chiral additives

Quentin Sallembien

Sorbonne Université

École doctorale de Physique et Chimie des Matériaux (ED 397)

Institut Parisien de Chimie Moléculaire / Équipe de Chimie des Polymères (UMR 8232)

Controlling handedness of triarylamine trisamide assemblies by means of circularly polarized light or chiral additives

Par Quentin SALLEMBIEN

Thèse de doctorat de Physique et Chimie des Matériaux

Dirigée par Matthieu RAYNAL

Présentée et soutenue publiquement le 15 avril 2021

Devant un jury composé de :

M. Stéphane BELLEMIN–LAPONNAZ	Directeur de recherche Université de Strasbourg	Rapporteur
M. Luis SÁNCHEZ	Professeur Université Complutense de Madrid	Rapporteur
M^{me} Valérie MARVAUD	Directrice de recherche Sorbonne Université	Examinatrice
M. Matthieu RAYNAL	Chargé de recherche Sorbonne Université	Directeur de thèse

À Alice

« Tout est grâce »
Sainte Thérèse

Remerciements

Qu'as-tu que tu n'aies reçu ?
I Cor. IV, 7.

En premier lieu, je souhaite remercier MM. Stéphane BELLEMIN–LAPONNAZ et Luis SÁNCHEZ (*¡Muchas gracias!*) d'avoir accepté d'être les rapporteurs de cette thèse. Je remercie également M^me^ Valérie MARVAUD d'en présider la soutenance, ainsi que pour l'aide qu'elle m'apporta lors de mes premiers essais photochimiques.

Je remercie vivement Matthieu RAYNAL, directeur de cette thèse haute en couleur qu'il a enrichi de son savoir étendu, et dont il aura su tirer les fils avec rigueur. Je suis aussi reconnaissant envers Laurent BOUTEILLER, directeur de l'équipe de chimie des polymères et co-encadrant de cette thèse, qui fut le premier à me recevoir au laboratoire et dont l'expertise scientifique a toujours aiguillé ces travaux.

Je tiens à exprimer toute ma gratitude à Sébastien BLANCHARD, qui a participé à cette étude en conduisant les expériences de RPE. Je le remercie pour sa disponibilité et son enthousiasme. Ma reconnaissance va également à Aline PERCOT et Céline PARIS, pour avoir réalisé les spectroscopies Raman. Un grand merci à Pamela AOUN, organicienne hors pair, pour son travail de synthèse et sa gentillesse. Je remercie Claire TROUFFLARD pour son expertise en RMN ainsi que pour ses conseils. Mes remerciements vont aussi à Jeanne CRASSOUS qui a eu l'amabilité d'apporter son expertise dans l'organisation du premier chapitre de cette thèse. Merci également à Cédric PRZYBYLSKI et Ludovic DUBREUCQ pour leurs analyses HRMS et MALDI-TOF des molécules présentées ici, ainsi qu'à Jorge ROYES MIR pour notre discussion fructueuse au sujet de la lumière polarisée circulairement. Je suis aussi reconnaissant envers Louis FENSTERBANK, directeur de l'IPCM, et Christian BONHOMME, qui m'a accueilli au laboratoire de chimie de la matière condensée de Paris pour y mener des expériences de spectroscopie. Je remercie Geoffroy GUILLEMOT pour son initiation à la spectroscopie dans l'infrarouge proche, Yanling LI pour le prêt de matériel optique, ainsi que Olivia REINAUD, Jacques CHOMILIER et Fabrice MATHEVET, membres du comité de suivi de cette thèse. J'exprime ma gratitude à Nadine WITKOWSKI et Akima SI-BACHIR, respectivement directrice

et secrétaire de l'école doctorale. J'associe à ces remerciements Dominique BONVENT, secrétaire de l'IPCM.

Je remercie Sylvie, Sylvie et Patricia, administratrice et gestionnaires de l'IPCM, pour leur sollicitude, ainsi que Bruno pour son aide précieuse en informatique et Omar pour ses compétences en chromatographie. Je salue amicalement Éric, agent d'entretien du couloir à la grande bonté et ami des lève-tôt. Je tiens à exprimer toute ma reconnaissance à Céline SAYAG, Bernold HASENKNOPF et Serge THORIMBERT, pour avoir accompagné mes premiers pas en tant qu'enseignant.

Que serait une thèse de doctorat sans ces compagnons de route que l'on nomme collègues et pour certains amis ? Ainsi, je remercie vivement Danilo, *bacalhau* joviale du bureau 516 ; Ahmad, barbe d'or de l'imitation et ornithologue en herbe ; Laura, rockeuse pyrénéenne internationale à la voix haut perchée ; Richard, homme confidentiel ; Dorian, sudiste bien informé ; Océane, à l'agenda de ministre ; qui, au-delà de cette description amusée, apportèrent les joies d'une camaraderie à ces heures passées au cinquième étage, entre les rotondes 43 et 53 du 4, place Jussieu de Paris. J'associe à ces remerciements Kajetan et Floriane, dont les goûts musicaux et la sympathie m'ont aussi donné l'envie d'avoir envie de venir chaque jour au laboratoire. Je salue amicalement Khaled, Mayte, Gaëtan, Gwendoline, Valentin, Pauline, Gaëlle, Laetitia, Sawsen, Adrian, Thomas, Julien, Léo et tous les autres membres de l'équipe de chimie des polymères, et plus largement de l'IPCM, pour leur fraternité. Enfin, j'ai une pensée pour Refka, inénarrable stagiaire qui m'aura tant appris.

Cette thèse est aussi l'aboutissement d'un parcours scolaire et universitaire auquel de nombreuses personnes ont concouru. Je suis ainsi reconnaissant envers MM. LANSMANT et MOLINARO, respectivement enseignants de physique-chimie et français au collège Jacques BREL de Villers-Bretonneux, ainsi que leur collègue de mathématiques, pour m'avoir permis de saisir qu'il n'y avait pas que le baobab dans ma main que je pouvais faire croître. J'exprime ma gratitude à Axel MARCHAL, professeur des universités en œnologie, homme brillant qui fut mon premier mentor. Je remercie également Didier ASTRUC, Jean-Louis BOBET, Denis DEFFIEUX et Alain FRITSCH qui, par leur soutien bienveillant, m'ont permis d'intégrer l'ENSCBP. Mes remerciements vont aussi à Philippe DESBOIS, qui m'a fait confiance et tant

appris chez BASF à Ludwigshafen, ainsi qu'à Bernard BERDEU, enseignant charismatique. Je suis également reconnaissant envers Sébastien LECOMMANDOUX, Stéphane CARLOTTI et Daniel TATON pour m'avoir aiguillé jusqu'ici. Enfin, c'est avec joie que j'évoque Antoine ROUSSELOT, Quentin VIRY, Johan HAMONNET, Raphaël PEPINO, Chloé BIZOT et Saïd EL LONE, acolytes du PJRDI.

Ces fruits viennent d'un arbre dont je suis le débiteur et l'obligé. Je pense à ma mère et mon père, mes grands-parents, mes aïeux et tous ceux qui me précédèrent et à qui je dois tout. Je remercie avec un amour fraternel ma sœur Tiffany et mon frère Gaëtan. Merci à Alexandre, dont l'amitié fidèle est une joie angélique. Je remercie ma belle-famille, en particulier François, Martine et Charles pour leur charité. Je rends grâce à Dieu pour le Père Georges, guide spirituel au cœur d'enfant. Je remercie Namratah, Delphine et Nancy, Cynthia, Julien et Adeline, ainsi que tous mes amis de jadis, dont nos chemins se sont séparés mais dont le souvenir m'accompagne. Puissent toutes ces personnes être bénies.

Je remercie Alice, mon épouse qui mit le grand jour dans mon âme et dont l'amour ineffable est une bénédiction. Je remercie et prie Dieu de nous offrir une longue vie pour continuer ce bonheur ensemble et avoir la joie de voir les enfants de nos enfants.

À Versailles, le huit mars deux mille vingt-et-un.

Quentin SALLEMBIEN

Table of contents

Abbreviations

AFM atomic force microscopy
BH biological homochirality
BTA benzene-1,3,5-tricarboxamide
CD circular dichroism
$CHCl_3$ chloroform
COSY correlation spectroscopy
CPL circularly polarized light
CPUL circularly polarized UV light
δ chemical shift in parts per million downfield from tetramethylsilane
DCE 1,2-dichloroethane
DCM dichloromethane
DFT density function theory
DMSO dimethyl sulfoxide
DNA deoxyribonucleic acid
DP_n degree of polymerization
e.e. enantiomer excess
EPR electron paramagnetic resonance
FT Fourier transform
HB hydrogen bond
HMBC heteronuclear multiple bond correlation
HOMO highest occupied molecular orbital
HRMS high-resolution mass spectrometry
HSQC heteronuclear single quantum correlation
IR infrared
ITO indium tin oxide
JMOD J-modulated spin-echo
MALDI matrix-assisted laser desorption ionization
mM millimolar (millimoles per liter)
MR majority-rules
m/z mass-to-charge ratio
NIR near-infrared
NMR nuclear magnetic resonance
PDA polydiacetylene
PPh_2 diphenylphosphine
rpm revolutions per minute
rt room temperature
SANS small angle neutron scattering
S&S sergeants-and-soldiers
SEM scanning electron microscope
SOMO single-occupied molecular orbital
str stretch
TA triarylamine
TATA triarylamine trisamide
UV ultraviolet
Vis visible

General Introduction

This introduction is divided into two independent chapters. Since the final goal of this thesis is part of the tremendous area of researches about the origin of the biological homochirality, a literature review about this topic will be presented first. It gives an overview of plausible scenarios, focusing on the emergence of the initial tiny enantiomeric imbalance. The reading of this first part is not compulsory for understanding the manuscript, but provides insight into the strategies implemented to elucidate the origin of biological homochirality. The second part addresses more specifically the context and objectives of the thesis. It deals with the amplification of chirality in supramolecular helical polymers and catalysts by means of chiral species or circularly polarized light (CPL).

Chapter I Chemical and Physical Scenarios Towards Biological Homochirality

Abstract

Chirality is a ubiquitous property with thought-provoking manifestations. As most living organisms, human beings are almost entirely composed of (*S*)-amino acids and (*R*)-sugars. This unequal distribution of chirality is commonly referred to as the biological homochirality (BH), the emergence of which is still a conundrum despite an extensive literature[1–15]. The original appearance of a minute enantiomeric excess[I] within a mixture of enantiomers, and the subsequent mechanisms leading to its enhancement up to enantiopurity as well as its retention, can be considered as two different phenomena. The plethora of possible scenarios that might lead to BH, as we know it today, must face the challenges associated with the formation of a chiral bias under the conditions and timescale of existence of the complex primitive bouillon. While a significant number of strategies exist for the enrichment/amplification of the initial chiral bias[16–20], only a few plausible propositions have been compelled that may explain enantiomer imbalance in relevant primordial biomolecules. Thus, after brief notes on chirality, most believable approaches towards the formation of the initial chiral imbalance will be addressed, with an emphasis on explaining clearly and concisely the underlying principles, together with their experimental evidences, showing merits and limitations of each approach. They were chosen for their compatibility with the putative primordial conditions, and the relevance of their experimental investigation with building blocks of Life: proteinogenic amino acids, biosugars, their intermediates or analogues. Finally, the aim of this literature review is to familiarize the novice with research dealing with BH, and to propose to the expert an updated and overall portrait of this interdisciplinary field.

[I] Determined as the difference in the number of two enantiomers divided by their sum, abbreviated as *e.e.* and expressed mathematically as *e.e.* = ((*R*-*S*)/(*R*+*S*)) × 100% with (*R*)/(*S*)-stereodescriptors of the CIP system to designate here the number of enantiomers.

Videmus nunc per speculum in aenigmate
At present we see indistinctly, as in a mirror
Car nous voyons, à présent, dans un miroir, en énigme
I Cor. XIII, 12.

I. Chirality: Brief History and definition(s)

Discussed from Plato to Kant, chirality was first a nameless concept dealing with mirror-image incongruence, *i.e.* the non-superimposability of some objects on their mirror-image (the so-called handedness)[21,22]. In the 19th-century, French advances in optics[23], crystallography[24] and chemistry[25] paved the way to the scientific study of chirality, which would soon unveil a puzzling phenomenon with a variety of manifestations[22,26,27].

Étienne-Louis Malus reported in 1809 the polarization of light[28] and François Arago, two years later, the optical rotation with slices of quartz[29]. In 1817, Jean-Baptiste Biot highlighted that several natural compounds, such as tartaric acid, rotated polarized light in solution[30]. Benefiting from his predecessors, Louis Pasteur studied in 1848 enantiomorphous crystals of the sodium ammonium salt of "paratartaric acid" (**Figure I.1**), a racemic mixture of tartaric acid coming from fermenting grape juice ('racemic' derives from the Latin *racemus* meaning a bunch of grapes). By manually sorting them and measuring their optical activity in solution, Pasteur found the rotations to be equal in absolute magnitude but opposite in direction. He concluded that paratartaric acid is a combination of two mirror-image molecules of tartaric acid, named as "dissymmetric"[II], and thereby discovered the molecular chirality[III,32]. In 1874, Jacobus Henricus van 't Hoff in Netherlands and Joseph-Achille Le Bel in France clarified this idea[33–35]. They independently emitted the theory of the tetrahedral structure of saturated carbon

[II] Even though both terms were used at that time[31], Louis Pasteur may have opted for 'dissymmetric' instead of 'asymmetric' because the 'asymmetry' corresponds to the absence of all symmetry elements, except the identity operation; while a dissymmetric object lacks certain symmetry elements, like chiral objects.

[III] The idea of molecular chirality was maybe not completely new to the Pasteur's mind because Sir John Herschel, an English polymath, suggested that optical activity in the non-crystalline state is owing to the "unsymmetrical" nature of molecules. Anyway, Louis Pasteur recognized to be a successor, Joseph Gal reported that he wrote in 1858: *« [une découverte] n'est jamais l'œuvre d'un seul homme »* ('a discovery is never the work of one man alone'). Translation of J. Gal[25].

which, bearing four different atoms or groups of atoms, can constitute an asymmetric carbon atom.

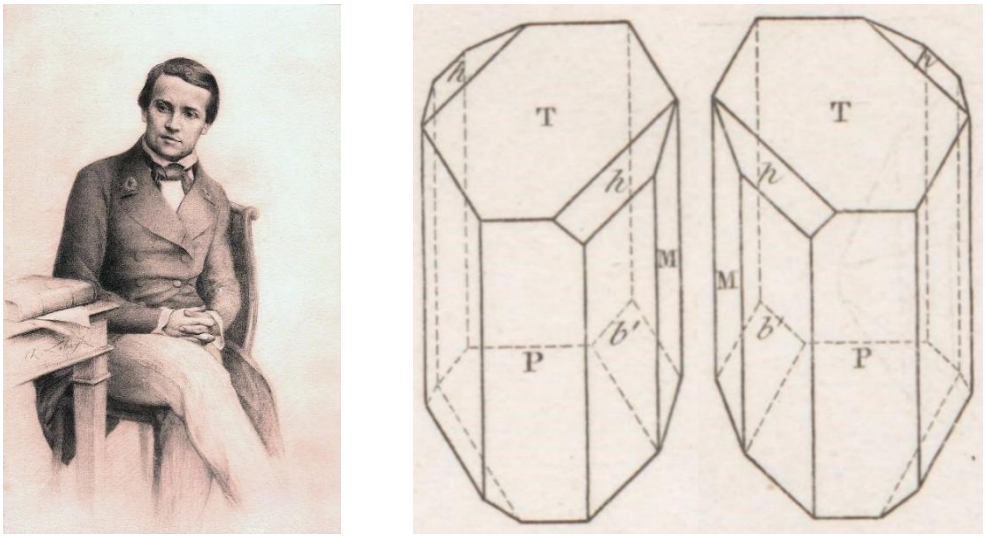

Figure I.1 Louis Pasteur's portrait by Charles Lebayle, around 1843[36]. Pasteur was also a talented artist[37], as is shown in his drawing of the enantiomorphous crystals of sodium ammonium tartrate (reprinted from [38]).

Nevertheless, it would appear that the first general definition of structural chirality was published nearly a half-century after Pasteur's discovery, in 1894, by Sir William Thomson (Lord Kelvin after his elevation to the peerage): "I call any geometrical figure, or group of points, *chiral*, and say that it has chirality if its image in a plane mirror, ideally realized, cannot be brought to coincide with itself."[39] The Lord Kelvin astutely used a word derived from the Proto-Indo-European[40] *ǵʰesr- through the Ancient Greek[41] χείρ (kheír), that both mean 'hand' – one of the first chiral object that we see. Chirality took additionally almost 70 years to be introduced in chemistry by Kurt Mislow[42] (1962) and became a standard terminology in stereochemistry in the 1970s[31], with the following definition: "an object is chiral if and only if it is not superposable on its mirror image; otherwise it is achiral.[43]"

In terms of point groups[22], indeed, chirality requires the absence of any improper axis of rotation (S_n), *i.e.* the lack of both mirror plane and center of inversion; but a chiral object can contain for example a proper rotation axis (C_n), such as tartaric acid that has a C_2 axis of

symmetry. In this sense, an asymmetric molecule is necessarily chiral, even if a chiral molecule is not necessarily asymmetric but inevitably dissymmetric[III].

In practice, chirality is all-pervasive, from elementary particles and spiral galaxies[22] to cucumber tendrils[44] and screws, and concerns various industries (e.g. pharma, agribusiness, cosmetic)[45–50] as well as academic research (visible in countless conferences encompassing not only the chemistry, physics, and biology but also the economy and arts, for instance)[51,52]. Among these studies, the emergence of chirality from scratch is unquestionably a tall order, in addition to be related to a fascinating topic: Life.

II. The Intriguing Homochirality[IV] of Life

Beyond chemistry, chirality plays a key role in living beings. In 1857, Louis Pasteur uncovered biological enantioselectivity by revealing the dramatic difference in the fermentation rate of the two tartaric acid enantiomers with an unidentified microorganism[56–58]. Following Pasteur's results, enantioselectivity at human receptors was first observed in 1886 by the Italian chemist Arnaldo Piutti[55]. He succeeded to isolate D-asparagine, enantiomer of the tasteless amino acid L-asparagine, and found that it was intensely sweet (**Figure I.2**)[59]. Arnaldo Piutti might have read the novel *'Through the Looking-Glass, and What Alice Found There'* published by Lewis Carroll fifteen years before, in 1871, and drew his inspiration from this artist's intuition: "How would you like to live in Looking-glass House, Kitty? […] Perhaps Looking-glass milk isn't good to drink" [said Alice to her kitten][7,22].

[IV] Use of 'homochiral' and derivatives, as synonyms of 'enantiomerically pure' or just 'enantiopure', is "strongly discouraged" by IUPAC recommendations of 1996[53]. J. Gal discussed this "controversy" and suggested to prefer 'unichiral' and derivatives in 1998[54] (used here[31,55]). Nonetheless, his paper is not available anymore and usage favors 'homochiral' to talk about the enantiopurity of biomolecules.

L-Asparagine

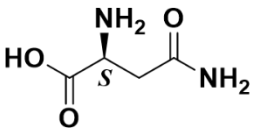

Tasteless

D-Asparagine

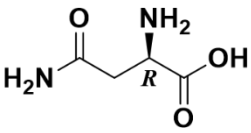

Sweet

Figure I.2 Arnaldo Piutti next to the chemical structures of the tasteless L- and sweet D-asparagine. Photograph of Arnaldo Piutti reprinted from Joseph Gal[55].

The biological enantioselectivity belongs to a mystery that shrouds chirality and links snails, neutrinos, and the *Mona Lisa*: the chiral asymmetry, *i.e.* the unequal distribution of chiral objects in Nature and Culture. Most snail shells are coiled clockwise[60], only *left*-handed neutrinos have been observed[61] and the three-quarter-view portrait is a famous example of left cheeks dominance in portraits[62]. Humans as well as coronaviruses, bacteria and otters are pieces of this puzzle through the intriguing biological homochirality: all life forms are almost exclusively composed of amino acids and sugars whose absolute configuration is (*S*) and (*R*), respectively[V,64,65]. Sugars are one of the constituents of nucleotides, building blocks of DNA and RNA which store genetic information and are involved in the synthesis of proteins: biomacromolecules made of amino acids participating as structural components within cells and controlling as enzymes all chemical reactions in living organisms[7,65–69]. In 2011, an analysis

[V] Proteinogenic amino acids and natural sugars are usually mentioned as L-amino acids (left-handed) and D-sugars (right-handed), according to the descriptors introduced by Emil Fischer, although this description "has no scientific basis and can easily lead to absurd consequences" according to Jack D. Dunitz[63]. It is worth noting that the natural L-cysteine is the exception to the rule using the Cahn–Ingold–Prelog system defined hereinabove: albeit the orientation of the respective amino, acid and side chains groups is identical to the other amino acids, the stereogenic carbon receives the chiral descriptor (*R*), due to the sulfur atom in the side chain which changes the priority sequence.

of the Swiss-Prot database counted only 837 D-isomers over a biomolecular dataset of 187,941,074 amino acids[70].

Strongly debated scenarios of chiral purity origin should address key problems that allows to classify them[10]: biogenic or abiogenic model, random or determinate mechanism, terrestrial or extra-terrestrial origin, local or universal influence? The overabundance of competitive explanations does so that "only a few […] have been experimentally examined in detail"[71], and Martin Quack, key player in this field, would even recognize the existence of "communities of belief"[72]. Thus, assuming the non-exhaustiveness, let us wander this garden of ideas, seeking the fruit which brought about the homochirality of Life.

III. Biogenic and Abiogenic Models

Emergence of Life and biomolecular homochirality must be tightly linked[73–76], but in such a way that needs to be cleared up. Considering the NASA definition of life, "a self-sustaining chemical system capable of Darwinian evolution"[77], and the "widespread presence of ribonucleic acid (RNA) cofactors and catalysts in today′s terran biosphere"[78], a strong hypothesis for the origin of Darwinian evolution and Life is "the abiotic formation of long-chained RNA polymers" with self-replication ability[79]. This was generally the starting point of the disagreement between tenants of biogenic and abiogenic models. In contrast with the former that described the chiral selection thanks to the life activity of the first organisms, the latter supposed that first biopolymers appeared in optically pure pools of their monomers, whose chiral purity would be the outcome of physical and chemical processes in prebiotic conditions.

Citing results of Blout, Doty *et al.* with glutamate derivatives in the 1950s[80–82], George Wald published in 1957 a seminal paper accounting for biotic theories[83]. Wald reasoned that, since polymers made of homochiral monomers likely propagate faster, are longer and have stronger secondary structures, it must have provided sufficient criteria to the chiral selection of amino acids thanks to the formation of their polymers in ad hoc conditions. This hypothesis was notably reinforced by Brack and Spach[84], confirming in 1971 the faster incorporation of monomers in polyglutamates derivatives with monomer units of the same chirality; and by Goldberg *et al.*[85], who reported in 1987 the stereoselective formation of di-, tri-, and tetra-

peptides from racemic mixtures of proteinogenic amino acids such as alanine, aspartic acid and glycine.

Yet, this kind of biotic theories was judged as "fundamentally speculative and imprecise as to mechanistic details", making them hard to be experimentally tested[6]. A classical counter-argument against biogenic models is based on the enantiomeric cross-inhibition phenomenon[3,5–7], since Idelson and Blout observed in 1958 that D-glutamate derivatives provoke the chain termination of L-glutamate oligomerization[86]. At the beginning of the 1980s[87], progress in the template-directed oligomerization of nucleotides allowed to mimic the putative self-replicating RNA at the origin of Life, and to strengthen this view and abiotic theories. Joyce *et al*. showed in 1984 that the guanosine oligomerization, directed by a polycytosine template, is inhibited within a racemic mixture of mononucleotides[88]. Four years later, Goldanskii and Kuz'min supported this observation with a mathematic model, and claimed that a homochiral system is a prerequisite to the emergence of any self-replicating systems[89].

This conclusion was tempered by subsequent studies. Bolli *et al.* demonstrated in 1997 that the enantiomeric cross-inhibition, at work in the oligomerization of mononucleotides, is less significant in the ligation of oligomers[90]. The co-oligomerization of tetramers of pyranosyl-RNA, in an equal mixture of all possible diastereomers, was found to be chiroselective and generate "predominantly homochiral" (*L*) and (*D*) sequences libraries. In 2001, Ghadiri *et al*. also observed the growth of homochirality in self-replicating polypeptides[91]. A homochiral 32-residue peptide replicator was shown to preferentially condensate electrophilic and nucleophilic 16-residue peptide fragments of the same handedness, even in the presence of their enantiomers. It entails a chiroselective autocatalytic cycle, where homochiral peptides accelerate their own reproduction, while heterochiral peptides are formed by an uncatalyzed reaction (**Figure I.3**). Fragments containing one stereochemical 'error' (e. g. one D-amino acid residue with 15 *L*-) could even act as a cross-catalytic template by coupling homochiral fragments of the same handedness than its most part.

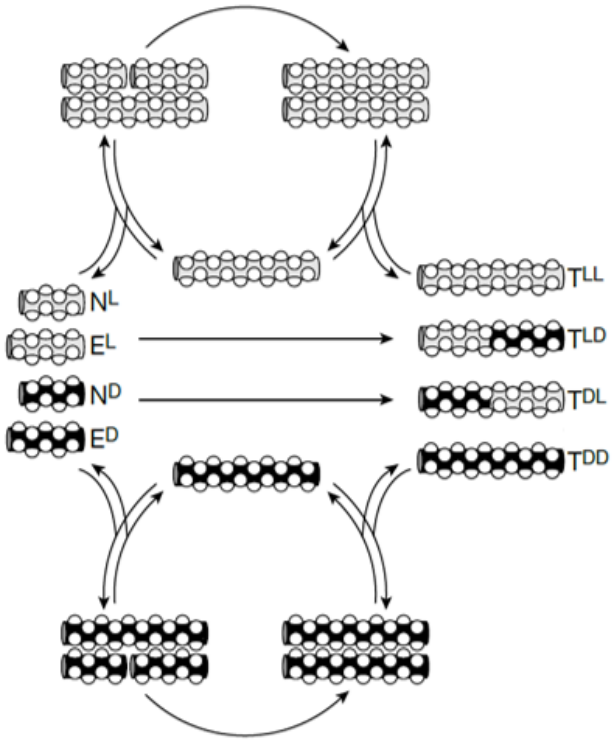

Figure I.3 Schematic representation of the stereoselective autocatalytic cycle reported by Ghadiri *et al.*[91] Homochiral peptides (T^{LL} and T^{DD}) are autocatalytically produced from an initial racemic mixture of oligopeptide (N^L + E^L + N^D +E^D), while heterochiral peptides (T^{LD} + T^{DL}) are formed by an uncatalyzed reaction.

Furthermore, Luisi and Lahav teams made interesting advances to find possible pathways from amino acids racemates to homochiral oligopeptides. They respectively took advantage of the asymmetric influence that could exist at the end of a propagating oligopeptide chain[92]; and of the "regio-enantioselection within racemic templates", resulting from the formation of short oligopeptides at the air/water or crystal/water interfaces, and following by their self-assembly into *β*-sheet colloidal-like aggregates[93].

This set of results indicates that the biogenic-abiogenic biological homochirality dichotomy is more complex that the question whether first living beings appear in racemic or homochiral pools of 'origin-of-Life' molecules[73,94]. The latter existence is actually improbable in timescales when deracemization processes and Life must have occurred. These crucial events should happen between harsh conditions – intense volcanism, asteroid bombardment and scorching heat[95,96] – prevailing during 700 million of years after the Earth formation, 4.5 billion

years ago, and the appearance of Life, 3.5 billion years ago at the latest[97,98]. At this time, deracemization inevitably suffered from its nemesis, racemization, which takes place in days or less in the current hot alkaline aqueous medium[10,99–102].

Conversely, even a racemate is very unlikely made of exactly equal amounts of enantiomers, due to natural fluctuations described statistically like coin tossing[103,104]. One mole of chiral molecules is expected to show a standard deviation of 1.9×10^{11}. Relating this variation to putative strong chiral amplification mechanisms and evolutionary pressures, Jay S. Siegel suggested that homochirality is an "imperative of molecular evolution"[105]. Previous results had indeed left the door open to the coexistence of homochiral biopolymers with opposite handedness and different sequence libraries[90]. Siegel imagined that among these biomacromolecules, some have special functions giving them the ability to replicate more quickly, until becoming the only representative and bearer of the chiral purity currently observed as a matter of chance.

Although the role of statistical fluctuations is highly controversial[10,102,106], the prominent explanation of Siegel has the merit to shine light on the family of theories supposing the existence of "two equal runners"[107], in coherence with some recent observations. D-amino acids, found in few living organisms and sometimes associated to diseases[64], as well as D-amino acid oxidases, proteins responsible for their elimination[7], are interpreted as relics of the struggle in early-life stages. Moreover, Life in both sides of the mirror was underpinned by the abilities either: for a D-RNA enzyme to catalyze the L-nucleotides coupling on an L-RNA template, with the same efficiency than the corresponding L-enzyme with D-substrates and D-template[108]; or for the polymerization of DNA and transcription into RNA to be catalyzed by the unnatural D-amino acid polymerase on an L-DNA template[109]. Finally, a strongly convincing evidence for this standpoint would be the discovery in sediments of primitive forms of Life based on a molecular machinery entirely composed of D-amino acids and L-sugars[107].

Overall, there is last years a growing number of advocates for models integrating evolutionary dynamics[110–112], and who consider that the "burden of chiral selectivity might have been shared [between abiotic and biotic factors] as complexity increased"[113,114], leading to the assumption that "homochirality would arise from competitive and cooperative chiral

recognition events, and not at as singular nor as an accidental event"[115]. A key phenomenon, adapted to this vision, is the spontaneous mirror-symmetry breaking (SMSB).

IV. The Spontaneous Mirror-Symmetry Breaking (SMSB)

Random mechanisms generate an unpredictable enantiomeric excess. SMSB processes are part of them by transforming "metastable racemic non-equilibrium stationary states (NESS) into one of two degenerate but stable enantiomeric NESSs"[102], with "a stochastic distribution of chiral signs between successive experiments or outcomes"[115]. Allowing on paper the emergence and retention of enantiopurity from scratch, SMSB is of interest and longstanding theoretically discussed in the biological homochirality context[1,14,20,89,102,116–121]. Without going into technicalities, well-done lately reviewed by Josep M. Ribó, David Hochberg *et al.*[14,102], the thermodynamical scenario of SMSB possesses similar physicochemical basis to that proposed in a combined approach of functions fundamental to Life, namely replication, metabolism and compartmentalization[79,102].

Systems able to lead to SMSB consist of enantioselective autocatalytic reaction networks, described through models dealing with either the transformation of achiral to chiral compounds, or the deracemization of racemic mixtures[102]. The former started to be modelled by Frank in 1953, through homochiral self-replication (like biological replicators) and heterochiral inhibition reactions (a chiral product accelerates its own formation, but slows down its mirror-image replication)[116]. Then, in place of the mutual inhibition between enantiomers but still performing SMSB, the limited enantioselective (LES) model considered the imperfection of the enantioselective autocatalysis (a chiral product also accelerates the formation of its mirror-image)[119], and hypercycle models coupled together different enantioselective autocatalytic reactions by mutual cross-catalysis (a chiral product accelerates another enantioselective autocatalytic reaction)[115,122].

Frank-like models are the only ones that have been yet evidenced in solution through the Soai reaction (an organozinc addition to a carbaldehyde, **Figure I.4**)[123–125], unfortunately irrelevant in primitive chemistry and the early-life environment (high exergonic organometallic reaction of unnatural substrates in anhydrous conditions)[11,73,102]. On the other hand, the LES

and hypercycle models appear credible in the case of Life originating in deep-sea hydrothermal vents, and during stages of compartmentalization of "interconnected RNA/protein and carbohydrate domains", respectively[102].

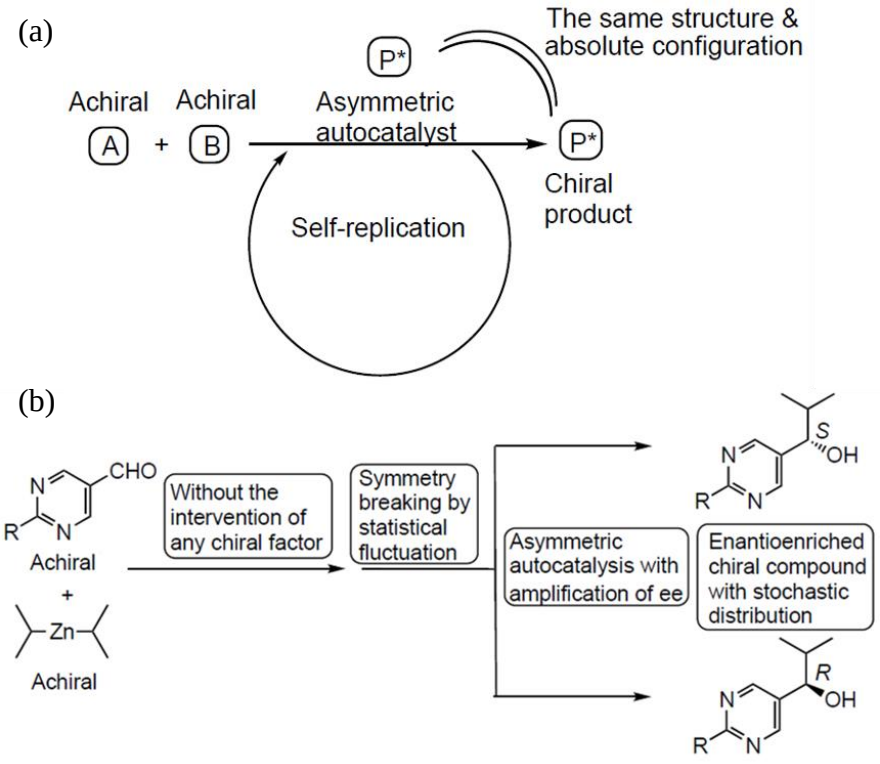

Figure I.4 (a) Principle of the asymmetric autocatalysis proposed by Soai. (b) Soai reaction in the absence of detected chirality, leading to a spontaneous absolute asymmetric synthesis. Reprinted from Soai *et al.*[125]

Many other models of spontaneous emergence of homochirality in far-from-equilibrium systems were emitted[126–128] and sparked off a controversy[129–135]. The polemic lies in their boundary conditions, which normally push and maintain the system far from thermodynamic equilibrium, enabling its enantioenrichment. They are accused of violating the principle of microscopic reversibility, by including unrealistic irreversible steps or inchoate external energy sources[20].

Classically, imposed boundary conditions involve "either systems open to matter exchange, or closed systems unable to equilibrate energy with their surroundings"[102]. In the absence of any chiral influence, the obtained metastable non-equilibrium stationary states are

exposed to statistical fluctuations, and evolve towards scalemic or homochiral NESSs, as long as the systems are far from equilibrium. This brings up some pitfalls of SMSB processes. First, they are so sensible that cryptochirality[VI] can bias the stochastic outcome towards one preferential enantiomer, and leads to a tedious interpretation of results[103]. Secondly, in this way, the statistical fluctuation is not truly amplified[102] and the deviation from the racemic state is inevitably temporary in a closed system insuring the micro-reversibility[137]. This is one reason why most of experimental applications of SMSB do not actually involve transformations (like in the three models above-mentioned), but rather the deracemization of racemic mixtures, followed by a phase transition in which boundary conditions and racemization vanish at the same time.

Crystals[16,138–140], as well as supramolecular assemblies at interfaces, in liquid crystals and solution[141–146], are in this regard an opportunity. In these systems, racemic mixtures, achiral and transiently chiral molecules (adopting enantiomorphic conformations or configurations, but separated by an energetic barrier too low compared to kT to prevent enantiomerization) assemble into homochiral domains, and generate local mirror-symmetry breaking[144]. The former by chirality discrimination of enantiomers, and the lasts by a stochastic chirality synchronization. However, supramolecular assemblies present obstacles. Their characterization is subjected to many artefacts[147] and their dynamic features, allowing strong chiral amplification properties through the cooperative transfer of a chiral bias from the monomer to the supra-macromolecular level (sergeants-and-soldiers principle)[148–150], make them even more sensitive to cryptochirality. Finally, to the best of our knowledge, despite recently reports on supramolecular assemblies exhibiting mirror-symmetry breaking manifestations of interest, they are generally too far from prebiotically relevant conditions and will be, as a result, only mentioned here and there. Conversely, crystals benefit from old-established studies.

[VI] Molecules whose chiral center bears substituents of very small difference[136], or chiral compounds in trace amounts, both under the level of sensibility of the most powerful characterisation technics[103], are cryptochiral.

V. Homochirality from Crystals

In fact, SMSB in the crystalline state was studied since the seminal works of Pasteur on the tartrate salt conglomerate, a racemic mixture of the two enantiomorphic crystals, each form containing only molecules of a single enantiomer[53,151]. According to Havinga theory, obtention of just one enantiomorph is possible upon a gentle cooling, when the crystal nucleation is rare and the growth rapid together with a fast inversion of configuration (racemization in solution), which allows to feed only monomers with matching chirality to the primary nuclei[152,153].

Egbertus Havinga reported in 1954[152] a set of experiments aimed at demonstrating the spontaneous resolution – enantiomeric preferential crystallization – of the conglomerate of allyl-ethyl-methyl-phenyl-ammonium iodide racemizing in chloroform (**Figure I.5**)[154,155]. Fourteen supersaturated solutions were gently heated in sealed tubes, then stored at 0°C to give crystals which were in 12 cases inexplicably more dextrorotatory (measurement of optical activity by dissolution in water, where racemization is not observed). Seven other supersaturated solutions were carefully filtered before chilling at 0°C, without crystallizing even after one year. Strongly cooled down, three crystalline products with no optical activity were obtained, while the four other ones showed a small optical activity ($[\alpha]_D$ = + 0.2°; + 0.7°; – 0.5°; – 3.0°). Feebly reproducible and giving rise to poor enantioenrichment, this technic was to the best of our knowledge scarcely used (e.g. with tri-*o*-thymotide[156] or 1,1'-binaphthyl[157]), even though it is also suitable for achiral molecules, which can crystallize into chiral space groups[VII] and follow this process (except the racemization step).

[VII] 65 of 230 crystallographic space group types are chiral[158–160]. Between 8 and 13% of achiral molecules crystallize as *conglomerate* crystals and less than 10% of chiral molecules. Concerning the latter, more than 90% form a *racemic compound* based on a single crystalline structure where both enantiomers are present in a 1:1 ratio[151]. This is the case for molecules with a greater affinity for the opposite enantiomer. *Solid solution* completes the picture (less than 1% of chiral molecules) where crystals are made of a racemic mixture of enantiomers in a random arrangement on the crystalline lattice[153].

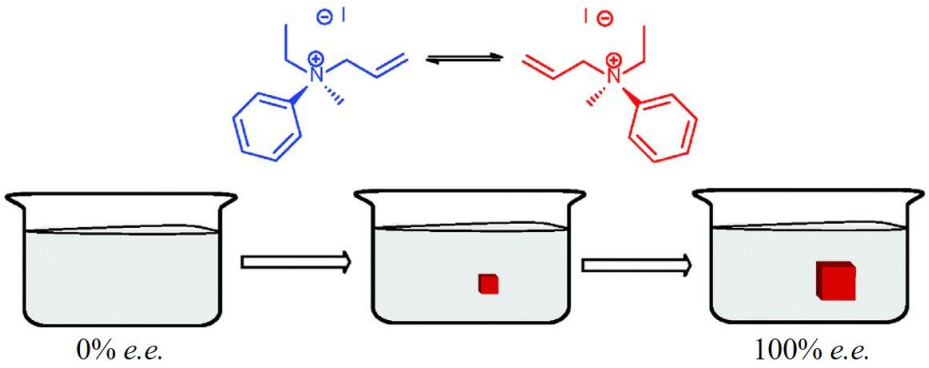

Figure I.5 Enantiomeric preferential crystallization of allyl-ethyl-methyl-phenyl-ammonium iodide described by Havinga[152]. A fast racemization in solution supplies the growing crystal with the appropriate enantiomer. Reprinted from Vlieg *et al.*[153]

More practical works were carried out on the intrinsically achiral sodium chlorate molecule $NaClO_3$. As reported by Kipping and Pope in 1898[161,162], $NaClO_3$ crystallizes by evaporation of water into a conglomerate, later attributed to the chiral cubic space group $P2_13$[163–165]. From static solution, $NaClO_3$ crystallization seems to undergo an uncertain resolution, similar to what Havinga published, with a statistically significant bias in favor of *d*-crystals, but likely due to the presence of bio-contaminants[166]. Interestingly, Kondepudi *et al.* showed in 1990[167] that magnetic stirring, during the growth of sodium chlorate crystals from a supersaturated solution, randomly orients the crystallization to only one enantiomorph, with a reproducible high average crystalline enantiomeric excess of ± 1. Further studies[168–171] revealed that the maximum degree of supersaturation is solely reached once, when the first primary nucleation occurs. At this stage, the magnetic stirring bar breaks up the first nucleated crystal into small fragments that have the same chirality than the 'Eve crystal', and act as secondary nucleation centers whence crystals grow (**Figure I.6**). This constitutes a SMSB process coupling homochiral self-replication plus inhibition through the supersaturation drop during secondary nucleation, precluding new primary nucleation and the formation of crystals of the mirror-image form[120]. This solution-to-solid deracemization strategy was also successfully employed to obtain enantioenriched crystalline material by seeding[172], under ultra-sonic field[173]

or thanks to beta particles[174]; with organic molecules such as 4,4'-dimethyl-chalcone[175] and 1,1'-binaphthyl[176] or in the enantioselective synthesis[VIII] of oxo-rhenium(V) complex[179].

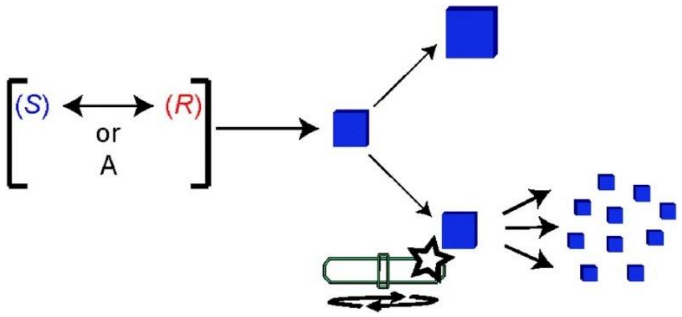

Figure I.6 Primary nucleation of an enantiopure 'Eve crystal' of random chirality, slightly amplified by growing in static conditions (top, Havinga-like), or strongly amplified by secondary nucleation thanks to the magnetic stirring (bottom, Kondepudi-like). Reprinted from Vlieg *et al.*[153]

Once the crystallization is over, solid-to-solid deracemization of conglomerates in their saturated solution is also possible: either in isothermal conditions by abrasive grinding with glass beads[180,181] or ultrasound[182] (attrition-enhanced deracemization); or thanks to temperature cycles[183,184]. Although this now called 'Viedma ripening' takes several hours to days[185] and is judged as easy to implement, the mechanism of this complex SMSB phenomenon is an ongoing highly topical question[14,102,186,187] that falls outside the scope of this report. Yet that did not prevent to exploit the Viedma ripening with many achiral materials[188,189] (but losing their "handedness" when dissolving, **Figure I.7a**) and, closer to our concerns[190], homochiral enantiomorphic crystals in equilibrium with solution phase under racemizing conditions (**Figure I.7b**), whose enantiomers can stem from prochiral substrates by chemical reaction (**Figure I.7c**).

[VIII] Enantio*selectivity* should not be confused with enantio*specificity*. The former corresponds to the preferential formation of one enantiomer over the other as defined by an external asymmetric field (e.g. a nonracemic chiral catalyst); whereas the latter is the preferential formation of one enantiomer over the other thanks to an internal or relayed asymmetric induction (the stereochemistry of the product arises from the chiral enantioenriched substrate)[53,177,178]. In this case, 'internal' means a chiral center bound to the reactive one and remaining during the reaction; 'relayed' indicates a chiral information introduced and removed in two separate steps surrounding the enantiospecific reaction. It is worth mentioning that substrates of an enantioselective reaction can be chiral but as a racemate, whose enantiomers orientate the reaction toward opposite configurations.

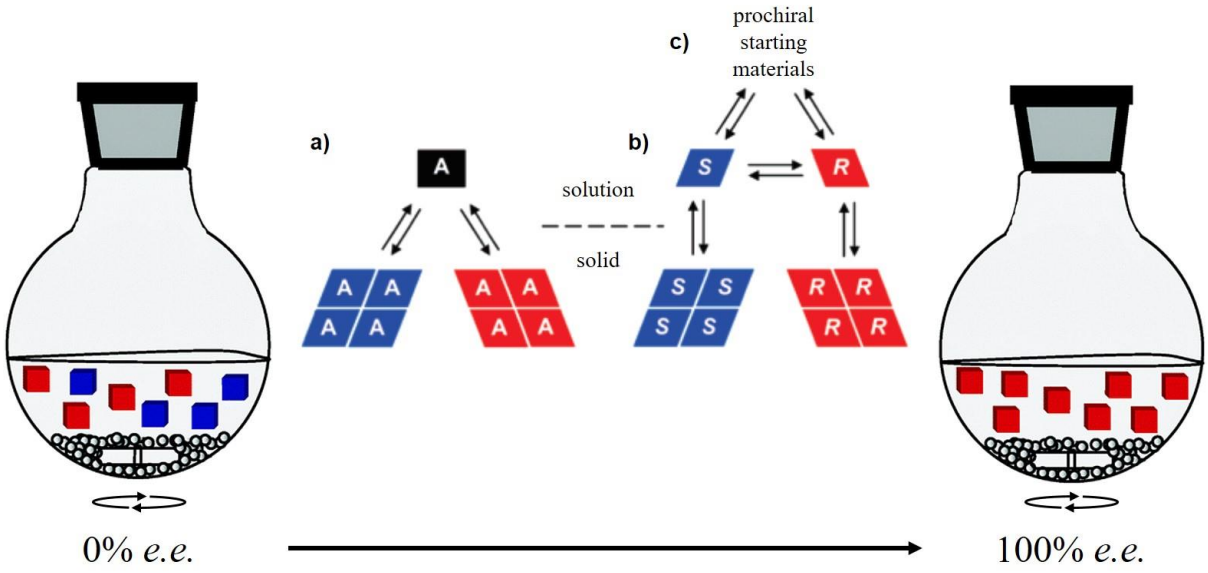

Figure I.7 Schematic representation of Viedma ripening and solution-solid equilibria of an intrinsically achiral molecule (a) and a chiral molecule undergoing solution-phase racemization (b). The racemic mixture can be the fruit of a chemical reaction between prochiral starting materials (c). The enantioenrichment in the case (a) occurs only in the solid state because, whatever the average crystalline enantiomeric excess, the molecule is still achiral (in solution). By contrast, a complete deracemization is possible after dynamic enantioselective crystallization (b) possibly together with chemical reaction (b + c). Adapted from Vlieg *et al.*[153,191]

Only three years after the first report about Viedma ripening in 2005 with sodium chlorate[180], it was successfully applied to the aspartic acid (a proteinogenic amino acid) in nearly racemic mixtures at high temperatures (>90°C)[192]. Indeed, like most proteinaceous amino acids under ambient conditions[151,192–195], the aspartic acid crystallizes as a racemic compound at room temperature (see the footnote VII), and was thereby deracemized from conglomerates kinetically obtained. Others proteinogenic amino acids such as alanine, leucine and glutamic acid, were also deracemized in a meta-stable state[192,195], or in salts with sulfonic acid derivatives[196,197], all starting from non-zero initial *e.es.* From a perfect racemic mixture, examples are fewer but notably, thiohydantoins (family of amino acids precursors) were successfully deracemized by attrition up to 96% *e.e.*[198].

Vlieg *et al.* opened up new prospects in 2014 by coupling attrition-enhanced deracemization (*cf.* Figure 4b) with a reversible organic reaction (*i.e.* the aza-Michael reaction)

between prochiral substrates (*cf.* Figure 4c) under achiral conditions to produce a chiral amine[199]. At high concentrations (1 to 2.5 mol/L), the conglomerate formed after half a day in the reacting mixture was besides grinded to give enantiopure crystals. This strategy of absolute asymmetric synthesis (AAS), which deals with the formation of enantiomerically enriched products without help of chiral chemical entities, was recently exploited with reactions and compounds of biological interest. Thanks to temperature cycles during Strecker reactions, Kawasaki *et al.* reported the formation of enantio-enriched α-aminonitriles, probable prebiotic intermediaries of α-amino acids, with *e.e.* higher than 99%[200]. The same enantiopurity was obtained by Sakamoto *et al.* in 2019 for the synthesis of N-succcinopyridine, an aspartic acid derivative, by the aza-Michael addition of maleic acid and pyridine involving attrition-enhanced deracemization[201].

Anyway, to face the conglomerate-dependence of Viedma ripening, a promising mechanochemical method to transform racemic compounds of amino acids into their corresponding conglomerates has been recently found[202]. Valine, leucine and isoleucine were milled one hour at the solid state to give their corresponding conglomerates, in a Teflon jar with a zirconium ball and in the decisive presence of zinc oxide.

VI. *Intermezzo:* Terrestrial or Extra-Terrestrial Origin?

All the previously mentioned scenarios suggest a terrestrial origin behind the original enantiomeric imbalance, and leave a question unanswered: how an Earth-based mechanism can explain enantioenrichment in extraterrestrial samples?[203,204] However, to stray from "geocentrism" is still worthwhile[IX]; another plausible scenario is the exogeneous delivery on Earth of enantioenriched molecules relevant for the appearance of Life. The body of evidence grew from the characterization of organic molecules, especially amino acids and sugars, and

[IX] Even a long time after Copernicus and Galileo, of course in a different sense.

their respective optical purity, in meteorites, comets[X] and laboratory-simulated interstellar ices[206].

The 100-kg Murchison's meteorite fallen in Australia in 1969 is generally considered as the standard reference for extraterrestrial organic matter (**Figure I.8**)[207]. In fifty years, its analyses revealed more than ninety α, β, γ and δ isomers of C_2 to C_9 amino acids, diamino acids, and dicarboxylic acids as well as numerous polyols including sugars (whose ribose[208], building block of RNA), sugar acids and alcohols, but also dicarboxylic and deoxy acids[206]. Unequal amounts of enantiomers were also found: as a quasi-exclusively *left*-handed predominance for amino acids[209–213] ranging from 0 to 26.3 ± 0.8% *e.es.* (highest *e.e.* go to non-proteinogenic α-methyl amino acids)[214]; and, when they are not racemates, only D-sugar acids with high *e.e.* up to 82% for xylonic acid[215]. Even if these measurements are scarce and need to be confirmed, particularly for sugars, enantiomeric excess matches between biological and extraterrestrial amino acids and sugar derivatives is an appealing preliminary set of results. Future space missions to asteroids, comets and Mars will indubitably shed light on this perspective.

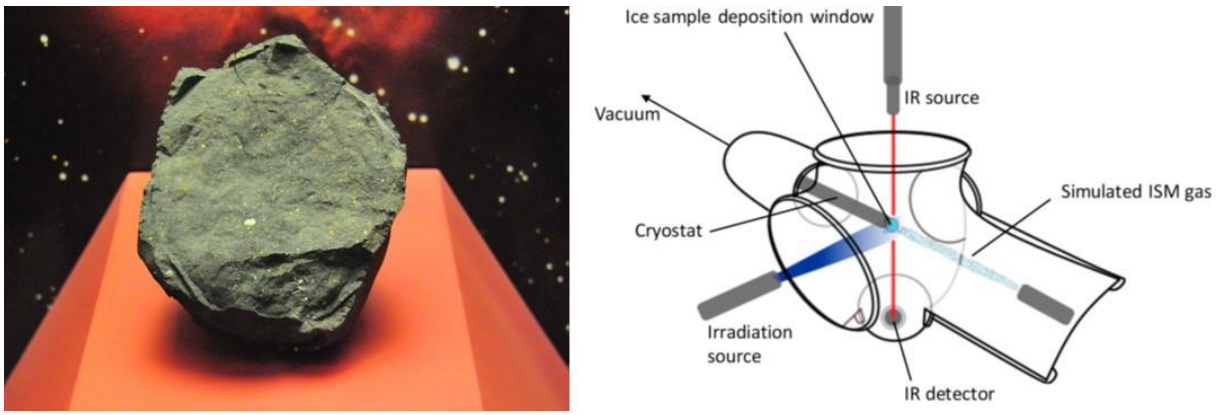

Figure I.8 On the left, a fragment of the meteorite landed in Murchison, Australia, in 1969, and exhibited at the National Museum of Natural History (Washington)[216]. On the right, scheme of the interstellar ice analogs preparation. A mixture of primitive gas molecules is deposited and irradiated under vacuum on

[X] Meteorites are fragments of asteroids originated from the outer space that landed on Earth. Comets are icy and dusty small bodies in orbit around the Sun, created at the same time as the solar system 4.6 billion years ago. Both are extraterrestrial reservoirs of organic compounds, meteorites are more accessible, but comets are better preserved and richer in molecular constituents[203,205].

a cooled window. Composition and thickness are monitored by infrared spectroscopy. Reprinted from Meierhenrich *et al.*[206]

To complete these analyses of the difficult-to-access outer space, laboratory investigations expanded on astrophysical ice analogs (**Figure I.8**)[217]. Natural ones are formed in interstellar clouds[218,219] on the surface of dust grains from which condensates a gaseous mixture of carbon, nitrogen and oxygen-based molecules (e.g. H_2O, CH_3OH, CH_4, NH_3, CO_2)[220], under the influence of a very low temperature (5–15 K)[221] and void. Subsequent photochemical processes in this mantle of frost are assumed to lead to complex molecules[222]. Since collapsing clouds gave birth to our solar system through the aggregation of dust grains[223], studies of their composition receive a keen interest to broaden our knowledge about the prebiotic environment. Experiments on simulated interstellar ices support the formation of many proteinaceous amino acids[224,225] and building blocks of RNA and DNA such as sugars[226], like ribose[227] and deoxyribose[228], as well as nucleobases (adenine, cytosine, uracil and thymine for example)[229].

These results, since they shift at best the biological homochirality origin in advance in space, are far from a magic solution. Nonetheless, they give incentives to explore scenarios based on determinate enantio-differentiating mechanisms, present not only on Earth but throughout the universe[230].

VII. Achiral-based Chemical Fields Towards Directed Homochirality Emergence

As noted above, the flip side of some SMSB phenomena through deracemization, taking advantage of phase transition, is the loss of the enantioenrichment upon dissolution, disassembly or melting[139]. Additionally, scenarios describing the advent of the biological homochirality presented so far, like pristine SMSB processes, are intrinsically random mechanisms. Regarding the bimodal distribution of homochirality that they anticipate for the entire Universe, these scenarios are frustrating rationales as long as the apparent matching handedness of terrestrial and extra-terrestrial Life building blocks is true. Nevertheless, SMSB can go hand in hand with deterministic chiral influences, resulting in enantiomeric excesses that

are not fortuitous but predictable. If a chiral effect penetrates long enough the medium and interacts with compounds or transition states of enantiomeric configurations or conformations, it can indeed distinguish them by providing different energies (diastereomerism)[144]. This can be seen as a Darwinian selection process where only the 'fittest' of both enantiomers 'survive'.

In this respect, the interesting absolute asymmetric synthesis within enantiomorphous crystals are set aside, on account of deviations from the principle of parsimony and plausible primordial conditions, by involving laborious enantiomorphous crystals and lattice-controlled asymmetric organometallic or photochemical reactions[139]. On the contrary, surfaces of crystalline structures are of interest[231–233], as a first step even without being paired with SMSB, by adsorption for example[234]. Indeed, some achiral crystals growing under constraints can present homochiral surfaces[139]. Minerals and metals can also have achiral bulk structures but surfaces intrinsically chiral or with chiral centers[234,235]. Selective adsorption is generally the consequence of reversible and preferential diastereoisomeric interactions between the chiral surface and one of the enantiomers[236], commonly described by the simple three-point model. But this model, assuming that only one enantiomer can present three groups that match three active positions of the chiral surface,[237] fails to fully explain chiral recognition which are the fruit of more subtle interactions[234].

Bonner *et al.* pioneered in 1974[238] studies about the chiral interactions between molecules and crystal surfaces. They showed a small 1.4 ± 0.4% asymmetric preferential adsorption of D- and L-alanine on *right*- and *left*-handed quartz (SiO_2), respectively. In 2001, Hazen *et al.*[239] significantly improved this enantioselectivity up to 10% with aspartic acid and calcite ($CaCO_3$), an abundant marine mineral known to adsorb amino acids and stick proteins[236]. About metallic surfaces, Attard *et al.*[240] first observed in 1999 enantioselectivity with platinum single-crystal electrodes through cyclic voltammetry measurements: oxidation of L-glucose is faster than D-glucose on the Pt(643)^S surface, and vice versa on Pt(643)^R. Yun and Gellman notably reported in 2013 the enantioselective separation of the racemic mixture of D- and L-aspartic acid on naturally chiral Cu(3,1,17)$^{R\&S}$ surfaces with an enantiomeric excess of 39 ± 3%[241].

To mimic the complete mirror-symmetry breaking present on Earth, a great contemporary challenge is the development of highly enantioselective surfaces[242]. Usually, the few kJ/mol difference in interaction energies between enantiomers results in a modest enantioselective adsorption. As such, the choice between metal surfaces may be oriented based on computational predictions of their enantiospecificity, as reported recently for a variety of α-amino acids and Ag/Cu/Pd/Pt(531) surfaces[243]. Widmer *et al.* emphasized in their turn the density of chiral binding sites as a determining criterion. Rather than metal surfaces presenting chiral kink sites just at the step edges of atomic terraces, they preferred the intermetallic palladium-gallium compound, whose non-centrosymmetric bulk structure appears on its entire (111) surface through a chiral atomic arrangement (**Figure I.9**)[244]. The prochiral molecule 9-ethynylphenantherene, forming two surface-enantiomers (*R*) or (*S*) when deposited, exhibits selective adsorption on PdGa mirror symmetric surfaces with enantiomeric excesses from 94 to 98%.

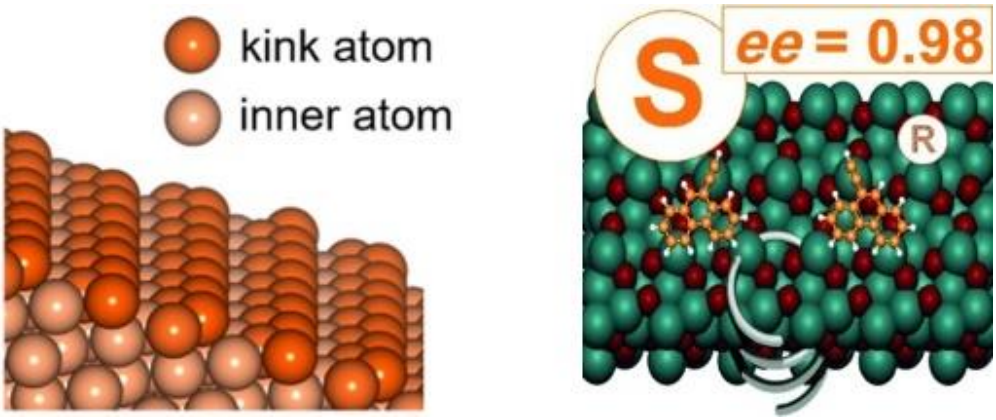

Figure I.9 Schematic representations of a step-kink metal surface (left) and the chiral surface PdGa:B($\bar{1}\bar{1}\bar{1}$)Pd$_1$ (Pd atoms in green and Ga in red) and 9-ethynylphenantherene (right), forming chiral adsorption complexes in *S*- and *R*-configuration. A remarkable enantiomeric excess of 98% in favor of *S* surface enantiomer was measured. Reprinted from Liu[243] and Widmer *et al.*[244]

Due to the extreme sensibility of his eponym autocatalytic process, Soai *et al.* successfully directed highly enantioselective syntheses with achiral-based systems thanks to chiral surface (quartz in the seminal paper of 1999[245]). To date, chiral crystalline solids or enantiotopic faces of achiral crystals (formed from achiral organic and inorganic constituents), as well as isotopic enantiomers (*i.e.* chiral only by isotopic substitution) and uncommon chiral

compounds (e.g. chiral helical silica[246] or cinnabar (mercury(II) sulfide)[247]) are some other chemical inductors that were successfully used, and carefully listed by Kenso Soai in 2019[125].

In the realm of the Viedma ripening, Noorduin *et al.* interestingly discovered in 2020 a way of propagating homochirality with molecules of relevance in the Strecker synthesis framework[248]. They demonstrated that within a family of compounds, an enantiopure additive (1-20 mol%) induces an enantioimbalance in a conglomerate by enantiospecific solid solution formation, then amplified by Viedma ripening up to a complete mirror-symmetry breaking. In fact, the additive promotes the crystallization of the enantiomer with the same absolute configuration, by incorporating in a thermodynamically controlled way into the bulk crystal lattice, without inducing noticeable change.

VIII. Physical Fields Towards Homochirality Emergence

VIII. 1. True and False Chirality

The chirality's definitions based on symmetrical arguments are adequate for stationary objects, but not when motion comes into play. To address this issue, Laurence D. Barron coined a refined definition in 1986, distinguishing between true and false chirality as follows: the "true chirality is shown by systems existing in two distinct enantiomeric states that are interconverted by space inversion, but not by time reversal combined with any proper spatial rotation" (unlike falsely ones, *cf.* **Figure I.10**)[249].

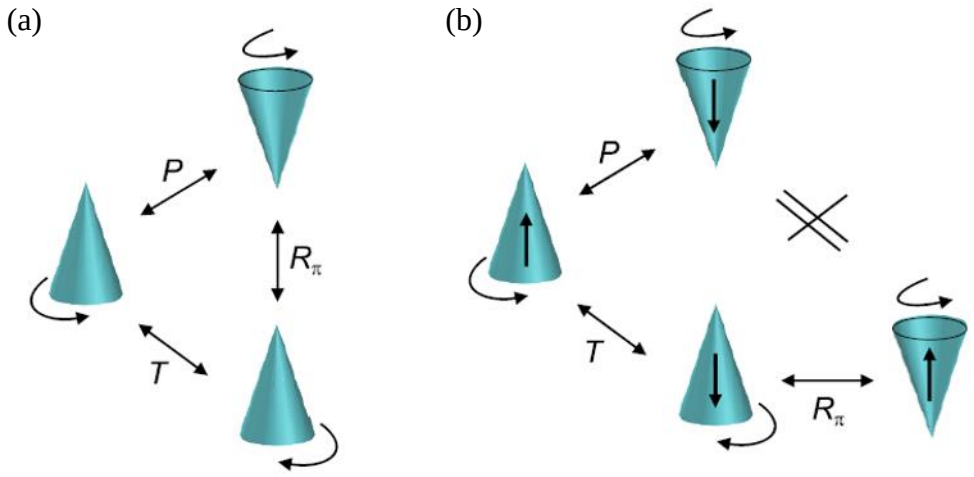

Figure I.10 Seminal examples of false and true chirality with (a) stationary and (b) translating spinning cones, respectively (translations are denoted by the vertical arrows). (a) The top stationary spinning cone generates under space inversion (*P*) and time reversal (*T*), followed by a rotation through 180° about an axis perpendicularly to the symmetry axis (R_π), an identical version to itself: it is falsely chiral. (b) Conversely, the top translating spinning cone is distinct from the bottom right translating spinning cone generated under *P* and *T*, followed by the 180° rotation: it is truly chiral. Reprinted from Buhse *et al.*[250]

To sort the wheat from the chaff in this way has the merit to make out truly chiral influences, that are the only ones to lift the degeneracy of enantiomers and induce enantioselection in an isotropic reaction system "that have been left to reach thermodynamic equilibrium (thermodynamic control)"[251]. Examples of true chirality, as part of this review's topic, are given hereinafter without further explanation on this concept, well introduced by its creator[252,253]. Note that Pasteur already believed in "dissymmetrical actions" of "cosmic order" to induce enantiomeric excess in chiral biological or chemical systems[254], but all his experimental attempts to produce any *e.es.* using magnetic, electric field or light failed[58]. This can be explained by the falsely chiral character of the forces he used.

Yet, the Barron's definition of chirality is not an absolute criterion to consider if a physical system is able to induce an enantiomeric excess. Falsely chiral influences may suffice for enantioenrichment in "reactions that have not attained equilibrium (kinetic control)"[251]. Micali *et al.* remarkably demonstrated in 2012, with a combination of rotational and

gravitational (magnetic) forces, that falsely chiral influences may bias a chemical process under kinetic conditions in favor of an enantiomeric state over the other[255,256]. Incidentally, this was in fact already observed by Dougherty *et al.* in 1980[257], but got entangled in the wider controversy about distinguishing between physical systems those capable of triggering absolute asymmetric synthesis[251].

Another falsely chiral system worthy of interest is a magnetic field operating far from equilibrium on aligned molecules, as in a crystal or at an interface[251,258]. In 2018, Banerjee-Ghosh *et al*. illustrated this scenario by showing that an achiral perpendicularly magnetized ferromagnetic (FM) substrate could enantioselectively adsorb polyalanine, cysteine and DNA[259]. Authors attributed this chiral effect to an exchange interaction between molecules and surface electrons spins, modulated by the magnetization direction that controls which enantiomer adsorbs faster (**Figure I.11**).

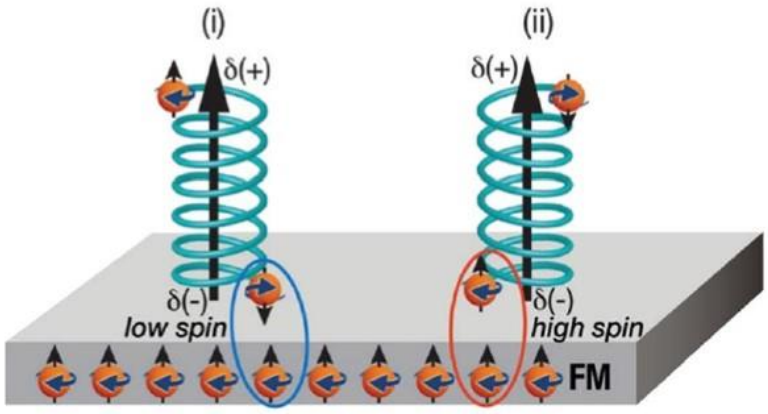

Figure I.11 Scheme of the enantiospecific interaction proposed by Banerjee-Ghosh *et al.* Enantiomers are sketched as opposite helices, electrons as orange balls with straight arrows indicating their spin orientation, which can be reversed for surface electrons by changing the magnetization direction. In contact with the perpendicularly magnetized FM surface, molecular electrons are redistributed to form a dipole, the spin orientation at each pole depending on the opposite chiral potentials of enantiomers. The substrate-molecular interaction (circled in blue and red), either stabilized when the two spins are antiparallel (i), or destabilized if parallel (ii), guides what enantiomer is preferentially adsorbed. Reprinted from Banerjee-Ghosh[259].

Concerning truly chiral influences, it exists some examples whose polarized photons and electrons are the most well-established and discussed hereinafter. Vortex motions,

comprising rotation plus transition, are also truly chiral systems. They can be induced by stirring, microfluidics as well as temperature gradients, and were notably found suitable to induce and control the supramolecular chirality of assemblies[260–273].

The combination of a static magnetic field with a light beam of arbitrary polarization also possesses true chirality, exploited by the magneto-chiral dichroism (MChD). This corresponds for chiral molecules to the differential absorption of a "light beam when an externally applied magnetic field is parallel or antiparallel to the direction of light propagation"[274]. MChD was first observed by Rikken and Raupach in 1997 with an europium(III) complex, and was further extended to other metal compounds and a few aggregates of organic molecules[274–277]. Photoresolution of Δ- and Λ-chromium(III) tris(oxalato) complexes by the help of MChD was accomplished in 2000 by Rikken and Raupach[278], with an enantioenrichment proportional to the magnetic field, *e.e.*/*B* being equal to 1×10^{-5} T^{-1}.

Applications of vortex and MChD with biomolecules of interest are conceivable, notably within the framework of hydrothermal vents for the former[270], and for the latter in neutron stars environment, of tremendous magnetic fields (10^8–10^{12} T) and synchrotron radiations[10,279].

Another surprising source of supposed truly chiral influences are plasma produced by the impact of extraterrestrial objects on Earth. Price and Furukawa teams reported, in 2013 and 2015, respectively, the nucleobases and/or proteinogenic amino acids formation in experiments simulating reactions upon celestial bodies impacts on analogs of icy planet surfaces or early oceans[280,281]. They launched a metallic projectile on targets composed of either ice mixtures made of NH_4OH, CO_2 and CH_3OH, or metal compounds (representative of simplified meteorites) and ammonium bicarbonate solution and gaseous nitrogen (as oceanic and atmospheric components). The attained pressure and temperature (up to 60 GPa and thousands Kelvin) allowed chemical reactions (and racemization, as Furukawa *et al.* evidenced later in similar fashion[282]), but were not enough to trigger plasma processes. Managadze *et al.* achieved this in 2016[283], by firing synthetic diamonds of ^{13}C at a tri-layered target of ammonium nitrate, graphite and steel. The impact generated a pressure of 170 GPa and a temperature of 3 to 4×10^4 K, enough to form, through the interaction between the projectile and targets materials, their

atomization and ionization, a plasma torch. Authors analyzed the shock product by matrix-assisted laser desorption/ionization associated with time-of-light mass spectrometry, (MALDI-TOF), laser desorption TOF and gas chromatography (GC) coupled with mass spectrometry instruments. The most striking result is certainly the formation of ^{13}C-enriched alanine with *e.e.* ranging from 7 to 25%, considered as a result of local and truly chiral electromagnetic fields in the plasma[284]. However, this first promising impact-produced enantioenrichment needs to be experimentally confirmed and theoretically detailed.

VIII. 2. The Circularly Polarized Light (CPL)

A long time before the discussions on the true or false nature of chiral influences, Joseph-Achille Le Bel and Jacobus Henricus van 't Hoff already proposed, at the end of the nineteenth century, to use circularly polarized light, a truly chiral electromagnetic wave existing in two enantiomorphic forms (*i.e.* the *left*- and *right*-handed CPL, **Figure I.12**), as chiral bias to induce enantiomeric excess[5,33,35,285]. Aimé Auguste Cotton strengthened this idea in 1895[286–288], when he reported the circular dichroism (CD) of an aqueous solution of potassium chromium(III) tartrate[XI].

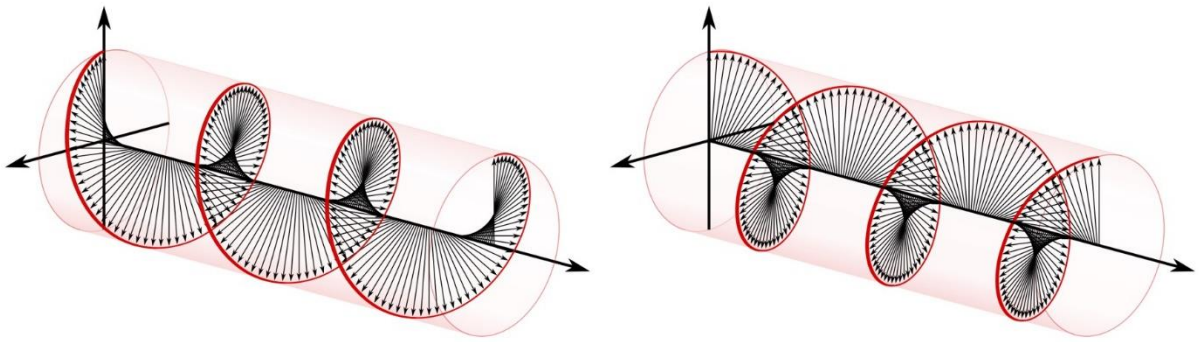

Figure I.12 *Left*- and *right*-circularly polarized light. The straight black arrow represents the electric field of constant magnitude, rotating in a plane perpendicular to the direction of propagation, *i.e.* the tip of the electric field vector describes a circle as time progress (the red line). When the observer is looking

[XI] Circular dichroism was in fact discovered in 1847 with amethyst quartz[289] but, unfortunately for Wilhelm Haidinger, it has not gone down in history[290].

against the direction the wave is traveling, the rotation of the electric field vector is *counterclockwise* or *clockwise* for *left*-circularly polarized (*l*-CPL) or *right*-circularly polarized (*r*-CPL), respectively[291].

Circular dichroism is a phenomenon, corresponding to the differential absorption of *l*-CPL and *r*-CPL at a given wavelength in the absorbance region of an optically active material, as well the spectroscopic method that measures it[292,293]. It is generally described as the difference in molar extinction coefficients of *l*-CPL and *r*-CPL ($\Delta\varepsilon = \varepsilon_{(l\text{-CPL})} - \varepsilon_{(r\text{-CPL})}$)[XII] as a function of the wavelength, and it manifests by the so-called Cotton effect, namely: CD reaches a positive maximum value on one side of the absorption band and a negative minimum on the other, "giving rise to a loop"[295]. Cotton effect originally constituted the ensemble of optical rotary dispersion (ORD) and CD, but is now commonly used to refer about only half of the bisignate CD signal since this part is often observed alone[290]. The Cotton effect is called positive when the CD first increases as the wavelength decreases, and negative if the CD first decreases. A racemic mixture does not show any CD, because enantiomers exhibit opposite Cotton effects which cancel each other out.

Indeed, enantiomers absorbing CPL of one handedness constitute non-degenerated diastereoisomeric systems, based on the interaction between two distinct chiral influences, one chemical and the other physical. Thus, one state of this system is energetically favored, and one enantiomer preferentially absorbs CPL of one polarization state (*r*- or *l*-CPL, **Figure I.13**).

[XII] However, for historical[290,294] and mathematical[293] reasons, CD spectra were initially – and sometimes still are – described in terms of ellipticity (θ, in radians) due to the legacy of an older chiroptical technique called optical rotatory dispersion (ORD) spectroscopy. ORD represents the rotation of a linearly polarized light (LPL) beam by an optically active material as a function of the wavelength. Given that in virtue of the superposition principle, CPL can be decomposed as two perpendicular LPL with equal amplitudes, and LPL viewed as the sum of *r*- and *l*-CPL of the same magnitude, ORD and CD are mathematically related: they are Kramers–Kronig transforms of each other.

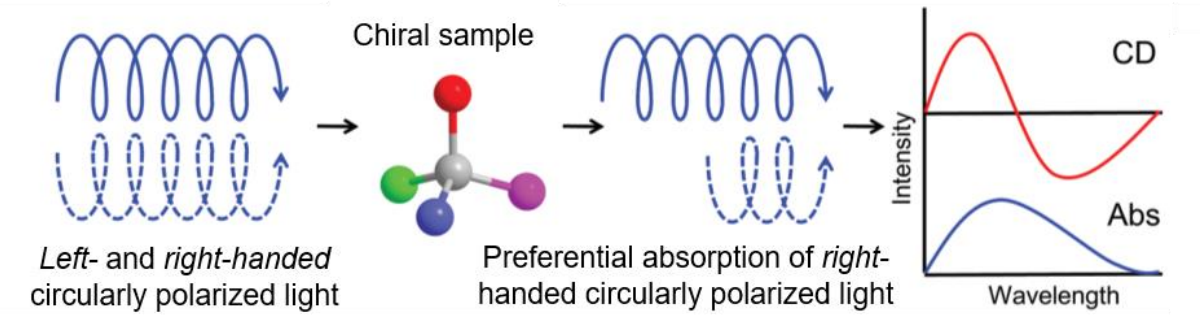

Figure I.13 Schematic illustration of circular dichroism. A chiral compound irradiated by *left*- and *right*-circularly polarized light absorbs preferentially the *r*-CPL, resulting in a negative Cotton effect in its spectral absorption range. Adapted from Liu *et al.*[296]

The dimensionless Kuhn anisotropy (or dissymmetry) factor *g* allows to quantitatively describe the chiroptical response of enantiomers (**Equation (I.1)**)[64]. The Kuhn anisotropy factor is expressed by the ratio between the difference in molar extinction coefficients of *l*-CPL and *r*-CPL (Δε), and the global molar extinction coefficient (ε)[297], where ε_L and ε_R are the molar extinction coefficients for *left*- and *right*-handed CPL, respectively. It ranges from -2 to +2, for a total absorption of *right*- and *left*-handed CPL, respectively and is wavelength-dependent. Enantiomers have opposite *g* values, corresponding to their preferential CPL polarization state absorption.

$$g = \frac{\Delta\varepsilon}{\varepsilon} = \frac{\varepsilon_L - \varepsilon_R}{\left(\frac{\varepsilon_L + \varepsilon_R}{2}\right)} \quad \textbf{(I.1)}$$

The differential absorption of CPL by enantiomers, chiral transition-states, or chiral conformations, allows the emergence of a chiral imbalance from a racemic mixture (by asymmetric photoresolution or photolysis) or through the formation of enantioenriched molecules from achiral substrates (by asymmetric photosynthesis)[298–300].

The asymmetric *photolysis* is based on the irreversible photochemical consumption at a higher rate of one enantiomer, within a racemic mixture which does not racemize during the process (**Figure I.14a**). Thereby, the enantioenrichment comes from the accumulation of the unreacted enantiomer. It depends both on the unequal molar extinction coefficients (ε_R and ε_S)

for CPL of the (*R*)- and (*S*)-enantiomers, governing the different rate constants, as well as the extent of reaction ξ. On the contrary, the asymmetric *photosynthesis* produces an enantioenriched medium by preferentially reacting with one enantiomer, while the substrate is kept racemic during the process thanks to a fast racemization (**Figure I.14b**). The enantioenrichment originates in this way from the asymmetric photosynthesis product. Under these conditions, the enantioimbalance of the product is equal to the excitation ratio $\varepsilon_R/\varepsilon_S$ of the substrate enantiomers, from which the enantiomeric excess can be calculated as $(\varepsilon_R - \varepsilon_S)/(\varepsilon_R + \varepsilon_S) = g/2$. Regarding the asymmetric *photoresolution*, it occurs within a mixture of enantiomers that do not interconvert mutually in the ground state, but only upon CPL excitation (**Figure I.14c**). Since the deactivating reverse reactions, regenerating the starting material in its ground state, should not be enantiodifferentiating, the deviation from the racemic mixture is only due to the difference of extinction coefficient (ε_R and ε_S) of each enantiomer toward the CPL used. While the combined enantiomer concentration ($C_R + C_S$) is constant during the photoresolution, the photostationary state (pss) is attained after a prolonged irradiation irrespective of the initial enantiomeric composition[301]. Without side reactions, the enantiomeric pss is reached when $\varepsilon_R C_R = \varepsilon_S C_S$, which can be rewritten into $(C_R/C_S)_{pss} = \varepsilon_R/\varepsilon_S$, allowing to calculate the $e.e._{pss}$ (*e.e.* at the photostationary state), considering the **Equation I.1**, equal to $(C_R - C_S)/(C_R + C_S) = g/2$. So, like the asymmetric photosynthesis *e.e.*, the photoresolution $e.e._{pss}$ only depends on the *g* value of enantiomers, whereas the *e.e.* in asymmetric photolysis is also influenced by the extent of reaction ξ.

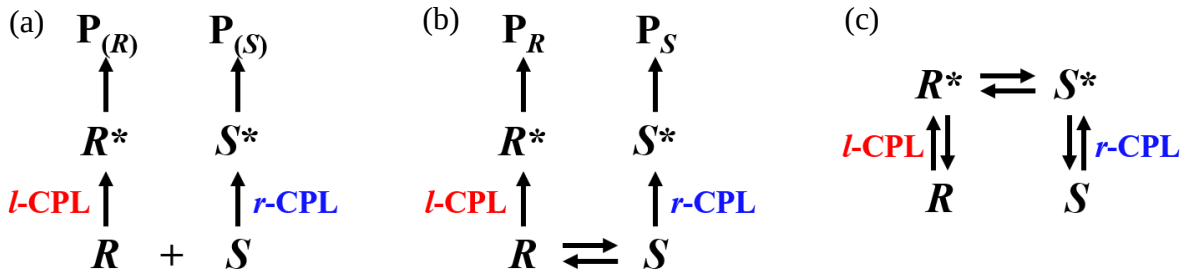

Figure I.14 Asymmetric (a) photolysis, (b) photosynthesis and (c) photoresolution mechanisms. In (a) and (b), upon irradiation of single-handed CPL, only the fastest transformation is represented, giving an idea of the major product. Note that the product of the asymmetric photolysis may also be chiral. *R* and

S denote (*R*)- and (*S*)-enantiomers, *R** and *S** their photoexcited state, and P the products possibly chiral (P_R and P_S).

The first CPL-induced asymmetric partial resolution dates back to 1968 thanks to Stevenson and Verdieck, who worked with octahedral oxalato complexes of chromium(III)[302]. Asymmetric photoresolution was further investigated for many organic molecules[303,304], macromolecules[305] and their assemblies[306]. They contain a photoresolvable functional group, such as overcrowded alkene, azobenzene, diarylethene, α,β-unsaturated ketone or fulgide[307].

Kagan *et al.* pioneered the field of asymmetric photosynthesis with CPL in 1971, through examining the hexahelicene photocyclization in the presence of iodine[308]. Next year, Calvin *et al.* reported *e.e.* up to 2% for an octahelicene in similar conditions[309]. Regarding amino acids, Takano *et al.* published in 2007 the detection of eleven of them, whose small but opposite *e.es.* for alanine (0.44 ± 0.31% *vs.* -0.65 ± 0.23%)[310]. They were generated upon the ultraviolet *r*- and *l*-CPL irradiation of macromolecular compounds, issued from proton-irradiated gaseous mixtures of CO, NH_3 and H_2O. One year before, Nuevo *et al.* had been the first to irradiate interstellar ice analogs composed of H_2O:$^{13}CH_3OH$:NH_3 (1:1:1) at 80K with CPL centered at 167 nm, which leads to the detection of alanine and 2,3-diaminopropanoic acid (an abundant non-proteinaceous amino acid), but with weak and not significant enantiomeric excesses[311]. They improved the pertinence of their set-up a few years later, by doubling the water content of ice mixtures and increasing the CPL wavelength (187 nm), where most α-amino acids have maximum CD, to reach an *e.e.* of 1.34 ± 0.40% *e.e.* for alanine[312]. The same team pursued its efforts by changing the substrates (ice analogs and/or residues coming from their irradiation with unpolarized UV, representing different stages of organic molecules in interstellar ices) and the photon energy of the irradiation CPL (188 and 122 nm)[313]. Sixteen amino acids were identified, and five of them (including alanine and valine) were analyzed by the innovative enantioselective two-dimensional GC × GC[314] coupled to TOF mass spectrometry, to show enantioenrichment up to 2.54 ± 0.28% *e.e.* Advantageously, all five amino acids exhibited *e.e.* of identical sign for a given polarization and wavelength, and whatever the substrate state as well, validating the possibility of a homogeneous CPL-induced asymmetry at any evolutionary stages of the interstellar ice-forming period.

Since its discovery by Kuhn *et al.* ninety years ago[315,316], through the enantioselective decomposition of ethyl-α-bromopropionate and *N*,*N*-dimethyl-α-azidopropionamide, the asymmetric photolysis of racemic mixtures has attracted a lot of interest. In the common case of "two competitive pseudo-first order photolytic reactions with unequal rate constants, k_S and k_R, for the (*R*) and (*S*) enantiomers, respectively"[64], and in the low *g* limit while knowing the extent of reaction ξ, the Kuhn anisotropy factor can be rewritten to predict the enantiomeric excess induced by the asymmetric photolysis (**Equation (I.2)**)[317].

$$g = 2\frac{k_R - k_S}{k_R + k_S}\,;\, e.e. \geq \left(1 - (1 - \xi)^{\frac{g}{2}}\right) \times 100\ (\%) \qquad \textbf{(I.2)}$$

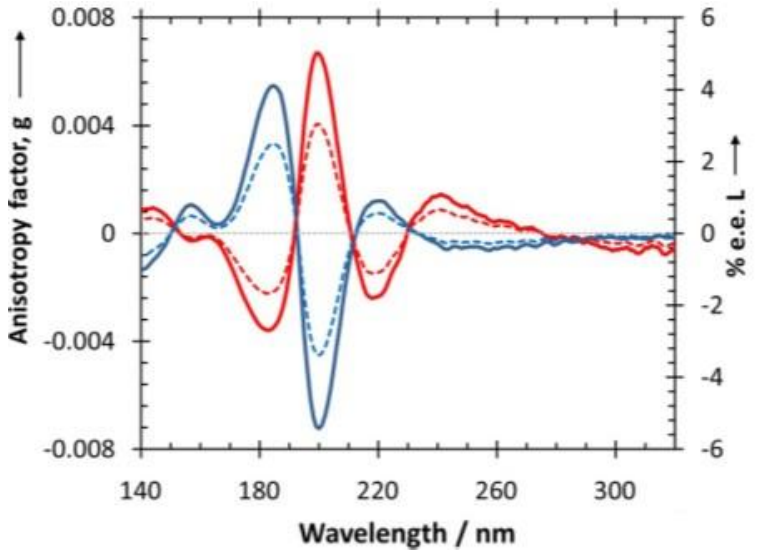

Figure I.15 Anisotropy spectra (thick lines, left ordinate) of isotropic amorphous D-alanine (red) and L-alanine (blue), in the vacuum–UV (<200 nm) and UV spectral region. Dashed lines represent the enantiomeric excess (right ordinate) that can be induced by photolysis of *rac*-alanine with either *left*- (in red) or *right*- (in blue) circularly polarized light at ξ = 0.9999. Positive *e.e.* value corresponds to scalemic mixture biased in favor of L-alanine. Note that the higher anisotropy factors and enantiomeric excesses are obtained below 190 nm as expected from **Equation I.2**. Reprinted from Meierhenrich *et al.*[317,318]

In 1974, the asymmetric photodecomposition of racemic camphor reported by Kagan *et al.*[319] (99% completed) reached 20% *e.e*, a long-lasting record in this domain. Three years later, Norden[320] and Bonner *et al.*[321] independently showed that enantioselective photolysis by UV-CPL was a viable source of symmetry-breaking for amino acids, by inducing *e.e.* up to 2% in aqueous solutions of alanine and glutamic acid for the latter, and 0.2% with leucine for the former. Leucine was then intensively studied thanks to a high anisotropy factor in the UV region[318]. The *e.e*. was increased up to 1.3% in 2001 (ξ = 0.55), thanks to Inoue *et al.* who highlighted the pH-dependence of the *g* value[322,323]. Since the early 2000s, Meierhenrich *et al.* notably get closer from astrophysically relevant conditions, by irradiating solid state samples with synchrotron vacuum ultraviolet (VUV)-CPL (below 200 nm). It made it possible to avoid the water absorption in the VUV, and allowed to reach electronic transitions having higher anisotropy factors (*cf.* **Figure I.15**)[324]. In 2005, a solid racemate of leucine was reported to reach 2.6% of *e.e.* after illumination with *r*-CPL at 182 nm (ξ not reported, *e.e.* given with a confidence interval at 95% of 0.16)[325]. More recently, the same team improved their results with amorphous samples of finely-tuned thickness, to achieve *e.es.* of 5.2 ± 0.5% and ± 4.2 ± 0.2% by photolysis of films of racemic leucine[326] and alanine[327,328], respectively. A similar enantioenrichment was stated in 2014 with gaseous photoionized alanine[329], which constitutes an appealing result taking into account the detection of interstellar gases such as propylene oxide[330] and glycine[331] in star-forming regions.

This experimental evidence for photochirogenesis gathers theories involving CPL as a source of chiral induction for biorelevant candidates, through photochemical processes on the surface of dust grains, next accreted into larger objects or incorporated to celestial bodies and delivered on the primitive Earth[332–334]. The occurrence of photochirogenesis on interstellar dust grains was supported by the detections of near-infrared light with significant circular polarization degrees (up to 22%[335]) in parsec-sized[XIII] star-forming regions, such as massive molecular clouds[337–343]. Cosmic circularly polarized photons arise from synchrotron radiations

[XIII] The parsec is an astronomical unit of length approximatively equal to 3.1×10^{16} meters or 3.26 light-years[336].

from neutron stars remnants of supernovae explosions[10], *bremsstrahlung*[XIV] or, presumably in interstellar clouds, through dichroic scattering (from spherical or magnetically aligned non-spherical dust) and/or extinction (along lined up grains)[345]. In addition, although it was not directly observed due to dust shielding, models predicted the generation of vacuum ultraviolet (VUV) and UV-CPL in such conditions[338], *i.e.* spectra region of light absorbed by amino acids and sugars.

Appealing hypotheses were formulated against the apparent contradiction between the molecular homogeneous handedness observed on Earth and on celestial bodies in our scope, and the fact that CPL is expected to be portioned into *left*- and *right*-handed contributions in equal abundance within the outer space, resulting in an enantiomeric preference that can vary (e.g. *l*- and *r*-CPL produced by a neutron star are equally emitted in vast conical domains in the space above and below its equator, where either *l*- and *r*-CPL prevails[10]). Bonner and Rubenstein already proposed in the 1980s a detailed scenario in which the solar system, revolving around the center of our galaxy, have repeatedly traversed a molecular cloud and accumulated enantioenriched incoming grains[346,347]. Authors assumed that this enantioenrichment would come from asymmetric photolysis induced by synchrotron CPL generated by a neutron star. They found this proposition more likely than enantioenrichment before the heating process of planet formation, or later by supernova synchrotron radiation. The sun was also rejected from viable CPL-source, despite the opposite circularly polarized sunlight measured between the morning and the afternoon[348,349], estimated as too low to induce a significant enantioenrichment[89,347,XV]. Later, Meierhenrich remarked in addition that, in molecular clouds, regions of homogeneous CPL polarization can exceed "the expected size of

---

[XIV] Electromagnetic radiation emitted as a result of the deceleration of high-energy charged particles, like electrons, impinging on matter[344], called by the German *bremsstrahlung*, literally 'braking radiation'. This light beam is expected to be circularly polarized when the mother particle is spin-polarized.

[XV] A nascent theory of Anup Sharma revisits this idea by proposing "(1) the selective absorption of UV-CPL by paramagnetic oxygen molecules due to magnetic circular dichroism (MCD) in the atmosphere of Archaean earth (4 to 2.5 billion years ago), (2) followed by the asymmetric photolysis of biomolecules by the resulting major CPL"[350,351]. MCD is the differential absorption of *l*- and *r*-CPL exhibiting by any molecules (chiral or not) oriented parallel to the direction of light propagation, and should not be confused with MChD. Even if the calculated enantiomeric excesses are very low (up to 10^{-10} for amino acids), they could coincide with the opposite handedness with sugars, and are potentially homogeneous over extended latitudes on Earth.

a protostellar disk – or our solar system"[337,352], allowing a unidirectional enantioenrichment "within our solar system, including comets"[7].

VIII. 2. 1. CPL and Spontaneous Mirror-Symmetry Breaking

Coupling CPL-induced enantioenrichment (by photoresolution) and amplification of chirality has been recognized as a valuable method to induce a preferred chirality to a range of assemblies and polymers[305,306,353–356]. The implementation of this coupled phenomena in the context of elucidating BH is rarer.

CPL was successfully used in the realm of the Soai reaction to orientate its enantioselectivity, either by using a chiroptical switchable additive, or by asymmetric photolysis of the racemic substrate. In 2004, Soai *et al.* illuminated during 48h a photoresolvable chiral olefin with *l*- or *r*-CPL, and mixed it with achiral diisopropylzinc and 2-alkynyl pyrimidine-5-carbaldehyde to afford the (*S*)- or (*R*)-5-pyrimidyl alkanol, respectively, in *e.e.* higher than 90%[357]. In 2005, they slightly photodecomposed a racemic mixture of pyrimidyl alkanol in with *l*- or *r*-CPL, and used the photolyzate as asymmetric autocatalyst with achiral aldehydes to give the corresponding (*S*)- or (*R*)-pyrimidyl alkanol, respectively, in *e.e.* higher than 99.5%[358].

In 2009, Vlieg *et al.* coupled CPL with the Viedma ripening to achieve a complete mirror-symmetry breaking[359], and which gave further support to deterministic processes towards BH. They employed an imine derivative of phenylglycinamide (named ***rac*-1**), for which deracemization by attrition was found to occur always in the same direction (the R-enantiomer) as a probable result of the minute levels of chiral impurities (note 13 in [191]). They next investigated whether this interference from the expected randomness can be overruled by CPL. They indeed discovered that irradiation of solid-liquid mixtures of ***rac*-1** led to complete deracemization, the direction of which being directly correlated to the circular polarization of light. Control experiments ruled out the possibility that the initial chiral bias is generated by photoresolution of ***rac*-1** by CPL. On contrary, the initial chiral bias originates from an unknown chiral photoproduct generated in solution after preferential absorption of CPL light by one of the enantiomers of ***rac*-1**. This photoproduct then serves as an "enantioselective crystal-growth inhibitor" which directs the deracemization process towards the other enantiomer of ***rac*-1**

(**Figure I.16**). In the context of BH, this work highlights that not only photolysis but also photosynthesis are potent mechanisms that can be exploited to direct the deracemization process by CPL when the latter is coupled to an amplification phenomenon.

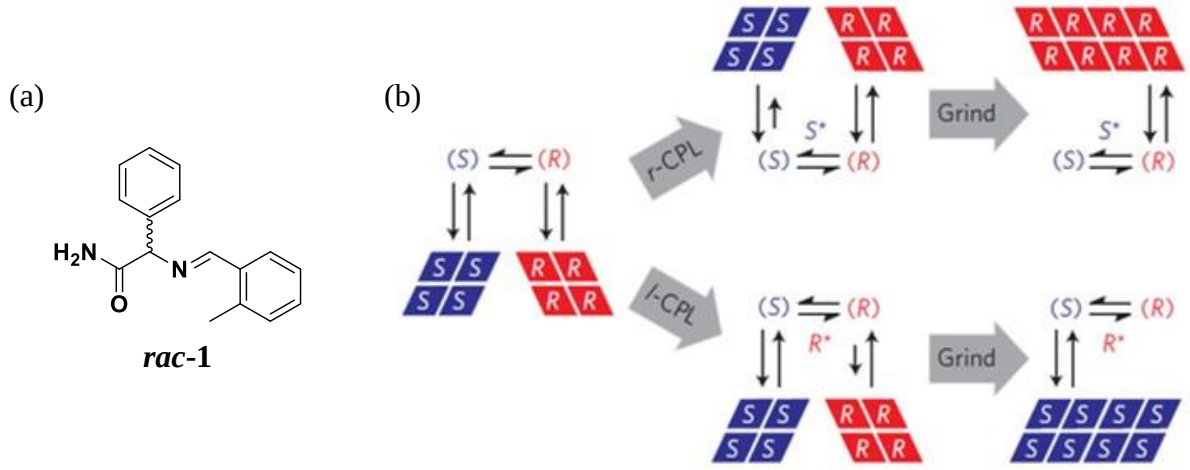

Figure I.16 (a) Molecular structure of ***rac*-1**. (b) CPL-controlled complete attrition-enhanced deracemization of ***rac*-1**. The CPL triggers the formation of a photoproduct (*S** and *R**) which acts as a crystallization inhibitor, favoring the crystal growth of the opposite enantiomer in the solution-solid mixture, subsequently fully enantioenriched by grinding. Reprinted from Vlieg *et al*.[359]

VIII. 3. Chiral Contributions Emanating from Other Elementary Particles

VIII. 3. 1. The Parity Violation (PV)

Universe is made of ultimate constituents called matter particles, or fermions, including quarks (which constitute protons and neutrons) and leptons (such as the electron and neutrinos)[XVI], interacting through fields, or forces, namely strong, electromagnetic, weak, and gravitational[360]. All, except gravity, are described in the Standard Model of Particle Physics (SMPP), which considers that fundamental forces are mediated by their respective interaction

[XVI] In fact, only 5% of the universe is made of fermions because dark matter and dark energy, not in the Standard Model of Particle Physics, account for 25 and 70%, respectively[360] – but that is another matter.

particles[XVII], named as gauge bosons[XVIII]: the gluon for the strong interactions between quarks; the photon for the electromagnetic interactions between electrically charged fermions (so all, except neutrinos); W^+, W^- and Z^0 bosons for the weak interactions between all fermions[360,361]. Indeed, interacting fermions transfer discrete amounts of energy, called quanta, by exchanging gauge bosons (**Figure I.17**).

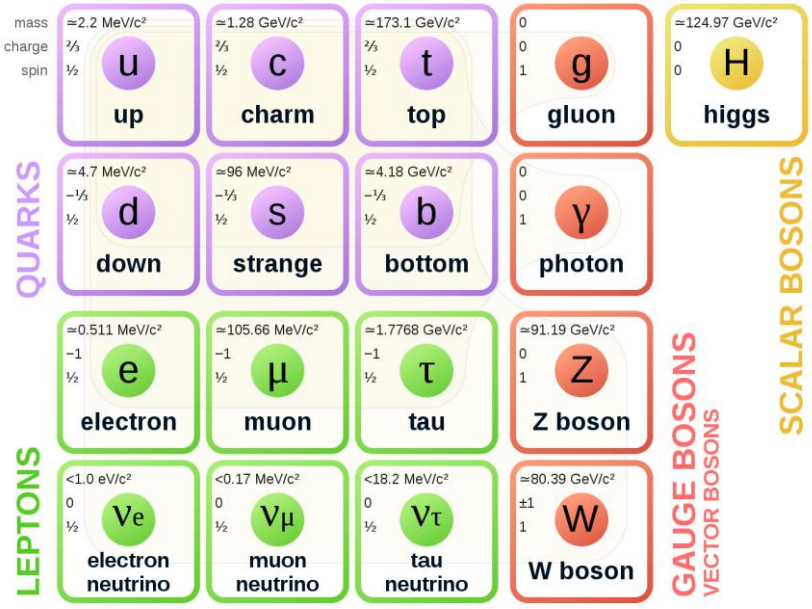

Figure I.17 Fermions and bosons of the Standard Model of Particle Physics[362].

Until the mid-20th century, fundamental interactions were thought to equally operate in a physical system and its image built through point reflection. In physicist's words, one assumed these laws were symmetric under space parity (*i.e.* invariant with respect to parity, or parity-even). Space parity is a symmetrical operation (*P*, usually only called parity) corresponding in a conventional three-dimensional space to an inversion around an arbitrary origin (**Figure I.18**).

[XVII] Gravitational force is insignificant on the scales of particle physics and its corresponding force-carrying particle, the "graviton", has not (yet?) been found[360,361].

[XVIII] The famous Higgs boson is not a gauge boson: it is not the interaction particle of a fundamental force but of the Brout–Englert–Higgs scalar field. This field gives mass to all particles with which it interacts (so all particles, including the Higgs boson itself, minus the massless gluons and photons)[360].

P transforms a *right*-handed cartesian coordinate system into a *left*-handed one (e.g. *P* replaces the cartesian coordinates of a point in space, x, y, z, by -x, -y, -z)[22].

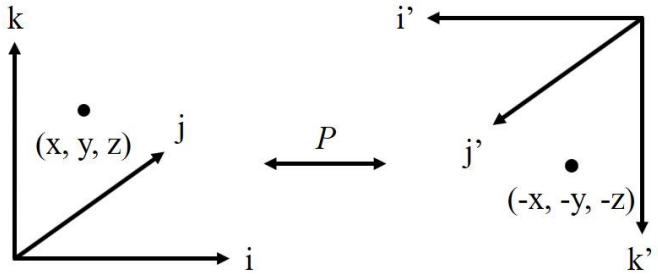

Figure I.18 The space parity symmetry (*P*) transforms a *right*-handed cartesian coordinate system (i, j, k) into a *left*-handed one (i', j', k'). j and j' point to the back and the front of the image plane, respectively. *P* is equivalent to a mirror reflection followed by a rotation of 180°. Inspired from Wagnière[22].

In 1956, T.-D. Lee and C.-N. Yang highlighted that parity conservation was only examined for strong and electromagnetic forces, and proposed experiments to test it in weak interactions[363]. Against all odds[XIX], Chien-Shiung Wu demonstrated few months later that the parity is violated in the weak force (which is hereby parity-odd)[364,365]. She showed that the transformation of unstable ^{60}Co nuclei into ^{60}Ni, by β^--decay of a neutron into a proton, emits, via an intermediate W^- boson, electrons of only *left*-handedness[XX]. In fact, solely *left*-handed

[XIX] It would seem that parity violation of weak interaction has cost 50$ to Richard Feynman[7,72].

[XX] Handedness of fermions, such as electrons, is more complex than molecular handedness and is described through two concepts, helicity and chirality[366–370].

Helicity is the projection of the particle's spin along its direction of motion (scalar product between the particle's spin and linear momentum: $\vec{\sigma} \cdot \hat{p}$, with the particle's spin $\vec{\sigma}$ and the unit vector in the particle's momentum direction $\hat{p} = \vec{p}/|\vec{p}|$). If the spin vector is parallel to the momentum direction, the state is called positive or *right*-handed, while antiparallel vectors indicate a negative or *left*-handed state. In other words, helical fermions are longitudinally spin-polarized particles which travel by tracing out a helical path, whose helicity is directed by the spin orientation. However, helicity is not relativistically invariant: its value changes according to the frame of reference. For example, the helicity of a massive particle is inverted when the reference frame speed is higher than the particle's motion.

Conversely, *chirality* is relativistically invariant and corresponds to the eigenvalue of the Dirac matrix operator γ_5. Loosely speaking, the particle's movement is described by a combination of forward and backward motion at the speed of light along the path, ± c according to the direction. The resultant momentum must be a superposition of these two internal velocity states. Therefore, chirality of a particle can be defined as "the spin

electrons were emitted because W^+ and W^- bosons (abbreviated as $W^\pm$ bosons), quanta of the weak charged-current interactions involving charge transfer, only couple with *left*-handed particles (**Figure I.19**)[370]. *Right*-handed particles are not subjected to weak interactions carried by $W^\pm$ bosons and, for example, neutrinos, that are only generated by processes mediated by $W^\pm$ bosons, are for this reason all *left*-handed in the universe[61].

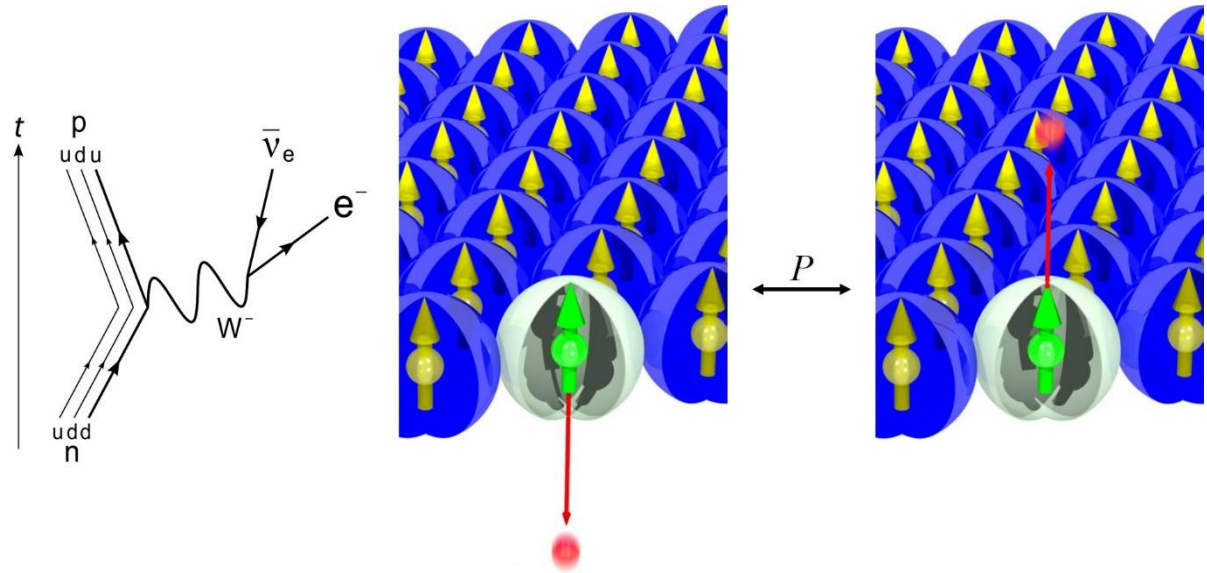

Figure I.19 Feynman diagram and scheme of the parity-violating β^--decay reported by Wu. Along time (*t*), a neutron (n) decays into a proton (p) by the conversion of a down quark (d) to an up quark (u) and the emission of a W^- boson which, in turn, decays into an electron neutrino ($\bar{\nu}_e$, the left arrow doesn't mean that the electron neutrino is a reagent but refers to its spin and indicates that it is an antiparticle) and an electron (e^-). On the right, cobalt-60 atoms and nuclei are shown as blue and yellow concentric

---

projection onto its internal velocity direction" and is a four-component description classified into positive *left*-handed and negative *right*-handed pairs.

In the case of massless particles (like neutrinos), or as long as the reference frame is slower than particles – in the so-called ultra-relativistic limit, only one internal velocity state is known and helicity is equal to chirality (e.g. left-handed chirality is equal to negative/left-handed helicity). Although this statement is strictly valid only for massless particles or when the massive fermions, such as electrons, are at high energies propagating near the speed of light, it remains useful in the low-energy regime to characterize the particle's handedness. Thus, like in most of the literature at the interface between chemistry and physics[371], particle's handedness and chirality refer in this report to helicity.

Regarding *P*, knowing that $\vec{\sigma}$ is a pseudo-vector (*i.e.* an axial vector, parity-even) whereas the unit vector of the linear momentum $\hat{p}$ is a true vector (*i.e.* a polar vector, parity-odd), the helicity is a pseudo-scalar operator which changes sign under space parity (parity-odd): a parity transformation turns a negative *left*-handed particle into a positive *right*-handed particle.

spheres, respectively. ^{60}Co atoms are magnetically polarized and their nuclear spin (indicating by yellow arrows) are all lined up. The β^--decay is sketched in the opaque part and notably leads to a nickel-60 atom (light-green sphere; nucleus represented by a green ball and the nuclear spin by a green arrow) and the emission of an electron (red sphere) whose linear momentum direction is indicated by the red arrow. Both parity inverted situations are figured: nuclear spins are not changed by *P* (parity-even) but the electron's linear momentum is (parity-odd). Experimentally, by conservation of angular momentum between the parent nucleus and decay products, the electron's spin (not sketched) is in the same direction than nuclear spins. The W^- bosons, just coupling with *left*-handed particles, decay into electrons with antiparallel spin/momentum vectors in such a way that only the situation depicted in the left part is encountered: parity violation (scheme reprinted from Berger and Stohner[370]).

The weak neutral current interactions, mediated by the Z^0 boson (and hence sometimes called Z forces), are without charge exchange and, just like the charged one, violate the space parity[372–376]. Thus, all weak interactions, carried by $W^{\pm}$ or Z^0 bosons, break the fundamental symmetry of space parity, which pushes physicists out of the Standard Model (SMPP cannot rationalize this PV) and has important consequences, perhaps even for the biological homochirality through three enantioenrichment ways: Parity-Violating Energy Difference (PVED) between enantiomers, the chiral fermions and indirectly their radiations in the *bremsstrahlung* case.

At the atomic scale, by the Z force, *right*-handed electrons are attracted to the nucleus, and *left*-handed ones repelled. Even if weak interactions are about thousand times less powerful than the electromagnetic force[371], this minute opposite contribution to the interactions between nuclei and electrons of different handedness lifts the degeneracy between enantiomers[XXI].

[XXI] Two other disconcerting effects of the weak forces parity violation bear mentioning. First, if usual enantiomers are not degenerated, as Laurence D. Barron wrote, "the true enantiomer of a chiral molecule (*i.e.* the 'opposite' object with identical energy to the original) is the molecule with the opposite absolute configuration but composed of antiparticles, being generated from the original by the combined CP operation"[377], C being the charge conjugation operation which changes normal particles to their antiparticles and vice-versa, and P the space parity operation. Secondly, all atoms are chiral. Not closely related to the biological homochirality, these aspects are not treated in this report and the interested reader may refer to the Barron's paper and, concerning the chirality of atoms, the seminal works of Zel'Dovich[378,379], Bouchiat[380] and Wieman[381], summarized here[370,371,382,383].

In achiral molecular geometries, electrons traveling in the same or opposite direction to their spin are, on average, in equal number, and the integrated electron chirality density over the whole molecule, called total electron chirality, is null. Nevertheless, the spin-orbit coupling, a relativistic effect occurring in the electromagnetic forces between the molecular nuclei and electrons, tends to oppose electron's spin axis and direction of motion[384]. In the vicinity of chiral regions, where molecules structure is akin to a helix, chiral electrons of opposite handedness to the helical shape are energetically favored by the spin-orbit coupling and consequently, molecules display 'spin-filtering' regions of different electron chirality density (**Figure I.20**). Beyond this, enantiomers, whose chiral geometries are interconverted by *P*, show imbalanced regions of opposite electron chirality density (so the total electron chirality is equal to $\pm$ x, with $x \neq 0$)[385,386]. The opposite contribution of the Z force between the nuclei and electrons – *right*-handed electrons are attracted whereas left ones are repelled – produces an energy shift in chiral molecules (and chiral transient forms): the enantiomer with slightly more *right*-handed electrons is stabilized, whilst the other with slightly more *left*-handed electrons is destabilized. In the sense of Barron, the PVED is a truly chiral influence.

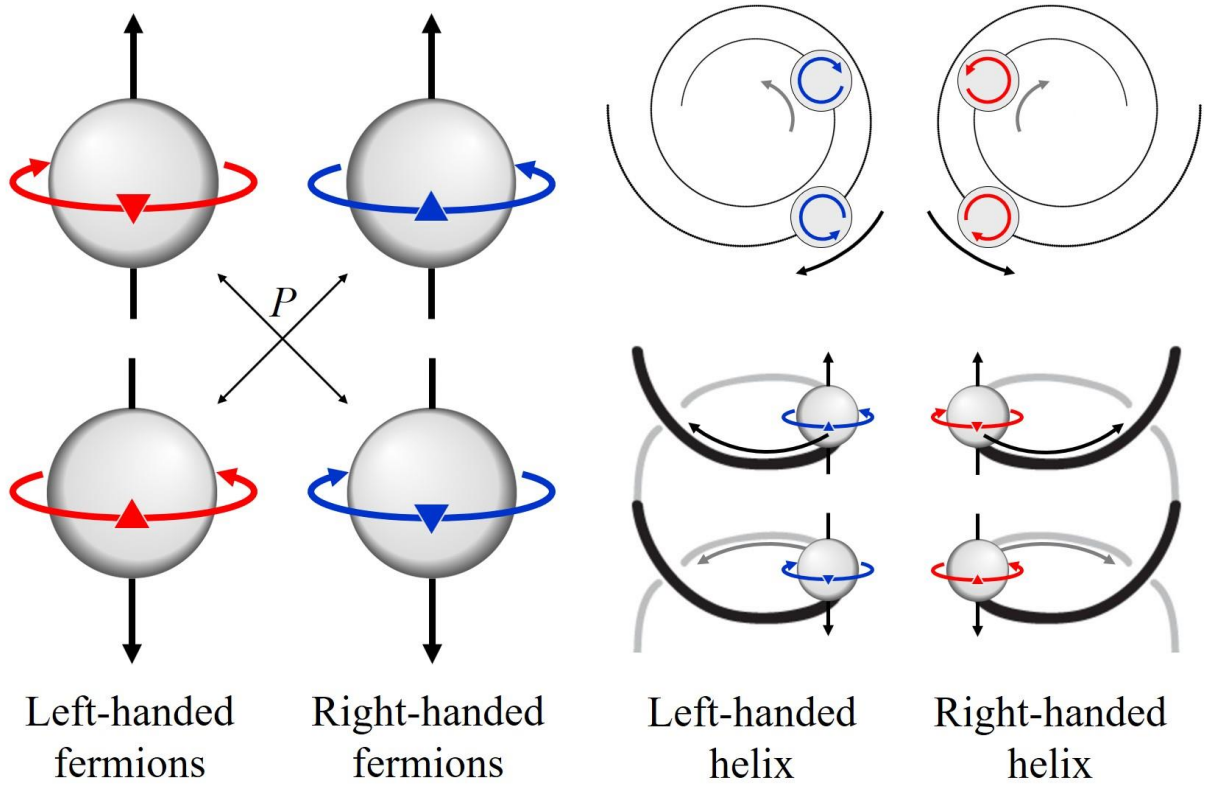

Figure I.20 *Left*-/*right*-handed fermions on the left; and on the right, the same particles (it would be electrons here) travelling on *left*-/*right*-handed helices, topped by an upper view. Fermions encircled with a blue (red) curvy arrow are *right*-(*left*-)handed; curvy arrows indicate in addition the sense of rotation of these spinning particles, whose angular momentum resultant direction is representing by the central triangle, pointing upward (right curvy arrow) or downward (left curvy arrow) for spin up or down, respectively; black/grey straight arrows show the motion's fermions direction. The particles' spin and direction of motion are antiparallel on the left (*left*-helical fermions) and parallel on the right (*right*-helical fermions). Spin-orbit coupling tends to oppose electron's orbit and spin. Hegstrom and Kondepudi explained that "for a *right*-handed helix, spin-orbit coupling favors down-spiraling for spin-up electrons and up-spiraling for spin-down electrons. In either case the spin axis of the electron tends to be aligned against the electron's direction of motion"[371]. Particles spin in opposite rotation direction to the orbit that they trace out along the helix. Helices drawing taken from Smyth[387].

Quantitative calculations of this parity-violating energy difference between enantiomers have been improved during these last four decades[388–391,71], to give for example about 10^{-11} J/mol for CHFClBr[392]. Although groups of Crassous/Darquié in France[393–397] and Quack in Switzerland[398–402] have been pursuing an experimental effort to measure PVED, thanks to

approaches based on spectroscopic technics and/or tunneling processes, no observation has confirmed it yet. Nonetheless, the tempting idea that PVED could be the source of the tiny enantiomeric excess amplified to the asymmetry of Life was put forward by Yamagata as early as 1966[403]. With this in mind, Mason, Tranter and MacDermott defended in the eighties and early nineties that L-amino acids, D-sugars, α-helix or β-sheet secondary structures, and other natural products are more stable than their enantiomorph due to the PVED[404–413]. Then, Quack[391] and Schwerdtfeger[414] refuted these results on the strength of finer calculations, and Lente[104,415] asserted that a PVED of around 10^{-13} J/mol causes an excess of only 6×10^{6} molecules in one mole (against 1.9×10^{11} for the standard deviation)[XXII]. In reply MacDermott claimed, by means of a new generation of PVED computations in agreement with other groups[416], that the enantiomeric excess of four gaseous amino acids found in the Murchison meteorite (at the solid state) could originate from their PVED[417].

Theoretical calculations in the 1980s of the PVED impact on SMSB gave contradictory results, depending on approaches and settled conditions in autocatalytic processes[118,418]. Recently, Blackmond *et al.* modelled experimental results of Soai reactions directed by isotopically chiral molecules, what allowed them to assess the energy threshold for controlling the mirror-symmetry breaking process outcome[419]. They estimated that the minimum enantiomeric excess required to overcome the statistical fluctuations effect lies between 3.5×10^{-7} to 3.5×10^{-8}%, corresponding to an energy difference within enantiomers between 1.5×10^{-7} and 1.5×10^{-8} kJ/mol. About five to seven orders of magnitude higher than the current highest estimations for PVED, this result weakens the Yamagata hypothesis, without being able to definitely discard it[20,419].

[XXII] Anyway, Quack himself did not rule out the PVED because of its smallness as possible origin for the bio-homochirality. He considered that even a minuscule energetic difference could play a key role within the framework of biological evolution and kinetic living beings[391]. PVED's supporters also questioned the Lente's result and argued that it could be more advantageous if estimated in the cold interstellar medium instead of at room temperature[230].

VIII. 3. 2. Chiral Fermions

Chiral fermions are other solutions proposed to overcome the conundrum of Life's asymmetry. They can be produced by supernovae explosions and interact with molecules in the proto-solar clouds[10,420–423]. Vester and Ulbricht suggested at the end of 1950s that high-energy enantiopure *left*-handed particles, truly chiral such as electrons, generated by β^--decay, could play[424,425]. From the sixties to the eighties[426–434], many attempted to show the validity of the "V–U hypothesis", generally by radiolysis of amino acids, but only ambiguous and irreproducible results were reported[3,435–437].

Last fifteen years have been bearing more fruits. The international collaboration RAMBAS (Radiation Mechanism of Biomolecular ASymmetry gathering Russian, Chinese and Japanese teams) proved in 2008[438,439] that (natural) *left*-handed electrons could induce: the synthesis of amino acids with minute *e.e.* (up to 0.005%) from primitive mixtures of compounds similar to the interstellar gas–dust clouds environment (CH_3OH, NH_3, H_2O, CO and metals); and the preferential enantioselective degradation in a racemate of D-amino acids, entailing the enantioenrichment of natural L-amino acids. Few years later, Dreiling demonstrated the electron-helicity-dependent dissociative electron attachment (DEA: $e^- + AB \rightarrow A^{\cdot} + B^-$) rate in halocamphors[440,441]. In the absence of *bremsstrahlung*, they confirmed that enantiomers interact in a different way with electrons, following their helicity.

On a different note, Walker underlined in 1985 that "80–90% of the radiation chemical effects of a high-energy particle are induced by secondary electrons (SEs)"[442]. These SEs ($< \approx$ 15 eV) arise from primary electrons, losing their energy and polarization in collisions, and are known to interact more with molecules due to closer energy levels, diluting the chiral effect of the electrons beam[425]. By using controlled sources of SEs – magnets or metallic substrates covered with chiral molecules, some have turned this trouble into new enantioenrichment technics, resting on principles that could be applied in the prebiotic universe.

In the asymmetrical reactions realm, in 2008, by irradiating adsorbed (*R*)- and (*S*)-2-butanol molecules with low-energy partly chiral electrons (10–15%), emitted by circularly-polarized-X-ray-excited magnetic substrate, Rosenberg *et al.*[443] measured a change of about ten percent in the rate of CO bond cleavage and calculated an *e.e.* around 25%, according to the

butanol/electrons handedness. Later, they succeeded to use better polarized electrons (60%) to dissociate Cl from epichlorohydrin (Epi) with a quantum yield 16% greater for the *S* form[444]. To achieve this, electrons are produced by X-ray irradiation of a gold substrate and spin-filtered by a chiral self-assembled overlayer of DNA before they reach the adlayer of Epi (**Figure I.21**).

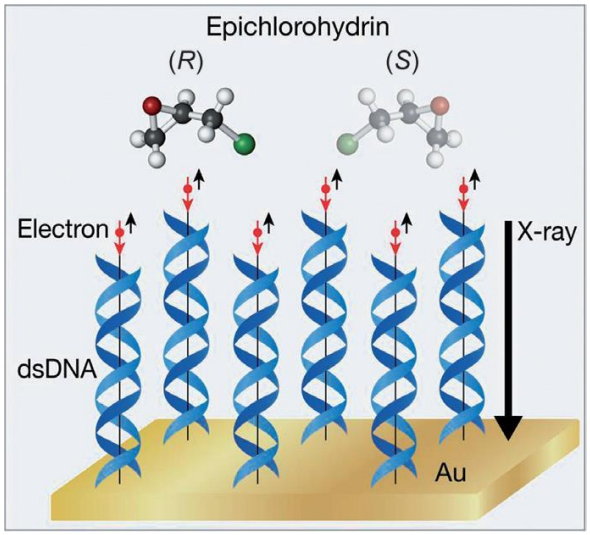

Figure I.21 Diagram of the enantioselective dissociation of epichlorohydrin by electrons, issued from the gold subjected to X-ray radiation and spin-polarized through a monolayer of double-stranded DNA (dsDNA). Red (black) arrows indicate the electron's spin (motion direction). They become polarized thanks to the so-called Chiral-Induced Spin Selectivity (CISS) effect, whose mechanism, including a strong spin-orbit coupling, is still unfathomed[445–447]. Reprinted from Rosenberg *et al.*[444]

In 2020, to demonstrate that the electron helicity itself can control the enantioselectivity in asymmetric reactions, Naaman *et al.* ruled out the confined surface effects and chemical chirality from the potential chiral bias sources[448]. Authors highlighted that spin-polarized electrons, produced by a magnetized Ni surface, could cross an achiral self-assembled monolayer (SAM) of carboxyl-terminated alkanethiols [$HS–(CH_2)_{x-1}–COO^-$] and cause an enantiospecific association with (*R*/*S*)-1-amino-2-propanol, leading to an *e.e.* of 20% in the reactive medium. The enantioselective electro-reduction of (1*R*/1*S*)-10-camphorsulfonic acid (CSA) was also governed by the chirality of electrons, injected through an electrode coated by an achiral SAM of 1-hexanethiol, with an *e.e.* of about 11.5% after the electrolysis of 80% of the initial amount of CSA.

Electrochirogenesis links these results with the biological homochirality through several theories, all based on an initial bias stemming from electrons[449,450]. Among them, strong fields and radiations of neutron stars could align ferrous magnetic domains in interstellar dust particles, and produce spin-polarized electrons, able to create an enantiomeric excess into adsorbed chiral molecules. One enantiomer from a racemate in a cosmic cloud would merely accrete on a magnetized domain in an enantioselective manner as well. Magnetic minerals of the prebiotic world, like pyrite (FeS_2) or Greigite (Fe_3S_4), might serve as an electrode in the asymmetric electrosynthesis of amino acids or purines, or a spin-filter in the presence of an external magnetic field in hydrothermal vents.

Among scenarios emanating from fundamental physics, and maybe outlandish for the layperson due to the use of complex concepts[230,421,423], the electron antineutrinos received in the 2010s greater interest, through the Supernova Neutrino Amino Acid Processing (SNAAP) model[451–453]. Electron antineutrinos are emitted after a supernova explosion, to cool the nascent neutron star, and, by a similar reasoning to that applied with neutrinos, they are all *right*-handed. Boyd *et al.* postulated that in the wake of neutron stars with strong magnetic and electric fields, *right*-handed electron antineutrinos selectively transform ^{14}N into ^{14}C, "depending on whether the spin of the ^{14}N is aligned or anti-aligned with that of the antineutrinos". In brief, since the reaction is expected to be more efficient in the antialignment case, and knowing that the spin orientation of ^{14}N nuclei is directly affected by the chirality of molecules, the destruction of amino acids in this situation is supposed to be enantioselective. Calculations predicted for amino acids enantiomeric excesses up to 0.02%, and an attractive *left*-handed dominance. Authors of this theory, similar to the magneto-optical processes, judged them more likely because of the possible "trapping of photons by the matter from the neutron star", and are currently seeking for feasible experimental tests.

IX. Conclusions and Perspectives of Biological Homochirality Studies

Questions accumulated while considering all the possible origins of the initial enantiomeric imbalance that have ultimately led to biological homochirality. When some

hypothesize a reason behind its emergence (such as for informational entropic reasons, resulting in evolutionary advantages towards more specific and complex functionalities)[1,115], others wonder whether if it is reasonable to reconstruct a chronology 3,500,000,000 years later[11]. Many are circumspect in front of the pile-up of scenarios and asserted that the solution is likely not expected in a near future (due to the difficulty to do all required control experiments, and fully understand the theoretical background of the putative selection mechanism)[72]. In parallel, the existence, and the extent, of a putative link between the different configurations of biologically-relevant amino acids and sugars also remain unsolved[135], and only Goldanskii and Kuz'min studied the effects of a hypothetical global loss of chiral purity in the future[89].

Nevertheless, great progress has been recently made in this old issue. The circularly polarized light is more and more convincing thanks to operational and analytical improvements. Increasingly accurate computational studies supply precious information, notably about SMSB processes, chiral surfaces and potential truly chiral physical influences. Efficient autocatalytic systems and deracemization processes were in addition highlighted notably the Soai reaction and the Viedma ripening. Space missions are also an opportunity: to study *in situ* organic matter, its conditions of transformations, and possible associated enantioenrichment; to elucidate the solar system origin and its history; and maybe, to find in other celestial bodies traces of opposite optical purity, what could indicate that the chiral selection of the terrestrial bio-homochirality could be a mere coincidence.

The current state-of-the-art indicates that further experimental investigations of the possible effect of physical chiral influences are needed. The photochirogenesis, attractive in many respects (CPL detection in space, detailed postulated scenarios, experimental proofs of *e.e.* within relevant conditions, and combination with SMSB), should still face pitfalls related to variable sources of extra-terrestrial CPL and the requirement of finely-tuned illumination conditions (almost full extent of reaction at the right place and moment of the evolutionary stages). Strong calls to organic chemists are also heard, to find asymmetric autocatalytic reactions credible in primordial conditions[14,125].

Anyway, the quest of the biological homochirality origin is fruitful in many respects. The first concerns one consequence of the asymmetry of Life: the contemporary challenge of

synthesizing enantiopure bioactive molecules. Indeed, many synthetic efforts are directed towards the generation of optically-pure molecules, to avoid potential side effects of racemic mixtures due to the enantioselectivity of biological receptors[XXIII]. These endeavors can undoubtedly draw inspiration from the range of deracemization and chirality induction processes conducted in connection with biological homochirality[5,109]. One example is the Viedma ripening, industrially relevant for a lot of molecules that display potent catalytic or therapeutic activities[185,455–461]. Other efforts are being made toward building-up sophisticated experiments and pushing their measurement limits to be able to detect tiny enantiomeric excesses, thus strongly contributing to important scientific instrumentation improvements and acquiring fundamental knowledge at the interface between chemistry, physics, and biology. Overall, this joint endeavor at the frontier of many fields is also beneficial to material sciences thanks to biomimicry and the introduction of chirality[139,462–467].

X. References

1 L. Morozov, *Orig. Life*, 1979, **9**, 187–217.
2 S. F. Mason, *Nature*, 1984, **311**, 19–23.
3 W. A. Bonner, *Orig. Life Evol. Biosph.*, 1991, **21**, 59–111.
4 J. L. Bada, *Nature*, 1995, **374**, 594–595.
5 B. L. Feringa and R. A. van Delden, *Angew. Chem. Int. Ed.*, 1999, **38**, 3418–3438.
6 W. A. Bonner, in *Topics in Stereochemistry*, John Wiley & Sons, Ltd, 2007, pp. 1–96.
7 U. Meierhenrich, *Amino acids and the asymmetry of life: caught in the act of formation*, Springer, Berlin, 2008.
8 A. Guijarro and M. Yus, *The Origin of Chirality in the Molecules of Life*, 2008.
9 R. Breslow and Z.-L. Cheng, *Proc. Natl. Acad. Sci.*, 2009, **106**, 9144–9146.
10 V. A. Tsarev, *Phys. Part. Nucl.*, 2009, **40**, 998–1029.
11 M. Ávalos, R. Babiano, P. Cintas, J. L. Jiménez and J. C. Palacios, *Tetrahedron Asymmetry*, 2010, **21**, 1030–1040.
12 P. Cintas and C. Viedma, *Chirality*, 2012, **24**, 894–908.
13 P. Cintas, Ed., *Biochirality: Origins, Evolution and Molecular Recognition*, Springer-Verlag, Berlin Heidelberg, 2013.
14 J. M. Ribó, D. Hochberg, J. Crusats, Z. El-Hachemi and A. Moyano, *J. R. Soc. Interface*, 2017, **14**, 20170699.
15 D. G. Blackmond, *Cold Spring Harb. Perspect. Biol.*, 2019, **11**, a032540.

[XXIII] Like in the infamous thalidomide molecule case, anti-inflammatory in its (*R*) form and teratogenic in the (*S*)[454].

16 P. Cintas, *Angew. Chem. Int. Ed.*, 2002, **41**, 1139–1145.
17 K. Soai, Ed., *Amplification of Chirality*, Springer Berlin Heidelberg, Berlin, Heidelberg, 2008, vol. 284.
18 J. M. Ribó, C. Blanco, J. Crusats, Z. El-Hachemi, D. Hochberg and A. Moyano, *Chem. - Eur. J.*, 2014, **20**, 17250–17271.
19 K. P. Bryliakov, Chemical Mechanisms of Prebiotic Chirality Amplification, https://spj.sciencemag.org/journals/research/2020/5689246/, (accessed November 16, 2020).
20 D. G. Blackmond, *Chem. Rev.*, 2020, **120**, 4831–4847.
21 A. Sevin, *FMSH - Fond. Maison Sci. Homme*, 2015, 11.
22 G. H. Wagnière, *On Chirality and the Universal Asymmetry. Reflections on Image and Mirror Image.*, VHCA, Verlag Helvetica Chimica Acta, Zürich (Switzerland)., 2007.
23 B. Kahr, *Chirality*, 2018, **30**, 351–368.
24 S. H. Mauskopf, *Trans. Am. Philos. Soc.*, 1976, **66**, 1–82.
25 J. Gal, *Helv. Chim. Acta*, 2013, **96**, 1617–1657.
26 R. Janoschek, Ed., *Chirality*, Springer Berlin Heidelberg, Berlin, Heidelberg, 1991.
27 M. Hargittai, *Appl. Phys. A*, 2007, **89**, 889–898.
28 É.-L. Malus, *Mém. Phys. Chim. Société Arcueil*, 1809, **2**, 143–158.
29 F. Arago, *Œuvres Fr. Arago Mém. Sci. Mém. Sur Polarisation Color. Gide Paris 1858*, 1811, **1**, 36–74.
30 J.-B. Biot, *Mém. Académie R. Sci. Inst. Fr.*, 1817, **2**, 41–136.
31 J. Gal, *Chirality*, 2011, **23**, 1–16.
32 L. Pasteur, *Comptes Rendus Hebd. Séances Académie Sci.*, 1848, **26**, 535–538.
33 J. H. van 't Hoff, *Voorstel tot uitbreiding der tegenwoordig in de scheikunde gebruikte structuur-formules in de ruimte: benevens een daarmee samenhangende opmerking omtrent het verband tusschen optisch actief vermogen en chemische constitutie van organische verbindingen.*, Utrecht, 1874.
34 J. H. van 't Hoff, *Arch. Néerl. Sci. Exactes Nat.*, 1874, **9**, 445–454.
35 J.-A. Le Bel, *Bull. Société Chim. Paris*, 1874, **22**, 337–347.
36 Portraits of Louis Pasteur - Louis Pasteur (1822-1895) - HISTORY - Institut Pasteur, https://phototheque.pasteur.fr:443/en, (accessed April 22, 2020).
37 J. Gal, *Nat. Chem.*, 2017, **9**, 604–605.
38 L. Pasteur, *Ann. Chim. Phys.*, 1850, **28**, 56–99.
39 W. Thomson, *Baltim. Lect. Mol. Dyn. Wave Theory Light Camb. Univ. Press Wareh. Lond. Revis. Ed. 1904*, 1894, 619.
40 Indo-European Lexicon, https://web.archive.org/web/20160420225029/http://www.utexas.edu/cola/centers/lrc/ielex/PokornyMaster-X.html, (accessed April 20, 2020).
41 Tabularium : dictionnaire Bailly, http://home.scarlet.be/tabularium/bailly/, (accessed April 20, 2020).
42 C. Djerassi, R. Records, E. Bunnenberg, K. Mislow and A. Moscowitz, *J. Am. Chem. Soc.*, 1962, 870–872.
43 K. Mislow, in *Topics in Stereochemistry*, ed. S. E. Denmark, John Wiley & Sons, Inc., Hoboken, NJ, USA, 2007, pp. 1–82.
44 S. J. Gerbode, J. R. Puzey, A. G. McCormick and L. Mahadevan, *Science*, 2012, **337**, 1087–1091.
45 H.-U. Blaser, *Rendiconti Lincei*, 2007, **18**, 281–304.

46 H.-U. Blaser, *Rendiconti Lincei*, 2013, **24**, 213–216.
47 A. Rouf and S. C. Taneja, *Chirality*, 2014, **26**, 63–78.
48 H. Leek and S. Andersson, *Molecules*, 2017, **22**, 158.
49 D. Rossi, M. Tarantino, G. Rossino, M. Rui, M. Juza and S. Collina, *Expert Opin. Drug Discov.*, 2017, **12**, 1253–1269.
50 D. Wu, F. Pan, W. Tan, L. Gao, Y. Tao and Y. Kong, *J. Sep. Sci.*, 2020, **43**, 337–347.
51 *Nature*, 2018, **555**, 414–414.
52 *Chirality*, 2020, **32**, 501–504.
53 G. P. Moss, *Pure Appl. Chem.*, 1996, **68**, 2193–2222.
54 J. Gal, *Enantiomer*, 1998, **3**, 263–273.
55 J. Gal, *Chirality*, 2012, **24**, 959–976.
56 L. Pasteur, *Comptes Rendus Hebd. Séances Académie Sci.*, 1857, **45**, 1032–1036.
57 L. Pasteur, *Comptes Rendus Hebd. Séances Académie Sci.*, 1858, **46**, 615–618.
58 J. Gal, *Chirality*, 2008, **20**, 5–19.
59 A. Piutti, *Comptes Rendus Hebd. Séances Académie Sci.*, 1886, **103**, 134–138.
60 M. Abe and R. Kuroda, *Development*, 2019, **146**, dev175976.
61 M. Drewes, *Int. J. Mod. Phys. E*, 2013, **22**, 1330019.
62 K. Blackburn and J. Schirillo, *Exp. Brain Res.*, 2012, **219**, 447–455.
63 J. D. Dunitz, *Angew. Chem. Int. Ed.*, 2019, **58**, 1248–1250.
64 H. Sugahara, C. Meinert, L. Nahon, N. C. Jones, S. V. Hoffmann, K. Hamase, Y. Takano and U. J. Meierhenrich, *Biochim. Biophys. Acta BBA - Proteins Proteomics*, 2018, **1866**, 743–758.
65 *Origins of Life on the Earth and in the Cosmos*, Elsevier, 2000.
66 Organic Chemistry - Paperback - Jonathan Clayden, Nick Greeves, Stuart Warren - Oxford University Press, https://global.oup.com/ukhe/product/organic-chemistry-9780199270293?cc=fr&lang=en&, (accessed April 22, 2020).
67 J. D. Watson and F. H. C. Crick, *Nature*, 1953, **171**, 737.
68 M. Yadav, R. Kumar and R. Krishnamurthy, *Chem. Rev.*, 2020, **120**, 4766–4805.
69 M. Frenkel-Pinter, M. Samanta, G. Ashkenasy and L. J. Leman, *Chem. Rev.*, 2020, **120**, 4707–4765.
70 G. A. Khoury, R. C. Baliban and C. A. Floudas, *Sci. Rep.*, 2011, **1**, 90.
71 M. Quack, in *Quantum Systems in Chemistry and Physics*, eds. K. Nishikawa, J. Maruani, E. J. Brändas, G. Delgado-Barrio and P. Piecuch, Springer Netherlands, Dordrecht, 2012, vol. 26, pp. 47–76.
72 M. Quack, *Angew. Chem. Int. Ed.*, 2002, **41**, 4618–4630.
73 K. Ruiz-Mirazo, C. Briones and A. de la Escosura, *Chem. Rev.*, 2014, **114**, 285–366.
74 N. Goldenfeld, T. Biancalani and F. Jafarpour, *Philos. Trans. R. Soc. Math. Phys. Eng. Sci.*, 2017, **375**, 20160341.
75 M. Preiner, S. Asche, S. Becker, H. C. Betts, A. Boniface, E. Camprubi, K. Chandru, V. Erastova, S. G. Garg, N. Khawaja, G. Kostyrka, R. Machné, G. Moggioli, K. B. Muchowska, S. Neukirchen, B. Peter, E. Pichlhöfer, Á. Radványi, D. Rossetto, A. Salditt, N. M. Schmelling, F. L. Sousa, F. D. K. Tria, D. Vörös and J. C. Xavier, *Life*, 2020, **10**, 20.
76 K. Michaelian, *Life*, 2018, **8**, 21.
77 NASA Astrobiology, https://astrobiology.nasa.gov/research/life-detection/about/, (accessed November 10, 2020).
78 S. A. Benner, E. A. Bell, E. Biondi, R. Brasser, T. Carell, H.-J. Kim, S. J. Mojzsis, A. Omran, M. A. Pasek and D. Trail, *ChemSystemsChem*, 2020, **2**, e1900035.

79 S. Bartlett and M. L. Wong, *Life*, 2020, **10**, 42.
80 E. R. Blout and M. Idelson, *J. Am. Chem. Soc.*, 1956, **78**, 3857–3858.
81 E. R. Blout, P. Doty and J. T. Yang, *J. Am. Chem. Soc.*, 1957, **79**, 749–750.
82 R. D. Lundberg and P. Doty, *J. Am. Chem. Soc.*, 1957, **79**, 3961–3972.
83 G. Wald, *Ann. N. Y. Acad. Sci.*, 1957, **69**, 352–368.
84 A. Brack and G. Spach, *Nat. Phys. Sci.*, 1971, **229**, 124–125.
85 S. I. Goldberg, J. M. Crosby, N. D. Iusem and U. E. Younes, *J. Am. Chem. Soc.*, 1987, **109**, 823–830.
86 M. Idelson and E. R. Blout, *J. Am. Chem. Soc.*, 1958, **80**, 2387–2393.
87 T. Kosikova and D. Philp, *Chem. Soc. Rev.*, 2017, **46**, 7274–7305.
88 G. F. Joyce, G. M. Visser, C. A. A. van Boeckel, J. H. van Boom, L. E. Orgel and J. van Westrenen, *Nature*, 1984, **310**, 602–604.
89 V. I. Goldanskii and V. V. Kuz'min, *AIP Conf. Proc.*, 1988, **180**, 163–228.
90 M. Bolli, R. Micura and A. Eschenmoser, *Chem. Biol.*, 1997, **4**, 309–320.
91 A. Saghatelian, Y. Yokobayashi, K. Soltani and M. R. Ghadiri, *Nature*, 2001, **409**, 797–801.
92 T. H. Hitz and P. L. Luisi, *Orig. Life Evol. Biosph.*, 2004, **34**, 93–110.
93 I. Weissbuch, R. A. Illos, G. Bolbach and M. Lahav, *Acc. Chem. Res.*, 2009, **42**, 1128–1140.
94 A. T. Borchers, P. A. Davis and M. E. Gershwin, *Exp. Biol. Med.*, 2004, **229**, 21–32.
95 M. M. Waldrop, *Science*, 1990, **250**, 1078–1080.
96 E. G. Nisbet and N. H. Sleep, *Nature*, 2001, **409**, 1083–1091.
97 V. R. Oberbeck and G. Fogleman, *Orig. Life Evol. Biosph.*, 1989, **19**, 549–560.
98 A. Lazcano and S. L. Miller, *J. Mol. Evol.*, 1994, **39**, 546–554.
99 J. L. Bada, in *Chemistry and Biochemistry of the Amino Acids*, ed. G. C. Barrett, Springer Netherlands, Dordrecht, 1985, pp. 399–414.
100 S. Kempe and J. Kazmierczak, *Astrobiology*, 2002, **2**, 123–130.
101 J. L. Bada, *Chem. Soc. Rev.*, 2013, **42**, 2186–2196.
102 J. M. Ribó and D. Hochberg, *Symmetry*, 2019, **11**, 814.
103 K. Mislow, *Collect. Czechoslov. Chem. Commun.*, 2003, **68**, 849–864.
104 G. Lente, *J. Phys. Chem. A*, 2006, **110**, 12711–12713.
105 J. S. Siegel, *Chirality*, 1998, **10**, 24–27.
106 A. K. Mann and H. Primakoff, *Orig. Life*, 1983, **13**, 113–118.
107 M. M. Green and V. Jain, *Orig. Life Evol. Biospheres*, 2010, **40**, 111–118.
108 J. T. Sczepanski and G. F. Joyce, *Nature*, 2014, **515**, 440–442.
109 Z. Wang, W. Xu, L. Liu and T. F. Zhu, *Nat. Chem.*, 2016, **8**, 698–704.
110 A. Brewer and A. P. Davis, *Nat. Chem.*, 2013, **6**, 569–574.
111 V. Sojo, *Orig. Life Evol. Biospheres*, 2015, **45**, 219–224.
112 Y. Chen and W. Ma, *PLOS Comput. Biol.*, 2020, **16**, e1007592.
113 D. G. Blackmond, *Cold Spring Harb. Perspect. Biol.*, 2010, **2**, a002147–a002147.
114 A. Korenić, S. Perović, M. M. Ćirković and P.-A. Miquel, *Prog. Biophys. Mol. Biol.*, 2020, **150**, 1–12.
115 J. M. Ribó, J. Crusats, Z. El-Hachemi, A. Moyano and D. Hochberg, *Chem Sci*, 2017, **8**, 763–769.
116 F. C. Frank, *Biochim. Biophys. Acta*, 1953, **11**, 459–463.
117 D. K. Kondepudi and G. W. Nelson, *Phys. Rev. Lett.*, 1983, **50**, 1023–1026.
118 L. L. Morozov, V. V. Kuz Min and V. I. Goldanskii, *Orig. Life*, 1983, **13**, 119–138.
119 V. Avetisov and V. Goldanskii, *Proc. Natl. Acad. Sci.*, 1996, **93**, 11435–11442.
120 D. K. Kondepudi and K. Asakura, *Acc. Chem. Res.*, 2001, **34**, 946–954.

121 J. M. Ribó and D. Hochberg, *Phys. Chem. Chem. Phys.*, 2020, **22**, 14013–14025.
122 M. Eigen and P. Schuster, *The Hypercycle: A Principle of Natural Self-Organization*, Springer-Verlag, Berlin Heidelberg, 1979.
123 K. Soai, T. Shibata, H. Morioka and K. Choji, *Nature*, 1995, **378**, 767–768.
124 T. Gehring, M. Busch, M. Schlageter and D. Weingand, *Chirality*, 2010, **22**, E173–E182.
125 K. Soai, T. Kawasaki and A. Matsumoto, *Symmetry*, 2019, **11**, 694.
126 R. Plasson, H. Bersini and A. Commeyras, *Proc. Natl. Acad. Sci. U. S. A.*, 2004, **101**, 16733–16738.
127 Y. Saito and H. Hyuga, *J. Phys. Soc. Jpn.*, 2004, **73**, 33–35.
128 F. Jafarpour, T. Biancalani and N. Goldenfeld, *Phys. Rev. Lett.*, 2015, **115**, 158101.
129 D. G. Blackmond and O. K. Matar, *J. Phys. Chem. B*, 2008, **112**, 5098–5104.
130 R. Plasson, *J. Phys. Chem. B*, 2008, **112**, 9550–9552.
131 D. G. Blackmond, *J. Phys. Chem. B*, 2008, **112**, 9553–9555.
132 D. G. Blackmond, *Chirality*, 2009, **21**, 359–362.
133 D. G. Blackmond, *Angew. Chem. Int. Ed.*, 2009, **48**, 2648–2654.
134 M. Stich, J. M. Ribó, D. G. Blackmond and D. Hochberg, *J. Chem. Phys.*, 2016, **145**, 074111.
135 F. Jafarpour, T. Biancalani and N. Goldenfeld, *Phys. Rev. E*, 2017, **95**, 032407.
136 T. Kawasaki, H. Tanaka, T. Tsutsumi, T. Kasahara, I. Sato and K. Soai, *J. Am. Chem. Soc.*, 2006, **128**, 6032–6033.
137 F. Ricci, F. H. Stillinger and P. G. Debenedetti, *J. Phys. Chem. B*, 2013, **117**, 602–614.
138 L. Pérez-García and D. B. Amabilino, *Chem. Soc. Rev.*, 2007, **36**, 941–967.
139 I. Weissbuch and M. Lahav, *Chem. Rev.*, 2011, **111**, 3236–3267.
140 G. An, P. Yan, J. Sun, Y. Li, X. Yao and G. Li, *CrystEngComm*, 2015, **17**, 4421–4433.
141 S. Azeroual, J. Surprenant, T. D. Lazzara, M. Kocun, Y. Tao, L. A. Cuccia and J.-M. Lehn, *Chem. Commun.*, 2012, **48**, 2292.
142 M. Liu, L. Zhang and T. Wang, *Chem Rev*, 2015, **115**, 7304–7397.
143 C. Tschierske and G. Ungar, *ChemPhysChem*, 2016, **17**, 9–26.
144 C. Tschierske, *Liq. Cryst.*, 2018, **45**, 2221–2252.
145 Y. Sang and M. Liu, *Symmetry*, 2019, **11**, 950.
146 B. Chang, X. Li and T. Sun, *Eur. Polym. J.*, 2019, **118**, 365–381.
147 G. Albano, G. Pescitelli and L. Di Bari, *Chem. Rev.*, 2020, **120**, 10145–10243.
148 A. R. A. Palmans and E. W. Meijer, *Angew. Chem. Int. Ed.*, 2007, **46**, 8948–8968.
149 P. Duan, H. Cao, L. Zhang and M. Liu, *Soft Matter*, 2014, **10**, 5428.
150 E. Yashima, N. Ousaka, D. Taura, K. Shimomura, T. Ikai and K. Maeda, *Chem. Rev.*, 2016, **116**, 13752–13990.
151 J. Jacques, A. Collet and S. H. Wilen, *Enantiomers, Racemates, and Resolutions*, Krieger Publishing Company, 1994.
152 E. Havinga, *Biochim. Biophys. Acta*, 1954, **13**, 171–174.
153 L.-C. Sögütoglu, R. R. E. Steendam, H. Meekes, E. Vlieg and F. P. J. T. Rutjes, *Chem. Soc. Rev.*, 2015, **44**, 6723–6732.
154 W. J. Pope and A. W. Harvey, *J. Chem. Soc. Trans.*, 1901, **79**, 74–87.
155 F. G. Holliman and F. G. Mann, *J. Chem. Soc. Resumed*, 1943, 550–554.
156 A. C. D. Newman and H. M. Powell, *J. Chem. Soc. Resumed*, 1952, 3747–3751.
157 R. E. Pincock and K. R. Wilson, *J. Am. Chem. Soc.*, 1971, **93**, 1291–1292.
158 H. Koshima and T. Matsuura, *J. Synth. Org. Chem. Jpn.*, 1998, **56**, 268–279.

159 E. Pidcock, *Chem. Commun.*, 2005, 3457.
160 M. Sakamoto, *J. Photochem. Photobiol. C Photochem. Rev.*, 2006, **7**, 183–196.
161 F. S. Kipping and W. J. Pope, *J. Chem. Soc. Trans.*, 1898, **73**, 606–617.
162 F. S. Kipping and W. J. Pope, *Nature*, 1898, **59**, 53–53.
163 W. H. Zachariasen, *Z. Für Krist. - Cryst. Mater.*, 1929, **71**, 517–529.
164 G. N. Ramachandran and K. S. Chandrasekaran, *Acta Crystallogr.*, 1957, **10**, 671–675.
165 S. C. Abrahams and J. L. Bernstein, *Acta Crystallogr. B*, 1977, **33**, 3601–3604.
166 J.-M. Cruz, K. Hernández-Lechuga, I. Domínguez-Valle, A. Fuentes-Beltrán, J. U. Sánchez-Morales, J. L. Ocampo-Espindola, C. Polanco, J.-C. Micheau and T. Buhse, *Chirality*, 2020, **32**, 120–134.
167 D. K. Kondepudi, R. J. Kaufman and N. Singh, *Science*, 1990, **250**, 975–976.
168 J. M. McBride and R. L. Carter, *Angew. Chem. Int. Ed. Engl.*, 1991, **30**, 293–295.
169 D. K. Kondepudi, K. L. Bullock, J. A. Digits, J. K. Hall and J. M. Miller, *J. Am. Chem. Soc.*, 1993, **115**, 10211–10216.
170 B. Martin, A. Tharrington and X. Wu, *Phys. Rev. Lett.*, 1996, **77**, 2826–2829.
171 Z. El-Hachemi, J. Crusats, J. M. Ribó and S. Veintemillas-Verdaguer, *Cryst. Growth Des.*, 2009, **9**, 4802–4806.
172 R.-Y. Qian and G. D. Botsaris, *Chem. Eng. Sci.*, 1998, **53**, 1745–1756.
173 Y. Song, W. Chen and X. Chen, *Cryst. Growth Des.*, 2008, **8**, 1448–1450.
174 S. Mahurin, M. McGinnis, J. S. Bogard, L. D. Hulett, R. M. Pagni and R. N. Compton, *Chirality*, 2001, **13**, 636–640.
175 D. J. Durand, D. K. Kondepudi, P. F. Moreira Jr. and F. H. Quina, *Chirality*, 2002, **14**, 284–287.
176 D. K. Kondepudi, J. Laudadio and K. Asakura, *J. Am. Chem. Soc.*, 1999, **121**, 1448–1451.
177 A. H. Cherney, N. T. Kadunce and S. E. Reisman, *Chem. Rev.*, 2015, **115**, 9587–9652.
178 In *Asymmetric Synthesis in Organophosphorus Chemistry*, Wiley-VCH Verlag GmbH & Co. KGaA, Weinheim, Germany, 2016, pp. 1–34.
179 W. K. Rybak, *Tetrahedron Asymmetry*, 2008, **19**, 2234–2239.
180 C. Viedma, *Phys. Rev. Lett.*, 2005, **94**, 065504.
181 B. Kaptein, W. L. Noorduin, H. Meekes, W. J. P. van Enckevort, R. M. Kellogg and E. Vlieg, *Angew. Chem. Int. Ed.*, 2008, **47**, 7226–7229.
182 C. Xiouras, J. Van Aeken, J. Panis, J. H. Ter Horst, T. Van Gerven and G. D. Stefanidis, *Cryst. Growth Des.*, 2015, **15**, 5476–5484.
183 C. Viedma and P. Cintas, *Chem. Commun.*, 2011, **47**, 12786.
184 F. Cameli, C. Xiouras and G. D. Stefanidis, *CrystEngComm*, 2018, **20**, 2897–2901.
185 A. H. Engwerda, H. Meekes, B. Kaptein, F. Rutjes and E. Vlieg, *Chem. Commun. Camb. Engl.*, 2016, **52**, 12048–12051.
186 W. L. Noorduin, W. J. P. van Enckevort, H. Meekes, B. Kaptein, R. M. Kellogg, J. C. Tully, J. M. McBride and E. Vlieg, *Angew. Chem. Int. Ed.*, 2010, **49**, 8435–8438.
187 R. R. E. Steendam, T. J. B. van Benthem, E. M. E. Huijs, H. Meekes, W. J. P. van Enckevort, J. Raap, F. P. J. T. Rutjes and E. Vlieg, *Cryst. Growth Des.*, 2015, **15**, 3917–3921.
188 D. T. McLaughlin, T. P. T. Nguyen, L. Mengnjo, C. Bian, Y. H. Leung, E. Goodfellow, P. Ramrup, S. Woo and L. A. Cuccia, *Cryst. Growth Des.*, 2014, **14**, 1067–1076.
189 S.-T. Wu, Y.-S. Zhang, B. Zhang, X.-L. Hu, X.-H. Huang, C.-C. Huang and N.-F. Zhuang, *Cryst. Growth Des.*, 2019, **19**, 2537–2541.

190 C. Viedma, *Astrobiology*, 2007, **7**, 312–319.
191 W. L. Noorduin, T. Izumi, A. Millemaggi, M. Leeman, H. Meekes, W. J. P. Van Enckevort, R. M. Kellogg, B. Kaptein, E. Vlieg and D. G. Blackmond, *J. Am. Chem. Soc.*, 2008, **130**, 1158–1159.
192 C. Viedma, J. E. Ortiz, T. de Torres, T. Izumi and D. G. Blackmond, *J. Am. Chem. Soc.*, 2008, **130**, 15274–15275.
193 C. Viedma, *Orig. Life Evol. Biosph.*, 2001, **31**, 501–509.
194 J. Huang and L. Yu, *J. Am. Chem. Soc.*, 2006, **128**, 1873–1878.
195 L. Spix, H. Meekes, R. H. Blaauw, W. J. P. van Enckevort and E. Vlieg, *Cryst. Growth Des.*, 2012, **12**, 5796–5799.
196 L. Spix, A. Alfring, H. Meekes, W. J. P. van Enckevort and E. Vlieg, *Cryst. Growth Des.*, 2014, **14**, 1744–1748.
197 L. Spix, A. H. J. Engwerda, H. Meekes, W. J. P. van Enckevort and E. Vlieg, *Cryst. Growth Des.*, 2016, **16**, 4752–4758.
198 N. Uemura, M. Hosaka, A. Washio, Y. Yoshida, T. Mino and M. Sakamoto, *Cryst. Growth Des.*, 2020, **20**, 4898–4903.
199 R. R. E. Steendam, J. M. M. Verkade, T. J. B. van Benthem, H. Meekes, W. J. P. van Enckevort, J. Raap, F. P. J. T. Rutjes and E. Vlieg, *Nat. Commun.*, 2014, **5**, 5543.
200 S. Miyagawa, S. Aiba, H. Kawamoto, Y. Tokunaga and T. Kawasaki, *Org. Biomol. Chem.*, 2019, **17**, 1238–1244.
201 N. Uemura, K. Sano, A. Matsumoto, Y. Yoshida, T. Mino and M. Sakamoto, *Chem. – Asian J.*, 2019, **14**, 4150–4153.
202 C. Viedma, C. Lennox, L. A. Cuccia, P. Cintas and J. E. Ortiz, *Chem. Commun.*, 2020, **56**, 4547–4550.
203 A. Burton and E. Berger, *Life*, 2018, **8**, 14.
204 D. P. Glavin, A. S. Burton, J. E. Elsila, J. C. Aponte and J. P. Dworkin, *Chem. Rev.*, 2020, **120**, 4660–4689.
205 W. M. Irvine, *Orig. Life Evol. Biosph.*, 1998, **28**, 365–383.
206 A. Garcia, C. Meinert, H. Sugahara, N. Jones, S. Hoffmann and U. Meierhenrich, *Life*, 2019, **9**, 29.
207 G. Cooper, N. Kimmich, W. Belisle, J. Sarinana, K. Brabham and L. Garrel, *Nature*, 2001, **414**, 879–883.
208 Y. Furukawa, Y. Chikaraishi, N. Ohkouchi, N. O. Ogawa, D. P. Glavin, J. P. Dworkin, C. Abe and T. Nakamura, *Proc. Natl. Acad. Sci.*, 2019, **116**, 24440–24445.
209 J. R. Cronin and S. Pizzarello, *Science*, 1997, **275**, 951–955.
210 J. R. Cronin and S. Pizzarello, *Adv. Space Res.*, 1999, **23**, 293–299.
211 S. Pizzarello and J. R. Cronin, *Geochim. Cosmochim. Acta*, 2000, **64**, 329–338.
212 S. Pizzarello, M. Zolensky and K. A. Turk, *Geochim. Cosmochim. Acta*, 2003, **67**, 1589–1595.
213 D. P. Glavin and J. P. Dworkin, *Proc. Natl. Acad. Sci.*, 2009, **106**, 5487–5492.
214 I. Myrgorodska, C. Meinert, Z. Martins, L. le Sergeant d'Hendecourt and U. J. Meierhenrich, *J. Chromatogr. A*, 2016, **1433**, 131–136.
215 G. Cooper and A. C. Rios, *Proc. Natl. Acad. Sci.*, 2016, **113**, E3322–E3331.
216 ArtBrom, *Murchison Meteorite*, 2008.
217 M. P. Bernstein, J. P. Dworkin, S. A. Sandford, G. W. Cooper and L. J. Allamandola, *Nature*, 2002, **416**, 401–403.
218 K. M. Ferrière, *Rev. Mod. Phys.*, 2001, **73**, 1031–1066.

219 Y. Fukui and A. Kawamura, *Annu. Rev. Astron. Astrophys.*, 2010, **48**, 547–580.
220 E. L. Gibb, D. C. B. Whittet, A. C. A. Boogert and A. G. G. M. Tielens, *Astrophys. J. Suppl. Ser.*, 2004, **151**, 35–73.
221 J. Mayo Greenberg, *Surf. Sci.*, 2002, **500**, 793–822.
222 S. A. Sandford, M. Nuevo, P. P. Bera and T. J. Lee, *Chem. Rev.*, 2020, **120**, 4616–4659.
223 J. J. Hester, S. J. Desch, K. R. Healy and L. A. Leshin, *Science*, 2004, **304**, 1116–1117.
224 G. M. Muñoz Caro, U. J. Meierhenrich, W. A. Schutte, B. Barbier, A. Arcones Segovia, H. Rosenbauer, W. H.-P. Thiemann, A. Brack and J. M. Greenberg, *Nature*, 2002, **416**, 403–406.
225 M. Nuevo, G. Auger, D. Blanot and L. d'Hendecourt, *Orig. Life Evol. Biospheres*, 2008, **38**, 37–56.
226 C. Zhu, A. M. Turner, C. Meinert and R. I. Kaiser, *Astrophys. J.*, 2020, **889**, 134.
227 C. Meinert, I. Myrgorodska, P. de Marcellus, T. Buhse, L. Nahon, S. V. Hoffmann, L. L. S. d'Hendecourt and U. J. Meierhenrich, *Science*, 2016, **352**, 208–212.
228 M. Nuevo, G. Cooper and S. A. Sandford, *Nat. Commun.*, 2018, **9**, 5276.
229 Y. Oba, Y. Takano, H. Naraoka, N. Watanabe and A. Kouchi, *Nat. Commun.*, 2019, **10**, 4413.
230 A. Dorta-Urra and P. Bargueño, *Symmetry*, 2019, **11**, 661.
231 R. M. Hazen and D. A. Sverjensky, *Cold Spring Harb. Perspect. Biol.*, 2010, **2**, a002162–a002162.
232 K.-H. Ernst, *Surf. Sci.*, 2013, **613**, 1–5.
233 C. Wattanakit, *Curr. Opin. Electrochem.*, 2018, **7**, 54–60.
234 F. Zaera, *Chem. Soc. Rev.*, 2017, **46**, 7374–7398.
235 M. V. Kelso, J. Z. Tubbesing, Q. Chen and J. A. Switzer, *J. Am. Chem. Soc.*, 2018, **140**, 15812–15819.
236 R. M. Hazen and D. S. Sholl, *Nat. Mater.*, 2003, **2**, 367–374.
237 V. Davankov, *Chirality*, 1998, **9**, 99–102.
238 W. A. Bonner, P. R. Kavasmaneck, F. S. Martin and J. J. Flores, *Science*, 1974, **186**, 143–144.
239 R. M. Hazen, T. R. Filley and G. A. Goodfriend, *Proc. Natl. Acad. Sci.*, 2001, **98**, 5487–5490.
240 A. Ahmadi, G. Attard, J. Feliu and A. Rodes, *Langmuir*, 1999, **15**, 2420–2424.
241 Y. Yun and A. J. Gellman, *Angew. Chem. Int. Ed.*, 2013, **52**, 3394–3397.
242 A. J. Gellman, Y. Huang, X. Feng, V. V. Pushkarev, B. Holsclaw and B. S. Mhatre, *J. Am. Chem. Soc.*, 2013, **135**, 19208–19214.
243 C. Chen, S. Yang, G. Su, Q. Ji, M. Fuentes-Cabrera, S. Li and W. Liu, *J. Phys. Chem. C*, 2020, **124**, 742–748.
244 J. Prinz, O. Gröning, H. Brune and R. Widmer, *Angew. Chem. Int. Ed.*, 2015, **54**, 3902–3906.
245 K. Soai, S. Osanai, K. Kadowaki, S. Yonekubo, T. Shibata and I. Sato, *J. Am. Chem. Soc.*, 1999, **121**, 11235–11236.
246 I. Sato, K. Kadowaki, H. Urabe, J. H. Jung, Y. Ono, S. Shinkai and K. Soai, *Tetrahedron Lett.*, 2003, **44**, 721–724.
247 H. Shindo, Y. Shirota, K. Niki, T. Kawasaki, K. Suzuki, Y. Araki, A. Matsumoto and K. Soai, *Angew. Chem. Int. Ed.*, 2013, **52**, 9135–9138.
248 I. Baglai, M. Leeman, K. Wurst, R. M. Kellogg and W. L. Noorduin, *Angew. Chem. Int. Ed.*, 2020, **59**, 20885–20889.

249 L. D. Barron, *J. Am. Chem. Soc.*, 1986, **108**, 5536–5539.
250 T. Buhse, J.-M. Cruz, M. E. Noble-Terán, D. Hochberg, J. M. Ribó, J. Crusats and J.-C. Micheau, *Chem. Rev.*, 2021, **121**, 2147–2229.
251 L. D. Barron, *Magnetochemistry*, 2020, **6**, 5.
252 M. Avalos, R. Babiano, P. Cintas, J. L. Jiménez, J. C. Palacios and L. D. Barron, *Chem. Rev.*, 1998, **98**, 2391–2404.
253 L. D. Barron, *Rendiconti Lincei*, 2013, **24**, 179–189.
254 L. Pasteur, *Observations sur les forces dissymétriques. In Comptes rendus hebdomadaires des séances de l'Académie des sciences. 1er juin 1874, tome 78, p. 1515-1518. In Œuvres de Pasteur. Réunies par Louis Pasteur Vallery-Radot. Tome premier. Dissymétrie moléculaire. Pages 360-363.*, Masson et cie, Paris, 1922.
255 N. Micali, H. Engelkamp, P. G. van Rhee, P. C. M. Christianen, L. M. Scolaro and J. C. Maan, *Nat. Chem.*, 2012, **4**, 201–207.
256 L. D. Barron, *Nat. Chem.*, 2012, **4**, 150–152.
257 D. Edwards, K. Cooper and R. C. Dougherty, *J. Am. Chem. Soc.*, 1980, **102**, 381–382.
258 L. D. Barron, *Science*, 1994, **266**, 1491–1492.
259 K. Banerjee-Ghosh, O. Ben Dor, F. Tassinari, E. Capua, S. Yochelis, A. Capua, S.-H. Yang, S. S. P. Parkin, S. Sarkar, L. Kronik, L. T. Baczewski, R. Naaman and Y. Paltiel, *Science*, 2018, **360**, 1331–1334.
260 J. M. Ribó, J. Crusats, F. Sagués, J. Claret and R. Rubires, *Science*, 2001, **292**, 2063–2066.
261 A. Tsuda, M. A. Alam, T. Harada, T. Yamaguchi, N. Ishii and T. Aida, *Angew. Chem. Int. Ed.*, 2007, **46**, 8198–8202.
262 M. Wolffs, S. J. George, Ž. Tomović, S. C. J. Meskers, A. P. H. J. Schenning and E. W. Meijer, *Angew. Chem. Int. Ed.*, 2007, **46**, 8203–8205.
263 Z. El-Hachemi, O. Arteaga, A. Canillas, J. Crusats, C. Escudero, R. Kuroda, T. Harada, M. Rosa and J. M. Ribó, *Chem. - Eur. J.*, 2008, **14**, 6438–6443.
264 A. D'Urso, R. Randazzo, L. Lo Faro and R. Purrello, *Angew. Chem. Int. Ed.*, 2010, **49**, 108–112.
265 J. Crusats, Z. El-Hachemi and J. M. Ribó, *Chem Soc Rev*, 2010, **39**, 569–577.
266 O. Arteaga, A. Canillas, J. Crusats, Z. El-Hachemi, J. Llorens, E. Sacristan and J. M. Ribo, *ChemPhysChem*, 2010, **11**, 3511–3516.
267 O. Arteaga, A. Canillas, J. Crusats, Z. El-Hachemi, J. Llorens, A. Sorrenti and J. M. Ribo, *Isr. J. Chem.*, 2011, **51**, 1007–1016.
268 P. Mineo, V. Villari, E. Scamporrino and N. Micali, *Soft Matter*, 2014, **10**, 44–47.
269 P. Mineo, V. Villari, E. Scamporrino and N. Micali, *J. Phys. Chem. B*, 2015, **119**, 12345–12353.
270 J. Sun, Y. Li, F. Yan, C. Liu, Y. Sang, F. Tian, Q. Feng, P. Duan, L. Zhang, X. Shi, B. Ding and M. Liu, *Nat. Commun.*, 2018, **9**, 2599.
271 Y. Sang, D. Yang, P. Duan and M. Liu, *Chem. Sci.*, 2019, **10**, 2718–2724.
272 Z. Shen, Y. Sang, T. Wang, J. Jiang, Y. Meng, Y. Jiang, K. Okuro, T. Aida and M. Liu, *Nat. Commun.*, 2019, **10**, 1–8.
273 M. Kuroha, S. Nambu, S. Hattori, Y. Kitagawa, K. Niimura, Y. Mizuno, F. Hamba and K. Ishii, *Angew. Chem. Int. Ed.*, 2019, **58**, 18454–18459.
274 K. Ishii, S. Hattori and Y. Kitagawa, *Photochem. Photobiol. Sci.*, 2020, **19**, 8–19.
275 G. L. J. A. Rikken and E. Raupach, *Nature*, 1997, **390**, 493–494.

276 G. L. J. A. Rikken, E. Raupach and T. Roth, *Phys. B Condens. Matter*, 2001, **294–295**, 1–4.
277 Y. Xu, G. Yang, H. Xia, G. Zou, Q. Zhang and J. Gao, *Nat. Commun.*, 2014, **5**, 5050.
278 G. L. J. A. Rikken and E. Raupach, *Nature*, 2000, **405**, 932–935.
279 A. G. Lyne, *Nature*, 1984, **308**, 605–606.
280 Z. Martins, M. C. Price, N. Goldman, M. A. Sephton and M. J. Burchell, *Nat. Geosci.*, 2013, **6**, 1045–1049.
281 Y. Furukawa, H. Nakazawa, T. Sekine, T. Kobayashi and T. Kakegawa, *Earth Planet. Sci. Lett.*, 2015, **429**, 216–222.
282 Y. Furukawa, A. Takase, T. Sekine, T. Kakegawa and T. Kobayashi, *Orig. Life Evol. Biospheres*, 2018, **48**, 131–139.
283 G. G. Managadze, M. H. Engel, S. Getty, P. Wurz, W. B. Brinckerhoff, A. G. Shokolov, G. V. Sholin, S. A. Terent'ev, A. E. Chumikov, A. S. Skalkin, V. D. Blank, V. M. Prokhorov, N. G. Managadze and K. A. Luchnikov, *Planet. Space Sci.*, 2016, **131**, 70–78.
284 G. Managadze, *Planet. Space Sci.*, 2007, **55**, 134–140.
285 J. H. van 't Hoff, *Die Lagerung der Atome im Raume.*, Friedrich Vieweg und Sohn, Braunschweig, 2nd edn., 1894.
286 A. A. Cotton, *Comptes Rendus Hebd. Séances Académie Sci.*, 1895, **120**, 989–991.
287 A. A. Cotton, *Comptes Rendus Hebd. Séances Académie Sci.*, 1895, **120**, 1044–1046.
288 A. A. Cotton, *Ann. Chim. Phys.*, 1896, **7**, 347–432.
289 W. Haidinger, *Ann. Phys. Chem.*, 1847, **146**, 531–544.
290 N. Berova, P. Polavarapu, K. Nakanishi and R. W. Woody, Eds., *Comprehensive Chiroptical Spectroscopy: Applications in Stereochemical Analysis of Synthetic Compounds, Natural Products, and Biomolecules, Volume 2*, Wiley: Hoboken, NJ, USA, 2012, vol. 2.
291 M. Bass and Optical Society of America, Eds., *Handbook of optics. Vol. 1: Fundamentals, techniques, and design*, McGraw-Hill, New York, NY, 2. ed., 1995.
292 M. Nič, J. Jirát, B. Košata, A. Jenkins and A. McNaught, Eds., *IUPAC Compendium of Chemical Terminology: Gold Book*, IUPAC, Research Triagle Park, NC, 2.1.0., 2009.
293 N. Berova, P. Polavarapu, K. Nakanishi and R. W. Woody, *Comprehensive Chiroptical Spectroscopy: Instrumentation, Methodologies, and Theoretical Simulations, Volume 1*, Wiley: Hoboken, NJ, USA, 2012, vol. 1.
294 P. Crabbé, *Tetrahedron*, 1964, **20**, 1211–1241.
295 T. M. Lowry, *Nature*, 1933, **132**, 552–552.
296 Y. Sang, J. Han, T. Zhao, P. Duan and M. Liu, *Adv. Mater.*, 2020, **32**, 1900110.
297 W. Kuhn, *Trans. Faraday Soc.*, 1930, **26**, 293–308.
298 H. Rau, *Chem. Rev.*, 1983, **83**, 535–547.
299 Y. Inoue, *Chem. Rev.*, 1992, **92**, 741–770.
300 P. K. Hashim and N. Tamaoki, *ChemPhotoChem*, 2019, **3**, 347–355.
301 Y. Inoue, *Chem. Rev.*, 1992, **92**, 741–770.
302 K. L. Stevenson and J. F. Verdieck, *J. Am. Chem. Soc.*, 1968, **90**, 2974–2975.
303 B. L. Feringa, R. A. van Delden, N. Koumura and E. M. Geertsema, *Chem. Rev.*, 2000, **100**, 1789–1816.
304 W. R. Browne and B. L. Feringa, in *Molecular Switches*, John Wiley & Sons, Ltd, 2011, pp. 121–179.
305 G. Yang, S. Zhang, J. Hu, M. Fujiki and G. Zou, *Symmetry*, 2019, **11**, 474–493.
306 H. K. Bisoyi and Q. Li, *Angew. Chem. Int. Ed.*, 2016, **55**, 2994–3010.

307 A. C. Evans, C. Meinert, C. Giri, F. Goesmann and U. J. Meierhenrich, *Chem. Soc. Rev.*, 2012, **41**, 5447.
308 H. Kagan, A. Moradpour, J. F. Nicoud, G. Balavoine and G. Tsoucaris, *J. Am. Chem. Soc.*, 1971, **93**, 2353–2354.
309 W. J. Bernstein, M. Calvin and O. Buchardt, *J. Am. Chem. Soc.*, 1972, **94**, 494–498.
310 Y. Takano, J. Takahashi, T. Kaneko, K. Marumo and K. Kobayashi, *Earth Planet. Sci. Lett.*, 2007, **254**, 106–114.
311 M. Nuevo, U. J. Meierhenrich, G. M. M. Caro, E. Dartois, L. d'Hendecourt, D. Deboffle, G. Auger, D. Blanot, J.-H. Bredehöft and L. Nahon, *Astron. Astrophys.*, 2006, **457**, 741–751.
312 P. de Marcellus, C. Meinert, M. Nuevo, J.-J. Filippi, G. Danger, D. Deboffle, L. Nahon, L. Le Sergeant d'Hendecourt and U. J. Meierhenrich, *Astrophys. J.*, 2011, **727**, L27.
313 P. Modica, C. Meinert, P. de Marcellus, L. Nahon, U. J. Meierhenrich and L. L. S. d'Hendecourt, *Astrophys. J.*, 2014, **788**, 79.
314 C. Meinert and U. J. Meierhenrich, *Angew. Chem. Int. Ed.*, 2012, **51**, 10460–10470.
315 W. Kuhn and E. Braun, *Naturwissenschaften*, 1929, **17**, 227–228.
316 W. Kuhn and E. Knopf, *Naturwissenschaften*, 1930, **18**, 183–183.
317 C. Meinert, J. H. Bredehöft, J.-J. Filippi, Y. Baraud, L. Nahon, F. Wien, N. C. Jones, S. V. Hoffmann and U. J. Meierhenrich, *Angew. Chem. Int. Ed.*, 2012, **51**, 4484–4487.
318 I. Myrgorodska, C. Meinert, S. V. Hoffmann, N. C. Jones, L. Nahon and U. J. Meierhenrich, *ChemPlusChem*, 2017, **82**, 74–87.
319 G. Balavoine, A. Moradpour and H. B. Kagan, *J. Am. Chem. Soc.*, 1974, **96**, 5152–5158.
320 B. Norden, *Nature*, 1977, **266**, 567–568.
321 J. J. Flores, W. A. Bonner and G. A. Massey, *J. Am. Chem. Soc.*, 1977, **99**, 3622–3625.
322 H. Nishino, A. Kosaka, G. A. Hembury, H. Shitomi, H. Onuki and Y. Inoue, *Org. Lett.*, 2001, **3**, 921–924.
323 H. Nishino, A. Kosaka, G. A. Hembury, F. Aoki, K. Miyauchi, H. Shitomi, H. Onuki and Y. Inoue, *J. Am. Chem. Soc.*, 2002, **124**, 11618–11627.
324 U. J. Meierhenrich, J.-J. Filippi, C. Meinert, J. H. Bredehöft, J. Takahashi, L. Nahon, N. C. Jones and S. V. Hoffmann, *Angew. Chem. Int. Ed.*, 2010, **49**, 7799–7802.
325 U. J. Meierhenrich, L. Nahon, C. Alcaraz, J. H. Bredehöft, S. V. Hoffmann, B. Barbier and A. Brack, *Angew. Chem. Int. Ed.*, 2005, **44**, 5630–5634.
326 U. J. Meierhenrich, J.-J. Filippi, C. Meinert, S. V. Hoffmann, J. H. Bredehöft and L. Nahon, *Chem. Biodivers.*, 2010, **7**, 1651–1659.
327 C. Meinert, S. V. Hoffmann, P. Cassam-Chenaï, A. C. Evans, C. Giri, L. Nahon and U. J. Meierhenrich, *Angew. Chem. Int. Ed.*, 2014, **53**, 210–214.
328 C. Meinert, P. Cassam-Chenaï, N. C. Jones, L. Nahon, S. V. Hoffmann and U. J. Meierhenrich, *Orig. Life Evol. Biospheres*, 2015, **45**, 149–161.
329 M. Tia, B. Cunha de Miranda, S. Daly, F. Gaie-Levrel, G. A. Garcia, L. Nahon and I. Powis, *J. Phys. Chem. A*, 2014, **118**, 2765–2779.
330 B. A. McGuire, P. B. Carroll, R. A. Loomis, I. A. Finneran, P. R. Jewell, A. J. Remijan and G. A. Blake, *Science*, 2016, **352**, 1449–1452.
331 Y.-J. Kuan, S. B. Charnley, H.-C. Huang, W.-L. Tseng and Z. Kisiel, *Astrophys. J.*, 2003, **593**, 848.
332 A. G. Griesbeck and U. J. Meierhenrich, *Angew. Chem. Int. Ed.*, 2002, **41**, 3147–3154.
333 C. Meinert, J.-J. Filippi, L. Nahon, S. V. Hoffmann, L. D'Hendecourt, P. De Marcellus, J. H. Bredehöft, W. H.-P. Thiemann and U. J. Meierhenrich, *Symmetry*, 2010, **2**, 1055–1080.

334 J. H. Bredehöft, N. C. Jones, C. Meinert, A. C. Evans, S. V. Hoffmann and U. J. Meierhenrich, *Chirality*, 2018, **26**, 373–378.
335 J. Kwon, M. Tamura, P. W. Lucas, J. Hashimoto, N. Kusakabe, R. Kandori, Y. Nakajima, T. Nagayama, T. Nagata and J. H. Hough, *Astrophys. J.*, 2013, **765**, L6.
336 E. E. Mamajek, G. Torres, A. Prsa, P. Harmanec, M. Asplund, P. D. Bennett, N. Capitaine, J. Christensen-Dalsgaard, E. Depagne, W. M. Folkner, M. Haberreiter, S. Hekker, J. L. Hilton, V. Kostov, D. W. Kurtz, J. Laskar, B. D. Mason, E. F. Milone, M. M. Montgomery, M. T. Richards, J. Schou and S. G. Stewart, *ArXiv151006262 Astro-Ph*.
337 J. Bailey, *Orig. Life Evol. Biosph.*, 2001, **31**, 167–183.
338 J. Bailey, A. Chrysostomou, J. H. Hough, T. M. Gledhill, A. McCall, S. Clark, F. Ménard and M. Tamura, *Science*, 1998, **281**, 672–674.
339 T. Fukue, M. Tamura, R. Kandori, N. Kusakabe, J. H. Hough, J. Bailey, D. C. B. Whittet, P. W. Lucas, Y. Nakajima and J. Hashimoto, *Orig. Life Evol. Biospheres*, 2010, **40**, 335–346.
340 J. Kwon, M. Tamura, J. H. Hough, N. Kusakabe, T. Nagata, Y. Nakajima, P. W. Lucas, T. Nagayama and R. Kandori, *Astrophys. J.*, 2014, **795**, L16.
341 J. Kwon, M. Tamura, J. H. Hough, T. Nagata, N. Kusakabe and H. Saito, *Astrophys. J.*, 2016, **824**, 95.
342 J. Kwon, M. Tamura, J. H. Hough, T. Nagata and N. Kusakabe, *Astron. J.*, 2016, **152**, 67.
343 J. Kwon, T. Nakagawa, M. Tamura, J. H. Hough, R. Kandori, M. Choi, M. Kang, J. Cho, Y. Nakajima and T. Nagata, *Astron. J.*, 2018, **156**, 1.
344 R. Jenkins, R. Manne, R. Robin and C. Senemaud, *Pure Appl. Chem.*, 1991, **63**, 735–746.
345 K. Wood, *Astrophys. J.*, 1997, **477**, L25–L28.
346 E. Rubenstein, W. A. Bonner, H. P. Noyes and G. S. Brown, *Nature*, 1983, **306**, 118–118.
347 W. A. Bonner and E. Rubenstein, *Biosystems*, 1987, **20**, 99–111.
348 J. R. P. Angel, R. Illing and P. G. Martin, *Nature*, 1972, **238**, 389–390.
349 M. D. Papagiannis, Ed., *The Search for Extraterrestrial Life: Recent Developments: Proceedings of the 112th Symposium of the International Astronomical Union Held at Boston University, Boston, Mass., U.S.A., June 18–21, 1984*, Springer Netherlands, Dordrecht, 1985.
350 A. Sharma, *Sci. Rep.*, 2017, **7**, 13295.
351 A. Sharma, *J. Biol. Phys.*, 2020, **46**, 283–295.
352 M. Buschermohle, D. C. B. Whittet, A. Chrysostomou, J. H. Hough, P. W. Lucas, A. J. Adamson, B. A. Whitney and M. J. Wolff, *Astrophys. J.*, 2005, **624**, 821–826.
353 J. Royes, V. Polo, S. Uriel, L. Oriol, M. Piñol and R. M. Tejedor, *Phys. Chem. Chem. Phys.*, 2017, **19**, 13622–13628.
354 J. Kim, J. Lee, W. Y. Kim, H. Kim, S. Lee, H. C. Lee, Y. S. Lee, M. Seo and S. Y. Kim, *Nat. Commun.*, 2015, **6**, 6959.
355 J. Hu, Y. Xie, H. Zhang, C. He, Q. Zhang and G. Zou, *Chem. Commun.*, 2019, **55**, 4953–4956.
356 E. E. Greciano, R. Rodríguez, K. Maeda and L. Sánchez, *Chem. Commun.*, 2020, **56**, 2244–2247.
357 I. Sato, R. Sugie, Y. Matsueda, Y. Furumura and K. Soai, *Angew. Chem. Int. Ed.*, 2004, **43**, 4490–4492.

358 T. Kawasaki, M. Sato, S. Ishiguro, T. Saito, Y. Morishita, I. Sato, H. Nishino, Y. Inoue and K. Soai, *J. Am. Chem. Soc.*, 2005, **127**, 3274–3275.
359 W. L. Noorduin, A. A. C. Bode, M. van der Meijden, H. Meekes, A. F. van Etteger, W. J. P. van Enckevort, P. C. M. Christianen, B. Kaptein, R. M. Kellogg, T. Rasing and E. Vlieg, *Nat. Chem.*, 2009, **1**, 729.
360 J. Woithe, G. J. Wiener and F. F. Van der Veken, *Phys. Educ.*, 2017, **52**, 034001.
361 W. N. Cottingham and D. A. Greenwood, *An Introduction to the Standard Model of Particle Physics*, Cambridge University Press, Cambridge, 2nd edn., 2007.
362 Particle Data Group, M. Tanabashi, K. Hagiwara, K. Hikasa, K. Nakamura, Y. Sumino, F. Takahashi, J. Tanaka, K. Agashe, G. Aielli, C. Amsler, M. Antonelli, D. M. Asner, H. Baer, Sw. Banerjee, R. M. Barnett, T. Basaglia, C. W. Bauer, J. J. Beatty, V. I. Belousov, J. Beringer, S. Bethke, A. Bettini, H. Bichsel, O. Biebel, K. M. Black, E. Blucher, O. Buchmuller, V. Burkert, M. A. Bychkov, R. N. Cahn, M. Carena, A. Ceccucci, A. Cerri, D. Chakraborty, M.-C. Chen, R. S. Chivukula, G. Cowan, O. Dahl, G. D'Ambrosio, T. Damour, D. de Florian, A. de Gouvêa, T. DeGrand, P. de Jong, G. Dissertori, B. A. Dobrescu, M. D'Onofrio, M. Doser, M. Drees, H. K. Dreiner, D. A. Dwyer, P. Eerola, S. Eidelman, J. Ellis, J. Erler, V. V. Ezhela, W. Fetscher, B. D. Fields, R. Firestone, B. Foster, A. Freitas, H. Gallagher, L. Garren, H.-J. Gerber, G. Gerbier, T. Gershon, Y. Gershtein, T. Gherghetta, A. A. Godizov, M. Goodman, C. Grab, A. V. Gritsan, C. Grojean, D. E. Groom, M. Grünewald, A. Gurtu, T. Gutsche, H. E. Haber, C. Hanhart, S. Hashimoto, Y. Hayato, K. G. Hayes, A. Hebecker, S. Heinemeyer, B. Heltsley, J. J. Hernández-Rey, J. Hisano, A. Höcker, J. Holder, A. Holtkamp, T. Hyodo, K. D. Irwin, K. F. Johnson, M. Kado, M. Karliner, U. F. Katz, S. R. Klein, E. Klempt, R. V. Kowalewski, F. Krauss, M. Kreps, B. Krusche, Yu. V. Kuyanov, Y. Kwon, O. Lahav, J. Laiho, J. Lesgourgues, A. Liddle, Z. Ligeti, C.-J. Lin, C. Lippmann, T. M. Liss, L. Littenberg, K. S. Lugovsky, S. B. Lugovsky, A. Lusiani, Y. Makida, F. Maltoni, T. Mannel, A. V. Manohar, W. J. Marciano, A. D. Martin, A. Masoni, J. Matthews, U.-G. Meißner, D. Milstead, R. E. Mitchell, K. Mönig, P. Molaro, F. Moortgat, M. Moskovic, H. Murayama, M. Narain, P. Nason, S. Navas, M. Neubert, P. Nevski, Y. Nir, K. A. Olive, S. Pagan Griso, J. Parsons, C. Patrignani, J. A. Peacock, M. Pennington, S. T. Petcov, V. A. Petrov, E. Pianori, A. Piepke, A. Pomarol, A. Quadt, J. Rademacker, G. Raffelt, B. N. Ratcliff, P. Richardson, A. Ringwald, S. Roesler, S. Rolli, A. Romaniouk, L. J. Rosenberg, J. L. Rosner, G. Rybka, R. A. Ryutin, C. T. Sachrajda, Y. Sakai, G. P. Salam, S. Sarkar, F. Sauli, O. Schneider, K. Scholberg, A. J. Schwartz, D. Scott, V. Sharma, S. R. Sharpe, T. Shutt, M. Silari, T. Sjöstrand, P. Skands, T. Skwarnicki, J. G. Smith, G. F. Smoot, S. Spanier, H. Spieler, C. Spiering, A. Stahl, S. L. Stone, T. Sumiyoshi, M. J. Syphers, K. Terashi, J. Terning, U. Thoma, R. S. Thorne, L. Tiator, M. Titov, N. P. Tkachenko, N. A. Törnqvist, D. R. Tovey, G. Valencia, R. Van de Water, N. Varelas, G. Venanzoni, L. Verde, M. G. Vincter, P. Vogel, A. Vogt, S. P. Wakely, W. Walkowiak, C. W. Walter, D. Wands, D. R. Ward, M. O. Wascko, G. Weiglein, D. H. Weinberg, E. J. Weinberg, M. White, L. R. Wiencke, S. Willocq, C. G. Wohl, J. Womersley, C. L. Woody, R. L. Workman, W.-M. Yao, G. P. Zeller, O. V. Zenin, R.-Y. Zhu, S.-L. Zhu, F. Zimmermann, P. A. Zyla, J. Anderson, L. Fuller, V. S. Lugovsky and P. Schaffner, *Phys. Rev. D*, 2018, **98**, 030001.
363 T. D. Lee and C. N. Yang, *Phys. Rev.*, 1956, **104**, 254–258.
364 C. S. Wu, E. Ambler, R. W. Hayward, D. D. Hoppes and R. P. Hudson, *Phys. Rev.*, 1957, **105**, 1413–1415.
365 C.-S. Wu, in *Nishina Memorial Lectures: Creators of Modern Physics*, ed. N. M. Foundation, Springer Japan, Tokyo, 2008, pp. 43–70.

366 L. A. Page, *Rev. Mod. Phys.*, 1959, **31**, 759–781.
367 E. J. Konopinski, *The Theory of Beta Radioactivity*, Oxford: Clarendon Press; London: Oxford University Press., 1966.
368 A. S. Goldhaber and M. Goldhaber, *Phys. Today*, 2011, **64**, 40–43.
369 R. Hong, M. G. Sternberg and A. García, *Am. J. Phys.*, 2017, **85**, 45–53.
370 R. Berger and J. Stohner, *Wiley Interdiscip. Rev. Comput. Mol. Sci.*, 2019, **9**, 25.
371 R. A. Hegstrom and D. K. Kondepudi, *Sci. Am.*, 1990, **262**, 108–115.
372 F. J. Hasert, H. Faissner, W. Krenz, J. Von Krogh, D. Lanske, J. Morfin, K. Schultze, H. Weerts, G. H. Bertrand-Coremans, J. Lemonne, J. Sacton, W. Van Doninck, P. Vilain, C. Baltay, D. C. Cundy, D. Haidt, M. Jaffre, P. Musset, A. Pullia, S. Natali, J. B. M. Pattison, D. H. Perkins, A. Rousset, W. Venus, H. W. Wachsmuth, V. Brisson, B. Degrange, M. Haguenauer, L. Kluberg, U. Nguyen-Khac, P. Petiau, E. Bellotti, S. Bonetti, D. Cavalli, C. Conta, E. Fiorini, M. Rollier, B. Aubert, L. M. Chounet, P. Heusse, A. Lagarrigue, A. M. Lutz, J. P. Vialle, F. W. Bullock, M. J. Esten, T. Jones, J. McKenzie, A. G. Michette, G. Myatt, J. Pinfold and W. G. Scott, *Phys. Lett. B*, 1973, **46**, 121–124.
373 F. J. Hasert, S. Kabe, W. Krenz, J. Von Krogh, D. Lanske, J. Morfin, K. Schultze, H. Weerts, G. H. Bertrand-Coremans, J. Sacton, W. Van Doninck, P. Vilain, U. Camerini, D. C. Cundy, R. Baldi, I. Danilchenko, W. F. Fry, D. Haidt, S. Natali, P. Musset, B. Osculati, R. Palmer, J. B. M. Pattison, D. H. Perkins, A. Pullia, A. Rousset, W. Venus, H. Wachsmuth, V. Brisson, B. Degrange, M. Haguenauer, L. Kluberg, U. Nguyen-Khac, P. Petiau, E. Belotti, S. Bonetti, D. Cavalli, C. Conta, E. Fiorini, M. Rollier, B. Aubert, D. Blum, L. M. Chounet, P. Heusse, A. Lagarrigue, A. M. Lutz, A. Orkin-Lecourtois, J. P. Vialle, F. W. Bullock, M. J. Esten, T. W. Jones, J. McKenzie, A. G. Michette, G. Myatt and W. G. Scott, *Phys. Lett. B*, 1973, **46**, 138–140.
374 C. Y. Prescott, W. B. Atwood, R. L. A. Cottrell, H. DeStaebler, E. L. Garwin, A. Gonidec, R. H. Miller, L. S. Rochester, T. Sato, D. J. Sherden, C. K. Sinclair, S. Stein, R. E. Taylor, J. E. Clendenin, V. W. Hughes, N. Sasao, K. P. Schüler, M. G. Borghini, K. Lübelsmeyer and W. Jentschke, *Phys. Lett. B*, 1978, **77**, 347–352.
375 C. Y. Prescott, W. B. Atwood, R. L. A. Cottrell, H. DeStaebler, E. L. Garwin, A. Gonidec, R. H. Miller, L. S. Rochester, T. Sato, D. J. Sherden, C. K. Sinclair, S. Stein, R. E. Taylor, C. Young, J. E. Clendenin, V. W. Hugnes, N. Sasao, K. P. Schüler, M. G. Borghini, K. Lübelsmeyer and W. Jentschke, *Phys. Lett. B*, 1979, **84**, 524–528.
376 L. Di Lella and C. Rubbia, in *60 Years of CERN Experiments and Discoveries*, WORLD SCIENTIFIC, 2014, vol. Volume 23, pp. 137–163.
377 L. D. Barron, *Chem. Phys. Lett.*, 1994, **221**, 311–316.
378 I. B. Zel'Dovich, *J Exptl Theor. Phys USSR*, 1957, **33**, 1531–1533.
379 I. B. Zel'Dovich, *J Exptl Theor. Phys USSR*, 1959, **36**, 964–966.
380 M. A. Bouchiat and C. Bouchiat, *J. Phys.*, 1974, **35**, 899–927.
381 C. S. Wood, S. C. Bennett, D. Cho, B. P. Masterson, J. L. Roberts, C. E. Tanner and C. E. Wieman, *Science*, 1997, **275**, 1759–1763.
382 M.-A. Bouchiat and L. Pottier, *Sci. Am.*, 1984, **250**, 100–111.
383 R. A. Hegstrom, J. P. Chamberlain, K. Seto and R. G. Watson, *Am. J. Phys.*, 1988, **56**, 1086–1092.
384 F. Faglioni and P. Lazzeretti, *Phys. Rev. E*, 2001, **65**, 011904.
385 R. Bast, A. Koers, A. S. P. Gomes, M. Iliaš, L. Visscher, P. Schwerdtfeger and T. Saue, *Phys Chem Chem Phys*, 2011, **13**, 864–876.
386 M. Senami and K. Ito, *Phys. Rev. A*, 2019, **99**, 012509.

387 D. R. Smyth, *Development*, 2016, **143**, 3272–3282.
388 D. W. Rein, R. A. Hegstrom and P. G. H. Sandars, *Phys. Lett. A*, 1979, **71**, 499–502.
389 R. A. Hegstrom, D. W. Rein and P. G. H. Sandars, *J. Chem. Phys.*, 1980, **73**, 2329–2341.
390 M. Quack, *Angew. Chem. Int. Ed. Engl.*, 1989, **28**, 571–586.
391 A. Bakasov, T.-K. Ha and M. Quack, *J. Chem. Phys.*, 1998, **109**, 7263–7285.
392 M. Quack and J. Stohner, *Phys. Rev. Lett.*, 2000, **84**, 3807–3810.
393 J. Crassous, C. Chardonnet, T. Saue and P. Schwerdtfeger, *Org. Biomol. Chem.*, 2005, **3**, 2218.
394 C. Stoeffler, B. Darquié, A. Shelkovnikov, C. Daussy, A. Amy-Klein, C. Chardonnet, L. Guy, J. Crassous, T. R. Huet, P. Soulard and P. Asselin, *Phys Chem Chem Phys*, 2011, **13**, 854–863.
395 N. Saleh, S. Zrig, T. Roisnel, L. Guy, R. Bast, T. Saue, B. Darquié and J. Crassous, *Phys. Chem. Chem. Phys.*, 2013, **15**, 10952.
396 S. K. Tokunaga, C. Stoeffler, F. Auguste, A. Shelkovnikov, C. Daussy, A. Amy-Klein, C. Chardonnet and B. Darquié, *Mol. Phys.*, 2013, **111**, 2363–2373.
397 N. Saleh, R. Bast, N. Vanthuyne, C. Roussel, T. Saue, B. Darquié and J. Crassous, *Chirality*, 2018, **30**, 147–156.
398 C. Fábri, Ľ. Horný and M. Quack, *ChemPhysChem*, 2015, **16**, 3584–3589.
399 P. Dietiker, E. Miloglyadov, M. Quack, A. Schneider and G. Seyfang, *J. Chem. Phys.*, 2015, **143**, 244305.
400 S. Albert, I. Bolotova, Z. Chen, C. Fábri, L. Horný, M. Quack, G. Seyfang and D. Zindel, *Phys. Chem. Chem. Phys.*, 2016, **18**, 21976–21993.
401 S. Albert, F. Arn, I. Bolotova, Z. Chen, C. Fábri, G. Grassi, P. Lerch, M. Quack, G. Seyfang, A. Wokaun and D. Zindel, *J. Phys. Chem. Lett.*, 2016, **7**, 3847–3853.
402 S. Albert, I. Bolotova, Z. Chen, C. Fábri, M. Quack, G. Seyfang and D. Zindel, *Phys. Chem. Chem. Phys.*, 2017, **19**, 11738–11743.
403 Y. Yamagata, *J. Theor. Biol.*, 1966, **11**, 495–498.
404 S. F. Mason and G. E. Tranter, *Chem. Phys. Lett.*, 1983, **94**, 34–37.
405 S. F. Mason and G. E. Tranter, *J. Chem. Soc. Chem. Commun.*, 1983, 117–119.
406 S. F. Mason and G. E. Tranter, *Proc. R. Soc. Lond. Math. Phys. Sci.*, 1985, **397**, 45–65.
407 G. E. Tranter, *Chem. Phys. Lett.*, 1985, **115**, 286–290.
408 G. E. Tranter, *Mol. Phys.*, 1985, **56**, 825–838.
409 G. E. Tranter, *Nature*, 1985, **318**, 172–173.
410 G. E. Tranter, *J. Theor. Biol.*, 1986, **119**, 467–479.
411 G. E. Tranter, *J. Chem. Soc. Chem. Commun.*, 1986, 60–61.
412 G. E. Tranter, A. J. MacDermott, R. E. Overill and P. J. Speers, *Proc. Math. Phys. Sci.*, 1992, **436**, 603–615.
413 A. J. MacDermott, G. E. Tranter and S. J. Trainor, *Chem. Phys. Lett.*, 1992, **194**, 152–156.
414 R. Wesendrup, J. K. Laerdahl, R. N. Compton and P. Schwerdtfeger, *J. Phys. Chem. A*, 2003, **107**, 6668–6673.
415 G. Lente, *Symmetry*, 2010, **2**, 767–798.
416 A. J. Macdermott, *Chirality*, 2012, **24**, 764–769.
417 A. J. MacDermott, T. Fu, R. Nakatsuka, A. P. Coleman and G. O. Hyde, *Orig. Life Evol. Biospheres*, 2009, **39**, 459–478.
418 D. K. Kondepudi and G. W. Nelson, *Nature*, 1985, **314**, 438–441.

419 N. A. Hawbaker and D. G. Blackmond, *Nat. Chem.*, 2019, **11**, 957–962.
420 A. G. W. Cameron and J. W. Truran, *Icarus*, 1977, **30**, 447–461.
421 P. Bargueño and R. Pérez de Tudela, *Orig. Life Evol. Biospheres*, 2007, **37**, 253–257.
422 P. Banerjee, Y.-Z. Qian, A. Heger and W. C. Haxton, *Nat. Commun.*, 2016, **7**, 13639.
423 J. Takahashi and K. Kobayashi, *Symmetry*, 2019, **11**, 919.
424 F. Vester, T. L. V. Ulbricht and H. Krauch, *Naturwissenschaften*, 1959, **46**, 68–68.
425 T. L. V. Ulbricht, *Q. Rev. Chem. Soc.*, 1959, **13**, 48–60.
426 T. L. V. Ulbricht and F. Vester, *Tetrahedron*, 1962, **18**, 629–637.
427 A. S. Garay, *Nature*, 1968, **219**, 338–340.
428 A. S. Garay, L. Keszthelyi, I. Demeter and P. Hrasko, *Nature*, 1974, **250**, 332–333.
429 W. A. Bonner, M. a. V. Dort and M. R. Yearian, *Nature*, 1975, **258**, 419–421.
430 W. A. Bonner, M. A. van Dort, M. R. Yearian, H. D. Zeman and G. C. Li, *Isr. J. Chem.*, 1976, **15**, 89–95.
431 L. Keszthelyi, *Nature*, 1976, **264**, 197–197.
432 L. A. Hodge, F. B. Dunning, G. K. Walters, R. H. White and G. J. Schroepfer, *Nature*, 1979, **280**, 250–252.
433 M. Akaboshi, M. Noda, K. Kawai, H. Maki and K. Kawamoto, *Orig. Life*, 1979, **9**, 181–186.
434 R. M. Lemmon, H. E. Conzett and W. A. Bonner, *Orig. Life*, 1981, **11**, 337–341.
435 T. L. V. Ulbricht, *Nature*, 1975, **258**, 383–384.
436 W. A. Bonner, *Orig. Life*, 1984, **14**, 383–390.
437 R. Naaman, D. N. Beratan and D. Waldeck, Eds., *Electronic and Magnetic Properties of Chiral Molecules and Supramolecular Architectures*, Springer Berlin Heidelberg, Berlin, Heidelberg, 2011, vol. 298.
438 V. I. Burkov, L. A. Goncharova, G. A. Gusev, K. Kobayashi, E. V. Moiseenko, N. G. Poluhina, T. Saito, V. A. Tsarev, J. Xu and G. Zhang, *Orig. Life Evol. Biospheres*, 2008, **38**, 155–163.
439 G. A. Gusev, K. Kobayashi, E. V. Moiseenko, N. G. Poluhina, T. Saito, T. Ye, V. A. Tsarev, J. Xu, Y. Huang and G. Zhang, *Orig. Life Evol. Biospheres*, 2008, **38**, 509–515.
440 J. M. Dreiling and T. J. Gay, *Phys. Rev. Lett.*, 2014, **113**, 118103.
441 J. M. Dreiling, F. W. Lewis, J. D. Mills and T. J. Gay, *Phys. Rev. Lett.*, 2016, **116**, 093201.
442 D. C. Walker, *Acc. Chem. Res.*, 1985, **18**, 167–173.
443 R. A. Rosenberg, M. Abu Haija and P. J. Ryan, *Phys. Rev. Lett.*, 2008, **101**, 178301.
444 R. A. Rosenberg, D. Mishra and R. Naaman, *Angew. Chem. Int. Ed.*, 2015, **54**, 7295–7298.
445 B. Göhler, V. Hamelbeck, T. Z. Markus, M. Kettner, G. F. Hanne, Z. Vager, R. Naaman and H. Zacharias, *Science*, 2011, **331**, 894–897.
446 R. Naaman and D. H. Waldeck, *Annu. Rev. Phys. Chem.*, 2015, **66**, 263–281.
447 R. Naaman, Y. Paltiel and D. H. Waldeck, *Nat. Rev. Chem.*, 2019, **3**, 250–260.
448 T. S. Metzger, S. Mishra, B. P. Bloom, N. Goren, A. Neubauer, G. Shmul, J. Wei, S. Yochelis, F. Tassinari, C. Fontanesi, D. H. Waldeck, Y. Paltiel and R. Naaman, *Angew. Chem. Int. Ed.*, 2020, **59**, 1653–1658.
449 K. Michaeli, N. Kantor-Uriel, R. Naaman and D. H. Waldeck, *Chem Soc Rev*, 2016, **45**, 6478–6487.
450 R. A. Rosenberg, *Symmetry*, 2019, **11**, 528.
451 M. A. Famiano, R. N. Boyd, T. Kajino and T. Onaka, *Astrobiology*, 2017, **18**, 190–206.

452 R. N. Boyd, M. A. Famiano, T. Onaka and T. Kajino, *Astrophys. J.*, 2018, **856**, 26.
453 M. A. Famiano, R. N. Boyd, T. Kajino, T. Onaka and Y. Mo, *Sci. Rep.*, 2018, **8**, 8833.
454 T. D. Stephens, C. J. W. Bunde and B. J. Fillmore, *Biochem. Pharmacol.*, 2000, **59**, 1489–1499.
455 M. W. van der Meijden, M. Leeman, E. Gelens, W. L. Noorduin, H. Meekes, W. J. P. van Enckevort, B. Kaptein, E. Vlieg and R. M. Kellogg, *Org. Process Res. Dev.*, 2009, **13**, 1195–1198.
456 W. L. Noorduin, B. Kaptein, H. Meekes, W. J. P. van Enckevort, R. M. Kellogg and E. Vlieg, *Angew. Chem. Int. Ed.*, 2009, **48**, 4581–4583.
457 R. R. E. Steendam, M. C. T. Brouwer, E. M. E. Huijs, M. W. Kulka, H. Meekes, W. J. P. van Enckevort, J. Raap, F. P. J. T. Rutjes and E. Vlieg, *Chem. – Eur. J.*, 2014, **20**, 13527–13530.
458 Q. Zhang, L. Jia, J.-R. Wang and X. Mei, *CrystEngComm*, 2016, **18**, 8834–8837.
459 I. Baglai, M. Leeman, R. M. Kellogg and W. L. Noorduin, *Org. Biomol. Chem.*, 2019, **17**, 35–38.
460 G. Belletti, C. Tortora, I. D. Mellema, P. Tinnemans, H. Meekes, F. P. J. T. Rutjes, S. B. Tsogoeva and E. Vlieg, *Chem. – Eur. J.*, 2020, **26**, 839–844.
461 W. Shimizu, N. Uemura, Y. Yoshida, T. Mino, Y. Kasashima and M. Sakamoto, *Cryst. Growth Des.*, 2020, **20**, 5676–5681.
462 C. Sanchez, H. Arribart and M. M. Giraud Guille, *Nat. Mater.*, 2005, **4**, 277–288.
463 C. Train, M. Gruselle and M. Verdaguer, *Chem. Soc. Rev.*, 2011, **40**, 3297–3312.
464 J. R. Brandt, F. Salerno and M. J. Fuchter, *Nat. Rev. Chem.*, 2017, **1**, 1–12.
465 S. M. Morrow, A. J. Bissette and S. P. Fletcher, *Nat. Nanotechnol.*, 2017, **12**, 410–419.
466 W. Jiang, D. Athanasiadou, S. Zhang, R. Demichelis, K. B. Koziara, P. Raiteri, V. Nelea, W. Mi, J.-A. Ma, J. D. Gale and M. D. McKee, *Nat. Commun.*, 2019, **10**, 2318.
467 K. Ariga, T. Mori, T. Kitao and T. Uemura, *Adv. Mater.*, 2020, **32**, 1905657.

Chapter II Supramolecular helical polymers displaying extremely high chirality amplification properties: implementation in asymmetric catalysis

Abstract

Although it has theoretical and industrial interests, to perform asymmetric reactions with little or no help of chiral entities is yet to be harnessed. Supramolecular polymers – chain-like molecular self-assemblies – constitute an opportunity in this regard. Their dynamic features bring about strong chirality amplification properties through the cooperative transfer of a chiral bias from the monomer to the supra-macromolecular level. Strategies for controlling the helicity of supramolecular polymers mainly constituted of achiral buildings blocks start to emerge. On one hand, by using a non-chemical but truly chiral bias – the circularly polarized light (CPL), the handedness of supramolecular polymers devoid of chiral centers can be biased and controlled thanks to the rotational direction of CPL. On the other hand, asymmetric catalysis with supramolecular polymers, generated upon co-assembly of many achiral metal complexes (catalytic centers) and few enantiopure complementary co-monomers, was successfully carried out. The supramolecular chirality is induced to the peripheral catalytic moiety, which in turn specifically directs the catalytic reaction towards the formation of a preferred enantiomer. Coupling both strategies constitute the final goal of this thesis. Indeed, controlling the handedness of helical supramolecular polymers by CPL and performing catalysis by centers present at the helix periphery, would constitute a general route towards absolute asymmetric catalysis.

I. Introduction

How chirality emerges from scratch? This question concerns the mysterious biological homochirality and one of its consequences: the contemporary challenge of synthesizing enantiopure bioactive molecules. Enantiopurity is reached either thanks to the resolution of racemates[1–7], for example through chromatographic or crystallization techniques; or by asymmetric synthesis[8–10] with microorganisms[11,12] as well as natural chiral building blocks (the "chiral pool")[13], auxiliaries[14] or catalysts[15–19]. While separating enantiomers is expensive and exploiting the chiral pool is limited, the nowadays well-known asymmetric catalysis still uses chiral species to transfer chirality to the desired final products. Indeed, all industrial processes rely on chiral compounds to produce new chiral products, which often translate into limited scope and additional cost. A great challenge is therefore to get rid of any chiral species to generate enantiopure molecules. This is the promise of absolute asymmetric synthesis (AAS), which deals with the formation of enantiomerically enriched products without help of chiral chemical entities[20,21].

To this end, studies aimed at elucidating biological homochirality are a source of inspiration (see Chapter I). Many examples of spontaneous mirror-symmetry breaking (SMSB) phenomena demonstrated that enantioenriched products can stem from achiral compounds or racemic mixtures[22,23]. For molecular systems, the most efficient processes which rely on auto-catalytic reaction (Soai reaction) or attrition-enhanced deracemization (Viedma ripening) have limited scope. For supramolecular and macromolecular systems, chirality discrimination or synchronization led to single-handed assemblies but the isolated building blocks display no optical chirality. In any case, the final chiral state is left to chance because it results from an amplification of an initial statistical fluctuation.

A physical field can therefore be envisaged to direct the outcome of the synthesis. Circularly polarized light is worthy of interest both in this regard and in the context of elucidating the origin of bio-homochirality. Circularly polarized UV–Visible electromagnetic radiations are easier to implement than sources of chiral fermions or combined magnetic field/light beam, and cover a broad spectrum since all molecules exhibiting circular dichroism can in principle be enantio-enriched by single-handed CPL. Three types of enantioselective

conversions exist: the preferential photolysis of one of the two enantiomers of a racemate (irreversible); the asymmetric photosynthesis of an enantioenriched product from a prochiral substrate (irreversible); and the asymmetric photoresolution, consisting of the deracemization of interconvertible enantiomers of a racemate (reversible)[24]. However, the enantiomeric excess resulting from the photoresolution process depends on the chiroptical response of molecules, quantified by the dissymmetry factor *g* (equal to $\Delta\varepsilon/\varepsilon$), which is usually quite small ($|g| \approx 10^{-4}$–10^{-2})[25,26], giving birth to *e.e.* of a few percent at best ($e.e._{pss} = g/2$ with $e.e._{pss}$ being the enantiomeric excess at the photostationary state of a reversible photoresolution process)[24]. Nevertheless, this small *e.e.* can be amplified by chiral synchronization if the chromophore is incorporated into larger entities like macromolecules or assemblies, through the cooperative transfer of a chiral bias from the monomer to the (supra-)macromolecular level. For instance, single-handed polymers[27], liquid crystalline phases[28] or supramolecular polymers[29–31] were obtained following CPL irradiation. Therefore, coupling reversible photoresolution by CPL and chirality amplification processes must be envisaged as an efficient strategy for promoting absolute asymmetric synthesis. The final step is to find a way to convert the CPL-controlled (supra-)macromolecular handedness into an AAS process. For this purpose, employing the CPL-oriented homochiral helices as asymmetric catalysts looks promising[32–34].

In this context and with the aim of defining the topic and objectives of this thesis, the following paragraphs will introduce the design of a new strategy able to afford absolute asymmetric synthesis in a rational and predictable manner, by means of supramolecular helical polymers of discotic low-molecular weight molecules supporting asymmetric metal catalysts. After a short overview of supramolecular polymers, and in particular helical assemblies made of disk-like molecules, their abilities to amplify chirality will be described, as well as the way to couple them with CPL and catalysis for AAS.

II. General Aspects of Supramolecular Polymers

The term polymer was first coined by Jöns Jakob Berzelius in 1832, when it vaguely referred to "colloidal aggregates of small particles or molecules"[35]. Almost one hundred years later, in 1920[36], Hermann Staudinger identified polymers with macromolecules through the hypothesis of *Hochmolekulare Verbindungen*, literally high-molecular weight compounds.

While another century passed, polymer materials, thereby understood as composed of macromolecules based on the multiple repetition of monomer units linked by covalent bonds, progressively invaded our lives and lands. Polymeric arrays of saccharides, peptides or nucleic acids were recognized in key functions of living organisms, and engineered polymers found innumerable applications in all product ranges thanks to a broad spectrum of structures and properties.

Over the last thirty years, supramolecular polymers emerged in a context where the high stability of macromolecular polymers became a drawback (for instance whether they transform into widespread wastes) and the reversibility coveted (e.g. for better stimuli-responsive properties). The field of supramolecular polymers has gradually drifted away from colloids and liquid crystals, by bringing together polymeric materials with supramolecular chemistry. Supramolecular polymers are self-assemblies of monomeric units (e.g. molecules, oligomers, dendrimers, foldamers or macromolecules) held together by reversible and directional noncovalent interactions, such as hydrogen bonds or π–π stacking[37]. Secondary interactions are actually a key component of natural and synthetic macromolecular polymers. Proteins secondary structures, the DNA double helix as well as the high mechanical properties of nylon have all to do with the combination of covalent and noncovalent interactions.

The uniqueness of supramolecular polymers lies in the nature of their cohesive forces. Noncovalent interactions are about ten times weaker than usual covalent bonds (up to some tens against hundreds kJ/mol)[38], which allows, through fine-tuning of their nature and arrangement, to reach intermediate bond lifetimes, typically ranging from milliseconds to the minute[39]. It makes them stable enough to give material properties to supramolecular polymers, although being reversible through dissociation-reassociation, even at room temperature, so that monomers spontaneously and continuously rearrange within polymeric structures. The dynamic nature of supramolecular polymers can serve many purposes, such as yielding materials adaptable to their environment, with more subtlety than in fully covalent systems[40]. Notably, the nature and structure of supramolecular polymers can be modulated, through either internal change on the chemical structures and composition of monomers, or thanks to one or multiple external stimuli (e.g. temperature, concentration, solvent polarity, redox potential, light, mechanical motion and so on[41–45]).

Passing through a critical condition, either by changing the concentration, the temperature or the solvent composition, usually triggers the supramolecular polymerization. Despite an untouched chemical structure of monomers in the case of self-assembly – owing to the absence of any chemical reaction, the formation of supramolecular assemblies mainly follows the two same mechanisms than their covalent counterparts, either isodesmic (supramolecular)/step–growth (covalent) or nucleation–elongation (supramolecular)/chain-growth (covalent) polymerizations (**Figure II.1**)[46–48]. In the isodesmic pathway the association constant between the monomer and growing chain is constant. On the contrary, the nucleation-elongation pathway is initiated by the formation of aggregates composed of few to tens molecules, which then grow at a different rate. Nucleation–elongation is either cooperative or anti-cooperative, and results in polymeric or oligomeric assemblies, respectively, if the elongation is faster or slower than nucleation. Like covalent ones, supramolecular polymerizations give birth to varied morphologies across all dimensions (from 0D nanoparticles and 3D networks to 1D rods and 2D sheets)[35,39,49,50]. Consequently, physical properties of supramolecular polymers resemble those of macromolecular materials – where entanglements and crosslinks do much contrary to the removal of few constitutional units, and thereby benefit from the well-established polymer theories. Altogether, the field of supramolecular polymers is now an integral part of the Polymer Science, no longer considered solely in terms of macromolecules, but finding again the meaning of a polymolecular association, in keeping with its etymological sense joining ‘many’ (*polús*) with ‘part’ (*méros*) as a fraction of a whole[50].

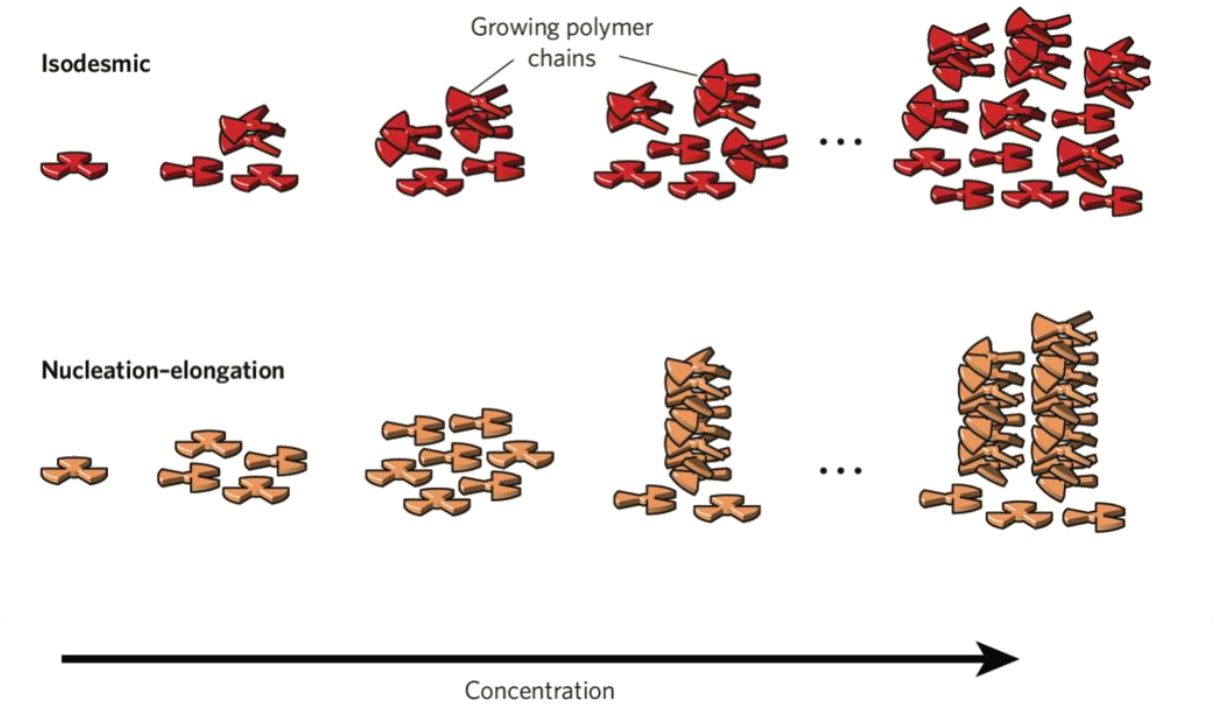

Figure II.1 Isodesmic and nucleation–elongation supramolecular polymerization mechanisms. Reprinted from de Greef and Meijer[51].

The conformational plasticity of the supramolecular aggregates also strongly subjects the self-assembly process to kinetic contributions, often up to non-equilibrium states[52]. One set of building-blocks can produce different aggregates, according to the "interplay between thermodynamic and kinetic pathways"[53]. A special use of such pathway complexity is the possibility to control the supramolecular polymerization, taking advantage of out-of-equilibrium species to drive the degree of polymerization with narrow dispersity, and to form supramolecular copolymers with the desired composition. In short, recent progress in the domain of supramolecular polymers is related to the control of their structure, their dynamic nature and their implementation in various fields.

III. Helical Supramolecular Polymers of Disk-like Molecules

Of the full range of morphologies adopted by supramolecular polymers, those adopting a helical configuration are particularly appealing[54,55], since Mother Nature showed the relevance of the helical geometry to achieve striking functionalities, such as improved stability and catalytic performance. By definition, helicity is the (axial) chirality of "an entity that has an axis about which a set of substituents is held in a spatial arrangement that is not superimposable on its mirror image"[56] (viz. of a spiral nature), and is specified by *P* (plus) or *M* (minus) stereodescriptors for *right*- and *left*-handed helices, respectively (*Δ* and *Λ* are also found in the same respect)[57]. *Right* (*left*-)-handed helical supramolecular polymers have monomers tracing out a clockwise (counter-clockwise, resp.) rotation moving away from the observer (see **Figure II.2** for an example of *right*-handed supramolecular helix). Note that in this way, helices are inherently chiral and do not need chiral building blocks. Supramolecular helices are found at various scales, especially when interactions between them favor superstructures, sometimes through several intermediary hierarchical levels from the nanometer to microns[54]. In this case, the handedness at one level does not presage of the one of the others[58].

Among the wide library of molecules able to form helical supramolecular polymers, disk-shaped molecules are an insightful class of monomers. They often display a rotational symmetry and consist of a flat and rigid aromatic core, connected to flexible peripheral chains by different linking groups (e.g. amide, urea). Discotic molecules self-assemble into nanometer-sized one-dimensional supramolecular assemblies, stabilized by a combination of aromatic interactions and hydrogen bonds. Derivatives of benzene-1,3,5-tricarboxamide (BTA), C_3-symmetrical molecule composed of a central aromatic ring connected at 1, 3 and 5 positions to side chains through amide bonds (**Figure II.2**), were perhaps the most extensively studied[59]. They owe this to their simple structure, wide accessibility and ease of chemical modifications, which allowed the in-depth understanding of their supramolecular self-assembly behavior[60–64]. It is in addition noteworthy that BTA compounds form helical supramolecular polymers. Indeed, from solution to helical stair-wise self-assemblies, the freedom of rotational motion of BTA molecules is reduced eventually yielding an axially chiral propeller-like assembly. This

structure is the lowest in energy, fruit of the compromise between maintaining both π–π staking and H-bond interactions between two successive BTA units in the stacks despite these interactions displaying different geometrical requirements (3.5 *vs.* 4.5 Å for π–π stacking and hydrogen bonds, respectively), which in turn leads to the tilt of amide groups out of the arene plane[65].

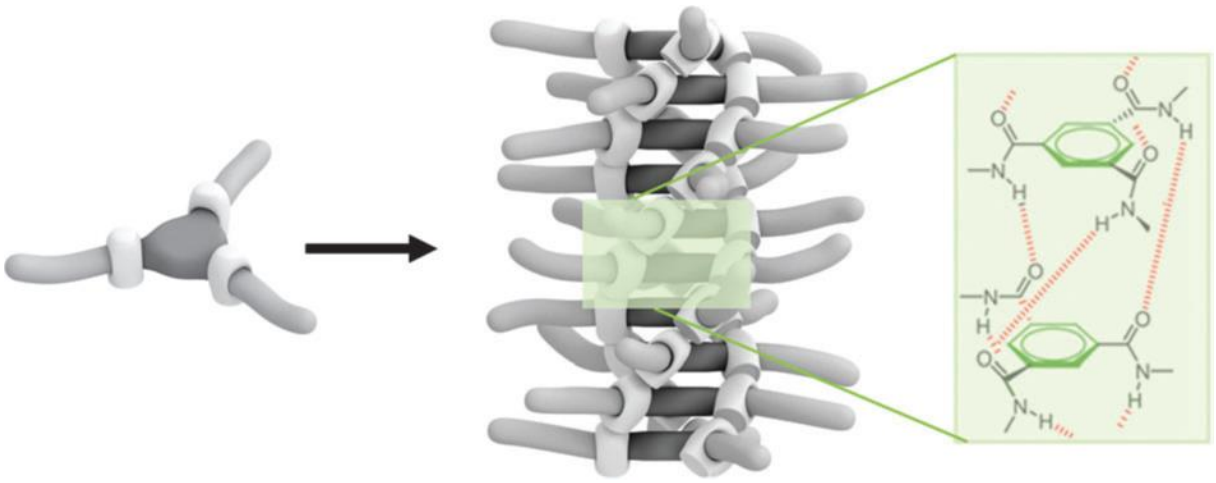

Figure II.2 Schematic representation of a *right*-handed helical supramolecular polymer built upon the assembly of benzene-1,3,5-tricarboxamide (BTA) by π–π stacking and a threefold hydrogen bonds network. Reprinted from Palmans *et al.*[59]

The helicity of supramolecular polymers is mainly characterized by microscopic and spectroscopic techniques. The strength of microscopes enables the morphological observation on the 10-100 nm scale (typical of bundles of fibrils), when "seeing is believing"[56] (e.g. in **Figure II.3**). Yet, results should be carefully interpreted, because the preparation of samples is mostly accompanied by phase change (e.g. evaporation in atomic force and scanning tunneling microscopies) and chemical treatment (e.g. staining with heavy metals in scanning and transmission electron microscopies) that might modify the self-assembly structure comparatively to the one present in solution. Cryogenic electronic microscopy can dispel doubts, since it preserves the solution-state by analyzing a thin film of vitrified liquid, but with difficulty for implementation in the case of organic solvents[66].

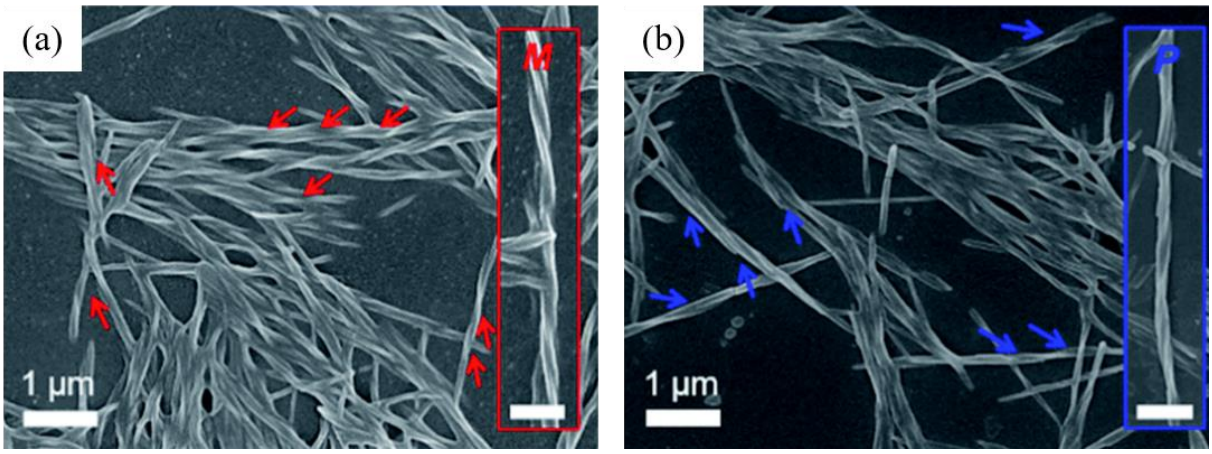

Figure II.3 Scanning electron microscopy images of (a) (*M*) *left*- and (b) (*P*) *right*-handed helical structures of BTA assemblies. Arrows point out the helical turns. Adapted from Liu *et al.*[67].

Chiroptical spectroscopic techniques, and especially the electronic circular dichroism (ECD), are tools of choice to monitor in a non-destructive way the dynamical processes of self-assemblies in solution, due to matching time scales and the ease of implementation[68–71]. By probing electronic transitions of chromophores absorbing circularly ultraviolet and visible light, ECD is sensitive to first-neighbor effects. It makes them relevant to elucidate molecular absolute configurations and the conformation of first-order supramolecular aggregates.

Usually, chromophores are not chiral *per se* and, at the monomeric state, their electronic transition exhibit either no CD if the molecule is achiral, or a quite undetectable CD signal of a few mdeg and a g value of about 10^{-4} when the chiral perturbation comes from a remote stereogenic element. However, as soon as molecules aggregate into supramolecular helices, their chromophores in close contact likely adopt a helical packing, associated to a strong bisignate Cotton effect around a hundred mdeg and a g value around 10^{-2}. This phenomenon, called exciton coupling, comes from the through-space interaction between chromophores that mutually perturbate each other. It leads to the in- or out-of-phase combination of their electronic transition dipole moments (TDMs), splitting the excited states into two energy levels of high and low energy, respectively, while the ground state remains unsplit.

Many information may be deduced at first glance from CD and UV-visible absorption spectra attributed to an exciton coupling (**Figure II.4**). Assemblies where molecules are arranged face-to-face, known as H-aggregates, only have an UV-active transition to the high-

energy state, which causes a hypsochromic (blue) shift of the absorption band. On the other hand, the UV-active transition of J-aggregates, where molecules are arranged head-to-tail, just reach the low-energy state and is accompanied by a bathochromic (red) shift of the absorption band. CD spectra allow to monitor the aggregation process, from the formation of helical assemblies to superstructures, since CD signals vary in a more sensitive and noticeable way than UV–visible ones. It gives also the sense of the helical arrangement of the electric TDMs of interacting chromophores. They shape a *right*-handed helix when the CD describe a positive exciton couplet (first positive upon decreasing wavelength then negative). That said, the helical sense of the TDMs should not be confused with the helicity of the supramolecular polymer, which might sometimes be different. In addition, the CD bands shape depends on many factors (distance and angle between chromophores, vibronic coupling, effects of other chromophores and chiroptical phenomena) that calls for caution when qualitatively and quantitatively interpreting CD spectra.

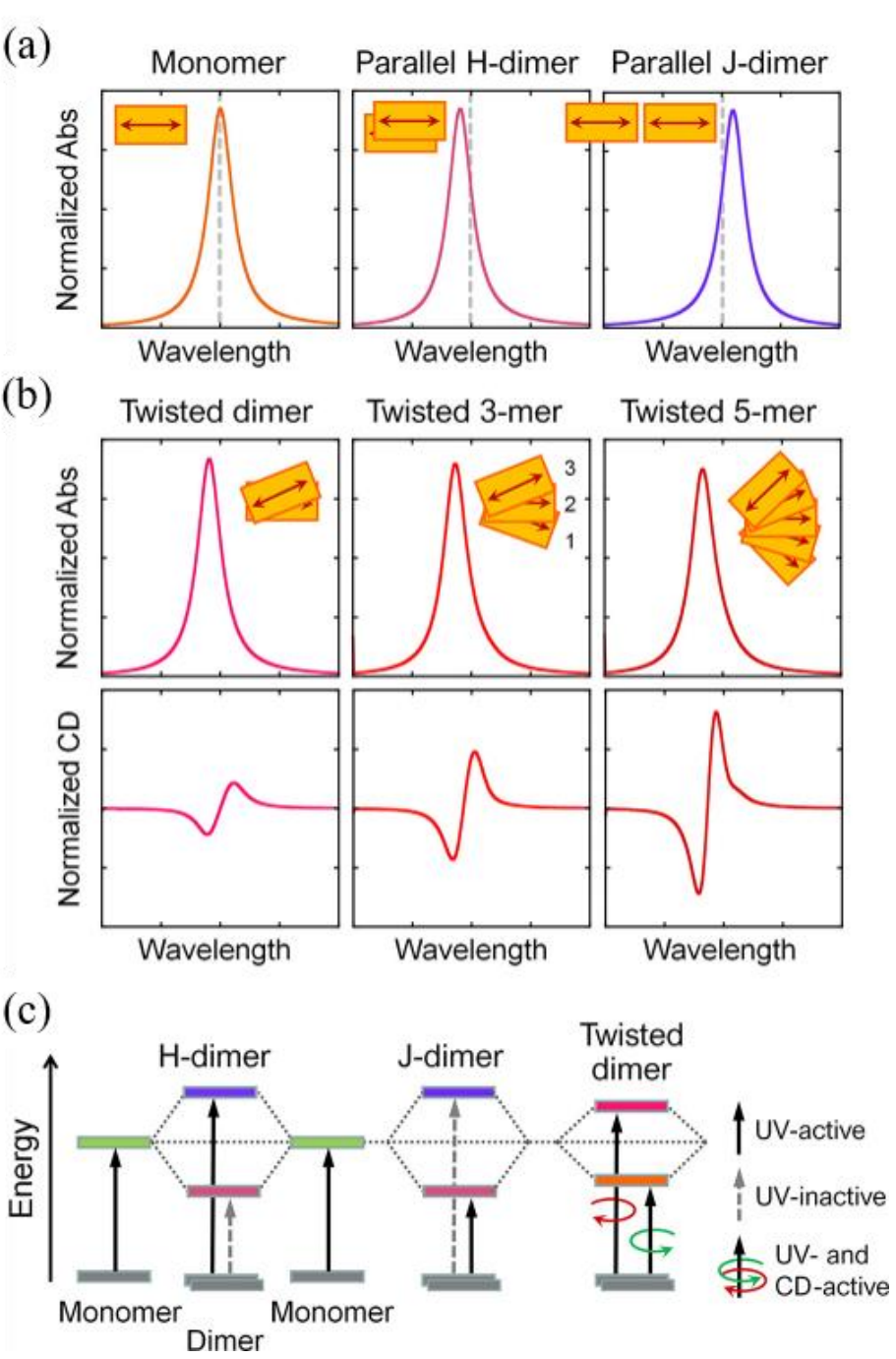

Figure II.4 Illustration of the exciton coupling mechanism for idealized models. (a) Absorption spectra of a monomer and achiral H- and J-dimers, leading to a hypsochromic and bathochromic shift of the absorption band, respectively. (b) Absorption and ECD spectra of a twisted dimer, trimer, and pentamer in a *right*-handed fashion. The double arrows denote the direction of the TDMs of interacting chromophores, sketched as orange rectangles, while the dashed vertical lines indicate the position of the monomer absorption band. The spectra are normalized per monomer. (c) Energy level diagrams showing

UV- and CD-active transitions for H-type, J-type, and twisted dimers. Reprinted from and partially citing Di Bari *et al.*[58]

In the majority of cases, the assembly of achiral monomers lead to the formation of *left*-handed and *right*-handed helices, in equal number (at least according to the limit of detection of the conventional analytical techniques employed) which is what is expected in the absence of chiral biases. However, in a limited number of examples[72–79], helical aggregates of preferential handedness have been detected upon the self-assembly of achiral BTA molecules. In the case reported by Meijer *et al.* in 2012, the supramolecular assembly of achiral BTAs with partially fluorinated side chains resulted in fibers with a repeatable bias towards one handedness, which was thus ascribed to cryptochirality (*i.e.* chiral compound below the detection limit)[72]. In contrast, Liu *et al.* unveiled a stochastic distribution in the predominant chirality of helical ribbons (bundles of fibers) within supramolecular gels of BTA substituted with ethyl cinnamate (**Figure II.5**)[73]. The authors attributed this to a spontaneous mirror-symmetry breaking phenomenon, promoted by the steric hindrance of ethyl cinnamate substituents during the primary formation of helical aggregates, generating homochiral domains of unpredictable helicity by chirality synchronization *via* a secondary crystallization process. Remarkably, these enantioenriched supramolecular scaffolds exhibit strong circularly polarized luminescence[74,XXIV], and were reproduced with molecules of which the amide groups were replaced by ester function, suggesting that H-bonding is not necessary to trigger this intriguing phenomenon[75]. Finally, by replacing the ethyl cinnamate groups by benzoic acids, the same authors obtained mirror symmetry-broken helical aggregates too, employed as ligands for the Cu^{2+}-catalyzed Diels–Alder asymmetric reaction, with enantiomeric excesses up to 46%, thanks to the diastereoisomeric environment at the periphery of twisted ribbons[76]. A strong limitation of this SMSB processes applied to catalysis is that the nature of the major enantiomer is left to chance and its optical purity also varies from one reaction to another.

[XXIV] Differential emission intensity of *right*- and *left*-handed circularly polarized light upon light excitation.

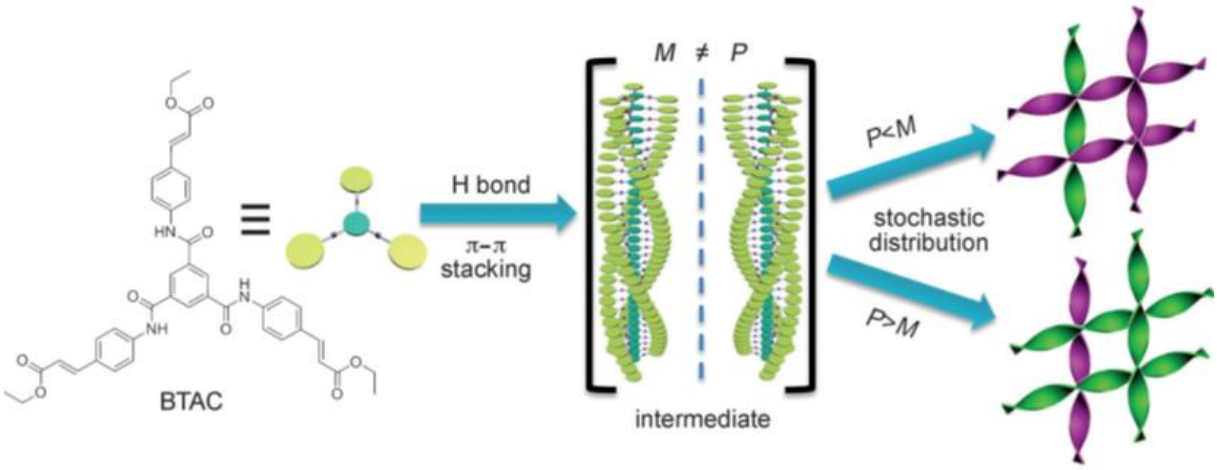

Figure II.5 Schematic representation of the hierarchical self-assembly of achiral tris(ethyl cinnamate) BTA (BTAC) into helical aggregates of supposed unequal conformation abundance, then bundling to form twisted ribbons of biased handedness. On 100 samples, 48 showed a *P* major conformation and 52 a *M* major conformation.

The most obvious chiral element which can be introduced to induce a preferential helicity is a chemical chiral group in building blocks, and a stereogenic center in side chains of the associative motif is the strategy mainly employed. In hindsight, enantiopure monomers establish a diastereomeric relationship between *P* and *M* helices, favoring one of both. At the supramolecular scale, the molecular chirality is cooperatively communicated to the helical assembly, from the twisted arrangement of the first monomers coming into contact upon aggregation. The helicity is thus governed by the building blocks, with an efficiency depending on "the distance of the chiral center to the assembly site, the strength of the noncovalent bonds, and the competition of the chiral and achiral interactions to name just a few."[56]

For instance, Meijer *et al.* measured the optical purity of assemblies of BTA monomers embedding chiral centers in their peripheral alkyl chains[80]. CD-silent at 90°C, the heptane solution of the **BTA-C8*** monomer exhibits a clear negative Cotton effect and a decrease in absorbance, accompanied by a hypsochromic shift of the main UV-Vis band at lower temperature (10°C, *cf.* **Figure II.6**). These changes correspond to the transition from chiral BTA as single molecules into H-aggregates, later ascribed by a combined experimental and computational study to *left*-handed helical supramolecular assemblies[61].

(a)

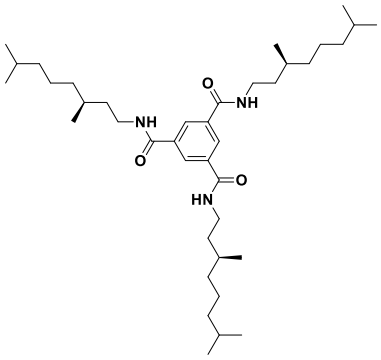

BTA-C8*

(b)

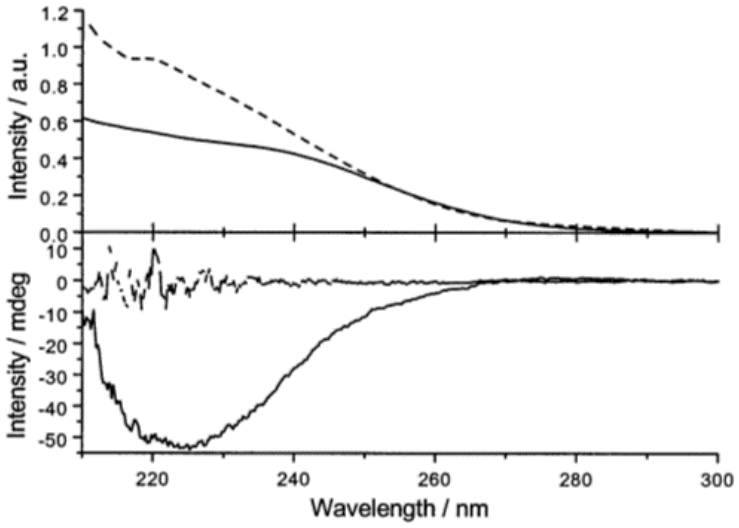

Figure II.6 (a) Molecular structure of the **BTA-C8*** used by Meijer *et al.*, substituted with (*S*)-3,7-dimethyloctyl. (b) Absorption (top) and circular dichroism (bottom) spectra at 90°C (dashed lines) and 10°C (solid lines) of **BTA-C8*** at 6.5×10^{-5} M in heptane. Reprinted from Meijer *et al.*[80]

IV. Chirality Amplification by Means of Chemical Chirality

As a result of their dynamic nature, the helical structure of a given supramolecular polymer will be affected by the experimental conditions such as concentration or temperature. Interestingly, this controllable manifestation of chirality can also be coupled with the enhancement of a chiral input, thanks to the strong cooperativity between monomeric units[81]. A tiny enantiomeric excess within monomers can be non-linearly amplified towards one preferential helix-sense[XXV]. The chirality amplification properties of supramolecular polymers was exploited through different approaches, mimicking the seminal works of Green *et al.* in the 1980s-90s with covalent – but dynamic – poly(isocyanate)s[84–86].

[XXV] With rare exceptions (two to the best of our knowledge)[82,83], only supramolecular polymers formed by nucleation-elongation, whose the mechanism has inherent cooperativity, show amplification of chirality[81].

The emblematic manifestations of asymmetry amplification properties are the "sergeants-and-soldiers" and "majority-rules" effects (S&S and MR, respectively). S&S and MR effects enable the control at the thermodynamic equilibrium of the polymer helicity, thanks to cooperative minute conformational biases induced by the monomer units up to single-handed helices. The S&S effect arises in copolymers of enantiopure ("sergeants") and achiral ("soldiers") monomer units, when a minor number of sergeants "is able to control the local conformation of an excess of soldiers, that cannot escape this influence except through rarely occurring helix reversals."[34] Similarly, the MR effect accounts for "copolymers constituted of a non-racemic (*i.e*. scalemic) mixture of enantiomeric monomers, in which the major enantiomer controls the main helicity of the polymer."[34] The combination of both S&S and MR effects is possible in the case of a terpolymer comprising achiral monomers (soldiers) and a scalemic mixture of chiral co-monomers (opposite sergeants). This so-called "diluted majority-rules" effect brings about enantioenriched helical aggregates too, with a handedness dictated by the most numerous sergeants. Thanks to the unrivaled dynamic properties of supramolecular polymers, note that the handedness of the helices can be inverted by changing the monomer feeding ratio. All these effects are illustrated in **Figure II.7**.

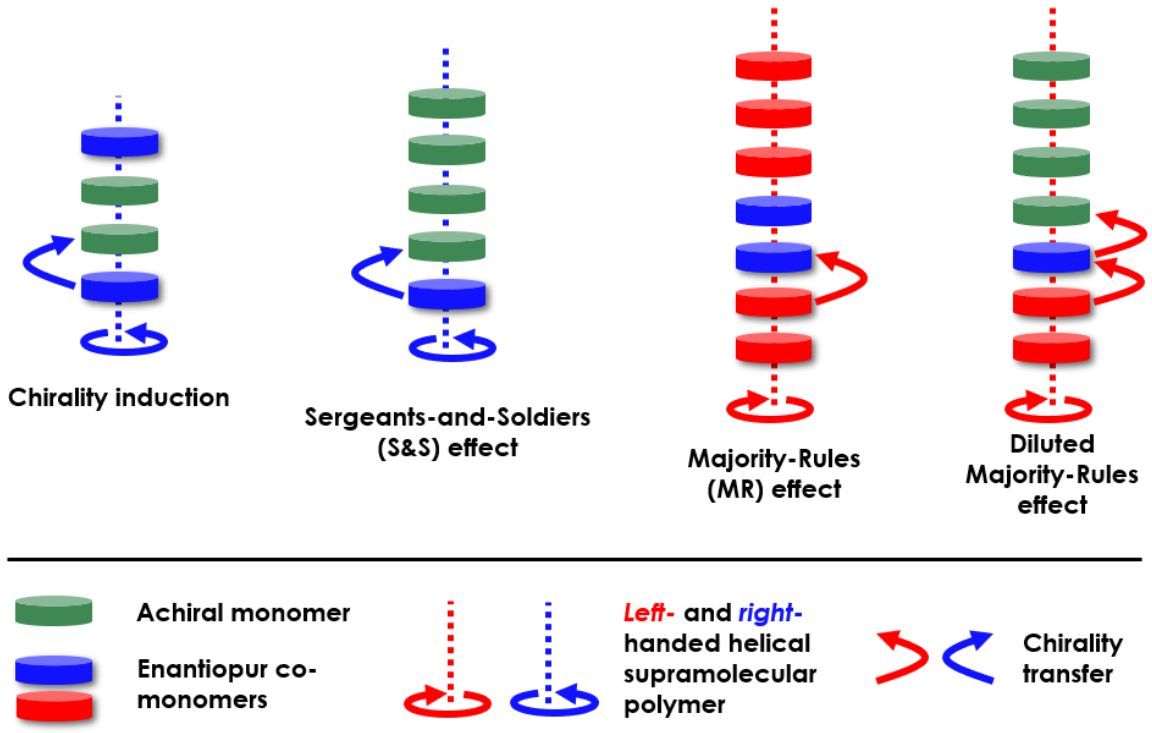

Figure II.7 Schematic illustration of chirality transfers in helical supramolecular polymers. The handedness of enantiopure monomers is induced to achiral co-monomers, thereby orientating the supramolecular chirality (chirality induction). Even in a minority, enantiopure molecules (sergeants) may dictate their chiral preference to achiral monomeric units (soldiers) and eventually to the helical scaffold (sergeants-and-soldiers effect). The supramolecular chirality of assemblies made of a scalemic mixture of opposite enantiomers is dictated by the enantiomer in majority, according to the majority-rules effect. In the presence of soldiers and both enantiomers, the most abundant sergeant governs the handedness of the assemblies.

Meijer *et al.* showed that amplification of chirality through S&S and MR effects is at work in supramolecular BTA polymers in 1997[87] and 2005[88], respectively. Homochiral BTA helices are formed for co-assemblies containing ca. 5% of enantiopure sergeants in the S&S mixture or a 20% *e.e.* in a scalemic mixture of enantiopure monomers in the MR mixture. Since then, the possibility of amplifying very weak chiral polarization was demonstrated for BTA and other supramolecular helical polymers. 6–10% of sergeants with isotope chirality, introduced by the substitution of a hydrogen by a deuterium into the alkyl side chains of a BTA monomer, are enough to impart a preferred but incomplete helicity to the resulting assemblies[89]. It

translated to a chiral preference of only 4.2 $J.mol^{-1}$ which, thanks to the high cooperativity, results in a helical structure with preferred handedness.

Again with BTA assemblies, our team reported in 2020 a counterintuitive beneficial effect of an achiral monomer unit on chirality amplification properties[90]. In the initially investigated sergeants-and-soldiers type mixture between **BTA^{PPh2}** and **BTA Cha** (**Figure II.8a**), more than fifty percent of the sergeants were required to get fully biased co-assemblies. However, upon addition of a second achiral BTA monomer (**a-BTA**), the chiral induction ability of the sergeants was considerably enhanced, and no more than 0.5% of sergeants was needed to afford single-handed helices (**Figure II.8b**). Similarly, the achiral additive improves the diluted majority-rules effect by making an enantiomeric excess of 10% in a scalemic mixture of enantiopure monomers mixed with soldiers enough to induce homochiral helical assemblies (**Figure II.8c**). Spectroscopic and scattering analytical techniques showed that the achiral additive does not modify the geometry and length of aggregates (>0.1 µm one-dimensional helical assemblies), but makes their hydrogen bonds network stronger and more regular, yielding more stable assemblies upon heating and less conformational defects such as helix reversals. These effects were related to the molecular structure of the additive, including a cyclohexyl group attached on the amide α-carbon "expected to reduce the conformational freedom of the amide functions and thus to rigidify the hydrogen-bonded network between the complementary monomers in the co-assemblies."[90]

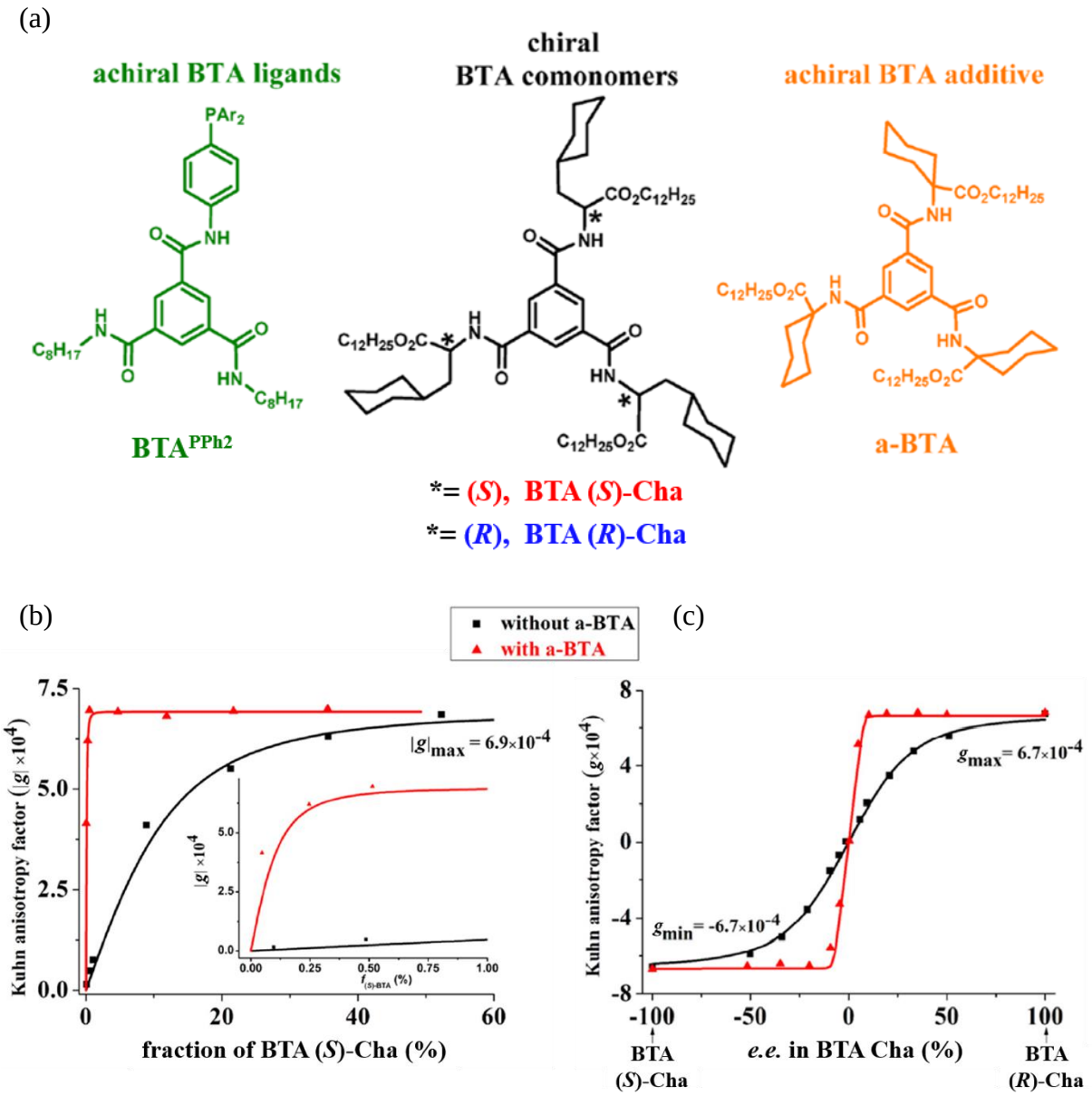

Figure II.8 (a) Structures of molecules used in the study of Raynal *et al.* Chirality amplification through the (b) S&S and (c) diluted majority-rules effects. Kuhn anisotropy factor (g) as a function of (b) the fraction of **BTA (*S*)-Cha** (sergeant) or (c) the optical purity of sergeants (**BTA Cha**) in the mixtures, with and without the additional achiral monomer (**a-BTA**). g was measured at a wavelength corresponding to the maximum CD (295 nm), and allows to normalize the tiny variations of absorbance. The plateau is attributed to the obtention of homochiral helices. Adapted from Raynal *et al.*[90]

The assemblies composed of triarylamine trisamide (TATA) also show great chirality amplification properties. This class of amine substituted by three aryl groups linked to side

chains *via* an amide bond exhibits a very high degree of chirality amplification: only 0.2-mol% of sergeants can fully control the handedness of the TATA helices[91]. Such a characteristic results from the dynamic chiral propeller-like structure of TATA arising from the three aryl groups swiveled out of the plane (depicted in **Figure II.9**). Indeed in triphenylamine, from which TATA derived from, the dihedral angle between the plane of the central NCCC moiety and those of the phenyl rings is around ± 45°[92,93], due to the competition between the delocalization of the lone pair electrons and the steric hindrance of aromatic rings. Additionally, in supramolecular assemblies, TATA molecules are held together by hydrogen bonds and aromatic interactions, which therefore connect the *Δ*- or *Λ*-propeller conformation of NCCC moiety to the handedness of the helices. Thereby, inverting the handedness of TATA helices would require a considerable energy in order to rotate amide and aryl groups of all assembled molecules (as illustrated in **Figure II.9**). In this way, helix reversals are scarce and a low fraction of sergeants allows to dictate the handedness of plenty of soldiers (0.2% which means one sergeant for 500 soldiers, *cf.* **Figure II.10b**).

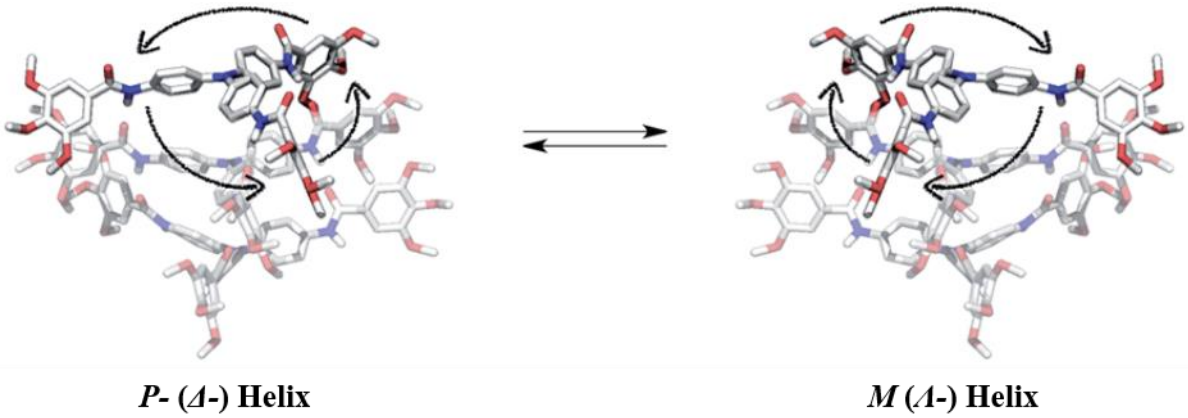

Figure II.9 Schematic representation of a trimeric TATA model close to the molecules used by Miyajima *et al.* (depicted in **Figure II.10a**), calculated by density function theory method (DFT) by them[91].

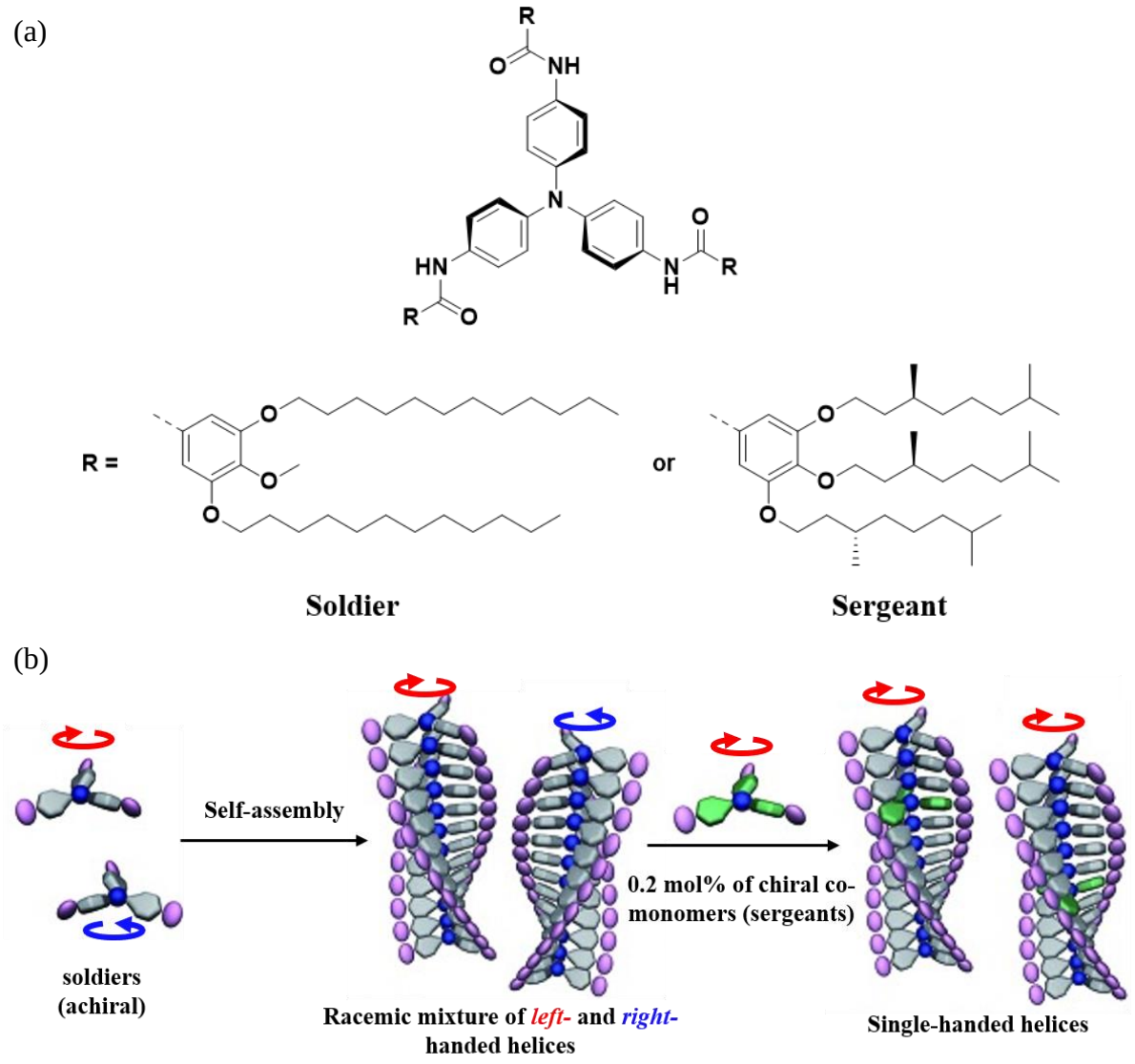

Figure II.10 (a) Structures of TATA molecules used by Miyajima *et al.* (b) Schematic illustration of the self-assembly and sergeants-and-soldier effect in an extremely chirally amplified helical TATA. Adapted from Miyajima *et al.*[91]

The strong amplification properties of supramolecular polymers enable a tiny enantiomeric imbalance to cooperatively proliferate, and produce single-handed helices in a well-controlled manner. SMSB phenomena confirmed that smallest cryptochiral and statistical influences may lead to macroscopic homochiral domains. It is then a short step to expect that non-chemical influences like CPL could be able to orientate the supramolecular helicity.

V. Chirality Amplification by Means of CPL

The dynamic nature of supramolecular polymers opens up many opportunities of control not only of their degree of polymerization, but also of their structure (e.g. shape or hierarchical level). The control of the supramolecular chirality of helical self-assemblies, directly impacting their (super)structures and properties, gained interest owing to multiplying and diversifying applications such as asymmetric supramolecular catalyst[34], chiral sensor and chromatographic stationary phase[94], materials for the production and detection of CPL[95], materials exhibiting magneto-chiral dichroism,[96] chiroptical switch for information storage[94], electron spin filter[97] and so on.

Modifying the environment of supramolecular polymers by means of an external stimulus (e.g. light irradiation, magnetic or mechanical fields) offers many possibilities such as "*in situ* morphological transformation of building blocks"[41]. Moreover, external stimuli like light irradiations are non-invasive[94,98,99], by preserving the chemical environment of supramolecular polymers from the addition of competitive or cryptochiral molecules. Furthermore, within external stimuli, the light is of interest because of its: remote control[98,99]; high "spatio-temporal resolution down to micron-scale and millisecond"[100]; tunability (wavelength, intensity, exposure time)[98–100] allowing site-specificity[98] for a controlled response[100]; easy processing[94]; biocompatibility and high penetrability[98]; applicability as an orthogonal stimulus or an energy input[99].

Light irradiation has thus many advantages to control the supramolecular helicity. Two main strategies exist: (i) chiroptical switch by means of the action of (non-chiral) light, (ii) induction of chirality and helicity inversion by means of CPL. The chiroptical switch between *right*- and *left*-handed helical polymers stems from the study of photochromic compounds (**Figure II.11a**), small organic molecules undergoing *trans*-to-*cis* isomerization or pericyclic reactions upon light irradiation[101,102]. They were first covalently linked to or mixed with chiral polymers or liquid crystalline phases, for which the chirality came from either their backbone (e.g. polypeptides), chiral pendant groups or dopants[101]. The mechanical motion triggered by isomerization or cyclization of photochromic molecules upon light irradiation, was able to cause handedness inversion in these dynamic nanostructures. The second strategy relying on

CPL has by far been less implemented. A switchable enantioenrichment can be induced in a racemic mixture of dynamical helical macromolecular or supramolecular structures by photoresolution. Within enantiomeric photobistable forms, each enantiomer of a racemate interconverts mutually upon CPL excitation, affording an enantioenriched photostationary-state (pss) enantiomeric mixture (**Figure II.11b**). The deviation from the racemic mixture is only due to the difference of the extinction coefficient (ε_R and ε_S) of each enantiomer toward the CPL used, since the deactivating reverse reactions, regenerating the starting material in its ground state, should not be enantiodifferentiating. The combined enantiomer concentration (C_R + C_S) is constant during the photoresolution, and the photochemical steady state is attained after a prolonged irradiation irrespective of the initial enantiomeric composition[24]. Without side reactions, the enantiomeric pss is reached when $\varepsilon_R C_R = \varepsilon_S C_S$, which can be rewritten into $(C_R/C_S)_{pss} = \varepsilon_R/\varepsilon_S$, allowing to calculate the *e.e.*$_{pss}$ (*e.e.* at the photostationary state), considering the **Equation I.1**, equal to $(C_R - C_S)/(C_R + C_S) = g/2$. Note that since photoresolvable helical structures are not interconverted in their ground state, but only through the excited (*R*)- and (*S*)-enantiomers (*R** and *S**), the photoresolved chiral structures are stable in absence of light, thereby representing a biased chiral center that may further be amplified.

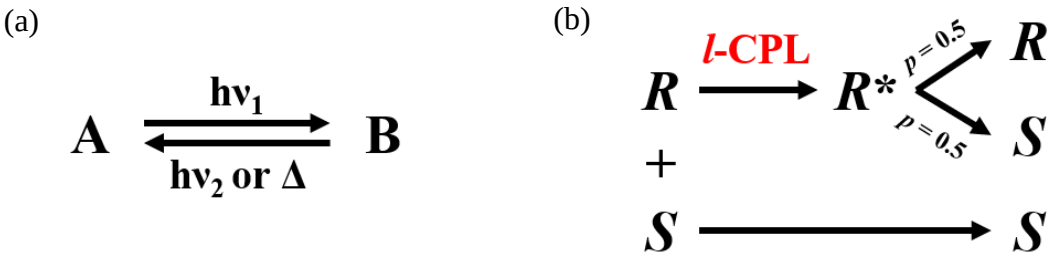

Figure II.11 (a) Photochromism and (b) photoresolution mechanisms. The photochromism is defined as the "reversible transformation of a molecular entity between two forms, A and B, having different absorption spectra, induced in one or both directions by absorption of electromagnetic radiation. The thermodynamically stable form A is transformed by irradiation into form B. The back reaction can occur thermally or photochemically"[103]. In (b), upon irradiation with single-handed CPL, only the preferential absorption is represented, giving an idea of the major transformation. *R* and *S* denote (*R*)- and (*S*)-enantiomers in the ground state, *R** the photoexcited state.

The pioneer work of Green, Salinger *et al.* does not involve an aggregation process, but is primordial in understanding how a preferred handedness can be induced by CPL to molecular systems adopting a helical configuration[104]. They synthesized polyisocyanate copolymers for which one of the monomers bears an axially chiral photoresolvable bicyclic ketone (G_1). Before irradiation, the ketone-containing group is in racemic mixture, and thus the polymer is CD silent. However, 24-hour light irradiation with *right*-handed CPL of the polymer solution triggers the rotation of the styryl group, promoting the formation of a preferential helicity, as highlighted by CD.

The photoresolution process is well understood at the molecular level: the styryl excited state is formed by intramolecular triplet-triplet energy transfer from the ketone group, which absorbs the light (**Figure II.12**). The unusually high anisotropy factor ($g \approx 0.05$ at 313 nm) of this axially-chiral ketone is ascribed to its rigid framework[105], which inhibits averaging of conformations having oppositely signed circular dichroism spectra. Irradiation of model monomers yields $e.e._{pss}$ of ca. 1% *e.e.*, in good agreement with the values estimated from their anisotropy factors. The authors also highlighted that depending on the *ortho*-, *meta*- or *para*-position of the spacer linking the aromatic photoresolvable chromophore with the polymer backbone, the chiral bias was more or less strong. Remarkably, even a small percentage of photoresolved chiral pendant group (2%, with an *e.e.* of ca. 1%, dispersed randomly among 98% of achiral pendants) was able to induce a measurable CD, thanks to the strong amplification of chirality through both the MR and S&S effects at work in this macromolecular structure. However, the optical purity of the polyisocyanate copolymers is not maximal, suggesting that the induction of chirality is not total, *i.e.* that both *right*-handed and *left*-handed fragments are present in the helices after CPL irradiation (as represented in **Figure II.13**). The results are very promising but two drawbacks can be delineated: i) the photoresolution requires an intramolecular energy transfer to the styryl group; it can thus be anticipated that any aromatic group interfering with this photochemical process will jeopardize the resolution process and ii) the irradiation time is long (24 h), which prevents a rapid stereochemical switch and may induce some (photo)-decomposition of the molecular units.

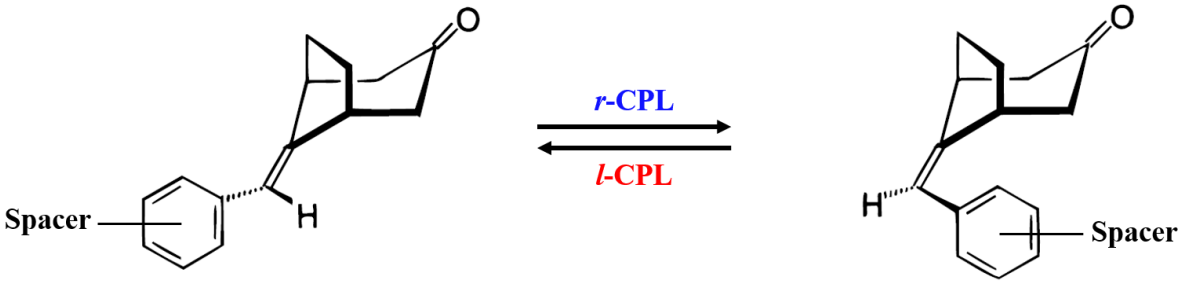

Figure II.12 Photoresolution of the axially chiral bicyclic ketone in polyisocyanate copolymers studied by Green, Salinger *et al.*[104]

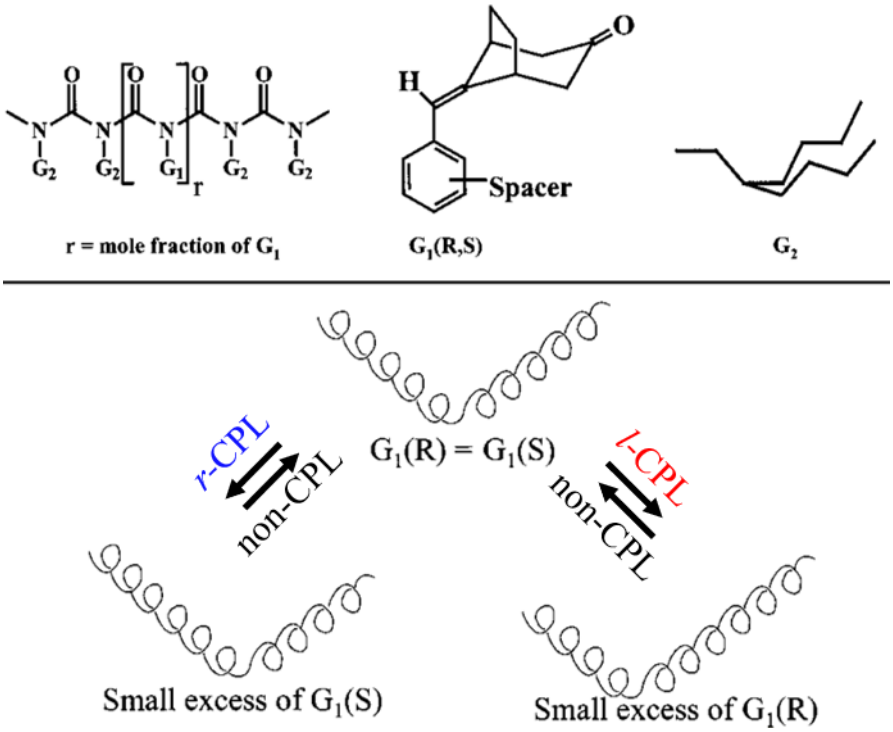

Figure II.13 (top) Molecular structure of the polyisocyanates synthesized by Green, Selinger *et al.*, bearing chiral photoresolvable ketone-containing group (G_1) and achiral alkyl pendant group (G_2). Spacers are two or three-atom linkers connecting the *ortho*, *meta*, and *para* positions of the bicyclic ketone to the polymer backbone. (bottom) Schematic illustration of the reversible and partial CPL-control helicity. Adapted from Green, Selinger *et al.*[104]

Following the seminal report of Green, Selinger *et al.* about the photoresolution of a helical polymer by CPL, a few other examples were reported for which the photoresolvable chromophore units were introduced in the main chain (e.g. axially chiral fluorene-based

polymers films[106–110]). Regarding the polyfluorene, the photoresolved groups are the twisted dyads composing the polymer backbone (**Figure II.14a**)[109].

In parallel, chromophores were also photoresolved in the aggregated state at the periphery of the macromolecular chains, resulting in a CPL-induced supramolecular chirality. This notably concerns azobenzene-containing polymers which form aggregates in thin films or liquid crystalline phases[111–120]. Considering azobenzene-containing pendant chains, the angular momentum of CPL is expected to generate an optomechanical torque (rotational force) upon impinging an absorbing medium with a subtle difference in the refractive index[121,122], like the optically anisotropic azobenzene stacks that exhibit long and short axes. Thereby, the CPL sets in rotational motion the initially non-helical π–π stacks of azobenzene pendants, thus twisting and giving them a preferential helical handedness which depend on the CPL direction (**Figure II.14b**)[120]. Fujiki *et al.* showed a convincing example of chiroptical switch of supramolecular chirality of the micrometer-size aggregates formed by achiral polymethacrylate functionalized by azobenzene units (**Figure II.15**)[120].

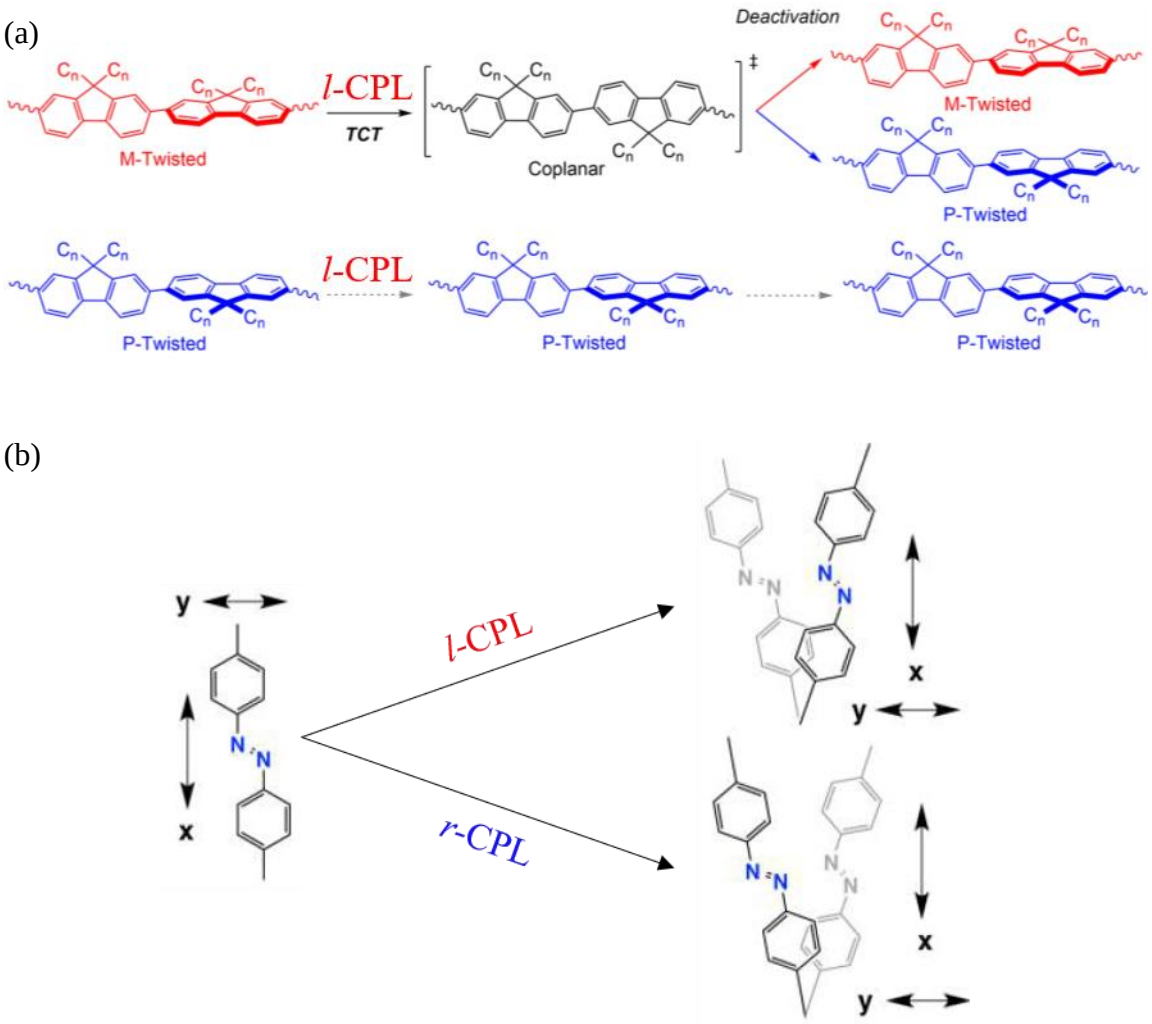

Figure II.14 (a) Chirality induction of polyfluorene derivatives by enantioselective photoexcitation by *left*-handed CPL. The *M*-twisted dyads composing the polymer absorb preferentially the *l*-CPL and consequently overgo a twisted-coplanar transition (TCT) leading to an achiral excited state, resulting in *M*- and *P*-twisted dyad in equal abundance upon deactivation. Meantime, the *P*-twisted feebly interacts with the *l*-CPL and is accumulated. Adapted from Nakano *et al.*[109] (b) CPL-induced helicity in π–π stacks of azobenzene pendants in achiral polymers, caused by the optomechanical torque generated by the interaction of the CPL angular momentum with the optically anisotropic azo stacks possessing long (x) and short (y) axes. Adapted from Fujiki *et al.*[120]

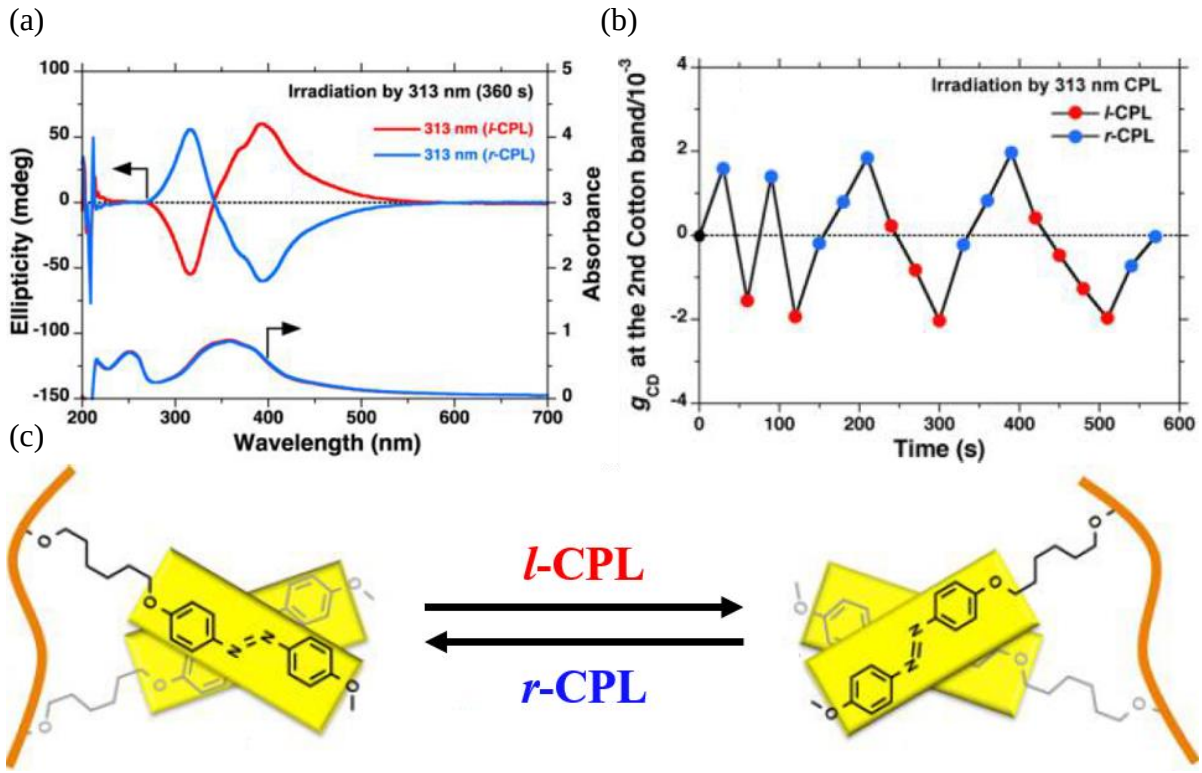

Figure II.15 (a) CD and UV−Vis analyses of the achiral polymethacrylate bearing azobenzene moieties synthesized by Fujiki *et al.* and aggregated in a dichloromethane/methylcyclohexane mixture, before and after irradiation with *left*- or *right*-handed CPL for 360 seconds. (b) Chiroptical switching of the Kuhn anisotropy factor under *l*- and *r*-CPL alternating irradiation. (c) Schematic representation of the chiroptical switch of stacked azobenzene groups. Adapted from Fujiki *et al.*[120]

Precedent examples show how a designed photoresolvable chromophore can induce a preferential chirality at the macromolecular or supramolecular scale. Nevertheless, the incorporation of the chiroptical switch in a molecular framework necessitates each time tedious syntheses to vary the position and nature of the chromophores or substituents, as well as optimized conditions of film or liquid crystalline phase formation[94]. Additionally, using photochromic compounds needs to face the problems of their dispersion inside the polymer matrix, but also requires the polymer scaffold to be "transparent" to the CPL signal which may otherwise impede the photoresolution process[99,100]. Finally, systems based on the aggregation of azobenzene moieties and polyfluorene derivatives uncovered the importance of the close-contact between entities to achieve an efficient chiral induction[108,123]. Recently, reversible control of the helical conformation of supramolecular polymers was achieved by means of CPL

irradiation. These examples are particularly intriguing because they deal with discotic molecules devoid of usual photoresolvable compounds.

To the best of our knowledge, the first example of such systems was provided by Kim *et al*. for triarylamine trisamide (TATA)-based helical supramolecular polymers. The supramolecular chirality (*left*- or *right*-handed helicity) of TATA polymers was found to be controlled by the rotational direction of the light (*left*- or *right*-handed CPL, respectively)[29]. To achieve this, Kim *et al*. employed a TATA monomer featuring straight diacetylene side chains (named as TATA-SDA). The TATA core was likely selected to exploit the fact that their self-assembly into well-defined columnar stacks, built upon aromatic and hydrogen interactions, can be triggered by light[124]. Indeed, Giuseppone *et al.* claimed that in chlorinated solvents, TATA molecules can be photo-oxidized into their radical cationic counterpart (triarylammonium radicals), species of more planar conformation than propeller-like neutral molecules, thereby favoring and initiating the aggregation of all TATA monomers into TATA stacks under dilute conditions. TATA self-assemblies were in addition pointed out to display extremely high amplification properties[91]. Regarding the diacetylene side chains, their use was probably inspired from the previous reports about the enantioselective synthesis of helical polydiacetylene (PDA) initiated by CPL, of fatty acids or disk-like molecules in films[118,119,125–127]. Notably, Zou *et al.* described in 2014 the enantioselective polymerization of a C_3-symmetrical disk-like diacetylene derivatives upon circularly polarized UV light (CPUL) irradiation. Their stacking into columnar liquid crystalline phase favored the asymmetric polymerization, by lining up the molecules in a suitable close contact to fulfill the steric requirements of the topochemical photopolymerization[128], as well as to ensure enough flexibility to the orientation of the polydiacetylene backbone by "the rotational force developed by CPL"[27,127].

In fact, Kim *et al.* demonstrated that the light irradiation with visible CPL was able to induce and control the supramolecular chirality of TATA polymers, under conditions for which the polymerization of the diacetylene units did not occur (**Figure II.16**). They postulated that upon photo-oxidation into triarylammonium radicals, the interaction of the CPL angular momentum "with the dipolar moment of π electrons in the triarylamine core induces a preferential handedness to the propeller-like molecules", which further acts as sergeants upon

stacking. In this way, the PDA formation upon CPUL irradiation only serves to covalently lock the biased helical supramolecular conformation induced by visible CPL. Whilst this observation was reported for TATA-SDA molecule in dilute solutions, a similar mechanism was proposed recently by the same group for the induction of supramolecular chirality in the film state for a related disk-like monomer[129], despite the fact that this monomer is not oxidized in presence of light.

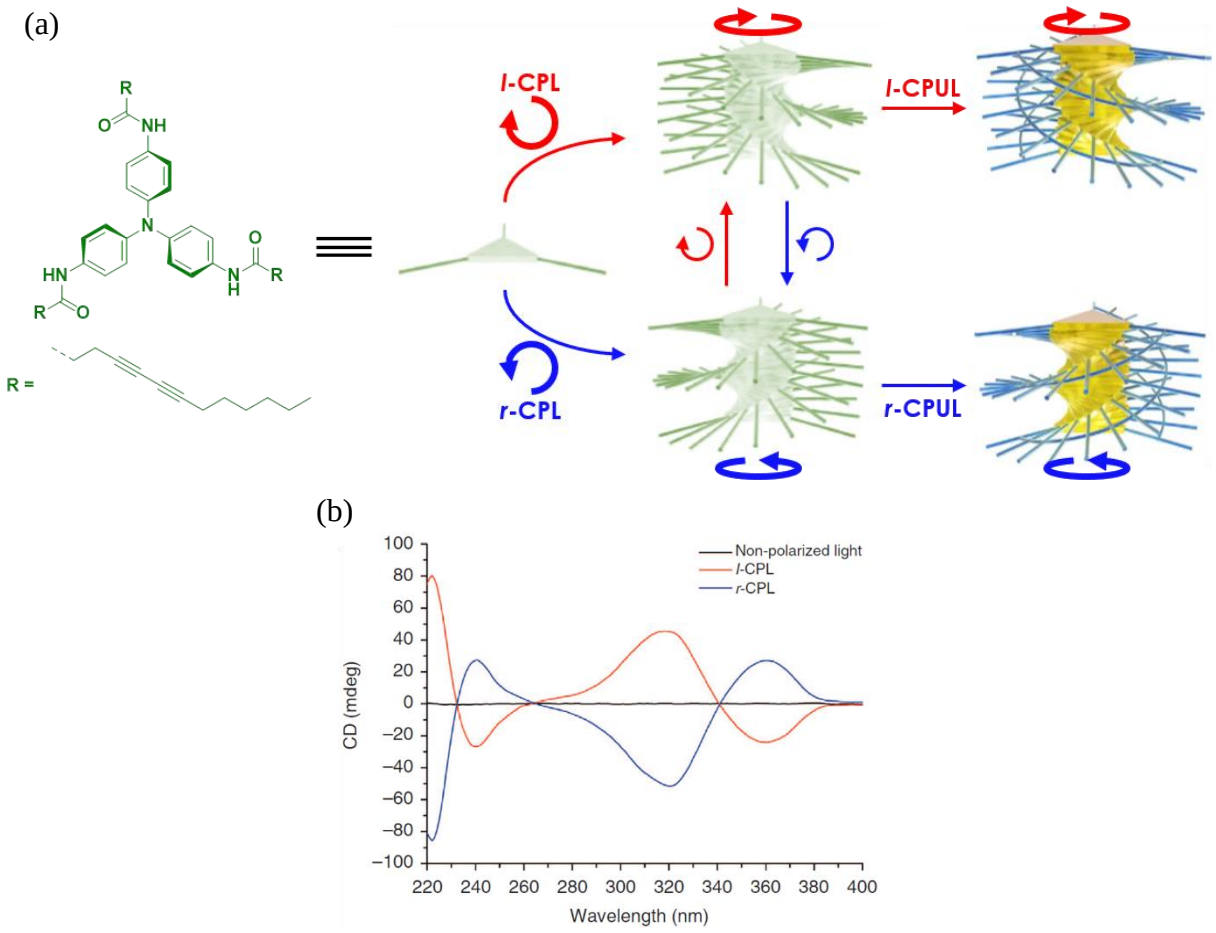

Figure II.16 (a) Schematic illustration of the induction, control and locking of helicity in TATA-SDA-based supramolecular polymer. (b) Circular dichroism measured from TATA-SDA in 1,2-dichloroethane at 2 g/L and -10°C, after irradiation with non-polarized light (black), *right*- (blue) or *left*-handed (red) circularly polarized light for 10 min at room temperature. Adapted from Kim *et al.*[29]

In 2019, Zou *et al.* reported that the helical handedness of porphyrin-based assemblies can be controlled by means of CPUL irradiation when the irradiation is performed during the first stages of a gelation process (**Figure II.17a**)[30]. The authors assumed that porphyrin

derivatives irradiated with UV light in chloroform are protonated, through the decomposition of chloroform into hydrogen chloride. This leads to dicationic porphyrin species that adopt a saddle structure "believed to facilitate symmetry breaking". A key point for the induction and propagation of chirality in this system is that self-assembly must occur during and after the CPUL irradiation. Indeed, the irradiation was carried out during 20 minutes, then the mirror-image CD spectra (**Figure II.17c**) was measured after 6 hours during which the sample was let in the dark and formed a gel. The gelation process was highlighted by the increase of viscosity during and after the irradiation (**Figure II.17b**), indicating the formation of long assemblies. Thereby, the authors asserted that the chiral bias was induced by the angular momentum of CPUL while interacting with π electrons of molecules upon protonation and stacking, which was then amplified upon stacking of the monomers leading to a preferential handedness for the eventually formed helical assemblies.

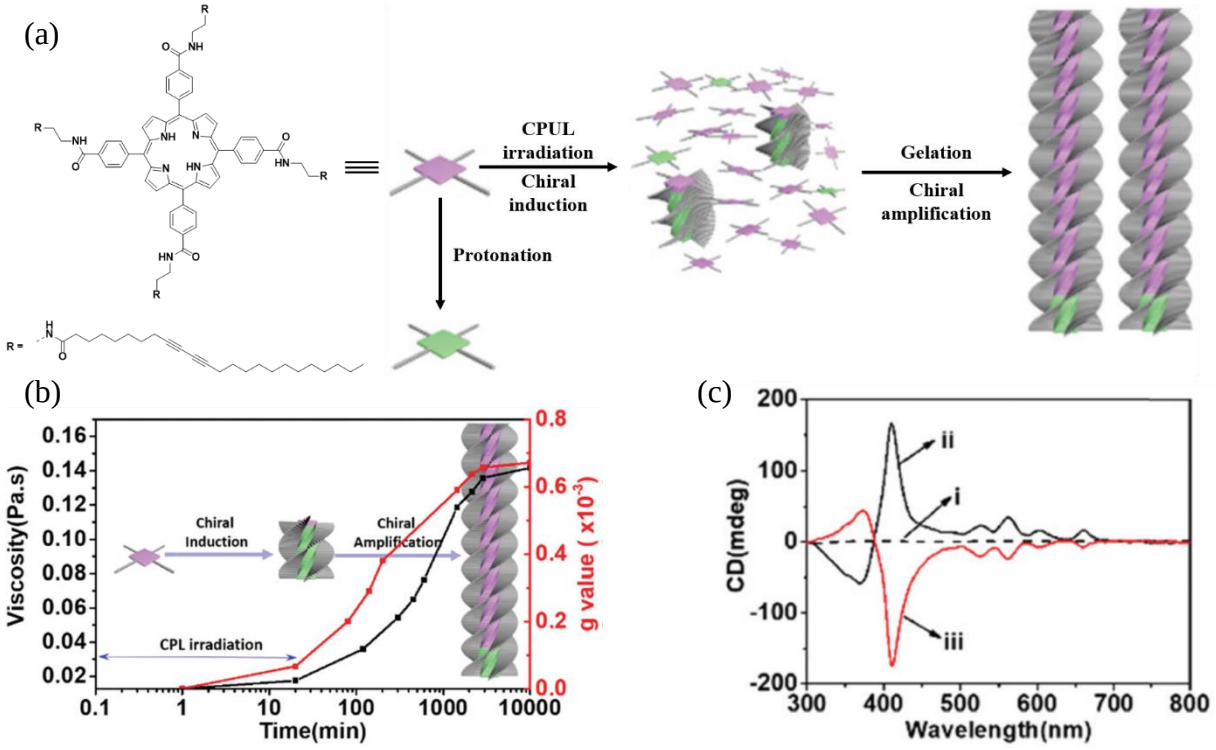

Figure II.17 (a) Molecular structure of the porphyrin derivative used by Zou *et al.* and schematic illustration of the whole chiral induction and amplification process upon circularly polarized UV light irradiation and formation of long assemblies. (b) Time-dependent viscosity and Kuhn anisotropy factor (λ = 410 nm) measurements. (c) Circular dichroism measured after irradiation with non-polarized light

(i), *right*- (ii) or *left*-handed (iii) circularly polarized light for 20 min at room temperature. Adapted from Zou *et al.*[30]

In 2020, Sánchez *et al*. demonstrated that CPL irradiation of the monomeric state of *N*-annulated perylenetetracarboxamides (at 95°C) yielded enantioenriched helical aggregates at room temperature (**Figure II.18**)[31]. Remarkably, they evidenced that the irradiation of aggregates already formed at room temperature did not induce any chiral bias (grey line in the CD and UV–Visible absorption spectra displayed in **Figure II.18b**). The irradiation is performed in methylcyclohexane and does not involve the formation of radical or protonated species.

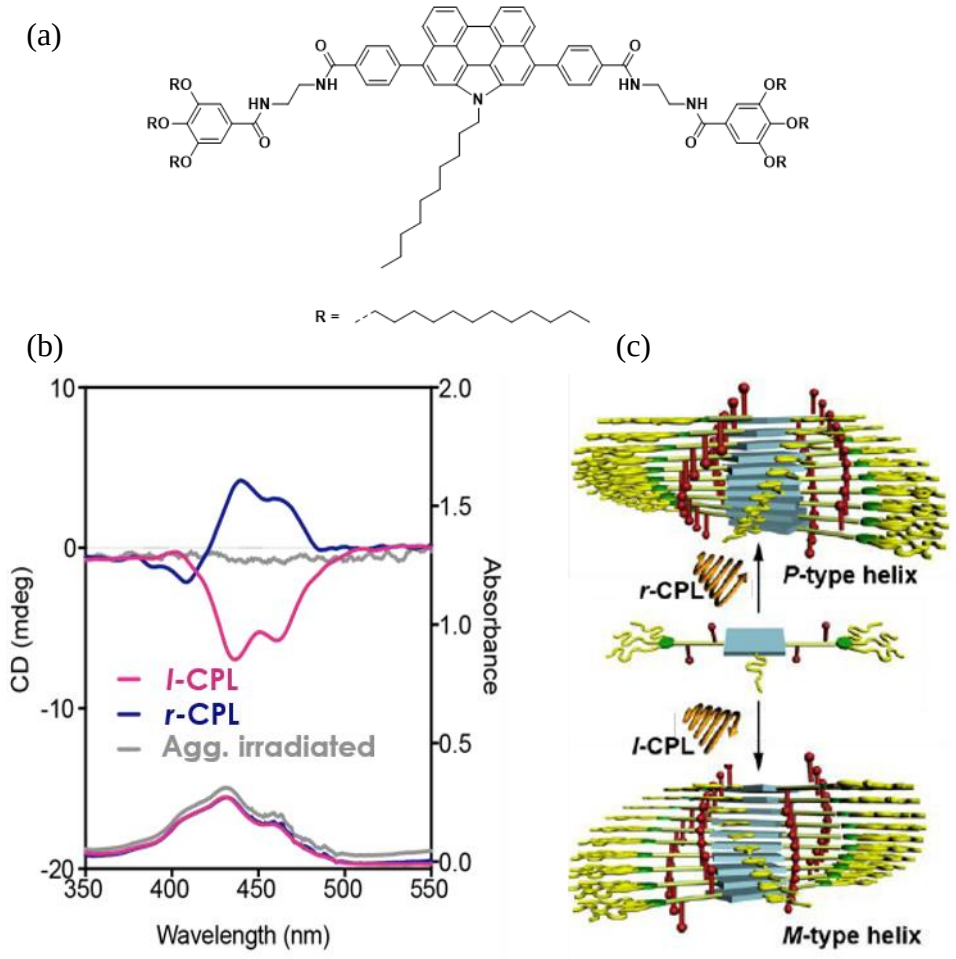

Figure II.18 (a) Molecular structure of the *N*-annulated perylenetetracarboxamide compound synthesized by Sánchez *et al.* (b) CD spectra at 20°C of solution irradiated by *left*- (pink) and *right*-handed (blue) CPL for one hour at 95°C in the monomeric state, or at 20°C in the aggregated state

(grey). (c) Schematic illustration of the enantioenriched helices formed upon cooling of CPL irradiated monomers. Adapted from Sánchez *et al.*[31]

Thus, by using a non-chemical but truly chiral bias – the circularly polarized light (CPL), the helical shape of supramolecular polymers devoid of chiral centers and designed photoresolvable units was biased and controlled in solution thanks to the rotational direction of CPL. The mechanisms at the origin of this effect are overall badly understood and likely differ from one system to another. For example, the combination of a photoresolution and a photochemical process leading to the formation of radical or protonated species is not always necessary. Likewise, the nature of the photoresolved units have not been established in these systems and the mechanism of chirality induction was referred to occur through the interaction between the angular momentum of CPL with π electrons of monomers. A key feature which is common to all these systems is the efficient amplification of the initial chiral bias thanks to the combination of S&S and MR effects upon assembly.

VI. Asymmetric Catalysts Built on a Chirally-Amplified Helical Scaffold

A promising direction towards absolute asymmetric synthesis is to exploit CPL-controlled helical supramolecular polymers as scaffold for asymmetric catalysis. Indeed, the supramolecular handedness of helical assemblies, made of disk-like molecules, was recently used as the chiral inducer in asymmetric organometallic reactions.

In 2013, Raynal *et al.* demonstrated this concept by synthesizing chiral BTA-based supramolecular polymers able to coordinate rhodium atoms. Applied to the asymmetric hydrogenation of dimethyl itaconate, they demonstrated the transfer of supramolecular chirality of the helical scaffold to the metal centers located at its periphery, which in turn promoted the reaction towards the formation of one preferential enantiomer (**Figure II.19**)[130]. In the first system, the monomer unit featured both a diphenylphosphine group (for metal coordination) and stereogenic centers (for chiral induction). On one hand, good selectivity (82% *e.e.*) was obtained even though the stereogenic center is located 12 atoms away from the metal. On the other hand, no enantioselectivity was observed under conditions that do not allow the formation

of supramolecular polymers. This result demonstrated that the selectivity came from the transfer of chirality of the helical supramolecular structure to the rhodium atoms.

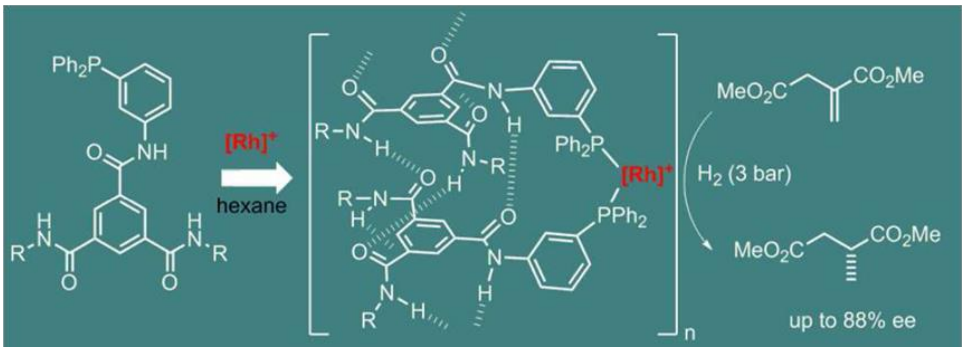

Figure II.19 Structure proposed for the auto-association of BTA into a helical supramolecular polymer able to transfer its supramolecular chirality to the metal center supported at its periphery. Reprinted from Raynal *et al.*[130]

In parallel, Liu *et al.* also evidenced the transfer of supramolecular chirality from helical assemblies made of L-glutamic acid-based gelators[131–133] to products of asymmetric copper-catalyzed Diels–Alder reaction, bismuth-catalyzed Mukaiyama aldol reaction and rhodium-catalyzed cyclopropanation. In all cases, chiral monomers were combined to metal precursors for generating the supramolecular helical catalysts.

Raynal *et al.* applied the aforementioned S&S effect to the design of asymmetric helical BTA catalysis[134]. They synthesized a library of C_3-symmetrical ester BTAs derived from amino acids, with a chiral center located in α position of the amide function (**Figure II.20a**). Then, they showed that a helical supramolecular polymer composed of achiral metal complexes (achiral ligand monomer units, soldiers) and enantiopure co-monomers (sergeants) can catalyze the hydrogenation of dimethyl itaconate with significant enantioselectivity (*e.e.* up to 85%, **Figure II.20b** and **c**). The non-linear relationship between the amount of chiral comonomers in the assemblies and the enantioselectivity of the catalytic reaction demonstrated that amplification of chirality through the S&S effect is at work in these supramolecular helical catalysts (**Figure II.20c**). The optimal selectivity is reached for mixtures containing no more than 20% of **BTA Ile** as sergeants, *i.e.* the amount required to get homochiral helices. A schematic representation of the helical catalytic co-assemblies is shown in **Figure II.20b**.

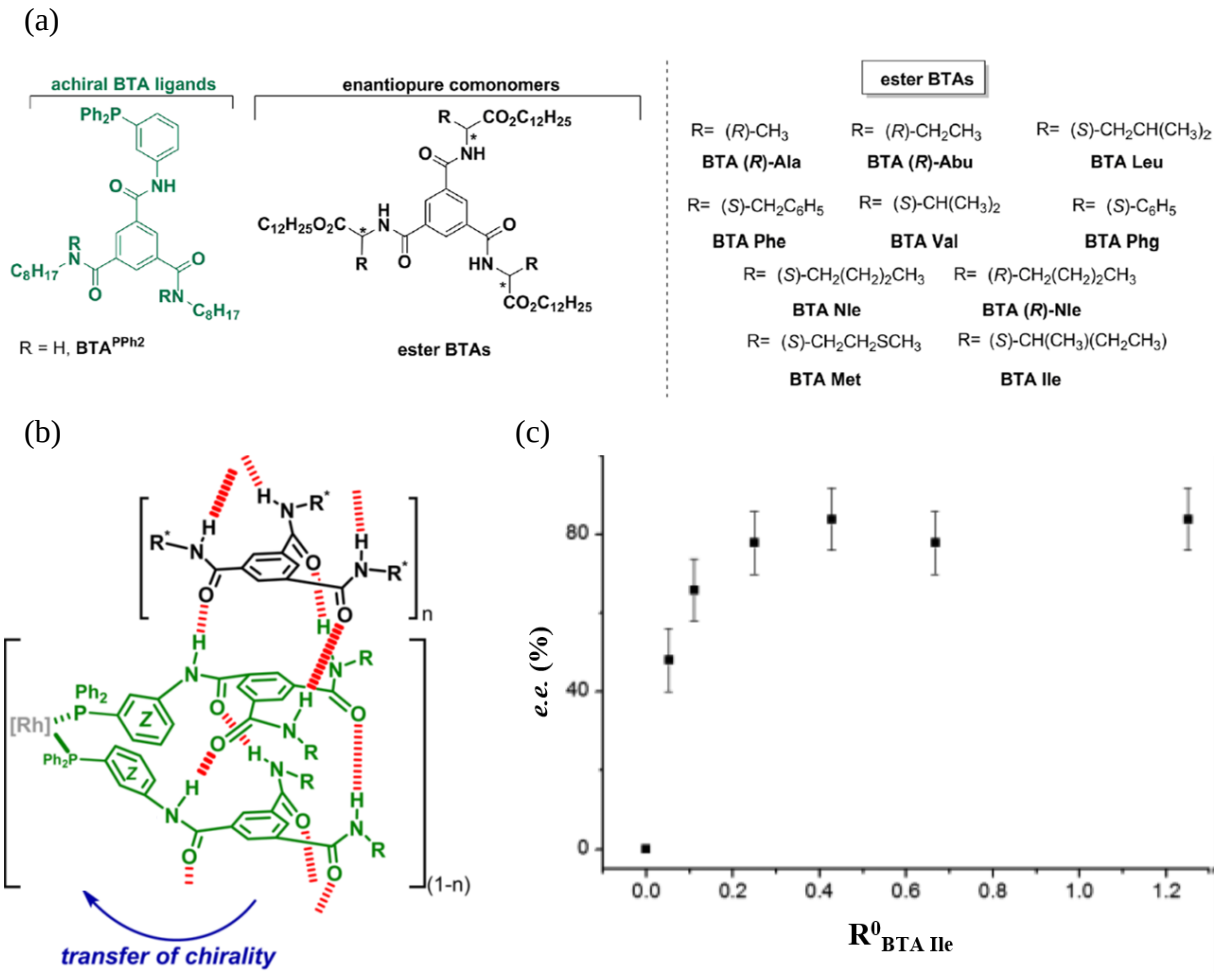

Figure II.20 (a) Molecular structure of BTA used in the asymmetric hydrogenation reaction. (b) Proposed supramolecular structure for the co-assembly of the achiral metal complex and enantiopure co-monomers, able to the transfer its supramolecular chirality to the catalytic center. (c) Enantioselectivity of the hydrogenation reaction as a function of the molar ratio between the chiral ester **BTA Ile** and the achiral ligand **BTA^{PPh2}** present in the catalytic mixture ($R^0_{BTA\ Ile}$). Adapted from Raynal *et al.*[134]

Raynal *et al.* also took advantage of the aforementioned BTA system including an achiral rigidifier, to improve the chirality amplification properties of the helical system and thus reduce the amount of sergeant. The achiral BTA additive (**a-BTA**) was thus mixed with achiral BTA ligands and enantiopure co-monomers (**BTA (*R*)-** or **(*S*)-Cha**), to be implemented in the copper-catalyzed hydrosilylation of the 1-(4-nitrophenyl)ethanone (NPnone) into 1-(4-nitrophenyl)ethanol (NPnol), by supporting copper at the periphery of assemblies (**Figure**

II.21a). In S&S mixtures, the enantioselectivity of the reaction catalyzed by supramolecular catalysts devoid of the achiral additive does not reach a plateau ($|e.e._{max}|$ = 57.6%), meaning that more than 50% of chiral BTA is required to get homochiral helices. Conversely, in the presence of **a-BTA**, only 0.25% of **BTA (*S*)-Cha** is necessary to attain 98% of the optimal selectivity, in agreement with the minimal chiral BTA amount needed to obtain homochiral helices (**Figure II.21b**). Likewise, the achiral additive allows a significant improvement of the diluted MR effect, viz. an optimal selectivity is reached with 20% *e.e.* scalemic mixture (*vs.* ⩾50% *e.e.* in absence of the **a-BTA**, **Figure II.21c**). Further optimization of the catalytic system, by decreasing the temperature down to 200 K (*vs.* 293 K), and by substituting the BTA ligand with methyl groups at the *meta* positions of the aromatic rings attached to the phosphorus atom, permits to operate with ppm levels of sergeants to produce highly enantioenriched NPnol (90% *e.e.*).

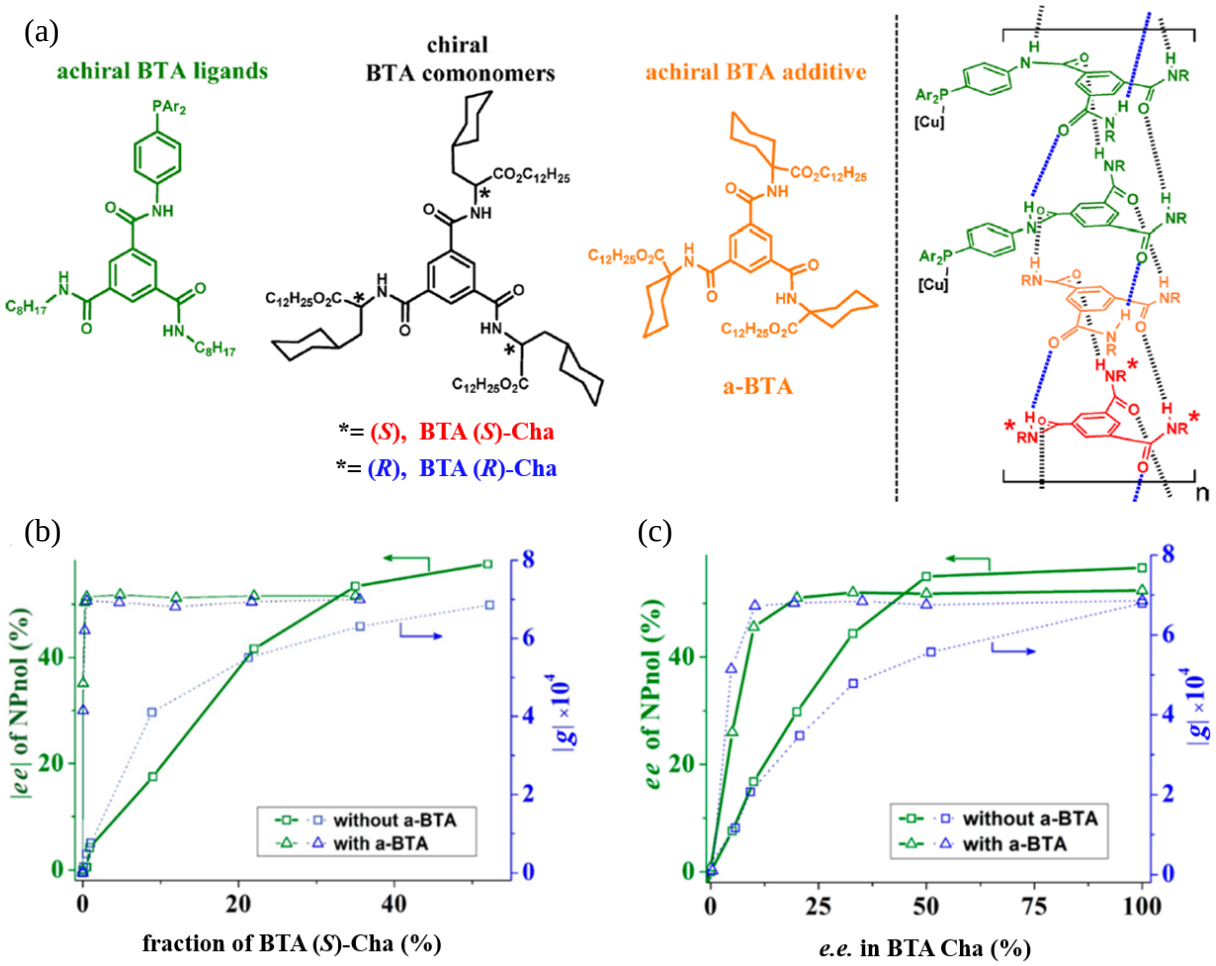

Figure II.21 (a) Chemical structures of the BTA monomers composing the helical supramolecular polymer exhibiting extremely high amplifications properties. (b–c) Plots of the enantioselectivity in NPnol and of the Kuhn anisotropy factor versus (b) the fraction of **BTA (*S*)-Cha** or (c) the optical purity in c-BTA in the catalytic mixtures. Adapted from Raynal *et al.*[90]

Majority-rules type helical BTA catalysts were also exploited to switch the enantioselectivity of an asymmetric hydrosilylation catalyzed by copper (**Figure II.22a**). The chirality of the supramolecular co-assembly, composed of a mixture of **BTA^{PPh2}**, **BTA (*S*)-Cha** and **BTA (*R*)-Cha**, can be reversed during the catalytic reaction (**Figure II.22b**), allowing to obtain alternately the product of configuration (*R*) or (*S*) with an optimal selectivity (**Figure II.22d**)[135]. This inversion of chirality results from the addition in the catalytic medium of the enantiopure co-monomer initially in minority. Thanks to their dynamic nature, supramolecular polymers integrate these co-monomers, which then become the most abundant in the co-

assemblies and, thanks to the MR effect (**Figure II.22c**), now impose their chiral preference to the stacks. This inversion of the handedness of the self-assemblies is then induced at the metal centers at their periphery, thus allowing the real-time control of the selectivity of the catalyst.

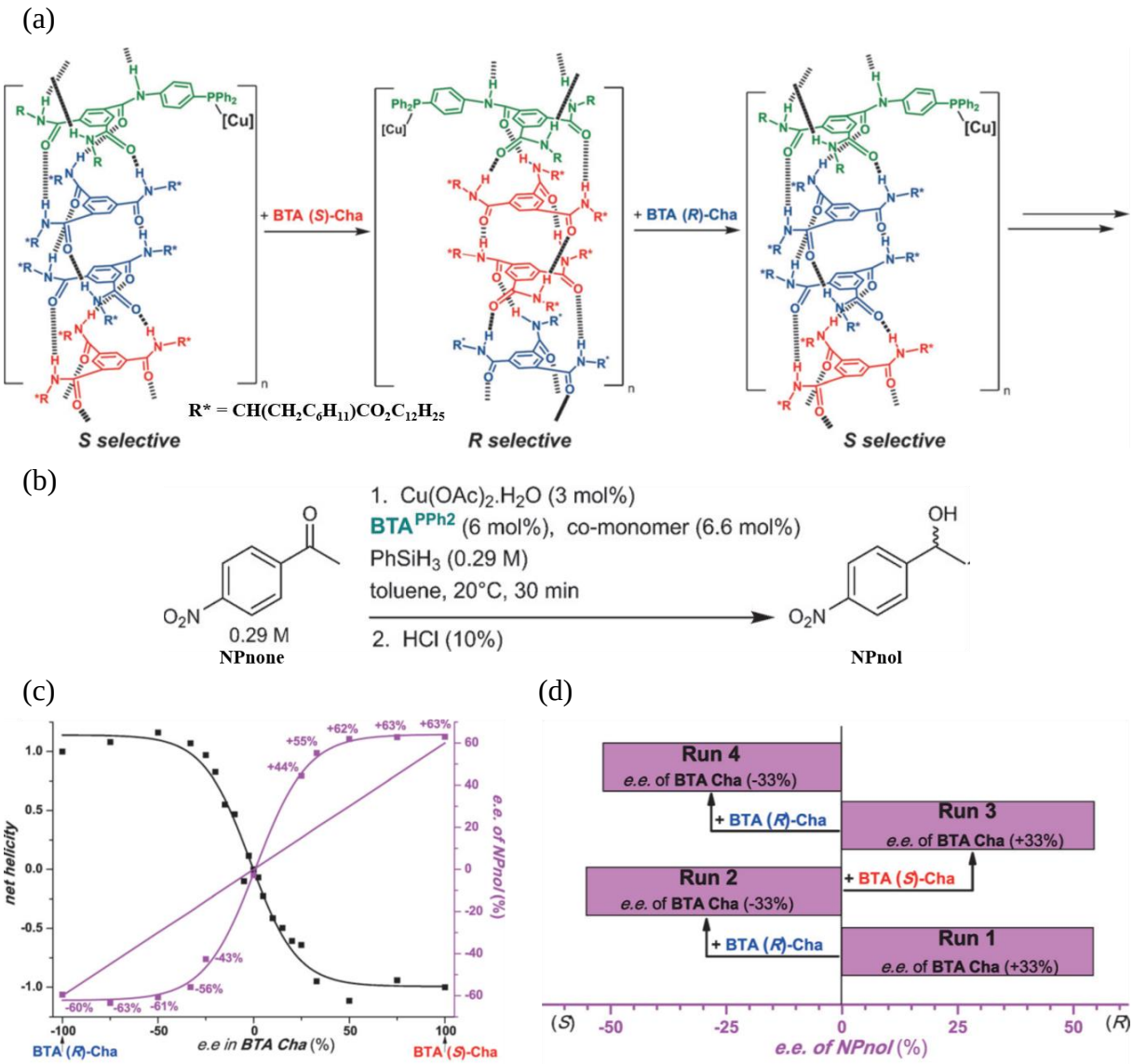

Figure II.22 (a) Proposed structure, based on spectroscopic and scattering analytical techniques, of the BTA-based supramolecular catalyst of switching supramolecular chirality, thanks to the addition of enantiopure co-monomers of opposite configuration. (b) Conditions of copper-catalyzed hydrosilylation of (1-(4-nitrophenyl)ethenone, NPnone) into (1-(4-nitrophenyl)ethanol, NPnol) employed in this study. (c) Correlation between the enantioselectivity and the supramolecular chirality of the helical supramolecular scaffold. Enantiomeric excess of the asymmetric catalyzed reaction (NPnol) and net

helicity as a function of the enantiomeric excess in chiral co-monomer (**BTA Cha**). The violet straight line represents the selectivity that would be obtained in absence of chirality amplification. The net helicity for the various co-assemblies was measured by CD spectroscopy by dividing the ellipticity of each mixture by the ellipticity of the mixture containing enantiopure **BTA Cha**. (d) Enantioselectivity of the copper-catalyzed hydrosilylation of 1-(4-nitrophenyl)ethanone into NPnol, upon sequential additions of enantiopure BTA of opposite handedness and reagents. Adapted from Raynal *et al.*[135]

Helical supramolecular polymers based on disk-like molecules were thus highlighted as efficient supports of metal centers for asymmetric reactions, with a correlation between the supramolecular chirality and the enantioselectivity of the catalyzed reaction. It was demonstrated that a tiny chiral bias could be amplified at the supramolecular level, prior to be transferred again down to the molecular level, leading to the synthesis of highly enantioenriched products. The sensitivity of BTA- and porphyrin-based supramolecular assemblies was also highlighted by SMSB phenomena, advantageously applied to asymmetric catalysis yet giving moderate enantiomeric excess[76,136]. It would be advantageous to replace the sergeants (in chirally-amplified BTA catalysts) and the randomness of the SMSB process by CPL, which is the ultimate objective of this thesis.

VII. Objectives of the Thesis and outline of the manuscript

As shown by the aforementioned literature, performing asymmetric reaction with little or no help of chiral entities that would have a general scope is yet to be harnessed. Helical supramolecular polymers composed of disk-like molecules are appealing materials. Chiral amplification phenomena cooperatively transfer an asymmetric bias from the monomer to the supra-macromolecular level, thanks to their dynamic features. Triarylamine trisamide derivatives (TATA) constitute in this regard an opportunity. On one hand, these monomers form supramolecular helices which display an extremely high degree of chirality amplification: only 0.2-mol% fraction of sergeants can fully control the handedness of supramolecular helices[91]. On the other hand, TATA-based helical supramolecular polymers generated upon illumination by circularly polarized light exhibit a switchable supramolecular chirality (*left*- or *right*-handed helicity) controlled by the rotational direction of CPL (*left*- or *right*-handed CPL, respectively)[29]. Two approaches are envisaged to build absolute asymmetric catalysts based on

CPL-oriented homochiral helices (**Figure II.23**): either by incorporating TATA molecules bearing metal-binding groups inside already CPL-oriented stacks of TATA molecules (1st strategy, explored in this thesis); or by directly controlling the handedness of assemblies of TATA ligands. Thereby, this thesis aims at paving the way towards absolute asymmetric catalysis, thanks to inducing and controlling the optical purity of helical TATA catalysts by means of circularly polarized light. In addition, an attempt to control the supramolecular chirality of TATA assemblies thanks to chiral additives is also investigated.

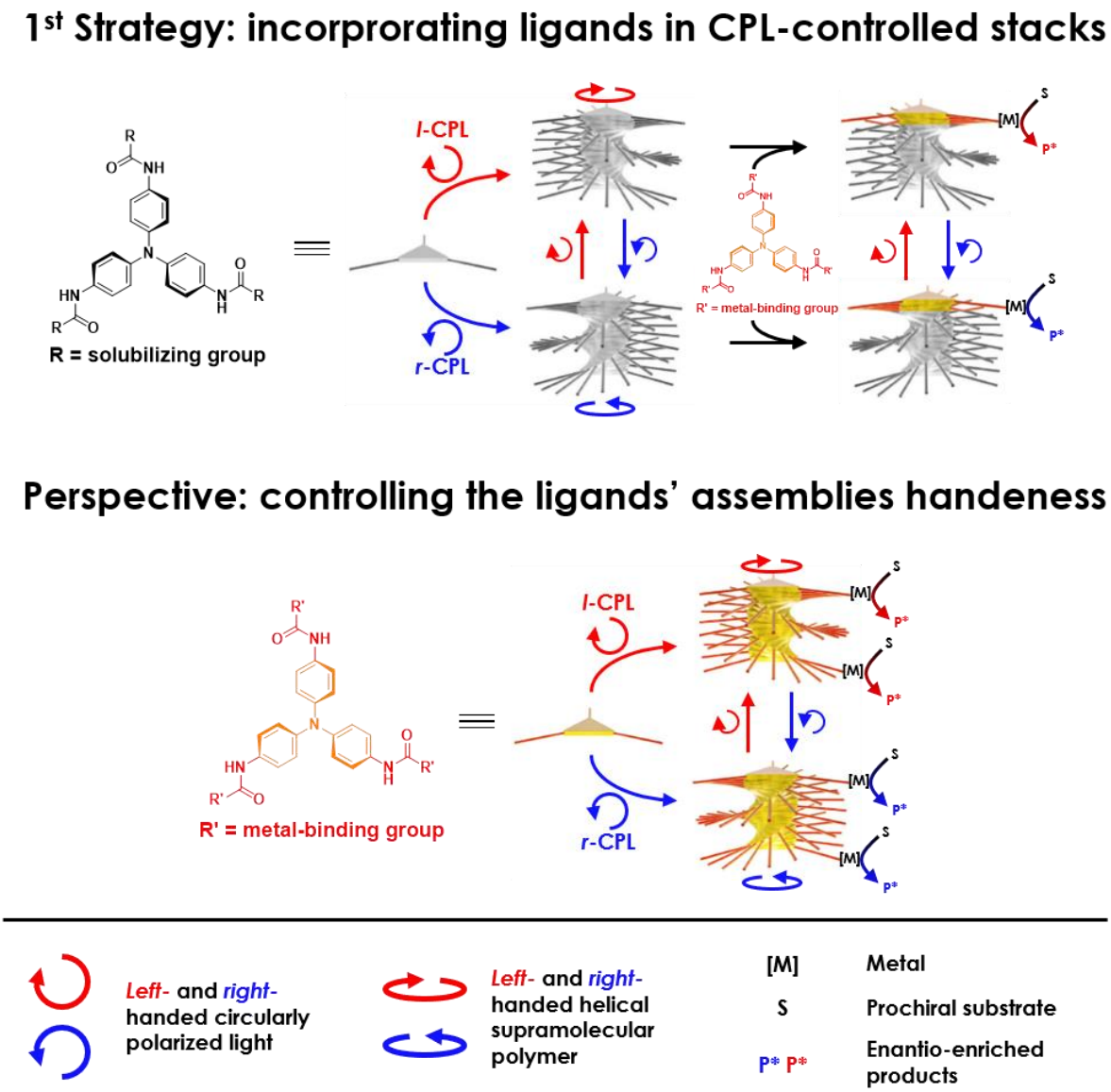

Figure II.23 Two strategies of absolute asymmetric catalysis by means of TATA-based helical supramolecular polymer with handedness controlled by circularly polarized light. For the first strategy,

the incorporated metal-binding monomer is represented at the top of the assemblies for simplicity but it is assumed that it will actually be distributed homogeneously inside the helices.

First, the association properties of structurally simple TATA monomers will be probed with and without light irradiation in Chapter III. TATA monomers with saturated side chains will be studied to highlight the conditions of assembly, as well as to probe the structure of the aggregates (e.g. shape, length and interactions between molecules). The effect of light irradiation will then be assessed on a variety of association states. The co-assembly between radical cationic species, generated upon light irradiation, and neutral molecules, as well as the type of interactions involved, will be particularly examined. A special attention will notably be paid for determining the nature of the hydrogen bond network. The aim of this chapter is to establish some guiding parameters that may lead to CPL-controlled supramolecular chirality of TATA-based assemblies.

Chapter IV focuses on reproducing the system reported by Kim *et al.*[29], and better understand the mechanism behind the control of supramolecular chirality by CPL irradiation. For this purpose, TATA-SDA monomer will be prepared and fully characterized. A first assessment of the properties of TATA-SDA in solution will identify its advantages and drawbacks, as well as give hints about its solubility and self-assembly capacities. The self-association properties of TATA-SDA will then be explored in various solvents. In chlorinated solvents, the assembly property of TATA-SDA molecules will be studied under different conditions (concentration, temperature, time) in order to evaluate the importance of these parameters on the nature and structure of self-assemblies. Next, the impact of CPL on self-association properties of TATA-SDA will be specifically studied. The difficulties encountered during CD measurements of the CPL-irradiated solutions and films will be stressed out. Finally, the possibility of controlling the handedness of TATA-SDA assemblies by CPL will be probed under a large range of conditions.

Finally, the synthesis and characterization of the designed TATA ligand will be presented in Chapter V. Preliminary studies aiming at inducing a preferential handedness to TATA ligand helical assemblies by means of chiral additives will be described.

VIII. References

1 J. Jacques, A. Collet and S. H. Wilen, *Enantiomers, Racemates, and Resolutions*, Krieger Publishing Company, 1994.
2 C. F. Poole, in *The Essence of Chromatography*, ed. C. F. Poole, Elsevier Science, Amsterdam, 2003, pp. 793–845.
3 H. Y. Aboul-Enein, *Chirality*, 2006, **18**, 772–772.
4 P. Piras and C. Roussel, *J. Pharm. Biomed. Anal.*, 2008, **46**, 839–847.
5 G. K. E. Scriba, Ed., *Chiral Separations*, Humana Press, Totowa, NJ, 2013, vol. 970.
6 R. Siedlecka, *Tetrahedron*, 2013, **69**, 6331–6363.
7 H. Lorenz and A. Seidel-Morgenstern, *Angew. Chem. Int. Ed.*, 2014, **53**, 1218–1250.
8 V. Farina, J. T. Reeves, C. H. Senanayake and J. J. Song, *Chem. Rev.*, 2006, **106**, 2734–2793.
9 D. L. Hughes, in *Comprehensive Chirality*, eds. E. M. Carreira and H. Yamamoto, Elsevier, Amsterdam, 2012, pp. 1–26.
10 J. J. Song, R. P. Frutos, T. Tampone, C. H. Senanayake and D. Krishnamurthy, in *Comprehensive Chirality*, eds. E. M. Carreira and H. Yamamoto, Elsevier, Amsterdam, 2012, pp. 46–72.
11 R. Wohlgemuth, *J. Chem. Technol. Biotechnol.*, 2007, **82**, 1055–1062.
12 K. M, M. T, S. S and T. M, *Appl. Microbiol. Biotechnol.*, 2016, **100**, 5747–5757.
13 H. U. Blaser, *Chem. Rev.*, 1992, **92**, 935–952.
14 J. Seyden-Penne, *Chiral Auxiliaries and Ligands in Asymmetric Synthesis*, Wiley, 1995.
15 S. Jaroch, H. Weinmann and K. Zeitler, *ChemMedChem*, 2007, **2**, 1261–1264.
16 C. A. Busacca, D. R. Fandrick, J. J. Song and C. H. Senanayake, *Adv. Synth. Catal.*, 2011, **353**, 1825–1864.
17 C. A. Busacca, D. R. Fandrick, J. J. Song and C. H. Senanayake, in *Applications of Transition Metal Catalysis in Drug Discovery and Development*, John Wiley & Sons, Ltd, 2012, pp. 1–24.
18 P. G. Bulger, in *Comprehensive Chirality*, eds. E. M. Carreira and H. Yamamoto, Elsevier, Amsterdam, 2012, pp. 228–252.
19 In *Active Pharmaceutical Ingredients in Synthesis*, John Wiley & Sons, Ltd, 2018, pp. 1–30.
20 B. L. Feringa and R. A. van Delden, *Angew. Chem. Int. Ed.*, 1999, **38**, 3418–3438.
21 K. Mislow, *Collect. Czechoslov. Chem. Commun.*, 2003, **68**, 849–864.
22 J. M. Ribó, D. Hochberg, J. Crusats, Z. El-Hachemi and A. Moyano, *J. R. Soc. Interface*, 2017, **14**, 20170699.
23 J. M. Ribó and D. Hochberg, *Symmetry*, 2019, **11**, 814.
24 Y. Inoue, *Chem. Rev.*, 1992, **92**, 741–770.
25 M. Wakabayashi, S. Yokojima, T. Fukaminato, K. Shiino, M. Irie and S. Nakamura, *J. Phys. Chem. A*, 2014, **118**, 5046–5057.
26 T. Mori, *Chem. Rev.*, 2021, **121**, 2373–2412.
27 G. Yang, S. Zhang, J. Hu, M. Fujiki and G. Zou, *Symmetry*, 2019, **11**, 474–493.
28 H. K. Bisoyi and Q. Li, *Angew. Chem. Int. Ed.*, 2016, **55**, 2994–3010.
29 J. Kim, J. Lee, W. Y. Kim, H. Kim, S. Lee, H. C. Lee, Y. S. Lee, M. Seo and S. Y. Kim, *Nat. Commun.*, 2015, **6**, 6959.
30 J. Hu, Y. Xie, H. Zhang, C. He, Q. Zhang and G. Zou, *Chem. Commun.*, 2019, **55**, 4953–4956.

31 E. E. Greciano, R. Rodríguez, K. Maeda and L. Sánchez, *Chem. Commun.*, 2020, **56**, 2244–2247.
32 R. P. Megens and G. Roelfes, *Chem. - Eur. J.*, 2011, **17**, 8514–8523.
33 S. E. Denmark, *ACS Cent. Sci.*, 2019, **5**, 1117–1119.
34 Y. Li, L. Bouteiller and M. Raynal, *ChemCatChem*, 2019, **11**, 5212–5226.
35 T. Aida and E. W. Meijer, *Isr. J. Chem.*, 2020, **60**, 33–47.
36 H. Staudinger, *Berichte Dtsch. Chem. Ges. B Ser.*, 1920, **53**, 1073–1085.
37 L. Brunsveld, B. J. B. Folmer, E. W. Meijer and R. P. Sijbesma, *Chem. Rev.*, 2001, **101**, 4071–4098.
38 F. Biedermann and H.-J. Schneider, *Chem. Rev.*, 2016, **116**, 5216–5300.
39 T. Aida, E. W. Meijer and S. I. Stupp, *Science*, 2012, **335**, 813–817.
40 D. B. Amabilino, D. K. Smith and J. W. Steed, *Chem. Soc. Rev.*, 2017, **46**, 2404–2420.
41 S. Yagai and A. Kitamura, *Chem. Soc. Rev.*, 2008, **37**, 1520–1529.
42 X. Yan, F. Wang, B. Zheng and F. Huang, *Chem. Soc. Rev.*, 2012, **41**, 6042–6065.
43 C. D. Jones and J. W. Steed, *Chem. Soc. Rev.*, 2016, **45**, 6546–6596.
44 X. Yao, T. Li, J. Wang, X. Ma and H. Tian, *Adv. Opt. Mater.*, 2016, **4**, 1322–1349.
45 S. Lee, K. Y. Kim, S. H. Jung, J. H. Lee, M. Yamada, R. Sethy, T. Kawai and J. H. Jung, *Angew. Chem. Int. Ed.*, 2019, **58**, 18878–18882.
46 T. F. A. De Greef, M. M. J. Smulders, M. Wolffs, A. P. H. J. Schenning, R. P. Sijbesma and E. W. Meijer, *Chem. Rev.*, 2009, **109**, 5687–5754.
47 M. M. J. Smulders, M. M. L. Nieuwenhuizen, T. F. A. de Greef, P. van der Schoot, A. P. H. J. Schenning and E. W. Meijer, *Chem. – Eur. J.*, 2010, **16**, 362–367.
48 P. K. Hashim, J. Bergueiro, E. W. Meijer and T. Aida, *Prog. Polym. Sci.*, 2020, **105**, 101250.
49 E. Busseron, Y. Ruff, E. Moulin and N. Giuseppone, *Nanoscale*, 2013, **5**, 7098–7140.
50 T. D. Clemons and S. I. Stupp, *Prog. Polym. Sci.*, 2020, **111**, 101310–101340.
51 T. F. A. de Greef and E. W. Meijer, *Nature*, 2008, **453**, 171–173.
52 A. Sorrenti, J. Leira-Iglesias, A. J. Markvoort, T. F. A. de Greef and T. M. Hermans, *Chem. Soc. Rev.*, 2017, **46**, 5476–5490.
53 J. Matern, Y. Dorca, L. Sánchez and G. Fernández, *Angew. Chem. Int. Ed.*, 2019, **58**, 16730–16740.
54 E. Yashima, N. Ousaka, D. Taura, K. Shimomura, T. Ikai and K. Maeda, *Chem. Rev.*, 2016, **116**, 13752–13990.
55 Y. Dorca, E. E. Greciano, J. S. Valera, R. Gómez and L. Sánchez, *Chem. – Eur. J.*, 2019, **25**, 5848–5864.
56 M. Liu, L. Zhang and T. Wang, *Chem Rev*, 2015, **115**, 7304–7397.
57 G. P. Moss, *Pure Appl. Chem.*, 1996, **68**, 2193–2222.
58 G. Albano, G. Pescitelli and L. Di Bari, *Chem. Rev.*, 2020, **120**, 10145–10243.
59 S. Cantekin, T. F. A. de Greef and A. R. A. Palmans, *Chem. Soc. Rev.*, 2012, **41**, 6125–6138.
60 P. J. M. Stals, J. C. Everts, R. de Bruijn, I. A. W. Filot, M. M. J. Smulders, R. Martín-Rapún, E. A. Pidko, T. F. A. de Greef, A. R. A. Palmans and E. W. Meijer, *Chem. - Eur. J.*, 2010, **16**, 810–821.
61 Y. Nakano, T. Hirose, P. J. M. Stals, E. W. Meijer and A. R. A. Palmans, *Chem. Sci.*, 2011, **3**, 148–155.
62 A. Desmarchelier, B. G. Alvarenga, X. Caumes, L. Dubreucq, C. Troufflard, M. Tessier, N. Vanthuyne, J. Idé, T. Maistriaux, D. Beljonne, P. Brocorens, R. Lazzaroni, M. Raynal and L. Bouteiller, *Soft Matter*, 2016, **12**, 7824–7838.
63 C. Kulkarni, E. W. Meijer and A. R. A. Palmans, *Acc. Chem. Res.*, 2017, **50**, 1928–1936.

64 G. Basuyaux, A. Desmarchelier, G. Gontard, N. Vanthuyne, J. Moussa, H. Amouri, M. Raynal and L. Bouteiller, *Chem. Commun.*, 2019, **55**, 8548–8551.
65 W. R. Henderson and R. K. Castellano, *Polym. Int.*, , DOI:https://doi.org/10.1002/pi.6111.
66 C. J. Newcomb, T. J. Moyer, S. S. Lee and S. I. Stupp, *Curr. Opin. Colloid Interface Sci.*, 2012, **17**, 350–359.
67 Y. Sang, D. Yang, P. Duan and M. Liu, *Chem. Sci.*, 2019, **10**, 2718–2724.
68 G. Gottarelli, S. Lena, S. Masiero, S. Pieraccini and G. P. Spada, *Chirality*, 2008, **20**, 471–485.
69 C. Yang and Y. Inoue, in *Comprehensive Chiroptical Spectroscopy*, eds. N. Berova, P. L. Polavarapu, K. Nakanishi and R. W. Woody, John Wiley & Sons, Inc., Hoboken, NJ, USA, 2012, pp. 317–353.
70 A. Mammana, G. T. Carroll and B. L. Feringa, in *Comprehensive Chiroptical Spectroscopy*, eds. N. Berova, P. L. Polavarapu, K. Nakanishi and R. W. Woody, John Wiley & Sons, Inc., Hoboken, NJ, USA, 2012, pp. 289–316.
71 G. Pescitelli, L. D. Bari and N. Berova, *Chem. Soc. Rev.*, 2014, **43**, 5211–5233.
72 P. J. M. Stals, P. A. Korevaar, M. A. J. Gillissen, T. F. A. de Greef, C. F. C. Fitié, R. P. Sijbesma, A. R. A. Palmans and E. W. Meijer, *Angew. Chem. Int. Ed.*, 2012, **51**, 11297–11301.
73 Z. Shen, T. Wang and M. Liu, *Angew. Chem. Int. Ed.*, 2014, **53**, 13424–13428.
74 Z. Shen, T. Wang, L. Shi, Z. Tang and M. Liu, *Chem. Sci.*, 2015, **6**, 4267–4272.
75 Z. Shen, Y. Jiang, T. Wang and M. Liu, *J. Am. Chem. Soc.*, 2015, **137**, 16109–16115.
76 Z. Shen, Y. Sang, T. Wang, J. Jiang, Y. Meng, Y. Jiang, K. Okuro, T. Aida and M. Liu, *Nat. Commun.*, 2019, **10**, 1–8.
77 S. C. Karunakaran, B. J. Cafferty, A. Weigert-Muñoz, G. B. Schuster and N. V. Hud, *Angew. Chem. Int. Ed.*, 2019, **58**, 1453–1457.
78 Y. Sang and M. Liu, *Symmetry*, 2019, **11**, 950.
79 B. Chang, X. Li and T. Sun, *Eur. Polym. J.*, 2019, **118**, 365–381.
80 L. Brunsveld, A. P. H. J. Schenning, M. A. C. Broeren, H. M. Janssen, J. A. J. M. Vekemans and E. W. Meijer, *Chem. Lett.*, 2000, **29**, 292–293.
81 A. R. A. Palmans and E. W. Meijer, *Angew. Chem. Int. Ed.*, 2007, **46**, 8948–8968.
82 C. Kulkarni, R. Munirathinam and S. J. George, *Chem. – Eur. J.*, 2013, **19**, 11270–11278.
83 J. Buendía, F. García, B. Yélamos and L. Sánchez, *Chem. Commun.*, 2016, **52**, 8830–8833.
84 M. M. Green, M. P. Reidy, R. D. Johnson, G. Darling, D. J. O'Leary and G. Willson, *J. Am. Chem. Soc.*, 1989, **111**, 6452–6454.
85 M. M. Green, N. C. Peterson, T. Sato, A. Teramoto, R. Cook and S. Lifson, *Science*, 1995, **268**, 1860–1866.
86 M. M. Green, J.-W. Park, T. Sato, A. Teramoto, S. Lifson, R. L. B. Selinger and J. V. Selinger, *Angew. Chem. Int. Ed.*, 1999, **38**, 3138–3154.
87 A. R. A. Palmans, J. A. J. M. Vekemans, E. E. Havinga and E. W. Meijer, *Angew. Chem. Int. Ed. Engl.*, 1997, **36**, 2648–2651.
88 J. van Gestel, A. R. A. Palmans, B. Titulaer, J. A. J. M. Vekemans and E. W. Meijer, *J. Am. Chem. Soc.*, 2005, **127**, 5490–5494.
89 S. Cantekin, D. W. R. Balkenende, M. M. J. Smulders, A. R. A. Palmans and E. W. Meijer, *Nat. Chem.*, 2011, **3**, 42–46.
90 Y. Li, A. Hammoud, L. Bouteiller and M. Raynal, *J. Am. Chem. Soc.*, 2020, **142**, 5676–5688.
91 T. Kim, T. Mori, T. Aida and D. Miyajima, *Chem Sci*, 2016, **7**, 6689–6694.

92 I. Reva, L. Lapinski, N. Chattopadhyay and R. Fausto, *Phys. Chem. Chem. Phys.*, 2003, **5**, 3844–3850.
93 V. A. Naumov, S. Samdal, A. V. Naumov, S. Gundersen and H. V. Volden, *Russ. J. Gen. Chem.*, 2005, **75**, 1956–1961.
94 L. Zhang, H.-X. Wang, S. Li and M. Liu, *Chem. Soc. Rev.*, 2020, **49**, 9095–9120.
95 Y. Sang, J. Han, T. Zhao, P. Duan and M. Liu, *Adv. Mater.*, 2020, **32**, 1900110.
96 C. Train, M. Gruselle and M. Verdaguer, *Chem. Soc. Rev.*, 2011, **40**, 3297–3312.
97 C. Kulkarni, A. K. Mondal, T. K. Das, G. Grinbom, F. Tassinari, M. F. J. Mabesoone, E. W. Meijer and R. Naaman, *Adv. Mater.*, 2020, **32**, 1904965.
98 Q. Zhang, D.-H. Qu and H. Tian, *Adv. Opt. Mater.*, 2019, **7**, 1900033.
99 L. Wang and Q. Li, *Chem. Soc. Rev.*, 2018, **47**, 1044–1097.
100 V. V. Jerca and R. Hoogenboom, *Angew. Chem. Int. Ed.*, 2018, **57**, 7945–7947.
101 B. L. Feringa, R. A. van Delden, N. Koumura and E. M. Geertsema, *Chem. Rev.*, 2000, **100**, 1789–1816.
102 W. R. Browne and B. L. Feringa, in *Molecular Switches*, John Wiley & Sons, Ltd, 2011, pp. 121–179.
103 M. Nič, J. Jirát, B. Košata, A. Jenkins and A. McNaught, Eds., *IUPAC Compendium of Chemical Terminology: Gold Book*, IUPAC, Research Triagle Park, NC, 2.1.0., 2009.
104 J. Li, G. B. Schuster, K.-S. Cheon, M. M. Green and J. V. Selinger, *J. Am. Chem. Soc.*, 2000, **122**, 2603–2612.
105 M. Suarez and G. B. Schuster, *J. Am. Chem. Soc.*, 1995, **117**, 6732–6738.
106 Y. Wang, T. Sakamoto and T. Nakano, *Chem. Commun.*, 2012, **48**, 1871–1873.
107 M. Fujiki, K. Yoshida, N. Suzuki, J. Zhang, W. Zhang and X. Zhu, *RSC Adv.*, 2013, **3**, 5213–5219.
108 Y. Wang, A. L. Kanibolotsky, P. J. Skabara and T. Nakano, *Chem. Commun.*, 2016, **52**, 1919–1922.
109 Y. Wang, T. Harada, L. Q. Phuong, Y. Kanemitsu and T. Nakano, *Macromolecules*, 2018, **51**, 6865–6877.
110 J. Cheng, F. Ge, Y. Xiang, H. Zhang, Y. Kuai, P. Hou, D. Zhang, L. Qiu, Q. Zhang and G. Zou, *J. Mater. Chem. C*, 2020, **8**, 6521–6527.
111 L. Nikolova, T. Todorov, M. Ivanov, F. Andruzzi, S. Hvilsted and P. S. Ramanujam, *Opt. Mater.*, 1997, **8**, 255–258.
112 G. Iftime, F. L. Labarthet, A. Natansohn and P. Rochon, *J. Am. Chem. Soc.*, 2000, **122**, 12646–12650.
113 M. Ivanov, I. Naydenova, T. Todorov, L. Nikolova, T. Petrova, N. Tomova and V. Dragostinova, *J. Mod. Opt.*, 2000, **47**, 861–867.
114 M.-J. Kim, B.-G. Shin, J.-J. Kim and D.-Y. Kim, *J. Am. Chem. Soc.*, 2002, **124**, 3504–3505.
115 Z. Zheng, J. Xu, Y. Sun, J. Zhou, B. Chen, Q. Zhang and K. Wang, *J. Polym. Sci. Part Polym. Chem.*, 2006, **44**, 3210–3219.
116 S.-W. Choi, S. Kawauchi, N. Y. Ha and H. Takezoe, *Phys. Chem. Chem. Phys.*, 2007, **9**, 3671–3682.
117 G. Cipparrone, P. Pagliusi, C. Provenzano and V. P. Shibaev, *Macromolecules*, 2008, **41**, 5992–5996.
118 G. Zou, H. Jiang, H. Kohn, T. Manaka and M. Iwamoto, *Chem. Commun.*, 2009, **0**, 5627–5629.

119 G. Zou, H. Jiang, Q. Zhang, H. Kohn, T. Manaka and M. Iwamoto, *J. Mater. Chem.*, 2009, **20**, 285–291.
120 L. Wang, L. Yin, W. Zhang, X. Zhu and M. Fujiki, *J. Am. Chem. Soc.*, 2017, **139**, 13218–13226.
121 Y. Tang and A. E. Cohen, *Phys. Rev. Lett.*, 2010, **104**, 163901.
122 Y. Zhao, A. A. E. Saleh, M. A. van de Haar, B. Baum, J. A. Briggs, A. Lay, O. A. Reyes-Becerra and J. A. Dionne, *Nat. Nanotechnol.*, 2017, **12**, 1055–1059.
123 A. Pietropaolo, Y. Wang and T. Nakano, *Angew. Chem. Int. Ed.*, 2015, **54**, 2688–2692.
124 J. J. Armao, M. Maaloum, T. Ellis, G. Fuks, M. Rawiso, E. Moulin and N. Giuseppone, *J. Am. Chem. Soc.*, 2014, **136**, 11382–11388.
125 G. Zou, H. Kohn, Y. Ohshima, T. Manaka and M. Iwamoto, *Chem. Phys. Lett.*, 2007, **442**, 97–100.
126 Y. Xu, H. Jiang, Q. Zhang, F. Wang and G. Zou, *Chem. Commun.*, 2013, **50**, 365–367.
127 G. Yang, L. Han, H. Jiang, G. Zou, Q. Zhang, D. Zhang, P. Wang and H. Ming, *Chem Commun*, 2014, **50**, 2338–2340.
128 H. Menzel, S. Horstmann, M. D. Mowery, M. Cai and C. E. Evans, *Polymer*, 2000, **41**, 8113–8119.
129 C. Park, J. Lee, T. Kim, J. Lim, J. Park, W. Y. Kim and S. Y. Kim, *Molecules*, 2020, **25**, 402.
130 M. Raynal, F. Portier, P. W. van Leeuwen and L. Bouteiller, *J. Am. Chem. Soc.*, 2013, **135**, 17687–17690.
131 Q. Jin, L. Zhang, H. Cao, T. Wang, X. Zhu, J. Jiang and M. Liu, *Langmuir*, 2011, **27**, 13847–13853.
132 J. Jiang, Y. Meng, L. Zhang and M. Liu, *J. Am. Chem. Soc.*, 2016, **138**, 15629–15635.
133 C. Yuan, J. Jiang, H. Sun, D. Wang, Y. Hu and M. Liu, *ChemCatChem*, 2018, **10**, 2190–2194.
134 A. Desmarchelier, X. Caumes, M. Raynal, A. Vidal-Ferran, P. W. N. M. van Leeuwen and L. Bouteiller, *J. Am. Chem. Soc.*, 2016, **138**, 4908–4916.
135 J. M. Zimbron, X. Caumes, Y. Li, C. M. Thomas, M. Raynal and L. Bouteiller, *Angew. Chem. Int. Ed.*, 2017, **56**, 14016–14019.
136 A. Arlegui, B. Soler, A. Galindo, O. Arteaga, A. Canillas, J. M. Ribó, Z. El-Hachemi, J. Crusats and A. Moyano, *Chem. Commun.*, 2019, **55**, 12219–12222.

Chapter III Effect of light on the structure of assemblies formed by triarylamine trisamide monomers

Abstract

In this chapter, the synthesis and characterization of triarylamine trisamide (TATA) monomers with saturated sides chains are described, as well as their association properties probed in presence and absence of light. The self-association properties of TATA monomers with C11 and C12 aliphatic side chains were examined into details in chloroform and in bulk (powder/film) by a variety of techniques: UV–Vis–NIR, FT–IR, ^{1}H NMR and EPR spectroscopy and SANS analyses. The nature of self-assemblies formed by these TATA molecules was found to drastically depend on the conditions (concentration, temperature, time) and our study reveals that several assemblies are actually in competition. Two types of TATA assemblies have been unambiguously determined: non-specific one-dimensional aggregates (at intermediate concentration); and ribbons composed of hydrogen-bonded helical stacks (at high concentration). Thin films were also prepared and were found to consist mainly of long stacks of hydrogen-bonded TATAs. The impact of light irradiation was investigated at room temperature in all these states and at low temperature for intermediate concentrations. The spectroscopic signature of the generated TATA$^{\bullet+}$ species has been determined, their number has been evaluated and the influence of these species on the nature of the assemblies has been scrutinized. At intermediate concentration radical and neutral molecules co-assemble into non-specific aggregates, however these assemblies have similar structure before and after integration of TATA$^{\bullet+}$ species. The delocalization of the unpaired electrons of TATA$^{\bullet+}$ species in these non-specific aggregates is slow as probed by ^{1}H NMR and EPR analyses. By decreasing the temperature, these non-specific aggregates transform into hydrogen-bonded stacks which likely incorporate a fraction of TATA$^{\bullet+}$ species. At higher concentration, generation of the TATA$^{\bullet+}$ species slightly shortens the ribbons composed of hydrogen-bonded stacks which further reveal the competitive nature of the co-assembly process. Only a part of the radical

cationic species are found to be present into the hydrogen-bonded stacks under these conditions. The unpaired electrons of $TATA^{\bullet+}$ species in these hydrogen-bonded co-assemblies appear to be localized according to EPR analysis. We attribute this surprising observation to the possible disorder present upon stacking of neutral and radical TATA molecules. Finally, drop casting a light irradiated solution of TATA yields a film for which both radical cationic and neutral TATA molecules are co-assembled within hydrogen-bonded stacks. In these co-assemblies, the unpaired electrons of the triarylammonium radicals are fully delocalized within the stacks, as demonstrated by EPR measurements. Our study reveals that neutral TATA monomers compete into different structures in solution, and that the nature of the dominant structure will impart the amount of generated $TATA^{\bullet+}$ species upon irradiation and the nature of resulting structure of the co-assemblies formed between neutral and radical species. The elucidation of complex (co-)assembly behavior between triarylammonium radicals and neutral TATA species is important for their implementation in optoelectronic devices and in the context of controlling their supramolecular chirality.

I. Introduction

Shirota *et al.* synthesized the first N-centered C_3-symmetric triarylamine trisamide (**TATA**) molecule with stearic side chains in 1996[1], and showed its ability to form a thermoreversible and electrochromic gel, turning green upon electrochemical oxidation[1,2]. Then, up to 2013, TATA molecules were decorated with a variety of functional groups (triscatechol and bisurea derivatives, benzenic end-groups and calix[4]-arene to name a few) to construct supramolecular assemblies such as tetrahedral cages[3,4] or higher-order assemblies[5], metal-organic polyrotaxanes[6], dendrimers[7], dyes[8] or to be used as nucleation agent for polypropylene[9].

Giuseppone *et al.* initiated the characterization of TATA aggregates in 2014[10], with the aim of developing functional nanomaterials[11,12]. Compared with systems based on triarylamine monoamides intensively studied by the same authors, and for which they evidenced a light-triggering self-assembly phenomenon[13–15], they reported that TATA molecules (with C11, C16 and C21 linear aliphatic side chains) form stable assemblies and gels at ambient conditions. Moreover, upon light irradiation of "preassembled TATA fibers" in diluted solutions (0.1 mM in $CHCl_3$), they claimed a stepwise co-assembly process between radical and neutral TATA molecules that eventually led to fibers in which unpaired electrons are fully delocalized by "intermolecular through-space charge-transfer between stacked triarylamine cores". Spectroscopic analyses and conductivity measurements support a metallic behavior of these fibers within gels, thin films or powders composed of this irradiated organic material. The radicals could heal defects in the course of their "diffusion through the columnar stacks".

More recently, the assembly properties of a TATA monomer decorated with three norbornene end groups have been determined[16]. Light irradiation in diluted solutions in $CHCl_3$ (0.1 mM) led to the stacking of the molecules but with no detectable delocalization of the triarylammonium radical cations, despite significant conductivity of the fibers (measured between ITO plates of a 17 mM tetrachloroethane solution). Covalent trapping of irradiated solutions was performed in the gel state in toluene, the corresponding fibers contain fully delocalized radicals.

It is also worth mentioning that assemblies of TATA molecules featuring amide functions connected by their N-center[17–21] or C-center[22–25] to the central triphenylamine moiety were also investigated in apolar solvents in the absence of light. These molecules embed stereogenic centers in their side chains and have been found to form long helical hydrogen-bonded assemblies. They also exhibit complex aggregation pathways. For example, the nature of the self-assemblies composed of a TATA featuring a (2*S*)-2,6-dimethylheptyl side chain was found to change as a function of the cooling rate. A slow or fast cooling of a hot solution of this molecule down to 10°C led either to the bundling of helical columnar stacks into superhelices, or to coagulated fibers which exhibit different chiroptical properties[26]. The same authors further probed the association of this chiral TATA in toluene upon cooling down to 0°C and ageing, and unveiled another type of assemblies thanks to a combined electronic/vibrational-CD study[27]. A third pathway leads to superhelices in which amide groups have not all the same orientation: they exhibit a (2:1)-conformation instead of a (3:0)-conformation in the two other structures. The effect of light on this intricate self-assembly behavior has not been reported.

Helical assemblies of TATA molecules, based on a combination of hydrogen bond and aromatic interactions similar to the ones formed by BTA molecules, have been experimentally confirmed in the solid state,[28–30] in solution[17], and computed (**Figure III.1**)[10,31]. However, it remains to be determined whether this structure is formed under the full range of the different conditions that have been implemented in the aforementioned studies (*i.e.* diluted solutions, gels, films, pure solvent or solvent mixtures). As the structure of hydrogen-bonded supramolecular polymers are highly sensitive to the conditions (concentration, temperature, solvent)[32], it is reasonable to anticipate that the structure of the assemblies would differ under these different conditions. In addition, the effect of light irradiation on the structure of self-assemblies, notably on the mechanism of the photo-oxidation of TATA which leads to fully delocalized radicals inside fibers, deserves further investigation. The hydrogen-bond network is likely to be affected upon co-assembly between neutral and radical cationic species and only short mixed aggregates have been computed[10]. Finally, competitive association pathways have been mentioned for related molecules in the literature and it would be interesting to probe whether similar pathways are at work for irradiated TATA assemblies.

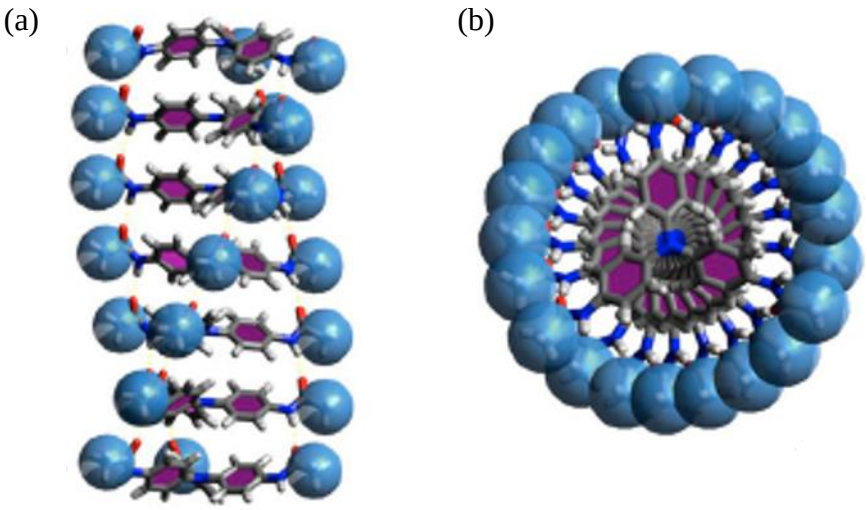

Figure III.1 (a) Side and (b) top views of the self-assembled structure of a TATA model, with methyl groups as side chains, calculated by density function theory method (DFT) by Giuseppone *et al.*[10]

Since our goal is to reproduce the control of supramolecular chirality which has been reported by Kim *et al.*[33] for a TATA molecule which requires several synthetic steps (Chapter IV), we decided to start by probing the assembly behavior of structurally simpler TATA analogues. TATA monomers with saturated side chains will be studied to highlight the conditions of assembly, as well as to probe the aggregates structure (e.g. shape, length and interactions between molecules). The effect of light irradiation and triarylammonium radicals will then be assessed on a variety of association states. The co-assembly between radical cationic species and neutral molecules, as well as the involved type of interactions, will be in particular examined. Notably, a special attention will be paid for determining the nature of the hydrogen bond network, which is likely the driving force of the CPL-controlled supramolecular chirality of TATA-based assemblies.

II. Synthesis, characterization and solubility tests

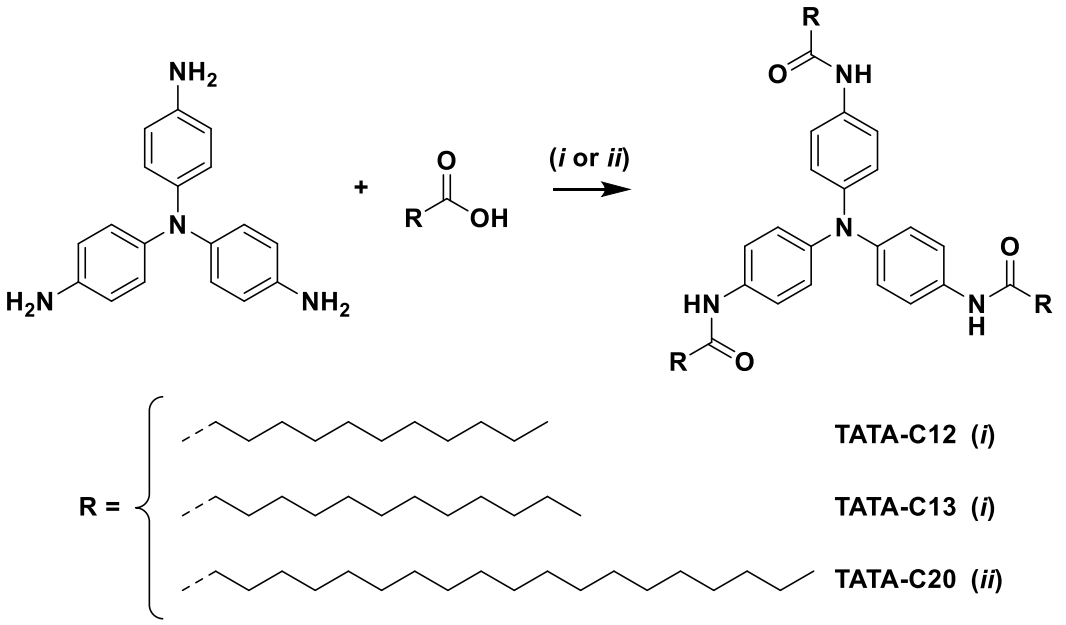

Figure III.2 Synthesis of TATA monomers. (*i*) DMAP/EDC·HCl/DMF (76% and 80% yield for **TATA-C12** and **TATA-C13**, respectively) and (*ii*) EDC·HCl/HOBt/triethylamine/DMF (80% yield for **TATA-C20**).

Gram-scale synthesis of TATA monomers has been achieved in one step from commercial tris(4-aminophenyl)amine, inspired by two existing procedures (*i*[34] and *ii*[33])[XXVI]. Amide bond forming reactions with three different saturated fatty acids gave similar yields for **TATA-C12**, **TATA-C13** and **TATA-C20**, with C11, C12 and C19 linear aliphatic side chains, respectively (**Figure III.2**). Each molecule has its own advantage: **TATA-C12** allowed to compare a part of our results with those reported by Giuseppone *et al.*[10]; **TATA-C13** is the saturated analogue of the TATA molecule reported by Kim *et al.* for CPL-controlled supramolecular chirality; while **TATA-C20** could help to reach a better solubility in apolar solvents (which is a key point for catalysis), thanks to its longer alkyl side chains. Additionally,

[XXVI] EDC·HCl, DMAP and HOBt are frequently used as additive for amide bond formation[35–37]. Notably, EDC·HCl forms with carboxylic acids an active *O*-acylisourea, that can directly react with the amine to give the desired product and a poorly soluble urea by-product.

TATA-C12 and **TATA-C13** could permit to explore a potential odd-even effect coming from the side chain. Overall, characterization by ^{1}H, ^{13}C and bidimensional NMR studies (**Figure SIII.34** to **Figure SIII.39**), as well as infrared spectroscopy, high-resolution mass spectrometry (HRMS) and elementary analyses demonstrated the high purity of the synthesized molecules.

Solubility tests at 1 mM concentration in solvents of various polarities allow to highlight the influence of the length of the side chains (**Table III.1**).

Table III.1 Solubility of **TATA-C12**, **TATA-C13** and **TATA-C20** (1 mM) after heating up to the boiling point. G = gel, I = insoluble, P = precipitation, S = soluble, η ↑ = viscosity increases.

Solvent	TATA-C12	TATA-C13	TATA-C20
Methylcyclohexane	I	I (η↑)	I (η↑)
Decalin	I (η↑)	I	I (η↑)
Toluene	P (η↑)	P (η↑)	G
Trifluorotoluene	I	I	I
DCM	S	P (η↑)	P
$CHCl_3$	S	S	P
1,2-DCE	P (η↑)	P (η↑)	P
MeOH	P	I	I
EtOH	S	S	I
Et_2O	I	I	I
THF	S	S	S
1,4-Dioxane	S	S	S
Acetone	P	I	I
Ethyl acetate	P	S	I
Acetonitrile	I	I	I
DMSO	S	S	P
DMF	S	S	S

Remarkably, while the long alkyl chains of **TATA-C20** imparts better solubility in toluene, leading to a gel, it precludes good solubility in $CHCl_3$. The low solubility of **TATA-C20** discarded its use in the rest of the study, since chlorinated solvents are necessary to the photo-oxidation of TATA, and mixtures of solvents were avoided to simplify the

interpretations. Interestingly, the increase of viscosity observed for many solutions of TATA likely reflects the presence of very long assemblies. Additional solubility tests were performed at a lower concentration (0.1 mM, **Table SIII.2**). **TATA-C13** is now soluble in decalin (accompanied by an increase of viscosity) and toluene, while **TATA-C20** is soluble in decalin (accompanied by an increase of viscosity). On the contrary, it is interesting to note that fluid solutions for **TATA-C12** and **TATA-C13** are observed at both at 0.1 mM and 1.0 mM in $CHCl_3$ which likely indicates the absence of long assemblies in this solvent.

III. Self-association properties without light

III. 1. Hydrogen bonding at various concentrations

TATA-C12 and **TATA-C13** were chosen to probe the self-association properties of TATA in chloroform, thanks to their good solubility in this solvent and the possibility of promoting the photo-oxidation reaction[10]. Knowing that the degree of supramolecular polymerization is related to the concentration and the temperature[32], the self-association of **TATA-C12** and **TATA-C13** was first investigated by FT–IR analyses in chloroform at various concentrations and at 20°C, after cooling hot solutions (**Figure III.3**).

TATA-C12 and **TATA-C13** exhibit a similar concentration-dependent FT–IR profile in the N-H region (C=O region in **Figure SIII.40**). At low concentration ($c \leqslant 0.6$ mM), **TATA-C12** and **TATA-C13** show a single absorption band at 3434 cm^{-1}, corresponding to the stretching vibration of free amide N-H. On the contrary, at high concentration ($c \geqslant 11.9$ mM), a strong absorption band is observed at 3292 cm^{-1}, which is characteristic of hydrogen bonded amide N-H. In this state, the solution forms a gel (*i.e.* it does not flow immediately when the vial is inverted), and the signal corresponding to free N-H is quite low, indicating a degree of aggregation higher than 0.6. This result is in agreement with the critical gelation concentration of 17.9 mM reported for **TATA-C12** by the inverted tube method[10]. The decrease of the fraction of free N-H and the increase of that of bonded N-H with concentration is indicative of the formation of intermolecular hydrogen bonds. This FT–IR result is in accordance with computed DFT models of TATA helical stacks, for which TATA monomers are connected by means of a threefold hydrogen bond network[10]. For intermediary concentrations ($2.3 \leqslant c \leqslant 6.0$ mM),

although the absorption band accounting for free N-H groups is intense ($\alpha_{Agg} \leqslant 0.3$), a flat and wide signal occurs between 3400 and 3250 cm^{-1}, suggesting the presence of different types of hydrogen bonded assemblies which are likely disordered and short aggregates.

In summary, TATA monomers showcase three different states as a function of the concentration:

1) molecules free of interactions through H-bonds (low concentration, *i.e.* ≤ 0.6 mM)[XXVII];
2) ill-defined hydrogen bonded aggregates (intermediate concentration);
3) well-defined hydrogen-bonded stacks (high concentration, *i.e.* ≥ 12 mM).

[XXVII] These molecules are not necessarily in the monomeric state and might interact by means of "non-specific" interactions (*vide infra*).

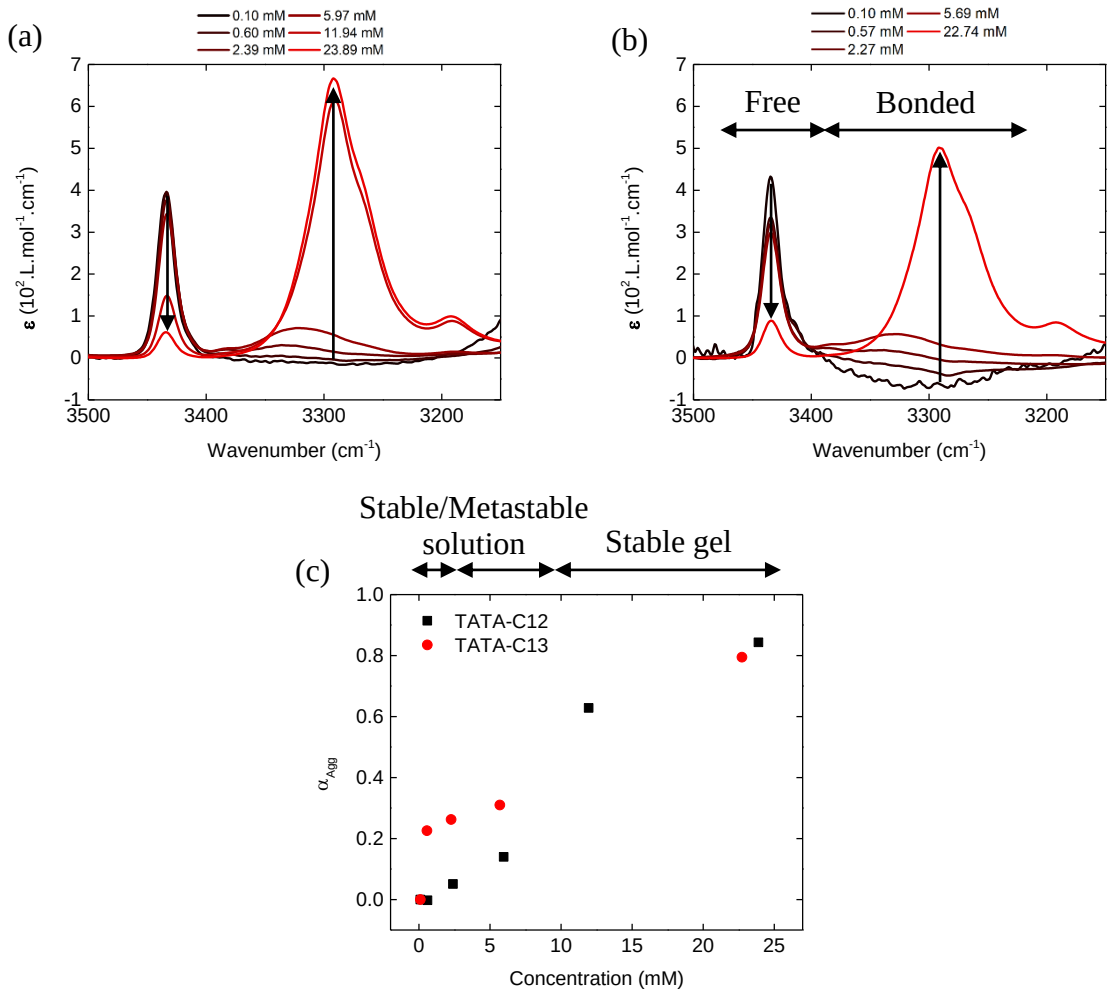

Figure III.3 Concentration-dependent FT–IR spectra of (a) **TATA-C12** and (b) **TATA-C13** in chloroform at 20°C. Zoom on the N-H region. (c) Evolution of the degree of aggregation as a function of the concentration, plotted according to (a) and (b). The degree of aggregation (α_{Agg}) is calculated from the evolution of the free N-H stretching vibration intensity (ν = 3434 cm^{-1}) as a function of the concentration.

III. 2. Association at low concentration: 0.1 mM

Having evidenced the three states of TATA molecules in chloroform at room temperature, we further explored each of them by varying analytical techniques and conditions (essentially time and temperature).

First, the low concentration regime was probed by UV–Vis–NIR and FT–IR absorption spectroscopy, right after dissolution at 40°C as well as two hours later (**Figure III.4**).

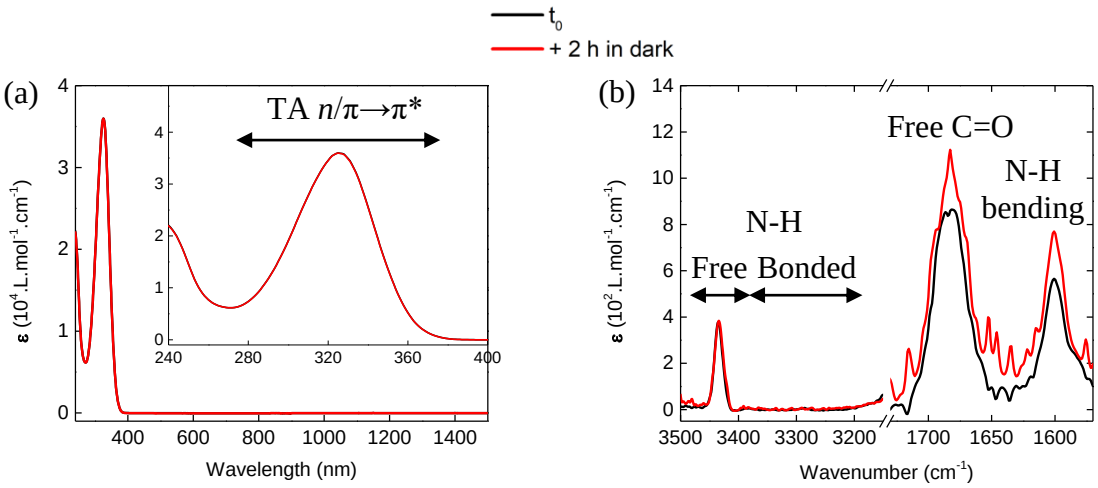

Figure III.4 TATA-C12 at 0.1 mM in chloroform after dissolution and after two hours in the dark. (a) UV–Vis–NIR absorption with a zoom in the UV range, and (b) FT–IR spectra with a zoom on the N-H and C=O regions.

After dissolution, the UV–Vis–NIR profile showed an absorption band with maximum at about 325 nm, attributed to mixed $n\rightarrow\pi^*$ and $\pi\rightarrow\pi^*$ electronic transitions of the triarylamine core[38]; while the FT–IR spectroscopy highlighted signals at 3434 cm^{-1}, 1683 cm^{-1} and 1601 cm^{-1}, corresponding to the free N-H[39,40], free C=O stretching (called amide *I*)[41] and N-H bending, respectively[17,42,43]. This result confirms that TATA molecules are not interacting by hydrogen bonds or aromatic interactions at 0.1 mM. Two hours later, the UV–Vis–NIR and FT–IR profiles remained the same, attesting the stability of the solution within this timescale.

The possibility of triggering the association by lowering the temperature was probed by FT–IR. A Variable-temperature (VT) analysis of **TATA-C13** in chloroform at 0.1 mM was carried out (**Figure III.5**).

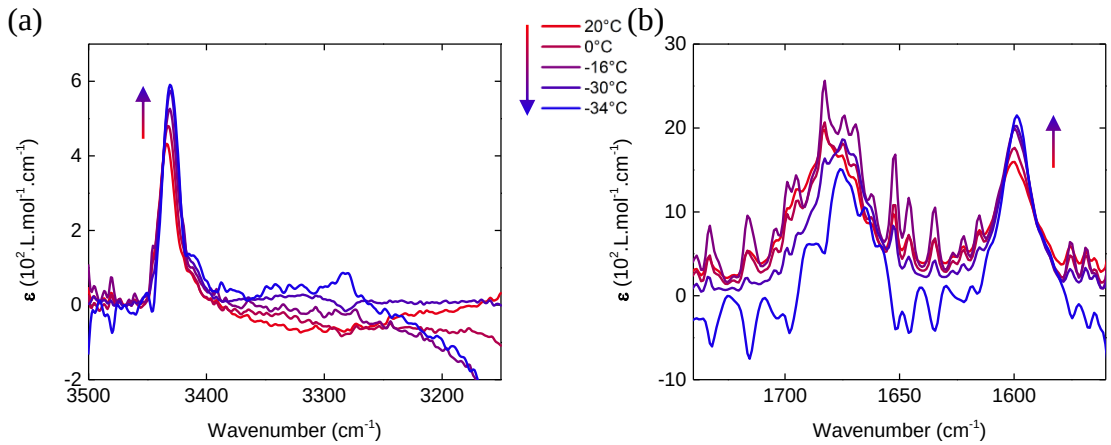

Figure III.5 Variable-temperature FT–IR analysis of **TATA-C13** at 0.1 mM upon cooling.

Upon cooling down to -34°C, **TATA-C13**, no significant change of the FT–IR spectrum is seen. Due to the chloroform contraction, a global hyper/bathochromic shifts of molar extinction coefficient can nevertheless be observed, especially at maxima of absorption ($\Delta\lambda$ = -3/-1 nm and $\Delta\varepsilon \approx 1.6/5.5 \times 10^4$ L.mol^{-1}.cm^{-1} at 3433cm^{-1} and 1600 cm^{-1}, respectively).

On combining the VT–FT–IR results with the UV–Vis–NIR and FT–IR analyses over time, we concluded that at low concentration, TATA molecules employed in this study are at the thermodynamic equilibrium and do not interact through hydrogen or aromatic interactions. They are likely under the form of free monomers, even though the presence of non-specific aggregates, *i.e.* molecules interacting through dispersive forces cannot be fully discarded (*vide infra*).

III. 3. At an intermediate concentration: 2.3 mM

Concentration-dependent FT–IR study suggested that TATA molecules at 2.3 mM exist as a mixture of non-hydrogen bonded species (predominantly) and ill-defined hydrogen-bonded aggregates. Thereby, Variable-time (Vt) and variable-temperature (VT) spectroscopic analyses were performed to explore the impact of these parameters on the association state. When possible, spectroscopic and scattering experiments were conducted under similar conditions, *i.e.* the time of analyses after dissolution were adapted in order to be similar for all analyses.

III. 3. 1. At room temperature

The influence of time on the nature of assemblies was carefully probed by UV–Vis–NIR and FT–IR spectroscopy (**Figure III.6**), to first assess whether assemblies are under metastable state, and to be consistent with the fact that, for technical reasons, SANS analyses have been performed several hours after dissolution.

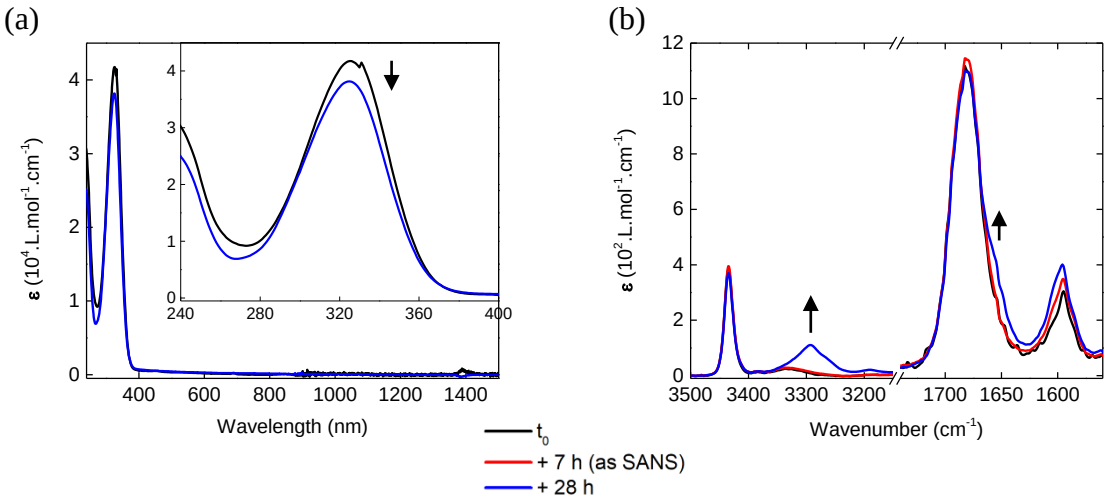

Figure III.6 TATA-C13 at 2.3 mM in chloroform. (a) UV–Vis–NIR absorption and (b) FT–IR spectra with a zoom on the N-H and C=O regions.

UV–Vis–NIR and FT–IR analyses of **TATA-C13** at 2.3 mM in chloroform confirmed that at t_0 and t_0 + 7 h, molecules do not interact through π–π stacking or H-bonding interactions (stable absorption bands at 325 nm, 3434 cm^{-1} and 1682 cm^{-1}). However, after 28 h, a clear decrease of the molar extinction coefficient at 325 nm, as well as the development of a symmetric absorption band at 3293 cm^{-1} (ascribed to hydrogen-bonded *trans* N-H stretching vibration[39,40,44,45]), support a progressive self-assembly by π–π stacking and hydrogen bonds of **TATA-C13** over time. The observation of a shoulder at 1654 cm^{-1}, ascribed to the stretching vibration of C=O groups interacting by hydrogen bonds, correlates favorably with this

finding[XXVIII]. This evolution with time substantiates a slow formation of helical columnar stacks built upon π–π stacking and a well-defined threefold hydrogen bonds network.

The metastable nature of the 2.3 mM solution appears more obviously when solutions are aged over weeks (**Figure III.7**). Photographs of the sample let in the dark during a few weeks depict a solution becoming opaque within a few days, then precipitating into a piece of gel floating in a clearer liquid (syneresis). Isolated from the rest of the solution by filtration, the precipitate was analyzed by FT–IR and showed amide bands solely at 3290 cm^{-1} and 1655 cm^{-1}, indicating that only hydrogen-bonded stacks are present in this gel (**Figure SIII.41**).

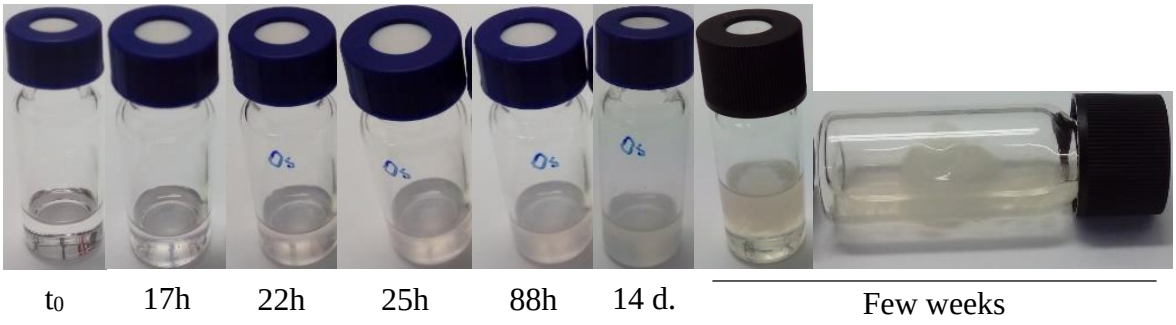

Figure III.7 Photographs of **TATA-C13** solutions over ageing. The solution became opaque then precipitated.

Small-Angle Neutron Scattering (SANS) gave additional information on the self-assembly behavior of **TATA-C13** in $CDCl_3$, at 2.3 mM and room temperature (**Figure III.8**). The scattered intensity is much higher than what is expected for monomers or dimers. In fact, it is close to the simulated curve, considering that all monomers assemble into rods. The deviation at low q values is possibly due to further aggregation of the rods. This might appear contradictory considering that no more than 5% of the molecules interact through hydrogen bonds at the time of the SANS analysis (t_0 + 7 h in **Figure III.6**). A change in the temperature of a few degrees would not induce a drastic increase of the aggregation degree (*vide infra*). So, one explanation might be put forward to give a rationale for the shape of the SANS curve: a

[XXVIII] $\Delta\alpha_{Agg} \approx 0.16$ between t_0 and + 28 h, as calculated from the evolution of the absorption of the hydrogen bonded N-H stretching vibration signal.

significant fraction of what have been surmised to be “monomers” are actually molecules likely aggregated through non-directional interactions (*i.e.* not detected by the spectroscopic measurements) and ill-defined hydrogen bonds (detected IR signals between 3400 cm^{-1} and 3250 cm^{-1}). These “non-specific” aggregates might be composed essentially of TATA associated through dispersion interactions.

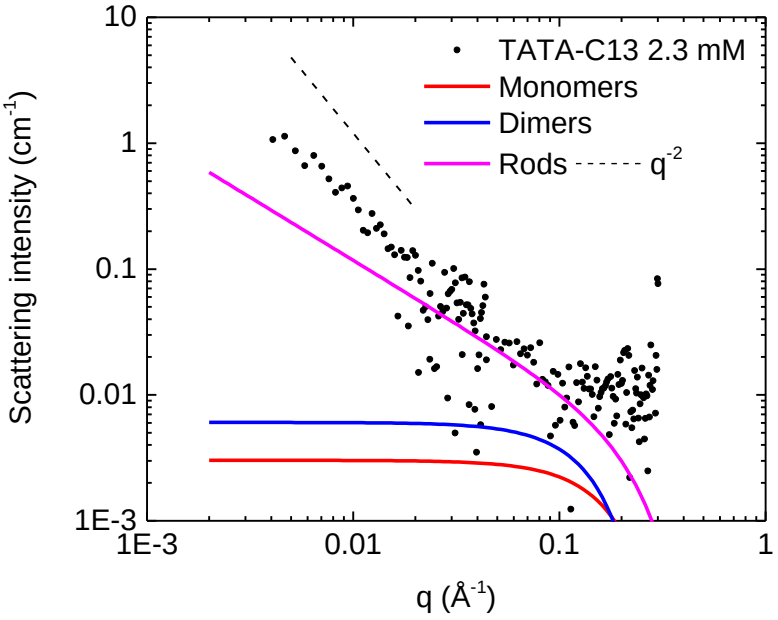

Figure III.8 SANS analysis of **TATA-C13** at 2.3 mM in $CDCl_3$ (7 hours after dissolution). Simulated curves for monomers, dimers or infinitely long rigid rods of circular cross-section (radius 2 nm) are shown together with the experimental data.

Taken together, these findings confirm the metastability of the 2.3 mM solutions in chloroform. Molecules seem kinetically trapped into disordered non-specific aggregates, that self-assemble with time into long self-assemblies, built upon π–π stacking and well-defined hydrogen bond interactions that eventually lead to an insoluble gel. It will be intriguing to determine the role, location and electronic state of TATA radicals generated under this metastable condition.

III. 3. 2. At low temperatures

VT analyses of **TATA-SDA** in chloroform at 2.3 mM were carried out by UV–Vis (**Figure III.9**) and FT–IR (**Figure III.10**) spectroscopy.

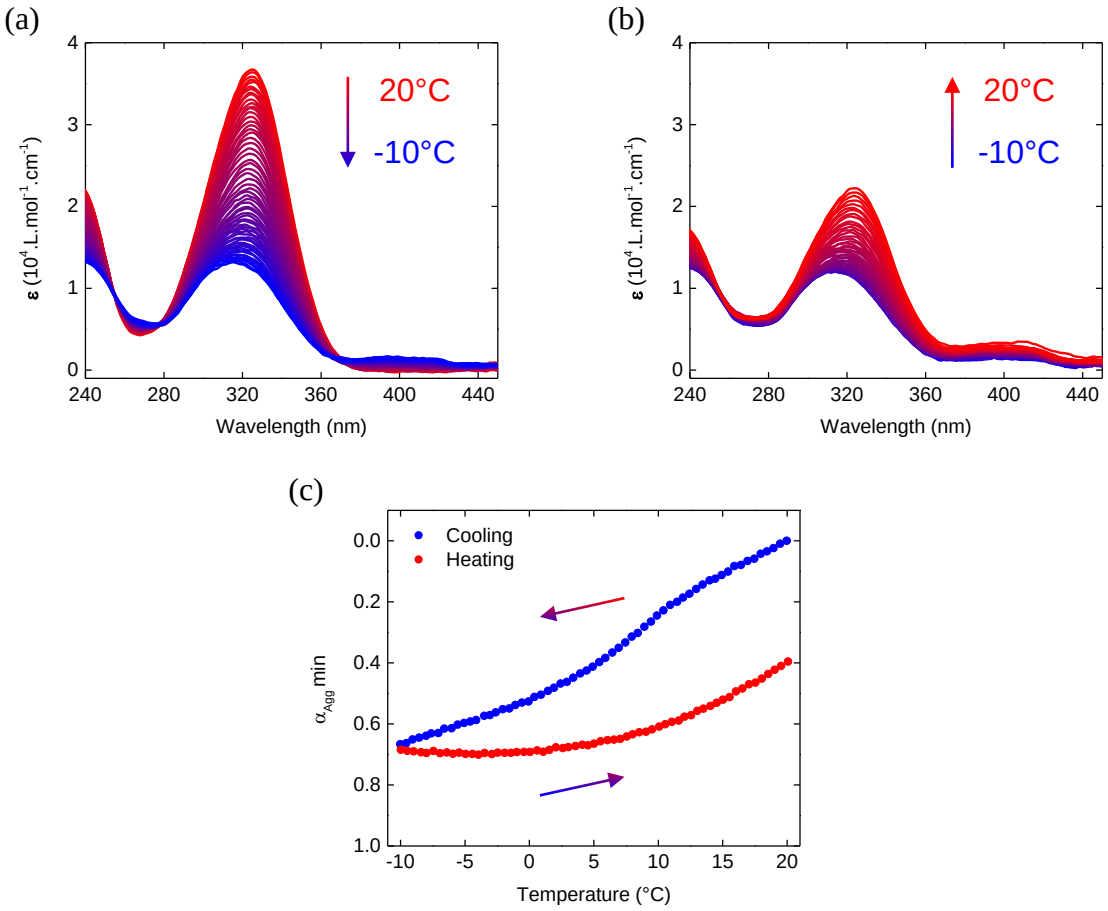

Figure III.9 Temperature-dependent UV–Vis analyses of **TATA-C13** in chloroform (2.3 mM) (a–b) UV–Vis absorption spectra recorded during a cooling-heating cycle between 20°C and -10°C, with a spectrum recorded every 0.5 °C at a rate of 0.5°C/min (each measurement took 30 seconds at constant temperature). (c) Evolution of the minimum degree of aggregation as a function of the temperature, as deduced from (a) and (b). The minimum degree of aggregation (α_{Agg} min) was calculated from the evolution of the absorption at 325 nm, as a function of the temperature, considering the low hypothesis of a fully aggregated state corresponding to an absorption equal to zero.

Contrary to the similar experiments performed on 0.1 mM solutions (**Figure III.5**), significant changes in the UV–Vis and FT–IR spectra of 2.3 mM solution were observed upon cooling. In UV–Vis,

strong hypo- and hypsochromic shifts of the major UV signal ($\Delta\varepsilon \approx -2.4 \times 10^4$ L.mol^{-1}.cm^{-1} and $\Delta\lambda = -10$ nm) are observed which indicate π–π stacking. After heating, the UV–Vis spectra are not identical: a similar shift in the opposite direction is observed but the intensity of the main UV band was not recovered ($\Delta\lambda = +10$ nm and $\Delta\varepsilon \approx +1.0 \times 10^4$ L.mol^{-1}.cm^{-1}), meaning that the disassembly process was incomplete. It is notable that both cooling and heating have been performed at low rates in order to favor thermodynamic control. The degree of aggregation actually follows two distinct pathways upon cooling and heating, drawing a thermal hysteresis which outlines kinetic contributions involved in the supramolecular polymerization, and the fact that 2.3 mM solutions at 20°C are metastable. Interestingly, the vibronically structured UV–Vis signal at around 400 nm increases upon cooling and heating as well. This complex absorption band was already noticed in triarylamine amides solutions and was attributed to stacks[46,47], and is in agreement with the remanence of aggregation at 20°C observed in this work. The increase of the molar extinction coefficient with the temperature is maybe the effect of a molecular rearrangement within aggregates, allowed by thermal energy.

VT–FT–IR analyses revealed that **TATA-C13** develops upon cooling well-defined H-bonding interactions, as evidenced by strong and symmetric absorption bands at about 3292 cm^{-1} and 1655 cm^{-1}, until reaching a degree of aggregation close to fully aggregated state (α_{Agg} = 0.91 at -10°C). No spectra have been recorded during the heating process except at room temperature, at a sufficiently long time after the cooling/heating process (black curve in **Figure III.10**). This spectrum indicates that, similarly to VT–UV–Vis analyses, only partial disassembly occurs when heating back to 20°C (free N-H/C=O signals at 3434 cm^{-1} and 1678 cm^{-1}, respectively). After the cooling/heating process, the degree of aggregation is still significant at room temperature and similar to the one determined by UV ($\alpha_{Agg,\ FT-IR}$ = 0.32 *vs.* $\alpha_{Agg,\ UV}$ min = 0.40), thus providing additional support for a thermal hysteresis between the assembly and disassembly processes.

However, the plots of the degree of aggregation upon cooling have different shapes depending on whether they are deduced from FT–IR or UV analyses. The FT–IR profile clearly highlights two phases, first from 20 to 16°C, where the degree of aggregation is close to zero, then a second phase for which α_{Agg} rapidly increases at lower temperature whereas the UV profile only shows a gradual increase of the degree of association. Possible explanations are either that the initial states of the analyzed solutions were different or that stacking of the TATA molecules occurred before they established hydrogen bonds.

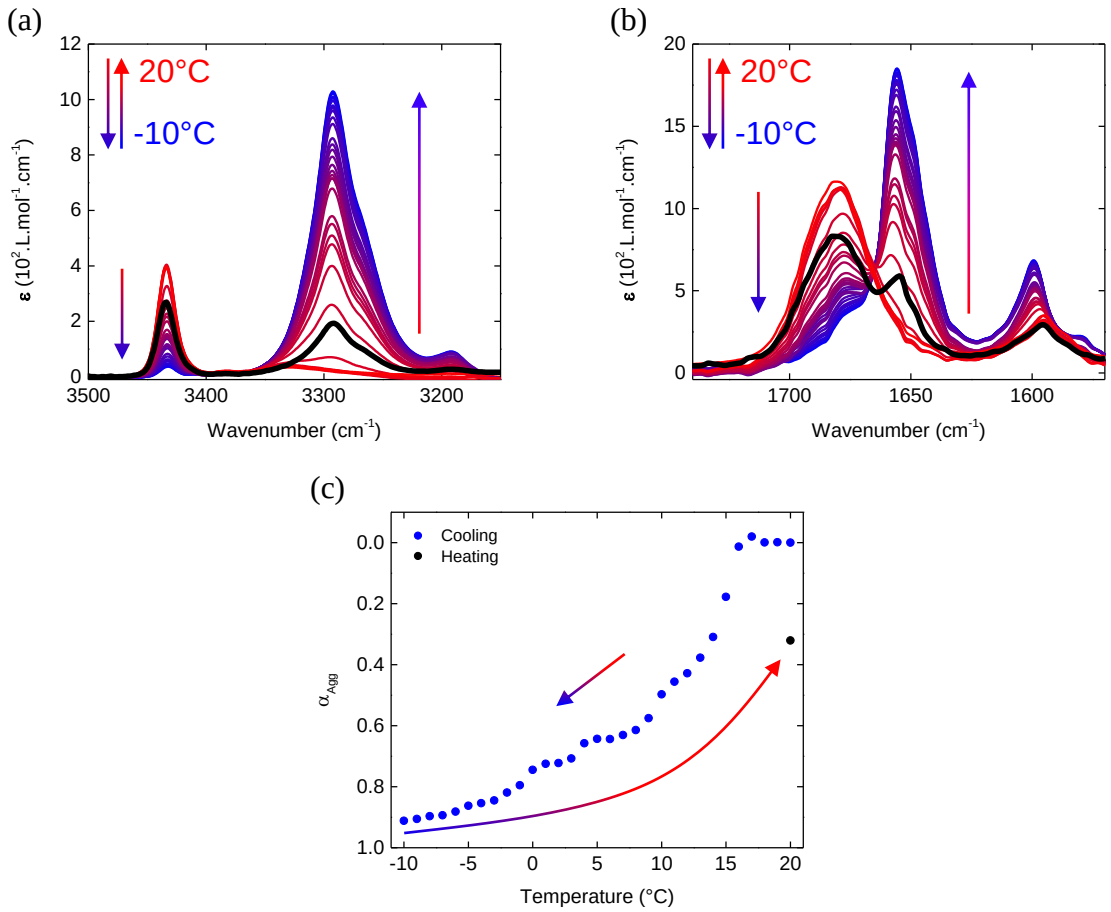

Figure III.10 Temperature-dependent FT–IR analyses of **TATA-C13** in chloroform (2.3 mM). (a–b) FT–IR absorption spectra recorded during a cooling process between 20°C and -10°C at a mean rate of about 0.4°C/min (red to blue lines), with spectra recorded every 1°C. A spectrum was recorded at 20°C after the cooling process (black line). Zoom on the (a) N-H and (b) C=O regions. (c) Evolution of the degree of aggregation as a function of the temperature, as deduced from (a) and (b). The degree of aggregation (α_{Agg}) was calculated from the evolution of the free N-H stretching vibration absorption signal at 3434 cm^{-1}, as a function of the temperature. The black dot corresponds to the degree of aggregation at 20°C, after the cooling process.

Both variable time- and temperature-UV–Vis/FT–IR analyses concurred well with a metastable state of 2.3 mM solutions of TATA monomers. The non-specific aggregates mainly present at 20°C transform into well-defined hydrogen bonded stacks slowly with time (over weeks) or upon cooling to -10°C. These hydrogen bonded stacks are prone to aggregation leading to the formation of gels that eventually precipitate from the solution.

III. 4. At high concentration: 11.4 mM

To identify the best conditions for co-assembly between radical cationic and neutral TATA species, highly concentrated solutions of TATA molecules (e.g. >10 mM) are of interest since they are expected to contain a higher content of stacked TATA monomers.

First, a 11.4 mM solution of **TATA-C13** in $CHCl_3$ was studied over time a by UV–Vis–NIR and FT–IR spectroscopy (**Figure III.11**).

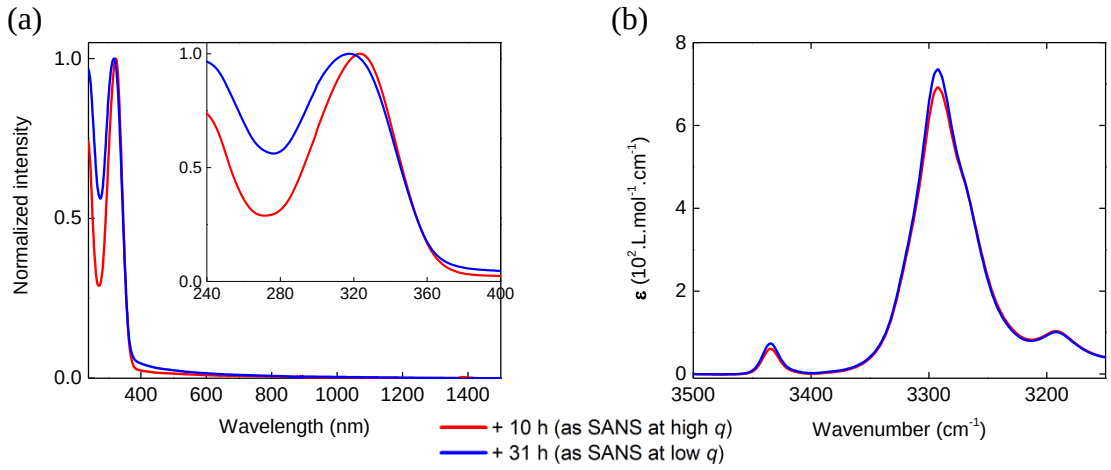

Figure III.11 TATA-C13 at 11.4 mM in chloroform. (a) UV–Vis–NIR absorption and (b) FT–IR spectra with a zoom on the N-H region. The gel-like nature of the solution prevents the preparation of samples with identical widths. As a consequence, the intensities of the analyses of the samples t_0 + 10 h and t_0 + 31 h have been normalized, yet enabling qualitative comparison of the shape of the bands.

The FT–IR absorption spectra 10 h and 31 h after dissolution are similar. They exhibit a large signal corresponding to bonded N-H (3292 cm^{-1}), indicating that most of the molecules are associated by hydrogen bonds in a stable fashion ($\alpha_{Agg} \approx 0.8$). The tiny contribution of free N-H bond (3435 cm^{-1}) suggests that either a small proportion of monomer is present, or that defects exist in the assemblies. On the other hand, both UV–Vis–NIR spectra show a slanting baseline, especially visible between 350 and 600 nm, that probably arises from diffusion of the light by very large aggregates. The spectrum recorded after 31 h manifests in addition a hypsochromic shift of 7 nm compared with the measurement after 10 h, that could suggest further π–π stacking.

Next, to extend our knowledge of the associated state in terms of shape and length, a solution of **TATA-C13** in $CDCl_3$ was probed by SANS at the same concentration (**Figure III.12**).

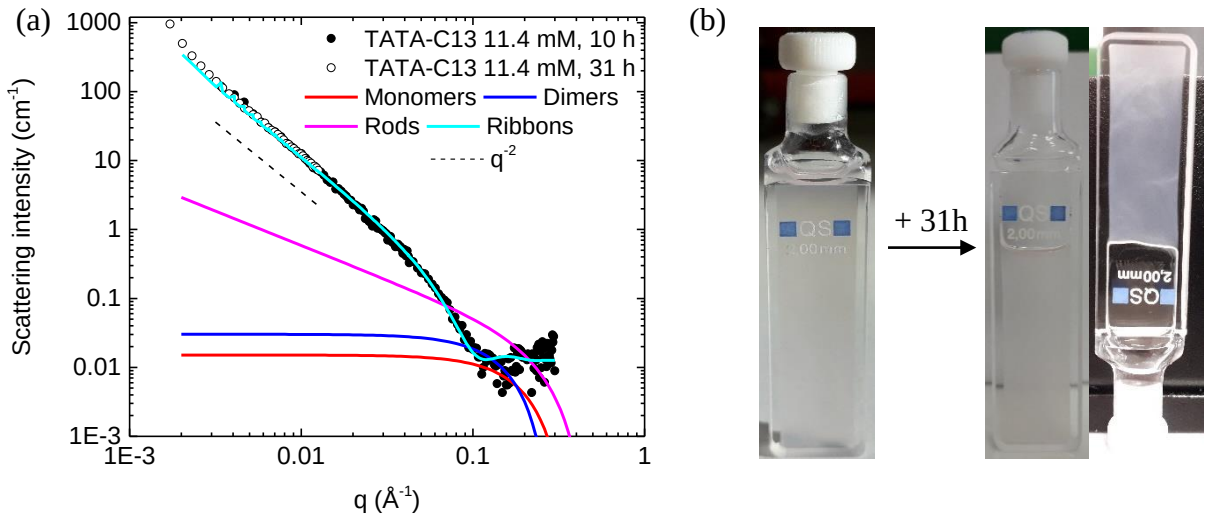

Figure III.12 (a) SANS analysis of **TATA-C13** at 11.4 mM in $CDCl_3$ (the fact that the two data sets overlap allows to verify their coherence and to discard the effect of time between measurements at low and high q values). Simulated curves for monomers, dimers and infinitely long rigid rods of circular cross-section are shown together with the experimental curve. The latter is fitted with a form factor for ribbons (*vide infra*). (b) Pictures of **TATA-C13** at 11.4 mM in $CDCl_3$ after dissolution and after SANS measurements (t_0 + 31h). Solution before ageing was a different sample, hence its volume is slightly different.

SANS analysis revealed that molecules are assembled into large and flat objects, with one dimension equal to 5.4 nm and the two others superior to 100 nm, as deduced from the fit of the experimental curve exhibiting a q^{-2} dependence of the scattering intensity at low q values. This result is in agreement with the presence of bundles of rods into very thick fibers or ribbons and this is consistent with the fact that the solution is opaque. A gel actually forms under these conditions (see pictures in **Figure III.12b**), sign of huge aggregates. Such a type of ribbons have been observed for freeze-fracture TEM image of **TATA-C12** in the gel state by Giuseppone *et al.* (**Figure III.13**)[10].

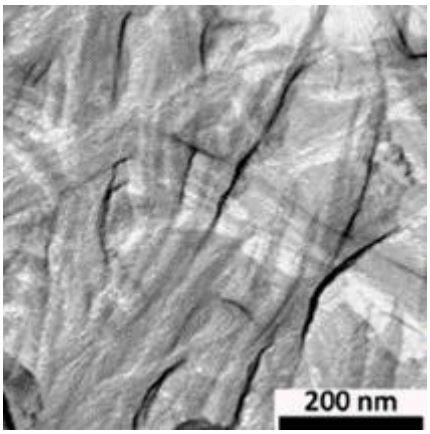

Figure III.13 Freeze-fracture TEM image showing the ribbons of **TATA-C12** in the gel state, performed by Giuseppone *et al.*[10] This technique allows to observe supramolecular assemblies as solvated, without entailing further crystallization that could misrepresent the structure present in the gel state.

UV–Vis–NIR/FT–IR spectroscopy and scattering analyses demonstrated that at 11.4 mM, TATA monomers self-assemble into hydrogen-bonded stacks under the form of ribbons, which are large two-dimensional objects existing at the frontier between solution and solid states. In addition, FT–IR analyses showed a small contribution of what could be free monomers or defects in stacks.

III. 5. In the solid state as thin film

To increase the degree of association of TATA monomers through hydrogen bonds, thin films were prepared by drop casting of TATA solutions at 2.3 mM in $CHCl_3$. They were analyzed by UV–Vis–NIR and FT–IR spectroscopies (**Figure III.14**).

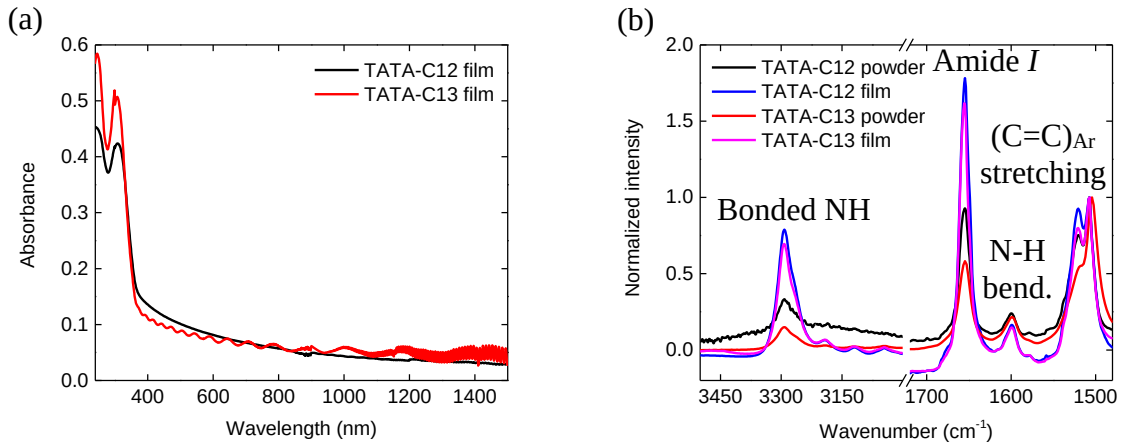

Figure III.14 (a) UV–Vis–NIR of **TATA-C12** and **TATA-C13** as thin film and (b) FT–IR analyses of **TATA-C12** and **TATA-C13** as powder and thin film. Thin films were obtained by drop casting of a chloroform solution of **TATA-C12**/**C13** at 2.3 mM.

UV–Vis–NIR spectra revealed that for both **TATA-C12** and **TATA-C13** the main UV absorption band is blue-shifted (λ_{max} = 308 nm *vs.* 325 nm for non-stacked molecules), and that scattering occurs, which is consistent with the formation of very large and disordered fibers. FT–IR analyses confirmed that TATA molecules in the film are assembled by hydrogen bonds (α_{Agg}>0.95). The solid-state analysis also allows to detect additional bands that have been assigned as shown in **Figure III.14b**. The alignment of the fibers in the film state has been assessed by an AFM analysis conducted by Giuseppone *et al.*[10] on **TATA-C12**.

III. 6. Summary of the self-assembly properties of TATA-C12 and TATA-C13 without light

The aim of the previous section was to study the self-association properties of TATA molecules, by highlighting the conditions necessary to promote their self-assembly, as well as the resulting structures and interactions involved therein. No significant differences between the association properties of **TATA-C12** and **TATA-C13** have been detected. Solutions in chloroform at three different concentrations and thin films were characterized allowing the following conclusions:

1) at 0.1 mM, no hydrogen-bonded stacks have been detected down to -34°C (α_{Agg} = 0); the presence of non-specific aggregates stabilized by dispersion interactions cannot be discarded;

2) 2.3 mM solutions are metastable at 20°C: TATA molecules are initially assembled into non-specific aggregates which tend to transform slowly over time into hydrogen-bonded stacks[10]. Similar stacks are observed upon cooling (α_{Agg} = 0.7–0.9 at -10 °C), and the strong hysteresis observed upon heating back to 20°C highlights the fact that the system is likely under kinetic control;

3) at 11.4 mM, TATA molecules are almost exclusively associated into ribbon-like superstructures made of bundles of individual hydrogen-bonded stacks ($\alpha_{Agg} \approx$ 0.8);

4) TATA molecules in thin films are exclusively associated into hydrogen-bonded stacks (α_{Agg}>0.95).

IV. Self-association properties with light

The next step was to assess the impact of light for the generation of TATA radical cations and their influence on the self-assembly under different initial conditions. For this purpose, two light irradiation setups were used: (H) a 23-W Philips halogen classic warm white 204 lumen lamp (delivering unpolarized light, **Figure SIII.42**); and (A) composed of a LED of an optical power of 1650 mW centered on 385 nm, a condenser lens, a linear polarizer and a quarter-wave Fresnel rhomb retarder[XXIX] (delivering CPL, **Figure SIII.43**). The latter setup is more powerful than the former, allowing shortened irradiation times.

[XXIX] Further used as CPL optical bench.

IV. 1. At low concentration: 0.1 mM

It was appealing to test whether light could trigger self-assembly starting from a solution that contains non-hydrogen bonded TATA molecules. According to Giuseppone *et al.*, the stacking of TATA molecules upon light irradiation is characterized by the following features:

1) the "appearance of a NIR absorption band at about 1130 nm (for shorter times of irradiation and corresponding to the presence of intermolecular through-space radical cation charge transfer between stacked triarylamine cores), followed by the appearance of an absorption band at about 830 nm (for longer times of irradiation and corresponding to more localized triarylammonium radical cations)"[16]. Giuseppone *et al.* notified this behavior upon irradiation of a chloroform solution of **TATA-C12** at 0.1 mM in the presence of "preassembled TATA fibers", as well as in a 0.1 mM chloroform solution of TATA decorated with norbornene end groups. The attribution of this band agrees well with previous reports of molecules composed of two triarylamines cores bridged by π-electron spacers[48–50], for which "photoexcited electron transfer from a neutral triphenylamine center to the triphenylamine radical cation center" occurs[48].

2) The "appearance of a typical three-line pattern on the EPR spectra (for unpaired electrons each localized on one triarylamine core)"[16] or "one-line pattern (for fully delocalized electrons between stacked triarylamine cores)"[10]. The former was measured in a 0.1 mM chloroform solution of TATA decorated with norbornene end groups, while the latter was measured in a 1 mM chloroform solution of **TATA-C12**. See **Figure SIII.44** for archetypal EPR signals of triarylamines[51].

3) The "disappearance of the ^{1}H NMR resonance signals corresponding to the triarylamine core"[16], observed with TATA molecules at quite high concentrations (5 mM[10] or 10 mM[16]). This is in part ascribed to the putative light-triggered self-assembly, promoted by triarylammonium radicals ($TATA^{\bullet+}$, photo-oxidation product of TATA molecules), thanks to their flattened geometry owing to the delocalization of the unpaired electron. In such a case, signals of protons directly affected by the assembly might broaden or disappear (e.g. aromatic and amide protons by π–π stacking or H-bonding). Indeed, TATA aggregates must be anisotropically oriented, hampering complete T2 spin-spin

relaxation. However, a second contribution exists, relative to the generation of triarylammonium radicals themselves. In this case, the spin electronic density in the triarylammonium core becomes significantly high (while negligible for the neutral triarylamine core), inducing a dramatic downfield shift of involved protons (out of the recorded window)[52]. Nonetheless, the broadening/disappearance of resonance signals of aromatic and amide hydrogens, as well as those at the vicinity of these groups, was even observed in the presence of less than one percent of radical in triarylamine monoamide molecules[13], and cannot be explained solely by this contribution. Accordingly, in triarylamine monoamides solutions, "both the formation of radicals and the molecular aggregation (producing regular or irregular structures) can lead to changes in the NMR spectrum"[52].

4) The "disappearance of the fluorescence around 500 nm after short irradiation times which indicates the presence of supramolecular polarons (fully delocalized electrons) quenching the aggregation induced emission of the stacked TATA molecules."[10,16]

Thereby, to investigate the putative light-triggered assembly in solutions of **TATA-C12** at 0.1 mM in chloroform, UV–Vis–NIR (**Figure III.15**), FT–IR (**Figure III.16**) and EPR (**Figure III.17**) analyses were carried out during light irradiation by a 23 W halogen lamp (optical bench similar to the one used by Giuseppone *et al.*[10,16]).

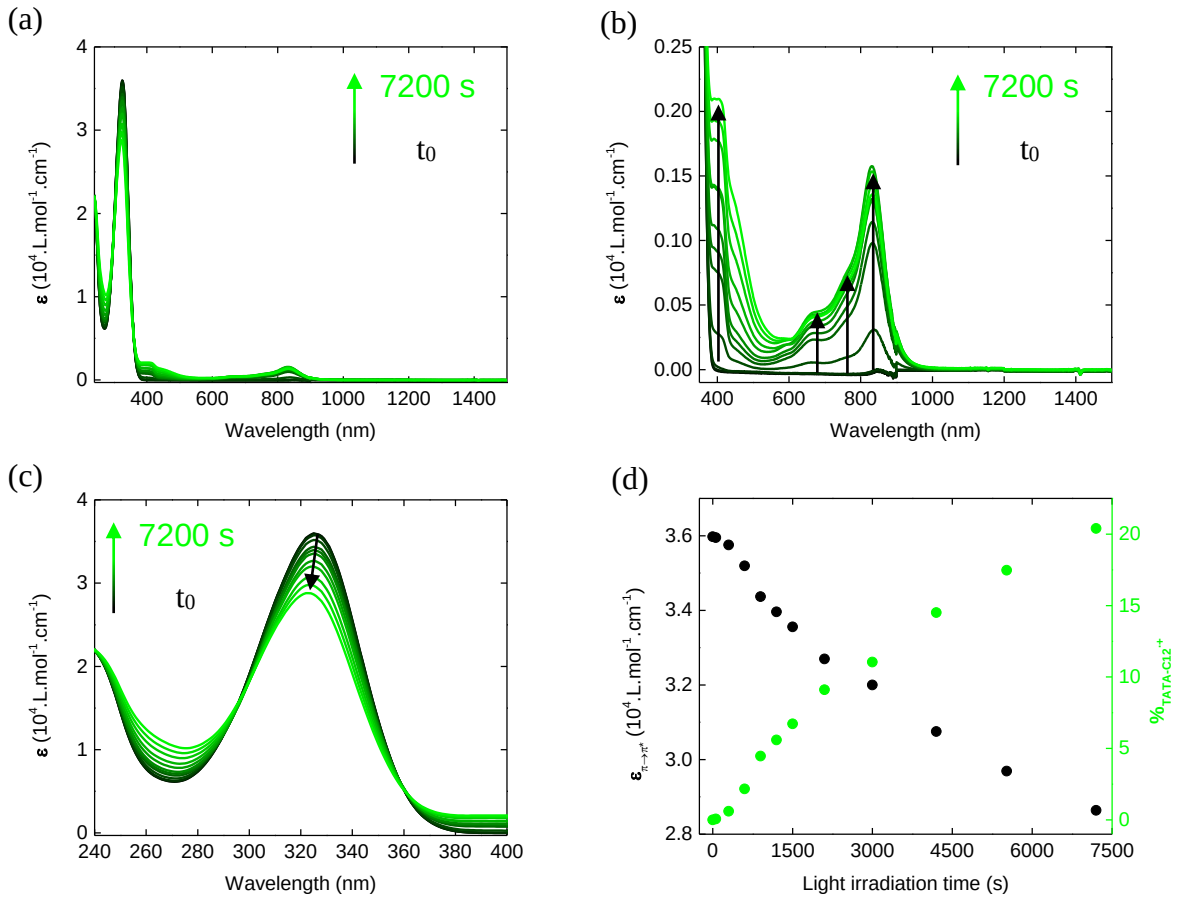

Figure III.15 (a–d) UV–Vis–NIR absorption spectra during light irradiation of a solution of **TATA-C12** in chloroform at 0.1 mM. (b–c) Zoom on the Vis–NIR and UV regions; (d) evolution of the absorption at 325 nm and estimation of the amount of **TATA-C12** radical cations, as a function of the light irradiation time. A 10 mm rectangular quartz cuvette was irradiated by (H) a 23-W Philips halogen classic warm white 204 lumen lamp placed at a few cm.

Throughout light irradiation, UV signals shifted (notably a hypo-/hypso-chromic shift for the main UV signal at 325 nm) and a set of absorption bands appeared in the Vis–NIR range (at about 400 nm and between 600 and 900 nm). Similar results were obtained with **TATA-C13** (**Figure SIII.45**). The evolution of the main UV band is similar to that measured upon stacking of neutral TATA molecules in absence of light (*vide supra*), in line with the literature assumptions on the light-triggered self-assembly. Nevertheless, another hypothesis to explain this behavior is the possible shift of the UV band (π→π*) due to production of triarylammonium radicals. This explanation is supported by the new absorption bands observed in the visible and

NIR regions, which are related to **TATA-C12$^{\bullet+}$** species. Indeed, the signal at about 400 nm can be attributed to a vibronically structured $\pi \rightarrow \pi^*$ ($S_0 \rightarrow S_1$) transition[53], while the vibronic bands between 600 and 900 nm are ascribed to the new HOMO→SOMO transitions ($D_0 \rightarrow D_1$, and $D_0 \rightarrow D_2$ for **TATA-C12$^{\bullet+}$** lacking C_3-symmetry as expected upon planarization, phenyl ring rotation or interaction with solvent molecules)[54]. All these bands were considered as a signature of localized triarylammonium radicals[10,13,14,16]. Moreover, the absence of signal around 1130 nm underpins the hypothesis of a solution composed of non-stacked molecules.

By considering that the UV changes are related to the generation of radicals only, the minimum amount of produced **TATA-C12$^{\bullet+}$** can be estimated (**Figure III.15d**) by recording the decrease of the 325-nm absorption band. In this way, a gradual increase of produced **TATA-C12$^{\bullet+}$** (up to ca. 20%) was assessed during light irradiation that does not reach any plateau. The order of magnitude is consistent with findings of Giuseppone *et al.* for the same absorption intensities of **TATA-C12$^{\bullet+}$** signals[10].

The effect of light irradiation was also followed by FT–IR spectroscopy (**Figure III.16**). The intensity of characteristic signals of free N-H and C=O decrease (by 21% after 7200 s for the N-H signal), but without being accompanied by an increase of absorption bands relative to hydrogen bonded N-H/C=O (expected at about 3290 cm^{-1} and 1655 cm^{-1}, respectively). On contrary, a new band appears at ca. 3200 cm^{-1} corresponding to N-H stretching vibration and maybe aromatic C-H stretching vibration[42] that are attributed to the newly formed **TATA-C12$^{\bullet+}$** species. It is expected that molar extinction coefficients and vibrational frequencies associated with the radical cationic molecule would be different to that of neutral TATA[43] and accordingly it is not possible to dissect whether the shift of the N-H band is also related to a change in the hydrogen-bonding nature of the amide group. Additionally, the amount of **TATA-C12$^{\bullet+}$** generated after irradiation is similar (ca. 20%) for FT–IR and UV analyses.

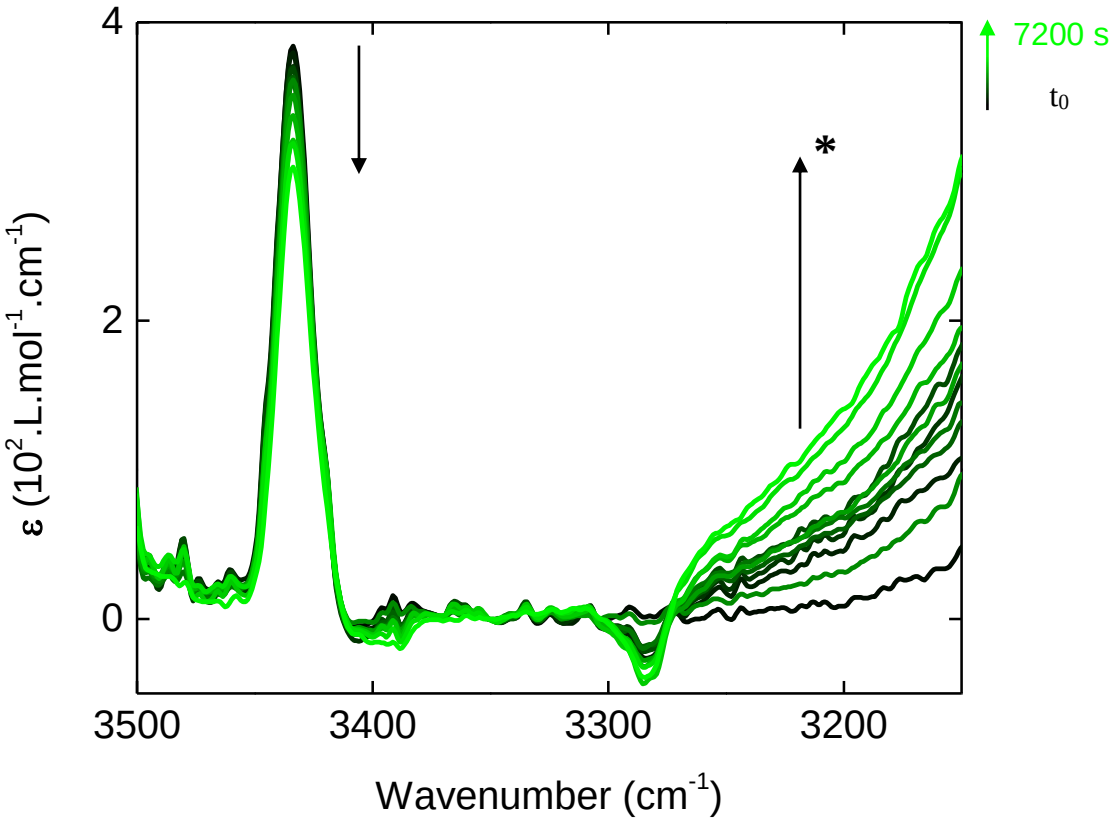

Figure III.16 FT–IR absorption spectra during light irradiation of a solution of **TATA-C12** in chloroform at 0.1 mM. The 2 mm CaF_2 cell was irradiated by (H) a 23-W Philips halogen classic warm white 204 lumen lamp placed at a few cm. *The absorption band visible at ca. 3200 cm^{-1} saturates at lower wavenumbers (<3150 cm^{-1}), as well as signals in the C=O region.

EPR spectroscopy may indicate both the amount of unpaired electrons as well as their nature (localized, partially or totally delocalized on one or many molecules) within the solution[55]. Here, the spectrum resembles the three-line pattern characteristic of unpaired radicals localized on one triarylamine core (**Figure III.17**). Quantification of the number of radicals relatively to TEMPO yields 3.8 mol% of **TATA-C12$^{\bullet+}$**. On one hand, it substantiates the isolated nature of molecules at this concentration, even when photo-oxidized, but on the other hand, this result gives a radical concentration five times lower than that determined by UV and FT–IR analyses (ca. 20%). There are two possible explanations which are not mutually exclusive for this discrepancy. First, the EPR quantification is based only on one measurement

of a reference solution composed of a quite different radical (a nitroxyl radical) at a greater concentration (all the TEMPO molecules at 4.9 mM are supposed to carry a radical), leading to an imprecise determination of the amount of TATA radicals. Secondly, this lack of correlation with UV and IR measurements could indicate an electronic interaction between neutral and radical TATA molecules within aggregates resulting in an overestimation of the amount of radicals by UV and IR analyses.

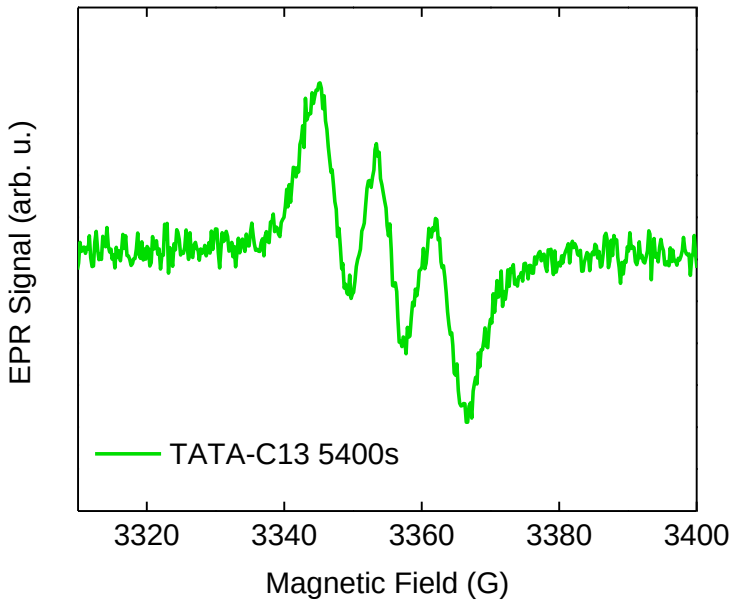

Figure III.17 EPR analysis of **TATA-C13** at 0.1 mM in chloroform, after 5400 s of light irradiation. The 10 mm rectangular quartz cuvette was irradiated by (H) a 23-W Philips halogen classic warm white 204 lumen lamp placed at few cm. The **TATA-C13** radical cation amount was estimated to be 3.8 mol% (in comparison with a reference solution of TEMPO at 4.9 mM).

Next, the reversibility of the oxidation process was assessed, as illustrated in **Figure III.18**. A sample irradiated at room temperature during 7200 seconds and enriched in **TATA-C12**$^{\bullet+}$, did not completely come back to its initial state after being left in the dark for 16 h. This result indicates that the recombination of charge carriers, through reactions with the reduced chlorinated products (e.g. the chloride radical anion[52,56–58]), is only partial within this timescale. More precisely, the absorption bands at around 800 nm and 3200 cm^{-1} almost completely disappear after 16 h in dark, while the main UV signal and the absorption band ascribing to the

free N-H vibration do not strongly evolve. This partial reversibility of the oxidation process might be due to the presence of both neutral and radical TATA molecules being mixed in the same non-specific aggregates.

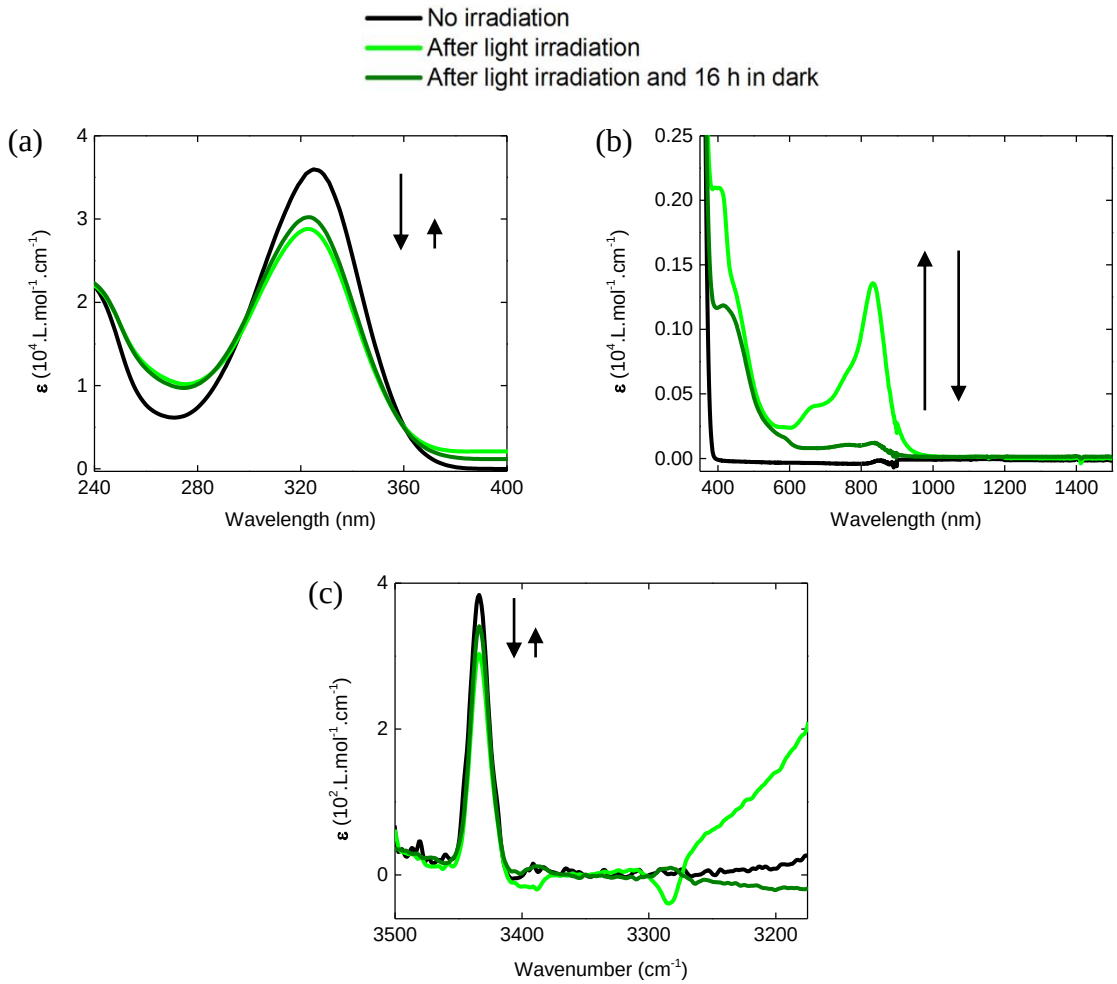

Figure III.18 (a–b) UV–Vis–NIR and (c) absorption spectra of **TATA-C12** at 0.1 mM in chloroform (black solid line), after 7200 seconds of light irradiation (green solid line), then left in dark 16 hours ("olive" green line). The 10 mm rectangular quartz cuvette and the 2 mm rectangular CaF_2 cell were irradiated by (H) a 23-W Philips halogen classic warm white 204 lumen lamp placed at a few cm.

In summary, analyses of 0.1 mM solutions of TATA molecules in chloroform evidence the formation of radical cationic species with characteristic signals in the Vis–Near IR region but also in the IR region. Our study discards the possibility that light triggers the self-assembly of all TATA molecules into well-defined H-bonded stacks since a significant fraction (ca. 80%)

of non-H-bonded molecules are detected after long irradiation time. Yet, the precise nature of the aggregates after light irradiation cannot be ascertained at this concentration.

IV. 2. At an intermediate concentration: 2.3 mM

It was demonstrated that 2.3 mM solutions of TATA are metastable at 20°C and that molecules, are first likely involved in non-specific aggregates and then self-assemble, with time or upon cooling, into hydrogen-bonded stacks. It seems promising to check the interaction between radical cations and neutral molecules under these conditions both at room temperature and upon cooling. In any case, freshly prepared solutions were irradiated, ensuring that the initial state is identical and does not involve a significant amount of hydrogen bonded species.

IV. 2. 1. Irradiation and analyses at room temperature

The UV–Vis–NIR absorption profile of irradiated solutions is similar to that of 0.1 mM solution. The absorption band at 325 nm shifts towards lower wavelengths and intensities, while new signals grow at about 400 nm and between 600 and 900 nm (**Figure III.19**). These evolutions reflect the photo-oxidation of **TATA-C12** into **TATA-C12**$^{\bullet+}$ with localized radicals, whose amount is estimated to ca. 40% after 1440 seconds of light irradiation, *i.e*. at its maximal value. This is corroborated by the green color of the solution once irradiated (**Figure III.20**), characteristic of triarylammonium radicals in chlorinated solutions[10,13,33]. The same profile was also measured with the **TATA-C13** molecule (**Figure SIII.46**), showing the reproducibility of the process.

Nevertheless, a prolonged light irradiation revealed a second phase in the evolution which is marked by a levelling off and a decrease of the number of generated radicals. This can be mainly observed by the decrease of the bands at 400 nm and 600–900 nm. This second phase leads to a partial reduction of the amount of radicals for **TATA-C12**, (**Figure III.19a** and **b)** and to full disappearance for **TATA-C13 (Figure SIII.46**). They might be due either to the reversible transformation of TATA$^{\bullet+}$ into dicationic species[54], or their irreversible transformation into a carbazole derivative. The latter occurs *via* intramolecular cyclization through covalent coupling of *ortho* carbons of two TA aromatic rings[59]. Given the unknown nature of the species formed during the second phase of the irradiation process, our

investigation of the impact of light will be limited to the first phase. In order to better assess the nature of the species formed upon irradiation, the photo-oxidation of **TATA-C12** and **TATA-C13** was investigated by EPR spectroscopy (**Figure III.21**).

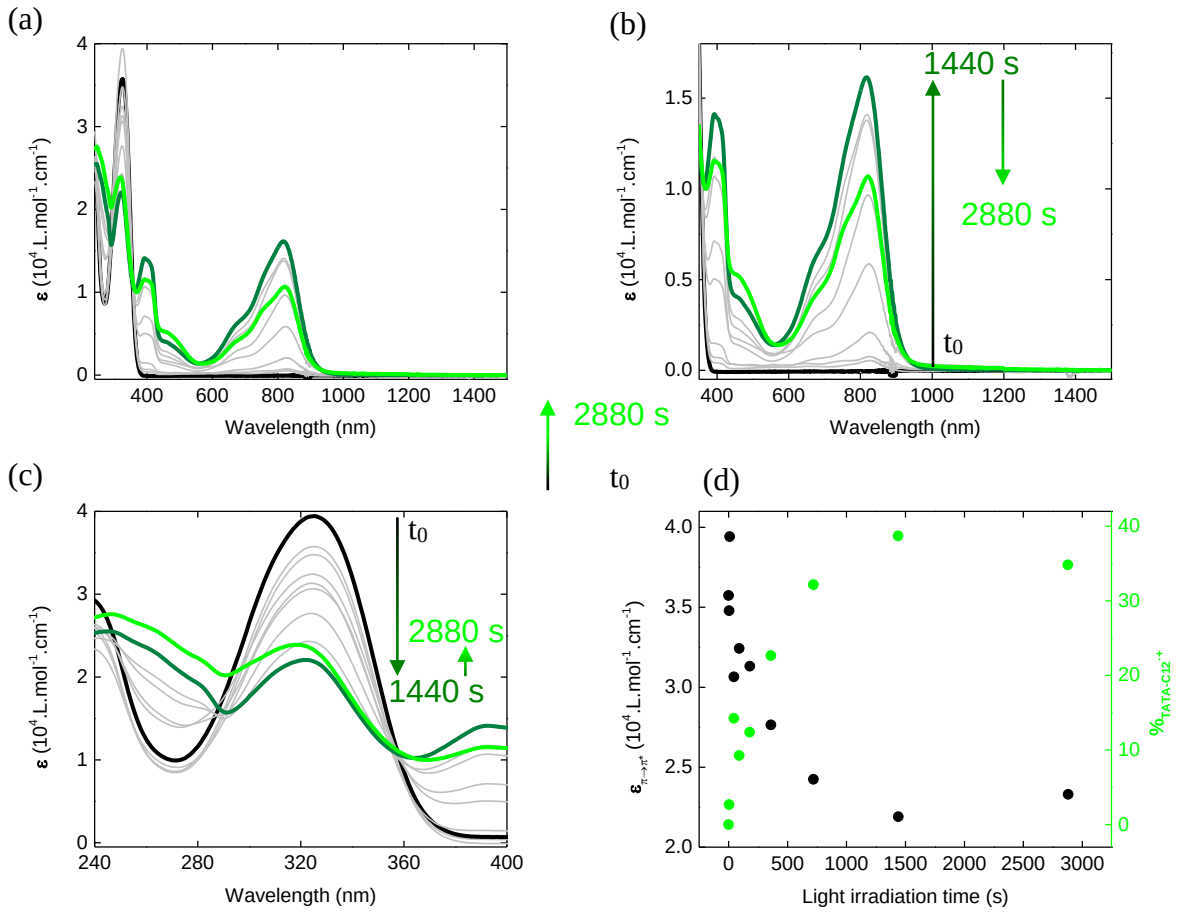

Figure III.19 (a–d) UV–Vis–NIR absorption spectra recorded during light irradiation of **TATA-C12** in chloroform at 2.3 mM. (b–c) Zoom on the Vis–NIR and UV regions; (d) evolution of the molar extinction coefficient at 325 nm and estimation of the amount of **TATA-C12** radical cations, as a function of the time of irradiation. The solution was irradiated in a 2 mm rectangular quartz cuvette by the setup A, with a surface optical power of 7.9 mW/cm^2.

Figure III.20 Picture showing solutions of **TATA-C12** at 2.3 mM in $CHCl_3$ after dissolution then after 10s, 45s, 90s, 180s, 360s, 720s and 1440s of light irradiation (from left to right). The solution was irradiated in a 2 mm rectangular quartz cuvette by the setup A, with a surface optical power of 7.9 mW/cm^2.

EPR spectroscopic measurements indicate the presence of isolated radical cationic TATA species, in a similar fashion for both **TATA-C12** and **TATA-C13** (**Figure III.21**). The evolution of the amount of $TATA^{\bullet+}$ species follows the same evolution than that assessed by UV–Vis–NIR. For **TATA-C13** solution, the EPR signals are not identical at the different times of irradiation: fewer radical cations are detected for the longest irradiation time as well as a small shift (one gauss) of the EPR. This could be interpreted as a first sign of irreversible transformation of the TATA chemical structure at the longer irradiation time. Finally, the amount of $TATA^{\bullet+}$ estimated by EPR is again lower than that determined by UV–Vis–NIR (by ca. a factor of 3), which implies that radical cationic species have an effect that exceeds their very presence. Like at 0.1 mM, they might be due to interactions between neutral and radical TATA molecules inside non-specific aggregates (*vide infra*).

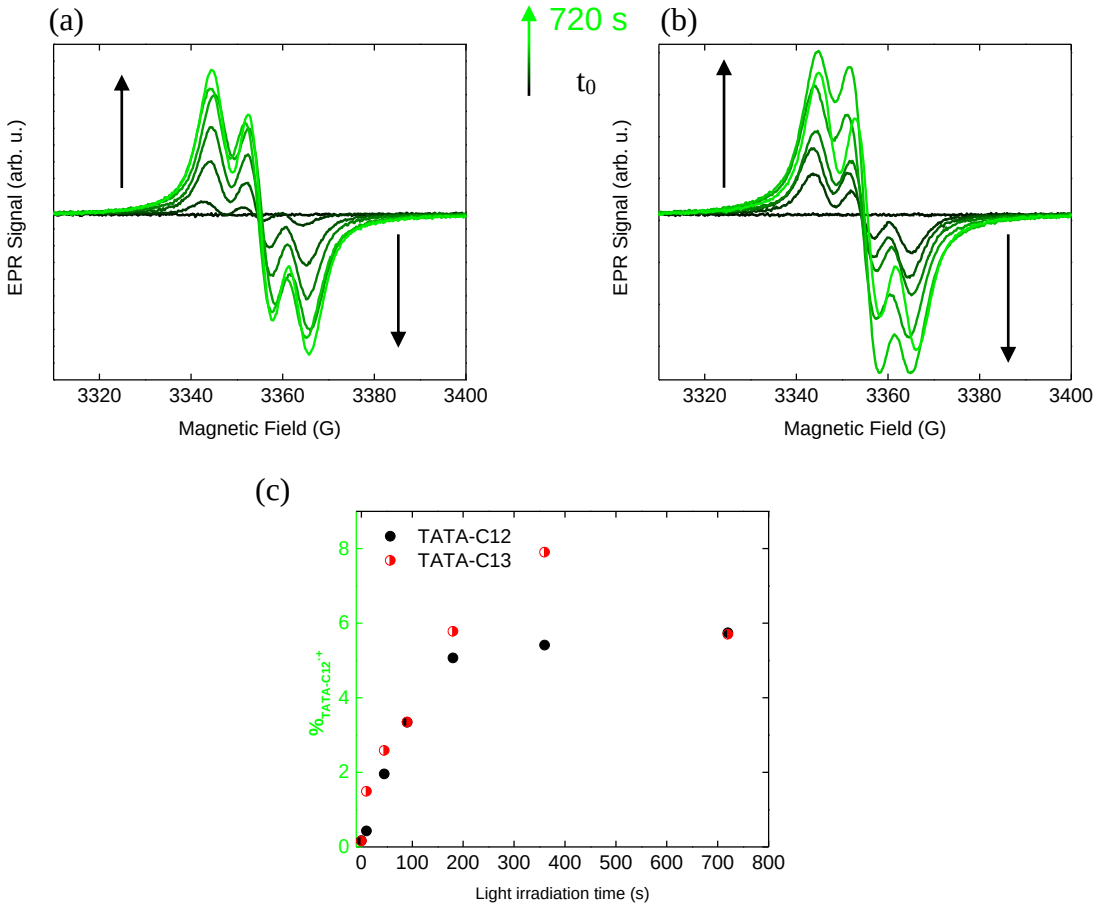

Figure III.21 EPR spectra during light irradiation of (a) **TATA-C12** and (b) **TATA-C13** 2.3 mM solutions in chloroform. (c) Evolution of the amount of **TATA-C12** and **TATA-C13** radical cations (upon calibration with a reference solution of TEMPO at 4.9 mM), as a function of the light irradiation time. The solution was irradiated in a 2 mm rectangular quartz cuvette by the setup A, with a surface optical power of 7.9 mW/cm^2.

FT–IR spectra (**Figure III.22**) measured during the light irradiation of a **TATA-C12** solution show a significant decrease of free N-H and C=O stretching vibrations (by 60% and 40%, respectively) and the concomitant apparition of a large band around 3200 cm^{-1} and a sharp band at 1566 cm^{-1}. The former was already observed for the irradiated 0.1 mM solutions whilst the larger observable spectrum window in the present case allows for the observation of the latter. These two bands can be attributed to the N-H (likely associated with C-H stretch) and amide C=O stretching frequencies of **TATA-C12**$^{\bullet+}$ species which are considerably shifted relatively to that of neutral species (by 115 cm^{-1} for the C=O band). On contrary, the bending

N-H frequency (1600 cm^{-1}) is not significantly affected by the presence of a radical cation in the molecule. By considering that the decrease of the N-H and C=O signal is only due to the formation of triarylammonium radicals, the amount of **TATA-C12**$^{\bullet+}$ was estimated to reach a plateau at 40–60% (**Figure III.22**) which is of the same order than the value determined by UV–Vis–NIR. However, this value is again significantly higher than that titrated by EPR, probably for a similar reason to that evoked for the 0.1 mM solution, *i.e.* that neutral and radical TATA species interact with each other and the new bands in the Vis-near IR and IR regions are related to both species.

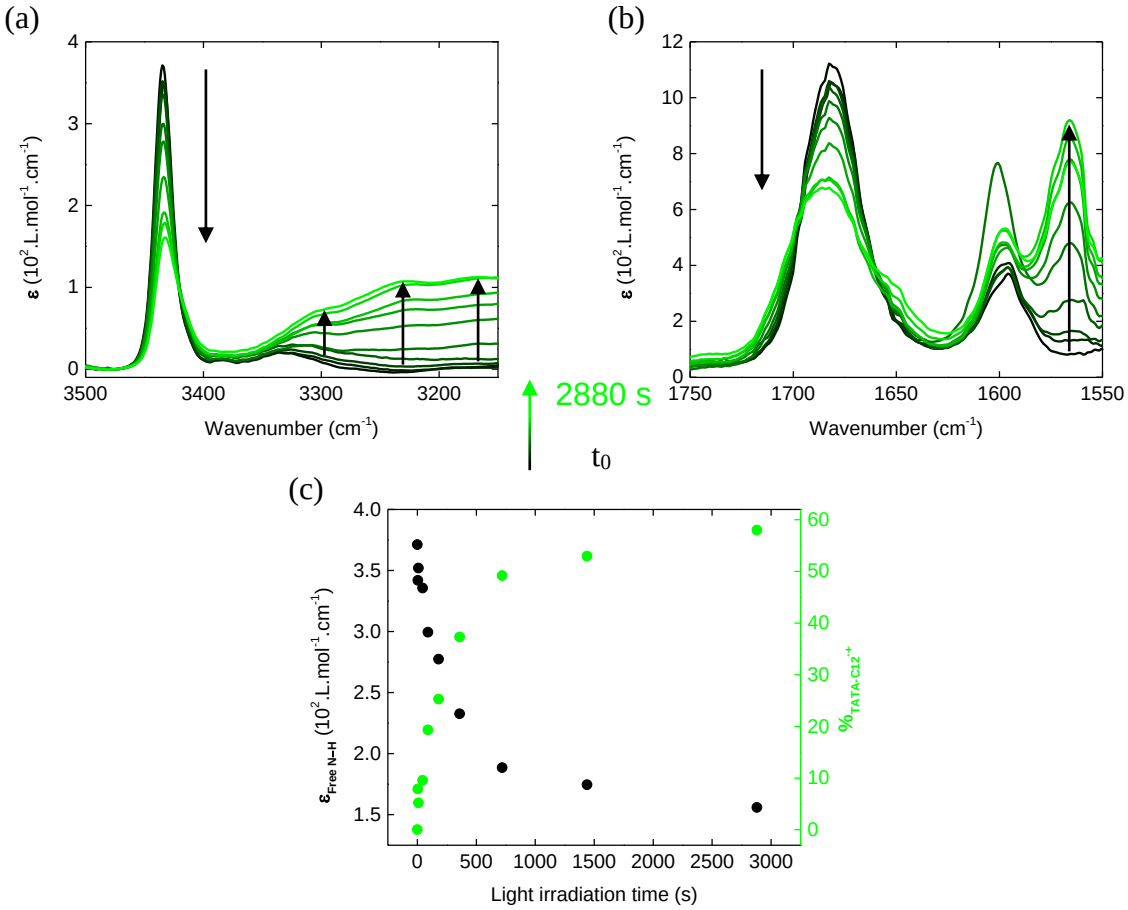

Figure III.22 (a–b) FT–IR absorption spectra during light irradiation of **TATA-C12** in chloroform at 2.3 mM, with a zoom on the (a) N-H and (b) C=O regions. (c) Evolution of the absorption at 3435 cm^{-1} (free N-H stretching vibration signal) and estimation of the amount of **TATA-C12**$^{\bullet+}$, as a function of the time of irradiation. The solution was irradiated in a 2 mm rectangular quartz cuvette by the setup A, with a surface optical power of 7.9 mW/cm^2.

To shed light on the nature of the co-assemblies, the chloroform solution of TATA at 2.3 mM was then analyzed by SANS ca. 7 h after being irradiated for 720 s. Of the radicals generated during the light irradiation (about 6% of radicals according to EPR[xxx]), about half of them (*i.e.* 3%) are likely to be present during the SANS measurement (see **Figure SIII.47** and **Figure SIII.48** with the accompanying discussion). These SANS data are depicted in **Figure III.23**, and compared with that of the non-irradiated sample.

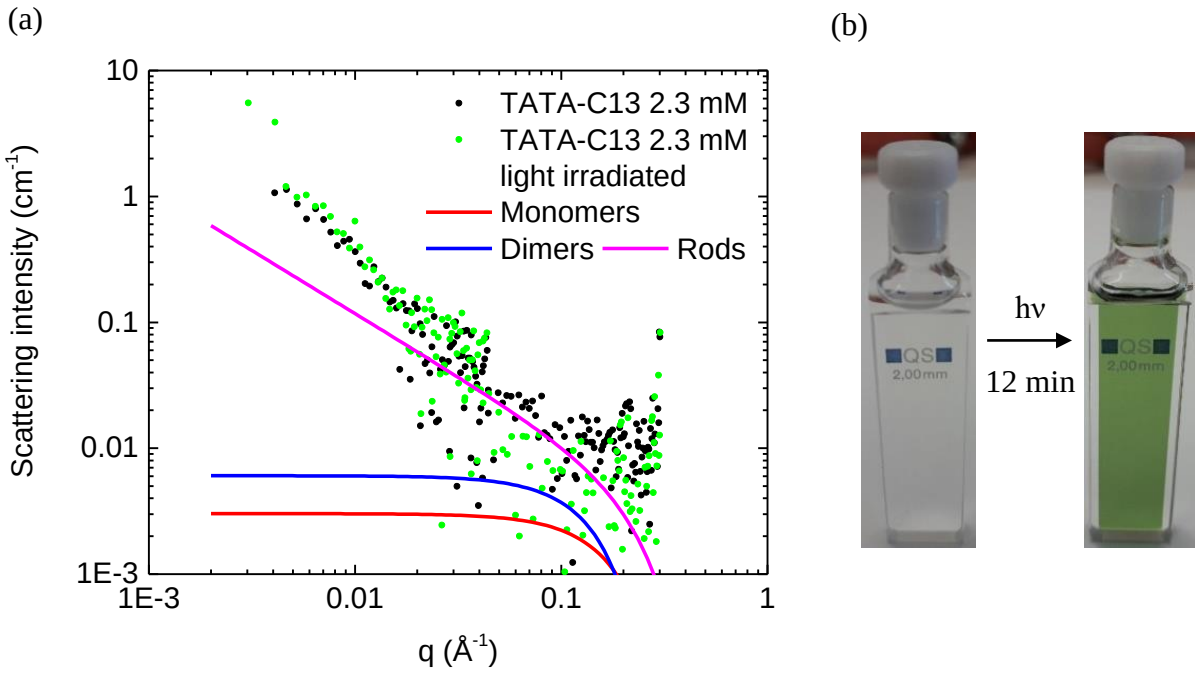

Figure III.23 (a) SANS analysis of **TATA-C13** at 2.3 mM in $CDCl_3$. Simulated curves for monomers, dimers or infinitely long rigid rods of circular cross-section are shown together with the experimental spectra. (b) Pictures of **TATA-C13** at 2.3 mM in $CDCl_3$ after dissolution and after irradiation. The solution was irradiated in a 2 mm rectangular quartz cuvette by the setup A, with a surface optical power of 7.9 mW/cm^2.

Both irradiated and non-irradiated samples exhibit virtually identical SANS curves. The 3% of radicals present in the sample have thus no significant influence on the structure of the

[xxx] By considering that the decrease of the N-H and C=O signal as well as of the main UV signal is only due to the formation of triarylammonium radicals, the amount of **TATA-C12**$^{\bullet+}$ was estimated at 50% by FT–IR (**Figure III.22**), of the same order than the value determined by UV–Vis–NIR (30%, **Figure III.19**).

assemblies. As the solution is initially composed of TATA molecules present in non-specific aggregates, our result indicate that the generation of a few percent of TATA radicals does not induce a dramatic structural transition.

As a complement to the previous analyses, the effect of a short time of irradiation on the nature of molecular and supramolecular species present in solution was probed by ^{1}H NMR (**Figure III.24**). First, before light irradiation, the sharpness of aromatic signals (1 and 2, zoom on this region on the left of **Figure III.24**) confirms the absence of long H-bonded stacks. After light irradiation, no new signals accounting for eventual undesired products issued from the irreversible transformation of triarylammonium radicals can be detected. However, it can be observed the broadening/disappearance of resonance signals of aromatic and amide hydrogens, as well as those at the vicinity of these groups (protons 1, 2, 3, 4 and 5 in **Figure III.24**). In the literature[10,13], this observation was attributed to a putative light-triggered self-assembly, promoted by triarylammonium radicals.

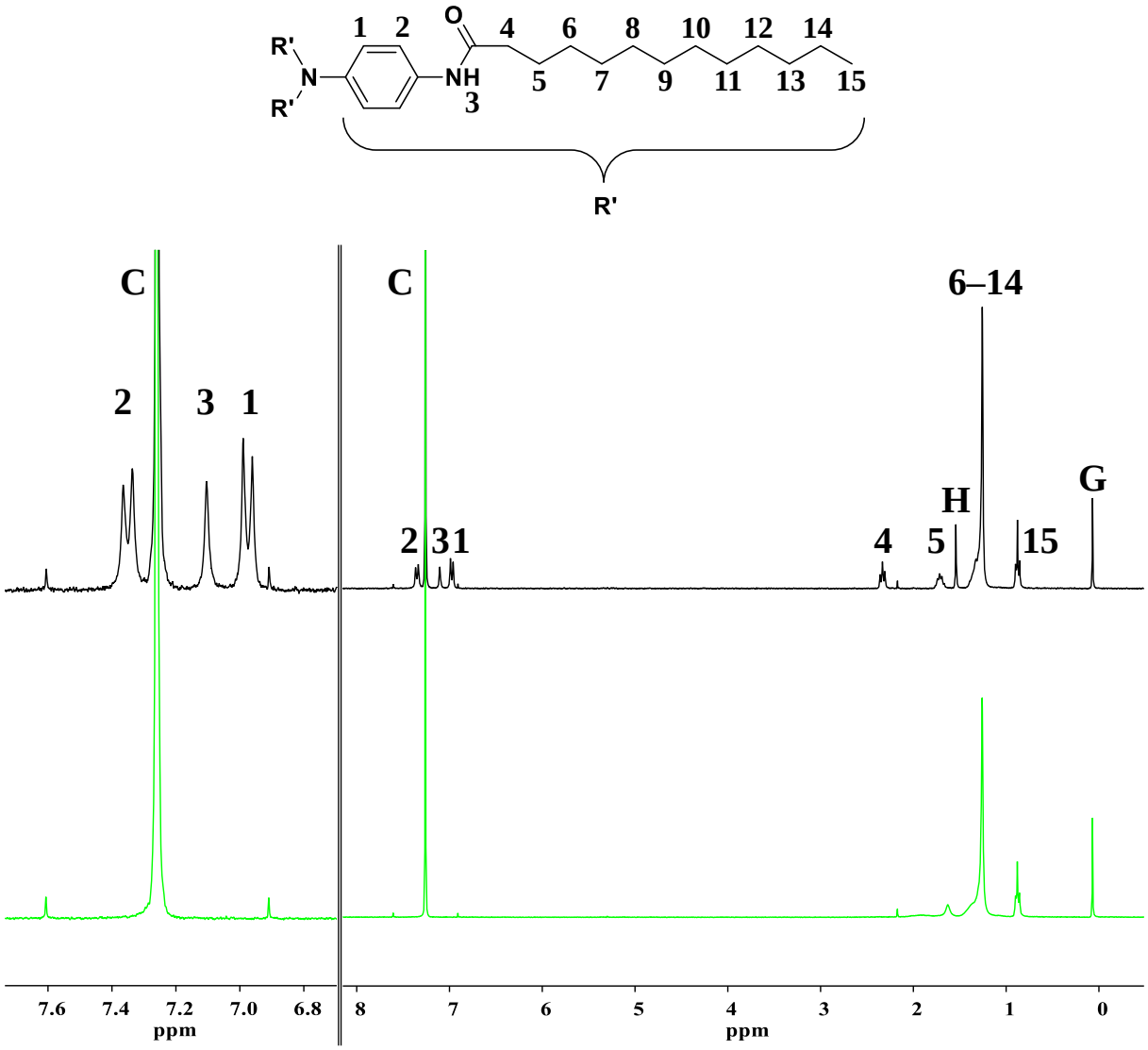

Figure III.24 ^{1}H NMR spectra of **TATA-C13** at 2.3 mM in $CDCl_3$, (top) before and (bottom) after light irradiation during one minute by the setup A, with a surface optical power of 7.9 mW/cm^2 (C, H and G are resonance peaks for residual chloroform, water and silicone grease, respectively). Left: zoom on the aromatic/amide region; right: full NMR spectra.

We propose a rationalization of the aforementioned analyses, which might appear contradictory when taken separately. Our data show that a significant proportion of non-hydrogen-bonded TATA molecules are present after light irradiation as detected by FT–IR analyses (40–60% for the maximal amount of generated TATA radicals). However, our data also suggest that neutral and radical TATA molecules co-assemble under these conditions: i) newly formed UV–Vis–NIR and FT–IR signals upon irradiation not only concern the oxidized

TATA species but also a large fraction of the neutral ones and ii) broadening/disappearance of ^{1}H NMR signals close to sticker units occur for all TATA molecules, not only for those which have been oxidized. Our conclusion is that under these conditions neutral and radical TATA species are co-assembled into large aggregates for which hydrogen-bonding is not the main driving force. Their general structure does not significantly differ from that of the non-specific aggregates present before irradiation as shown by SANS data even though a local reoorganization of the molecules cannot be discarded. The radicals appear to be localized according to EPR. At first sight, this seems in contradiction with the fact that all the TATA molecules seem to interact with each other according to NMR. However, it can be rationalized by considering the different timescales of ^{1}H NMR (µs) and EPR (ns) techniques. The transfer of radicals between oxidized and neutral molecules is sufficiently rapid to affect all molecules on the NMR timescale, but too slow to be detected by EPR. The relatively slowness of the exchange process might be related to a non ideal stacking of the aggregates. Finally, the fact that only a limited number of neutral TATA molecules could be oxidized under these conditons might also be atributed to the presence of TATA homoassemblies and mixed TATA/TATA$^{\bullet+}$ aggregates, prior and after irradiation, respectively.

IV. 2. 2. Irradiation at room temperature and analyses at -10°C

We identified (subsection III. 3. 2) that cooling is a suitable trigger for promoting the self-assembly of TATA solutions (2.3 mM) into hydrogen bonded stacks. Thereby, the effect of light irradiation at room temperature on the structure of the hydrogen-bonded assemblies formed upon cooling was assessed by variable-temperature FT–IR analyses (**Figure III.25**).

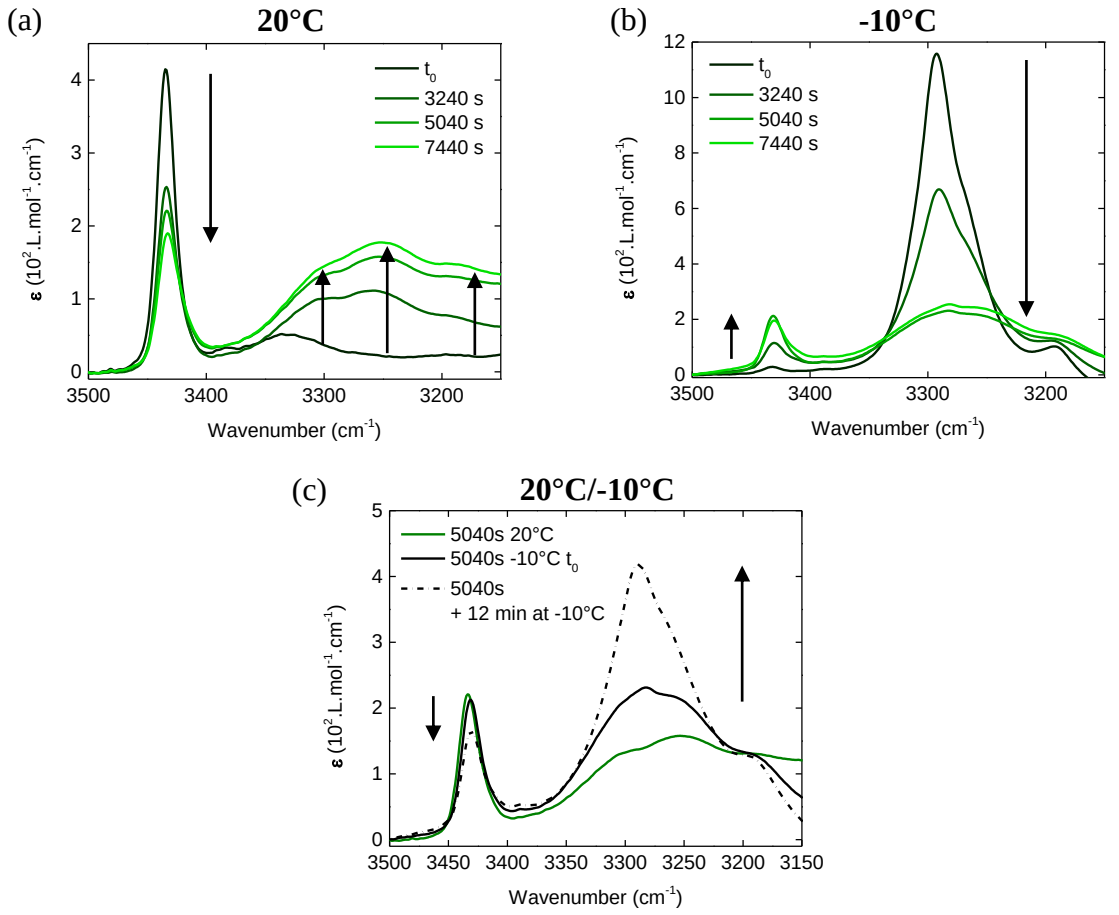

Figure III.25 (a–c) FT–IR spectra of light irradiated solutions of **TATA-C13** at 2.3 mM in $CHCl_3$, zoom on the N-H region. The solution was irradiated for 3240, 5040 or 7440 seconds at room temperature, and the spectrum was measured at 20°C (a) and then at -10°C (b); (c) the solution irradiated by light for 5040 s at room temperature was measured at -10°C immediately after cooling and 12 min later after being in the dark at the same temperature. The solution was directly irradiated in the FT–IR 2 mm rectangular CaF_2 cell by the setup A, with a surface optical power of 7.9 mW/cm^2.

The FT–IR spectrum recorded at room temperature after 3240 s irradiation indicated that the number of radicals generated is of ca. 40%, similar to the aforementioned experiments, then the 5040 s and 7440 s solutions are on the plateau (ca. 50%). Upon cooling to -10°C immediately after irradiation, significant changes in the intensity and shape of the N-H bands are seen. The fraction of free N-H has considerably reduced whilst that attributed to bonded N-H has increased. Comparison with FT–IR spectra of the non-irradiated solution at the same temperature is particularly insightful (**Figure III.25b**). The proportion of free N-H is higher for light-irradiated solutions which translated into a difference in the degree of aggregation: from 0.93 for the non-irradiated solution, to 0.72 (3240 s), 0.49 (5040 s) and

0.53 (7440 s) for the irradiated solutions. Likewise, the signal for bonded N-H significantly broadens when the irradiation time increases which is due to a higher proportion of radicals. This suggests that the formation of TATA radical cations significantly reduces the ability of TATA molecules to aggregate into hydrogen-bonded stacks. Recombination of the radicals in the dark increases the degree of association by hydrogen bond of TATA molecules but without reaching that of the non-irradiated solution. The fact that the band for bonded N-H at -10°C is sharper than the band centered on 3250 cm^{-1} at room temperature might indicate that co-assembly between neutral and radical TATA species occurs, at least partially. Accordingly, it is likely that $TATA^{\bullet+}$ species compete between two structures upon cooling: hydrogen-bonded stacks and a structure similar to that observed at room temperature and for which a large fraction of molecules are not hydrogen-bonded[XXXI].

IV. 3. At 11.4 mM

In the previous part, $TATA^{\bullet+}$ species have been generated under conditions for which the degree of association of neutral TATA molecules through well-defined hydrogen bonds was small. It was thus important to probe the effect of light on already existing hydrogen-bonded assemblies. The effect of light irradiation was thus assessed on a gel of **TATA-C12** at 11.4 mM in chloroform, which was further analyzed by UV–Vis–NIR and FT–IR analyses (**Figure III.26**).

[XXXI] A similar effect was observed when comparing the fate of non-irradiated and irradiated 2.3 mM solutions with time (**Figure SIII.46b**). Between t_0 and + 28 h, $\Delta\alpha_{Agg\ non\text{-}irradiated} \approx 0.16$ *vs.* $\Delta\alpha_{Agg\ irradiated} \approx 0.05$, as calculated from the evolution of the absorption of the hydrogen bonded N-H stretching vibration signal.

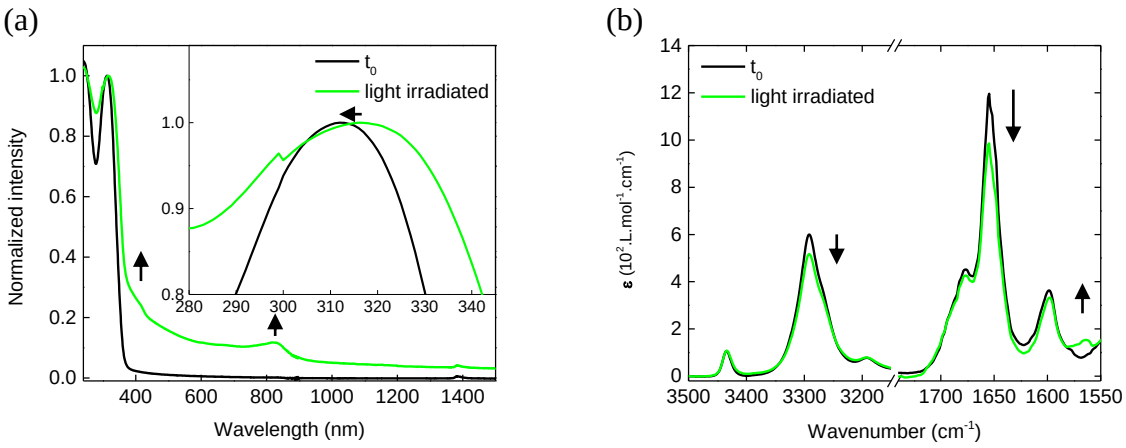

Figure III.26 (a) UV–Vis–NIR absorption and (b) FT–IR spectra at room temperature of **TATA-C12** solution at 11.4 mM in $CHCl_3$ after dissolution (black) and after light irradiation for 12 minutes (green). (a) the light irradiated sample exhibits a sloping baseline because of scattering. This effect is always present in a certain extent at this concentration, but does not prevent the interpretation of the absorption profile shape. (b) Zoom on the N-H, C=O and N-H (bending) regions. The solution was irradiated in a 2 mm rectangular quartz cuvette by the setup A, with a surface optical power of 7.9 mW/cm^2. * = **TATA-C12**$^{\bullet+}$.

After 12 minutes of irradiation, radicals generated from the 11.4 mM solution are less numerous than those formed from the 2.3 mM solution (the same set-up has been used). This can be seen by the weak intensity of the UV–Vis–NIR and FT–IR bands that are characteristic of TATA$^{\bullet+}$ species. The amount of radicals generated under these conditions was lower than 2% (as estimated by EPR, versus ca. 6% for the 2.3 mM solution). The degree of association of **TATA-C12** species into hydrogen-bonded stacks is high and not significantly affected by the irradiation ($\alpha_{Agg} \approx 75\%$). It can thus be deduced that because of the tight hydrogen-bonded self-assemblies, TATA molecules are less prone to oxidation.

UV–Vis–NIR analyses performed 10 h and 31 h after the end of the irradiation time, demonstrate that the triarylammoniums are still present in the solution (at least 1%), as evidenced by the absorption bands around 400 nm and between 600 and 900 nm (**Figure SIII.49**). These results indicate that radical cationic species are persistent, which is likely the sign of co-assembly between radical cationic and neutral species. To better apprehend the shape

and size of the assemblies of this system, a sample was analyzed by SANS measurement and compared with the non-irradiated one (**Figure III.27**).

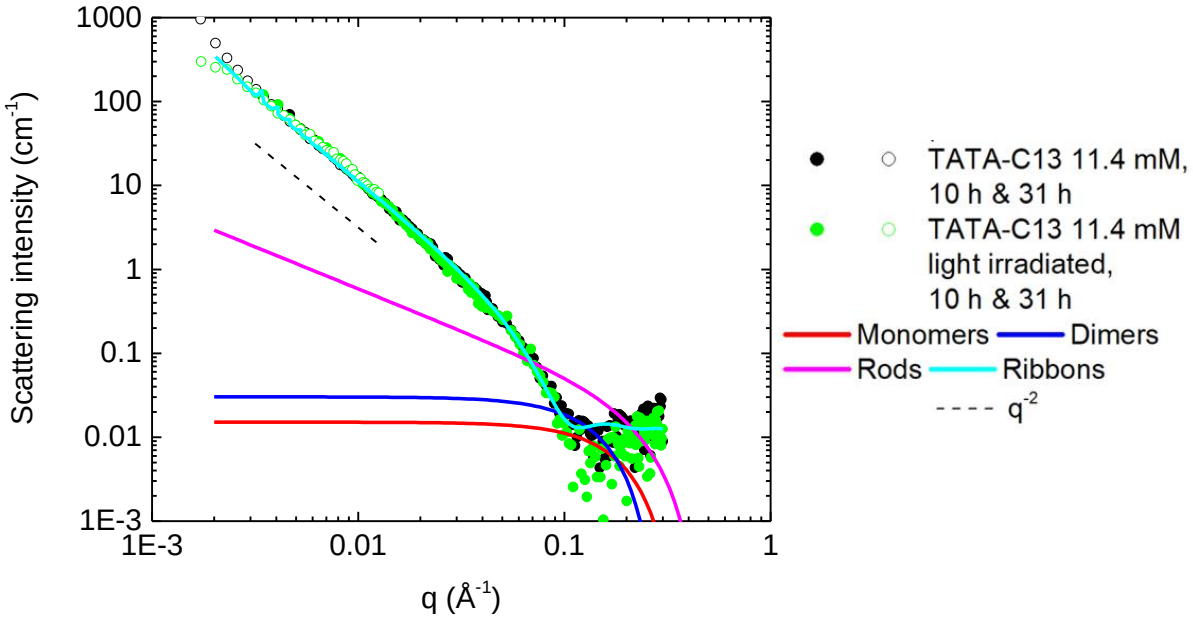

Figure III.27 SANS analysis of **TATA-C13** at 11.4 mM in $CDCl_3$ (the fact that the two datasets overlap allows to verify their coherence and to discard the effect of time between measurements at low and high q values). Simulated curves for monomers, dimers, and infinitely long rigid rods of circular cross-section together with the experimental results. The latter is fitted with a form factor for ribbons (turquoise blue, see the text). The solution was irradiated for 12 minutes in a 2 mm rectangular quartz cuvette by the setup A, with a surface optical power of 7.9 mW/cm^2.

SANS analyses of irradiated and non-irradiated solutions are again very similar and indicate the presence of ribbons (diameter = 5.4 nm). The only difference is that for the irradiated sample the q^{-2} dependence is not maintained until the lowest measured q values, suggesting that the ribbons are shorter after irradiation. This is certainly the result of the aforementioned competition of $TATA^{\bullet+}$ species between hydrogen-bonded stacks and mostly non-hydrogen-bonded aggregates. The presence of large ribbons, even after irradiation, agrees well with the photographs displaying a gel, whatever the conditions. In coherence with the persistence of $TATA^{\bullet+}$ species 31 h after the end of the irradiation, the gel pictured in **Figure III.28** is strongly green.

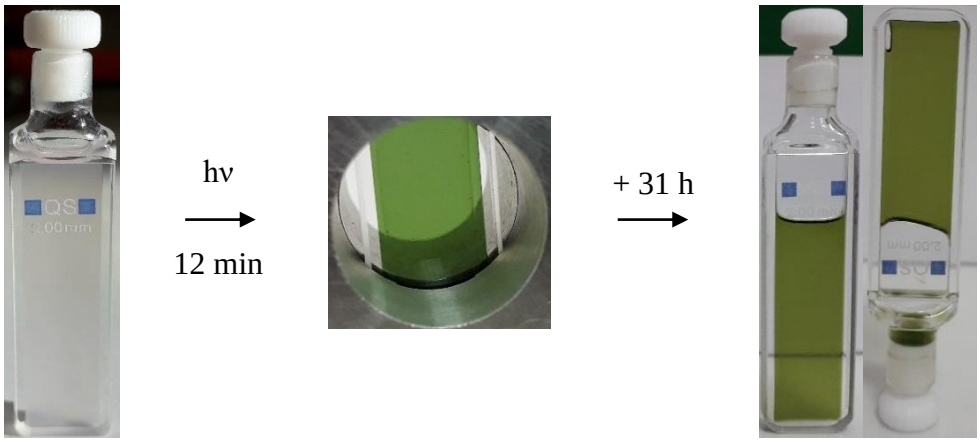

Figure III.28 Pictures of **TATA-C13** at 11.4 mM in $CDCl_3$ after dissolution, irradiation (12 minutes) and 31 h later. The solution after dissolution (left) is a different sample, hence its volume is slightly different. The solution was irradiated in a 2 mm rectangular quartz cuvette by the setup A, with a surface optical power of 7.9 mW/cm^2.

To summarize, the combined UV–Vis–NIR, FT–IR and SANS analyses suggested that the formed TATA$^{\bullet+}$ species are at least in part co-assembled with the neutral TATA species within ribbons which consist of hydrogen-bonded stacks. However, analysis of the irradiated gels by EPR reveal that the radicals are localized (**Figure SIII.51b**). To ascertain that the radicals are present in the hydrogen-bonded stacks we conducted the following experiments.

A solution of **TATA-C12** at 11.4 m in chloroform was irradiated for 12 minutes or 24 minutes, and centrifugated for 15 minutes in the dark to separate the supernatant from the gel (*i.e.* under the influence of the centrifugation, the gel expulses a part of its liquid by syneresis but was partly dissolved because of a slight heating of the machine). The gel was then rinsed four times with fresh chloroform in order to get a wet gel, which was eventually dried under nitrogen to give a dry gel. A scheme of the procedure is depicted in **Figure III.29**. A similar procedure was followed after irradiation of a solution of **TATA-C13** for 12 minutes (except that the gel was not dried). This process was followed for each step by UV–Vis–NIR, FT–IR and EPR spectroscopy. The data obtained for sample of **TATA-C12** irradiated for 24 minutes are shown in **Figure III.30** and **Figure III.31**. The EPR results for **TATA-C12** (12 minutes of irradiation) and **TATA-C13** (12 minutes) are presented in **Figure SIII.51**.

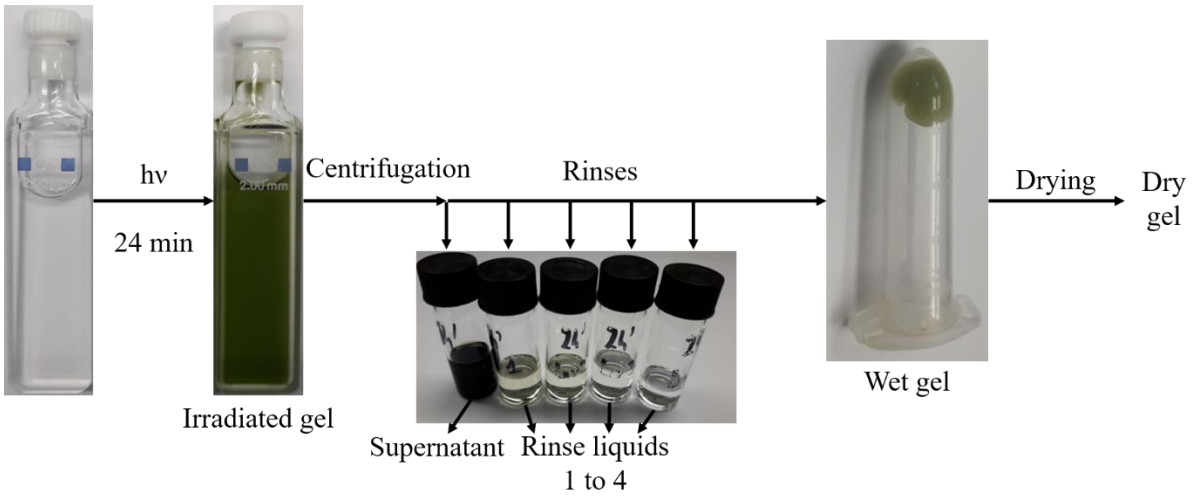

Figure III.29 Scheme of the separation of the gel and solution phases for **TATA-C12** at 11.4 mM in chloroform. The solution was irradiated for 24 min and centrifugated to give the supernatant (dark green liquid) and the pellet (green gel). This gel was then rinsed four times with fresh chloroform to obtain a 'wet gel', which was eventually dried under nitrogen yielding a 'dry gel'. The solution was irradiated in a 2 mm rectangular quartz cuvette by the setup A, with a surface optical power of 7.9 mW/cm^2.

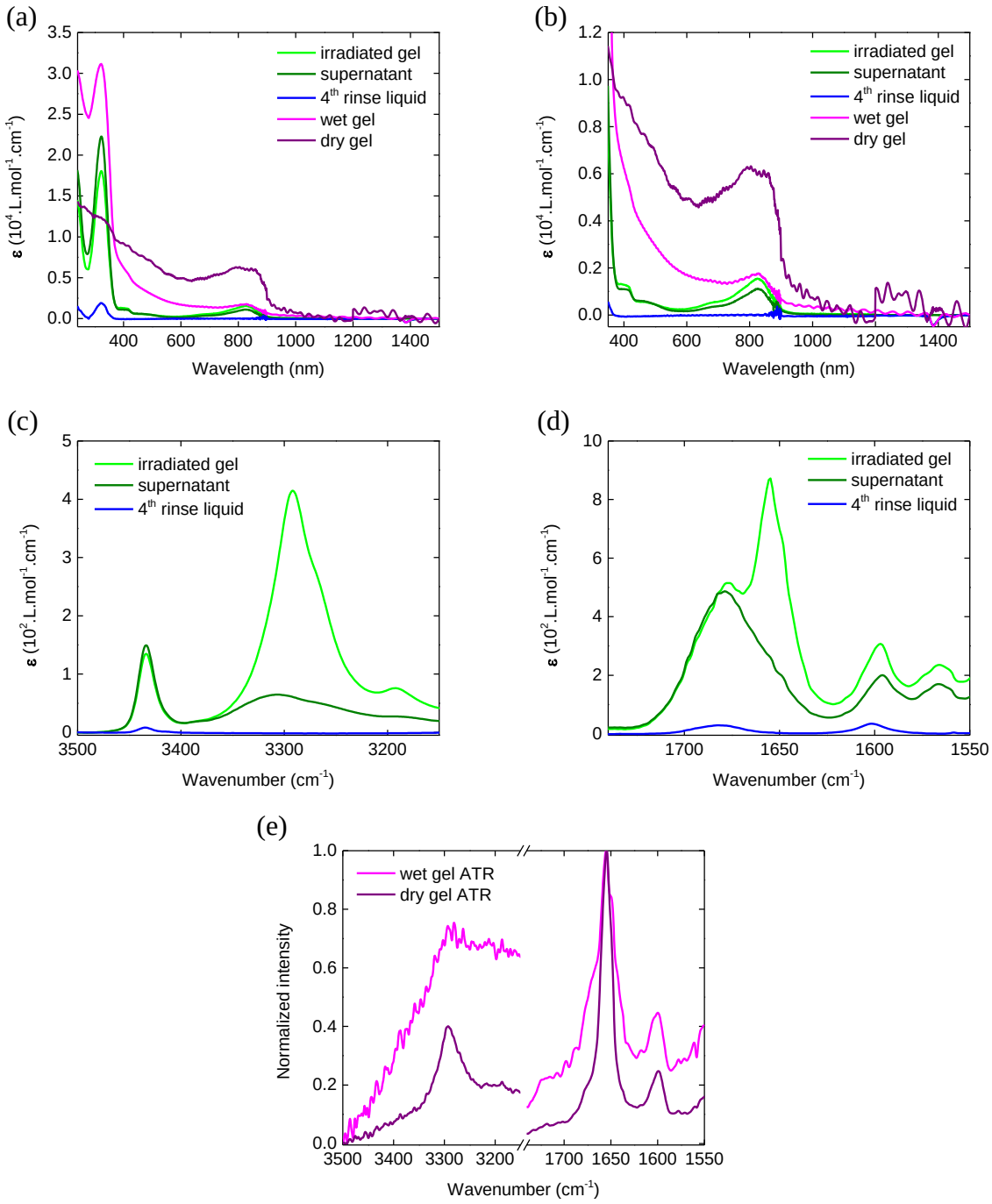

Figure III.30 (a–e) Analyses of the different solutions and gels issued form the centrifugation of **TATA-C12** gel at 11.4 mM in chloroform. (a–b) UV–Vis–NIR absorption with (b) a zoom on the Vis–NIR region, and (c–e) FT–IR spectra with a zoom on the (c and e) N-H and (d) C=O regions. The solution was irradiated in a 2 mm rectangular quartz cuvette by the setup A, with a surface optical power of 7.9 mW/cm^2.

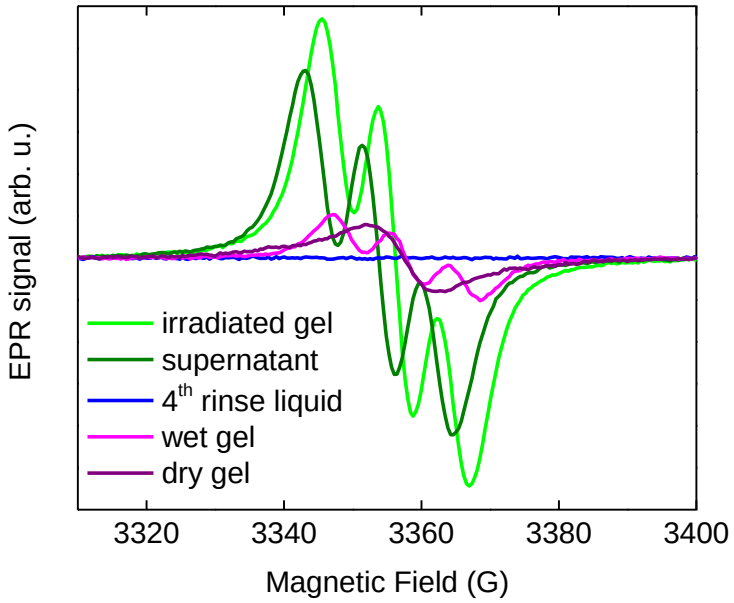

Figure III.31 EPR spectra of the different solutions and gels issued form the centrifugation of an irradiated sample of **TATA-C12** at 11.4 mM in chloroform. The solution was irradiated for 24 minutes in a 2 mm rectangular quartz cuvette by the setup A, with a surface optical power of 7.9 mW/cm^2. The slight shift in magnetic fields between signals is likely due to the variety of physical states probed (gel, liquid, solid). Same EPR spectra are plotted as a function of the normalized magnetic field, to observe their shape independently on the microwave frequency (**Figure SIII.50**). Thanks to the comparison with a reference solution of TEMPO at 4.9 mM, it was possible to determine that from the pristine gel, 1.8% of molecules were photo-oxidized into radical cationic species inside the irradiated gel. Then, the supernatant caught 75% of these triarylammonium radicals, consequently the wet/dry gels less than 25%.

The gel after irradiation (named « irradiated gel » in figures) contains ca. 1.8% of TATA$^{\bullet+}$ as determined by EPR. As mentioned above, the radicals in these gels appear as mainly localized despite TATA molecules being mostly associated into hydrogen-bond stacks. The supernatant caught 75% of these radicals and its FT–IR spectrum is consistent with a mixture of neutral and radical TATA molecules, likely co-assembled into non-specific aggregates. The radicals in these aggregates are localized as observed above for the irradiated 2.3 mM solutions. The wet gel still contains radicals that even if present in low amount (<0.5%) are undoubtedly located in the hydrogen-bonded stacks. The fact that the liquid corresponding to the 4th washing

of the gel does not contain radicals indeed indicate that the remaining radicals are “trapped” into aggregates and FT–IR analysis of the wet gel indicate that only hydrogen-bonded stacks are present. Despite these observations, EPR analysis indicates that again the radicals are localized in the hydrogen-bonded stacks present in this wet gel. No significant differences are seen in the UV–Vis–NIR and FT–IR analyses of the wet and the dry gels. However, EPR signals displayed by the wet and dry gels are markedly different: the radicals in the dry gel are this time fully delocalized as indicated by the characteristic single-line pattern. These results can be rationalized as follows: $TATA^{\bullet+}$ species generated upon irradiation segregate between hydrogen-bonded stacks and non-specific aggregates. In the hydrogen-bonded assemblies, the stacking of the TATA molecules is not optimal and some defects might exist in the H-bonds network that preclude a full delocalization of the radicals. The transfer of radicals between neutral and radical species is presumably slow in the stacks present in the wet gel. However, in the dry state, the stacking of the TATA molecules in the hydrogen-bonded assemblies likely contains fewer defects and allows for a full and rapid delocalization of the radicals.

IV. 4. As thin film

The possibility of having an efficient packing of the neutral and radical TATA species in the solid state was further investigated through the formation of films. Solution of **TATA-C12** and **TATA-C13** at 2.3 mM in chloroform were light irradiated (from 10 seconds to 24 minutes) at room temperature and drop-casted over KBr pellets and 0.1 mm quartz cell, dried and analyzed by FT–IR and UV–Vis–NIR spectroscopy (in **Figure III.32** for **TATA-C12**, and in **Figure SIII.52** for **TATA-C13**). 100 µL of each solution was also filled in quartz tubes, and dried under a nitrogen flow (as depicted in **Figure SIII.53**) to be analyzed by EPR spectroscopy.

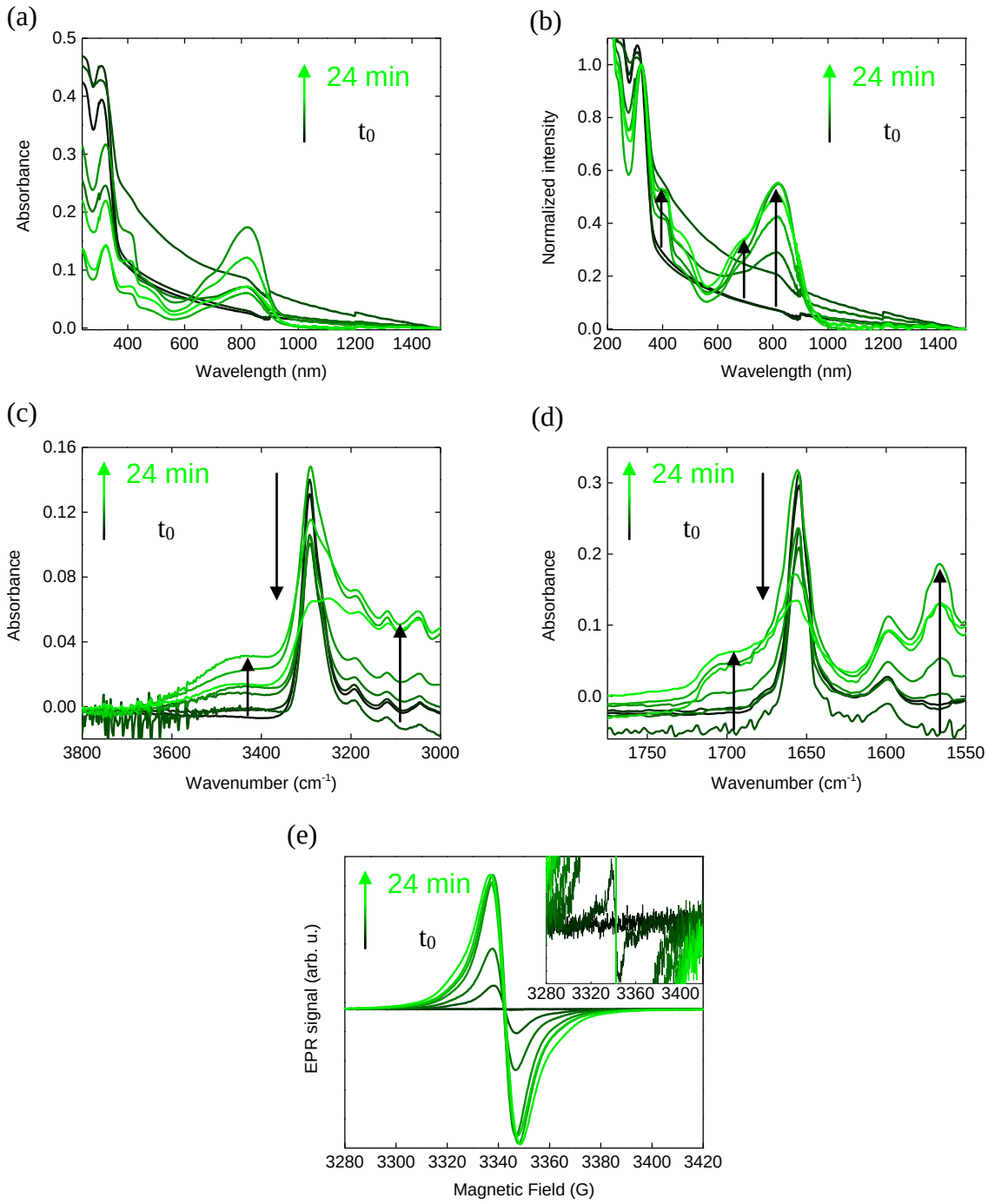

Figure III.32 (a–b) UV–Vis–NIR absorption (in normalized intensity in (b), to facilitate the shape interpretation), (c–d) FT–IR (zoom on the (c) N-H and (d) C=O regions) and (e) EPR spectra of thin films obtained after light irradiation for 10 s, 45 s, 90 s, 3 min, 6 min, 12 min or 24 min of **TATA-C12** solutions at 2.3 mM in $CHCl_3$. The solutions were irradiated in a 2 mm rectangular quartz cuvette by

the setup A, with a surface optical power of 7.9 mW/cm^2. Thin films were obtained by deposition on 0.1 mm lamellar quartz cells or on KBr pellets of the solutions.

UV–Vis–NIR results depict an increasing concentration of triarylammonium radicals from 45 seconds to 6 minutes of light irradiation (from 0 to 6% of radicals based on the EPR assessment displayed in **Figure III.21**), time after which the number of radical cationic species seems to be stable. The film thus likely contains the maximal amount of TATA$^{\bullet+}$ generated under these conditions, *i.e.* 6% according to the EPR results (**Figure III.21**). This is more than 10 times the amount of radicals present in the aforementioned dry gel.

All EPR spectra exhibit a one-line pattern indicative of fully delocalized unpaired electrons among TATA fibers, as measured in the dry gel in the previous section. Interestingly, EPR signals tend to overlap from 3 minutes of light irradiation, supporting the hypothesis of a rapidly reached plateau of TATA$^{\bullet+}$ species. Importantly, no specific charge transfer band is observed in the NIR region indicating that the UV band at 800 nm is identical for both delocalized and localized TATA radicals.

The FT–IR spectra contain the expected bands at 3300 cm^{-1} and 1655 cm^{-1} for hydrogen bonded stacks as well as the bands at 3200 cm^{-1} and 1570 cm^{-1} indicative of the presence of TATA$^{\bullet+}$ species. Upon light irradiation, the intensity of the former bands decreases while that of the latter bands increases which is consistent with the formation of TATA$^{\bullet+}$ species. More intriguingly, increasing the number of radicals in the film also leads to the outbreak and increase of broad bands at 3400 cm^{-1} and 1700 cm^{-1} for amide N-H and C=O, respectively. This resembles the frequencies associated with non-hydrogen-bonded species, *i.e*. free amide functions. Accordingly, it appears that HB defects are created when the number of radicals into the stacks increase. This phenomenon does not prevent full delocalization of the radicals probably because the fibers keep a sufficient correlation length. Giuseppone *et al*. actually reported that the correlation length increases for irradiated fibers of **TATA-C12** relatively to non-irradiated ones[10].

The strategy of drying an irradiated solution essentially composed of non-hydrogen-bonded TATA molecules offers the advantage of modulating the amount of TATA$^{\bullet+}$ species present into stacks. Moreover, these stacks contain fully delocalized unpaired electrons.

V. Conclusion

This chapter aimed at investigating the self-association properties of TATA with saturated side chains, to highlight the conditions of assembly, as well as to probe the aggregates structure (e.g. shape, length and interactions between molecules). The effect of light irradiation was then assessed on a variety of association states. The co-assembly between radical cationic species, generated by light irradiation, and neutral molecules, as well as the involved type of interactions, were particularly examined. Notably, a special attention has been paid for hydrogen bonds, directional by nature and which could likely be the driving force of the CPL-controlled supramolecular chirality of TATA-based assemblies. The result of our investigation is schematized in **Figure III.33** and summarized below.

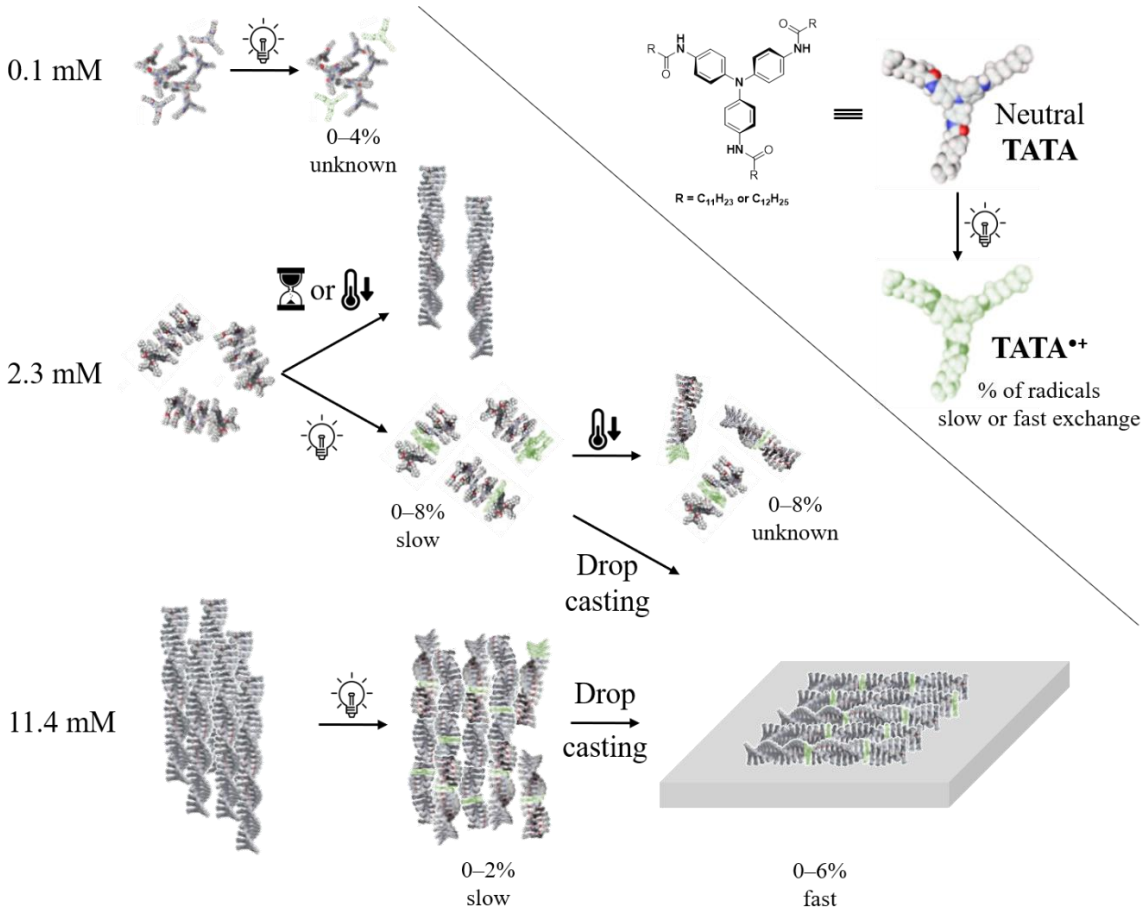

Figure III.33 Schematic representation of the different self-assembly pathways explored in this study, with and without light irradiation, for TATA monomers with C11 and C12 aliphatic side chains in chloroform and as thin film. Molecular structures adapted from Giuseppone *et al.*[26]

After the gram-scale synthesis of TATA with C11 or C12 linear aliphatic side chains, their solubility tests and concentration mapping allowed us to identify three different concentrations exhibiting distinct association states: 1) at 0.1 mM, where TATA molecules are essentially as free monomers, even if the presence of non-specific aggregates is also possible; 2) at 2.3 mM, where TATA molecules are mostly present as non-specific aggregates made of dispersion and ill-defined H-bonding interactions. These aggregates transform upon time or cooling, into hydrogen-bonded helical stacks; 3) at 11.4 mM, where TATA molecules are mostly involved in ribbon-like superstructures made of fibrils of individual hydrogen-bonded stacks. Finally, only thin films are composed exclusively of hydrogen-bonded stacks.

At 0.1 mM the formation of radical cationic species with localized unpaired electrons do not trigger TATA self-assembly into well-defined H-bonded stacks, but we cannot rule out the formation of non-specific co-aggregates between radical cationic and neutral species. At 2.3 mM, neutral and radical TATA species co-assemble into one-dimensional non-specific aggregates. Their structure is likely similar to those existing before irradiation, for which hydrogen-bonding is not the main driving force, and the disorder present into these aggregates precludes the fast delocalization of unpaired electrons. Upon cooling, it is likely that $TATA^{\bullet+}$ species compete between two structures: hydrogen-bonded stacks and non-specific aggregates. At 11.4 mM, $TATA^{\bullet+}$ species generated upon irradiation are distributed both in hydrogen-bonded stacks and in non-specific aggregates. In the H-bonded assemblies, the stacking of the TATA molecules is not optimal and some defects might exist, that prevent fast delocalization of $TATA^{\bullet+}$ charges. However, in the film state, the stacking of the TATA molecules likely contains fewer defects and allow for a full and rapid delocalization of the radicals.

These complex manifestations offer a few conditions where the co-assembly of triarylammonium radicals with neutral species could lead to a control of the supramolecular chirality. Thin films are promising, by directly incorporating molecules that have interacted with light inside well-defined hydrogen-bonded helical stacks. Light-promoted non-specific and hydrogen-bonded co-assemblies at 2.3 mM and 11.4 mM are also of interest, as long as the orientation force is kept and could be transferred to more stable and directional stacks upon time or cooling. Last, if triarylammonium radicals are likely biased by CPL through

photoresolution, other species like short aggregates (e.g. nuclei) involving few molecules could also interact with a CPL radiation directing their nascent helical conformation.

VI. Supporting Information

VI. 1. Supplementary Figures

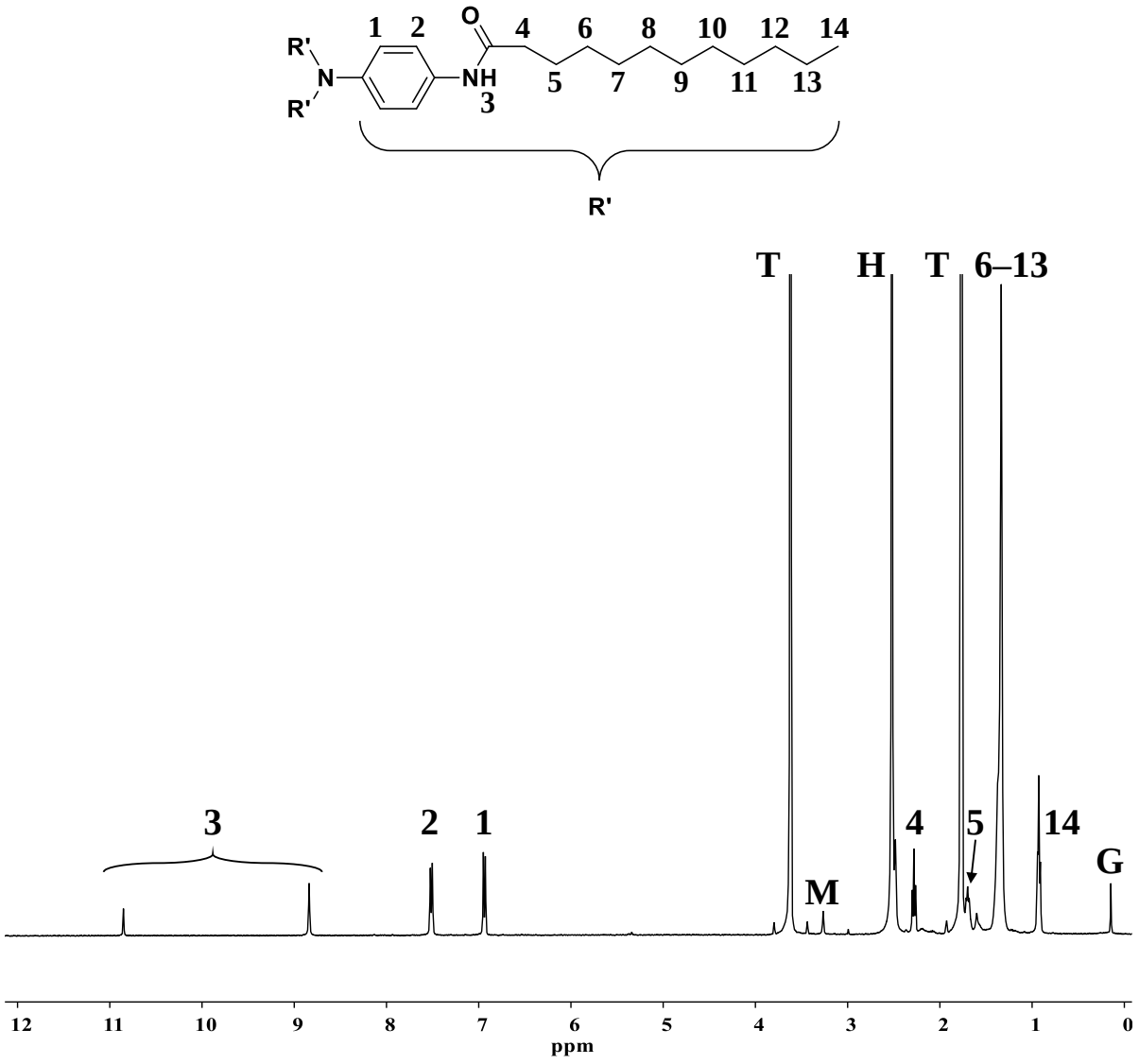

Figure SIII.34 ^{1}H NMR analysis in THF-d_8 of **TATA-C12** (T, M, H and G are resonance peaks for residual THF, methanol, water and silicone grease, respectively).

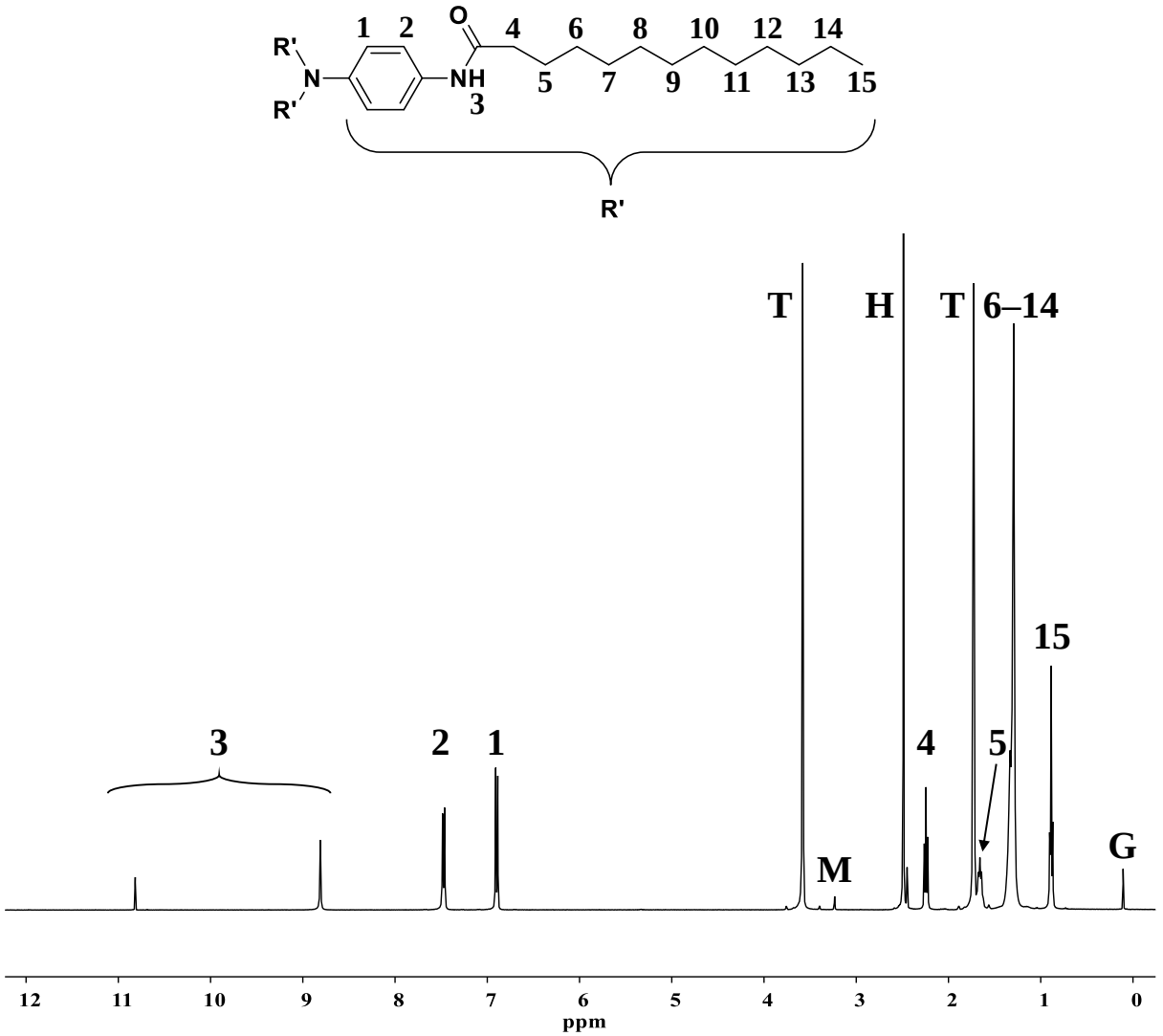

Figure SIII.35 ^{1}H NMR analysis in THF-d_8 of **TATA-C13** (T, M, H and G are resonance peaks for residual THF, methanol, water and silicone grease, respectively).

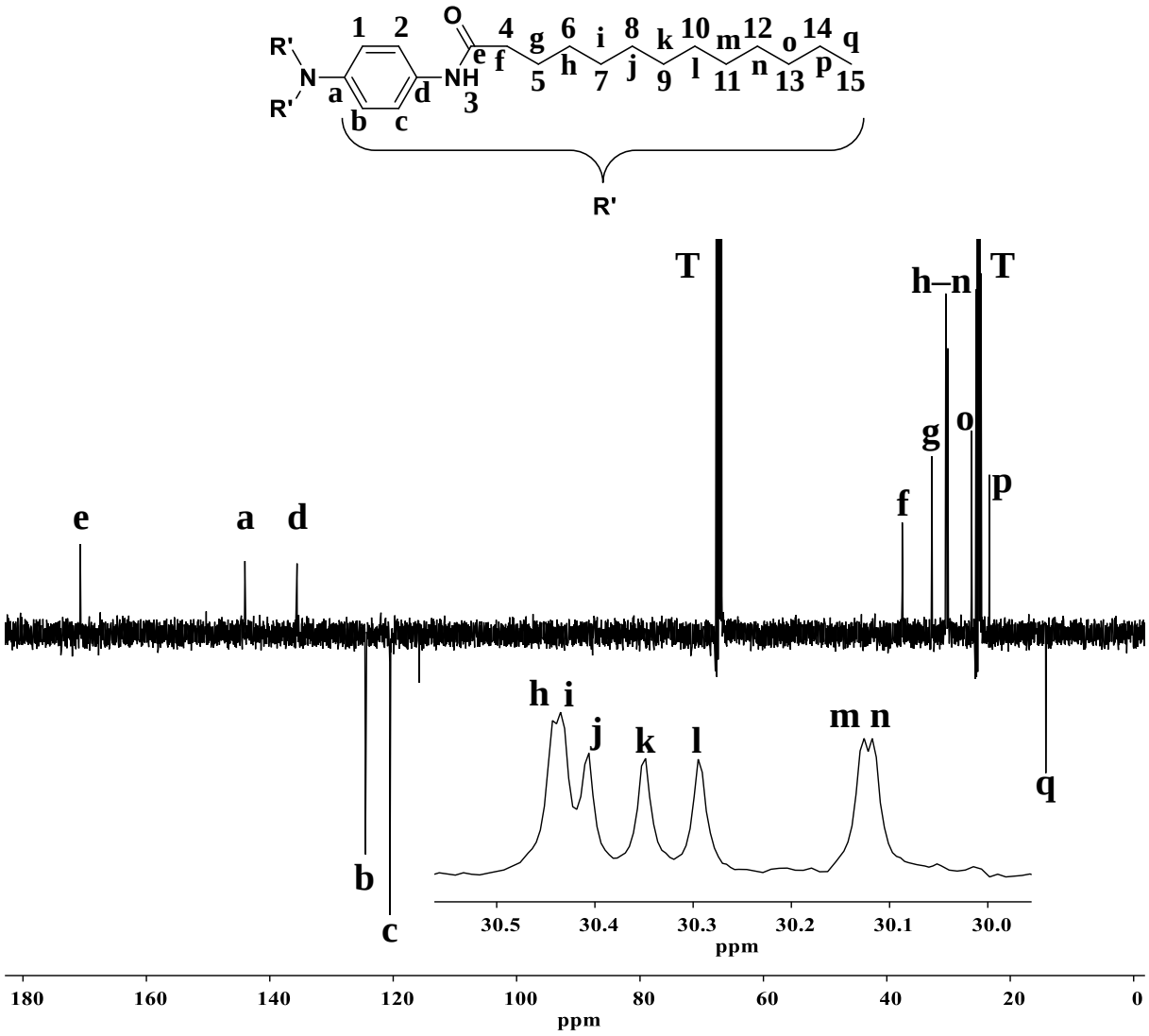

Figure SIII.36 $^{13}C\{^{1}H\}$–JMOD NMR analysis of **TATA-C13** in THF-d_8 (T is for resonance peaks of residual THF).

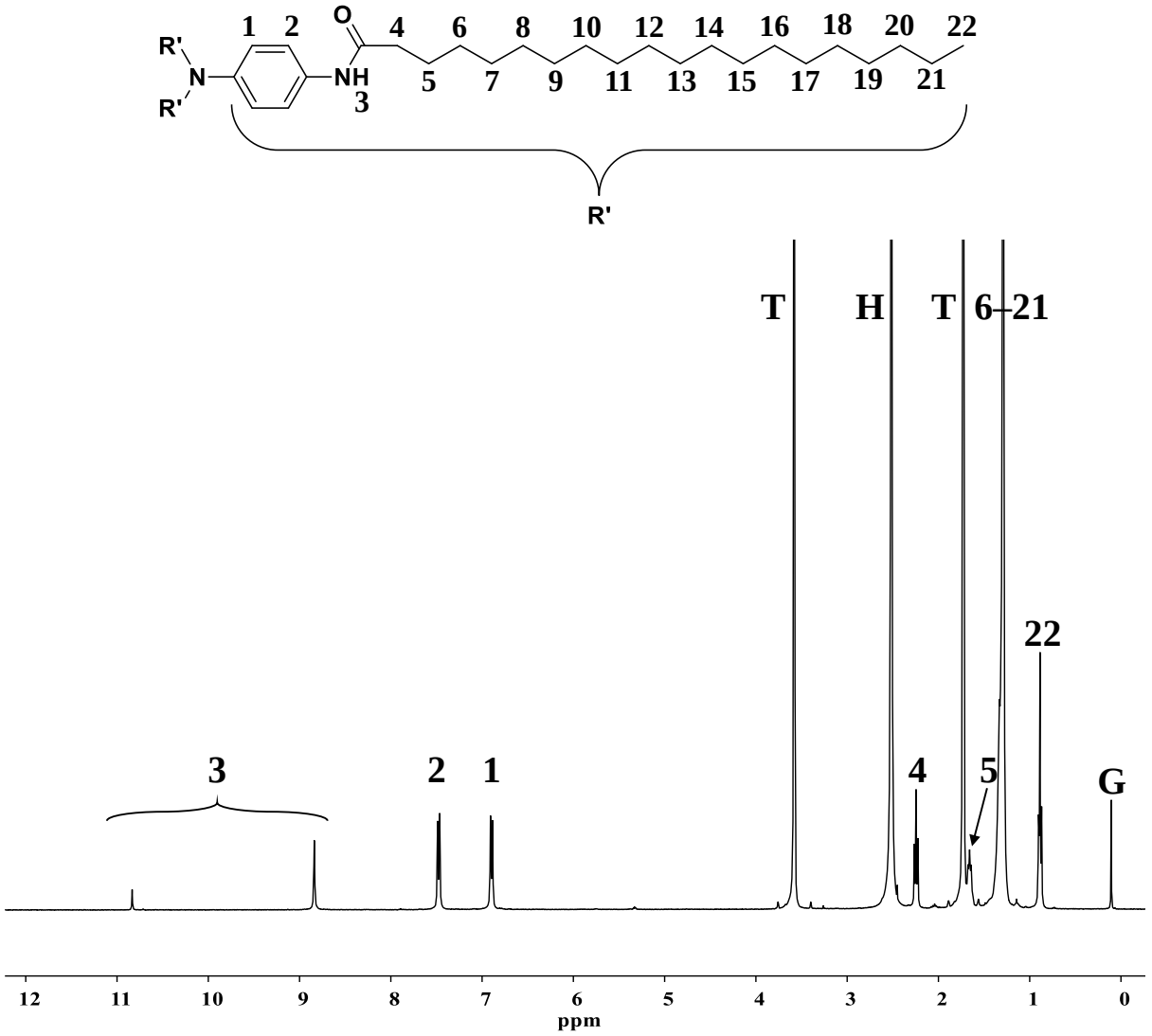

Figure SIII.37 ^{1}H NMR analysis in THF-d_8 of **TATA-C13** (T, H and G are resonance peaks for residual THF, water and silicone grease, respectively).

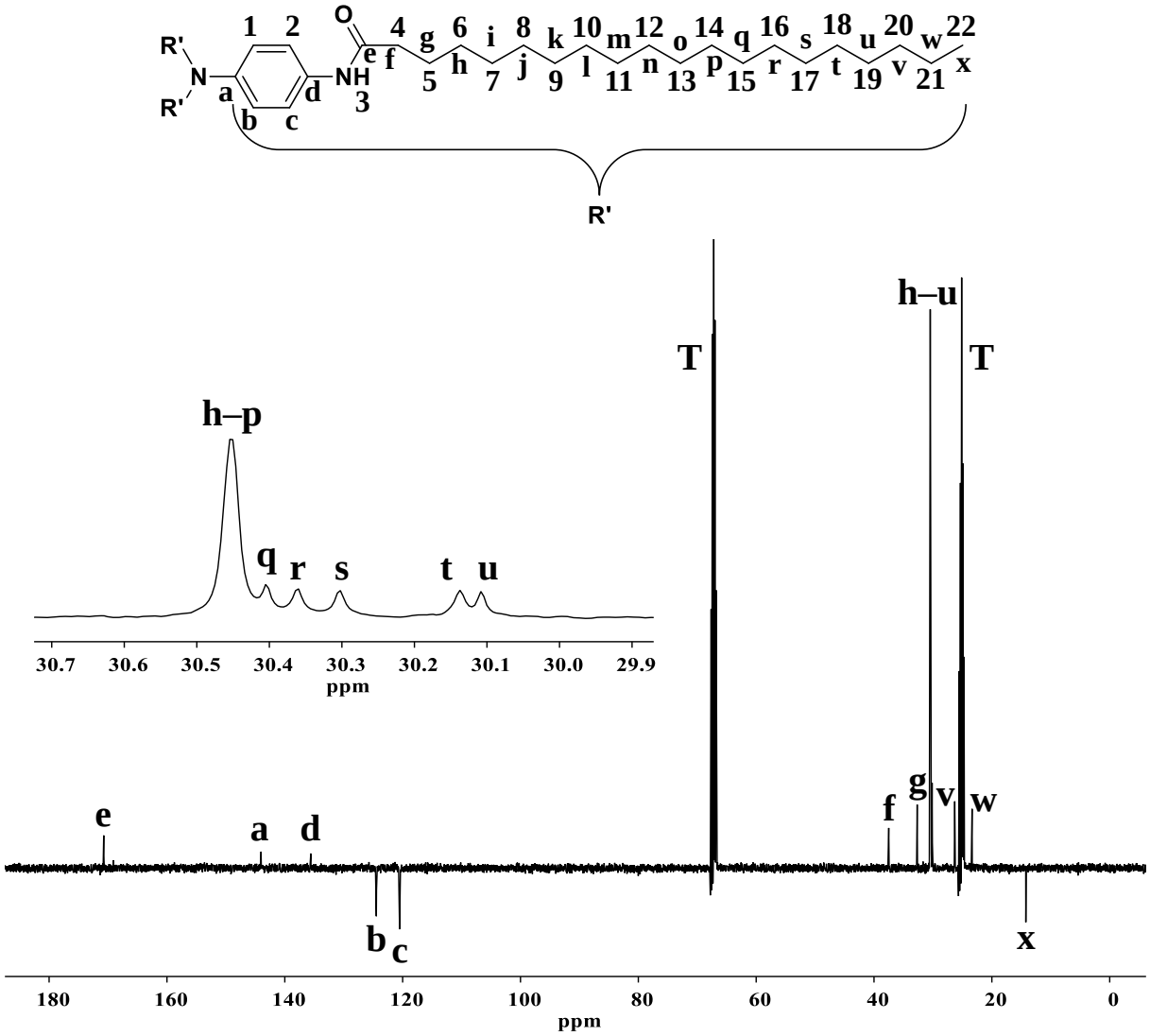

Figure SIII.38 $^{13}C\{^{1}H\}$–JMOD NMR analysis of **TATA-C20** in THF-d_8 (T is for resonance peaks of residual THF).

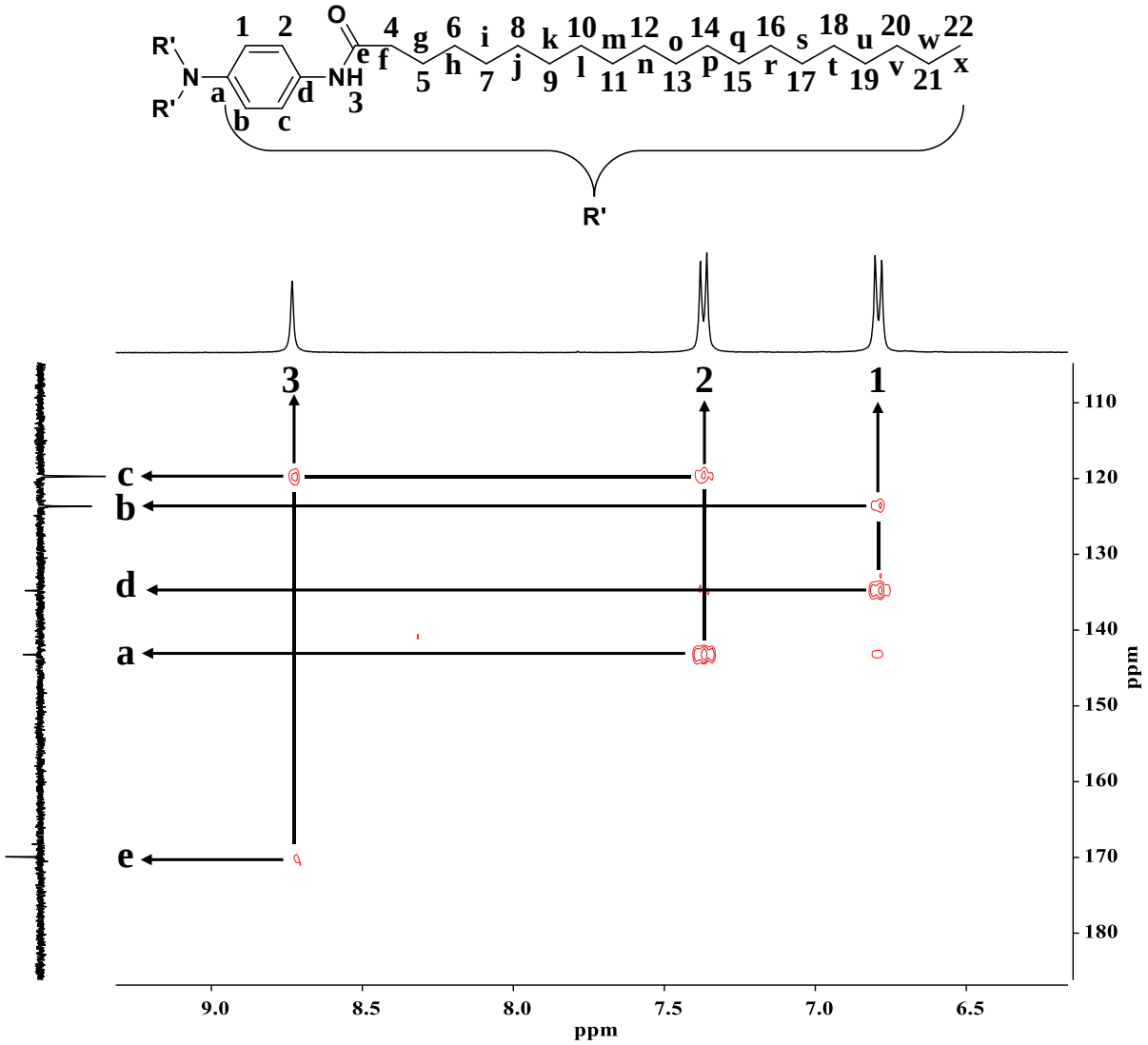

Figure SIII.39 ^{1}H–^{13}C HMBC NMR analysis in THF-d_8 of **TATA-C20**, with a zoom on the region of interest.

Table SIII.2 Solubility of **TATA-C13** and **TATA-C20** (0.1 mM) after heating up to the boiling point. I = insoluble, P = precipitation, S = soluble, η ↑ = viscosity increases.

Solvent	TATA-C13	TATA-C20
Methylcyclohexane	I	I (η↑)
Decalin	S (η↑)	S (η↑)
Toluene	S	P
Trifluorotoluene	I	I

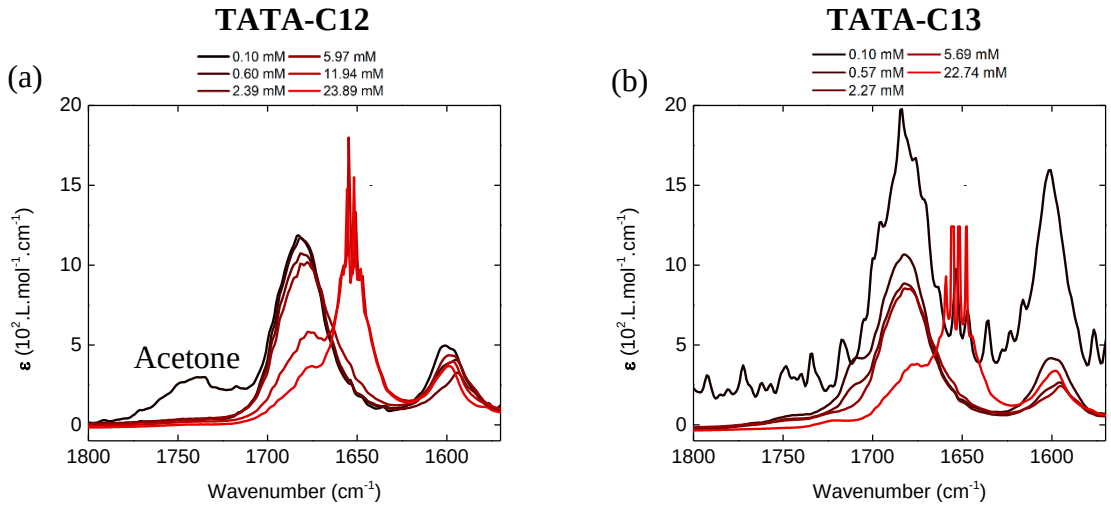

Figure SIII.40 Concentration-dependent FT–IR spectra of (a) **TATA-C12** and (b) **TATA-C13** in chloroform at 20°C. Zoom on the C=O region, saturating at 23.89 mM and at 22.74 mM for (a) **TATA-C12** and (b) **TATA-C13**, respectively. * = solutions saturated. (a) The absorption band around 1750 cm^{-1} is attributed to C=O stretching vibrations of residual acetone.

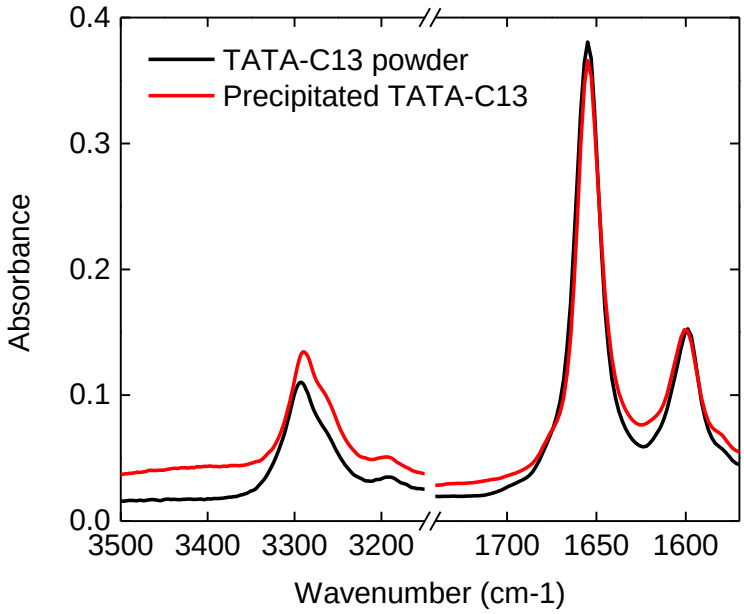

Figure SIII.41 FT–IR analyses of **TATA-C13** as powder and of the gel formed over few weeks inside the solution at 2.3 mM in chloroform, and retrieved by filtration.

Figure SIII.42 Photographs of the (H) 23-W Philips halogen classic warm white 204 lumen lamp, placed in an opaque box to block the surrounding light during irradiations.

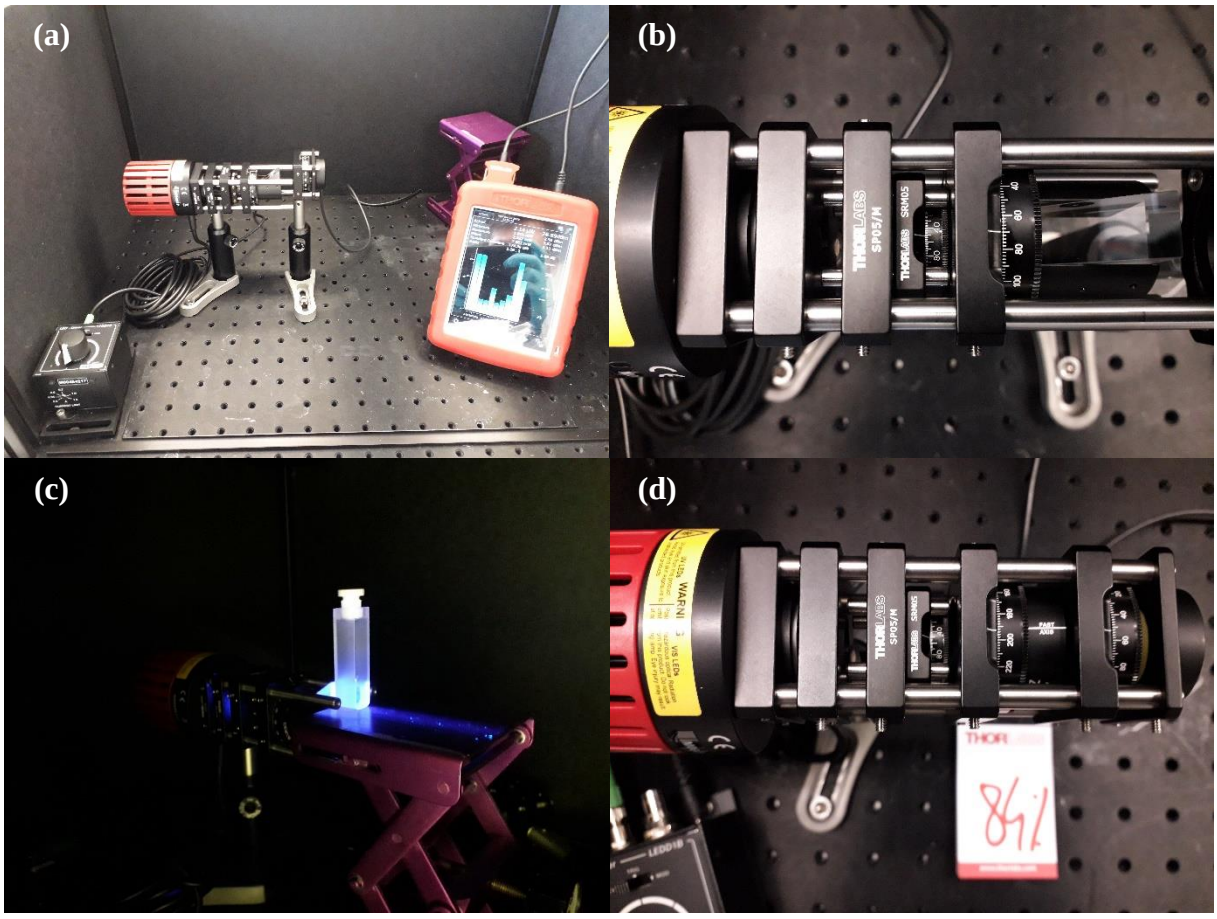

Figure SIII.43 Photographs of the setups A (a–c) and the "modified-setup A" (d) in an opaque optical enclosure, made of black hardboards, and installed on an aluminum breadboard. From left to right in the picture (a) or (b), the setup A is composed of a LED (in red), a condenser lens, a linear polarizer (in a cage rotation mounting) and a quarter-wave Fresnel rhomb retarder (also in a cage rotation mounting); from left to right in the picture (d), the "modified-setup A" is composed of a LED, a condenser lens, a

linear polarizer (like A) and a quarter-wave plate specially designed (instead of a Fresnel rhomb retarder like in A). The components following the quarter-wave plate in picture (a) and (d) are a linear polarizer and a photodiode, linked to an optical power meter console, visible in the picture (a) on the right. These two components served to measure the optical power of the light emitted by setups A and B, as a function of the direction of the axis of polarization of the linear polarizer preceding the photodiode. The photograph (c) presents the light irradiation of a 10 mm rectangular quartz cuvette by the setup A.

Figure SIII.44 EPR signals measured by Lancaster *et al.* for triarylamine-based radical cations[51]. (left) Three-line pattern, corresponding to unpaired electrons localized on one triarylamine; (center) five-line pattern, ascribing to unpaired electrons partially delocalized between two triarylamines; (right) one-line pattern, attributing to unpaired radicals fully delocalized without energetic barrier to the charge transfer.

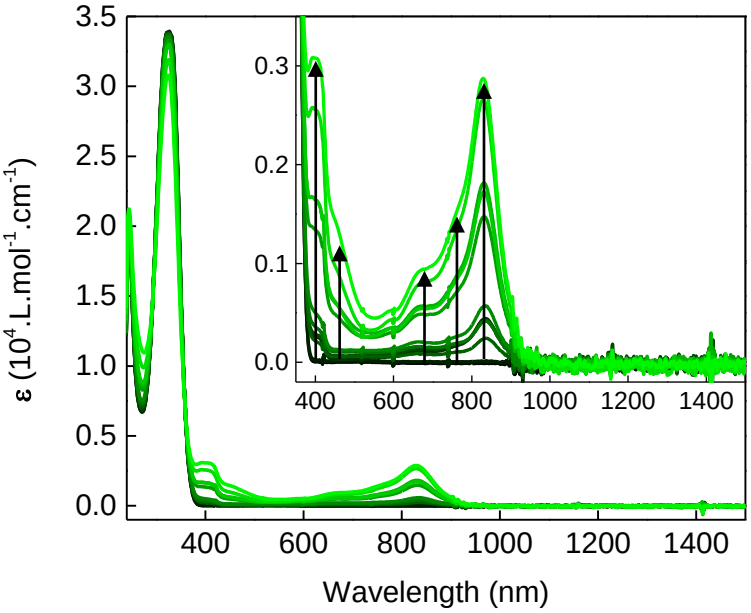

Figure SIII.45 UV–Vis–NIR absorption spectrum during light irradiation of a solution of **TATA-C13** in chloroform at 0.1 mM. The 10 mm rectangular quartz cuvette was irradiated at few cm by the setup A, with a surface optical power of 7.9 mW/cm^2.

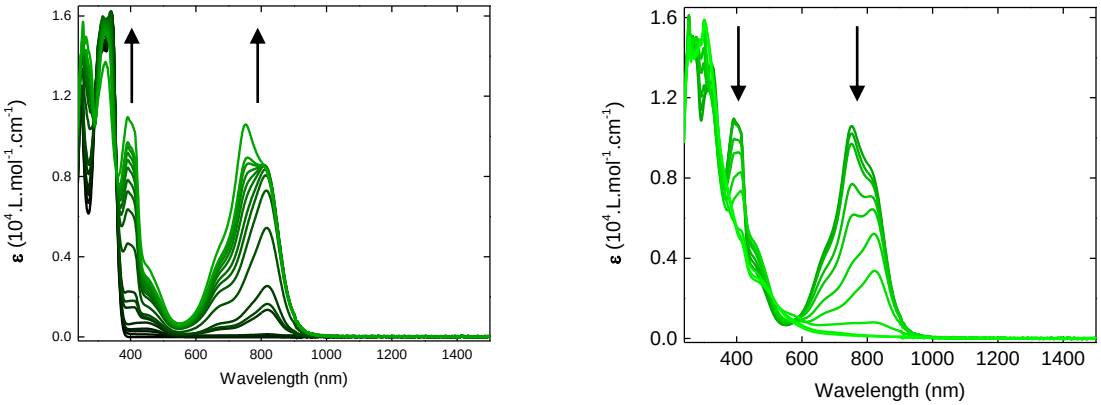

Figure SIII.46 UV–Vis–NIR absorption spectra during light irradiation of **TATA-C13** in chloroform at 2.3 mM. Two major phases: increasing molar extinction coefficient the first 200 seconds (left), then decreasing molar extinction coefficient until 5400 seconds (right). Molar extinction coefficients below 350 nm saturate. The 1 mm rectangular quartz cuvette was irradiated at few cm by the setup A, with a surface optical power of 7.9 mW/cm^2.

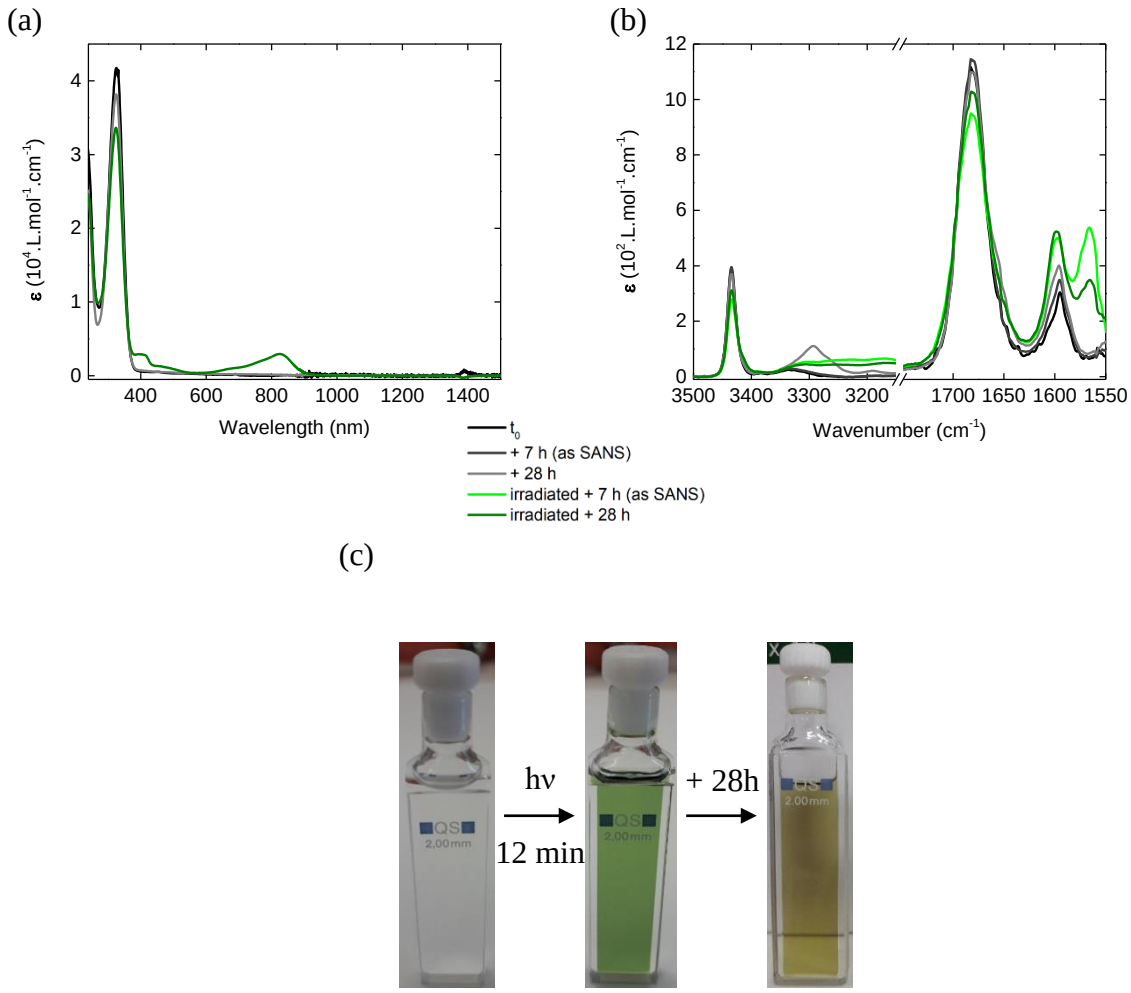

Figure SIII.47 (a) UV–Vis–NIR absorption and (b) FT–IR spectra of **TATA-C13** at 2.3 mM in $CHCl_3$ after 7 and 28 hours in dark after light irradiation (lime and olive green) or no irradiation (dark and light gray). (b) Zoom on the N-H and C=O regions. (c) Pictures of **TATA-C13** in CDCl3 at 2.3 mM after dissolution, after irradiation and after 28 hours in dark. Solutions after dissolution and light irradiation are models and were not used for SANS, hence their volume is slightly different. The solution was irradiated in a 2 mm rectangular quartz cuvette by the setup A, with a surface optical power of 7.9 mW/cm^2.

Since SANS measurements were realized several hours after the irradiation for practical reasons, UV–Vis–NIR and FT–IR analyzes were carried out to probe the system in this timescale and beyond (**Figure SIII.47**), what gives an overview about the persistence of radical cationic species. 7 hours after the light irradiation, the intensity of the free N-H vibration signal indicates that about 25% of radicals are still there, against 50% immediately after the light

irradiation. This result underlines the long persistence of triarylammonium radicals, estimated by EPR too: about 1.5% of radicals are detected 18 hours after the light irradiation in similar conditions, against ca. 6% just after the light irradiation (**Figure SIII.48**).

Even a day after the light irradiation, both UV–Vis–NIR and FT–IR spectra point out the presence of radical cationic species (Vis–NIR absorption bands around 400 nm as well as between 600 and 900 nm; IR signals between 3300 cm^{-1} and 3150 cm^{-1} as well as at 1566 cm^{-1}), as also evidenced by the photograph of an analog solution (**Figure SIII.47c**, the brownish color is likely due to the formation of irreversible photo-products). Interestingly, the FT–IR result proves that triarylammonium radicals have an impact on the self-assembly formed upon ageing (+ 28 h): a lower intensity for the free N-H/C=O signals, and a wide absorption band between 3300 cm^{-1} and 3150 cm^{-1} instead of a symmetric signal at 3293 cm^{-1}. It would seem that triarylammonium radicals hamper the formation of well-defined networks of hydrogen bonds, key component of helical columnar stacks.

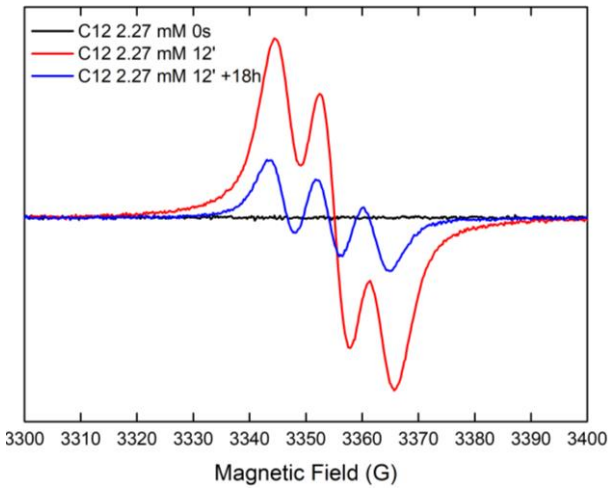

Figure SIII.48 EPR spectra of **TATA-C12** at 2.3 mM in $CHCl_3$ before and after light irradiation then 18h left in the dark. The solution was irradiated in a 2 mm rectangular quartz cuvette by the setup A, with a surface optical power of 7.9 mW/cm^2.

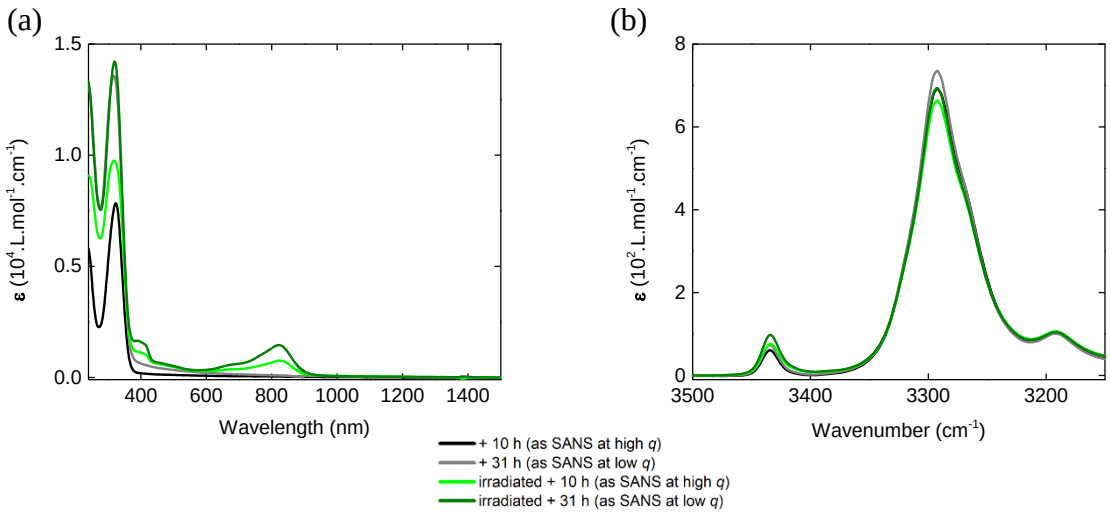

Figure SIII.49 (a) UV–Vis–NIR absorption and (b) FT–IR spectra at room temperature of **TATA-C13** at 11.4 mM in $CHCl_3$ after ageing 10 and 31 hours in dark after light irradiation for 12 minutes (lime and olive green) or without irradiation (dark and gray). (a) The higher molar extinction coefficient of signals corresponding to radical cationic species is due to the anisotropy of the sample, as shown actually by the overall higher molar extinction coefficient, at 325 nm too, and not to their increase in number of triarylammonium radicals. (b) Zoom on the N-H region. The solution was irradiated in a 2 mm rectangular quartz cuvette by the setup A, with a surface optical power of 7.9 mW/cm^2.

In order to assess to what extent the system could come back to its initial state, the effect of time was then probed by the same spectroscopic analyses (**Figure SIII.49**). The light-irradiated sample shows the same FT–IR profile than the non-irradiated one, indicating that the weak shorten effect disappeared upon ageing.

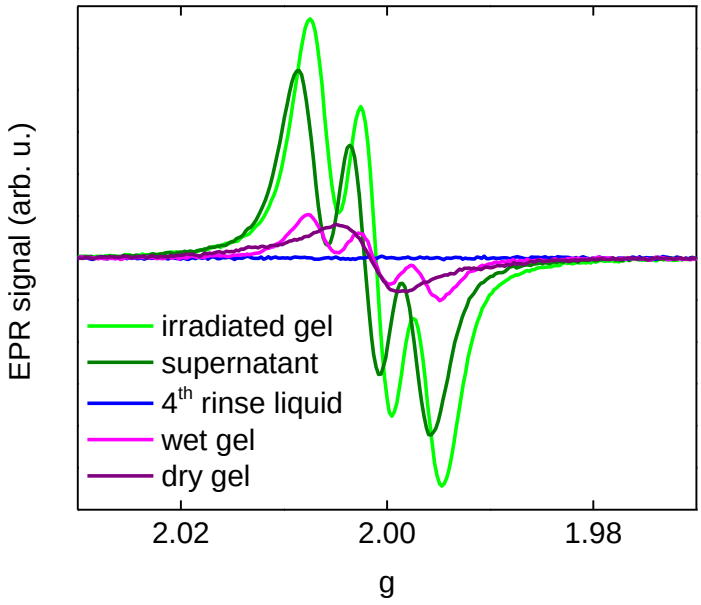

Figure SIII.50 EPR spectra of the dissection of **TATA-C12** at 11.4 mM in chloroform, plotted as a function of the normalized magnetic field to observe their shape independently on the microwave frequency. The solution was irradiated 24 minutes in a 2 mm rectangular quartz cuvette by the setup A, with a surface optical power of 7.9 mW/cm^2. The slight shift in g between signals is likely due to the variety of physical states probed (gel, liquid, solid).

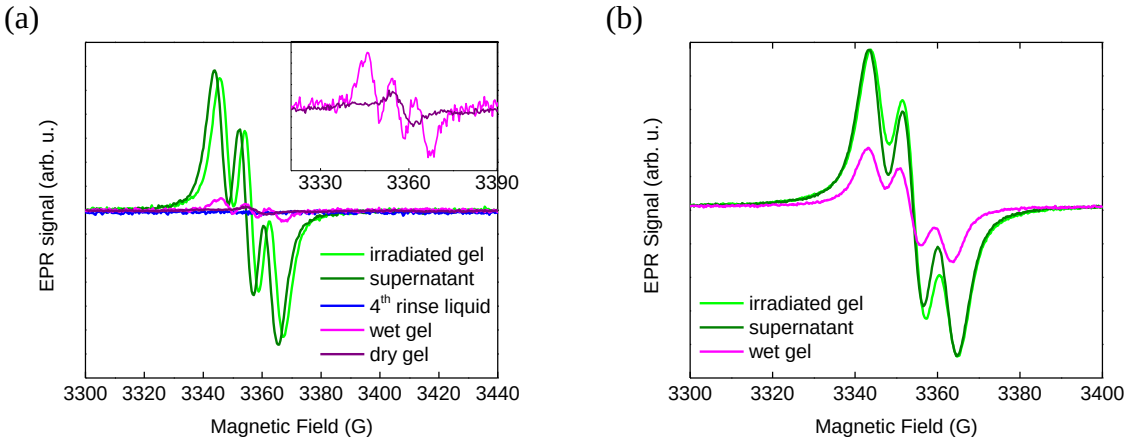

Figure SIII.51 EPR spectra of the dissection of (a) **TATA-C12** and (b) **TATA-C13** at 11.4 mM in chloroform. The solutions were irradiated 12 minutes in a 2 mm rectangular quartz cuvette by the setup A, with a surface optical power of 7.9 mW/cm^2.

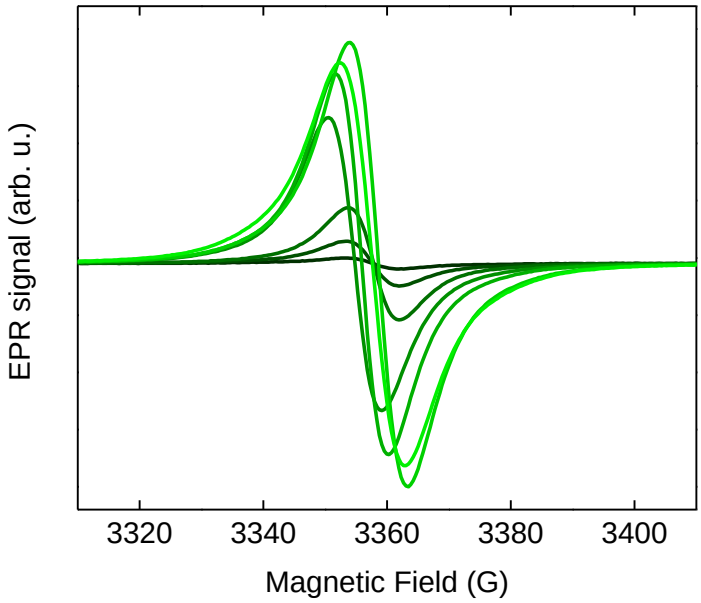

Figure SIII.52 EPR spectra of thin films during light irradiation of **TATA-C13** at 2.3 mM in $CHCl_3$. The solutions were irradiated in a 2 mm rectangular quartz cuvette by the setup A, with a surface optical power of 7.9 mW/cm^2.

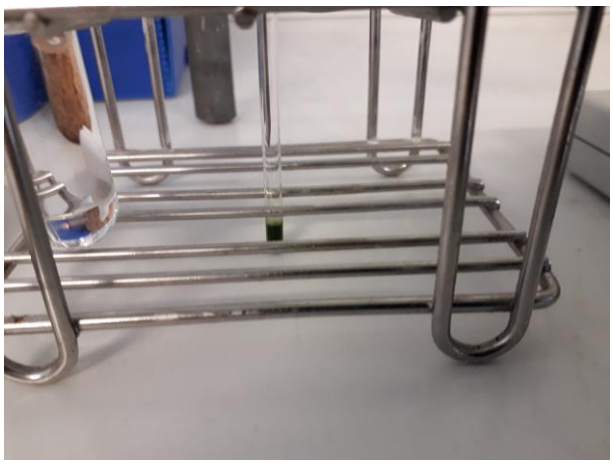

Figure SIII.53 EPR tube containing the thin film of a light irradiated **TATA-C12** solution at 2.3 mM in chloroform. The film formation was carried out upon nitrogen flushing. The solution was irradiated in a 2 mm rectangular quartz cuvette by the setup A, with a surface optical power of 7.9 mW/cm^2.

VI. 2. Experimental section

VI. 2. 1. Materials

n-Dodecanoic acid, *n*-tridecanoic acid, *n*-Eicosanoic acid, triethylamine, *N*-(3-dimethylaminopropyl)-*N′*-ethylcarbodiimide hydrochloride (EDC·HCl), 4-(Dimethylamino)pyridine (DMAP), and Hydroxybenzotriazole (HOBt) were purchased from Acros, Alfa Aesar, Sigma-Aldrich, Fluorochem or TCI suppliers and used as received. Unless otherwise noted, chromatography-grade solvents were used as received. Dried toluene was obtained from a Solvent Purification System (SPS, IT-Inc). Chloroform was filtered over basic alumina, distilled over CaH_2 and stored under argon atmosphere in a Schlenk flask before use in all of the experiments. C_7D_8, $CDCl_3$ and DMSO-d_6 were bought from Eurisotop and used without further purification.

VI. 2. 2. Methods

NMR spectra were recorded on a Bruker Avance 400 or 300 spectrometer and calibrated to the residual solvent peak: DMSO-d_6 (^{1}H: 2.50 ppm; ^{13}C: 39.52 ppm), THF-d_8 (^{1}H: 3.58 and 1.72 ppm; ^{13}C: 67.21 and 25.31 ppm), MeOD (^{1}H: 3.31 ppm; ^{13}C: 49.00 ppm), Toluene-d_8 (^{1}H: 7.09, 7.01, 6.97 and 2.08 ppm; ^{13}C: 137.48, 128.87, 127.96, 125.13 and 20.43 ppm), or $CDCl_3$ (^{1}H: 7.26 ppm; ^{13}C: 77.16 ppm). Peaks are reported with their corresponding multiplicity (s: singlet (br for broad); d: doublet, t: triplet; q: quartet; quint: quintuplet; hept: heptuplet; dd: doublet of doublets, dt: doublet of triplets; td: triplet of doublets), integration and J coupling constant given in Hertz.

Exact mass measurements (HRMS) were obtained on TQ R30-10 HRMS spectrometer by ESI^+ ionization and are reported in *m/z* for the major signal.

Solubility tests were carried out inside screw cap vials with 2 mL of solvent.

Fourier-Transform Infrared (FT–IR) measurements were performed on a Nicolet iS10 spectrometer. Solution spectra were measured in CaF2 cells of various pathlength (1 and 2 mm, according to the concentration) and were corrected for air, solvent and cell absorption. Films

were measured on KBr pellets and corrected for air and cell absorption. Thin films were obtained by deposition on KBr pellets of a solution of TATA.

The Attenuated total reflectance (ATR) FT–IR spectra for solids were collected on a Bruker tensor 27 FT–IR spectrometer equipped with the ATR platinum module, with a detector RT-DLaTGS and the OPUSv5.5 software (Bruker Optics, Germany) was set up with the following parameters. The spectral resolution was fixed to 4 cm^{-1}, the number of scans to 32, the selected spectral range between 4000 and 400 cm^{-1}, and the main peaks were reported (m: medium, s: strong, w: wide).

UV–Vis–NIR absorption spectra were measured with a Varian Cary 5000 spectrophotometer and corrected of the absorption of air, solvent, and cell contribution at the same temperature. Data were recorded with the following parameters: double beam mode, 600 $nm.min^{-1}$ sweep rate, 1 nm data pitch, 2 nm bandwidth, and between 1500 and 200 nm. Source changed at 300 nm while detector and gratings changeover took place at 900 nm. At high concentration, unlike CaF_2 cells employed in FT–IR spectroscopy – which are filled like cuvettes, the filling with a jellifying solution of 0.01 mm lamellar quartz cells is quite tedious, due to the lamellar feature and the thinness of cells, and could lead to inhomogeneous samples. Thin films were obtained by deposition on 0.1 mm lamellar quartz cells of a solution of TATA.

UV–Vis absorption spectra were extracted from CD analyses and obtained after correction of the absorption of air, solvent, and cell contribution at the same temperature. Circular dichroism (CD) measurements were performed on a Jasco J-1500 spectrometer equipped with a Peltier thermostatted cell holder and Xe laser. Data were recorded with the following parameters: 50, 100 or 200 $nm.min^{-1}$ sweep rate, 0.05, 0.5 or 1 nm data pitch, 1 or 2 nm bandwidth, and between 700 or 400 and 220 or 200 nm.

Small-angle neutron scattering (SANS) measurements were made at the LLB (Saclay, France) on the PA20 instrument, at three distance-wavelength combinations to cover the 2.4×10^{-3} to 0.46 Å q^{-1} range, where the scattering vector q is defined as usual, assuming elastic scattering, as $q = (4\pi/\lambda)\sin(\theta/2)$, where θ is the angle between incident and scattered beam. Data were corrected for the empty cell signal and the solute and solvent incoherent background. A

light water standard was used to normalize the scattered intensities to cm^{-1} units. The data was fitted with the DANSE software SasView.

X-band EPR spectra were recorded in non-saturating conditions on a Bruker ELEXSYS 500 spectrometer at room temperature. Typical experimental conditions were: 9.396 GHz microwave frequency, 2 mW microwave power, 0.1 mT modulation amplitude, 100 kHz modulation frequency. Simulations were performed using the EasySpin program[60].

VI. 3. Syntheses of TATA

VI. 3. 1. Synthesis of TATA-C12

n-Dodecanoic acid (1.555 g, 7.763 mmol, 4.5 equiv.), EDC·HCl (1.488 g, 7.762 mmol, 4.5 equiv.) and DMAP (991 mg, 8.112 mmol, 4.7 equiv.) were dissolved inside a round-bottom flask in 75 mL of anhydrous *N*,*N*-dimethylformamide at room temperature under argon. 10 minutes after, tris(4-aminophenyl)amine (500 mg, 1.722 mmol, 1 equiv.) was added to the solution at room temperature under argon. The reactive medium was stirred at room temperature under stirring (250 rpm) and followed by ^{1}H NMR. After 43h30, the reaction mixture was poured in brine (100 mL) and extracted with non-stabilized THF (3 x 150 mL). The organic layer was washed with brine (4 x 150 mL), saturated $NaHCO_3$ (up to pH = 8), dried over $MgSO_4$ and condensed in a rotary evaporator, to yield the crude product, which was further recrystallized in ethanol, then dried *in vacuo* to give the product as an off-white solid (1.10 g, 76% yield). ^{1}H NMR (THF-d_8, 400 MHz, 300 K): δ (ppm) = 10.85 (s, 0.50H), 8.84 (s, 2.50H), 7.51 (d, J = 8.4 Hz, 6H), 6.94 (d, J = 8.5 Hz, 6H), 2.28 (t, J = 7.4 Hz, 6H), 1.70 (q, J = 7.0 Hz, 6H), 1.35 (m, 48H), 0.93 (t, J = 6.5 Hz, 9H). FT–IR (ATR, cm^{-1}): 817 (m), 1272 (m), 1316 (m), 1406 (m), 1467 (m), 1508 (s), 1600 (m), 1655 (s), 2851 (m), 2921 (m), 3293 (m).

VI. 3. 2. Synthesis of TATA-C13

n-Tridecanoic acid (1.672 g, 7.803 mmol, 4.5 equiv.), EDC·HCl (1.496 g, 7.803 mmol, 4.5 equiv.) and DMAP (996 mg, 8.150 mmol, 4.7 equiv.) were dissolved inside a round-bottom flask in 75 mL of anhydrous *N*,*N*-dimethylformamide at room temperature under argon. 10 minutes after, tris(4-aminophenyl)amine (504 mg, 1.734 mmol, 1 equiv.) was added to the solution at room temperature under argon. The reactive medium was stirred at room temperature

under stirring (250 rpm) and followed by ^{1}H NMR. After 42h, the reaction mixture was poured in brine (100 mL) and extracted with non-stabilized THF (3 x 150 mL). The organic layer was washed with brine (4 x 150 mL), saturated $NaHCO_3$ (up to pH = 8), dried over $MgSO_4$ and condensed in a rotary evaporator, to yield the crude product, which was further recrystallized in ethanol and ethyl acetate, then dried in vacuo to give the product as an off-white solid (1.22 g, 80% yield). ^{1}H NMR (THF-d_8, 400 MHz, 300 K): δ (ppm) = 10.82 (s, 0.25H), 8.81 (s, 2.75H), 7.47 (dd, J = 9.0, 3.0 Hz, 6H), 6.90 (dd, J = 8.9, 3.0 Hz, 6H), 2.24 (t, J = 7.4 Hz, 6H), 1.66 (q, J = 7.2 Hz, 6H), 1.31 (m, 54H), 0.89 (t, J = 7.0 Hz, 9H). ^{13}C{^{1}H} NMR (THF-d_8, 100 MHz, 300 K): δ (ppm) = 170.71, 144.03, 135.58, 124.47, 120.52, 37.50, 32.68, 30.44 (2), 30.41, 30.35, 30.29, 30.13, 30.12, 26.29, 23.37, 14.24. FT–IR (ATR, cm^{-1}): 519 (m), 721 (m), 818 (m), 1244 (m), 1269 (m), 1313 (m), 1404 (m), 1466 (m), 1504 (s), 1599 (m), 1655 (m), 2851 (m), 2920 (m), 3292 (m). HRMS (ESI, *m/z*): calculated for $C_{57}H_{90}N_4O_3Na$, $[M+Na]^+$: 901.6905, found: 901.6909. Elemental analysis: calculated for $C_{57}H_{90}N_4O_3$: C 77.85, H 10.32, N 6.37, found: C 76.36, H 10.89, N 6.24.

VI. 3. 3. Synthesis of TATA-C20 (inspired from Kim *et al.*[33])

n-Eicosanoic acid (2.442 g, 7.812 mmol, 4.5 equiv.) was dissolved in 120 mL of anhydrous *N*,*N*-dimethylformamide. Then EDC·HCl (1.498 g, 7.812 mmol, 4.5 equiv.) was added to the solution at 0°C under argon, followed by the dropwise addition of triethylamine (0.791 g, 7.812 mmol, 4.5 equiv.), and the reaction was stirred for 10 min at 0°C. HOBt (1.056 g, 7.812 mmol, 4.5 equiv.) was then added in one portion and the reaction was stirred for 10 min at 0°C. Finally, tris(4-aminophenyl)amine (504 mg, 1.736 mmol, 1 equiv.) was added at 0°C, and the red reactive medium was stirred at 60°C. After 43h, the reaction mixture was quenched with brine (100 mL) and extracted with diethyl ether (3 x 100 mL). The organic layer was washed with brine, HCl at 10% and $NaHCO_3$, dried over $MgSO_4$ and condensed *in vacuo* yielding the crude product, which was further recrystallized in ethanol and ethyl acetate and dried over vacuum to give the product as off-white solid (1.63 g, 80% yield). ^{1}H NMR (THF-d_8, 400 MHz, 300 K): δ (ppm) = 10.83 (s, 0.30H), 8.84 (s, 2.70H), 7.48 (d, J = 8.6 Hz, 6H), 6.90 (d, J = 8.0 Hz, 6H), 2.24 (t, J = 7.4 Hz, 6H), 1.66 (q, J = 7.0 Hz, 6H), 1.29 (m, 96H), 0.89 (t, J = 7.0 Hz, 9H). ^{13}C{^{1}H} NMR (THF-d_8, 100 MHz, 300 K): δ (ppm) = 170.73, 144.03, 135.59, 124.46, 120.52, 37.50, 32.68, 30.45 (m), 30.40, 30.36, 30.30, 30.14, 30.11, 26.30,

23.36, 14.24. FT–IR (ATR, cm^{-1}): 517 (m), 719 (m), 818 (m), 1244 (m), 1269 (m), 1315 (m), 1406 (m), 1466 (m), 1504 (s), 1601 (m), 1655 (m), 2851 (m), 2918 (m), 3286 (m). HRMS (ESI, *m/z*): calculated for $C_{78}H_{132}N_4O_3Na$, $[M+Na]^+$: 1196.0192, found: 1196.0194. Elemental analysis: calculated for $C_{78}H_{132}N_4O_3$: C 79.80, H 11.43, N 4.77, found: C 77.69, H 11.67, N 4.64.

VII. References

1 Y. Yasuda, Y. Takebe, M. Fukumoto, H. Inada and Y. Shirota, *Adv. Mater.*, 1996, **8**, 740–741.
2 Y. Yasuda, T. Kamiyama and Y. Shirota, *Electrochimica Acta*, 2000, **45**, 1537–1541.
3 M. Albrecht, I. Janser and R. Fröhlich, *Synthesis*, 2004, **2004**, 1977–1982.
4 B. Wu, F. Cui, Y. Lei, S. Li, N. de Sousa Amadeu, C. Janiak, Y.-J. Lin, L.-H. Weng, Y.-Y. Wang and X.-J. Yang, *Angew. Chem. Int. Ed.*, 2013, **52**, 5096–5100.
5 A. D'Urso, N. Marino, M. Gaeta, M. S. Rizzo, D. A. Cristaldi, M. E. Fragalà, S. Pappalardo, G. Gattuso, A. Notti, M. F. Parisi, I. Pisagatti and R. Purrello, *New J. Chem.*, 2017, **41**, 8078–8083.
6 B.-C. Tzeng, A. Chao, T. Selvam and T.-Y. Chang, *CrystEngComm*, 2013, **15**, 5337–5344.
7 G. Gattuso, G. Grasso, N. Marino, A. Notti, A. Pappalardo, S. Pappalardo and M. F. Parisi, *Eur. J. Org. Chem.*, 2011, **2011**, 5696–5703.
8 W.-S. Huang, S. Liu, W.-K. Li, D. L. Goldfarb, L. Vyklicky, M. Glodde, P. R. Varanasi, World Intellectual Property Organization, WO2011022221A2, 2011.
9 N. Mohmeyer, B. Müller, N. Behrendt, J. Hillenbrand, M. Klaiber, X. Zhang, P. Smith, V. Altstädt, G. M. Sessler and H.-W. Schmidt, *Polymer*, 2004, **45**, 6655–6663.
10 J. J. Armao, M. Maaloum, T. Ellis, G. Fuks, M. Rawiso, E. Moulin and N. Giuseppone, *J. Am. Chem. Soc.*, 2014, **136**, 11382–11388.
11 E. Busseron, Y. Ruff, E. Moulin and N. Giuseppone, *Nanoscale*, 2013, **5**, 7098–7140.
12 E. Moulin, J. J. Armao and N. Giuseppone, *Acc. Chem. Res.*, 2019, **52**, 975–983.
13 E. Moulin, F. Niess, M. Maaloum, E. Buhler, I. Nyrkova and N. Giuseppone, *Angew. Chem. Int. Ed.*, 2010, **49**, 6974–6978.
14 E. Moulin, F. Niess, G. Fuks, N. Jouault, E. Buhler and N. Giuseppone, *Nanoscale*, 2012, **4**, 6748–6751.
15 V. Faramarzi, F. Niess, E. Moulin, M. Maaloum, J.-F. Dayen, J.-B. Beaufrand, S. Zanettini, B. Doudin and N. Giuseppone, *Nat. Chem.*, 2012, **4**, 485–490.
16 T. Liang, D. Collin, M. Galerne, G. Fuks, A. V. Jentzsch, M. Maaloum, A. Carvalho, N. Giuseppone and E. Moulin, *Chem. – Eur. J.*, 2019, **25**, 14341–14348.
17 T. Kim, T. Mori, T. Aida and D. Miyajima, *Chem Sci*, 2016, **7**, 6689–6694.
18 H. Seo, M. Go, H. Choi, K. Y. Kim, Y. Choi, S. S. Lee, S. H. Jung and J. H. Jung, *Chem. – Asian J.*, 2018, **13**, 2847–2853.
19 K. Y. Kim, C. Kim, Y. Choi, S. H. Jung, J. H. Kim and J. H. Jung, *Chem. - Eur. J.*, 2018, **24**, 11763–11770.
20 X. Cao, A. Gao, D. Liu, N. Zhao, Q. Ding and Y. Li, *Supramol. Chem.*, 2018, **30**, 674–680.

21 M. Go, H. Choi, K. Y. Kim, C. J. Moon, Y. Choi, H. Miyake, S. S. Lee, S. H. Jung, M. Y. Choi and J. H. Jung, *Org. Chem. Front.*, 2019, **6**, 1100–1108.
22 B. Adelizzi, I. A. W. Filot, A. R. A. Palmans and E. W. Meijer, *Chem. - Eur. J.*, 2017, **23**, 6103–6110.
23 B. Adelizzi, A. Aloi, A. J. Markvoort, H. M. M. Ten Eikelder, I. K. Voets, A. R. A. Palmans and E. W. Meijer, *J. Am. Chem. Soc.*, 2018, **140**, 7168–7175.
24 N. J. Van Zee, B. Adelizzi, M. F. J. Mabesoone, X. Meng, A. Aloi, R. H. Zha, M. Lutz, I. A. W. Filot, A. R. A. Palmans and E. W. Meijer, *Nature*, 2018, **558**, 100–103.
25 B. Adelizzi, A. Aloi, N. J. Van Zee, A. R. A. Palmans, E. W. Meijer and I. K. Voets, *ACS Nano*, 2018, **12**, 4431–4439.
26 A. Osypenko, E. Moulin, O. Gavat, G. Fuks, M. Maaloum, M. A. J. Koenis, W. J. Buma and N. Giuseppone, *Chem. – Eur. J.*, 2019, **25**, 13008–13016.
27 M. A. J. Koenis, A. Osypenko, G. Fuks, N. Giuseppone, V. P. Nicu, L. Visscher and W. J. Buma, *J. Am. Chem. Soc.*, , DOI:10.1021/jacs.9b11306.
28 J. J. Armao, I. Nyrkova, G. Fuks, A. Osypenko, M. Maaloum, E. Moulin, R. Arenal, O. Gavat, A. Semenov and N. Giuseppone, *J. Am. Chem. Soc.*, 2017, **139**, 2345–2350.
29 S. Akahane, T. Takeda, N. Hoshino and T. Akutagawa, *Cryst. Growth Des.*, 2018, **18**, 6284–6292.
30 B. Kiflemariam, D. Collin, O. Gavat, A. Carvalho, E. Moulin, N. Giuseppone and J.-M. Guenet, *Polymer*, 2020, **207**, 122814.
31 F. Zhang, F. Yang, Y. Gong, Y. Wei, Y. Yang, J. Wei, Z. Yang and M.-P. Pileni, *Small*, 2020, **16**, 2005701.
32 T. F. A. De Greef, M. M. J. Smulders, M. Wolffs, A. P. H. J. Schenning, R. P. Sijbesma and E. W. Meijer, *Chem. Rev.*, 2009, **109**, 5687–5754.
33 J. Kim, J. Lee, W. Y. Kim, H. Kim, S. Lee, H. C. Lee, Y. S. Lee, M. Seo and S. Y. Kim, *Nat. Commun.*, 2015, **6**, 6959.
34 M. Raynal, F. Portier, P. W. van Leeuwen and L. Bouteiller, *J. Am. Chem. Soc.*, 2013, **135**, 17687–17690.
35 L. A. Carpino, *J. Am. Chem. Soc.*, 1993, **115**, 4397–4398.
36 C. A. G. N. Montalbetti and V. Falque, *Tetrahedron*, 2005, **61**, 10827–10852.
37 A. El-Faham and F. Albericio, *Chem. Rev.*, 2011, **111**, 6557–6602.
38 M. Sumimoto, D. Yokogawa, M. Komeda, H. Yamamoto, K. Hori and H. Fujimoto, *Spectrochim. Acta. A. Mol. Biomol. Spectrosc.*, 2011, **81**, 653–660.
39 F. S. Parker, in *Applications of Infrared Spectroscopy in Biochemistry, Biology, and Medicine*, Springer US, Boston, MA, 1971, pp. 165–172.
40 D. Lin-Vien, N. B. Colthup, W. G. Fateley and J. G. Grasselli, in *The Handbook of Infrared and Raman Characteristic Frequencies of Organic Molecules*, eds. D. Lin-Vien, N. B. Colthup, W. G. Fateley and J. G. Grasselli, Academic Press, San Diego, 1991, pp. 155–178.
41 D. Lin-Vien, N. B. Colthup, W. G. Fateley and J. G. Grasselli, in *The Handbook of Infrared and Raman Characteristic Frequencies of Organic Molecules*, eds. D. Lin-Vien, N. B. Colthup, W. G. Fateley and J. G. Grasselli, Academic Press, San Diego, 1991, pp. 117–154.
42 K. Shizu, T. Sato, K. Tanaka and H. Kaji, *Chem. Phys. Lett.*, 2010, **486**, 130–136.
43 M. U. Munshi, G. Berden, J. Martens and J. Oomens, *Phys. Chem. Chem. Phys.*, 2017, **19**, 19881–19889.
44 C. G. Cannon, *Spectrochim. Acta*, 1960, **16**, 302–319.
45 P. Wu and H. W. Siesler, *J. Infrared Spectrosc.*, 1999, **7**, 65–76.

46 Y. Domoto, E. Busseron, M. Maaloum, E. Moulin and N. Giuseppone, *Chem. – Eur. J.*, 2015, **21**, 1938–1948.
47 E. Busseron, J.-J. Cid, A. Wolf, G. Du, E. Moulin, G. Fuks, M. Maaloum, P. Polavarapu, A. Ruff, A.-K. Saur, S. Ludwigs and N. Giuseppone, *ACS Nano*, 2015, **9**, 2760–2772.
48 C. Lambert and G. Nöll, *J. Am. Chem. Soc.*, 1999, **121**, 8434–8442.
49 S. Yeh, *Electrochem. Commun.*, 2003, **5**, 373–377.
50 T.-F. Yang, K. Y. Chiu, H.-C. Cheng, Y. W. Lee, M. Y. Kuo and Y. O. Su, *J. Org. Chem.*, 2012, **77**, 8627–8633.
51 K. Lancaster, S. A. Odom, S. C. Jones, S. Thayumanavan, S. R. Marder, J.-L. Brédas, V. Coropceanu and S. Barlow, *J. Am. Chem. Soc.*, 2009, **131**, 1717–1723.
52 I. Nyrkova, E. Moulin, J. J. Armao, M. Maaloum, B. Heinrich, M. Rawiso, F. Niess, J.-J. Cid, N. Jouault, E. Buhler, A. N. Semenov and N. Giuseppone, *ACS Nano*, 2014, **8**, 10111–10124.
53 A. T. Haedler, S. R. Beyer, N. Hammer, R. Hildner, M. Kivala, J. Köhler and H.-W. Schmidt, *Chem. - Eur. J.*, 2014, **20**, 11708–11718.
54 S. Amthor, B. Noller and C. Lambert, *Chem. Phys.*, 2005, **316**, 141–152.
55 M. M. Roessler and E. Salvadori, *Chem. Soc. Rev.*, 2018, **47**, 2534–2553.
56 A. Maroz, R. Hermann, S. Naumov and O. Brede, *J. Phys. Chem. A*, 2005, **109**, 4690–4696.
57 H. H. Richtol, E. A. Fitzgerald and P. Wuelfing, *J. Phys. Chem.*, 1971, **75**, 2737–2741.
58 O. Brede and S. Naumov, *Chem. Soc. Rev.*, 2010, **39**, 3057–3071.
59 R. Reynolds, L. L. Line and R. F. Nelson, *J. Am. Chem. Soc.*, 1974, **96**, 1087–1092.
60 S. Stoll and A. Schweiger, *J. Magn. Reson.*, 2006, **178**, 42–55.

Chapter IV Self-association properties of TATA-SDA and effects of CPL

Abstract

In this chapter, a triarylamine trisamide monomer, **TATA-SDA**, featuring three diacetylene side chains was synthesized and its association properties probed in presence and absence of CPL. Both **TATA-SDA** (this Chapter) and **TATA-C13** (Chapter III) feature a C12 aliphatic side chain which only differs by presence and absence of unsaturation, respectively. Accordingly, when possible, a qualitative comparison between the assembly-properties of these two monomers will be given. The self-association properties of **TATA-SDA** were investigated in toluene and chlorinated solvents (DCE and $CHCl_3$) as well as in bulk (powder/film) by a variety of techniques: SANS, UV–Vis–NIR, FT–IR and CD spectroscopy. The nature of self-assemblies formed by **TATA-SDA** drastically depends on the conditions. In toluene, **TATA-SDA** molecules stack into long one-dimensional self-assemblies, built upon well-defined hydrogen bonds. In 1,2-dichloroethane and chloroform, **TATA-SDA** molecules self-assemble into different structures depending on the conditions (concentration, temperature, time). Two assemblies have been identified: non-specific aggregates mainly devoid of H-bonding interactions; and hydrogen-bonded (HB) stacks. Thin films were also prepared and were found to consist mainly of HB stacks of **TATA-SDA**. The impact of CPL irradiation was then investigated in all these states (2.3 mM at room temperature or with variable temperature, at 11.7 mM and in the solid state as thin film), especially by determining the production of **TATA-SDA**$^{\bullet+}$ species and their impact on self-assemblies. It was actually found that these species have little influence on the nature of self-assemblies both present in solution and film, and conditions of co-assembly with neutral species were probed. Finally, CD measurements were carried out in CPL-illuminated DCE solutions of **TATA-SDA** in order to track the possibility of generating **TATA-SDA** helical assemblies with a preferred handedness, dictated by the rotational direction of CPL. Our studies faced the challenges of measuring the true CD signature of highly (possibly orientated) aggregated systems. Even so, we can rule out the possibility of using CPL to direct

the handedness of **TATA-SDA** assemblies in the conditions stated in the literature (2.3 mM in DCE)[1].

I. Introduction

The main objective of this thesis was to use TATA helical assemblies, whose handedness is controlled by the rotational direction of CPL light, as a scaffold for asymmetric catalysis. The preliminary investigation, with TATA of saturated side chains, allowed to gain knowledge about the TATA self-association properties, as well as their behavior under light irradiation (Chapter III). Next, the bridge to catalysis was either the incorporation of TATA ligands into CPL-oriented stacks of TATAs, or by directly irradiating TATA ligands by CPL. The former option appears at first sight more feasible since Kim *et al*. reported in 2015 the possibility of controlling the handedness of TATA assemblies by CPL[1].

To achieve this challenging goal, Kim *et al.* employed a TATA monomer featuring diacetylene side chains (named **TATA-SDA**), selected to exploit: the light-triggering self-assembly of TATA molecules described by Giuseppone *et al.*[2], assuming by Kim *et al.*[1] to amplify the chiral bias induced by CPL irradiation at the monomer level upon stacking into hydrogen-bonded helices; whilst the diacetylene side chains helped to lock the resulting supramolecular chirality by topochemical photopolymerization. **TATA-SDA** solutions at 2.3 mM in 1,2-dichloroetane (DCE) were irradiated "with a hand-held lamp having 400–600 nm range of wavelength and 450 nm of maximum intensity with power of 1.5W at rt", then analyzed by circular dichroism (CD) spectroscopy at -10°C, to reveal the biased supramolecular chirality of helical assemblies.

DCE was likely chosen instead of $CHCl_3$, used by Giuseppone *et al.* with similar TATAs[2], because of its lower polarity, probably promoting the self-assembly of **TATA-SDA**. Curiously, the impact of the temperature for irradiation (20°C) and spectroscopic measurements (-10°C) as well as the initial structure of the irradiated assemblies were not discussed by the authors, although we found in the previous chapter that the assembly properties of **TATA-C12** and **TATA-C13**, two structurally analogues of **TATA-SDA**, are clearly affected by these two parameters. Additionally, triarylammonium radicals formed upon light irradiation are claimed

to trigger the assembly of **TATA-SDA** by means of well-defined aromatic and H-bonding interactions but the presence of the latter was not characterized in the conditions of CD analyses. Moreover, it remains to be determined what mechanism at the origin of the chiral induction is at work in this system. On one hand, the chiral bias that could be transferred to neutral monomers by photoresolution was possibly short-lived, since the energetic barrier for interconversion between the two mirror-like forms is likely weak (calculated at 4.8 kcal/mol for the triphenylamine[3]). On the other hand, it is reported that the handedness of the helical assemblies can be switched reversibly without going through the monomer state[1].

Therefore, the aim of this chapter was first to perform in-depth analyses of the system reported by Kim *et al.*[1] For this purpose, this chapter will present the synthesis of **TATA-SDA** and its full characterization. A first assessment of **TATA-SDA** in solution will identify advantages and drawbacks of this molecule, as well as give hints about its solubility and self-assembly capacities. The **TATA-SDA** self-association properties will then be explored in toluene and chlorinated solvents, especially by the help of UV–Vis–NIR and FT–IR absorption spectroscopies, as well as by SANS analyses. In particular in DCE and chloroform, the **TATA-SDA** molecules will be studied under different conditions (concentration, temperature, time) to evaluate the importance of these parameters on the nature of self-assemblies formed by **TATA-SDA**. Next, the impact of light on self-association will be specifically studied for **TATA-SDA**. When possible, a qualitative comparison between the assembly-properties of **TATA-SDA** (this chapter, DCE) and **TATA-C13** (Chapter III, $CHCl_3$) will be given. The difficulties encountered during CD measurements will be stressed out. Finally, the possibility of controlling the handedness of **TATA-SDA** assemblies by CPL will be probed under a large range of conditions.

II. Synthesis and Characterization of TATA-SDA

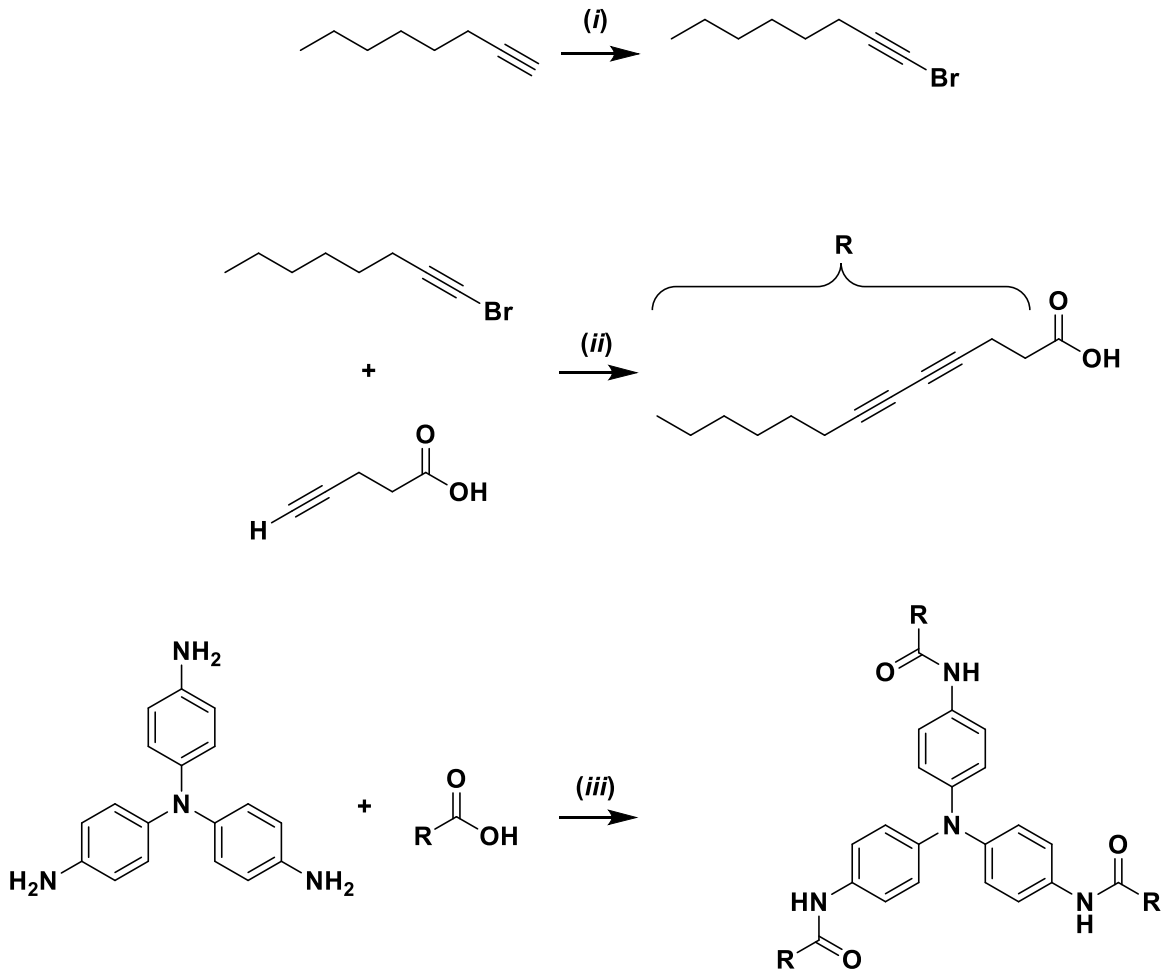

Figure IV.1 Synthesis of **TATA-SDA**. (*i*) N-bromosuccinimide/acetone/$AgNO_3$ (84%<yield <100%), (*ii*) CuCl/*n*-$BuNH_2$/NH_2OH·HCl (71%<yield<100%) and (*iii*) DMAP/EDC·HCl/THF (20%<yield<40%).

The synthesis of **TATA-SDA** has been achieved in three steps: the bromination of 1-octyne, a Cadiot–Chodkiewicz coupling of the resulting bromoalkyne with 4-pentynoic acid and the amide bond forming reaction between the corresponding straight diacetylenic acid, and commercial tris(4-aminophenyl)amine (**Figure III.2**). The first two steps were adapted from

the literature[5,6]. After recrystallization in a mixture of ethanol and heptane[XXXII], hundreds of milligrams of **TATA-SDA** were obtained as an amorphous reddish solid, as reported by Kim *et al.*[1] **TATA-SDA** was fully characterized by ^{1}H, ^{13}C and bidimensional NMR studies (**Figure SIV.39** to **Figure SIV.43**), as well as by IR spectroscopy, high-resolution mass spectrometry (HRMS) and MALDI-TOF (**Figure SIV.44**) analyses. Seven batches (I–VII) of **TATA-SDA** have been produced following the same procedure and they all show sufficient and equal purity (as probed by ^{1}H NMR, **Figure IV.2**). The purity of batch VI was also confirmed by elementary analysis.

[XXXII] Although Kim *et al.* only reported a recrystallization in ethanol[1], heptane was found to reduce the solubility of **TATA-SDA** at rt, improving the yield.

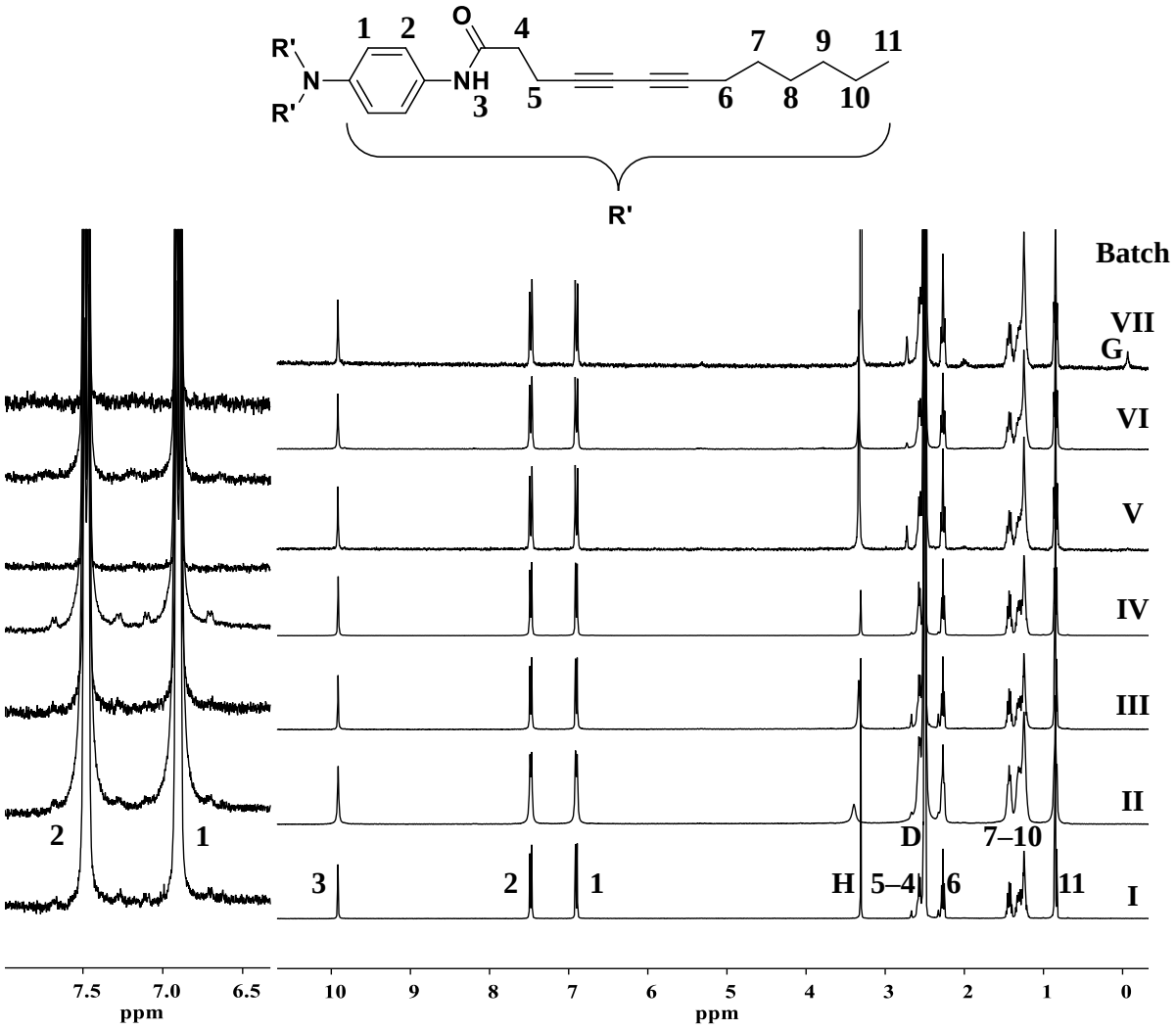

Figure IV.2 ^{1}H NMR analysis in DMSO-d_6 of all batches of **TATA-SDA** used in this study, accompanied by a zoom on the region of aromatic resonance peaks (H, D and G are resonance peaks for residual water, DMSO and silicone grease, respectively).

Dissolution of **TATA-SDA** in DMSO or 1,2-dichloroethane at room temperature yields an initially red colored solution, which undergoes precipitation over a few hours (**Figure SIV.45**). Filtration over 0.20 µm with PTFE filters allowed to recover a yellowish liquid (typical color of TATA solutions)[1,2], the red particles being ascribed by Raman and UV–Vis spectroscopies to polydiacetylene (**Figure IV.3**). Both the solution before filtration and the precipitate showed signals which are a hallmark of polydiacetylene (PDA)[7–13], *i.e.* the C≡C and C=C stretching vibrations at 2120 cm^{-1} and 1520 cm^{-1} (Raman), as well as an absorption band with maximum intensity at 540 nm (UV–Vis, **Figure IV.4**). The amount of PDA in the as-

synthesized seven batches of **TATA-SDA** was very low, as demonstrated by the unchanged absorption of main UV–Vis signals after filtration and the consistency of the aforementioned set of analyses. However, in order to limit its potential influence on the assembly process and generation of radicals, the amount of PDA in the samples was maintained as low as possible by performing filtration or additional recrystallization.

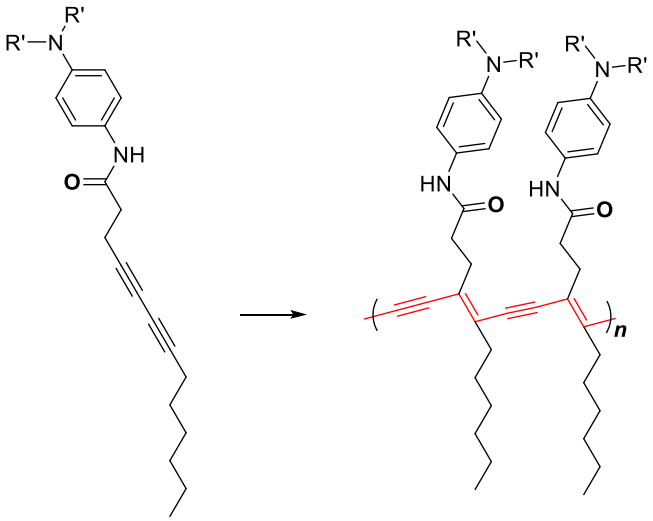

Figure IV.3 Schematic representation of the formation of polydiacetylene from **TATA-SDA**.

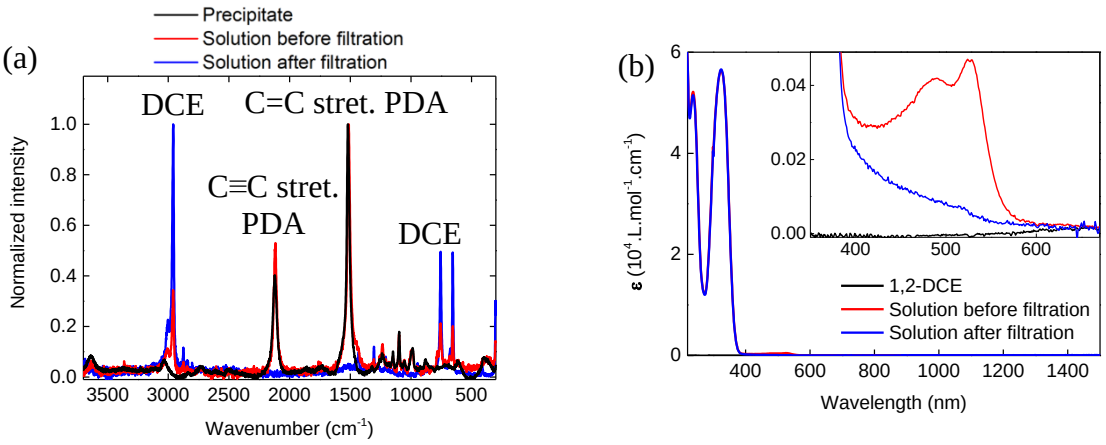

Figure IV.4 TATA-SDA solutions in DCE before and after filtration over 0.2 µm PTFE filter. (a) Raman spectra of **TATA-SDA** as solid and in solution at 2.3 mM in DCE. (b) UV–Vis–NIR spectra of DCE and of **TATA-SDA** at 2.3 mM in DCE. Characteristic C≡C and C=C stretching vibrations, or red-type absorption bands of polydiacetylene, with maximum intensity at about 2120 cm^{-1}, 1520 cm^{-1} and 540 nm, respectively, disappear after filtration (blue lines).

III. Self-association properties without CPL

III. 1. Solubility tests

Solubility tests at 1 mM in solvents of various polarities allow to showcase the influence of diacetylenic units of **TATA-SDA** (**Table IV.1**). Compared with **TATA-C13**, **TATA-SDA** showed a better solubility in toluene and chlorinated solvents, such as DCM and 1,2-dichloroethane, key solvents to trigger its photooxidation. The insolubility of **TATA-SDA** in alkanes, such as methylcyclohexane and decalin, is also an advantage for its purification. Finally, the increase of viscosity observed for **TATA-SDA** in toluene likely reflects the presence of very long assemblies (III. 2).

Table IV.1 Solubility of **TATA-C13** and **TATA-SDA** (1 mM) after heating up to the boiling point. I = insoluble, P = precipitation, S = soluble, η ↑ = viscosity increases.

Solvent	TATA-C13	TATA-SDA
Methylcyclohexane	I (η↑)	I
Decalin	I	I
Toluene	P (η↑)	S (η↑)
Trifluorotoluene	I	I
DCM	P (η↑)	S
$CHCl_3$	S	S
DCE	P (η↑)	S
MeOH	I	S
EtOH	S	S
Et_2O	I	I
THF	S	S
1,4-Dioxane	S	S
Acetone	I	S
Ethyl acetate	S	S
Acetonitrile	I	S
DMSO	S	S
DMF	S	S

III. 2. In Toluene

TATA-SDA at 5.8 mM in toluene forms a strong gel (*i.e.* it does not flow immediately when the vial is turned). FT–IR analysis revealed absorption bands at 3290 and 1660 cm^{-1} (**Figure IV.5**), corresponding to the stretching vibrations of N-H and C=O groups involved in hydrogen bonding[14,15]. The symmetry of signals likely documents one type of intermolecular hydrogen bonds, and the fact that free N-H/C=O absorption bands (at about 3410 and 1690 cm^{-1}, respectively) are barely detected points out that most of molecules are associated. This FT–IR result is in accordance with computed DFT models of TATA helical stacks for which TATA monomers are connected by means of a threefold hydrogen bond network (**Figure IV.6**)[1,2,16], like **TATA-C12** and **TATA-C13** molecules investigated in the previous chapter.

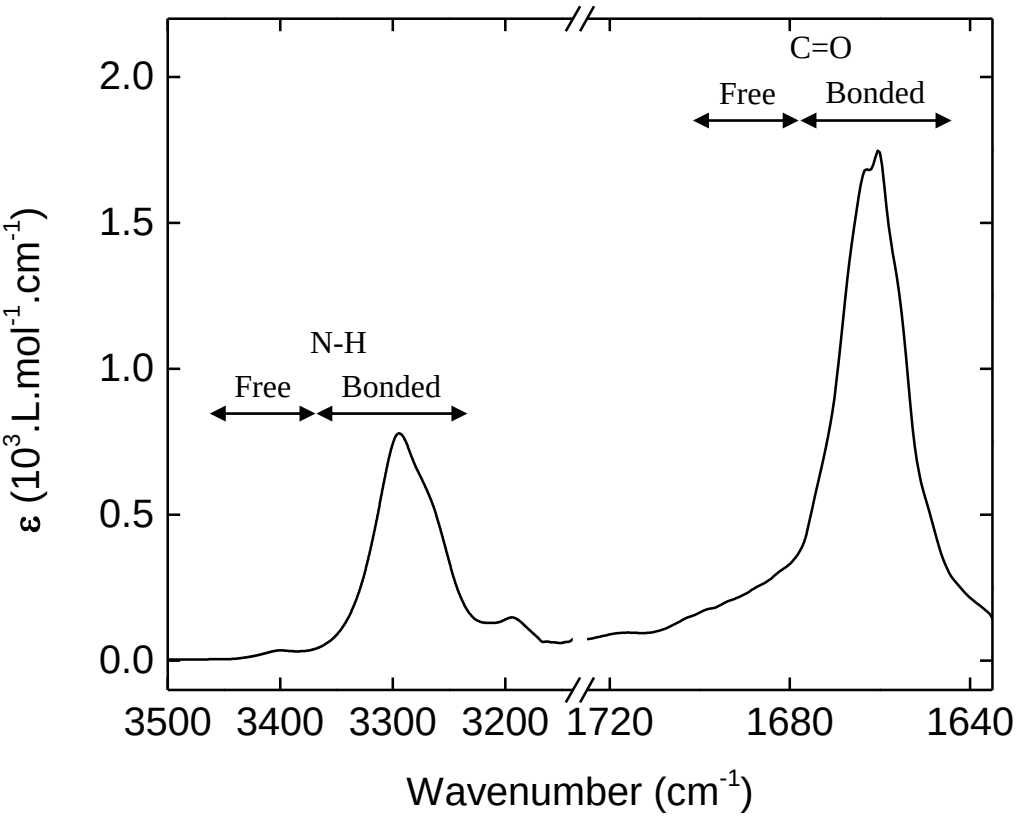

Figure IV.5 FT–IR analysis of **TATA-SDA** at 5.8 mM in toluene at 20°C. Zoom on the N-H and C=O regions.

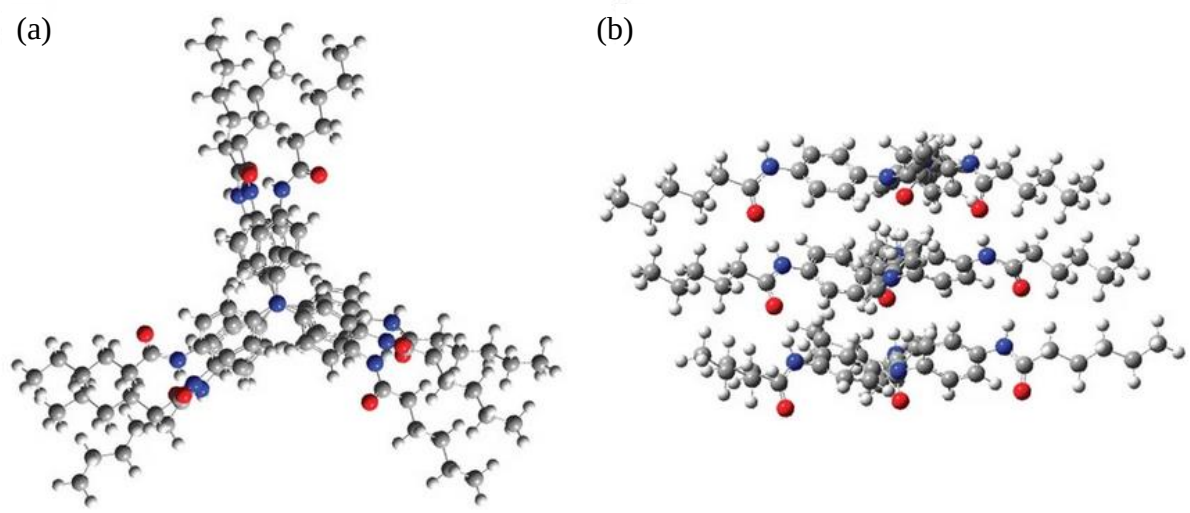

Figure IV.6 (a) Top and (b) side views of the self-assembled structure of a **TATA-SDA** model, with *n*-pentyl groups as side chains, calculated by density function theory method (DFT) by Kim *et al.*[1]

SANS analyses of **TATA-SDA** at 1.8, 3.5 and 7.0 mM in toluene-d_8 confirm the presence of rigid cylinders at all concentrations, as shown by the q^{-1} dependence of the scattered intensity at low q values (**Figure IV.7**). This dependence is maintained down to the lowest measured q values, meaning that much of **TATA-SDA** assemblies were longer than 350 Å (*i.e.* more than 80 molecules by assuming distance between stacked TPA moieties of 4.2 Å). The geometrical radius (r) and the number of molecules (n) in the cross-section of columnar stacks were deduced from the fit of curves with a form factor for rigid rods with a circular cross-section and a uniform scattering length density (**Figure IV.7**). Interestingly both r and n values increase with the concentration reaching up to 28 Å and 3.3 molecules, respectively, at 7.0 mM. This establishes the propensity of single rows of **TATA-SDA** molecules to bundle into larger and larger fibers, which appears to be a common feature of TATA molecules (*cf.* the ribbons of **TATA-C13** fibrillar aggregates at 11.4 mM in $CHCl_3$ described in Chapter III, as well as the litterature[2,17]).

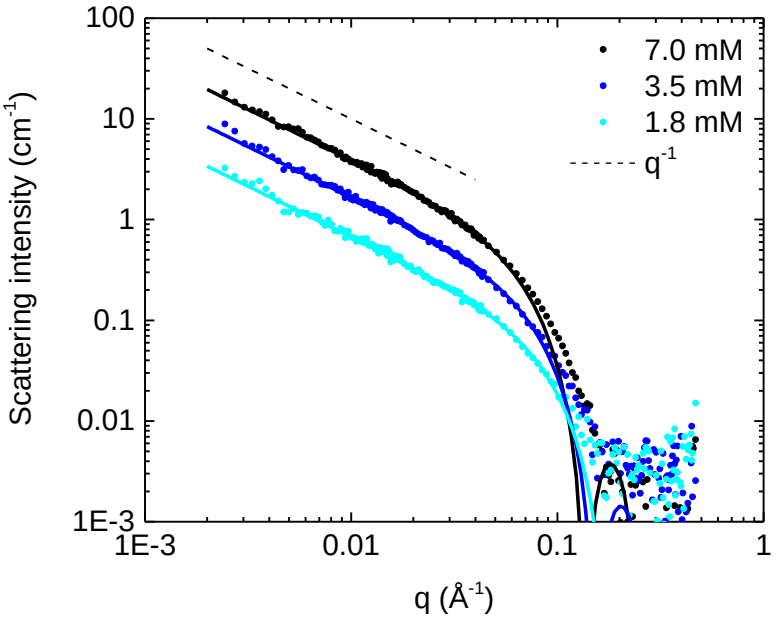

C (mM)	n	r (Å)
7.0	3.3	28
3.5	2.8	25
1.8	2.4	22

Figure IV.7 Left: SANS curves with corresponding fits for solutions in toluene-d_8 of **TATA-SDA** at 20°C and different concentrations. Right: data deduced from the fit, C = concentration, n = number of molecules in the cross-section and r = geometrical radius.

FT–IR and SANS analyses of **TATA-SDA** in toluene substantiated the formation of long one-dimensional self-assemblies, built upon well-defined hydrogen bond interactions between molecules.

III. 3. In 1,2-dichloroethane

The observation of hydrogen-bonded assemblies in toluene prompted us to investigate the self-association properties of **TATA-SDA** in chlorinated solvents, and particularly in 1,2-dichloroethane, since this is the solvent employed by Kim *et al.* to induce chirality with CPL[1]. Chloroform was also investigated as photo-oxidation of TATA in this solvent is more facile, due to its high oxidizing ability[16]. The nature and stability of the self-assemblies were probed under different conditions as discussed below. When possible, spectroscopic and scattering experiments were conducted under close conditions, *i.e.* the time of analyses after dissolution were adapted in order to be similar. The influence of time on the nature of assemblies was

carefully probed to first assess whether assemblies are under thermodynamic state and to be consistent with the fact that, for technical reasons, SANS analyses have been performed several hours after dissolution.

III. 3. 1. At 2.3 mM and room temperature

The first condition explored in 1,2-dichloroethane mimicked the one employed by Kim *et al.*[1]. After dissolution, the UV–Vis profile showed a main absorption band with a maximum at about 325 nm, and a less intense one at 235 nm, attributed to mixed $n \rightarrow \pi^*$ and $\pi \rightarrow \pi^*$ electronic transitions of the triarylamine core[18]. FT–IR spectroscopy highlighted signals at 3410 cm^{-1} and 1690 cm^{-1}, corresponding to the free N-H/C=O stretching vibrations signals, respectively (**Figure IV.8**)[14,15]. This result indicates that **TATA-SDA** molecules at 2.3 mM are not stacked just after dissolution. Eight hours (as SANS measurements) and 28 h after dissolution, the UV–Vis–NIR and FT–IR profiles remained the same, attesting the stability of the solution within this timescale and suggesting that **TATA-SDA**, in DCE at 2.3 mM and room temperature, does not form hydrogen-bonded assemblies.

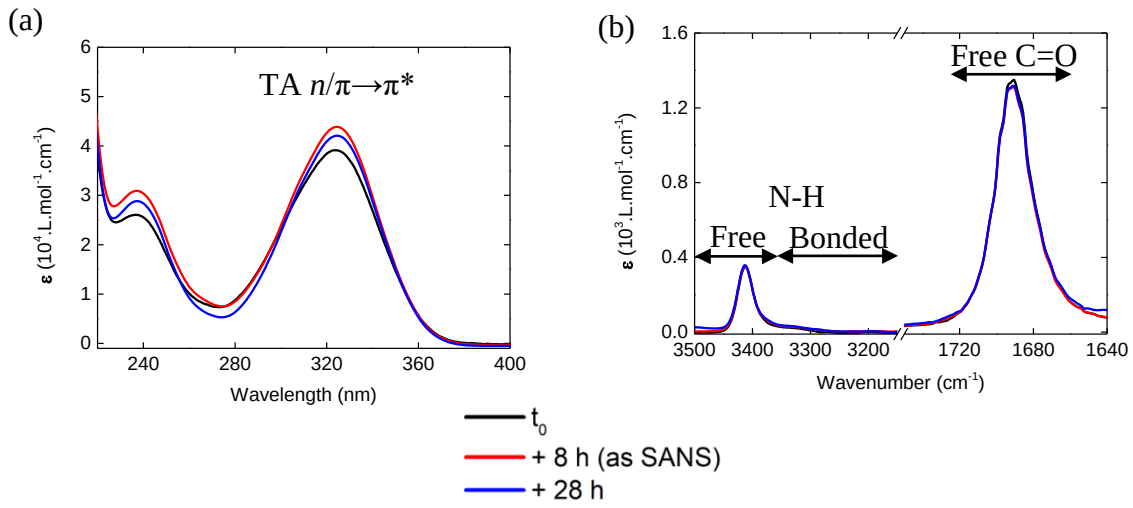

Figure IV.8 TATA-SDA at 2.3 mM in DCE[XXXIII]. (a) UV–Vis absorption and (b) FT–IR spectra with a zoom on the N-H and C=O regions.

[XXXIII] The variation of intensity between measurements in (a) came from a little difference of liquid thickness across the optical pathlength, due to the change of lamellar quartz cells of slightly different pathlengths. Anyway,

SANS technique gave additional information on the behavior of **TATA-SDA** in DCE, at 2.3 mM and room temperature. The shape of the scattering intensity, is inconsistent with a solution exclusively composed of monomers and dimers, but does not show a clear dependence with the wave vector q. This means that the solution contained a significant fraction of non-specific aggregates of unknown shape or length, in a similar fashion to what was observed with **TATA-C13** solutions at the same concentration.

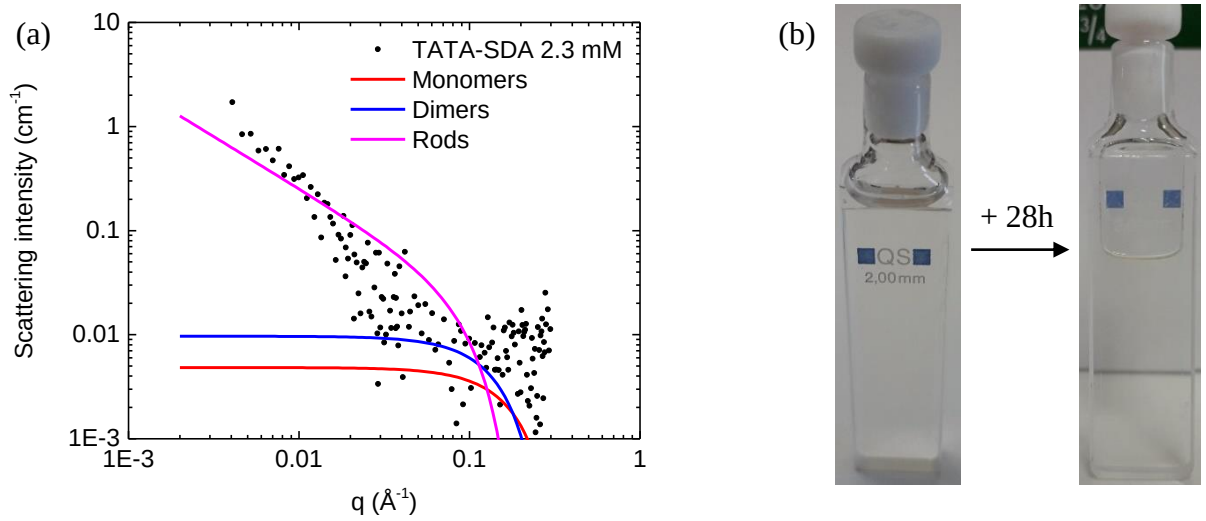

Figure IV.9 (a) SANS analysis of **TATA-SDA** at 2.3 mM in DCE-d_4. Simulated spectra for monomers, dimers or infinitely long rigid rods of circular cross-section are shown together with the experimental spectrum. (b) Pictures of **TATA-SDA** at 2.3 mM in DCE-d_4 after dissolution then after SANS measurements (t_0 + 28h). Solution before ageing was not used for SANS, hence its volume is slightly different.

Combined UV–Vis, FT–IR and SANS measurements evidenced that in DCE at 2.3 mM and at room temperature, **TATA-SDA** is mainly under the form of non-specific aggregates devoid of well-defined H-bonding and of unknown shape or length. Unlike **TATA-C13**, no significant formation of long assemblies of **TATA-SDA** occurs with time. This statement is in

---

the ratio of molar extinction coefficient between the signals at about 325 and 240 nm are the same, ruling out photo-oxidation or assembly processes.

accordance with the visual observation of the yellowish solution, remaining transparent, homogeneous and fluid after 28 hours (**Figure IV.9b**), while **TATA-C13** solutions forms an insoluble gel in the meantime. Analogous analyses in chloroform gave virtually identical results (**Figure SIV.46** to **Figure SIV.48**). In this condition, the diacetylenic units seems to favor the formation of non-specific aggregates.

III. 3. 2. At 2.3 mM and various temperatures

Next we probed the aggregation properties of **TATA-SDA** in chlorinated solvents (2.3 mM) at lower temperatures, since CD measurements of CPL-irradiated solutions were reported at -10°C by Kim *et al.*[1], and because the previous chapter demonstrated the relevance of cooling to trigger the self-assembly into hydrogen-bonded stacks. Variable-temperature (VT) analyses of **TATA-SDA** in DCE at 2.3 mM were carried out by UV–Vis and FT–IR spectroscopy. A first set of analyses was conducted upon heating a cooled solution. Upon heating from -17°C, **TATA-SDA** molecules are predominantly associated up to -10°C by hydrogen bonds and π–π stacking, as shown by strong absorption bands at about 3290 cm^{-1} and 1660 cm^{-1}, and hypo/hypsochromic shifts of the major UV signal compared with the profile at 20°C ($\Delta\varepsilon \approx 1 \times 10^4$ $L.mol^{-1}.cm^{-1}$ and $\Delta\lambda = 5$ nm), respectively (**Figure IV.10a**, **b** and **c**). Hydrogen-bonded stacks thus formed upon cooling the aforementioned non-specific aggregates. These stacks are stable between -17 and -10°C with a degree of aggregation of ca. 0.7 (**Figure IV.10d**), which either means that these aggregates are short or exist as a mixture of long assemblies and monomers (*vide infra*). The plot of the degree of association versus the temperature (orange dots in **Figure IV.10d**) reveals that disassembly occurs in two steps: first gradually up to ca. 10°C then abruptly between 10°C and 20°C, range for which half of aggregates are disrupted. This two-step process is even more obvious from the monitoring of the absorbance of the main UV–Vis band (black dots in **Figure IV.10d**). By analogy with self-assemblies identified in toluene, two consecutive phenomena probably happened in DCE throughout this temperature range: the unbundling of fibrils accompanied and pursued by their disassembly, maybe following two different kinetics and mechanisms (referring to an isodesmic bundling and a cooperative assembly, as already outlined for the assembly of structurally related TATA monomers[17]).

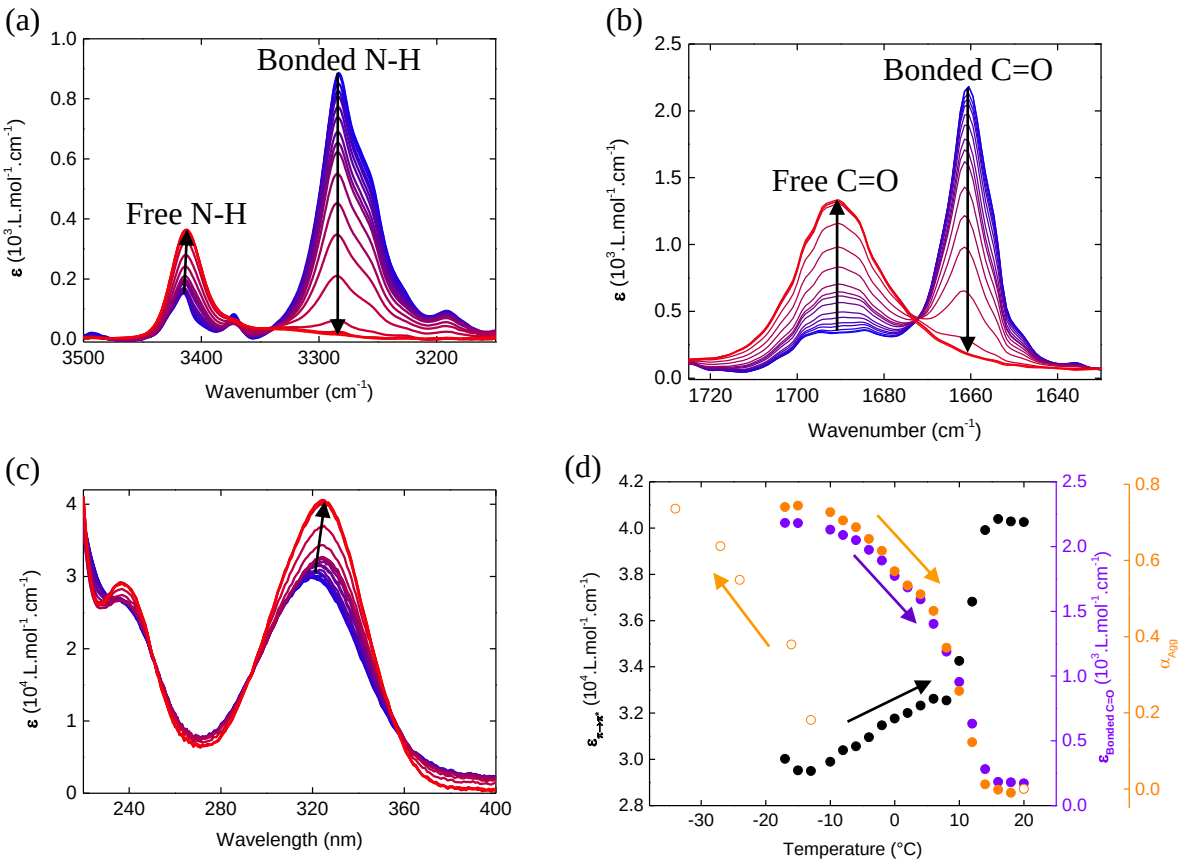

Figure IV.10 Temperature-dependent (a–b) FT–IR and (c) UV–Vis absorption spectra of **TATA-SDA** at 2.3 mM in DCE, recorded during a heating process between -17°C and 20°C for a rate of 0.4 and 0.2 °C/min, respectively. (d) Evolution of the absorption at 323 nm/1690 cm^{-1} and of the degree of aggregation as a function of the temperature, plotted from (c), (b) and another dataset upon cooling at a rate of 1.4°C/min. The degree of aggregation (α_{Agg}) is calculated from the evolution of the free C=O stretching (ν = 1690 cm^{-1}) vibration intensity as a function of the temperature.

FT–IR spectra were also recorded upon cooling a solution from 20°C to -34 °C (empty orange dot in **Figure IV.10d**). Interestingly, the formation of hydrogen-bonded stacks only starts below -10°C, although the disassembly upon heating happened at 10°C. The distinct evolution of the degree of aggregation upon cooling and heating, characterized by two different temperatures of elongation for assembly and disassembly processes, under cooling and heating, respectively, is the proof of a thermal hysteresis or the fact that the rates of heating/cooling were too fast to reach the thermodynamic state. Nevertheless, since hydrogen-bonded stacks

are formed upon cooling, these conditions appear highly suitable for the induction of chirality by CPL.

III. 3. 3. At 11.7 mM

The possibility of forming long helical hydrogen-boned stacks at room temperature was investigated by increasing the concentration. By analogy with **TATA-C12** and **TATA-C13** (Chapter III), a higher concentration of 11.7 mM was thus examined. The fist key point is to mention that even though hydrogen-bonded stacks are present at this concentration (as shown by UV–Vis and FT–IR analyses), the degree of association is relatively low ($\alpha_{Agg} \approx 0.21$ after dissolution, **Figure IV.12**) comparatively to what was observed for **TATA-C12** solutions in $CHCl_3$ at similar concentrations ($\alpha_{Agg} \approx 0.63$). Secondly, a slow but significant evolution of the assemblies is observed with time. Indeed, UV–Visible analyses recorded at different intervals of time after dissolution showed marked hypo- and hypso-chromic shifts of the major absorption band over 2.5 days, implying that molecules interact more and more by π–π stacking (**Figure IV.11**). UV–Vis and FT–IR data performed over the course of 24 h confirm this assessment (**Figure IV.12**). These analyses highlight a slow and modest self-assembly during the first hours (from $\alpha_{Agg} \approx 0.21$ to $\alpha_{Agg} \approx 0.35$); then an apparent decrease of association occurs as sketched, with a decrease of bonded N-H and increase of free N-H.

The key interpretation of these equivocal findings is given by SANS analyses (performed ca. 9/29 hours after dissolution, **Figure IV.13**). At low q values, the scattering intensity followed the profile of rigid rods for q values >0.2 $Å^{-1}$ (*i.e.* a q^{-1} dependence) then a q^{-4} dependence for q values <0.2 $Å^{-1}$. It indicates that the solution contains a mixture of rod-like aggregates and bigger structures with a smooth interface, assimilated to the particles visible in **Figure IV.14**. According to the SANS precision, the rod-like objects constitute a significant fraction of the introduced **TATA-SDA** monomers (possibly >50%).

FT–IR profile can be rationalized by **TATA-SDA** molecules being progressively self-assembled, or joined somehow to larger aggregates at the limit of solubility, until a balance is reached for which assemblies are embedded in large structures and precipitate. Therefore, photographs show insoluble particles dispersed in a fluid liquid rather than being trapped into a gel (**Figure IV.14**). Taken together, these results at high concentration described a metastable

two-step assembly process. After dissolution, soluble hydrogen-bonded stacks are present which probably co-exist with the aforementioned non-specific aggregates and monomers because the degree of association by hydrogen-bonded is modest. Thereafter, self-assembly occurs slowly over time leading to insoluble particles as exhibited by SANS and pictures.

Remarkably, this complex behavior of **TATA-SDA** at 11.7 mM depends on the solvent, since the same experiments realized in chloroform exhibit a different trend (**Figure SIV.48** to **Figure SIV.50**). In chloroform at 11.7 mM, the **TATA-SDA** solution mainly exhibits free monomers ($\alpha_{Agg} \approx 0.20$) and remains stable over time, homogenous and fluid. The scattering intensity profile in SANS at low q values is close to a q^{-1} dependence, indicating that no precipitation occurs. Combined analyses surmised that **TATA-SDA** in $CHCl_3$ (11.7 mM) form a mixture of specific (*i.e.* hydrogen-bonded) and non-specific (*i.e.* non-hydrogen-bonded) aggregates. The higher polarity of $CHCl_3$ over DCE might explain the better solubility of **TATA-SDA** assemblies in the former solvent.

TATA-SDA thus appears to exhibit a significantly lower tendency to aggregate into soluble HB-stacks relatively to **TATA-C13** as demonstrated by the lower degree of association by HB measured just after dissolution both in DCE and $CHCl_3$. Likewise, assemblies formed over time for **TATA-SDA** in DCE precipitate whilst they remain soluble in $CHCl_3$. The exact nature of the assemblies present in the DCE precipitate cannot be fully characterized, but they likely consist of hydrogen-bonded stacks whilst monomers and non-specific aggregates remain in solution. The fact that **TATA-SDA** HB stacks tend to form thicker assemblies which precipitate is likely the result of side chains interdigitation, which is maybe promoted by interactions between diacetylenic units. This could be also the sign of the formation of another type of hierarchical structure, such as coagulated fibrils instead of superhelices or vice versa. On one hand, precipitation of hydrogen-bonded stacks of **TATA-SDA** molecules might constitute a strategy to kinetically trap the helically-biased assemblies. On the other hand, insoluble nanoparticles are less suitable for characterization and for further implementation in catalysis.

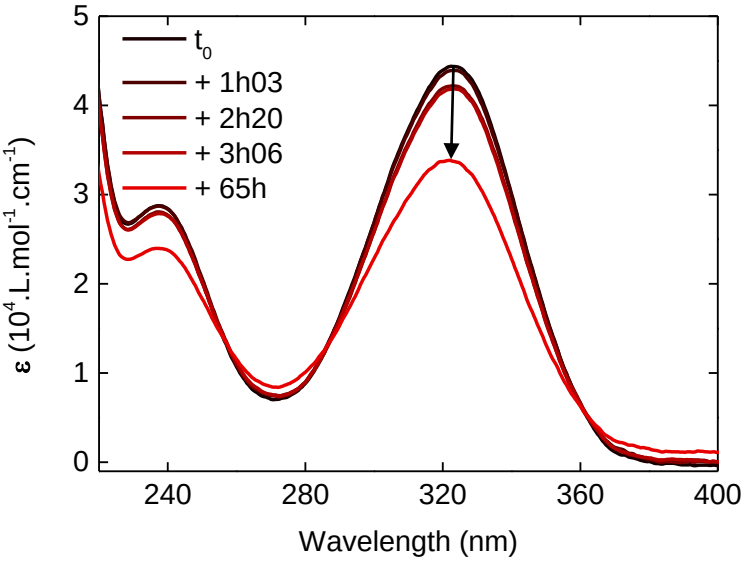

Figure IV.11 UV–Vis absorption spectra of **TATA-SDA** at 11.7 mM in DCE following time, within a sealed cylindrical quartz cuvette.

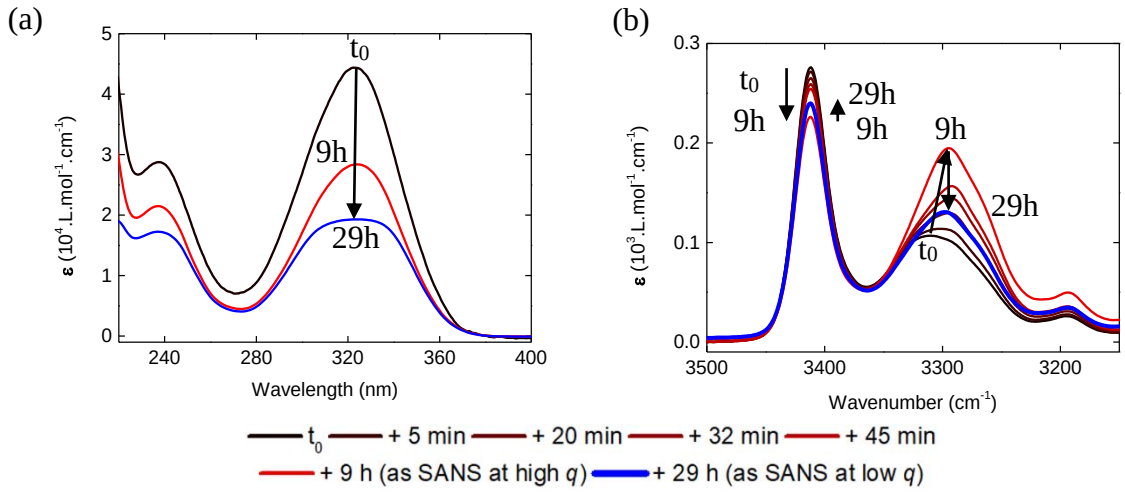

Figure IV.12 TATA-SDA at 11.7 mM in DCE. (a) UV–Vis absorption and (b) FT–IR spectra with a zoom on the N-H region (C=O region is not shown because of signal saturation). These UV–Vis absorption data have the advantage to be in the same time conditions than FT–IR and SANS measurements, but have been done in lamellar quartz cells, whence minuscule leaks sufficed to cause a very strong assembly or a loss of solution. Any quantitative interpretation must be avoided, on contrary to FT–IR measurements that were operated inside a sealed CaF_2 cell.

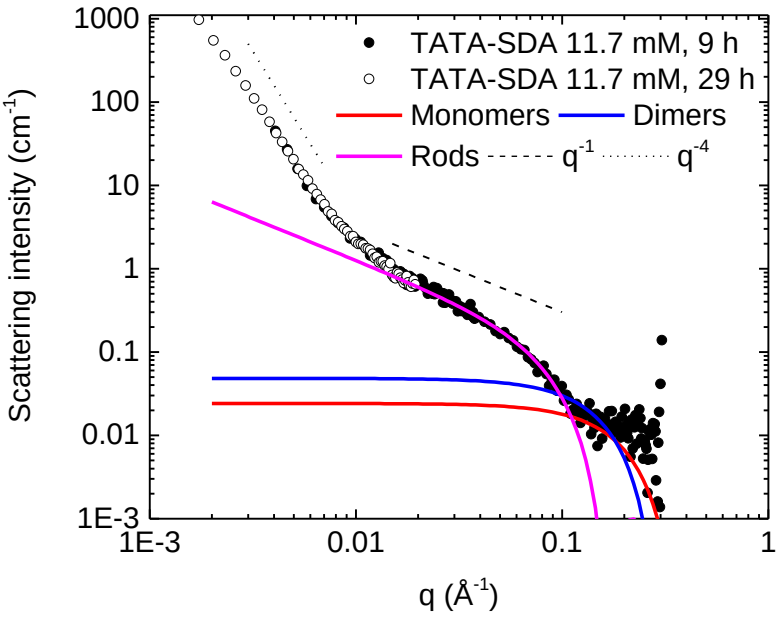

Figure IV.13 SANS analysis of **TATA-SDA** at 11.7 mM in DCE-d_4. Simulated spectra for monomers, dimers or infinitely long rigid rods of circular cross-section are shown together with the experimental spectrum.

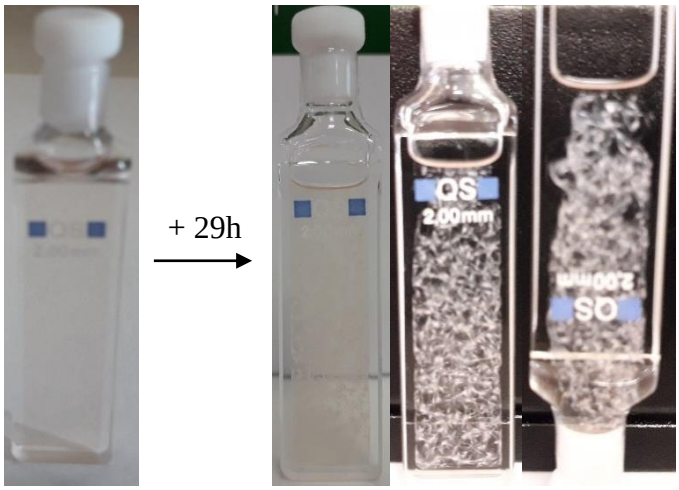

Figure IV.14 Pictures of **TATA-SDA** at 11.7 mM in DCE-d_4 after dissolution and after SANS measurements (t_0 + 29h). Solution before ageing was not used for SANS, hence its volume is slightly different.

III. 3. 4. As thin film

In order the increase the degree of association of **TATA-SDA** monomers, thin films were prepared and analyzed by UV–Vis–NIR and FT–IR spectroscopy.

Solution of **TATA-SDA** at 2.3 mM in DCE were drop-casted on lamellar quartz cell or KBr pellets and studied by UV–Vis–NIR or FT–IR (**Figure IV.15**). Normalized UV–Vis absorption signals revealed a flattened and shifted (- 5 nm) π→π* absorption band as well as a slanting baseline for the film (likely due to scattering large aggregates). This corroborates the stacking of **TATA-SDA** molecules in the film.

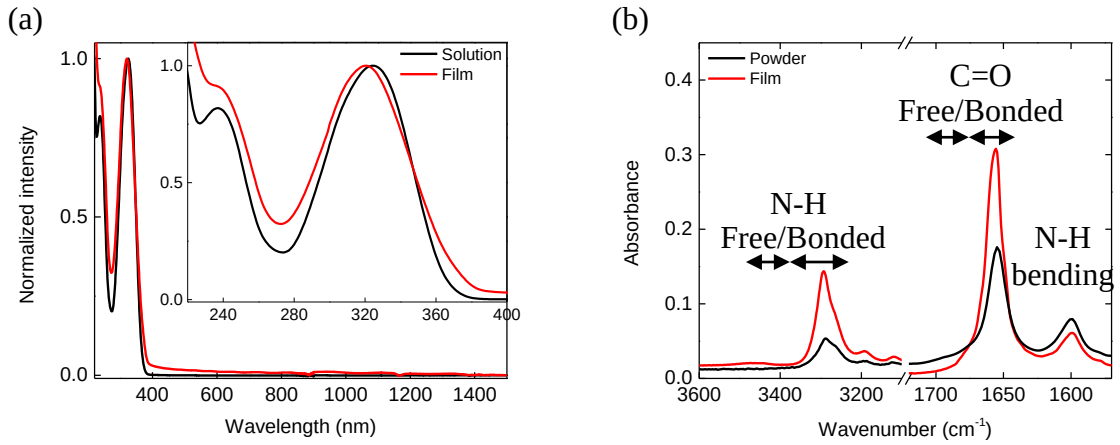

Figure IV.15 (a) UV–Vis–NIR absorption spectra of **TATA-SDA** in DCE at 2.3 mM, and as a thin film obtained by deposition of solution on lamellar quartz cell. (b) FT–IR analyses of **TATA-SDA** as powder, and as a thin film obtained by deposition on KBr pellets of a DCE solution of **TATA-SDA** at 2.3 mM. Zoom on the N-H and C=O regions.

FT–IR analyses confirmed that most of the molecules in the film are assembled by hydrogen bonds (α_{Agg} >99%, signals at 3290 cm^{-1} and 1655 cm^{-1}), similarly to what is found by analysis of the powder. A broad band between 3600 and 3400 cm^{-1} suggest that the H-bonding assemblies possess some defects, as a possible consequence of the amorphous nature of the solid present in the film. The high degree of association of **TATA-SDA** molecules in film agrees well with our studies performed on films of **TATA-C12** and **TATA-C13** (Chapter III).

IV. Self-association properties with CPL

The main aim was to control by CPL the supramolecular chirality of assemblies made of **TATA**. In the previous part, the self-association properties of **TATA-SDA** under four different conditions suitable for their oxidation have been precisely determined:

1) at 2.3 mM and room temperature in $CHCl_3$ and DCE (monomers and a significant fraction of non-specific aggregates);

2) at 2.3 mM in DCE at low temperature (hydrogen-bonded stacks mainly);

3) at 11.7 mM in DCE and $CHCl_3$ at room temperature after dissolution (mixture of soluble non-specific aggregates and hydrogen-bonded stacks) and with time: mixture of soluble non-specific aggregates and hydrogen-bonded stacks in $CHCl_3$ and mixture of soluble non-specific aggregates and insoluble particles, the latter probably composed of hydrogen-bonded stacks, in DCE.

4) Thin films (hydrogen-bonded stacks, high degree of association).

The next step was to assess the impact of light on the generation of radical cation **TATA-SDA** molecules and their influence on the nature of the resulting self-assemblies. For this purpose, two light irradiation setups for the generation of CPL were used: (A) composed of a LED of an optical power of 1650 mW centered on 385 nm, a condenser lens, a linear polarizer and a quarter-wave Fresnel rhomb retarder; (B) composed of the same components than A, except that quarter-wave plate specially designed to be optimal at 385 nm was used instead of the Fresnel rhomb (**Figure SIII.43**). Indeed, the Fresnel rhomb retarder is effective for a wide UV–Visible-NIR range, but is less precise and exhibits less efficient retardance at 385 nm. Thereby, the A-setup allows to reach a maximum circular polarization degree of 78% against 86% for B. The set of conditions employed for light irradiation – the setup, optical power, cell and other if needed – despite not being often accurately described in literature, have been systematically varied since all these parameters are expected to lead to different final chemical states. Consequently, the exact conditions of illumination are systematically specified, and unreliable comparisons avoided. The four aforementioned conditions are re-investigated under

CPL irradiation first with the aim of determining the influence of CPL on the structure of assemblies by means of NMR, FT–IR, SANS and UV–Vis–NIR analyses. The state of the unpaired electron has not been probed by EPR, but analogy with **TATA-C13** assemblies will be disclosed when possible. The potential helically biased nature of the co-assemblies will be probed in a dedicated section.

IV. 1. At 2.3 mM and room temperature

DCE, 2.3 mM and room temperature were selected to record the spectroscopic signature and estimate the amount of **TATA-SDA** radicals formed upon photo-oxidation, under conditions as close as possible of what Kim *et al.* mentioned[1].

In ^{1}H NMR, the broadening/disappearance of resonance signals of aromatic and amide hydrogens, as well as those at the vicinity of these groups, is the first hallmark of photo-oxidation of **TATA-SDA** molecules (protons 1, 2, 3 and 4 in **Figure IV.16**). Analogous experiment was carried out in chloroform, giving a complete disappearance of the same protons (**Figure SIV.52**). As in the case of TATA molecules with saturated side chains, this effect is likely caused by the co-assembly of radical cationic and neutral species within disordered non-specific aggregates, resulting in a transfer of unpaired electrons between molecules observed on the NMR timescale. The irradiated solution was characterized further by FT–IR and UV–Vis–NIR analyses.

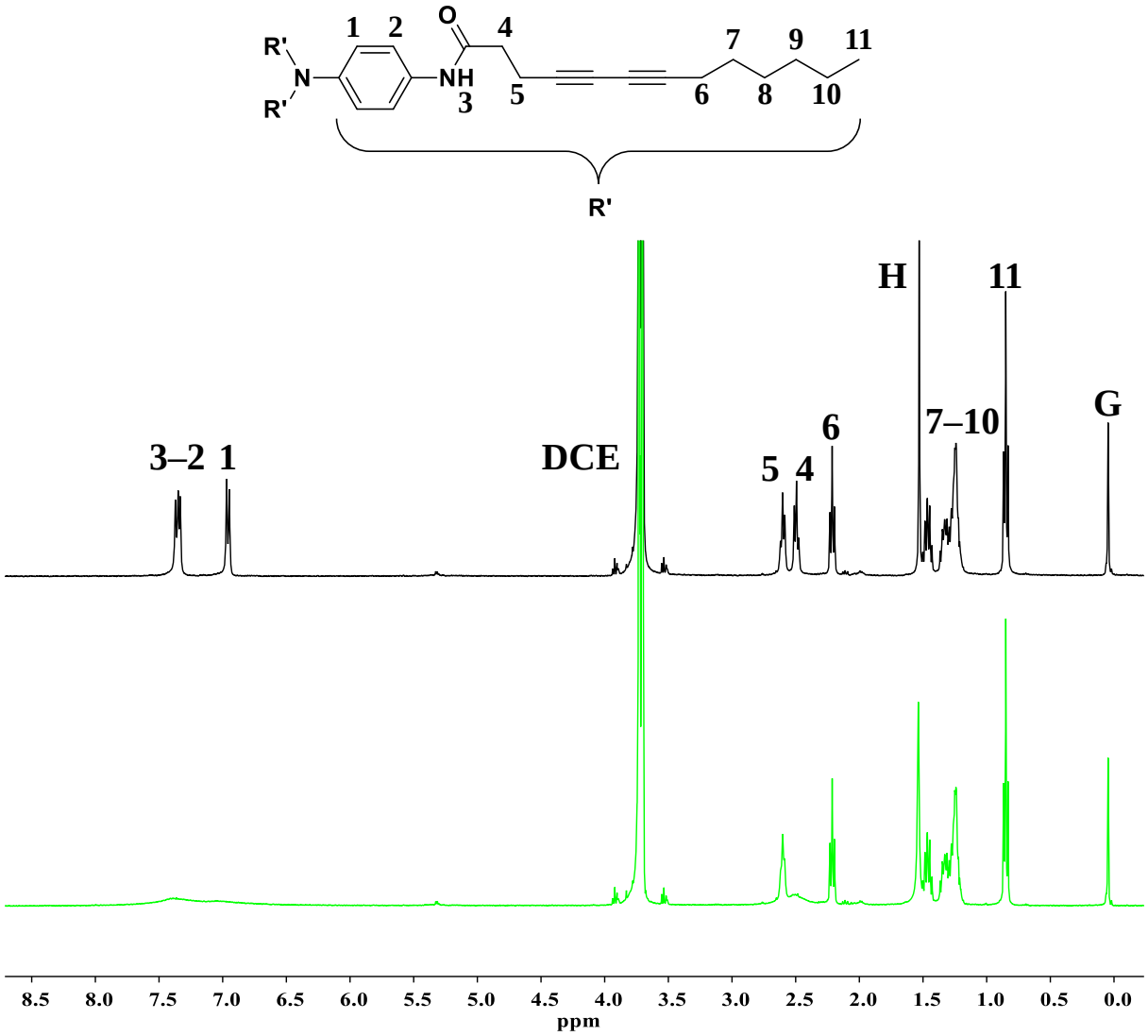

Figure IV.16 ^{1}H NMR spectra of **TATA-SDA** at 2.3 mM in DCE-d_4, before (top) and after (bottom) exposure to ambient light during one day (DCE, H and G are resonance peaks for residual DCE, water and silicone grease, respectively).

The photo-oxidation of **TATA-SDA** molecules was then probed by UV–Vis–NIR absorption spectroscopy in DCE (**Figure IV.17**) and in chloroform (**Figure SIV.54**) for different time of irradiation (up to 1800 s and 5100 s, respectively). Similarly to **TATA-C12** and **TATA-C13**, the main UV–Vis signals shift (notably a hypo-/hypso-chromic shift for the signal at 324 nm) and a set of absorption bands appear (at about 400 nm and between 600 and 900 nm) which corroborate the formation of $TATA^{\bullet+}$ species. As a reminder, the signal at about 400 nm is likely a vibronically structured $\pi \rightarrow \pi^*$ ($S_0 \rightarrow S_1$) transition[19], while the bands of

vibrational structure between 600 and 900 nm are ascribed to the new HOMO→SOMO transitions ($D_0 \rightarrow D_1$ and $D_0 \rightarrow D_2$ depending on the symmetry of the molecule)[20]. All these bands are considered as a signature of triarylammonium radicals in solution[2,21,22]. The bands between 600 and 900 nm increase in intensity for irradiation time up to 12 minutes then decrease until almost disappearing for 30 minutes of irradiation (red curves in **Figure IV.17e** and **f**). This suppression of the band characteristic of $TATA^{\bullet+}$ species is likely the sign of these radicals being reversibly or irreversibly transformed into side photoproducts such as $\mathbf{TATA^{2+}}$ dicationic species[20] or carbazole derivatives[23], respectively.

Coupling information related to both bands at 325 nm and 600-900 nm thus allows to monitor the fate of $\mathbf{TATA\text{-}SDA^{\bullet+}}$ during the two steps of the irradiation process (**Figure IV.17e** and **f**). The irradiation process thus follows two stages: i) $TATA^{\bullet+}$ species are generated and their number increases in the first stage, ii) the number of $TATA^{\bullet+}$ species decreases and photoproducts are concomitantly generated in the second stage. Triarylammonium radicals in chloroform exhibit the expected green color (**Figure SIV.55**)[1,2,21]. In $CHCl_3$, the same trend is observed but the amount of radicals generated at the end of the first stage is higher (up to 17% in DCE and 23% in $CHCl_3$), which is likely the sign of a higher oxidizing ability of **TATA-SDA** in chloroform. Such a two-step process was also observed for **TATA-C12** (2.3 mM in $CHCl_3$), for a maximum amount of $TATA^{\bullet+}$ species at the end of the first stage of about 40% (but for a different optical set up)[XXXIV]. Considering that EPR spectroscopy measured in these conditions a maximal concentration of $\mathbf{TATA\text{-}C12^{\bullet+}}$ species of about 6% (Chapter III), it means that by comparison, the photo-oxidation of **TATA-SDA** in DCE likely results only in a few percent of $\mathbf{TATA\text{-}SDA^{\bullet+}}$ species, overestimated by UV–Vis–NIR spectroscopy.

[XXXIV] A thicker pathlength for a lower optical power. The shape of the 600-900 bands for **TATA-SDA** in DCE is also significantly different from that of **TATA-SDA** and **TATA-C12** in $CHCl_3$.

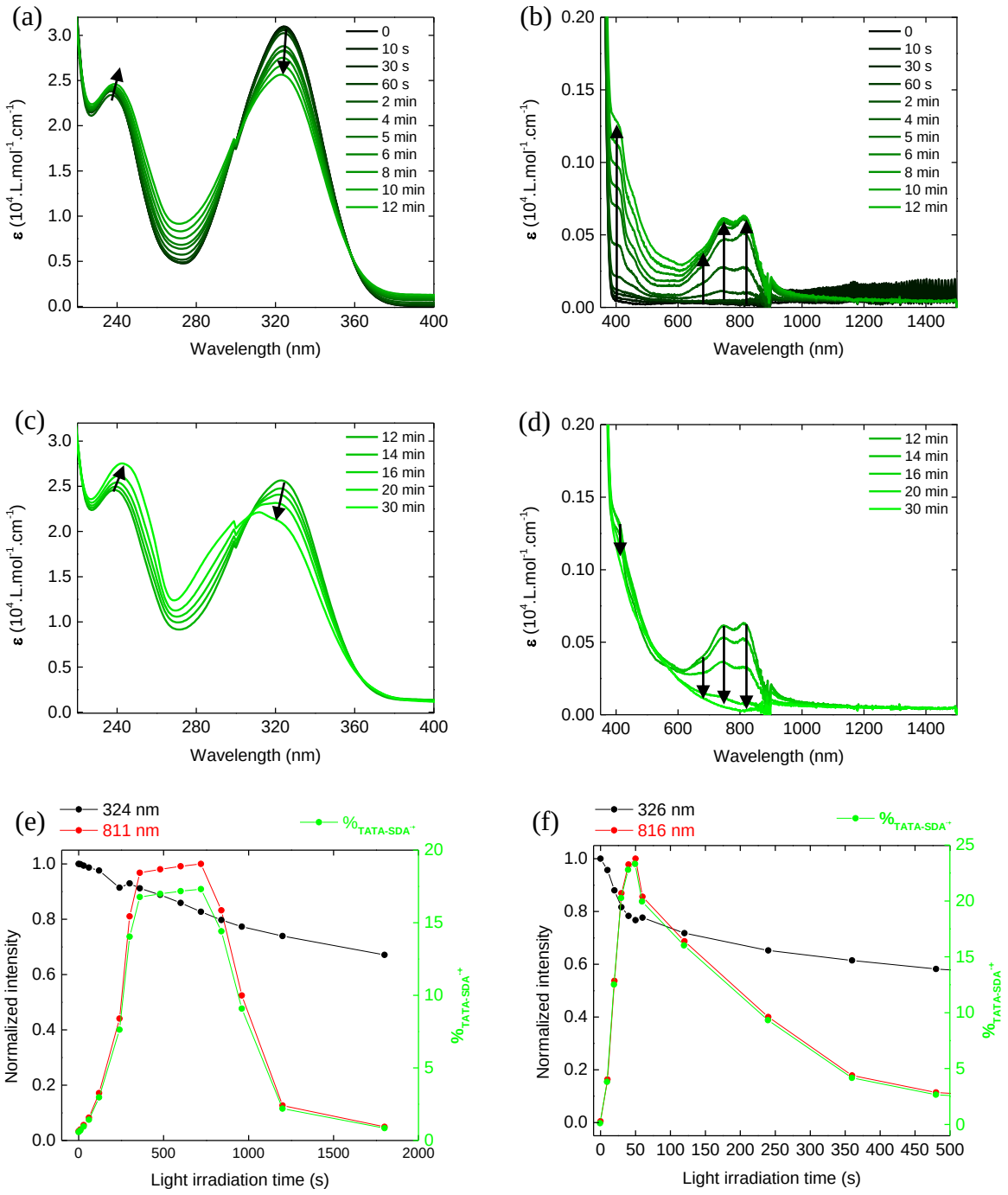

Figure IV.17 UV–Vis–NIR absorption spectra during light irradiation of a 2.3 mM solution of **TATA-SDA** in DCE. (a–b) first 12 min of light irradiation; (c–d) from 12 to 30 min of light irradiation; (e–f) evolution of the absorption at 324/326 nm and 811/816 nm (normalized intensity) in (e) DCE and (f) chloroform, respectively, and estimation of the amount of **TATA-SDA** radical cations as a function of the light irradiation time. This amount is first calculated according to the decrease of absorption at

324/326 nm, up to the light irradiation time corresponding to the maximum absorption at 811/816 nm, and according to the absorption at 811/816 nm. The 0.1 mm lamellar quartz cell was irradiated by the setup A, with a surface optical power of about 13.6 mW/cm^2. Noisy signals at 300 and 900 nm are due to changeovers of light source then detector and grating. (b) Wave interferences are observed in the NIR region.

The reversibility upon ageing in dark was then probed and confirmed, as depicted in **Figure IV.18**. A sample irradiated up to the second stage (molar extinction coefficient at 324 nm lower than at 240 nm) was left in the dark leading to a full recovery of the initial UV absorption spectrum. A second light irradiation leads to the same UV profile as after the first light irradiation. This reversibility discards the significant formation of carbazole compounds in this condition, and is more likely the sign of the formation of dicationic species, *i.e*. **TATA-SDA^{2+}** species[20,XXXV].

[XXXV] The characteristic signal of TATA^{2+} species is similar to the Vis–NIR profile at the end of second stage: a "broad and unsymmetrical absorption signal at about 530 nm"[20].

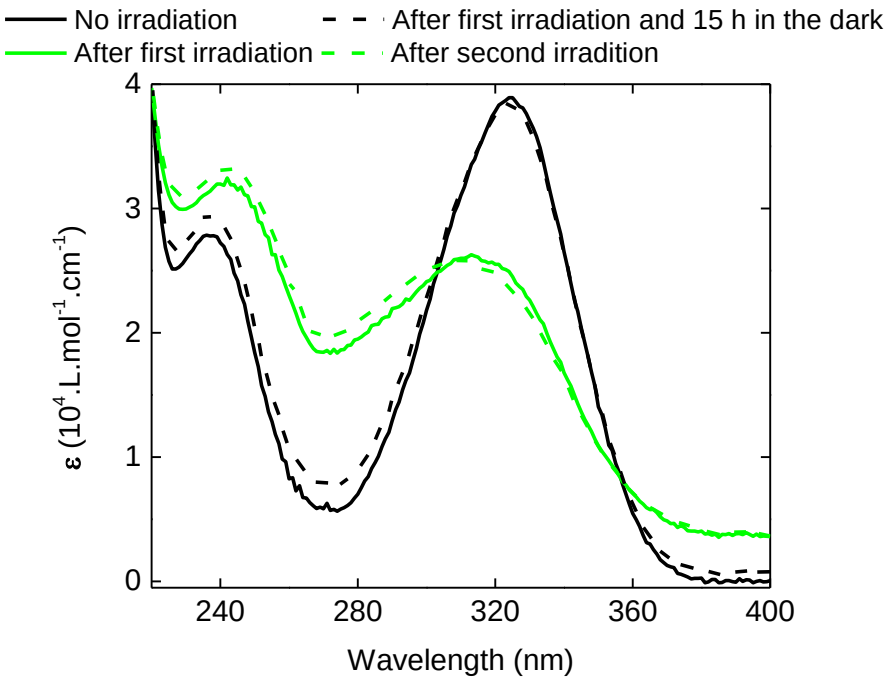

Figure IV.18 UV–Vis absorption spectra of **TATA-SDA** at 2.3 mM in DCE (black solid line), after 5700 seconds of light irradiation (1st irradiation, green solid line), then left in dark 15 hours (black dashed line) and again 5700 seconds of light irradiation (2nd irradiation, green dashed line). The 0.1 mm cylindrical quartz cuvette, inside the thermostatted CD-cell holder, was irradiated at 20°C by the setup B at a surface optical power of 33.7 mW/cm^2.

The photo-oxidation of **TATA-SDA** was further investigated by varying the setup (**Figure SIV.57**) and the sources (**Figure IV.19**). A single exponential decay of the absorption band at 323 nm was observed and as expected, the photo-oxidation efficiency increases with the surface optical power of the lamp. Thereby, note that the end of the two stages is marked by a plateau at a molar extinction coefficient inversely proportional to the lamp optical power, which is likely the reflect of the **TATA-SDA** amount that can be transformed in this configuration into radical cationic and then into dicationic species.

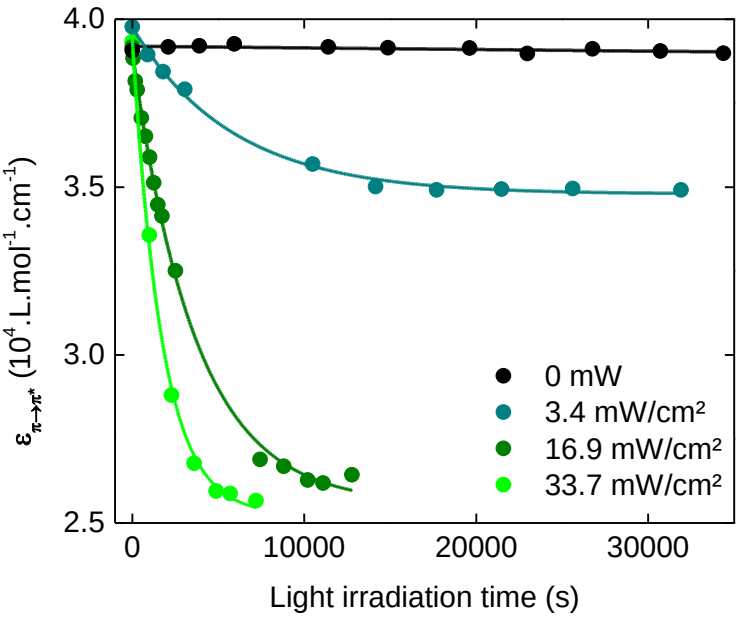

Figure IV.19 Evolution of the absorption at 323 nm of **TATA-SDA** at 2.3 mM in DCE, as a function of the light irradiation time, for three different surface optical power sources. The evolution of the absorption without illumination in the dark is shown for comparison. The data are fitted with an exponential decay model. The 0.1 mm cylindrical quartz cuvette, inside the thermostatted CD-cell holder, was irradiated at 20°C by the setup B.

Light irradiation of **TATA-SDA** was next conducted for two different times (8 and 16 min), and solutions were analyzed by FT–IR and UV–Vis–NIR spectroscopy (**Figure IV.20** for FT–IR and **Figure SIV.53** for UV–Vis–NIR). Thanks to the UV–Vis–NIR spectroscopic analysis, the formation of **TATA-SDA**$^{\bullet+}$ is attested both after 8 and 16 minutes of light irradiation, conditions in which the percentage of radicals is estimated at about 11 and 16%, respectively[XXXVI]. The presence of triarylammonium radicals is in addition corroborated by the color change of the light yellow solution turning into green (**Figure IV.20b**)[1,2,21]. FT–IR absorption spectra showed that after light irradiation, no shift or additional absorption bands similar to those found for **TATA-C12**$^{\bullet+}$ and **TATA-C13**$^{\bullet+}$ species can be detected. Only free

[XXXVI] For the sake of clarity, a part dedicated to the study of UV–Vis–NIR absorption under light irradiation follows this discussion.

N-H and C=O stretching vibrations signals are present, discarding the possibility that light triggers the formation of hydrogen-bonded stacks. Conversely, a chloroform solution irradiated in similar conditions showed an absorption band at 1565 nm, characteristic of $TATA^{\bullet+}$ species (**Figure SIV.46d**). Thus, radical cationic species in DCE are likely too few to be detected by FT–IR.

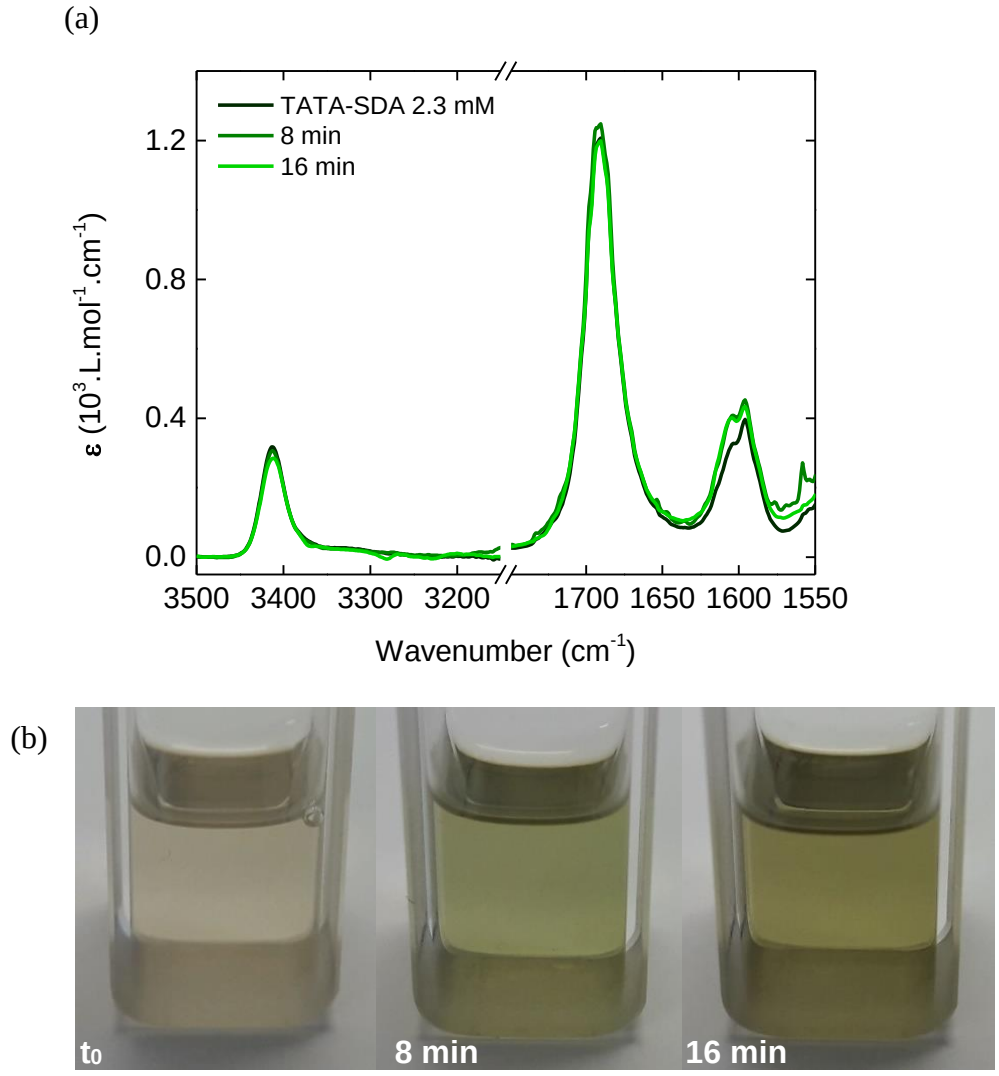

Figure IV.20 (a) FT–IR absorption spectra of (b) solutions of **TATA-SDA** at 2.3 mM in DCE before and after 8 and 16 minutes of light irradiation. The solution was irradiated in a 10 mm rectangular quartz cuvette by the setup A, with a surface optical power source of about 13.6 mW/cm^2. According to the evolution of the UV–Vis–NIR profile (**Figure SIV.53**), the percentage of radicals at 8 and 16 min was estimated at about 11 and 16%.

This spectroscopic study was completed by SANS measurements (**Figure IV.21**), performed 8 hours after the irradiation process (12 min, inducing approximatively 13% of radicals[XXXVII] within the first stage of photo-oxidation). UV–Vis–NIR and FT–IR analyses were realized in the same timescale than the scattering experiment: **TATA-SDA**$^{\bullet+}$ seem to be absent after 8 h, as suggested by the comparison with the UV–Vis–NIR profile of the non-irradiated sample, demonstrating that the reversibility is faster than what previous observations suggested; and FT–IR evidenced only free N-H and C=O stretching vibration signals at 3410 cm^{-1} and 1690 cm^{-1}, respectively (**Figure SIV.56**). The solution remains homogeneous and fluid after irradiation and 28 h in the dark (**Figure SIV.56**). The SANS profile was not affected by irradiation, indicating that the radicals generated after irradiation and their recombination do not significantly affect the structure of the non-specific aggregates present prior to irradiation.

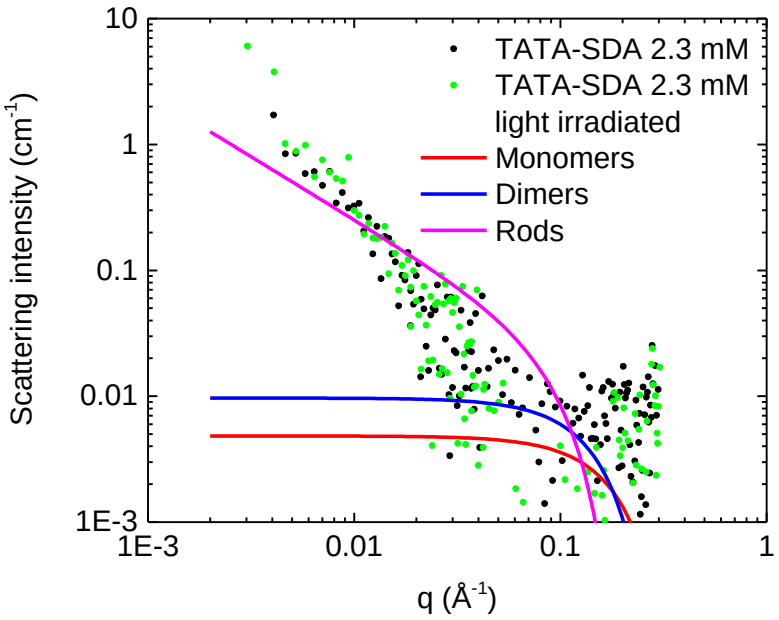

Figure IV.21 SANS analysis of **TATA-SDA** at 2.3 mM in DCE-d_4. Simulated spectra for monomers, dimers or infinitely long rigid rods of circular cross-section are shown together with the experimental

[XXXVII] Estimated on the basis of the UV–Vis–NIR results illustrated in **Figure IV.19**, *mutatis mutandis* (e.g. the optical power, the irradiated surface, the irradiation time).

spectra. The solution was irradiated 12 minutes in a 2 mm rectangular quartz cuvette by the setup A, with a surface optical power of 7.9 mW/cm^2.

Taken together, these results indicated that only a few **TATA-SDA**$^{\bullet+}$ are formed upon light irradiation in DCE, which did not show any effect on the association state of **TATA-SDA** at 2.3 mM and room temperature. Additionally, these triarylammonium radicals are likely further oxidized into dicationic species. In chloroform, even if triarylammonium radicals were easier to detect, and likely persisted more in solution with time than in DCE, their lack of effect on the globally non-hydrogen-bonded associated state of **TATA-SDA** at 2.3 mM and room temperature was the same (**Figure SIV.46** to **Figure SIV.48**).

IV. 2. At 2.3 mM and various temperatures

Having highlighted the absence of effects of **TATA-SDA**$^{\bullet+}$ on non-specific aggregates, the next stage was to move towards conditions that favors the formation of HB stacks. Previously, it was shown that a decreasing temperature triggered the assembly of **TATA-SDA** at 2.3 mM in DCE. It was thus highly interesting to examine the impact of light irradiation and radical cationic species on the self-assembly and aggregates favored by low temperatures.

To this end, the light irradiation of **TATA-SDA** at 2.3 mM was conducted for two different times (8 and 16 min, which likely correspond to a few percent of triarylammonium radicals), and solutions were analyzed by VT–FT–IR spectroscopy (**Figure IV.22**). Upon cooling, FT–IR evidenced the absence of impact of light irradiation on the self-association of **TATA-SDA** down to -35°C, close from the melting point of DCE at -36°C.

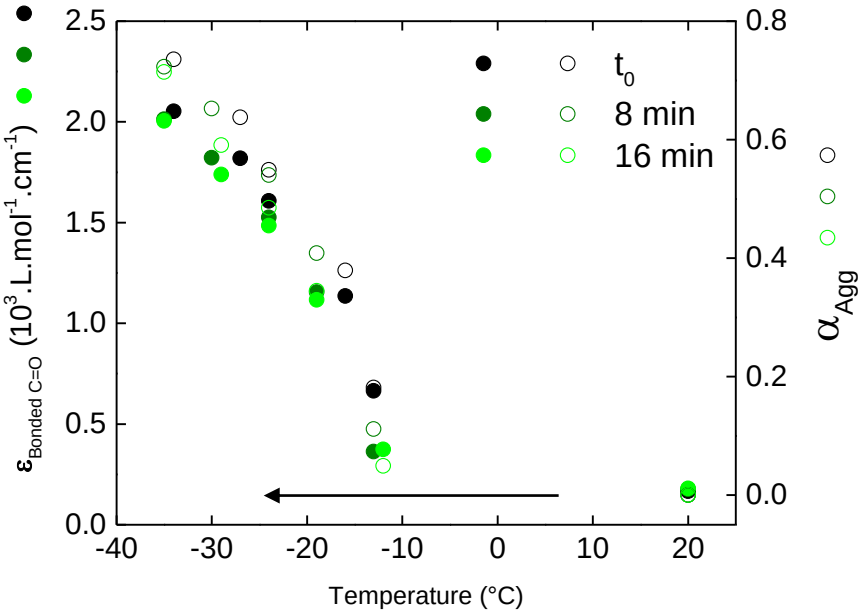

Figure IV.22 Evolution of the absorption at 1658 cm^{-1} (corresponding to bonded C=O, solid circles) and of the degree of aggregation (hollow circles), as a function of the temperature, for solutions of **TATA-SDA** at 2.3 mM in DCE irradiated 8, 16 minutes or not. The solution was irradiated in a 10 mm rectangular quartz cuvette by the setup A, with a surface optical power of about 13.6 mW/cm^2. According to the evolution of the UV–Vis–NIR profile (**Figure SIV.53**), the percentage of radicals at 8 and 16 min was estimated at about 11 and 16%.

Next, the behavior of the photo-oxidation and triarylammonium radicals was probed upon cooling, by light irradiating solutions with the setup B at high and low surface optical powers (33.7 and 3.4 mW/cm^2), during a short (15 min) or long time (120 min for the highest power or 360 min for the lowest). These setups corresponded to those whose results were illustrated in **Figure IV.19**. The temperature parameter was also explored, by carrying out light irradiation at 20°C (as it was always the case previously), but also under cooling: from 60°C to 20°C and from 60°C to -15°C. The irradiation performed at various temperatures raise the opportunity to test if triarylammonium radicals impacted differently the self-assemblies when produced: at 20°C, when molecules are not hydrogen bonded or upon cooling from 60°C, a temperature close from the boiling point of DCE (84°C) thus promoting the motion of molecules. Irradiation was also performed down to -15°C, thus potentially highlighting the

influence of the formation of radicals during the formation of the hydrogen-bonded stacks. The absorption of the principal UV signal at about 325 nm was followed at each step, and are presented in **Figure IV.23**.

By comparing the UV molar extinction coefficient at 20°C between the light irradiation at 20°C and while cooling from 60°C to 20°C, the effect of the photo-oxidation upon cooling looks inconsistent or inexistent (considering that the decrease in intensity at 20°C or higher is only due to the formation of **TATA-SDA**$^{\bullet+}$). At -15°C, the molar extinction coefficient at 325 nm is higher when the solution was light irradiated, especially upon cooling from 60°C to -15°C. It was evidenced that the UV intensity may decrease either because of the formation of hydrogen-bonded stacks (expected at -15°C) or upon the formation of **TATA-SDA**$^{\bullet+}$. Thereby, a weaker decrease in absorption after irradiation upon cooling could suggest that the formation of **TATA-SDA** radical cations slightly reduces the ability of TATA molecules to aggregate into hydrogen-bonded stacks. It could be the result of the competition of TATA$^{\bullet+}$ species between hydrogen-bonded stacks and non-specific aggregates, as observed with **TATA-C12** and **TATA-C13** in the previous chapter.

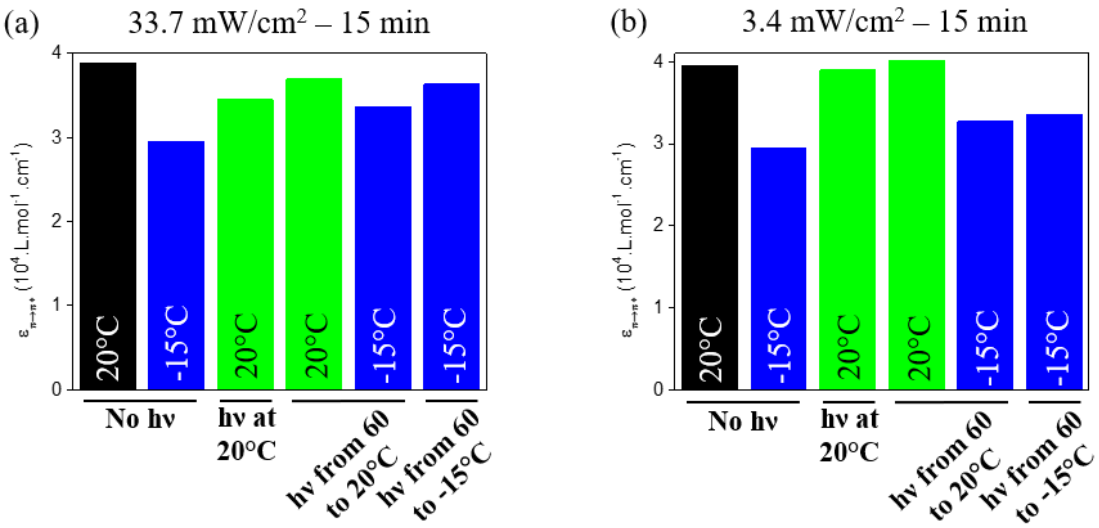

Figure IV.23 Absorption at 325 nm of **TATA-SDA** at 2.3 mM in DCE at 20°C (black columns), after light irradiation (green columns) and cooling at -15°C (blue columns). The light irradiation of 15 minutes involved the setup B at (a) 33.7 mW/cm^2 or (b) 3.4 mW/cm^2. For each optical power–light

irradiation time couple, the solution was irradiated at a constant temperature ("at 20°C") or under cooling (from "60 to 20°C" or from "60 to -15°C") at a constant rate. In the last case, measurements at 20°C were carried out upon heating from -15°C, after the light irradiation (apparently acceptable knowing the reversibility of the self-assembly and the short time between analyzes at -15 then 20°C). The 0.1 mm cylindrical quartz cuvette, inside the thermostatted CD-cell holder, was irradiated by the setup B. Thanks to comparative calculations, *mutatis mutandis*, the estimated percentage of radicals was about 15% (a) or 2% (b).

IV. 3. At 11.7 mM

Afterwards, By comparison with 2.3 mM, the light irradiation of solutions at 11.7 mM in DCE was less examined, since Kim *et al.* did not mention this concentration for the control by CPL of the handedness of **TATA-SDA** assemblies[1]. Nevertheless, the larger fraction of hydrogen-bonded stacks was of interest, even if the assemblies only evolved modestly with the time, as it was confirmed by the small decrease of the main UV–Vis absorption band in **Figure IV.24**. Maybe it is because under the timeframe of the experiment described here, no or limited aggregation occurs.

In $CHCl_3$, UV–Vis–NIR and FT–IR spectroscopic results both exhibited typical signatures of **TATA-SDA**$^{\bullet+}$ species (absorption bands at 400 nm and between 600 and 900 nm, as well as at 1565 cm^{-1}, **Figure SIV.49c** and **d**, and a strongly green solution after irradiation, visible in **Figure SIV.50**). However, the degree of aggregation appeared significantly lower than with **TATA-C12** ($\alpha_{Agg} \approx 0.35$ *vs.* 0.75), and the scattering profile unmodified by the light irradiation (**Figure SIV.48**). The solution likely still contains after irradiation a mixture of non-specific and hydrogen-bonded aggregates in similar proportions.

In DCE, the photo-oxidation of **TATA-SDA** was surveyed with different surface optical powers, as function of the irradiation time (**Figure IV.24**). Like for 2.3 mM solutions, the molar extinction coefficient at 323 nm followed a single exponential decay, which is consistent with the formation of triarylammonium radicals, but also with a second stage generating dicationic TATA species. The decrease in optical power also reduced the decay rate. The reversibility upon ageing in dark was also assessed, as illustrated in **Figure SIV.58**. A sample irradiated 8640 s at room temperature at a lamp optical power of 33.7 mW/cm^2 (so likely in presence of

radical cationic and dicationic species), did not completely come back to its initial state after being left in the dark for 16 h. This may be the result of the self-assembly and a beginning of precipitation that took place during ageing, but it can be also the hallmark of the persistence of **TATA-SDA**$^{\bullet+}$, which could have been favored by a putative co-assembly with neutral species, as observed at high concentration in chapter III.

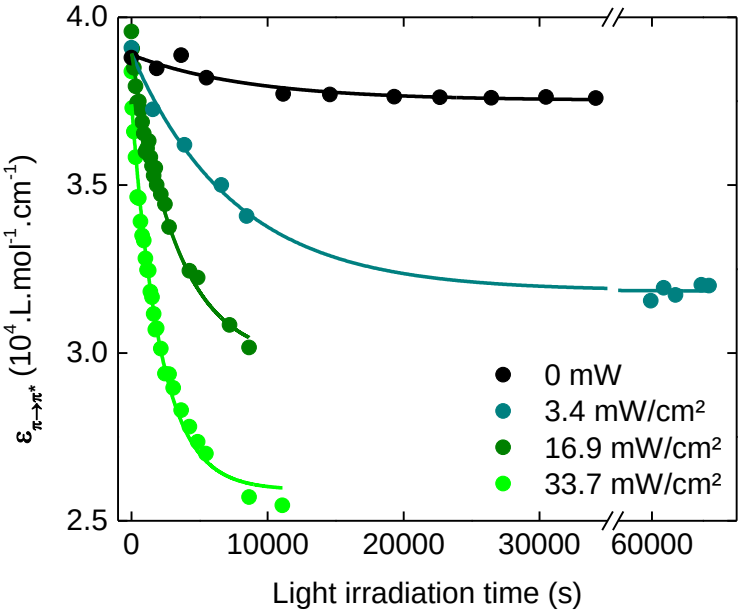

Figure IV.24 Evolution of the absorption at 323 nm as a function of the light irradiation time, for three different optical powers and for the non-illuminated solution in the dark. The data are fitted with an exponential decay model. The 0.01 mm cylindrical quartz cuvette, inside the thermostatted CD-cell holder, was irradiated at 20°C by the setup B. A precise determination of the amount of triarylammonium radicals formed is not possible due to the presence of hydrogen-bonded species in the initial conditions.

Solutions of **TATA-SDA** at 11.7 mM in DCE were light irradiated during 12 minutes and probed several hours later by a combination of UV–Vis–NIR/FT–IR/SANS analyses (**Figure IV.25** and **Figure IV.26**). Triarylammonium radicals formed upon light irradiation, of which traces seem still visible by UV–Vis–NIR spectroscopy 10 and 30 hours later (higher molar extinction coefficient between 400 and 600 nm), did not have a major impact on the association of **TATA-SDA**, as revealed by SANS and FT–IR analyses.

Nevertheless, it was possible to detect a rupture in the q^{-4} dependence of the scattering intensity at low q values, which might indicate that the particles formed after precipitation are smaller. A slight difference is also observed in the UV–Vis and FT–IR analyses of irradiated and non-irradiated solutions: the former contained a higher number of aggregated **TATA-SDA** molecules. This result could be attributed to the fact that assemblies doped with triarylammonium radicals are slightly more soluble than those devoid of it. This hypothesis seems interesting in the context of CPL-controlled supramolecular chirality, since the radicals can transfer their chirality to the helical co-assemblies.

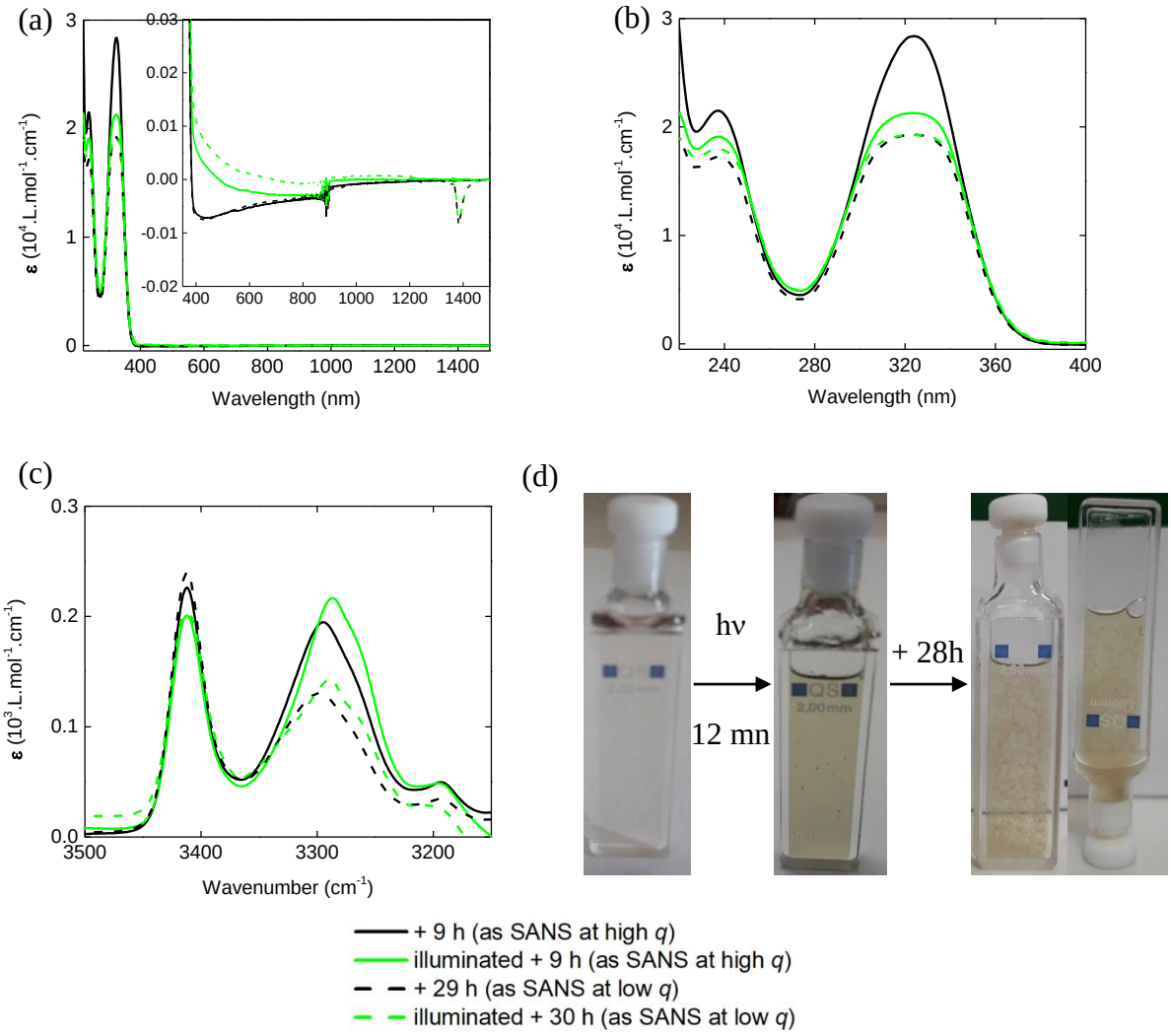

Figure IV.25 (a–b) UV–Vis–NIR absorption and (c) FT–IR spectra of **TATA-SDA** at 11.7 mM in DCE with (green) and without (black) light irradiation and ageing, under the same conditions than SANS

measurements. Zoom on the Vis–NIR and UV regions in (a) and (b), respectively. (d) Solutions after light irradiation and ageing (the first solution was not used for SANS, hence its volume slightly differs). The solution was irradiated in a 2 mm rectangular quartz cuvette by the setup A, with a surface optical power of 7.9 mW/cm^2.

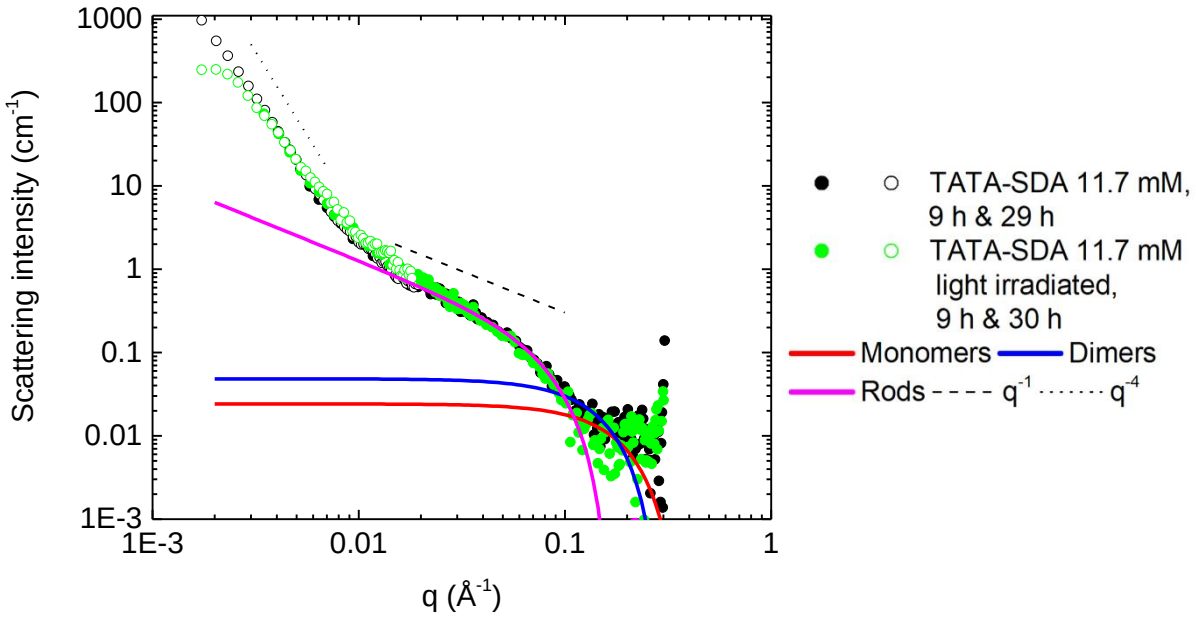

Figure IV.26 SANS analysis of **TATA-SDA** at 11.7 mM in DCE-d_4. Simulated spectra for monomers, dimers or infinitely long rigid rods of circular cross-section are shown together with the experimental spectra. The solution was irradiated in a 2 mm rectangular quartz cuvette by the setup A, with a surface optical power of 7.9 mW/cm^2.

IV. 4. As thin film

Solutions of **TATA-SDA** at 2.3 mM in DCE were light irradiated with the setup A at room temperature, inducing approximatively 10% of radical cationic species after 10 min of irradiation (first stage of photo-oxidation), and leaving only a few triarylammonium radicals after 30 min of irradiation[XXXVIII], (see UV–Vis–NIR analyses of the solutions before drop

[XXXVIII] Estimated on the same basis as for SANS measurements at 2.3 mM, *i.e.* based on the UV–Vis–NIR results depicted in **Figure SIV.59**.

casting in **Figure SIV.59**). Then these solutions were drop-casted on quartz lamellar cell and KBr pellets to give a green thin film, analyzed by UV–Vis–NIR and FT–IR, respectively (**Figure IV.27**).

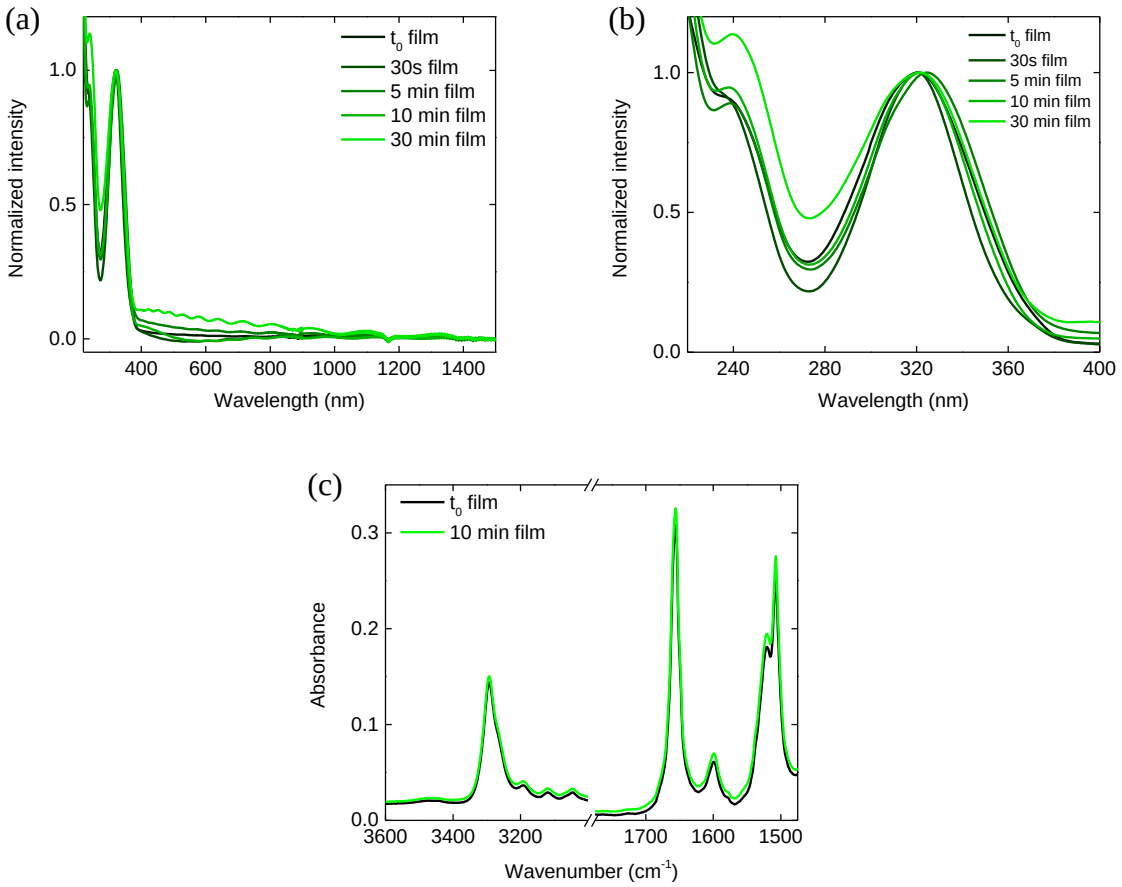

Figure IV.27 (a–b) UV–Vis–NIR and (c) FT–IR spectra of **TATA-SDA** as green thin film, obtained by deposition a lamellar quartz cell, or on KBr pellets, respectively, of irradiated solutions (from 30 seconds to 30 minutes). The spectra of the non-irradiated DCE solution was shown for comparison.

As mentioned in the previous part, the amount of $TATA^{\bullet+}$ generated in DCE is very low. The radicals cannot be detected in the thin films by FT–IR and are hardly observed by UV–Vis–NIR. The green color of the films ascertains the presence of radical cationic species (probably in very small amount, <<1%). This small amount of radicals does not lead to a drastic change in the structure of the assemblies, hydrogen-bonded stacks are present for both non-irradiated and irradiated solutions. Radical and neutral species are likely co-assembled into

these HB stacks, by analogy to our observation of co-assemblies involving neutral and radical **TATA-C13** species in thin films.

To sum up the part IV, we probed the formation and the behavior of **TATA-SDA**$^{\bullet+}$ in four different conditions. The goal was to investigate the impact of radical cationic species on assemblies, and above all to track the conditions for which **TATA-SDA**$^{\bullet+}$ integrate stacks, likely the prerequisite of a control of their supramolecular chirality (**Table IV.2**).

TATA-SDA is less prone to aggregation into soluble HB stacks in DCE and $CHCl_3$ than **TATA-C13** and tends to form insoluble particles with time at higher concentration (*vs.* syneresis gel for **TATA-C13**). The amount of radicals generated in DCE is significantly lower than in $CHCl_3$. This can be hardly improved by changing the light set up or increasing the irradiation time because mono radical cations tend to transform into dications. The difficulty to detect the radicals and their tendency to recombine in the dark prevents a definitive understanding of their fate. By analogy with the previous chapter, it is likely that the scarce amount of radicals generated co-assemble with neutral **TATA-SDA** molecules into non-specific aggregates at 2.3 mM.

At 2.3 mM upon cooling, part of the radicals generated at rt likely co-assemble with neutral molecules into HB stacks. A similar conclusion can be made at 11.4 mM, condition for which particles precipitate over time which likely contain mixed HB stacks of radical and neutral **TATA-SDA** molecules. Thin films are also composed of mixed assemblies, but again the amount of radicals in these films is extremely low. We assume that despite the low amount of TATA$^{\bullet+}$ generated in DCE, it can be enough to direct the handedness of assemblies since we also note that the amount of radicals generated in the study of Kim *et al.* is also low (**Figure IV.28**)[1]. With this in mind, the supramolecular chirality potentially biased by CPL irradiation could be pursued across these conditions by circular dichroism analyses.

Table IV.2 Recap chart of assemblies formed by **TATA-C13** and **TATA-SDA** in chloroform and 1,2-dichloroethane. ++, + and – before $TATA^{\bullet+}$ denote the level of radical cationic species generated by light irradiation and estimated by UV–Vis–NIR analysis. ++, + and – denote the level of confidence about co-assembly between neutral and radical cationic species.

	TATA-C13 $CHCl_3$		**TATA-SDA $CHCl_3$**		**TATA-SDA DCE**	
	Before hν	After hν	Before hν	After hν	Before hν	After hν
2.3 mM rt	soluble non-HB stacks	soluble non-HB stacks + $TATA^{\bullet+}$ before phase II –	soluble non-HB stacks	soluble non-HB stacks + $TATA^{\bullet+}$ before phase II –	soluble non-HB stacks	soluble non-HB stacks – $TATA^{\bullet+}$ before phase II –
2.3 mM with time	soluble non-HB slowly transforming into HB stacks (gel)	soluble non-HB stacks ++ $TATA^{\bullet+}$ before phase II +	soluble non-HB stacks	soluble non-HB stacks + $TATA^{\bullet+}$ before phase II –	soluble non-HB stacks	soluble non-HB stacks – $TATA^{\bullet+}$ before phase II –
2.3 mM upon cooling	HB stacks	shortened HB stacks ++ $TATA^{\bullet+}$ before phase II +			HB stacks	HB stacks – $TATA^{\bullet+}$ before phase II +
11.7 mM	in/soluble ribbons of HB stacks	in/soluble ribbons of HB stacks ++ $TATA^{\bullet+}$ before phase II +	soluble non-HB and HB stacks	soluble non-HB and HB stacks + $TATA^{\bullet+}$ before phase II +	soluble non-HB stacks and insoluble bundles of HB stacks	soluble non-HB stacks and insoluble bundles of HB stacks – $TATA^{\bullet+}$ before phase II +
Thin films	aligned HB stacks	aligned HB stacks ++ $TATA^{\bullet+}$ before phase II ++	aligned HB stacks	aligned HB stacks ++ $TATA^{\bullet+}$ before phase II ++	aligned HB stacks	aligned HB stacks – $TATA^{\bullet+}$ before phase II ++

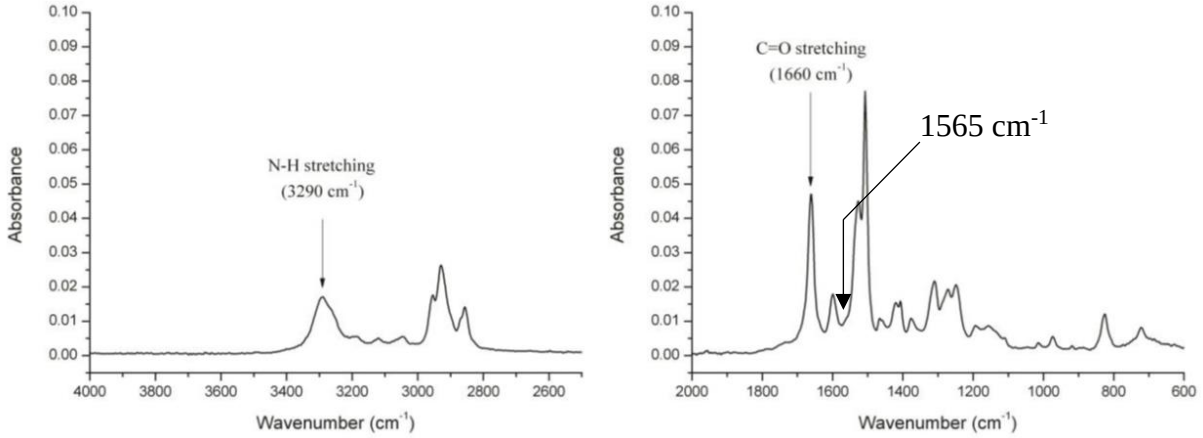

Figure IV.28 ATR-IR spectra of light irradiated then drop casted DCE solution of **TATA-SDA** at 2.3 mM. No signals characteristic of radical cationic species (e.g. at 1565 cm^{-1}) are present. Adapted from Kim *et al.*[1]

V. Towards CPL-biased supramolecular chirality

V. 1. Pitfalls of CD measurements

Before looking for the possibility of controlling the handedness of TATA helical assemblies by the orientation of the CPL, it was crucial to verify that **TATA-SDA** self-assemblies without illumination provided *right*- and *left*-handed supramolecular helices in equal amount (*i.e.* their solutions are CD-silent). During the course of our studies, we actually found that this is not always the case. In the following, we will highlight experiments for which CD signals were obtained from non-illuminated solutions. Pay attention that in the following figures, CD and LD signals will often be presented on the same plot as thick and dotted lines, respectively.

Spectroscopic analyses of **TATA-SDA** solution at 2.3 mM in DCE at 20 °C and -10°C, are shown in **Figure IV.29** for the **TATA-SDA** synthesized as batch IV. Surprisingly, solutions from this batch systematically gave a strong CD signal at -10°C whose shape is consistent with that expected for helically biased TATA assemblies. A similar CD spectrum was obtained by Kim *et al.*[1] for their CPL-irradiated solutions (**Figure IV.29a** *vs.* **d**). Importantly here, CD and LD spectra have fully different shapes (**Figure IV.29b**). The range of analyses performed on

this batch as well as the other batches (^{1}H and ^{13}C NMR, HRMS, MALDI–TOF and FT–IR) indicate that this batch is perfectly clean, so the bias was attributed to cryptochirality: *i.e.* chiral molecules below the detection level. This hypothesis was in line with the extremely high amplification properties reported for TATA helical assemblies[24], suggesting that a tiny chiral influence might somehow lead to an excess of one helical handedness.

Two examples of CD active solution issued from batch IV are shown in **Figure IV.29a**, which have identical shape but different intensity. The variable CD intensity displayed in **Figure IV.29a** come in part from a different amount of **TATA-SDA**, as suggested by the UV–Vis absorptions shown in **Figure IV.29c**. Although these samples have been recorded in different lamellar quartz cells, it cannot totally explain why one CD signal is double the other while molar extinction coefficients have a difference lower than 20%. An inhomogeneous distribution of cryptochiral compounds inside the powder, or the potential impact of sample thermal histories, might also explained these different CD magnitudes.

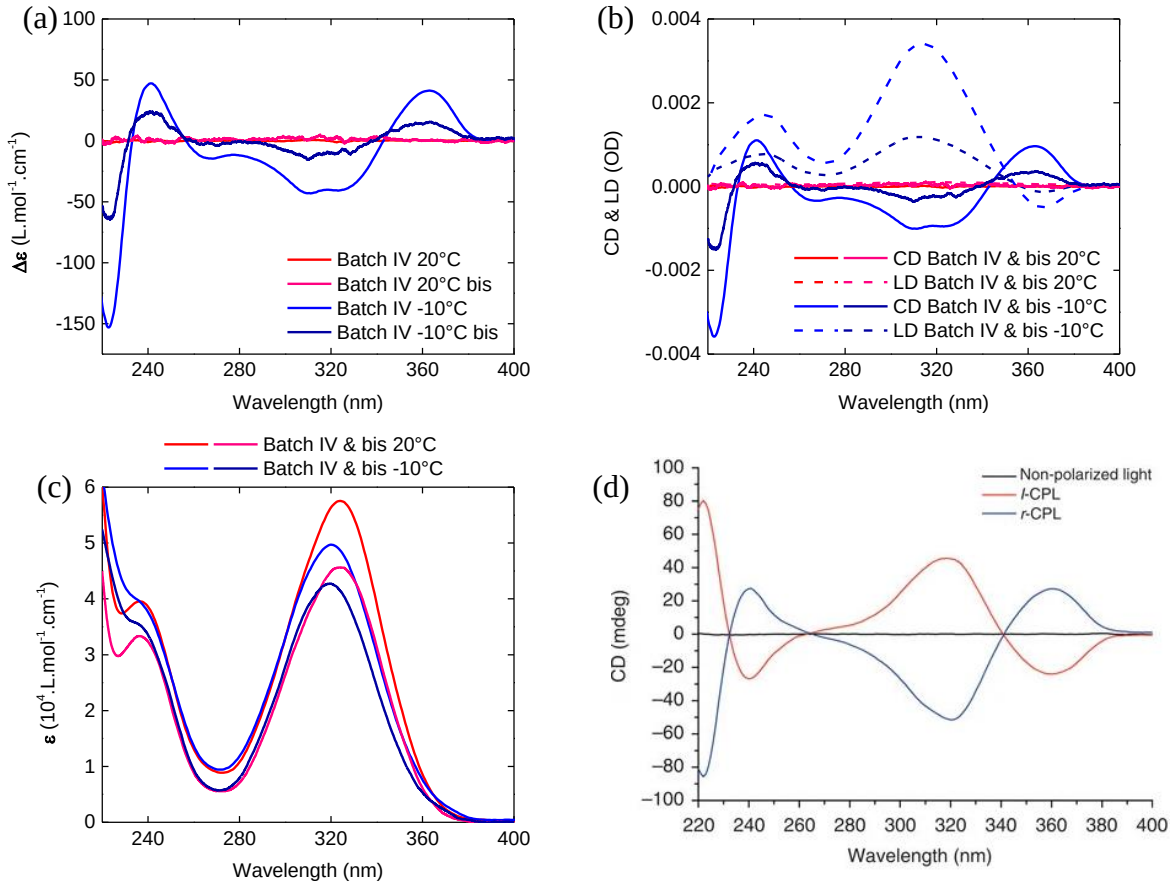

Figure IV.29 CD (a), CD + LD (b) and UV–Vis absorption (c) analyses of **TATA-SDA** (batch IV) at 2.3 mM in DCE at 20°C and -10°C. (d) For comparison, CD spectra reported by Kim *et al.* of **TATA-SDA** a 2.3 mM in DCE at -10°C, after irradiation with non-polarized light (black), *l*-CPL (red) and *r*-CPL (blue)[1].

Cryptochirality was not observed for all batches, and for a certain batch it appears only sporadically. For example, solutions from batch V were analyzed many times at 2.3 mM and -10°C but exhibited CD signal similar to the one observed for batch IV only for one sample analyzed at -10°C (black curve, **Figure IV.30a**). Note here that again CD and LD exhibit drastically different shapes. It indicated that cryptochirality could be sporadic, maybe due to incoming impurities or an exceptional spontaneous mirror symmetry breaking process. The latter could have been favored by the slightly different sample thermal histories, as implied by the tiny differences in the absorption spectra (**Figure IV.30c**). Taking into account these

cryptochirality/SMSB phenomena, any measured CD-active samples must be repeated and reproduced with different batches before any conclusion.

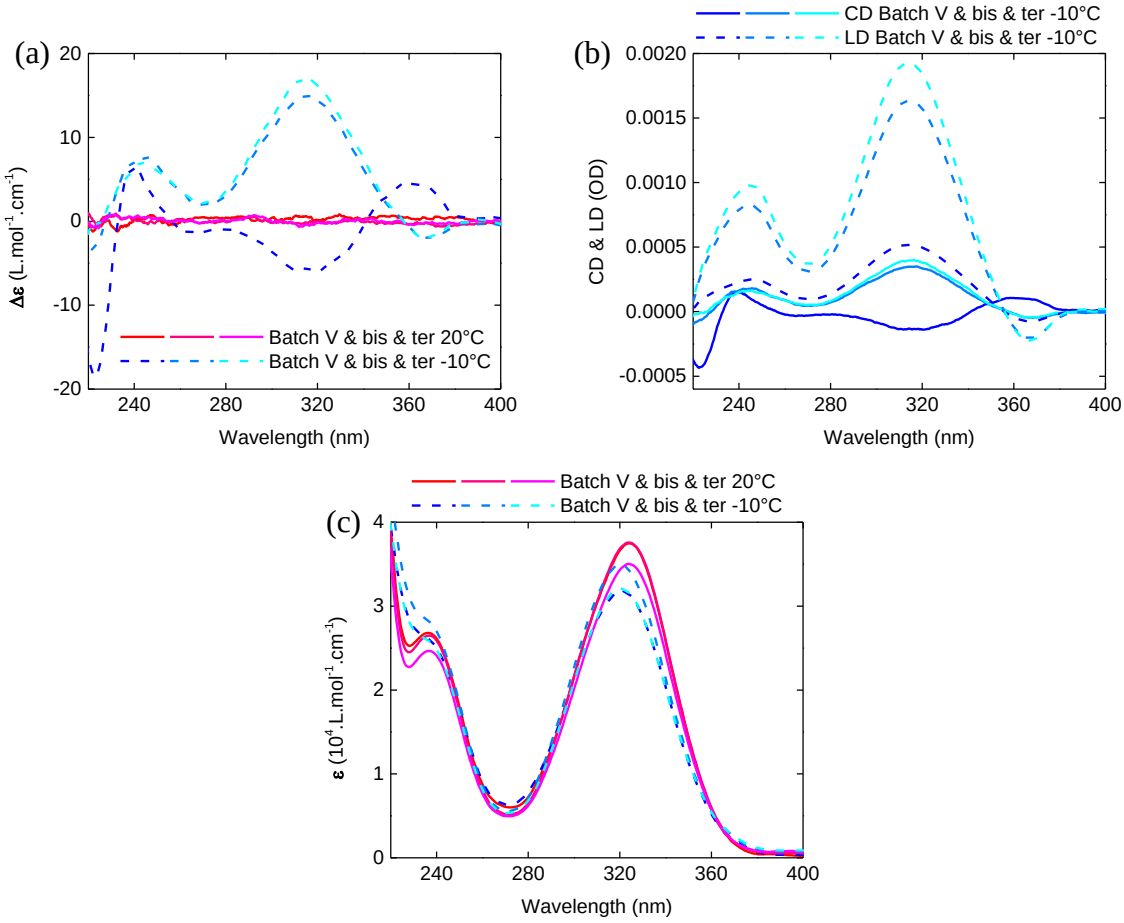

Figure IV.30 CD (a–b), LD (b) and UV–Vis (c) analyses of **TATA-SDA** (batch V) at 2.3 mM in DCE at 20°C and -10°C.

Furthermore, samples "bis" and "ter", depicted in **Figure IV.30**, were also CD-active anyway. But these CD signals exhibit a shape which is not consistent with helically-biased TATA assemblies[1,24,25]. Rather, the CD spectra have a similar shape than the linear dichroism spectra (LD, **Figure IV.30b** for a comparison in the same unit), with an intensity that appeared to be correlated to the LD magnitude.

This observation highlights the complex interplay between circular and linear dichroisms, thoroughly discussed by Di Bari *et al.*[26] Particularly present in solid samples, the interferences of macroscopic anisotropies with CPL light generate linear dichroism and linear

birefringence (LB), and these phenomena can sometimes couple with the nonideal characteristics of spectrophotometers, to significantly contribute to the measured CD spectrum. Indeed, the linear dichroism corresponds to the differential absorption of light linearly polarized in parallel and perpendicularly to an orientation axis, while the circularly polarized light can be reduced to the sum of perpendicular linearly polarized light with a phase shift of λ/4. Thus a non-zero LD may have an impact on the measured CD, often in a complex way that cannot be distinguished or subtracted[26–28]. In these conditions, the observed CD, effect of a real difference of absorption of *left*- and *right*-CPL, is different from the isotropic CD (CD_{iso}), the component of CD which is independent of sample orientation and which reflects the chiral nature of the supramolecular assemblies. With this in mind, CD and LD must be always compared and carefully interpreted.

Fortunately, simple experimental procedures may partly assess the consequences of macroscopic anisotropies and spectrophotometer artifacts on the observed CD[XXXIX]. For example, since the macroscopic anisotropies (*i.e.* LD and LB) are related to an orientation axis, a CD-active sample contaminated with LD and LB contributions will change its CD profile upon flipping by 180° the sample around its vertical axis. In our case, this was illustrated by the CD analysis of the 5th batch of **TATA-SDA** in DCE at -10°C for which the CD signal decreases in intensity upon flipping (**Figure IV.31a**). Secondly, a continuous rotation of the sample about the optical axis during the CD analysis can also allow to identify artifacts coming from the spectrophotometer optics[XL] as shown in **Figure IV.31b**.

[XXXIX] The CD measurement by a spectroscopic Mueller matrix polarimeter based on four photoelastic modulators, that can distinguish all circular and linear dichroisms and birefringences[29–31], could be also highly interesting, at least to identify reliable conditions of CD emergence and observation.

[XL] On one hand, the sawtooth signal observed in **Figure IV.31b** may be due to the periodic vibration induced by the rotation of the cell inside the CD spectrophotometer, affecting the measurement. On the other hand, CD spectrophotometers use a modulator which exhibits a regular sinusoidally time-dependent birefringence (*i. e.* this optical unit induce a sinusoidal phase difference to light), so the dependence of the output intensity of the CD/LD is also sinusoidal. In this way, CD artefacts may come "from a coupling between an intrinsic static birefringence of the modulator unit and a LD of the sample"[28], artefacts that can be periodically in interference depending on the orientation of the sample, impacting both LD and CD in the case of LD-induced CD.

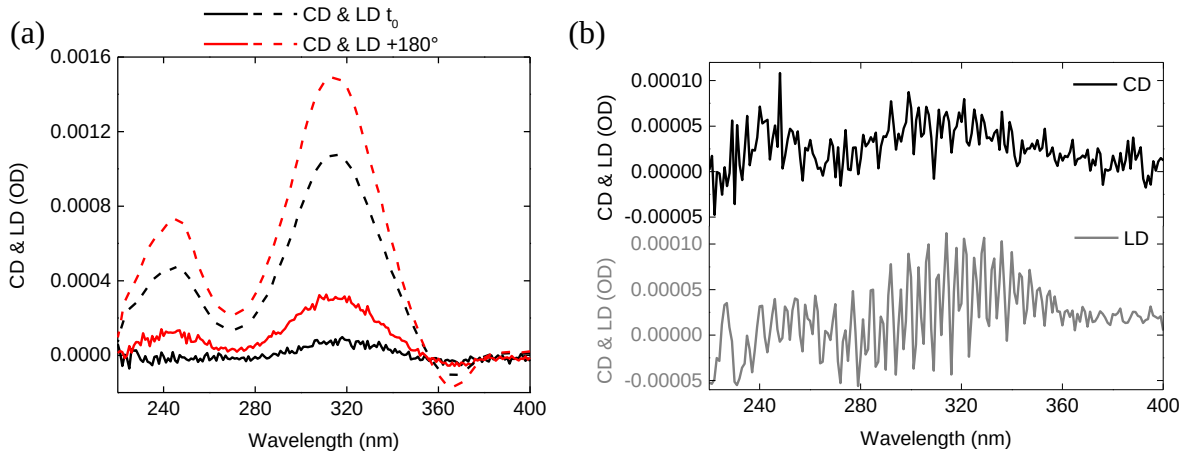

Figure IV.31 (a–b) CD + LD analyses of **TATA-SDA** (batch V) at 2.3 mM in DCE. (a) analysis was measured at -10°C in a thermostatted rotative cylindrical cell, while the (b) analysis was measured at about -20°C in a non-thermostatted rotative cylindrical cell.

Our in-depth characterization of the self-assembly properties of **TATA-SDA** monomers (section III) indicates that insoluble particles, likely composed of HB stacks of **TATA-SDA** molecules bundled through interdigitation of their side chains, might form in a certain number of cases: at low temperature and at room temperature for 11.7 mM. The same macroscopic objects are likely to be present in thin films therefore, each measured CD for **TATA-SDA** samples are discussed in comparison with the linear dichroism and, sometimes, under flipping and rotation. If the CD was quite different from CD_{iso} (*i.e.* the one expected for isolated one-dimensional helical TATA assemblies), but instead followed in shape and relative intensity the LD signal, it will be mainly attributed to LD contributions and named as CD/LD (occasionally confirmed by sample flipping). That is why the CD measured for "bis" and "ter" samples issued from batch V were attributed to CD stemming from LD contributions, and not from biased supramolecular chirality.

Nonetheless, LD contributions did not prevent to measure CD coming from biased supramolecular helices, as reported with the sample issued from batch IV in **Figure IV.29b** and in **Figure IV.32**. In the latter example, the LD and CD signals between 360 and 380 nm have opposite signs which might be the sign of the presence of a 'true' CD signal (CD_{iso}) in this region.

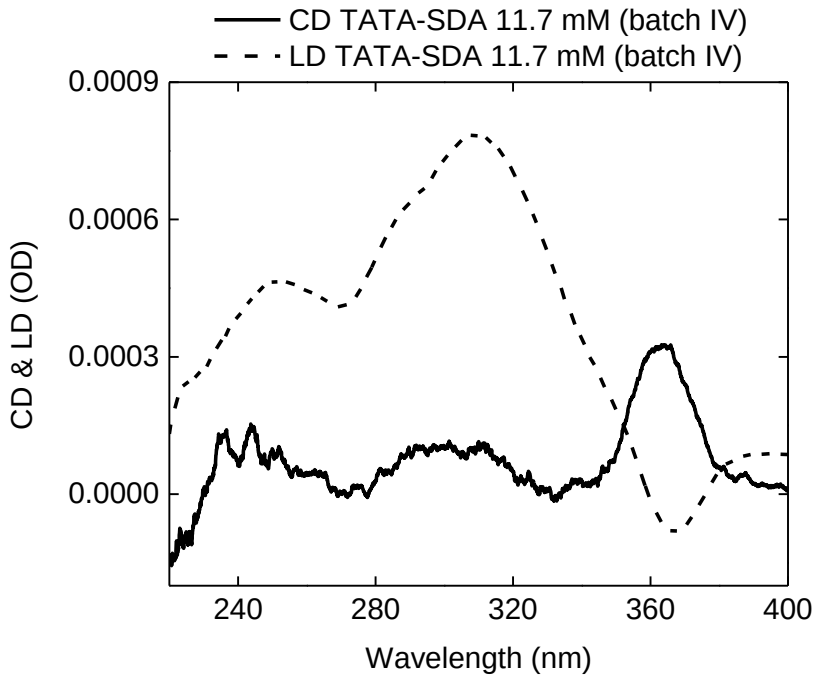

Figure IV.32 CD + LD analyses of **TATA-SDA** (batch IV) in DCE at 11.7 mM and 20°C.

Solutions of batch VI, intensively studied in our quest for CPL-triggered CD, never displayed a CD ascribed to cryptochirality, but CD signals are observed at low temperature, as illustrated in **Figure IV.33**, which have identical shape as LD signals. Indeed, a solution of this batch at 2.3 mM clearly shows a CD that could be assigned to LD, even though the LD signal in that case is tiny (absorbance of 0.0008).

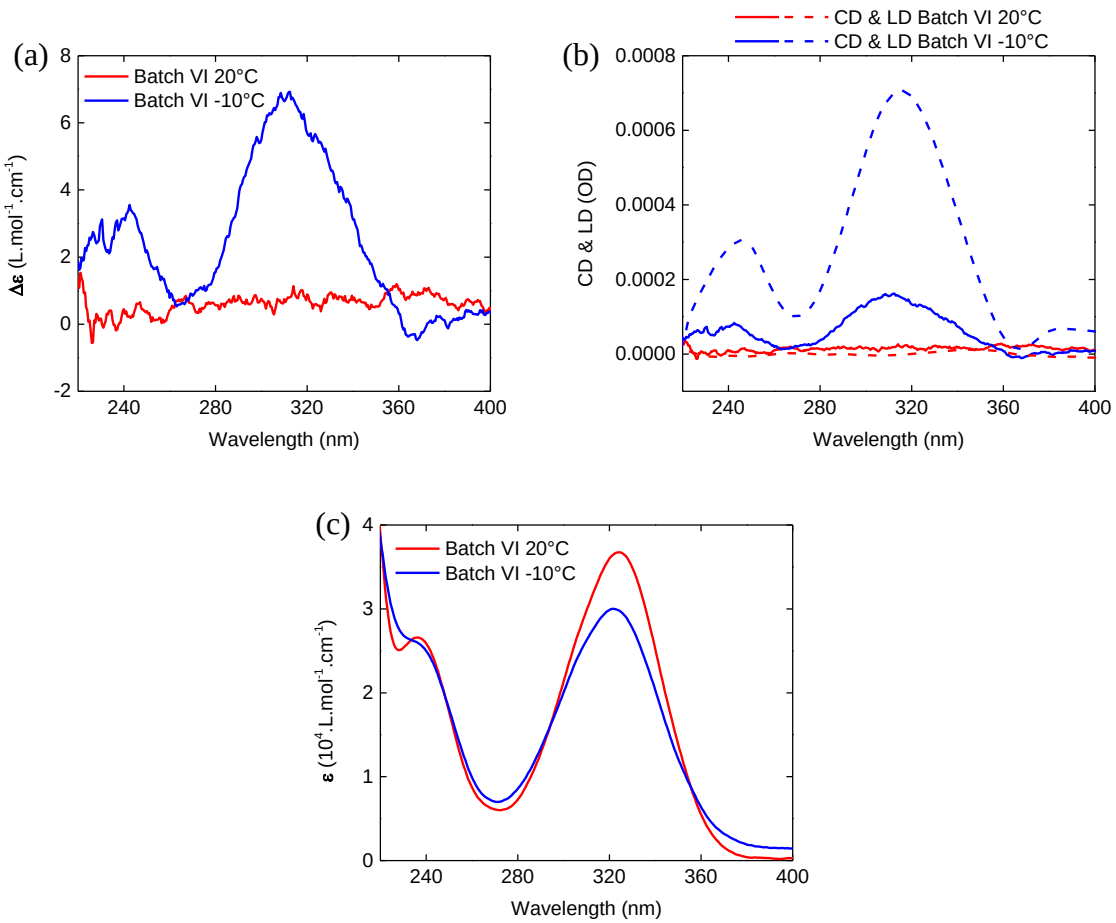

Figure IV.33 CD (a–b), LD (b) and UV–Vis (c) analyses of **TATA-SDA** (batch VI) at 2.3 mM in DCE at 20°C and -10°C.

In summary, CD measurements are more intricate for samples which contain assemblies that can possibly be aligned macroscopically, as suspected for **TATA-SDA** in the aforementioned conditions. More precisely, **TATA-SDA** molecules, by tending to assemble into soluble and insoluble huge aggregates, are prone to macroscopic anisotropies that can induce a CD which is not the result of a biased supramolecular chirality. Consequently, a particular attention was paid to ascertain the origin of the observed CD signal. CD is then systematically compared with the LD in the same unit (OD = optical density)[32,33], but without considering the subtraction of LD from CD, due to the complex relationship between both.

Considering the rather complex self-assembly behavior of **TATA-SDA** in DCE, which depends on concentration, temperature, time and matter state conditions, the irradiation with circularly polarized light were carried out under the four conditions previously studied:

1) at 2.3 mM and room temperature (V. 2);

2) at 2.3 mM with variable temperature (V. 3);

3) at 11.7 mM (V. 4);

4) in thin films obtained by drop-casting a 2.3 mM solution at room temperature (V. 5).

For conditions 1 and 2, CD analyses were performed at -10°C, *i.e.* the temperature needed to promote aggregation into hydrogen-bonded stacks whilst for conditions 3 and 4, analyzes were performed both at room and low temperature since helical HB assemblies are already present at rt. Another fundamental distinction exists between these conditions: conditions 1 and 4 involved the light irradiation of solutions composed of monomers and non-specific aggregates, before to undergo self-assembly upon cooling or evaporation. For conditions 2 irradiation occurs during aggregation (irradiation is performed under cooling), and for conditions 3 irradiation occurs on already (partly) hydrogen-bonded **TATA-SDA** molecules. This variety of conditions will allow us to probe if the chiral induction from CPL can be transferred to already formed HB stacks of **TATA-SDA**. Pay attention that the amount of radicals generated and the structure of the assemblies has not been precisely determined under all these different conditions, the aim was rather to find a condition suitable for chirality induction.

For each condition, the set of experiments are compiled in a table together with the relevant parameters such as the setup employed, its surface optical power, its degree of circular polarization, the (post-)irradiation time as well as the (post-)irradiation and measurement temperatures. The result in terms of CD is also given for all entries: “No CD” for CD-silent samples; “CD/LD” for CD likely issued from LD; “CD” for CD likely emanating from biased supramolecular chirality. “CD/LD” and “CD” might both be mentioned for a given sample, when the contribution of the LD was not enough to give a rationale to all the CD bands of a given CD spectrum.

V. 2. At 2.3 mM and room temperature

Results of CD measurements of CPL irradiations for samples of **TATA-SDA** at 2.3 mM and room temperature are listed in **Table IV.3**. It was the simplest condition and also the one reported by Kim *et al.*[1]

Table IV.3 Recap chart of CD measurements made on various samples of **TATA-SDA** (batch V) at 2.3 mM in DCE irradiated at constant temperature (room temperature or thermostatted at 20°C). Container of solutions, lamp optical power, irradiation time and measurement temperature were notably modulated. The light irradiation was carried out by the setup B at a surface optical power of 33.7 mW/cm^2 and a degree of circular polarization of 83%.

Entry		**Irradiated solution container**	**Irradiation time (min)**	**Measurement temperature (°C)**	**Result**
1	a	2 mm quartz cuvette	1	-10	CD/LD
	b		5		
	c		10		
2	a	2 mm quartz cuvette	1	≈ -20	CD/LD
	b		5		
	c		10		
3	a	4 mL glass vial without cap	1	-15	CD/LD
	b		5		

Samples were light irradiated at room temperature and analyzed at low temperature to trigger the formation of HB stacks. Only the batch V was used for these experiments, after checking the absence of cryptochirality as mentioned in **Figure IV.30**.

In conditions closest to those mentioned by Kim *et al.*[1] (entry 1), CD and LD have similar shapes, likely the proof of macroscopic anisotropies due to long aggregates (**Figure IV.34a**). Unfortunately, since the shape and the relative intensity of the CD accurately follow the same pattern than the LD, no biased supramolecular chirality seemed to have been arisen.

To probe the contributions from LD and artifacts, samples were placed after irradiation in a freezer below -20°C, that might provide a stronger self-assembly (entry 2). Out of the freezer, the very low temperature of the cell, coupled with the strength of self-assemblies

revealed by the formation of a gel, allowed to analyze samples in a rotative non-thermostatted cell-holder, able to quickly rotate (330 rpm) the cell during CD measurement. Since a gel is still present at the end of the measurements, it was assumed that self-assemblies kept their integrity all along the CD analysis. CD and LD signals, displayed in **Figure IV.34b**, have both a sawtooth-like waveform, and the envelope that they drew had the same shape than CD/LD signals in **Figure IV.34a**. Since a CD stemming from a biased supramolecular chirality is invariant upon rotation[26], these signals proved that the CD/LD observed in **Figure IV.34a** and elsewhere mainly came from LD and artifacts.

We were also interested to avoid any interference between the CPL beam and the solution. Accordingly, the experiments listed in the entry 3 of **Table IV.3** allowed a direct light irradiation of solutions, through the top of an uncapped vial. Nevertheless, again CD/LD arose upon cooling this sample down to -15°C.

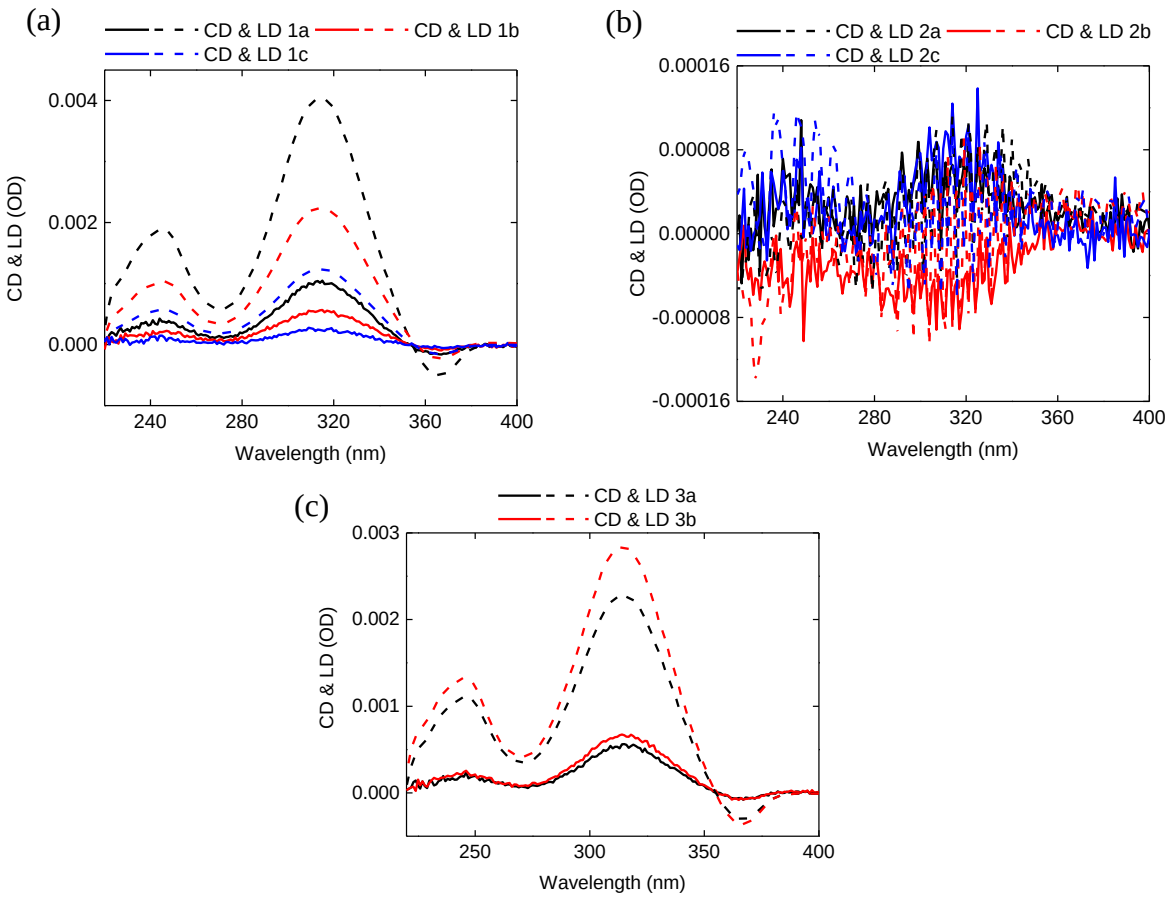

Figure IV.34 CD + LD (a–c) analyses of **TATA-SDA** at 2.3 mM in DCE, light irradiated at 20°C (**Table IV.3**). (b) analyses were measured at about -20°C in a non-thermostatted rotative cylindrical cell. For information, the legend reads: "CD & LD 1a" = "CD" (solid line) "& LD" (dashed line) of the experiment described in the entry "1a" of the previous table.

Another set of conditions involved the light irradiation of samples upon cooling from 60°C to 20°C. However, these conditions may actually be assimilated to light irradiation at 20°C, since no distinction was evidenced previously in the subsection IV. 2. Again, only CD induced by LD contributions were observed under these conditions (**Table SIV.8** and from **Figure SIV.60** to **Figure SIV.63**).

V. 3. At 2.3 mM with variable temperature

The production of **TATA-SDA**$^{\bullet+}$ in the non-specific aggregates prior to HB stacking by cooling appeared to be inefficient method to bias the supramolecular chirality. Thus, variable

temperatures for the irradiation of 2.3 mM solutions were investigated. In our mind, it could more favorably trigger the chiral induction process by generating **TATA-SDA**$^{\bullet+}$ concomitantly to the formation of HB stacks. Also, in the case of a putative mechanism involving a key chiral interaction between light and a nucleus or a nascent aggregate, performing the irradiation upon cooling might be interesting. Since kinetic contributions were likely highlighted upon cooling (*cf.* **Figure IV.10**), the time after irradiation and the cooling rate were also modulated. Experiments are listed in **Table IV.4**.

Table IV.4 Recap chart of trials with **TATA-SDA** (batch VI) at 2.3 mM in DCE irradiated upon cooling from 60°C to -15°C. The light irradiation was carried out by the setup B with the solution in a thermostatted 0.1 mm quartz cuvette. Lamp optical power and the irradiation time were notably modulated. The degree of circular polarization is equal to 83% (for a surface optical power of 33.7 mW/cm^2) or 86% (for a surface optical power of 3.4 mW/cm^2). The CD and LD were measured at -15°C.

Entry			**Lamp optical power (mW/cm^2)**	**Irradiation time (min)**	**Result**
1	a	i	33.7	15	CD/LD
		ii		120	
	b	i	3.4	15	
		ii		360	

These experiments were carried out with a fine control of temperature during light irradiation, thanks to CD thermostatted cell-holder illustrated in **Figure SIV.57**. Two different lamp optical powers (33.4 and 3.4 mW/cm^2) were also tested for a long and short irradiation time (15 and 120 min at high power and 15 and 360 min at low power). CD/LD results are depicted in **Figure IV.35**, and the different gradients of temperature are described in **Figure SIV.63**.

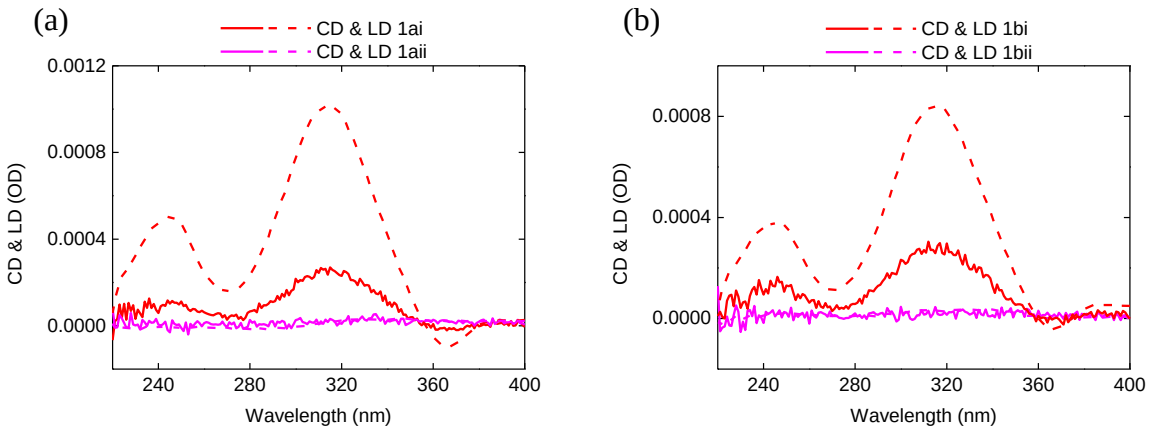

Figure IV.35 CD + LD (a–b) analyses of **TATA-SDA** at 2.3 mM in DCE, irradiated with a surface optical power of 33.7 (a) or 3.4 mW/cm^2 (b) and an irradiation time of 15 minutes (i) or 120 (33.7 mW/cm^2) /360 (3.4 mW/cm^2) minutes (ii).

Unfortunately, the result is that CD has the exact LD shape, devoid of any hints of CD bands arising out of biased supramolecular chirality for short irradiations (1ai and 1bi in red). In case of the long time of irradiations (1aii and 1bii in pink), both CD and LD are null. In these last conditions, the amount of radical cationic species is likely higher, and limits the formation of long aligned aggregates (as observed for the shortening of the particles).

Unlike Kim *et al.*[1], the conditions at a concentration of 2.3 mM probed in this study did not result in traces of biased supramolecular chirality upon CPL irradiation. It might suggest a complex behavior of the **TATA-SDA** self-assembly, with kinetic contributions not explored in this first set of experiments or the possibility that the experiments made by Kim *et al.* have been actually performed under different conditions.

V. 4. At 11.7 mM

Knowing that at higher concentration, **TATA-SDA** slowly aggregates into insoluble particles constituted of hydrogen-bonded stacks, 11.7 mM solutions were examined further in the hope to get CPL-induced CD spectra.

Table IV.5 Recap chart of trials, with **TATA-SDA** (batch VI) at 11.7 mM in DCE irradiated at 20°C or upon cooling. Lamp optical power, irradiation time as well as irradiation and measurement temperatures were notably modulated. The light irradiation was carried out by the setup B with the solution in a thermostatted 0.1 mm quartz cuvette. Lamp optical power and the irradiation time were notably modulated. The degree of circular polarization is either equal to 83% (for a surface optical power of 33.7 mW/cm^2), 84% (for a surface optical power of 16.9 mW/cm^2) or 86% (for a surface optical power of 3.4 mW/cm^2).

Entry				**Lamp optical power (mW/cm^2)**	**Irradiation time (min)**	**Irradiation temperature (°C)**	**Measurement temperature (°C)**	**Result**
1	a			33.7	185	20	20	No CD
	b			16.9	144			
	c			3.4	1281			
2	a	i		33.7	15	60 to 20	-15	CD/LD
		ii				60 to -15		
	b	i	I	3.4	15	60 to 20		
			II		15	60 to -15		
		ii			360	60 to -15		

In keeping with the kinetic contributions highlighted at 20°C, long light irradiations were first undertaken at different lamp powers (33.4, 16.9 and 3.4 mW/cm^2 for 185, 144 and 1281 min, respectively) and room temperature (entry 1, **Table IV.5**). It likely broke the giant aggregates (as evidenced by the absence of LD), but did not trigger biased aggregates towards one handedness.

Next, a set of experiments was undertaken with a fine control of temperature during light irradiation (entry 2, **Table IV.5** and **Figure SIV.64**), CD/LD results are depicted in **Figure IV.36** and gradients of temperature are described in **Figure SIV.64**. Unfortunately, all conditions gave more or less the same result: a CD of the exact LD shape, devoid of any hints of CD bands coming from a biased supramolecular chirality.

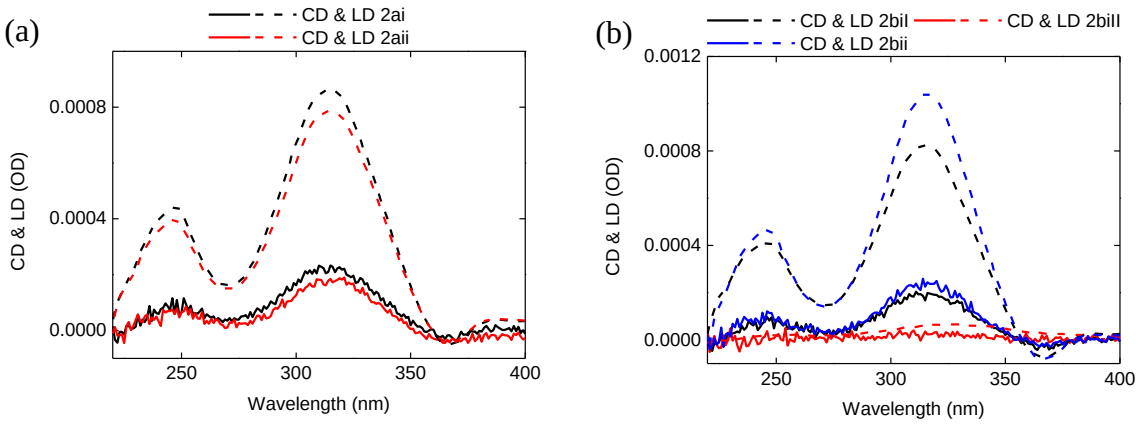

Figure IV.36 CD + LD (a–b) analyses of **TATA-SDA** at 11.7 mM in DCE at -15°C, light irradiated with a surface optical power of 33.7 (a) or 3.4 mW/cm^2 (b), and variable temperature from 60°C to 20°C or -15°C.

It is important to note that for the aforementioned experiments, the spectroscopic measurements were carried out immediately after the light irradiation, preventing from an investigation of structures formed in the long run upon ageing. It was the goal of the following experiments (**Table IV.6**), where solutions of **TATA-SDA** at 11.7 mM in DCE were irradiated from 60°C to room temperature (upon aggregation), for a short (0.5 min, 3a) or an intermediate time (5 min, 3b), and analyzed immediately (3ai and 3bi) or after ageing at rt for several hours (3aii and 3bii).

Table IV.6 Recap chart of trials, with **TATA-SDA** (batch V) at 11.7 mM in DCE irradiated upon cooling from 60°C to rt. Lamp optical power, irradiation time as well as irradiation and measurement temperatures were notably modulated. The light irradiation was carried out by the setup B with the solution in a 2 mm quartz cuvette. Lamp optical power and the irradiation time were notably modulated. The degree of circular polarization is either equal to 83%, for a surface optical power of 33.7 mW/cm^2).

Entry			**Irradiation time (min)**	**Ageing in the dark before measurement**	**Measurement temperature (°C)**	**Result at**	
						20°C	-10°C
3	a	i	0.5	No	20	No CD	
		ii		Yes, 45h at rt	20 & -10	**CD/LD + CD**	CD/LD
	b	i	5	No	20 & -10	CD/LD	CD/LD
		ii		Yes, 65h at rt	20 & -10	No CD	No CD

Samples irradiated for 5 minutes were not of interest (CD/LD for 3bi or no CD/LD at all for 3bii, even at -10°C; **Figure IV.37c**). Conversely, the solution irradiated for 30 seconds from 60°C to rt then kept at room temperature for 45h exhibited at 20°C an additional CD band between 350 and 380 nm, whereas the same solution lacking ageing does not show this band (**Figure IV.37a**). This Cotton effect was in addition insensitive to rotation of the cell. Upon analysis of this solution at -10°C, LD appears on the whole spectrum range which precludes the determination of the fate of this band upon cooling (**Figure IV.37b**). This can be due to the effects of a strong LD because of additional bundling of oriented and disoriented aggregates into unbiased scaffolds formed upon cooling. This CD_{iso} signal observed at 20°C is likely the sign of an efficient influence of CPL, probably by taking advantage of the slow interaction between radicals and neutral **TATA-SDA** monomers or aggregates having interacted with CPL, and the subsequent assembly occurring during the ageing time. The fact that the same phenomenon was not observed for a ten times longer irradiation suggests the requirement of a finely-tuned time of irradiation. Anyway, this experiment, coupling light irradiation under ageing of the solution at room temperature in the dark for almost two days, is promising and must be reproduced and repeated with CPL of opposite handedness to further ascertain the presence of helically-biased TATA assemblies.

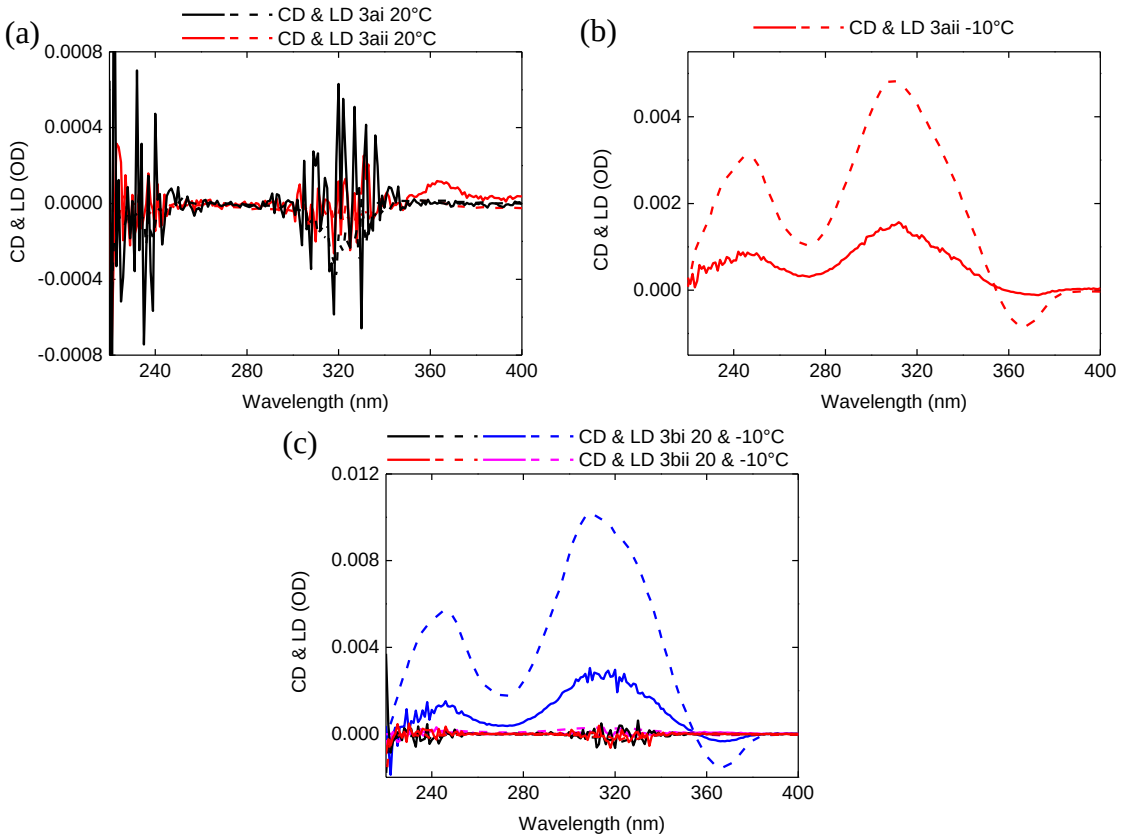

Figure IV.37 CD + LD (a–c) analyses of **TATA-SDA** at 11.7 mM in DCE, light irradiated with variable temperature, from 60°C to room temperature, and analyzed at 20°C (a) or -10°C (b–c). (a) analyses were measured in a rotative cylindrical cell.

V. 5. As thin film

A possible drawback of the previous conditions is the fact that the degree of association reached after irradiation is uncomplete. To maximize the probability of co-assembly into hydrogen-bonded stacks, thin films were prepared by drop casting CPL-irradiated solutions of **TATA-SDA** at 2.3 mM in DCE. In this way, **TATA-SDA** solutions, were light irradiated in a 2 mm rectangular quartz cuvette by the setup A, with a surface optical power of 7.9 mW/cm^2, then drop casted on 0.1 mm lamellar quartz cell and evaporated under the fume hood (**Table IV.7**, results depicted in **Figure IV.38**).

Table IV.7 Recap chart of trials with **TATA-SDA** (batch VI) at 2.3 mM in DCE irradiated by the setup B with a surface optical power of 33.7 mW/cm^2 (degree of circular polarization equal to 83%), at rt and in a 2 mm quartz cuvette. The solution was then drop-casted on lamella of 0.1 mm quartz cell to be analyzed as thin films at 20°C. The irradiation time was modulated.

Entry		**Light irradiation time (min)**	**Result**
1	a	0.5	CD/LD
	b	5	
	c	10	
	d	30	

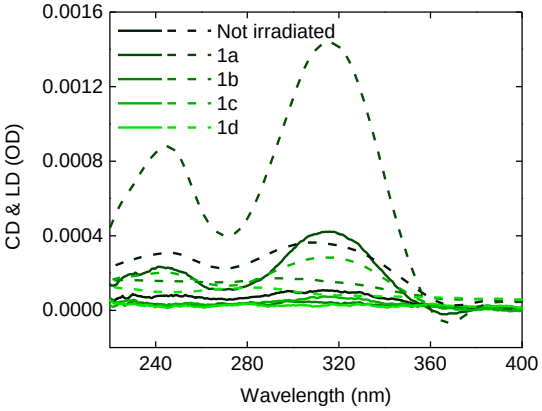

Figure IV.38 CD + LD analyses of **TATA-SDA** at 2.3 mM in DCE, irradiated in a 2 mm rectangular quartz cuvette by the setup A, with a surface optical power of 7.9 mW/cm^2, then drop casted on 0.1 mm lamellar quartz cell and evaporated under the fume hood.

Even though a low amount of radicals is generated in DCE, the co-assembly by H-bonding interactions of neutral and radical cationic species of **TATA-SDA** is highly probable. Nevertheless, only CD contaminated by LD were detected in the probed thin films. Furthermore, it appears that longer a solution was irradiated, the weaker the CD/LD signals in the film. It could indicate that the light irradiation has an impact on the formation of long aligned aggregates, in agreement with some of the aforementioned experiments and the fact that disassembly of HB stacks of **TATA-C13** was observed in thin films. However, it is not known if in the present conditions, the amount of radical generated before casting is enough to induce such a phenomenon.

Alternatively, it can be envisaged to irradiate the solutions during the drop casting process to generate radicals concomitantly to the formation of HB stacks as attempted in the aforementioned experiments for which solutions were irradiated at variable temperatures.

VI. Conclusion

Towards our objective to design an absolute asymmetric catalyst constructed with CPL-biased TATA scaffolds, the major preliminary stages were to investigate TATA self-assemblies, and then to be able to reproduce and understand the CPL control of supramolecular chirality of **TATA-SDA** aggregates. With this purpose, **TATA-SDA** has been synthesized in three steps and fully characterized. A first assessment of **TATA-SDA** in solution highlighted the presence of PDA, as well as the way to remove it, and demonstrated the solubility of **TATA-SDA** at mM in toluene and chlorinated solvents, key for photo-oxidation and catalytic purposes.

The self-association properties were thus probed in toluene and chlorinated solvents. In toluene, **TATA-SDA** stacked into long one-dimensional hydrogen-bonded helical stacks. In 1,2-dichloroethane, **TATA-SDA** molecules were studied under four different conditions. At 2.3 mM and room temperature, **TATA-SDA** formed a stable solution composed of a significant fraction of non-hydrogen-bonded aggregates. Variable-temperature analyses of **TATA-SDA** in DCE at 2.3 mM outlined under cooling a reversible self-assembly into hydrogen-bonded stacks. At 11.7 mM, although **TATA-SDA** molecules were self-assembled and soluble in chloroform, the 1,2-dichloroethane solutions revealed that precipitation of giant aggregates made of bundles of hydrogen-bonded stacks occurs while non-hydrogen-bonded assemblies and free monomers remain in solution. Finally, a solution of **TATA-SDA** at 2.3 mM in DCE were drop-casted to yield thin films, of structure close to that of the powder, *i.e.* composed of almost fully hydrogen-bonded stacks. The degree of association was virtually total in the latter conditions but only partial at 2.3 mM under low temperatures and at 11.7 mM.

In 1,2-dichloroethane and chloroform, the production of **TATA-SDA**$^{\bullet+}$ by CPL was proven, but their impact on self-assemblies found as quite weak. CD measurements were carried out in DCE, solvent used by Kim *et al.*[1] and leading to an associated state of **TATA-SDA** similar to that found in chloroform except that the stacks tend to precipitate at 11.7 mM. The amount of radicals generated in DCE is also lower than that in $CHCl_3$. The study was performed by keeping in mind CD-related issues, such as spectrophotometer artifacts and anisotropies entailed by samples containing macroscopically-orientated aggregates. Towards finding the conditions of emergence of CPL-controlled supramolecular chirality, all previously

investigated conditions were involved (from soluble non-HB stacks to solid HB stacks, soluble HB stacks and mixed soluble and insoluble HB stacks), and many parameters were modulated, such as the light setup, its surface optical power, its degree of circular polarization, the (post-)irradiation time as well as the (post-)irradiation and measurement temperatures. Unlike Kim *et al.*[1], the CPL irradiation of 2.3 mM solutions strictly before self-assembly and thin film formation or upon cooling, appeared to be inefficient to bias the supramolecular scaffolds. On the other hand, irradiation of 11.7 mM solution and conservation in the dark for allowing further aggregation led to a CD devoid of LD influence. Further experiment, such as irradiation by *r*-CPL and *l*-CPL are necessary to demonstrate the possibility of biasing the handedness of **TATA-SDA** helical assemblies under these conditions.

Taken together, this study evidences that radical cationic species have only disordered and/or weak interactions in most solute conditions, and can hardly transfer a putative chirality. Moreover, this chirality is likely weak or even inexistent in **TATA-SDA**$^{\bullet+}$ monomers, due to their quite planar conformation, as well as in the non-specific aggregates that they may form with neutral species, devoid of directional H-bonding interactions. In fact, even the neutral monomers, whose interconversion energetic barrier between the two mirror-like propeller geometries is close to 4.8 kcal/mol,[3] may probably not keep a chiral configuration in excess after having interacted with CPL.

In light of these conclusions, one of the prerequisite to the CPL-controlled supramolecular chirality is likely to irradiate objects able to retain their chiral configuration while stacking. In the case of TATA molecules, nascent pre-nuclei aggregates, held together by a threefold hydrogen bond network, could be the solution. The light irradiation of molecules in the course of self-assembly could orientate the first helical conformation of their stack (the first pitch), thanks to a relatively weak stability of these objects before their elongation. This hypothesis is in line with the CD-active 11.7 mM solution after 2 days, irradiated upon ongoing association and let long enough to elongate and exhibit a possible enantioenrichment.

This is also consistent with three works recently published. Kim *et al.* revealed in 2020 the CPL-biased supramolecular chirality of one-dimensional stacks in thin films[4]. For this purpose, they irradiated molecules with a tris(stilbene)amine core and diacetylene side chains

linked by amide groups in non-chlorinated solutions (*i.e.* in benzene) “during self-assembly and solution casting”. They claimed that in the absence of triarylammonium radicals, the optomechanical force of CPL, through the interaction of its angular momentum with the dipolar moment of π electrons in the triarylamine core, induces a preferential handedness to the propeller-like molecules during the photoexcitation, which further acts as sergeants upon stacking. The negligible contributions of LD and spectrophotometer artefacts was attested by rotating and flipping the sample. In the same vein, Zou *et al.*[34] controlled the handedness of porphyrin-based assemblies by means of CPL irradiation during the first stages of a gelation process. Also, they asserted that the chiral bias comes from the deformation of the planar structure of porphyrin rings under the influence of CPL through photoresolution. Finally, Sánchez *et al.* demonstrated that irradiation with CPL of N-annulated perylenetetracarboxamides in the monomeric state at high temperature could induce, upon cooling, enantioenriched helical aggregates[35].

For TATA molecules, the key is likely a fine-tuned set of parameters to take advantage of ongoing aggregates at high concentration over ageing/cooling or at moderate concentration upon thin film formation. The catalytic purpose will impose to find a balance between: chirality induction to enough molecules/short aggregates to afford an almost complete excess towards one supramolecular chirality (to favor one diastereoisomeric environment to catalytic centers at the periphery of assemblies); chirality induction to a system remaining soluble.

VII. Supporting Information

VII. 1. Supplementary Figures

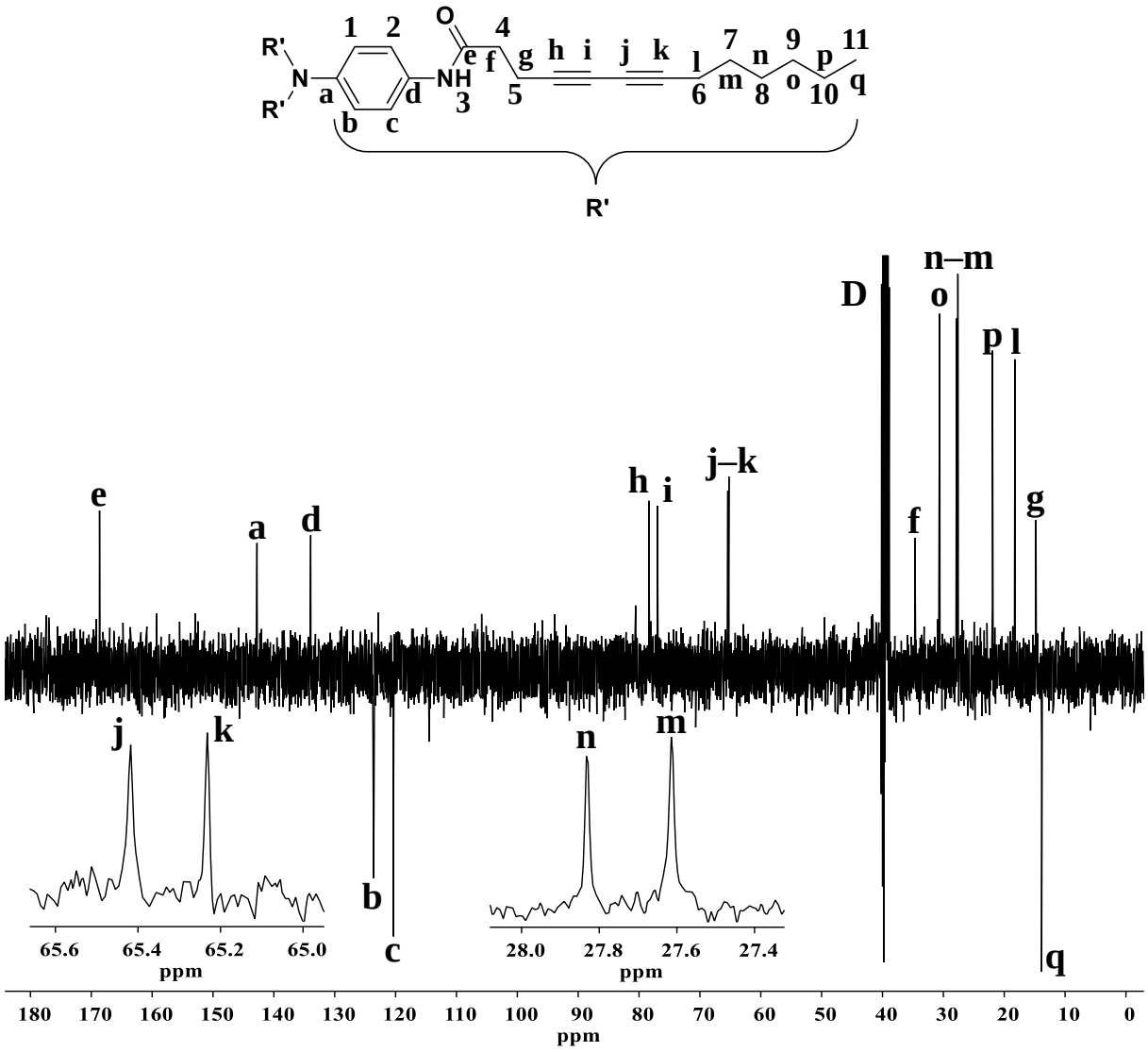

Figure SIV.39 $^{13}C\{^{1}H\}$–JMOD NMR analysis of **TATA-SDA** in DMSO-d_6 (D is resonance peak for residual DMSO).

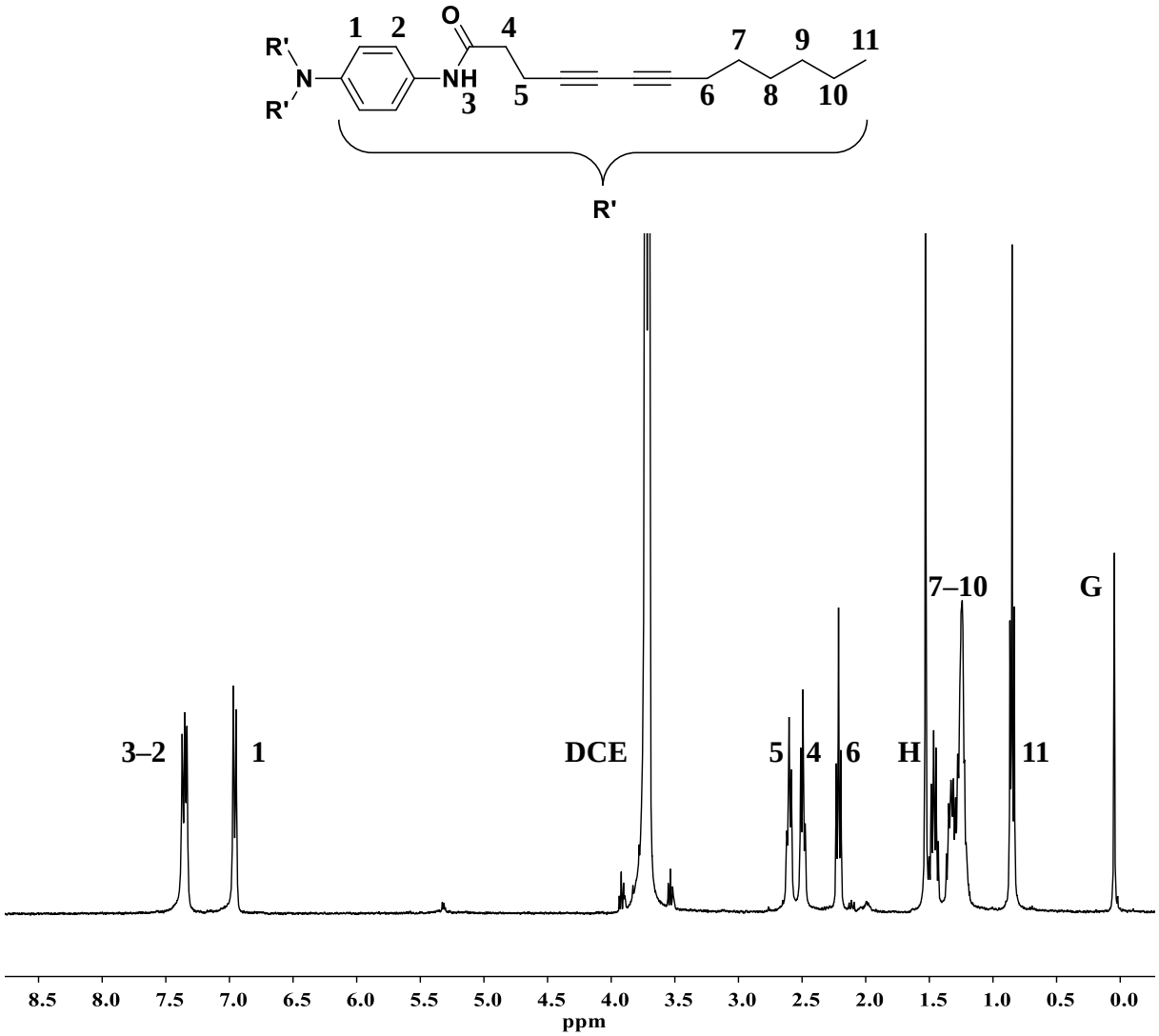

Figure SIV.40 ^{1}H NMR analysis in DCE-d_4 of **TATA-SDA** (DCE, H and G are resonance peaks for residual DCE, water and silicone grease, respectively).

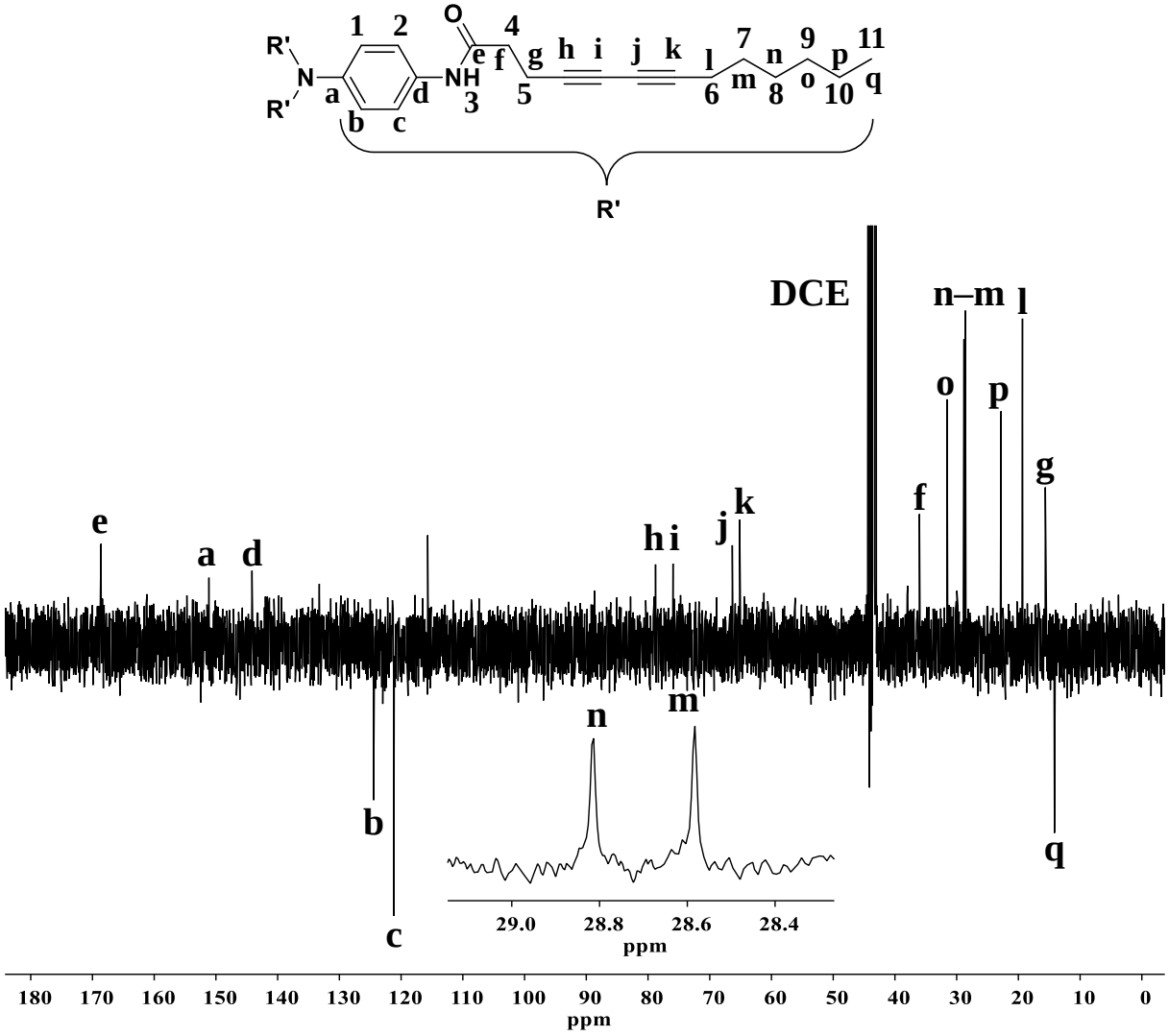

Figure SIV.41 $^{13}C\{^{1}H\}$–JMOD analysis of **TATA-SDA** at 2.3 mM in DCE-d_4.

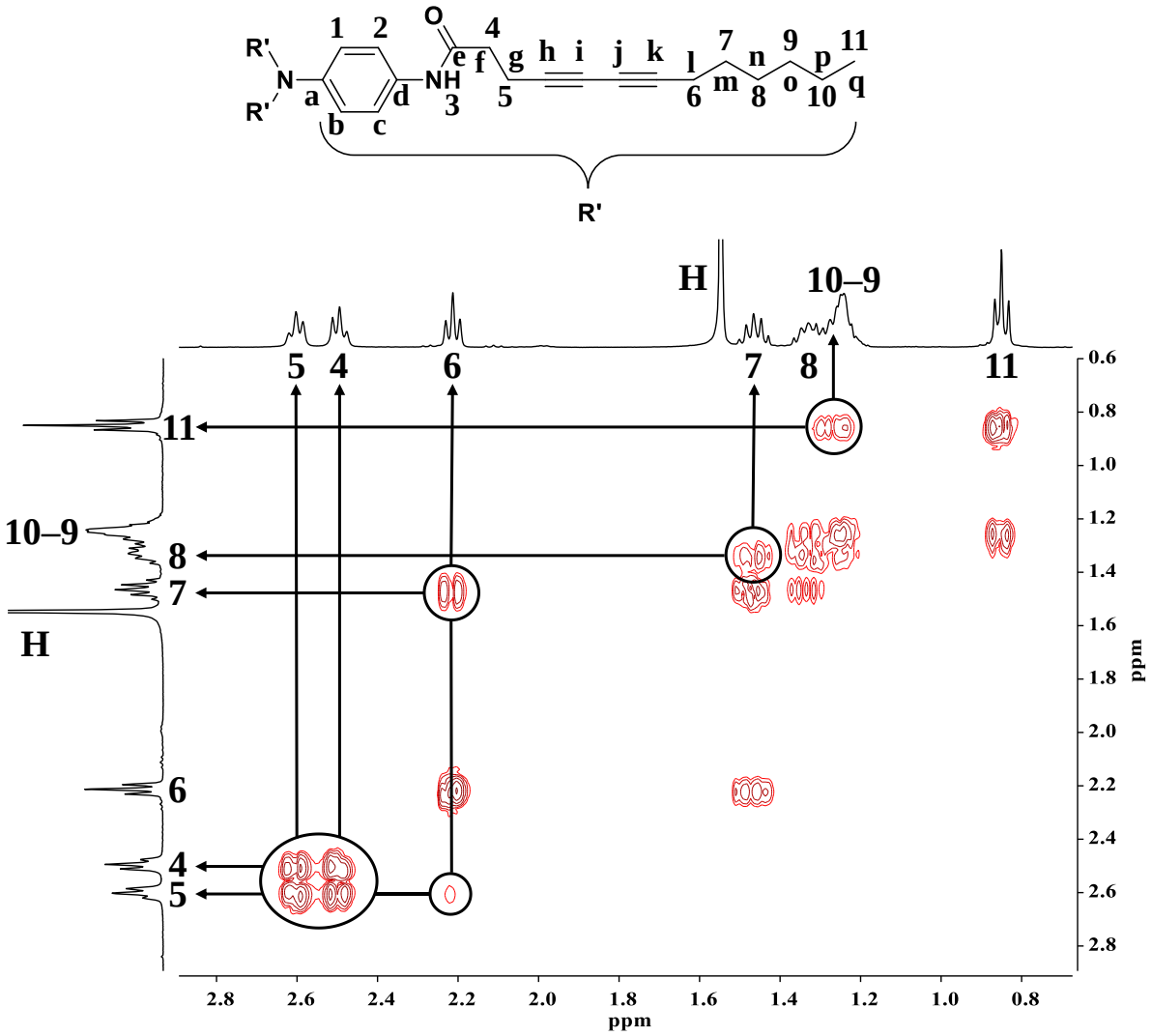

Figure SIV.42 ^{1}H–^{1}H COSY NMR analysis in DCE-d_4 of **TATA-SDA**, zoom on the region of interest (H is resonance peak for residual water).

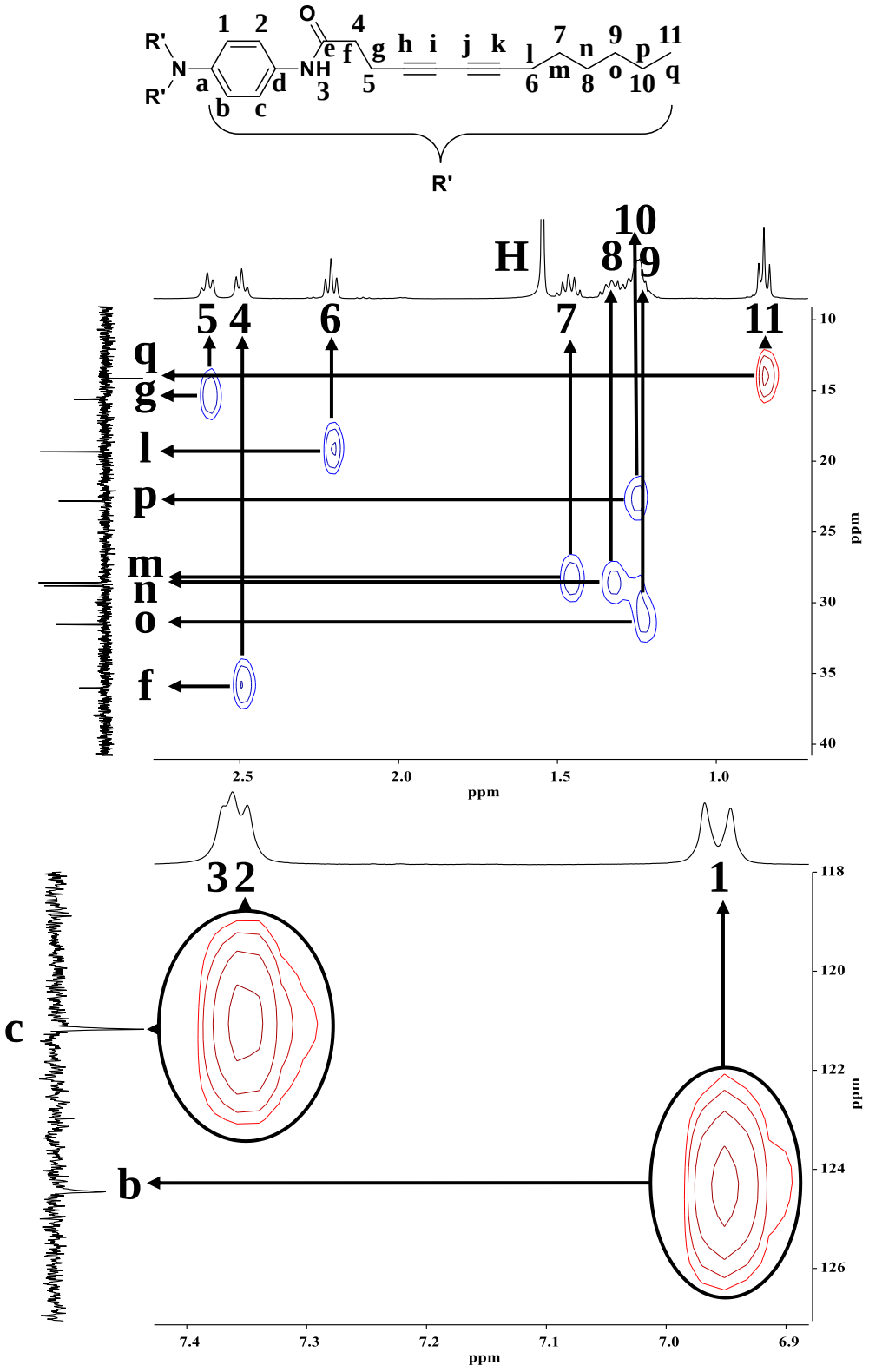

Figure SIV.43 ^{1}H–^{13}C edited HSQC NMR analysis in DCE-d_4 of **TATA-SDA**, zoom on the regions of interest (H is resonance peak for residual water).

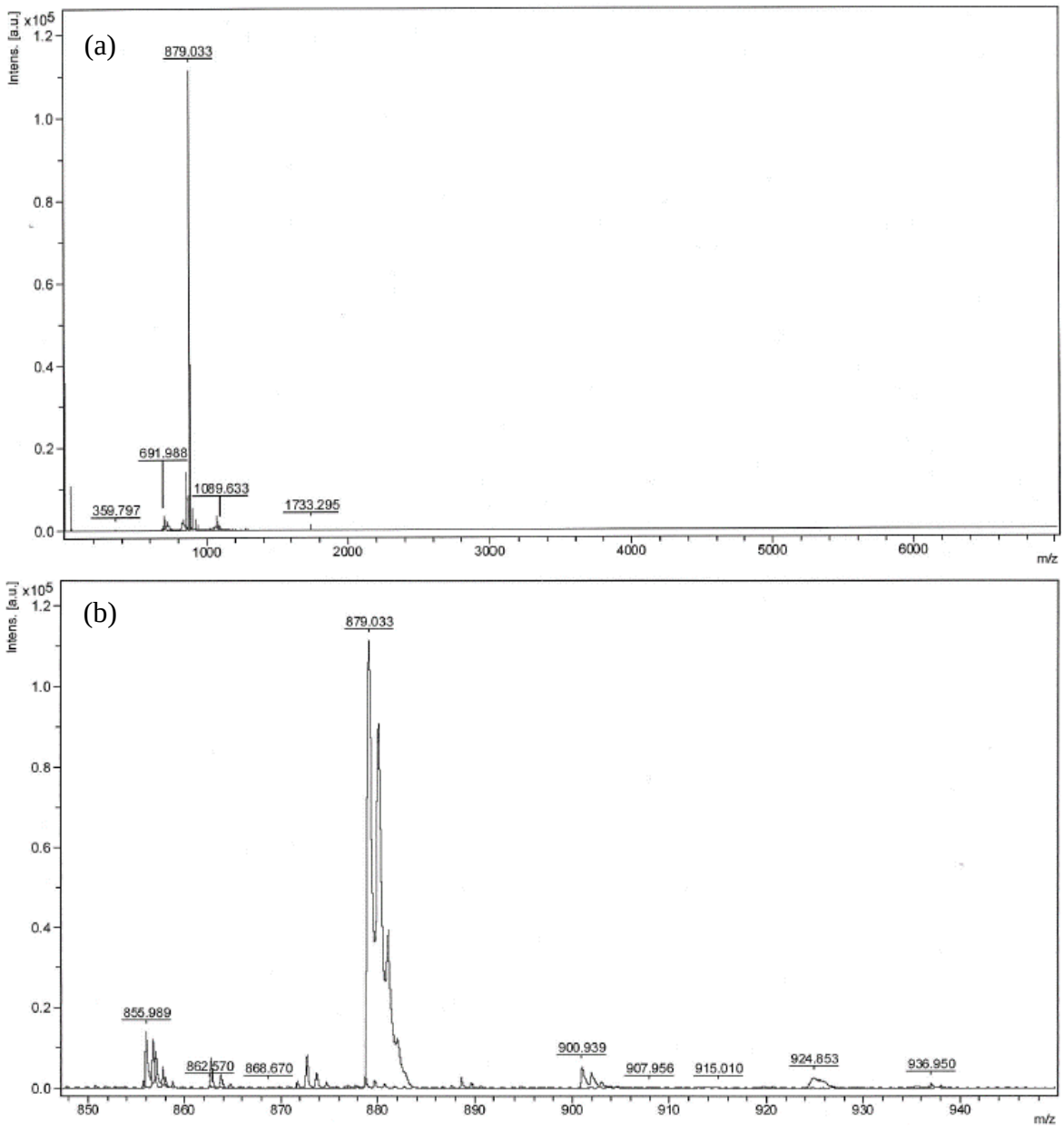

Figure SIV.44 (a–b) MALDI-TOF spectra of **TATA-SDA** acquired in α-cyano-4-hydroxycinnamic acid (CHCA) with NaI. (a) full region spectrum and (b), zoom at *m/z* ranging from 847 to 949. The main signals at 855.989 and 879.033 were assigned as [**TATA-SDA** + H]$^+$ and [**TATA-SDA** + Na]$^+$, respectively. The feeble peak at 1733.295 is attributed to [**TATA-SDA$_2$** + Na]$^+$.

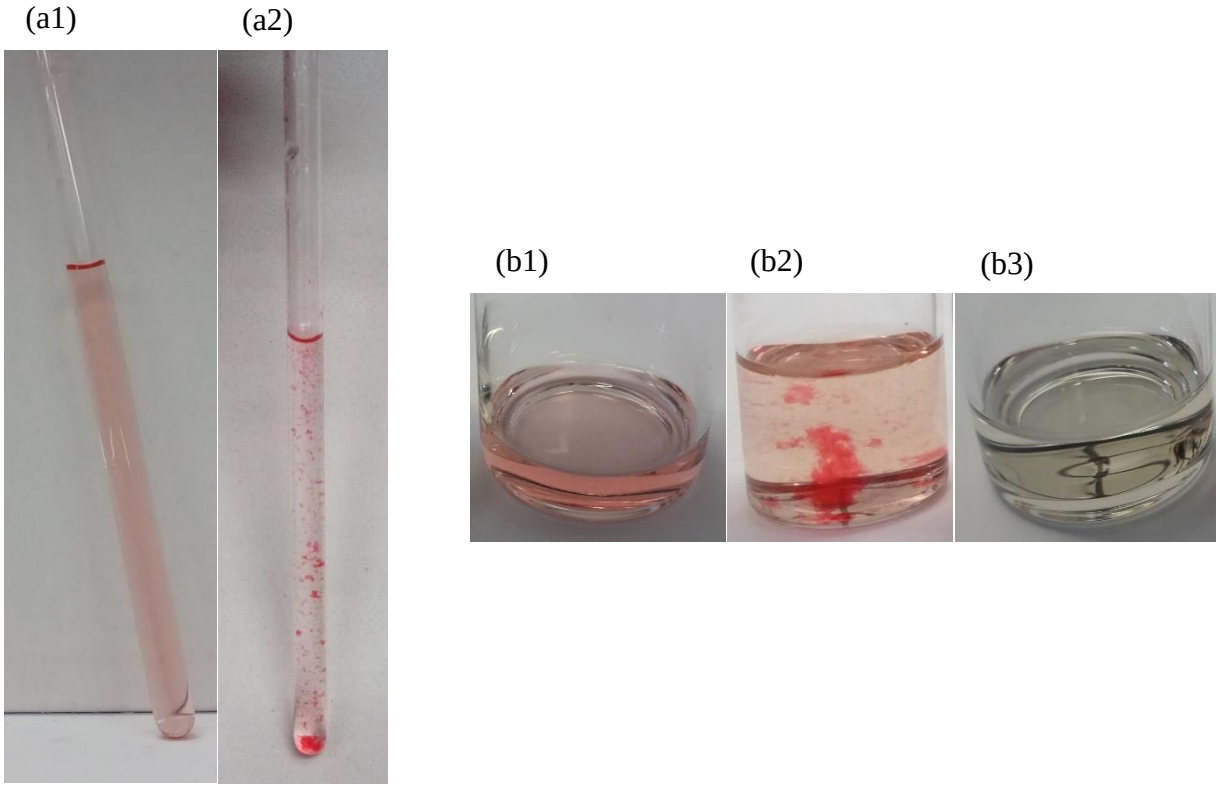

Figure SIV.45 TATA-SDA at 2.3 mM in DMSO (a) and 1,2-dichloroethane (b) after dissolution (a1 & b1) and the day after (a2 & b2). Filtration over a 0.20 µm filter removes red particles (b3).

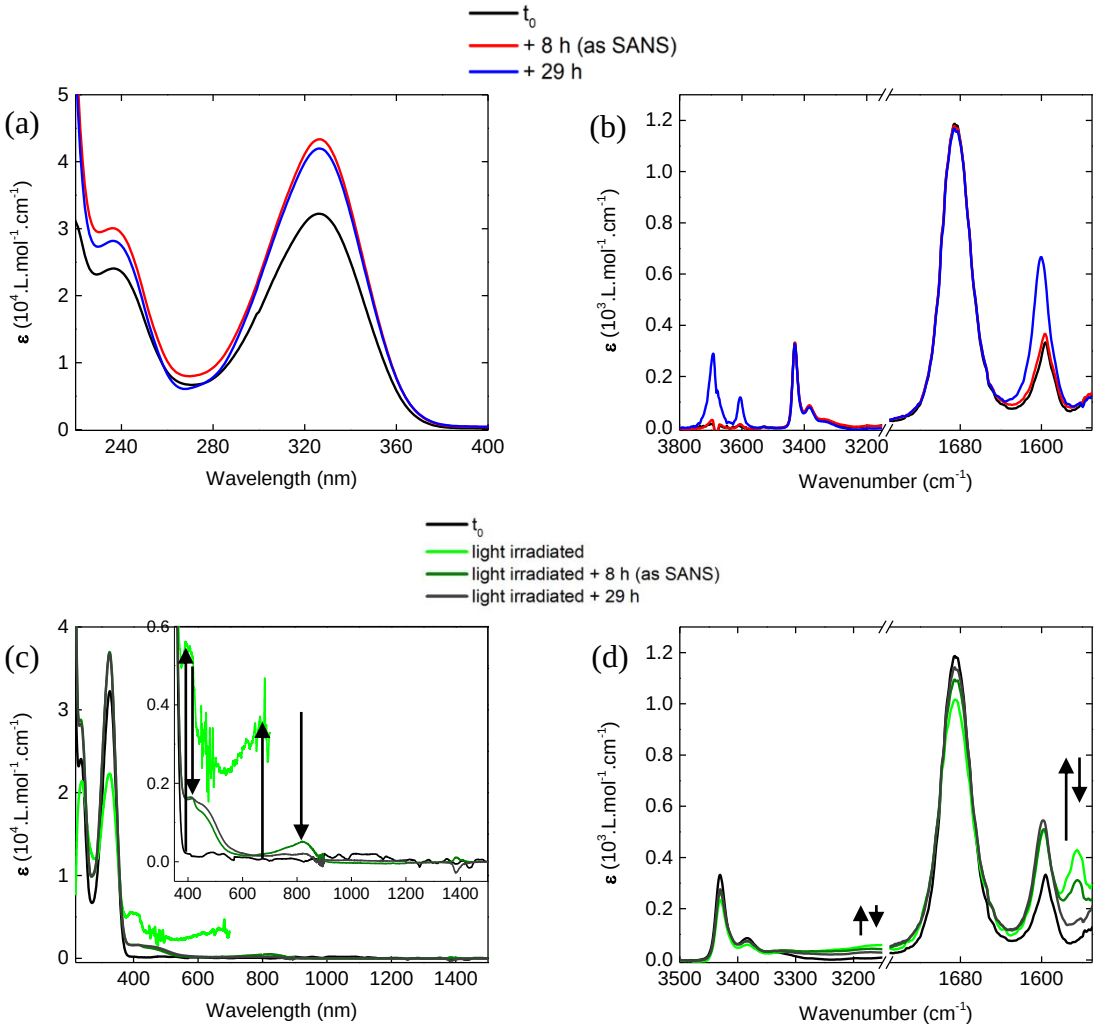

Figure SIV.46 (a–d) **TATA-SDA** at 2.3 mM in chloroform. (a) UV–Vis absorption and (b) FT–IR spectra with a zoom on the H_2O, N-H and C=O regions. The variation of intensity between measurements in (a) came from a little difference of liquid thickness across the optical pathlength, due to the change of lamellar quartz cells of slightly different pathlengths. Anyway, the ratio of molar extinction coefficient between the signals at about 320 and 240 nm are the same, ruling out photo-oxidation or assembly processes. (b) Signals between 3800 and 3600 cm^{-1} correspond to OH stretching vibrations of water, which contributes to the strong increase of the absorption at 1600 cm^{-1}, due to interactions between water and the carbonyl function of the **TATA-SDA** amide. The appearance of a new small absorption band at 3380 cm^{-1} in the N-H region, and not accompanied by a new signal in the C=O region, could be the sign of an interaction between N-H groups of **TATA-SDA** and Cl atoms of chloroform, smaller than DCE and maybe more disposed to approach **TATA-SDA**. (c) UV–Vis–NIR absorption and (d) FT–IR spectra before irradiation (black lines) and after light irradiation ("lime" green lines) and 8 or 29 hours of ageing ("olive" and "dark" green lines), in the same conditions than SANS

measurements. Zoom on the Vis–NIR region in (c). Zoom on the N-H and C=O regions in (d). The absorption band appearing at 1565 cm^{-1}, after light irradiation in chloroform, is the signature of **TATA-SDA**$^{\bullet+}$, through phenyl ring and C-N stretching vibrations. The solution was irradiated in a 2 mm rectangular quartz cuvette by the setup A, with a surface optical power of 7.9 mW/cm^2.

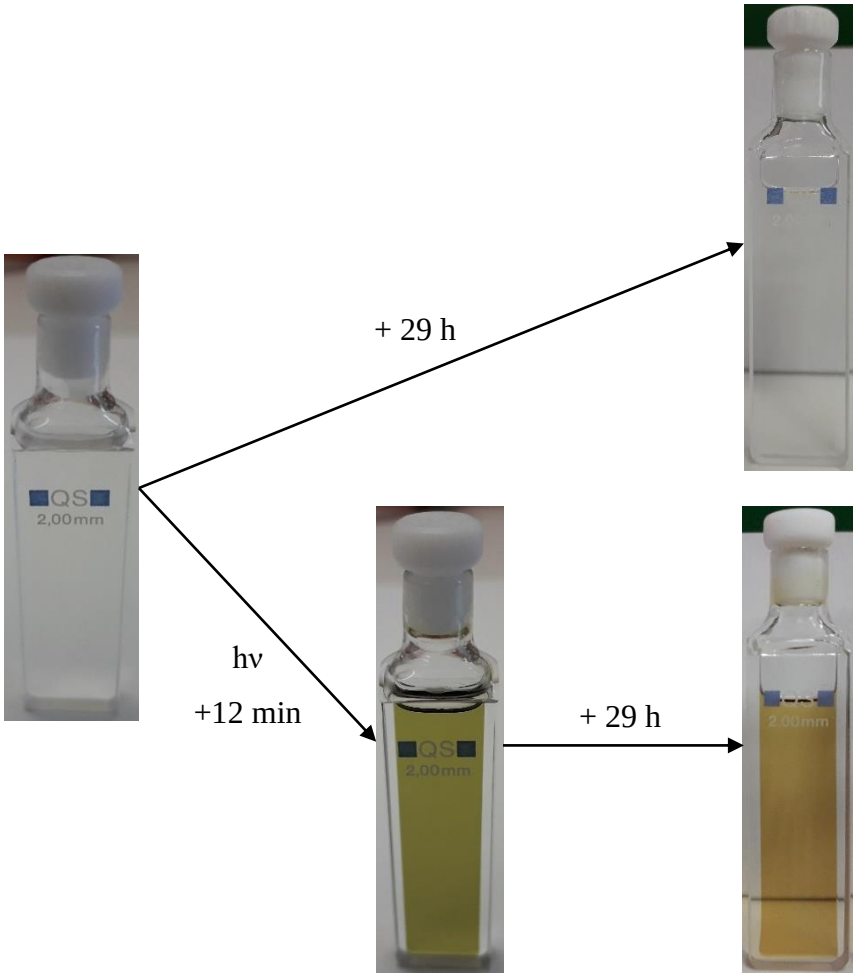

Figure SIV.47 TATA-SDA at 2.3 mM in chloroform. Solutions after light irradiation and/or ageing (solutions on the left and the middle are models and were not used for SANS, hence their volume are slightly different). The solution was irradiated in a 2 mm rectangular quartz cuvette by the setup A, with a surface optical power of 7.9 mW/cm^2.

(a)

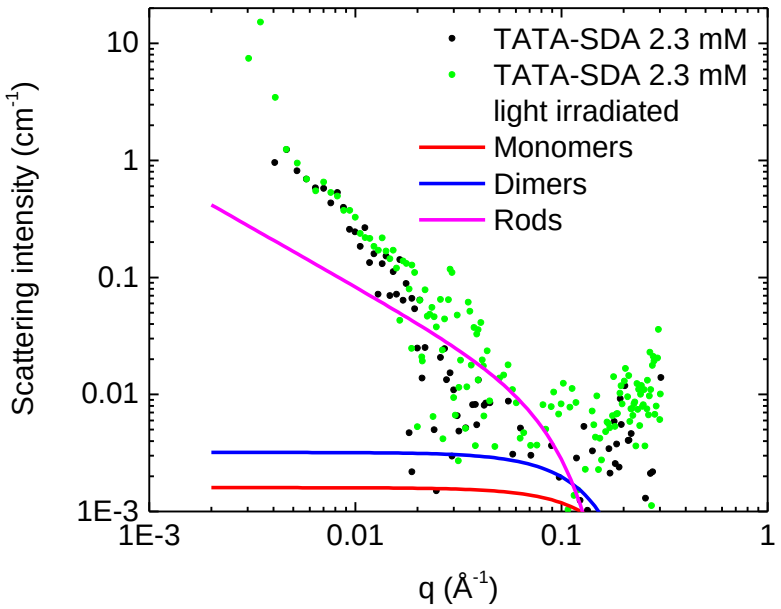

(b)

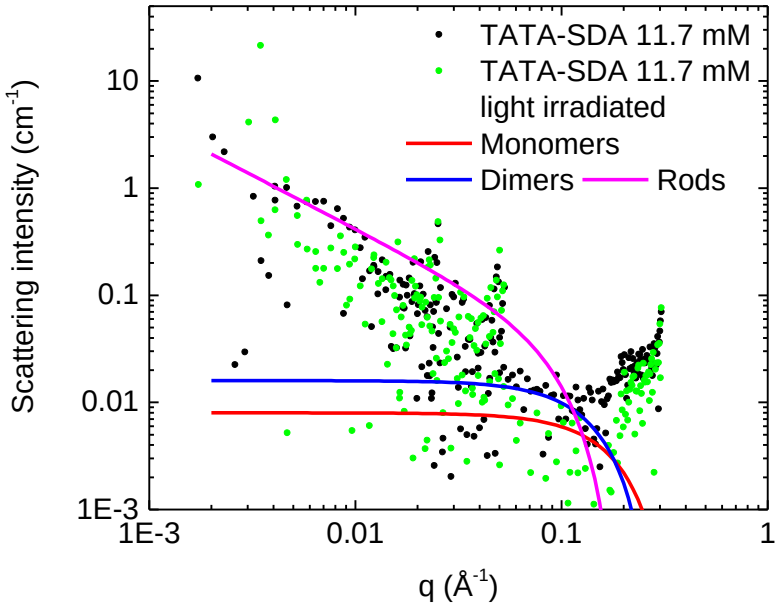

Figure SIV.48 SANS analyses of **TATA-SDA** at 2.3 (a) and 11.7 (b) mM in $CDCl_3$. Simulated spectra for monomers, dimers or infinitely long rigid rods of circular cross-section are shown together with the experimental spectra. The solutions were irradiated in a 2 mm rectangular quartz cuvette by the setup A, with a surface optical power of 7.9 mW/cm^2.

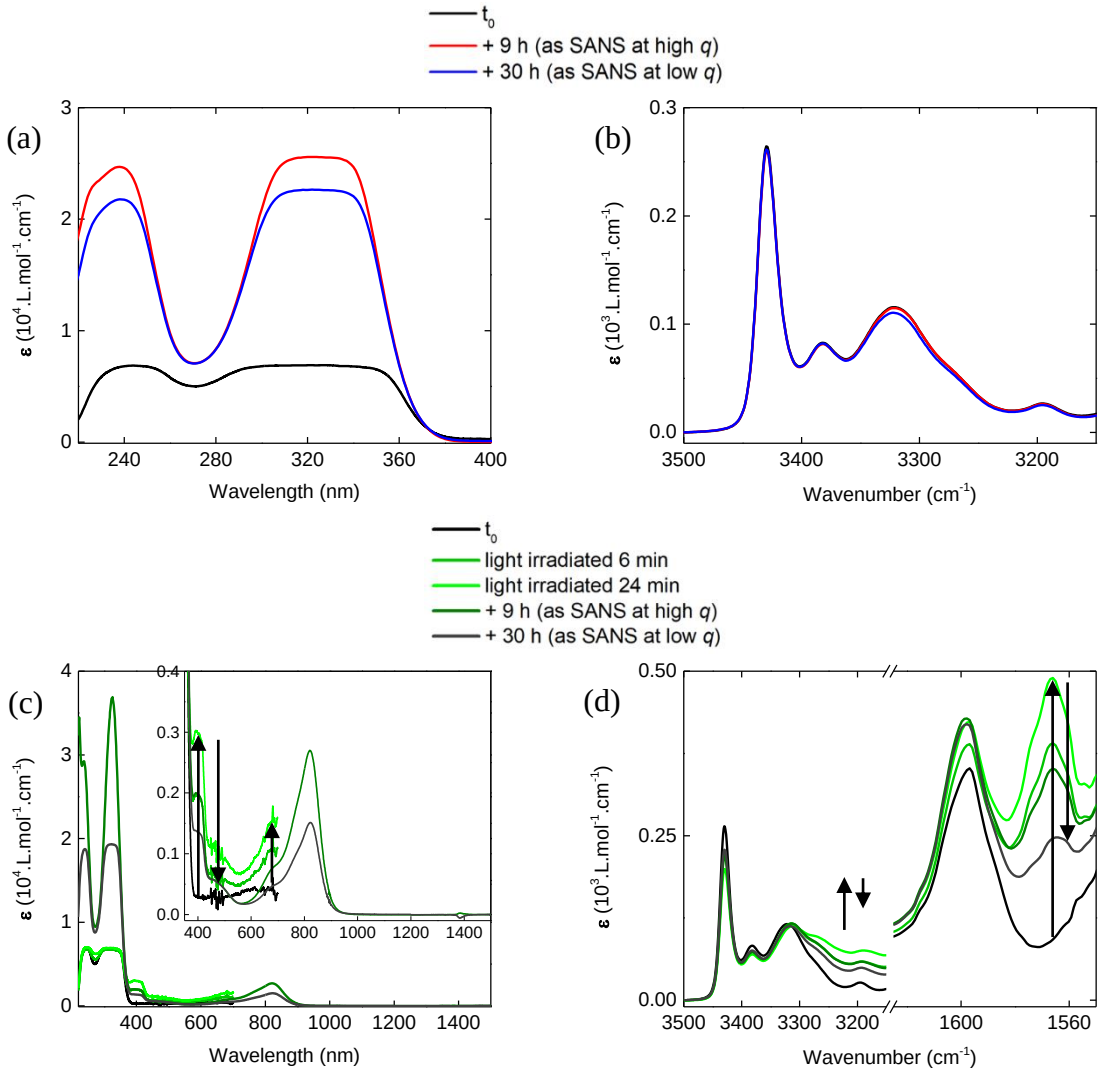

Figure SIV.49 (a–d) **TATA-SDA** at 11.7 mM in chloroform. (a) UV–Vis absorption and (b) FT–IR spectra with a zoom on the N-H and C=O regions. The variation of intensity between measurements in (a) came from a little difference of liquid thickness across the optical pathlength, due to the change of lamellar quartz cells of slightly different pathlengths. (c) UV–Vis–NIR absorption and (d) FT–IR spectra before irradiation (black lines) and after 6 or 24 of light irradiation ("lime" green lines) and 9 or 30 hours of ageing ("olive" and "dark" green lines), in close conditions compared with SANS measurements (light irradiation of 12 min, ageing of 9 and 30h). Zoom on the Vis–NIR region in (c). Zoom on the N-H and C=O regions (d). The solution was irradiated in a 2 mm rectangular quartz cuvette by the setup A, with a surface optical power of 7.9 mW/cm^2.

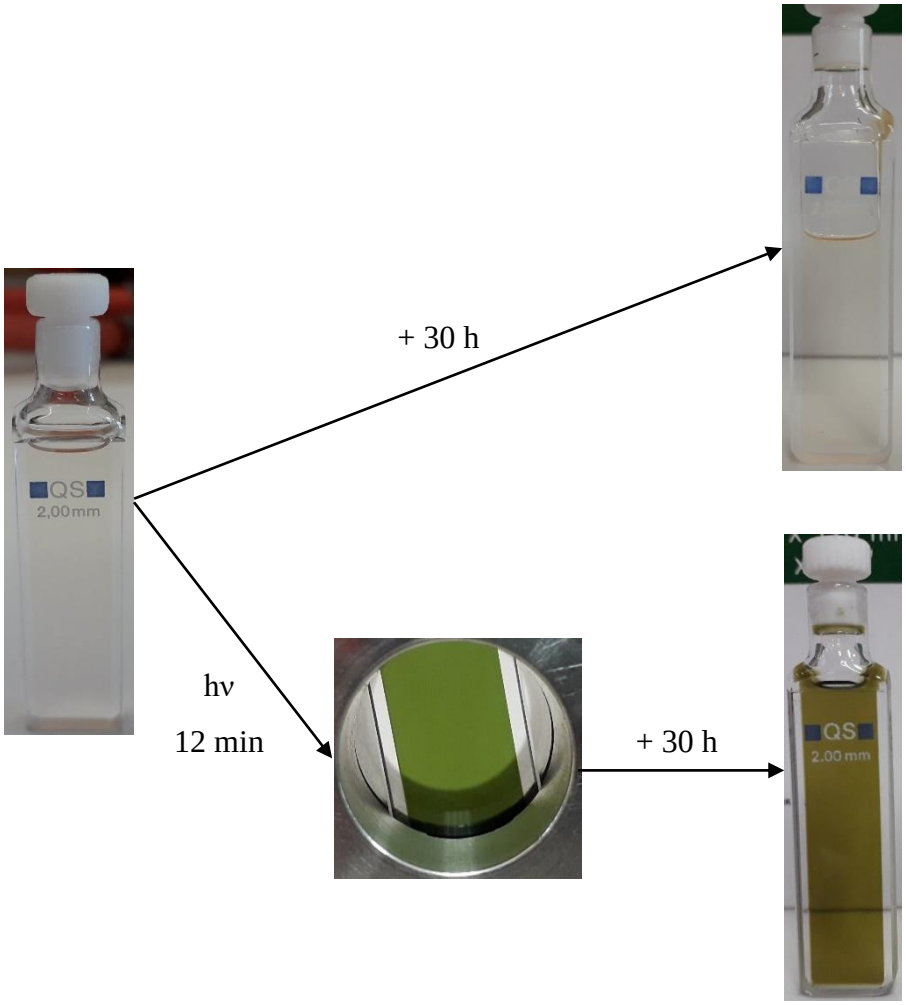

Figure SIV.50 TATA-SDA at 11.7 mM in chloroform. Solutions after light irradiation and/or ageing (solution on the left is model and was not used for SANS, hence its volume is slightly different). The photograph on the middle shows the solution in its cell holder rightly after SANS measurement. The solution was irradiated in a 2 mm rectangular quartz cuvette by the setup A, with a surface optical power of 7.9 mW/cm^2.

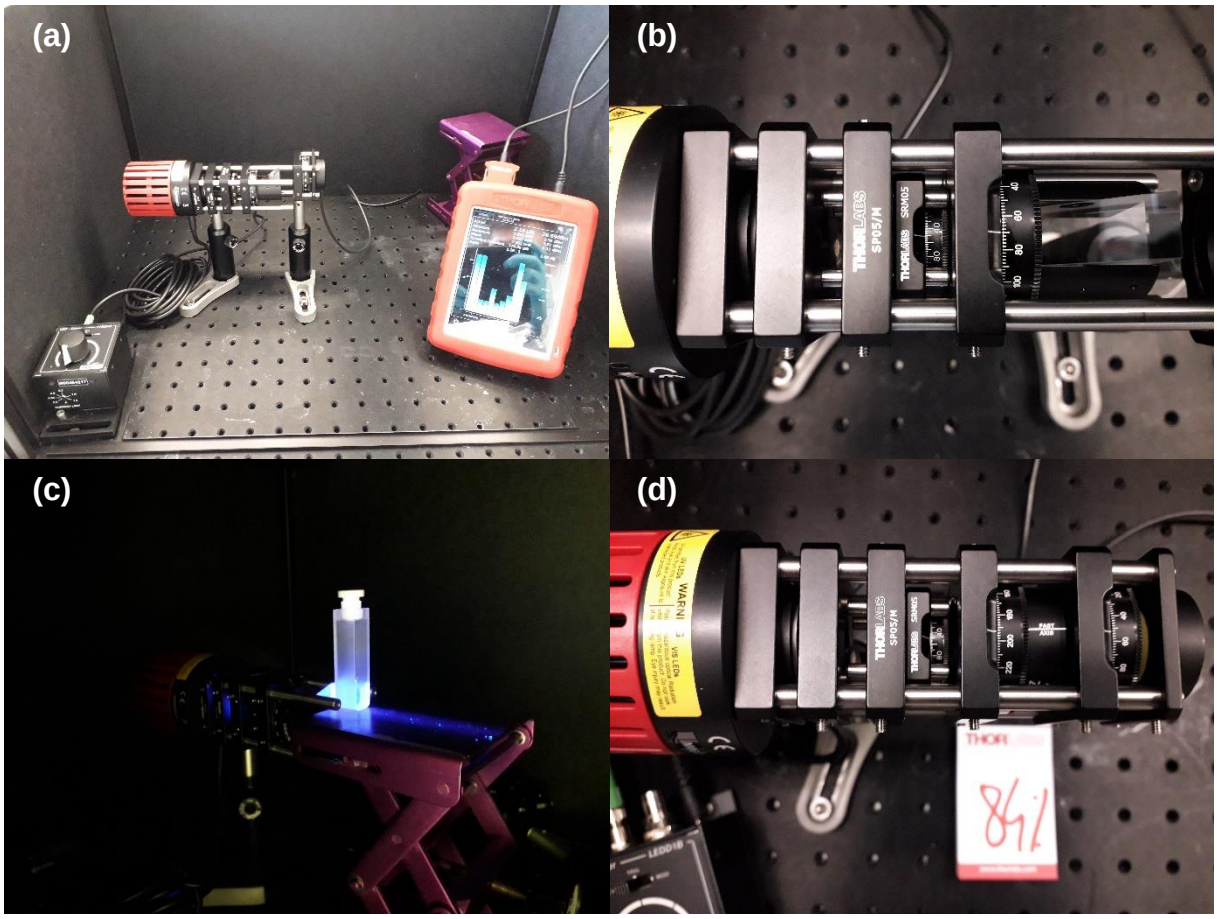

Figure SIV.51 Photographs of the setups A (a–c) and B (d) in an opaque optical enclosure, made of black hardboards, and installed on an aluminum breadboard. From left to right in the picture (a) or (b), the setup A is composed of a LED (in red), a condenser lens, a linear polarizer (in a cage rotation mounting) and a quarter-wave Fresnel rhomb retarder (also in a cage rotation mounting); from left to right in the picture (d), B is composed of a LED, a condenser lens, a linear polarizer (like A) and a quarter-wave plate specially designed (instead of a Fresnel rhomb retarder like in A). The components following the quarter-wave plate in picture (a) and (d) are a linear polarizer and a photodiode, linked to an optical power meter console, visible in the picture (a) on the right. These two components served to measure the optical power of the light emitted by setups A and B, as a function of the direction of the axis of polarization of the linear polarizer preceding the photodiode. By calculating the ratio of the lowest and the highest optical powers, it was possible to determine the degree of circular polarization of the light. The A-setup allows to reach a maximum circular polarization degree of 78% against 86% for B. The photograph (c) presents the light irradiation of a 10 mm rectangular quartz cuvette by the setup A.

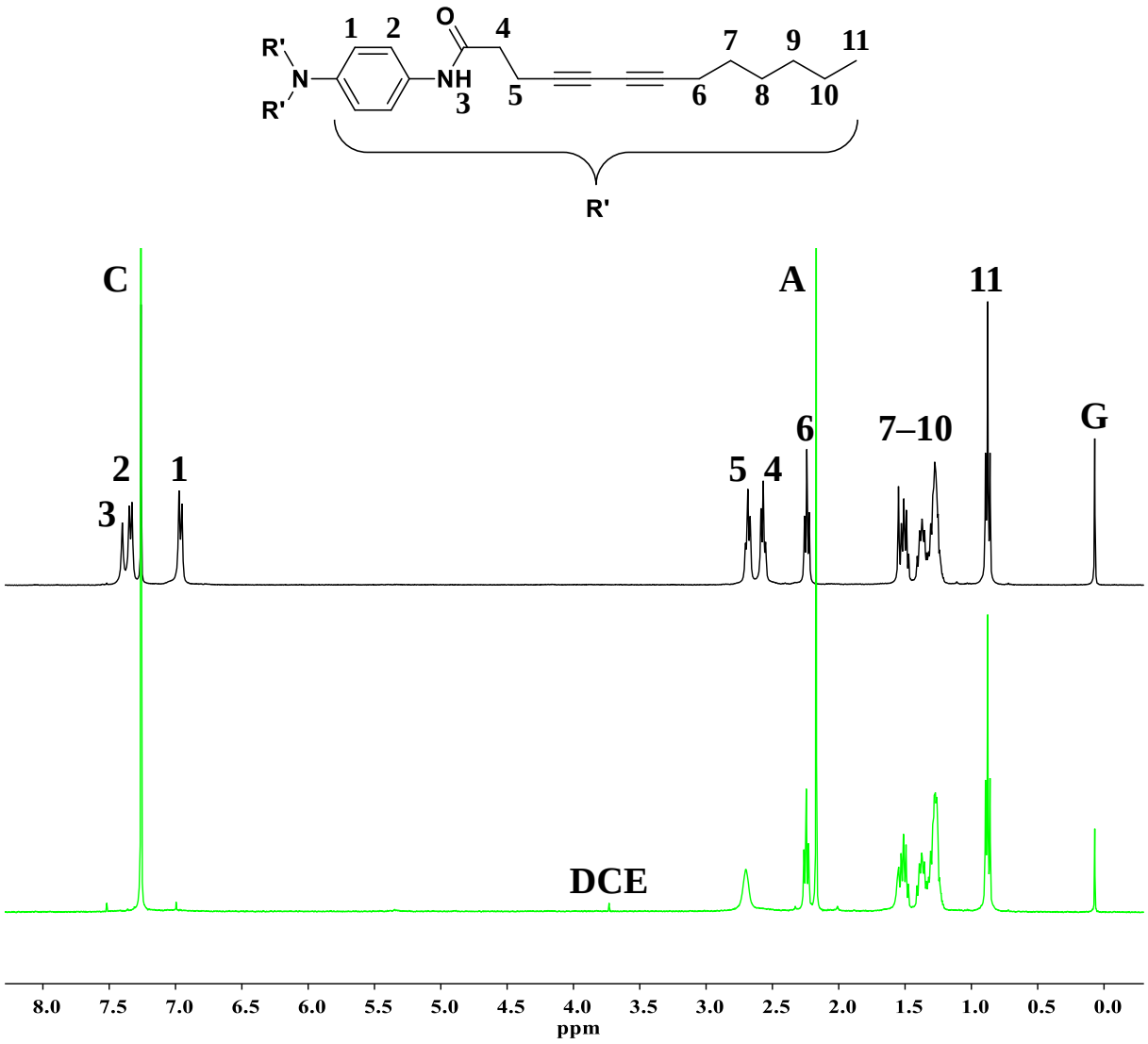

Figure SIV.52 ^{1}H NMR spectra of **TATA-SDA** at 2.3 mM in $CDCl_3$, (top) before and (bottom) after exposure to ambient light (C, DCE, A and G are resonance peaks for residual $CHCl_3$, 1,2-dichloroethane, acetone and silicone grease, respectively). Residual DCE was likely present in the tube prior to analysis.

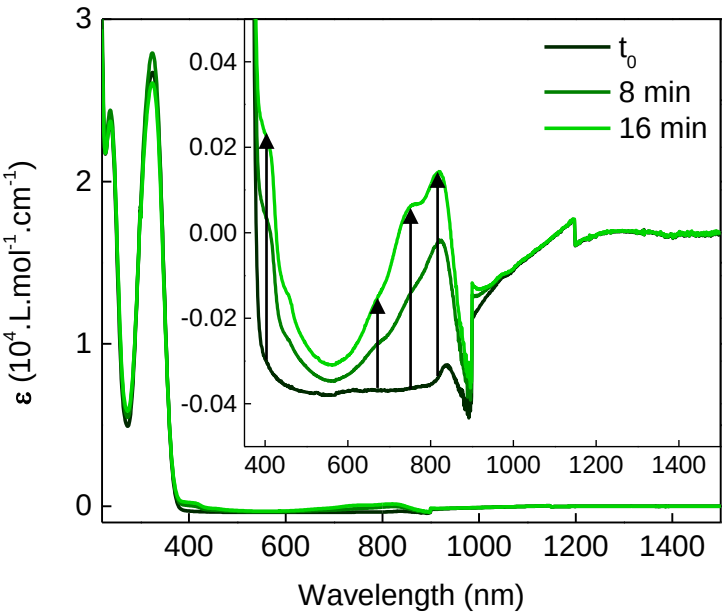

Figure SIV.53 UV–Vis–NIR absorption spectra of solutions of **TATA-SDA** at 2.3 mM in DCE before and after 8 and 16 minutes of light irradiation. The solution was irradiated in a 10 mm rectangular quartz cuvette by the setup A, with a surface optical power source of about 13.6 mW/cm^2. Noisy signals at 300 and 900 nm are due to changeovers of light source then detector and grating. The large bump in the NIR region comes from a slight apparatus misalignment. According to the evolution of the molar extinction coefficient at 811 nm (considered as increasing also after 16 minutes, even if it probably started to decrease before, at about 12 min); and compared with the evolution of the molar extinction coefficient at the same wavelength for the irradiation of a 0.1 mm lamellar cell at the same surface optical power in similar conditions with a low diffusion; integrating the difference of illuminated surface; and in the absence of skin effect, the percentage of radicals at 8 and 16 min is about 11 and 16%.

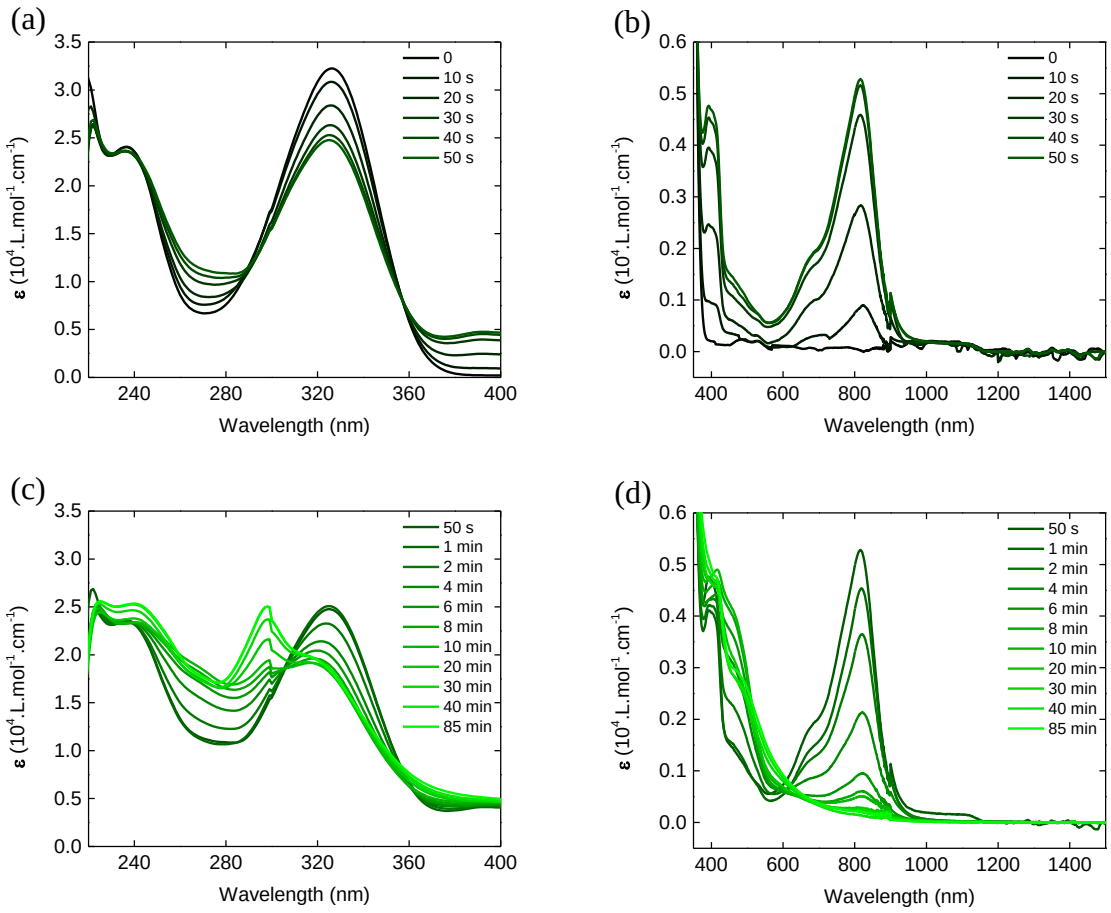

Figure SIV.54 UV–Vis–NIR absorption spectra during light irradiation of **TATA-SDA** at 2.3 mM in chloroform. (a–b) first 50 seconds of light irradiation; and (c–d) from 50 seconds to 85 min of light irradiation. The 0.1 mm lamellar quartz cell was irradiated by the setup A, with a surface optical power of about 13.6 mW/cm^2. Sharp changes at 300 and 900 nm are due to changeovers of light source then detector and grating.

Figure SIV.55 Photograph at the end of the light irradiation of **TATA-SDA** at 2.3 mM in chloroform. The same photograph is displayed on the right, with brightness and contrast corrections, to better show the irradiated part of the solution (on the bottom of the cell) whose triarylammonium radicals have not diffused significantly.

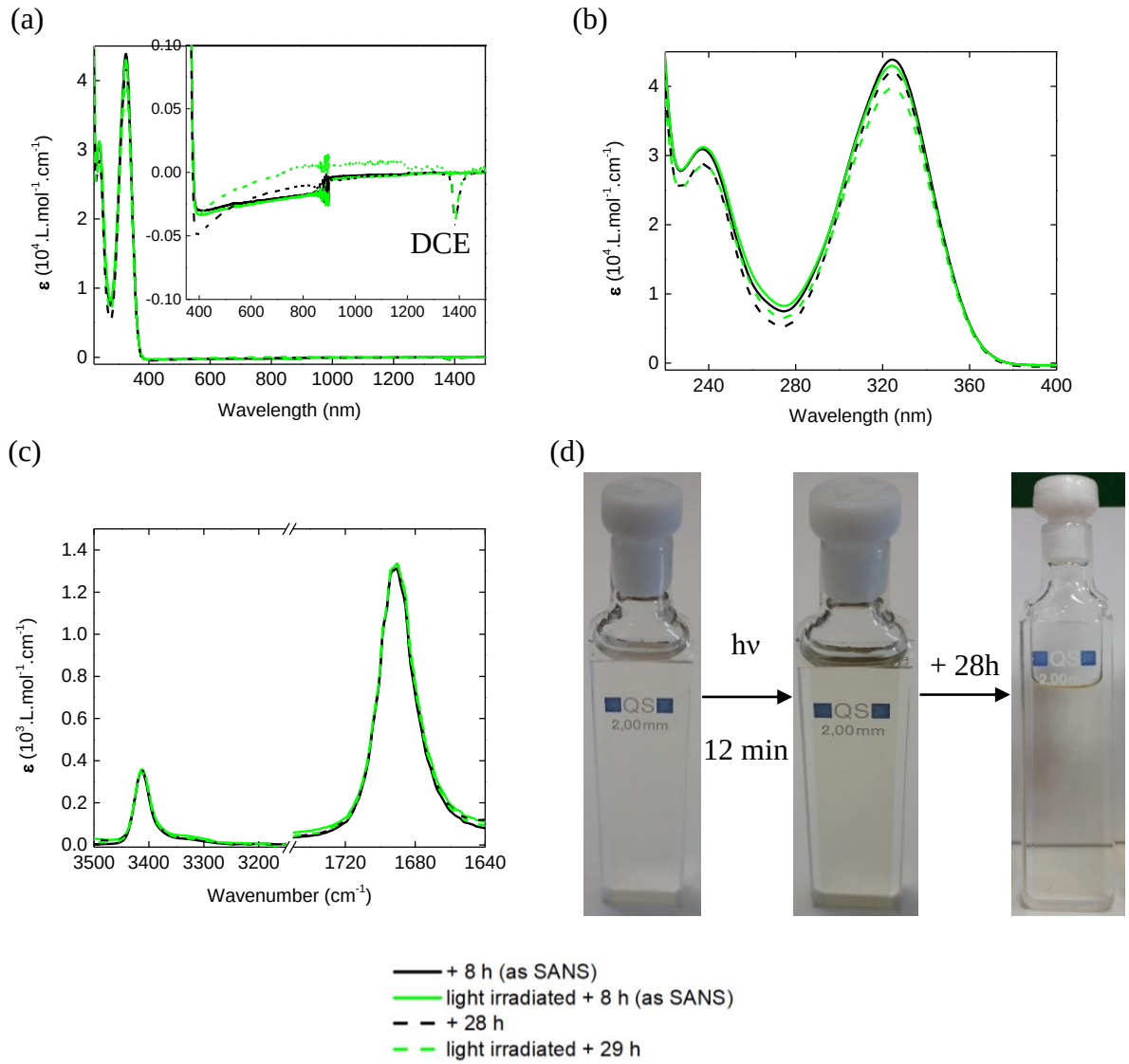

Figure SIV.56 (a–b) UV–Vis–NIR absorption and (c) FT–IR spectra of **TATA-SDA** at 2.3 mM in DCE after light irradiation (solid lines) and ageing (dashed lines), in the same conditions than SANS measurements. Zoom on the Vis–NIR and UV regions in (a) and (b), respectively. (d) Solutions after light irradiation and ageing (two first solutions are models and were not used for SANS, hence their volume are slightly different). The solution was irradiated in a 2 mm rectangular quartz cuvette by the setup A, with a surface optical power of 7.9 mW/cm^2.

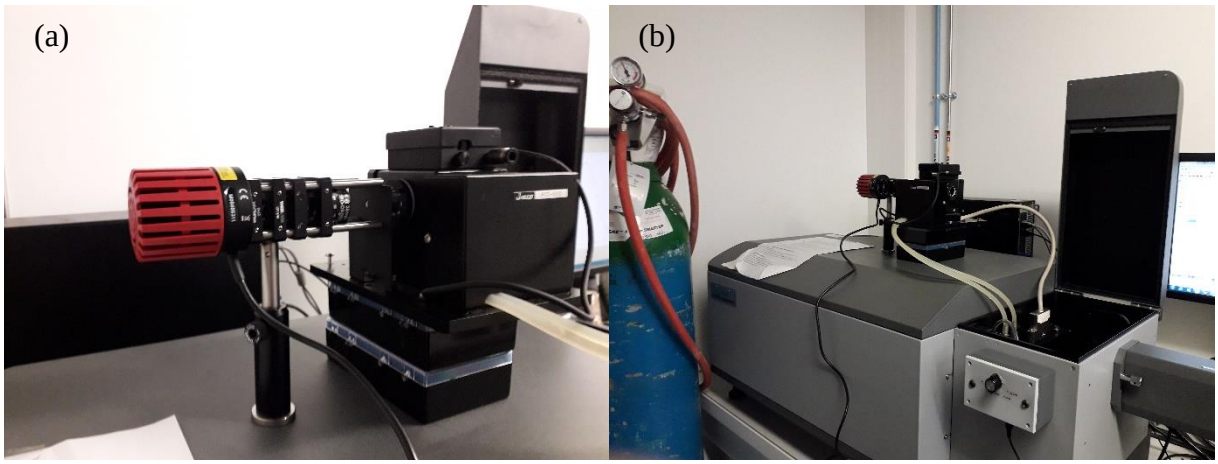

Figure SIV.57 (a–b) Photographs of the setup B, in position to irradiate a quartz cell in the Circular Dichroism spectrophotometer thermostatted cell-holder. This apparatus was covered with an opaque box to block the surrounding light during irradiations.

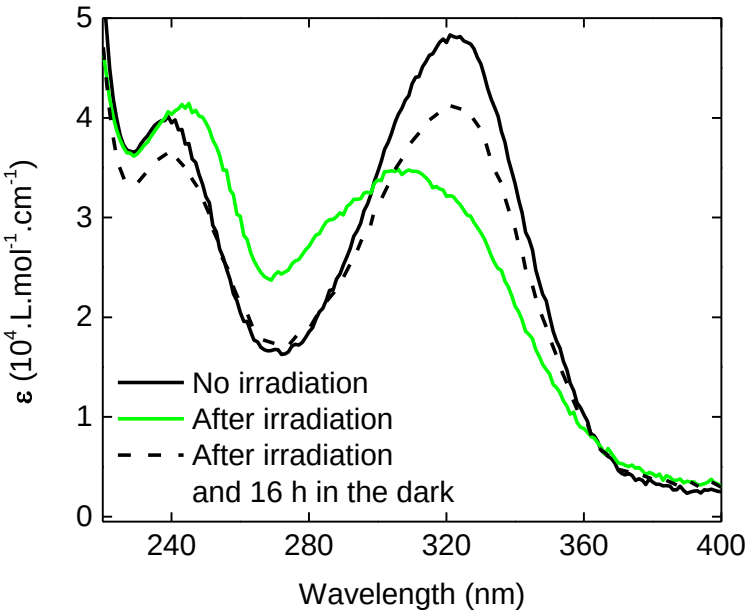

Figure SIV.58 UV–Vis absorption spectra of **TATA-SDA** at 11.7 mM in DCE (black solid line), after 8640 seconds of light irradiation (green solid line), then left in dark 16 hours (black dashed line). The 0.01 mm cylindrical quartz cuvette, inside the thermostatted CD-cell holder, was irradiated at 20°C by the setup B at a surface optical power of 33.7 mW/cm^2.

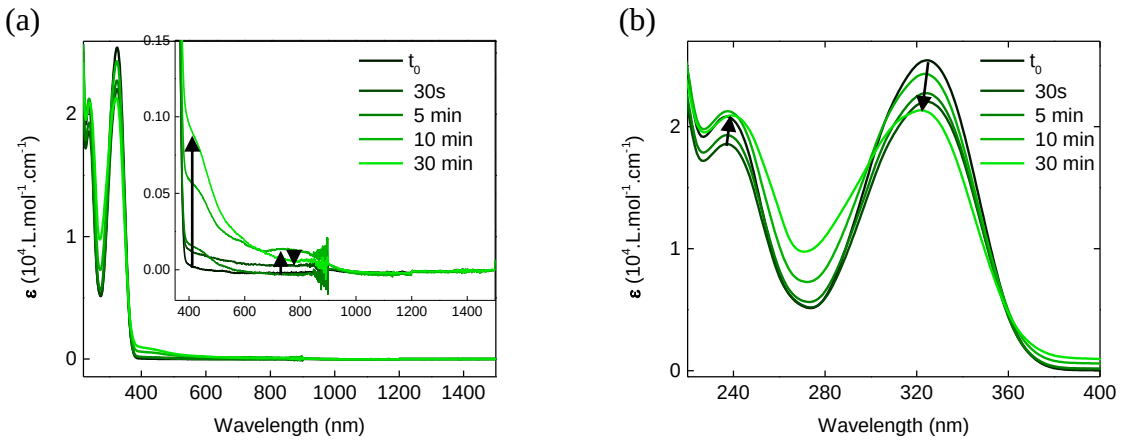

Figure SIV.59 (a–b) UV–Vis–NIR absorption during light irradiation of **TATA-SDA** at 2.3 mM in DCE, before thin film preparation. The solutions were irradiated in a 2 mm rectangular quartz cuvette by the setup A, with a surface optical power of 7.9 mW/cm^2.

Table SIV.8 Recap chart of trials aiming to find CD emergence conditions, with **TATA-SDA** (batch V for entries 1 to 5 and batch VI for entries 6 to 7) at 2.3 mM in DCE irradiated upon cooling from 60°C to 20°C. Container of solutions, lamp optical power, irradiation time as well as irradiation and measurement temperatures were notably modulated. The degree of circular polarization is equal to 83% (for a surface optical power of 33.7 mW/cm^2) or 86% (for surface optical powers of 3.4 or 0.3 mW/cm^2).

Entry			Irradiated solution container	Setup/ Lamp optical power (mW/cm^2)	Irradiation time (min)	Temperature change Gradual/ Quench	Measurement temperature (°C)	Result
1	a		2 mm quartz cuvette	B/33.7	1	G	-10	CD/LD
	b				5			
	c				10			
2	a		2 mm quartz cuvette	B/33.7	10	G + 2h	≈ -20	CD/LD
	b					G + 3 days	≈ -20	
3	a	i	2 mm quartz cuvette	B/33.7	0.5	G	-10	CD/LD
		ii				Q	-17	
	b	i			5	G	-10	
		ii				Q	-17	
4	a		4 mL glass vial without cap	B/33.7	1	Q	-15	CD/LD
	b				5			
5	a		2 mm quartz cuvette	B/3.4	60	G	-10	CD/LD
	b			B/0.3				
6	a		2 mm quartz cuvette	B/3.4	10	G	-15	CD/LD
	b			B/0.3	15			
7	a	i	Thermostatted 0.1 mm quartz cuvette	B/33.7	15	G	-15	CD/LD
		ii			120			

	b	i		B/3.4	15			
		ii			360			

The first entry described light irradiations upon chilling from 60 to rt, before a gradual decrease of temperature down to -10°C for the CD analysis (a). Only CD emanating from LD were measured, as it was evidenced by the modification of the CD/LD signals upon cell flipping (**Figure SIV.60b**). These conditions were further probed with a gradual decrease down to a lower temperature (<-20°C, to allow rotative CD measurements), at which samples were kept 2 hours or 3 days (to maybe favor potential key rearrangements within aggregates). In both cases, CD and LD signals, displayed in **Figure SIV.60c**, had a sawtooth-like waveform, similar to those described previously, likely indicating only LD and artifacts.

The entry 3 described experiments where samples were also quenched at a very low temperature (-17°C), to maybe foster the incorporation of **TATA-SDA**$^{\bullet+}$ into stacks, but gave only LD-induced CD (**Figure SIV.60d**). As previously, a direct light irradiation of solutions, through the top of an uncapped vial, was tried in these conditions (entry 4 *vs.* 3), but was unsuccessful (**Figure SIV.61a**).

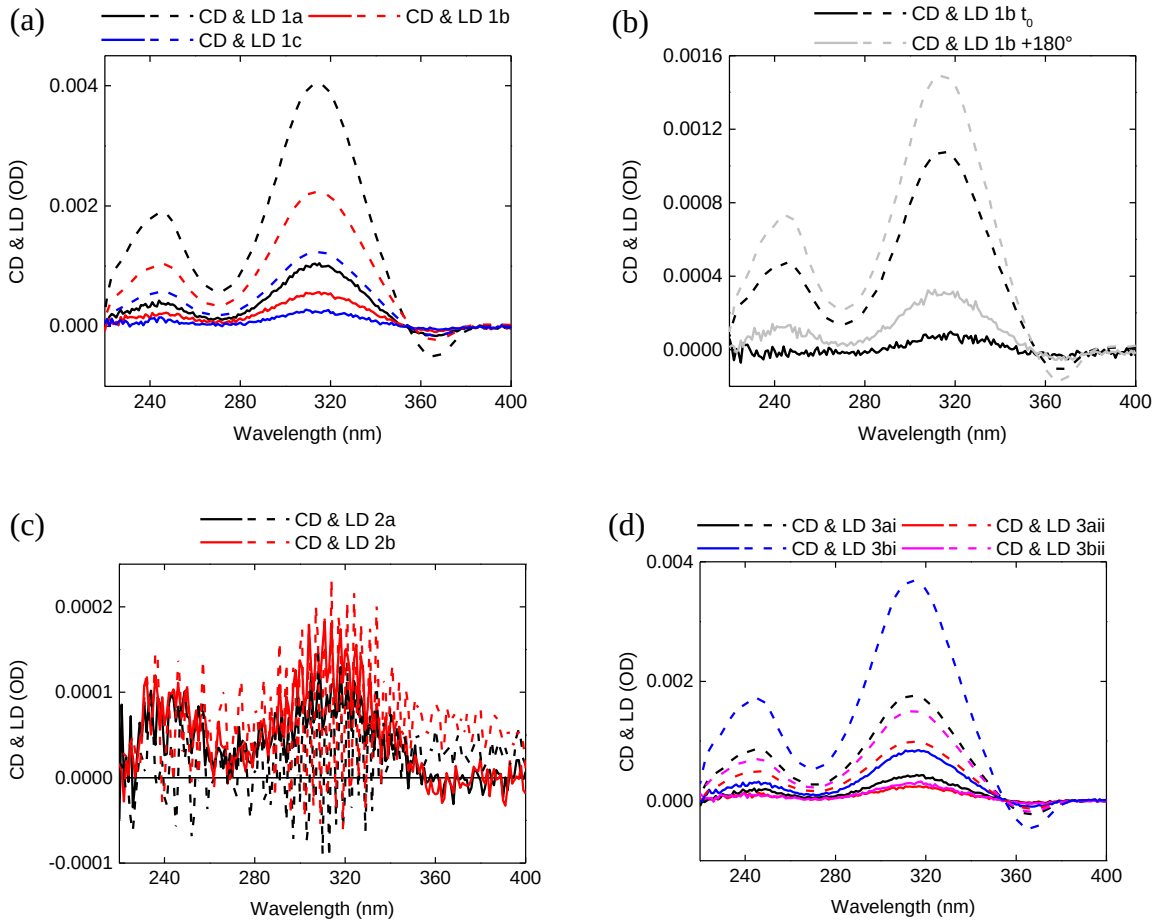

Figure SIV.60 CD + LD (a–d) analyses of **TATA-SDA** at 2.3 mM in DCE, light irradiated with variable temperature, from 60°C to room temperature. (c) analyses were measured at about -20°C in a non-thermostatted rotative cylindrical cell.

Still in the spirit of experiments upon chilling down to room temperature, the fifth and sixth entries presented light irradiations at a lower optical power (3.4 and 0.3 mW/cm^2) for long (entry 5) and intermediate (entry 6) durations. It allowed to investigate the effect a CPL which interacted with **TATA-SDA**, but with less efficiency into their conversion to triarylammonium radicals. It opened the door to the possible greater impact of neutral molecules having interacted with CPL, to integrate and orientate aggregates, compared with triarylammonium radicals. Nevertheless, only CD polluted by LD were obtained (**Figure SIV.61b** and **c**).

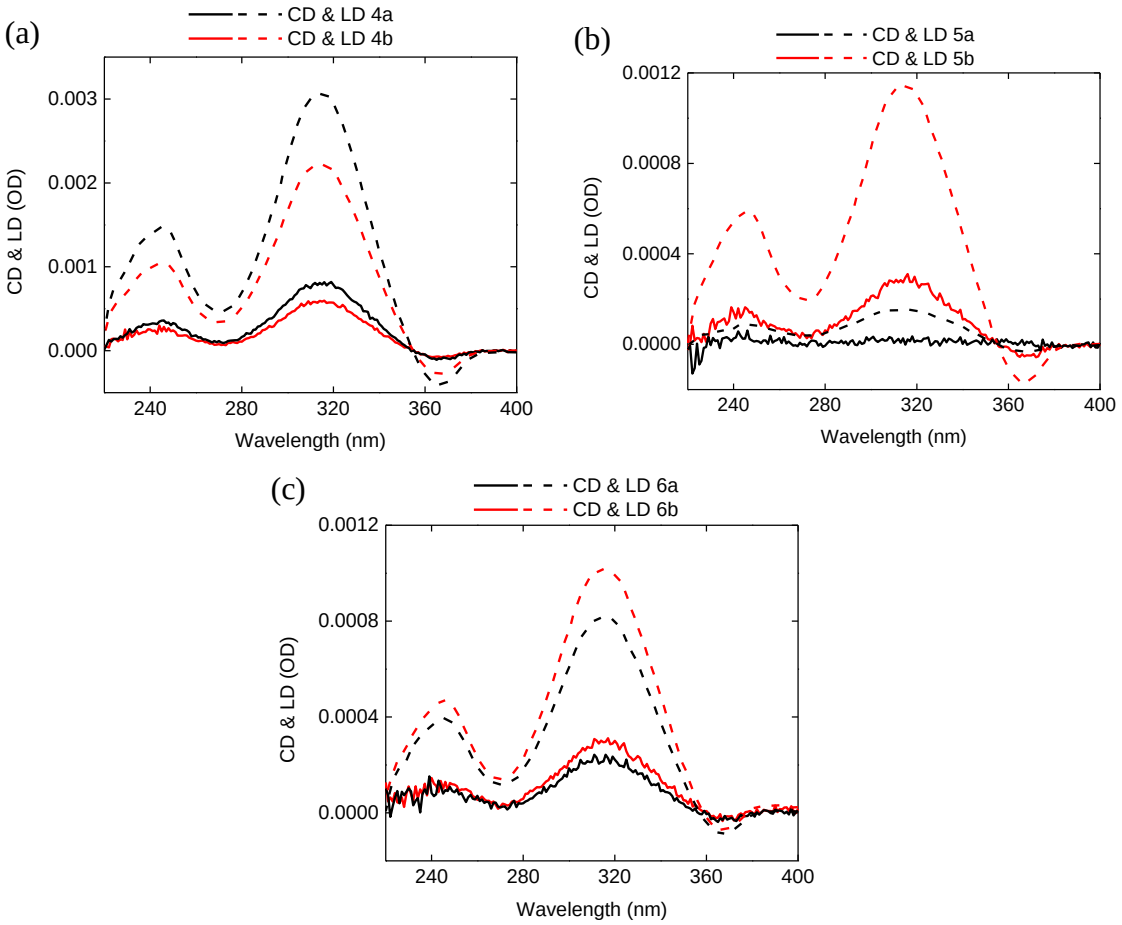

Figure SIV.61 CD + LD (a–c) analyses of **TATA-SDA** at 2.3 mM in DCE, light irradiated with variable temperature, from 60°C to room temperature.

A final set of experiments at 2.3 mM was carried out with a fine control of temperature during light irradiation (entry 7), thanks to the apparatus involving the CD thermostatted cell-holder illustrated in **Figure SIV.57**. It tested two different lamp optical powers (33.4 and 3.4 mW/cm^2), for a long and short irradiation time (15 and 120 min at high power, while 15 and 360 min at low power), upon cooling down from 60°C to 20°C. It covered a variety of parameters already studied, but with more accuracy on temperature gradients. CD/LD results are depicted in **Figure SIV.62**, and gradients of temperature described in **Figure SIV.63**. Unfortunately, all conditions gave more or less the same result: a CD of the exact LD shape, devoid of any hints of CD bands arising out of biased supramolecular chirality.

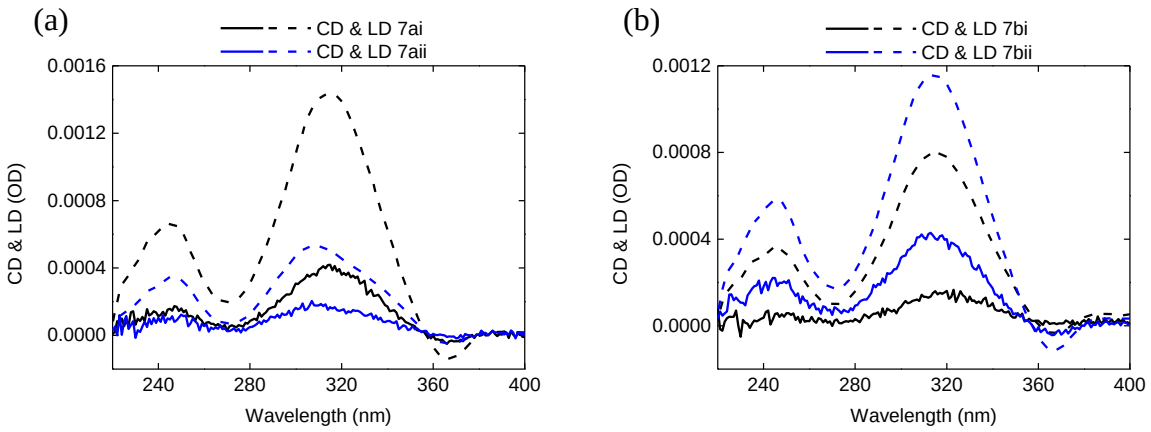

Figure SIV.62 CD + LD (a–b) analyses of **TATA-SDA** at 2.3 mM in DCE, light irradiated with a surface optical power of 33.7 (a) or 3.4 mW/cm^2 (b), and an irradiation time of 15 minutes (i) or 120 (33.7 mW/cm^2) /360 (3.4 mW/cm^2) minutes (ii).

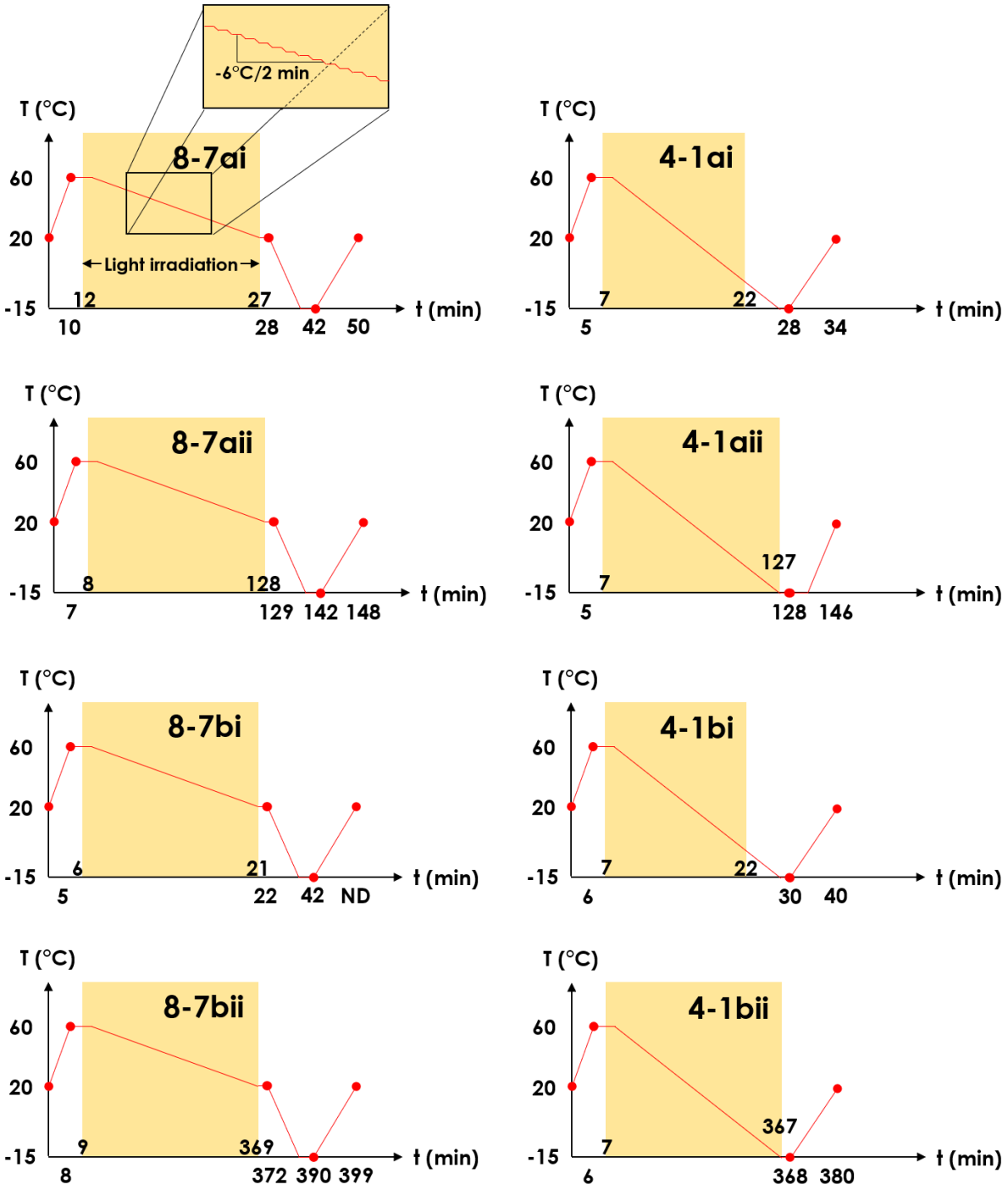

Figure SIV.63 Temperature gradients during the light irradiation of experiments 1 in **Table IV.4** and 7 in **Table SIV.8**. Red points correspond to UV–Vis and CD–LD measurements, and yellow rectangles to periods of irradiation. ND = not defined.

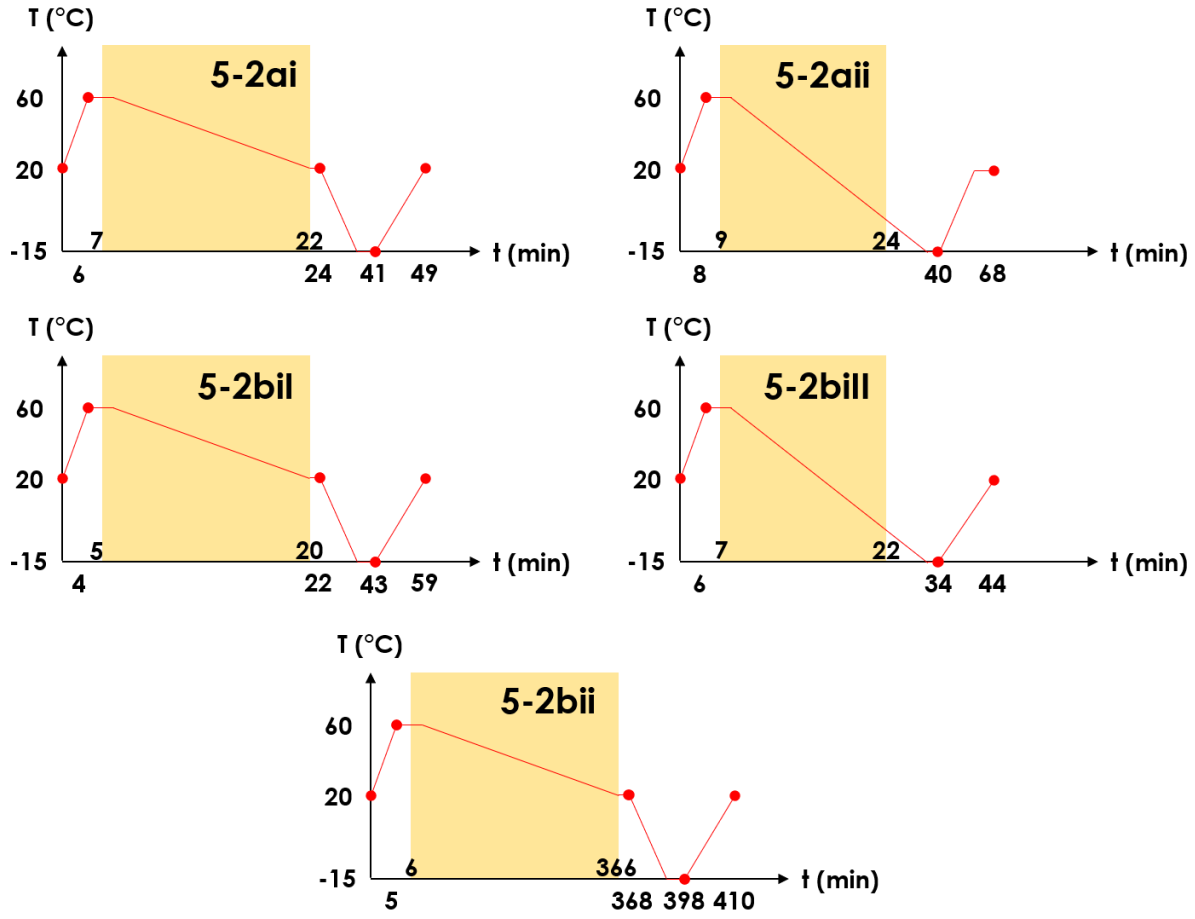

Figure SIV.64 Temperature gradients during the light irradiation of experiments 2 in **Table IV.5**. Red points correspond to UV–Vis and CD–LD measurements, and yellow rectangles to periods of irradiation.

VII. 2. Experimental section

VII. 2. 1. Materials

1-octyne, *N*-bromosuccinimide (NBS), silver nitrate, copper (I) chloride, *n*-Butylamine, hydroxylammonium chloride, 4-pentynoic acid, *N*-(3-dimethylaminopropyl)-*N*′-ethylcarbodiimide hydrochloride (EDC·HCl) and 4-(Dimethylamino)pyridine (DMAP) were purchased from Acros, Alfa Aesar, Sigma-Aldrich, Fluorochem or TCI suppliers and used as received. Unless otherwise noted, chromatography-grade solvents were used as received. Dried toluene was obtained from a Solvent Purification System (SPS, IT-Inc). 1,2-dichloroethane and chloroform were filtered over basic alumina, distilled over CaH_2 and stored under argon

atmosphere in a Schlenk flask before use in all of the experiments. C_7D_8, $CDCl_3$, DMSO-d_6 and 1,2-dichloroethane-d_4 were bought from Eurisotop and used without further purification.

VII. 2. 2. Methods

NMR spectra were recorded on a Bruker Avance 400 or 300 spectrometer and calibrated to the residual solvent peak: DMSO-d_6 (^{1}H: 2.50 ppm; ^{13}C: 39.52 ppm), 1,2-dichloroethane-d_4 (^{1}H: 3.73 ppm; ^{13}C: 43.60 ppm) or $CDCl_3$ (^{1}H: 7.26 ppm; ^{13}C: 77.16 ppm). Peaks are reported with their corresponding multiplicity (s: singlet (br for broad); d: doublet, t: triplet; q: quartet; quint: quintuplet; hept: heptuplet; dd: doublet of doublets, dt: doublet of triplets; td: triplet of doublets), integration and J coupling constant given in Hertz.

Exact mass measurements (HRMS) were obtained on TQ R30-10 HRMS spectrometer by ESI^+ ionization and are reported in *m/z* for the major signal.

Solubility tests were carried out inside screw cap vials with 2 mL of solvent.

Fourier-Transform Infrared (FT–IR) measurements were performed on a Nicolet iS10 spectrometer. Solution spectra were measured in CaF2 cells of various pathlength (1 and 2 mm, according to the concentration) and were corrected for air, solvent and cell absorption. Films were measured on KBr pellets and corrected for air and cell absorption.

The Attenuated total reflectance (ATR) FT–IR spectra for solids were collected on a Bruker tensor 27 FT–IR spectrometer equipped with the ATR platinum module, with a detector rt-DLaTGS and the OPUSv5.5 software (Bruker Optics, Germany) was set up with the following parameters. The spectral resolution was fixed to 4 cm^{-1}, the number of scans to 32, the selected spectral range between 4000 and 400 cm^{-1}, and the main peaks were reported (m: medium, s: strong, w: wide).

Raman measurements were performed on a Bruker Senterra instrument integrated an Olympus BX51 optical microscope. Data were recorded with a grating of 1200 lines/mm giving a spectral resolution of about 4 cm^{-1}, a doubled Nd:Yag excitation laser (532 nm) and an 50x Olympus lens leading to an analysis diameter of about 3 µm. An Edge filter allowed the

rejection of the Rayleigh emission, and the Raman diffusion was detected by a CCD cooled by a Pelletier element. Acquisitions were managed by the OPUS software.

Circular dichroism (CD) measurements were performed on a Jasco J-1500 spectrometer equipped with a Peltier thermostatted cell holder and Xe laser. Data were recorded with the following parameters: 50, 100 or 200 $nm.min^{-1}$ sweep rate, 0.05, 0.5 or 1 nm data pitch, 1 or 2 nm bandwidth, and between 700 or 400 and 220 or 200 nm. Spectra were corrected for air, solvent, and cell contribution at the same temperature. Molar extinction coefficients are reported in $L.mol^{-1}.cm^{-1}$ and expressed as follows: $\Delta\varepsilon = \theta/(32982 \times l \times c)$ where θ is the measured ellipticity in mdeg, l is the optical pathlength in cm, and c is the concentration in $mol.L^{-1}$. CD and linear dichroism (LD) are also reported in optical density (OD) and expressed as follows: $OD = \theta/32982$ and $OD = LD/10$ where LD is the measured LD in dOD. CD measurements at temperature lower than 10°C were carried out under a nitrogen gas flux, to avoid any water condensation.

UV–Vis absorption spectra were extracted from CD analyses and obtained after correction of the absorption of air, solvent, and cell contribution at the same temperature.

UV–Vis–NIR absorption spectra were measured with a Varian Cary 5000 spectrophotometer and corrected of the absorption of air, solvent, and cell contribution at the same temperature. Data were recorded with the following parameters: double beam mode, 600 $nm.min^{-1}$ sweep rate, 1 nm data pitch, 2 nm bandwidth, and between 1500 and 200 nm. Source changed at 300 nm while detector and gratings changeover took place at 900 nm.

Small-angle neutron scattering (SANS) measurements were made at the LLB (Saclay, France) on the PA20 instrument, at three distance-wavelength combinations to cover the 2.4×10^{-3} to 0.46 Å q^{-1} range, where the scattering vector q is defined as usual, assuming elastic scattering, as $q = (4\pi/\lambda)\sin(\theta/2)$, where θ is the angle between incident and scattered beam. Data were corrected for the empty cell signal and the solute and solvent incoherent background. A light water standard was used to normalize the scattered intensities to cm^{-1} units. The data was fitted with the DANSE software SasView. The number *n* of molecule in the cross-section can be derived from n_L (the number of molecules per unit length) by assuming an average

intermolecular distance of 4.2 Å, which is the spacing between aromatic rings in **TATA-SDA** helical assemblies calculated by Kim *et al*. by DFT[1].

VII. 3. Synthesis of TATA-SDA

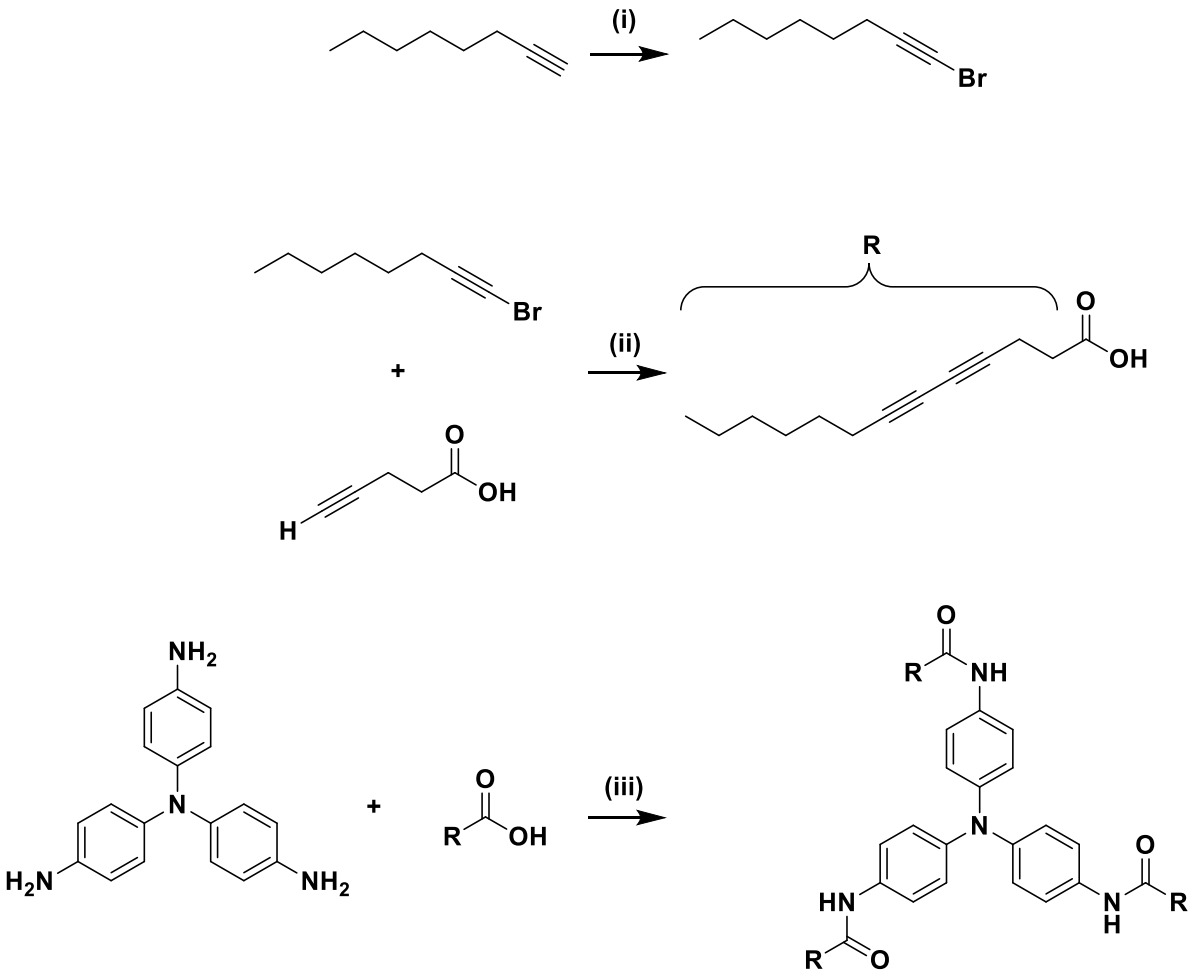

VII. 3. 1. Synthesis of 1-bromo-1-octyne (adapted from Tsuji *et al.*[6])

1-octyne (5 g, 45.4 mmol) was dissolved in acetone (230 mL) under argon. NBS (8.9 g, 49.9 mmol) was added under argon and after NBS dissolution, $AgNO_3$ (2.28 g, 13.4 mmol) was added and the reaction mixture was stirred for 3h at room temperature under argon (the reaction was followed by ^1H NMR spectroscopy). After quenching by adding H_2O (100 mL, formation of a precipitate), the mixture was filtered off and the filtrate was extracted with Et_2O (50 mL × 3). The organic layer was dried over $MgSO_4$ and evaporated *in vacuo*. The crude was purified

by flash column chromatography with petroleum ether/diethyl ether as eluent (7 g, 84% yield). ^{1}H NMR ($CDCl_3$, 400 MHz, 300 K): δ (ppm) = 2.20 (t, J = 6.7 Hz, 2H), 1.60-1.10 (m, 8H), 0.88 (t, J = 7.1 Hz, 3H).

VII. 3. 2. Synthesis of trideca-4,6-diynoic acid (adapted from Nie and Wang[5])

Copper (I) chloride (96 mg, 0.97 mmol) was added to a 30% vol *n*-$BuNH_2$ aqueous solution (77 mL) at room temperature, which resulted in the formation of a blue solution. Crystals of hydroxylamine hydrochloride were added to discharge the blue color. 4-Pentynoic acid (2 g, 20.38 mmol) was then added to the solution and the reaction mixture was cooled with an ice/water bath. Bromoalkyne (5 g, 26.44 mmol) in diethyl ether (40 mL) was added dropwise to the cooled reaction mixture. After the addition of bromoalkyne (usually 15-30 min), the cooling bath was removed. The reaction mixture was stirred at room temperature for 4 new hours. Occasionally adding small amount of hydroxylamine hydrochloride was necessary to keep the color of the reaction light yellow. The reaction was quenched with HCl (2M) and the pH was adjusted to 2. The reaction mixture was extracted with ethyl acetate (5 x 100 mL). The combined organic layer was dried over $MgSO_4$, concentrated under reduced pressure and precipitated in 4 mL of heptane (3 g, 71% yield). ^{1}H NMR ($CDCl_3$, 400 MHz, 300 K): δ (ppm) = 9.90 (br s, 1H), 2.60 (m, 4H), 2.24 (t, J = 7.0 Hz, 2H), 1.51 (q, J = 14.5, 7.0 Hz, 2H), 1.45-1.20 (m, 6H), 0.89 (t, J = 7.0 Hz, 3H).

VII. 3. 3. Synthesis of tris(4-trideca-4,6-diynamidophenyl)amine (inspired from Bouteiller *et al.*[36])

Trideca-4,6-diynoic acid (1.17 g, 5.67 mmol) was dissolved in 100 mL of non-stabilized and dried THF, under argon. DMAP (740 mg, 6.06 mmol), EDC·HCl (1.09 g, 5.69 mmol) and tris(4-aminophenyl)amine (366 mg, 1.26 mmol) were added respectively as solid, and the reaction mixture was left under reflux for 72 h at 70°C under Argon. After 72 h, HCl (1 M, 100 mL) was added to the mixture and the organic phase was washed with saturated solution of HCO_3 (100 mL) and then with Brine (100 mL). The organic phase was dried over $MgSO_4$ and condensed in a rotary evaporator, to yield the crude product. The crude was purified by flash silica column chromatography yielding two fractions: a small fraction of pure **TATA-SDA** with hexane/AcOEt (1:1) and another fraction with DCM/MeOH (9:1). Both fractions were

recrystallized using EtOH/heptane (45 mg + 170 mg = 215 mg, 20%). ^{1}H NMR (DMSO-d_6, 400 MHz, 300 K): δ (ppm) = 9.91 (s, 3H_3), 7.48 (d, J = 8.9 Hz, 6H_2), 6.90 (d, J = 8.8 Hz, 6H_1), 2.58 (dt, J = 7.0 Hz, 12$H_{5–4}$), 2.27 (t, J = 6.9 Hz, 6H_6), 1.43 (q, J = 6.9 Hz, 6H_7), 1.28 (m, 18$H_{8–10}$), 0.85 (t, J = 6.8 Hz, 9H_{11}). ^{13}C{^{1}H} NMR (DMSO-d_6, 100 MHz, 300 K): δ (ppm) = 168.64, 142.78, 133.95, 123.60, 120.35, 78.37, 76.98, 65.42, 65.23, 34.66, 30.60, 27.83, 27.61, 21.92, 18.24, 14.79, 13.85. FT–IR (ATR, cm^{-1}): 517 (m), 719 (m), 818 (m), 1244 (m), 1271 (m), 1313 (m), 1406 (m), 1466 (m), 1504 (s), 1601 (m), 1655 (m), 2851 (m), 2920 (m), 3288 (m). HRMS (ESI, *m/z*): calculated for $C_{57}H_{66}N_4O_3H$, $[M+H]^+$: 855.5208, found: 855.5196. Elemental analysis: calculated for $C_{57}H_{66}N_4O_3$: C 80.06, H 7.78, N 6.55, O 5.61, found: C 80.18, H 7.73, N 6.51, O 6.43 (the higher oxygen content is attributed to the hygroscopic nature of the molecule).

VIII. References

1 J. Kim, J. Lee, W. Y. Kim, H. Kim, S. Lee, H. C. Lee, Y. S. Lee, M. Seo and S. Y. Kim, *Nat. Commun.*, 2015, **6**, 6959.

2 J. J. Armao, M. Maaloum, T. Ellis, G. Fuks, M. Rawiso, E. Moulin and N. Giuseppone, *J. Am. Chem. Soc.*, 2014, **136**, 11382–11388.

3 I. Reva, L. Lapinski, N. Chattopadhyay and R. Fausto, *Phys. Chem. Chem. Phys.*, 2003, **5**, 3844–3850.

4 X. Nie and G. Wang, *J. Org. Chem.*, 2006, **71**, 4734–4741.

5 T. Fujihara, Y. Horimoto, T. Mizoe, F. B. Sayyed, Y. Tani, J. Terao, S. Sakaki and Y. Tsuji, *Org. Lett.*, 2014, **16**, 4960–4963.

6 M. Kamath, W. H. Kim, L. Li, J. Kumar, S. Tripathy, K. N. Babu and S. S. Talwar, *Macromolecules*, 1993, **26**, 5954–5958.

7 C. Kvarnström, A. Petr, P. Damlin, T. Lindfors, A. Ivaska and L. Dunsch, *J. Solid State Electrochem.*, 2002, **6**, 505–512.

8 K. Seto, Y. Hosoi and Y. Furukawa, *Chem. Phys. Lett.*, 2007, **444**, 328–332.

9 J. Wu, H. Wang, S. Xu and W. Xu, *J. Phys. Chem. A*, 2015, **119**, 1303–1308.

10 J. Huo, Z. Hu, G. He, X. Hong, Z. Yang, S. Luo, X. Ye, Y. Li, Y. Zhang, M. Zhang, H. Chen, T. Fan, Y. Zhang, B. Xiong, Z. Wang, Z. Zhu and D. Chen, *Appl. Surf. Sci.*, 2017, **423**, 951–956.

11 S. Spagnoli, E. Briand, I. Vickridge, J.-L. Fave and M. Schott, *Langmuir*, 2017, **33**, 1419–1426.

12 The Handbook of Infrared and Raman Characteristic Frequencies of Organic Molecules | ScienceDirect, https://www.sciencedirect.com/book/9780124511606/the-handbook-of-infrared-and-raman-characteristic-frequencies-of-organic-molecules, (accessed September 21, 2018).

13 D. Lin-Vien, N. B. Colthup, W. G. Fateley and J. G. Grasselli, in *The Handbook of Infrared and Raman Characteristic Frequencies of Organic Molecules*, eds. D. Lin-Vien, N. B. Colthup, W. G. Fateley and J. G. Grasselli, Academic Press, San Diego, 1991, pp. 117–154.
14 D. Lin-Vien, N. B. Colthup, W. G. Fateley and J. G. Grasselli, in *The Handbook of Infrared and Raman Characteristic Frequencies of Organic Molecules*, eds. D. Lin-Vien, N. B. Colthup, W. G. Fateley and J. G. Grasselli, Academic Press, San Diego, 1991, pp. 155–178.
15 I. Nyrkova, E. Moulin, J. J. Armao, M. Maaloum, B. Heinrich, M. Rawiso, F. Niess, J.-J. Cid, N. Jouault, E. Buhler, A. N. Semenov and N. Giuseppone, *ACS Nano*, 2014, **8**, 10111–10124.
16 A. Osypenko, E. Moulin, O. Gavat, G. Fuks, M. Maaloum, M. A. J. Koenis, W. J. Buma and N. Giuseppone, *Chem. – Eur. J.*, 2019, **25**, 13008–13016.
17 M. Sumimoto, D. Yokogawa, M. Komeda, H. Yamamoto, K. Hori and H. Fujimoto, *Spectrochim. Acta. A. Mol. Biomol. Spectrosc.*, 2011, **81**, 653–660.
18 A. T. Haedler, S. R. Beyer, N. Hammer, R. Hildner, M. Kivala, J. Köhler and H.-W. Schmidt, *Chem. - Eur. J.*, 2014, **20**, 11708–11718.
19 S. Amthor, B. Noller and C. Lambert, *Chem. Phys.*, 2005, **316**, 141–152.
20 E. Moulin, F. Niess, M. Maaloum, E. Buhler, I. Nyrkova and N. Giuseppone, *Angew. Chem. Int. Ed.*, 2010, **49**, 6974–6978.
21 E. Moulin, F. Niess, G. Fuks, N. Jouault, E. Buhler and N. Giuseppone, *Nanoscale*, 2012, **4**, 6748–6751.
22 R. Reynolds, L. L. Line and R. F. Nelson, *J. Am. Chem. Soc.*, 1974, **96**, 1087–1092.
23 T. Kim, T. Mori, T. Aida and D. Miyajima, *Chem Sci*, 2016, **7**, 6689–6694.
24 B. Adelizzi, I. A. W. Filot, A. R. A. Palmans and E. W. Meijer, *Chem. - Eur. J.*, 2017, **23**, 6103–6110.
25 G. Albano, G. Pescitelli and L. Di Bari, *Chem. Rev.*, 2020, **120**, 10145–10243.
26 Å. Davidsson and B. Norden, *Spectrochim. Acta Part Mol. Spectrosc.*, 1976, **32**, 717–722.
27 Å. Davidsson, B. Nordén and S. Seth, *Chem. Phys. Lett.*, 1980, **70**, 313–316.
28 O. Arteaga, Z. El-Hachemi and A. Canillas, *Phys. Status Solidi A*, 2008, **205**, 797–801.
29 O. Arteaga, J. Freudenthal, B. Wang and B. Kahr, *Appl. Opt.*, 2012, **51**, 6805–6817.
30 O. Arteaga, A. Canillas, Z. El-Hachemi, J. Crusats and J. M. Ribó, *Nanoscale*, 2015, **7**, 20435–20441.
31 J. W. Verhoeven, *Pure Appl. Chem.*, 1996, **68**, 2223–2286.
32 Z. Shen, Y. Sang, T. Wang, J. Jiang, Y. Meng, Y. Jiang, K. Okuro, T. Aida and M. Liu, *Nat. Commun.*, 2019, **10**, 1–8.
33 C. Park, J. Lee, T. Kim, J. Lim, J. Park, W. Y. Kim and S. Y. Kim, *Molecules*, 2020, **25**, 402.
34 J. Hu, Y. Xie, H. Zhang, C. He, Q. Zhang and G. Zou, *Chem. Commun.*, 2019, **55**, 4953–4956.
35 E. E. Greciano, R. Rodríguez, K. Maeda and L. Sánchez, *Chem. Commun.*, 2020, **56**, 2244–2247.
36 M. Raynal, F. Portier, P. W. van Leeuwen and L. Bouteiller, *J. Am. Chem. Soc.*, 2013, **135**, 17687–17690.

Chapter V Synthesis, self-assembly properties of achiral TATA ligands and probing of the effect of chiral additives

Abstract

In this chapter, the multi-step synthesis and characterization of two triarylamine trisamide monomers bearing a triphenylphosphine group (**TATA$^{m–PPh2}$** and **TATA$^{p–PPh2}$**) are described, which differ from each other by the position of the PPh_2 group on the phenylene linker. The association properties of **TATA$^{p–PPh2}$** are probed in absence of light by UV–Vis–NIR and FT–IR spectroscopy. These analyses show the reversible formation of long helical assemblies, built upon π–π stacking and hydrogen bonds. Solutions at 1.8 mM in toluene and at 1 mM in decalin are highly associated at 20°C ($\alpha_{Agg} \approx 0.75$ and 0.93, respectively), while at 1.8 mM in dichloromethane, **TATA$^{p–PPh2}$** molecules are almost totally free at 20°C and assembled at -10°C ($\alpha_{Agg} \approx 0.95$). Then, a library of enantiopure small molecules, notably including amino acids ester and citronellol derivatives, are employed to attempt to bias the handedness of **TATA$^{p–PPh2}$** helical stacks. Additions in toluene, dichloromethane or decalin of these chiral additives (10 mol% or 100 mol%) do not succeed to bias supramolecular handedness, but rather lead to a shortening of assemblies. (−)-α-Pinene and (*R*)-limonene are finally used as solvent for **TATA$^{p–PPh2}$**, to test if their chirality could be transferred to the aggregates. Despite **TATA$^{p–PPh2}$** molecules being soluble and hydrogen bonded in these solvents, no CD accounting for helically biased **TATA$^{p–PPh2}$**-assemblies was detected.

I. Introduction

Controlling the handedness of dynamic helical structures may be achieved by solubilizing achiral molecules in a chiral solvent. Indeed, monomer units interact with their neighbors, the co-monomers as well as solvent molecules constituting their surrounding environment. In fact, most of the physical and chemical properties of solutes are influenced by the solvent, through a subtle balance of attractive and repulsive interactions[1]. Although the chiral induction of solvent molecules to achiral free species is usually weak, the chiral bias can be amplified along the main chain of helical polymers to generate homochiral helices[2].

Green *et al.* pioneered this approach in 1993, by measuring the CD spectra of solutions of an achiral polyisocyanate in (*S*)-1-chloro-2-methylbutane or (*R*)-chloroalkanes[3]. The observation of significant CD signals demonstrated that the chiral solvent was able to bias the handedness of the macromolecules. Chiral solvents or additives were subsequently used to control the macromolecular helicity of a range of covalent polymers. Yashima *et al.* proved that a polyphenylacetylene bearing a carboxylic function could adopt a preferential helical handedness in the presence of chiral amines or amino alcohols in DMSO, thanks to H-bonding interactions[4]. In 1999, they unveiled that this preference is memorized when the chiral amine is replaced by an excess of a more basic achiral amino alcohol[5]. Optically inactive aggregates of macromolecules were also biased thanks to chiral alcohols[6], enantiopure limonene[7] or mixtures composed of achiral solvents and limonene[8,9]. Supramolecular chirality could be inverted depending on the configuration of the major enantiomer of limonene present in solution.

Chirality induction from solvent or chiral additives was also accomplished in supramolecular polymers of low-molecular-weight monomeric units. Meijer *et al.* first demonstrated this strategy in 1997 with benzene-1,3,5-tris(3,3'-diamido-2,2'-bipyridine) (BTABP) assemblies, built exclusively upon π–π stacking, in (*S*)-2,6-dimethyloctane[10]. It demonstrated that intermolecular interactions other than hydrogen bonds can cooperatively transfer the chirality, from the monomer to the supra-macromolecular level. The same team reported similar manifestations with oligo(p-phenylenevinylene) assemblies, mixed in methylcyclohexane with citronellic acid, thanks to host-guest interactions within assemblies[11], or in citronellol as solvent due to its ability to interact with assemblies through H-bonding

interactions[12]. Our team also demonstrated that dynamic nanotubes composed of a racemic mixture of chiral bisurea monomers could be biased in limonene[13]. Likewise, single-handed helical fibers, made of perylene bisamide derivatives, were obtained by Würthner *et al.* in enantiopure limonene[14].

Interestingly, Suginome *et al.* implemented this strategy for developing a class of asymmetric helical catalysts operating in chiral solvents[2]. First, they induced a preferential helical handedness to macromolecular catalysts based on poly(quinoxaline-2,3-diyl)s bearing triphenylphosphine groups, by dissolution in THF/limonene mixture. The optical purity of limonene was also varied from 6.7% to 100% *e.e.* Single-handed helices could in turn catalyze the palladium-mediated reaction to afford high enantioselectivity (up to 98% *e.e.* for the Suzuki-Miyaura cross-coupling, 95% *e.e.* for the styrene hydrosilylation, and 89% *e.e.* for the silaboration). Remarkably, the Suzuki-Miyaura coupling was also achieved in achiral solvent with 45% *e.e.* thanks to a helical macromolecular scaffold exhibiting "chiral memory". Dissolution of the polymer in limonene and removal of the latter leads to a kinetic effect for which the biased helicity was sufficiently memorized to induce a noticeable enantioselectivity in the forthcoming catalytic reaction.

Thereby, the objective of this chapter is double. On one hand, we aimed at designing, synthesizing and probing the self-association of TATA ligands, to pave the way for their irradiation with CPL, or incorporation into TATA stacks of CPL-controlled handedness. On the other hand, we tried to take advantage of extremely high amplification properties uncovered in TATA molecules by Miyajima *et al.*[15], to induce a preferential handedness to TATA ligand helical assemblies by means of chiral additives.

II. Synthesis, characterization and solubility tests

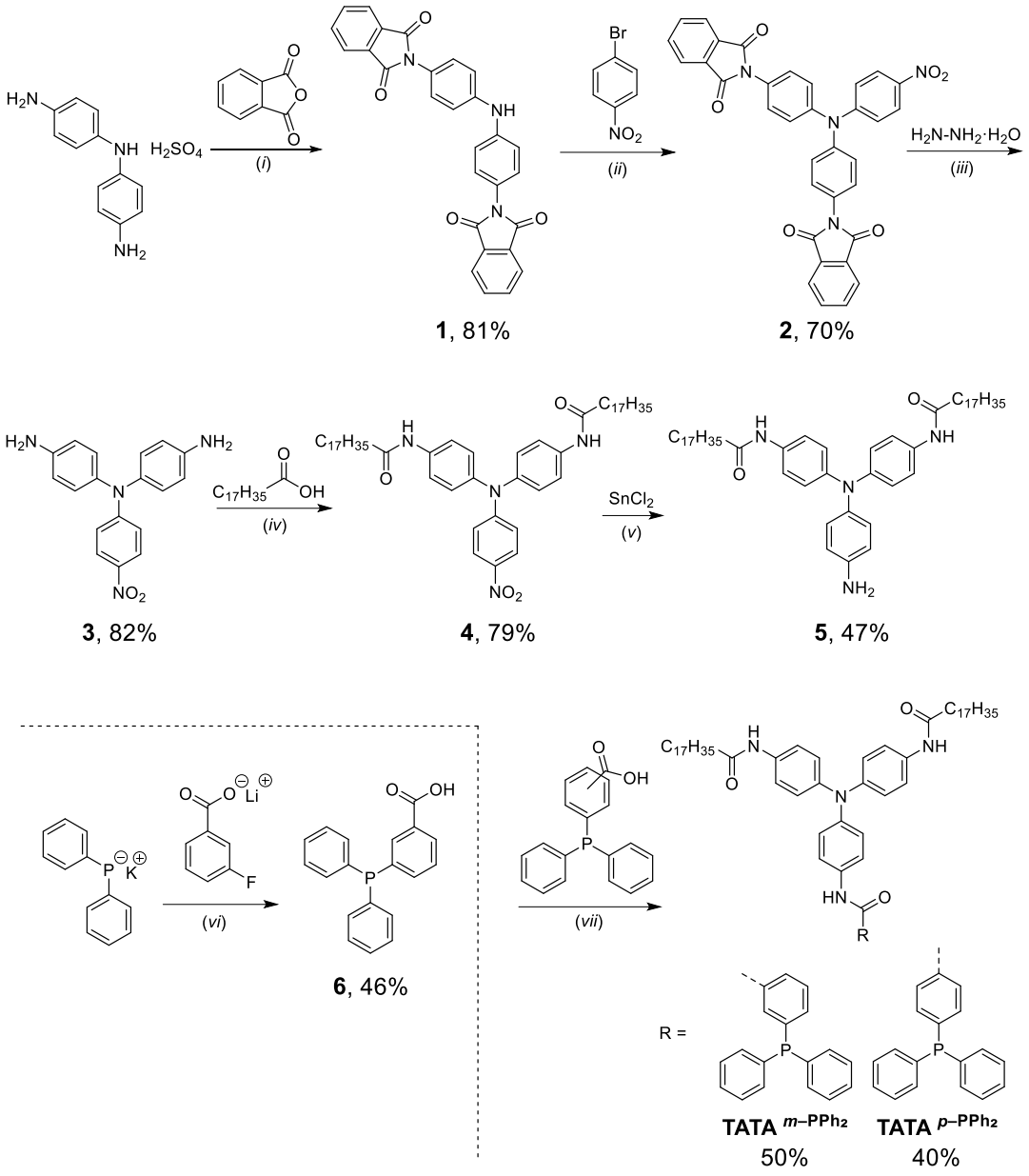

Figure V.1 Syntheses of **TATA$^{m–PPh2}$** and **TATA$^{p–PPh2}$**. (*i*) Acetic acid, *N*-Methyl-2-pyrrolidone, 125°C, 24 h (81% yield). (*ii*) Cs_2CO_3, $Pd(OAc)_2$, RuPhos, THF, Ar, 90°C, 18 h (70% yield). (*iii*) EtOH, 90°C, 3 h 30 (82% yield). (*iv*) DMAP, EDC·HCl, THF, Ar, 90°C, 3 days (79% yield). (*v*) MeCN/EtOH, Ar, 95°C, 17 h (47% yield). (*vi*) THF, 70°C, 26 h then HCl (46% yield). (*vii*) DMAP, EDC·HCl, THF, Ar, 70°C, 48 h (50% and 40% yield for **TATA$^{m–PPh2}$** and **TATA$^{p–PPh2}$**, respectively).

Two TATA molecules featuring a metal-coordinating group (a triarylphosphine) were synthesized for the first time thanks to a 6-step procedure (**Figure V.1**). They differ from the position (*meta* or *para*) of the PPh_2 unit on the phenylene linker. In analogy with helical BTA catalysts, it is expected that the position of the PPh_2 group will greatly affect the assembly and catalytic properties of the TATA ligands.

The synthetic pathway started with the protection of the two primary amines of commercial 4,4'-diaminodiphenylamine sulfate hydrate into phthalimides[XLI]. It was achieved with phthalic anhydride and catalyzed by acetic acid, in *N*-methyl-2-pyrrolidone (NMP). Next, for the formation of the triarylamine core, the nucleophilic aromatic substitution of **1** with 1-fluro-4-nitrobenzene turned out to be inefficient, despite the use of weak bases (K_2CO_3 or Cs_2CO_3), dry DMSO and high temperatures (110–140°C). We hypothesized that the extended electron delocalization, up to the phthalimide groups, decreases the reactivity of the diarylamine. A palladium-catalyzed cross-coupling amination (Buchwald-Hartwig reaction) was then envisaged, known to be now among the most versatile methods to form C–N bonds, including triarylamines[17]. To achieve this, we opted for: cesium carbonate, a weak base with an excellent functional group tolerance, and leading to high reaction rates; palladium acetate, the most commonly used source of Pd in amination reactions; an electron-rich and bulky ligand, RuPhos, considered as the phosphine of choice for the arylation of diarylamines; and 1-bromo-4-nitrobenzene[18–20]. Interestingly, the product was obtained with an appreciable yield (70%) and isolated from the reactive medium only by drying and several washings (hydrochloric acid, dichloromethane, ethyl acetate and methanol).

The third step consisted in the deprotection of the two amine functions from the corresponding phtalimide using hydrazine hydrate, a variant of the Gabriel synthesis named the Ing-Manske procedure[21,22]. The phtalimide reacts exothermically with hydrazine to yield through proton transfer a phthalylhydrazide and the targeted amine. Long aliphatic side chains, issued from stearic acid, were then coupled to bis(4-aminophenyl)(4-nitrophenyl)amine **3**, to

[XLI] The synthesis of bis(4-aminophenyl)(4-nitrophenyl)amine **3** in one step by nucleophilic substitution of deprotonated 4,4'-diaminodiphenylamine sulfate hydrate with 1-fluro-4-nitrobenzene (similarly to Kulszewicz-Bajer *et al.*[16]) and a base did not proceed cleanly.

increase the solubility of the final products comprising six aromatic rings and three amide functions. The amide bond forming reaction was accomplished following the same way as in the two previous chapters (with DMAP and EDC·ECl additives). Next, the reduction of the nitro group was performed with tin chloride dihydrate, in line with a procedure already reported with triarylamines by Giuseppone *et al.*[23]. In parallel, 3-(diphenylphosphino)benzoic acid was formed thanks to the phosphanylation of 3-fluorobenzoic acid[XLII] using a solution of PPh_2K in THF. Finally, **TATA$^{m\text{–}PPh2}$** and **TATA$^{p\text{–}PPh2}$** molecules were synthesized through the usual amide bond forming reaction between **6** and 3-diphenylphosphino benzoic acid and 4-diphenylphosphino benzoic acid, respectively. Purification by flash column chromatography over silica yielded both TATA ligands in the pure form as confirmed by NMR analyses. Even though not optimized, all steps proceed with satisfactory yields (7% overall yield) allowing the TATA ligands to be obtained in the hundred of mg scale.

Solubility tests at 1 mM in solvents of various polarities allowed to highlight the influence of the position of the PPh_2 unit on the phenylene linker (**Table V.1**).

[XLII] After the deprotonation of the free acid with lithium hydroxide, Stelzer *et al.* remarked that the carboxylate in the *meta*-position "does not activate the fluorine sufficiently for nucleophilic displacement under these conditions"[24].

Table V.1 Solubility of **TATA$^{m–PPh2}$** and **TATA$^{p–PPh2}$** (1 mM) after heating up to the boiling point. G = gel, I = insoluble, P = precipitation, S = soluble, η ↑ = viscosity increases.

Solvent	TATA$^{m–PPh2}$	TATA$^{p–PPh2}$
Methylcyclohexane	S	I
Decalin	S	G
Toluene	S	S (η↑)
Trifluorotoluene	P (η↑)	P (η↑)
DCM	S	S
$CHCl_3$	S	S
1,2-DCE	S	S
MeOH	P	P
EtOH	S	S
Et_2O	I	I
THF	S	S
1,4-Dioxane	S	S
Acetone	S	S
Ethyl acetate	S	S
Acetonitrile	P	P
DMSO	S	S
DMF	S	S

Remarkably, both TATA ligands are soluble in a large range of solvents, including chlorinated solvents. Even if the **TATA$^{p–PPh2}$** molecule has a lower solubility than **TATA$^{m–PPh2}$** in methylcyclohexane, the increase of viscosity observed in toluene, or even a gel in decalin, likely reflects the presence of very long assemblies in solvents of interest for analytic and catalytic purposes[25–28]. Accordingly, the self-association properties of **TATA$^{p–PPh2}$** were studied in more details.

III. Self-association properties of TATA$^{p–PPh2}$

III. 1. In toluene

TATA$^{p–PPh2}$ at 1.8 mM in toluene forms a strong gel at 20°C (*i.e.* it does not flow immediately when the vial is turned). FT–IR analysis revealed absorption bands at 3290 and 1645 cm^{-1} (**Figure V.2a** and **b**), corresponding to the stretching vibrations of N-H and C=O groups involved in hydrogen bonding[29,30]. The symmetry of signals likely documented one type

of intermolecular hydrogen bonds, and the fact that free N-H/C=O absorption bands (around 3420 and 1690 cm^{-1}, respectively) are barely detected pointed out that most of molecules are associated ($\alpha_{Agg} \approx 0.75$ at 20°C[XLIII]). Cooling down to 0°C led to a minimal increase of the aggregation state, highlighting that molecules are almost all involved in aggregates at 20°C. These FT–IR analyses corroborate the formation of hydrogen-bonded network[23,31,32], similarly to **TATA-C12**, **TATA-C13** and **TATA-SDA** molecules investigated in the previous chapters.

The C_2-symmetric nature of **TATA*p*–PPh2** core was evidenced when the solution was heated to 80°C in order to reach the dissociated state. FT–IR analysis revealed a broad absorption band between 3450 cm^{-1} and 3300 cm^{-1}, centered on 3414 cm^{-1}, and two signals at 1698 cm^{-1} and 1686 cm^{-1} (**Figure V.2a** and **b**), corresponding to the stretching vibrations of free N-H and C=O groups[29,30] of different natures. UV–Vis profile of **TATA*p*–PPh2** displayed an absorption band with maximum at about 304 nm at 20°C or 0°C (**Figure V.2c**), attributed to mixed n→π* and π→π* electronic transitions of the triarylamine core[33], which is hyper/bathochromic shifted upon heating to 80°C ($\Delta\varepsilon \approx 0.2 \times 10^4$ $L.mol^{-1}.cm^{-1}$ and $\Delta\lambda = 22$ nm). Both FT–IR and UV analyses are in agreement with an almost complete disassembly of the hydrogen-bonded stacks upon heating. Toluene is thus a suitable solvent for chiral induction studies and catalysis.

[XLIII] Considering that molecules are mainly isolated at 80°C.

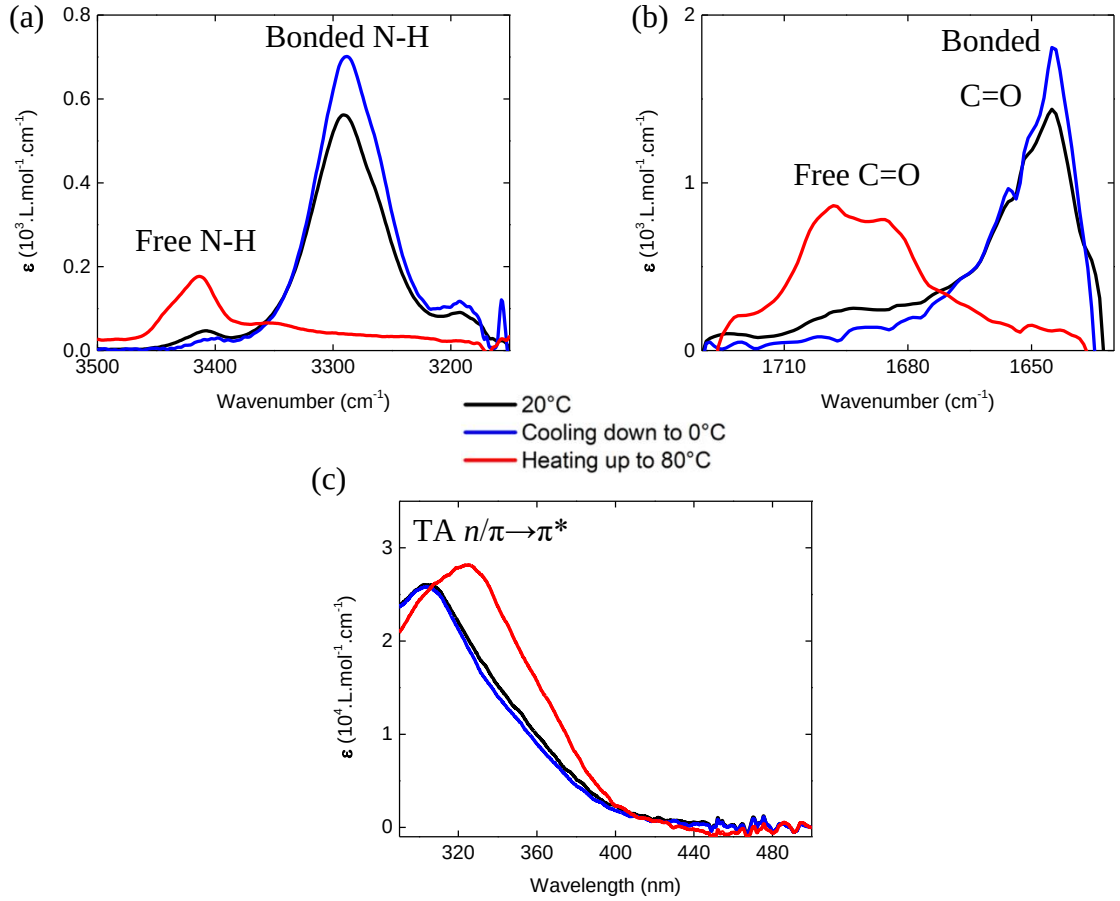

Figure V.2 Temperature-dependent (a–b) FT–IR and (c) UV–Vis analyses of **TATA$^{p–PPh2}$** in toluene (1.8 mM), with a zoom on the (a) N-H and (b) C=O regions. Spectra were recorded at 20°C, 0°C and 80°C.

III. 2. In dichloromethane

The observation of hydrogen-bonded assemblies in toluene prompted us to investigate the self-association properties in a chlorinated solvent, in particular dichloromethane. After dissolution at 1.8 mM, the UV–Vis profile highlighted an absorption band with maximum at a high wavelength (*i.e.* at 326 nm, **Figure V.3a**), and the FT–IR spectrum notably exhibited signals at 3428 cm^{-1} and 1683 cm^{-1}, corresponding to the free N-H/C=O stretching vibrations signals, respectively (**Figure V.3b** and **c**)[29,30], while being devoid of contributions accounting for hydrogen bonded amide groups. In this way, both UV–Vis and FT–IR results suggest that **TATA$^{p–PPh2}$** molecules are isolated.

Upon cooling down to -10°C, FT–IR analysis revealed absorption bands at 3288 and 1652 cm^{-1} (**Figure V.2a** and **b**), corresponding to the stretching vibrations of hydrogen bonded N-H and C=O groups ($\alpha_{Agg} \approx 0.95$), and the UV–Vis spectroscopy showed strong hypo/hypsochromic shifts of the main UV signal ($\Delta\varepsilon \approx 0.5 \times 10^4$ $L.mol^{-1}.cm^{-1}$ and $\Delta\lambda = 23$ nm), both indicating that almost all molecules are involved in hydrogen-bonded stacks. Interestingly, the UV–Vis analysis demonstrated that the initial state is not found again upon heating from -10°C to 20°C. It suggests a kinetic contribution of the association process and the fact that **TATA*p*–PPh2** in DCM is in a metastable state, similarly to the observation made for **TATA-C12** (Chapter III) and **TATA-SDA** (Chapter IV).

To conclude, FT–IR and UV–Vis analyses of **TATA*p*–PPh2** in dichloromethane revealed that cooling is needed to get hydrogen-bonded stacks ($\alpha_{Agg} \approx 0.95$ at -10°C), which constitutes a promising result in the purpose of generating mixed neutral and radical assemblies.

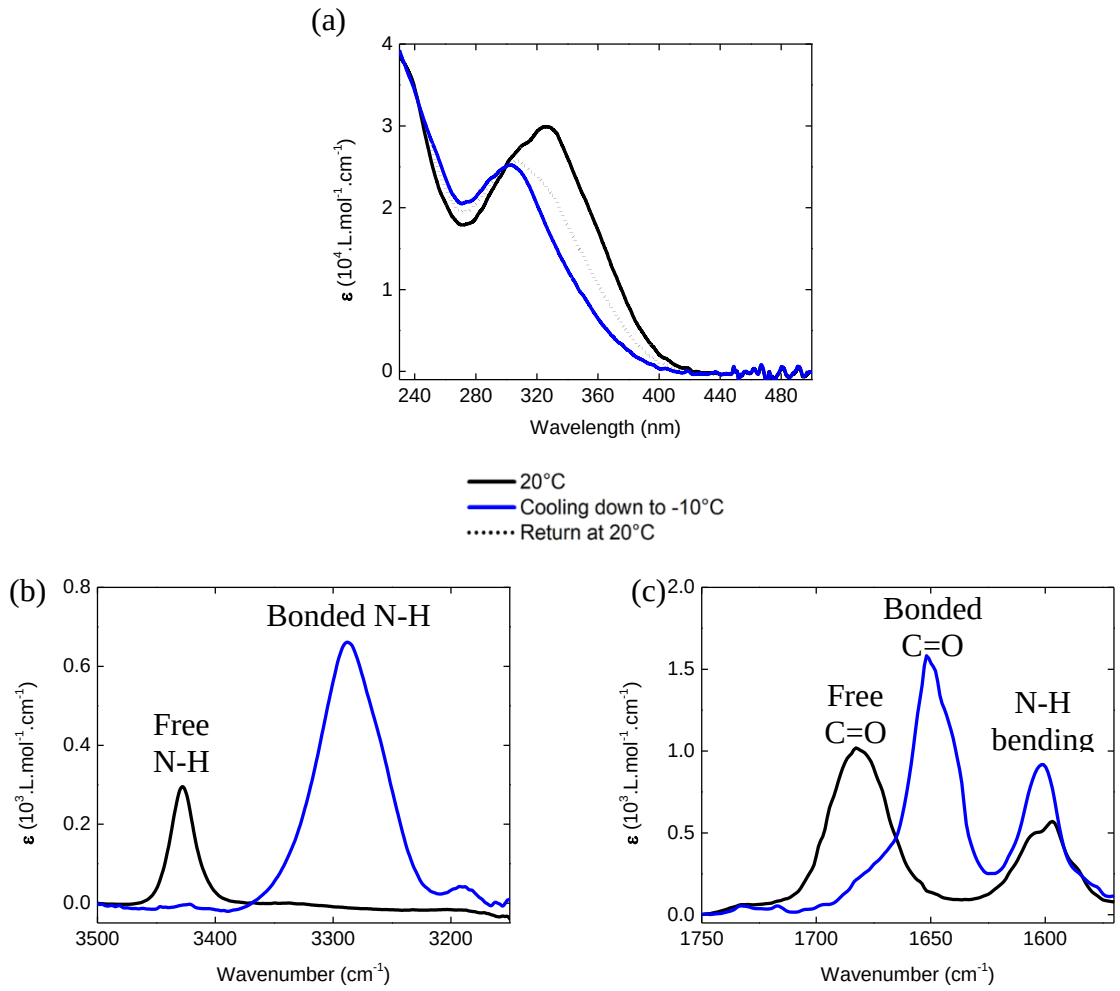

Figure V.3 Temperature-dependent (a) UV–Vis and (b–c) FT–IR analyses of **TATA$^{p\text{–PPh2}}$** in dichloromethane (1.8 mM), with a zoom on the (b) N-H and (c) C=O regions. Spectra recorded at 20°C, -10°C and 20°C again after the cooling process.

III. 3. In decalin

The self-association properties of **TATA$^{p\text{–PPh2}}$** were further probed in decalin at 1 mM, concentration for which a strong gel is formed at 20°C. Decalin has a high boiling point (190°C) which might be useful to reach the dissociated state. Thus, Variable-temperature (VT) analyses of **TATA$^{p\text{–PPh2}}$** in decalin at 1 mM were carried out by UV–Vis (**Figure V.4a**) and FT–IR (**Figure V.4b**, **c** and **d**) spectroscopy.

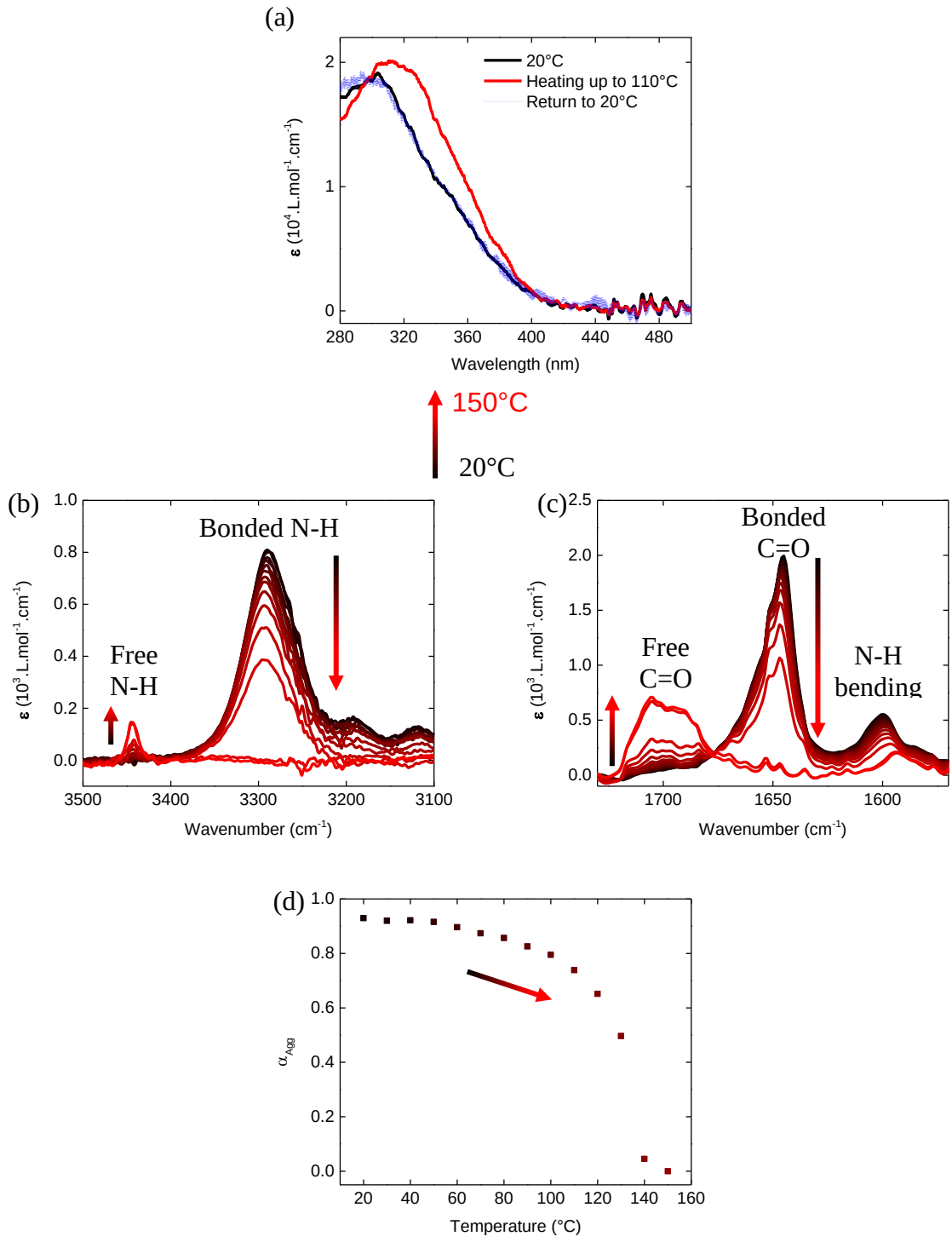

Figure V.4 Temperature-dependent (a) UV–Vis and (b–c) FT–IR analyses of **TATA$^{p\text{–}PPh2}$** in decalin (1 mM), with a zoom on the (b) N-H and (c) C=O regions. (a) UV–Vis spectra were recorded at 20°C, then after heating up to 110°C and at 20°C after the heating process. (b–c) FT–IR spectra were recorded during a heating process between 20°C and 150°C for a rate of 0.7°C/min. (d) Evolution of the degree

of aggregation as a function of the temperature, as deduced from (c). The degree of aggregation (α_{Agg}) was calculated from the evolution of the free C=O stretching vibration absorption signal at 1706 cm^{-1}, as a function of the temperature.

FT–IR and UV–Vis analyses are consistent with the presence of hydrogen bonded stacks at 20°C (**Figure V.4a**, **b** and **c**). The observation of a gel at 1 mM at 20°C indicates that these stacks are long.

Significant changes in the UV–Vis and FT–IR spectra were observed upon heating. In UV–Vis, moderate hyper- and bathochromic shifts of the major UV signal ($\Delta\varepsilon \approx 0.1 \times 10^4$ $L.mol^{-1}.cm^{-1}$ and $\Delta\lambda = 10$ nm) are measured, which indicate a loss of π–π stacking, maybe just partial because of the upper temperature limit at 110°C. VT–FT–IR analyses confirmed that **TATA$^{p\text{–PPh2}}$** molecules disassemble upon heating, as evidenced by the presence of bands associated to free amide units. The evolution of the degree of aggregation between 20°C and 150°C shows first a moderate decrease up to 100–120°C, which is consistent with the partial disassembly at 110°C revealed by UV–Vis spectroscopy, followed by a dramatic drop. Conversely, the plateau reached by the degree of aggregation below 50°C is very high ($\alpha_{Agg} \approx 0.93$) which indicates that most of the molecules are in the hydrogen-bonded stacks, in agreement with the presence of a gel.

In brief, UV–Vis and FT–IR spectroscopic analyses performed at various temperatures, showed the ability of **TATA$^{p\text{–PPh2}}$** to form reversible long assemblies of helical hydrogen-bonded stacks in various solvents. While molecules are associated in gels at 20°C in toluene at 1.8 mM and in decalin at 1 mM, the dichloromethane solution at 1.8 mM exhibits only isolated molecules. Nevertheless, **TATA$^{p\text{–PPh2}}$** molecules stack upon cooling down to -10°C in dichloromethane. Heating disrupts almost completely the supramolecular assemblies formed in toluene and decalin. Knowing precisely in what conditions **TATA$^{p\text{–PPh2}}$** molecules self-assemble into helical stacks, it was possible to try to bias their handedness with chiral additives.

IV. Towards biased supramolecular chirality by chiral additives

A library of enantiopure small molecules (**Figure V.5**) was selected to attempt to bias the handedness of helical stacks formed in toluene, dichloromethane and decalin by **TATA^{p-PPh2}** molecules. These additives – alcohols, aldehydes, amino acids, amino alcohol, bromo alkane, methyl esters of various amino acids or citronellol derivatives – cover a broad spectrum of functional groups (including hydroxyl, amine, sulfide, ester, cyclohexyl, alkenyl, aldehyde, bromo or phenyl groups) which might develop various interactions with **TATA^{p-PPh2}** molecules. Some of them have already proved successful in the context of controlling the main chain chirality of polymers (e.g. **A8**[2], **A9**[12] and **A11**[2]).

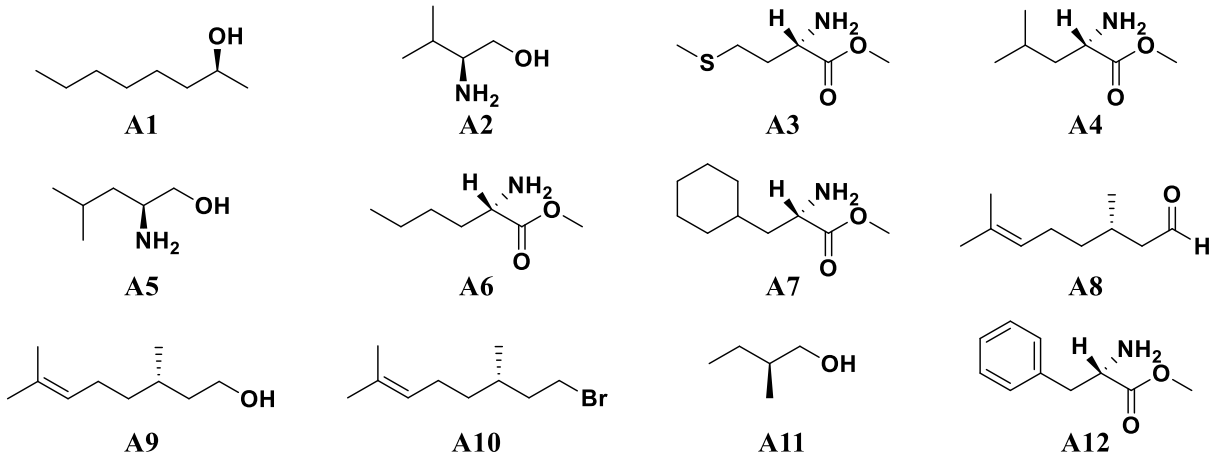

Figure V.5 Chiral additives used in this study. **A1**: (*S*)-(+)-2-octanol; **A2**: (*S*)-(+)-2-amino-3-methyl-1-butanol; **A3**: L-methionine methyl ester; **A4**: L-leucine methyl ester; **A5**: (*S*)-(+)-leucinol; **A6**: L-norleucine methyl ester; **A7**: β-cyclohexyl-L-alanine methyl ester; **A8**: (*S*)-(−)-citronellal; **A9**: (*S*)-(−)-ß-citronellol; **A10**: (*S*)-(+)-citronellyl bromide; **A11**: (*S*)-(−)-2-methylbutanol; **A12**: L-phenylalanine methyl ester.

Mixtures of **TATA^{p-PPh2}** and chiral additives were prepared in the appropriate solvent, and heated up to 100°C or 120°C for one hour (for toluene or decalin solutions, respectively), or gently heated (for DCM) prior to analyses. It was very appealing to test the methyl ester of phenyl alanine because of the presence of both an aromatic ring and HB groups but unfortunately, **A12** was only tested

in DCM because of its low solubility in the two other solvents. DCM was also tested only for this additive since the TATA/additive interactions were expected to be weaker in this solvent.

IV. 1. With 10 mol% of chiral additives in toluene or dichloromethane

First, chiral additives were added in small portions at 10 mol% in toluene or dichloromethane (for **A12**), with the aim of benefiting from extremely high amplification properties of **TATA$^{p\text{–}PPh2}$**.

In toluene at 1.8 mM and 20°C, CD, LD and FT–IR results of the TATA ligand alone as well as mixtures of the TATA ligand with four chiral additives (**A4**, **A7**, **A8** and **A11**) are displayed in **Figure V.6**; whereas the CD and LD analyses of the other mixtures are presented in **Figure SV.16** and all UV–Vis absorption spectra are in **Figure SV.17**.

Solutions exhibit no CD but rather a small LD signal which was already present in the ligand solution (**Figure V.6a**). This can be due to the presence of very long and aligned fibers, *i.e.* the sample is slightly anisotropic. Yet, all the solutions formed a strong gel and no significant effect of the chiral additive is seen on the spectroscopic signature of the hydrogen-bonded stacks. Obviously, no interaction occurs between the tested additives and the stacks of the TATA ligand in these conditions.

The same result was obtained with the chiral additive **A12** in dichloromethane at -10°C (**Figure V.7a** for the CD and LD spectra, **b** and **c** for FT–IR analyses), *i.e.* no significant effect of the additive on the nature of the assemblies is observed and the solutions are CD silent. Nevertheless, small signals are detected at 3400 cm^{-1} and 1682 cm^{-1} for the mixture which might be attributed to some defects induced by the presence of the additive. This potential competitive behavior of the additive **A12** was maybe the result of interactions between one of its phenyl, amine and/or ester functions with aromatic and amide groups of **TATA$^{p\text{–}PPh2}$** molecules.

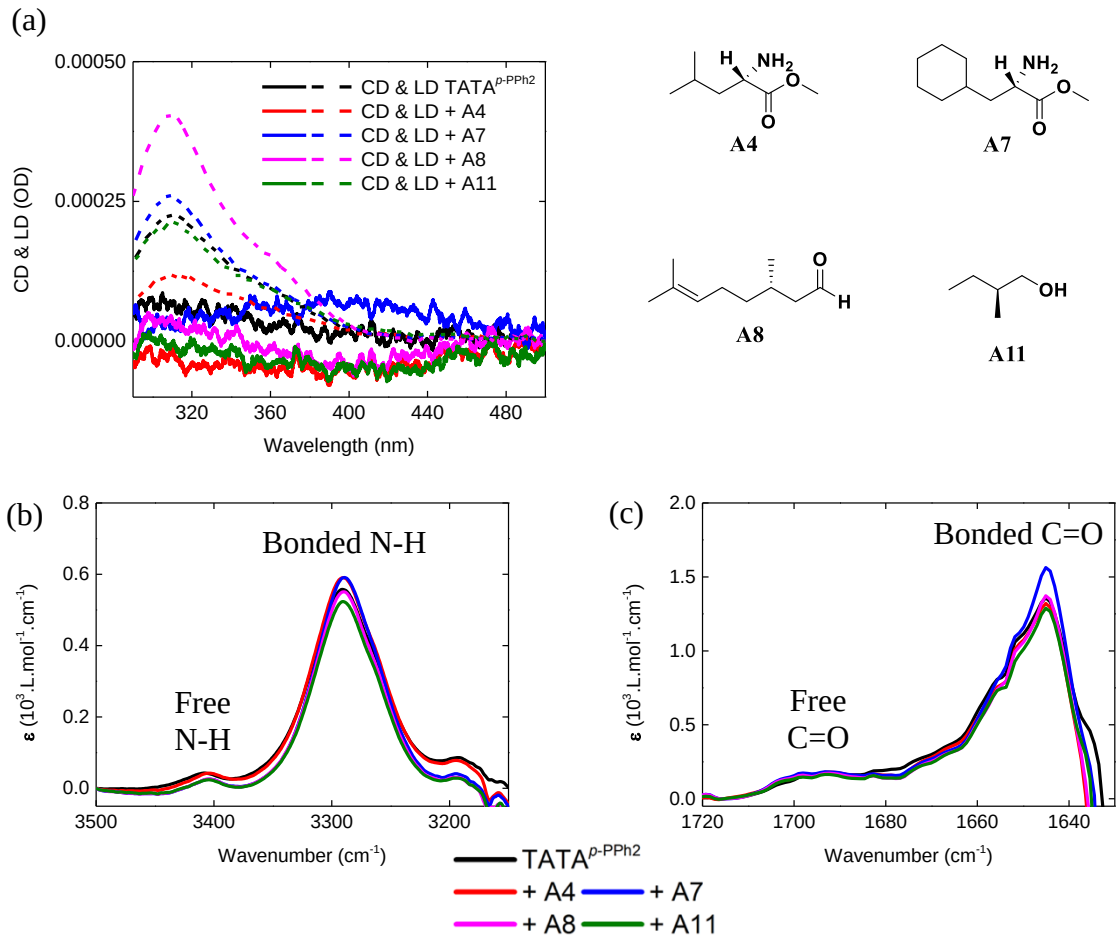

Figure V.6 (a) CD (solid lines) + LD (dashed lines) and (b–c) FT–IR analyses of **TATA$^{p\text{–}PPh2}$** in toluene (1.8 mM) at 20°C and of mixtures of **TATA$^{p\text{–}PPh2}$** (1.8 mM) with the additives **A4**, **A7**, **A8** or **A11** (0.2 mM, 10 mol%, molecular structures on the top right corner), with a zoom on the (b) N-H and (c) C=O regions.

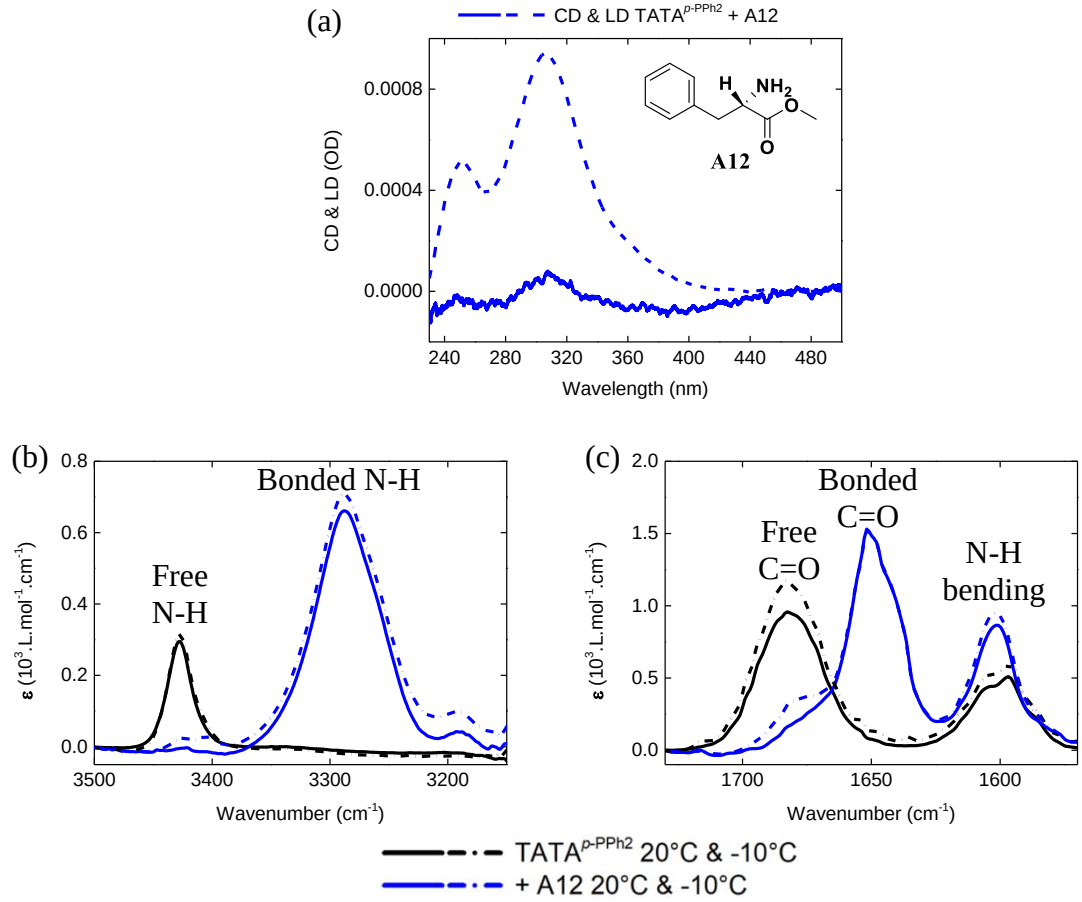

Figure V.7 (a) CD (solid line) + LD (dashed line) and (b–c) FT–IR analyses of **TATA$^{p\text{–}PPh2}$** in dichloromethane (1.8 mM) at 20°C then at -10°C and of the mixture of **TATA$^{p\text{–}PPh2}$** (1.8 mM) and **A12** (0.2 mM, 10 mol%, molecular structure in (a)) with a zoom on the (b) N-H and (c) C=O regions.

IV. 2. With 100 mol% of chiral additives in toluene or dichloromethane

In light of the results of the mixtures containing 10 mol% of chiral additives, the concentration was increased up to 100 mol%, to reach a stoichiometric **TATA$^{p\text{–}PPh2}$**/chiral

additive ratio. The aim was to favor interactions and chiral induction. In decalin at 1.8 mM and 20°C, CD, LD and UV–Vis analyses of the different mixtures are shown in **Figure V.8**.

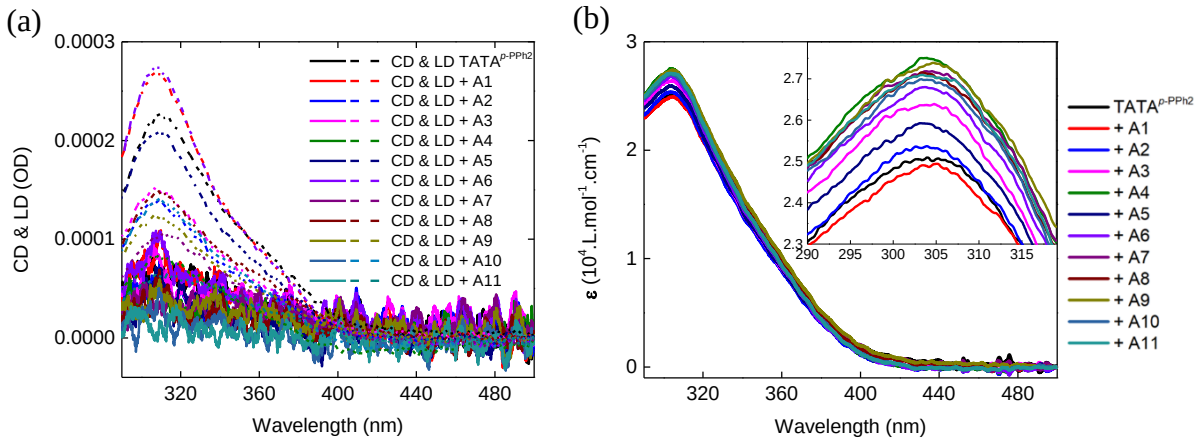

Figure V.8 (a) CD (solid lines) + LD (dashed lines) and (b) UV–Vis analyses of **TATA$^{p\text{–}PPh2}$** in toluene (1.8 mM) at 20°C, and of the mixtures of **TATA$^{p\text{–}PPh2}$** with additives **A1** to **A11** (1.8 mM each, 1/1 ratio).

All solutions exhibit only weak CD signals, together with LD contributions of similar shape and variable intensity. The gel state is maintained for all mixtures. Relatively to UV signal of the pure TATA ligand, a small hyperchromic shift of the main UV absorption band at 305 nm is observed for all mixtures except that of **A1**. The larger this shift, the lower the LD contribution which might be consistent with a competitive character of the additives that decreases the anisotropy of the samples. However, this interaction is likely weak and non-directional as no transfer of chirality is detected. In dichloromethane, the addition of **A12** did not make the **TATA$^{p\text{–}PPh2}$** sample CD-active either (**Figure V.9**). Again, a weak competitive effect of **A12** is detected at -10°C (ε = 2.82 *vs.* 2.67 *vs.* 2.52 L.mol^{-1}.cm^{-1} for 100%mol-mixture, 10%mol-mixture and pure TATA ligand, respectively).

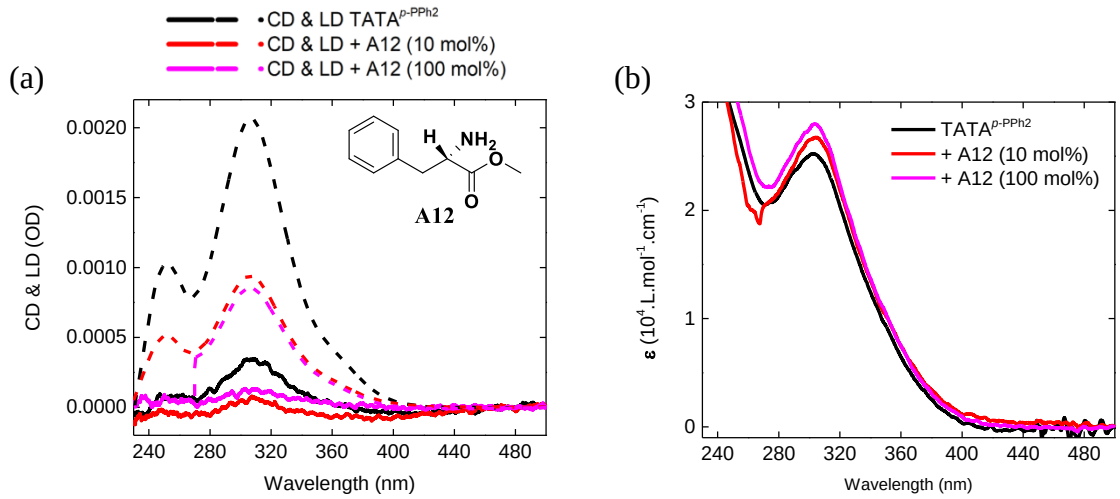

Figure V.9 (a) CD (solid lines) + LD (dashed lines) and (b) UV–Vis analyses of **TATA$^{p\text{–PPh2}}$** in dichloromethane (1.8 mM) at -10°C, and of the mixtures of **TATA$^{p\text{–PPh2}}$** (1.8 mM) and **A12** (0.2 mM, 10 mol% or 1.8 mM, 1/1 ratio; molecular structure in (a)).

IV. 3. With 100 mol% of chiral additives in decalin

The effect of 100 mol% of additives on assemblies was then probed in decalin, an apolar solvent which could favor interactions between **TATA$^{p\text{–PPh2}}$** stacks and chiral molecules. However, only the additives **A1**, **A5**, **A8**, **A9**, **A10** and **A11** (alcohols, one amino alcohol and citronellol derivatives) were soluble in decalin at this concentration (*i.e.* 1 mM).

The ligand solution exhibits at 20°C a CD signal together with a strong LD contribution of similar shape (**Figure V.10a**). This is likely due to the presence of very long and aligned fibers, *i.e.* the sample is slightly anisotropic. The mixture with (*S*)-(+)-2-octanol (**A1**) was investigated by CD and LD spectroscopy at 20 °C (**Figure V.10a**, UV–Vis analyses in **Figure SV.19a**) and thanks to variable-temperature (VT) FT–IR spectroscopy (**Figure V.10b** and **Figure SV.19b** and **c**). A weak CD signal is measured, likely emanating from LD a contribution which follows the same profile. Upon flipping the sample around its vertical axis, a CD mirror image is observed, outlining the absence of a biased supramolecular chirality. Like the trend observed for mixtures in toluene, the UV–Vis molar extinction coefficient of the solution containing the additive **A1** is higher than that of the ligand alone, which could suggest some interactions between **A1** and **TATA$^{p\text{–PPh2}}$**. Likewise, VT–FT–IR measurements highlighted a

plateau at lower degree of aggregation with the additive than for the ligand alone ($\alpha_{Agg} \approx 0.85$ *vs.* 0.93), meaning that **TATA$^{p–PPh2}$** molecules develop less hydrogen bonds between them, which can be explained by some interaction with (*S*)-(+)-2-octanol. Unfortunately, these interactions do not induce a detectable bias to TATA supramolecular helices

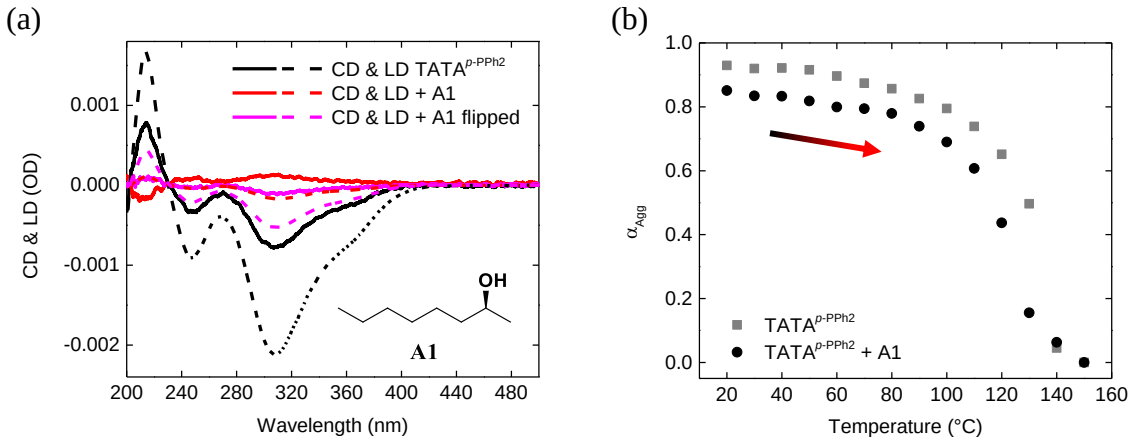

Figure V.10 (a) CD (solid lines) + LD (dashed lines) analyses of **TATA$^{p–PPh2}$** in decalin (1 mM) at 20°C and of the mixture of **TATA$^{p–PPh2}$** (1 mM) with **A1** (1 mM, 100 mol%, molecular structure on the bottom right corner) in decalin at 20°C. (b) Evolution of the degree of aggregation as a function of the temperature, as deduced from **Figure V.4** and **Figure SV.19**. The degree of aggregation (α_{Agg}) was calculated from the evolution of the free C=O stretching vibration absorption signal at 1706 cm^{-1}, as a function of the temperature.

CD and LD analyses for the mixtures containing 100 mol% of the additive **A5**, **A8** or **A9** are depicted in **Figure V.11**, while UV–Vis absorption spectra are shown in **Figure SV.20**. Even though no CD_{iso} was found, these experiments indicate that LD contributions, being erratic as they depend on the macroscopic orientation of fibers, can lead to mirror-image CD between samples.

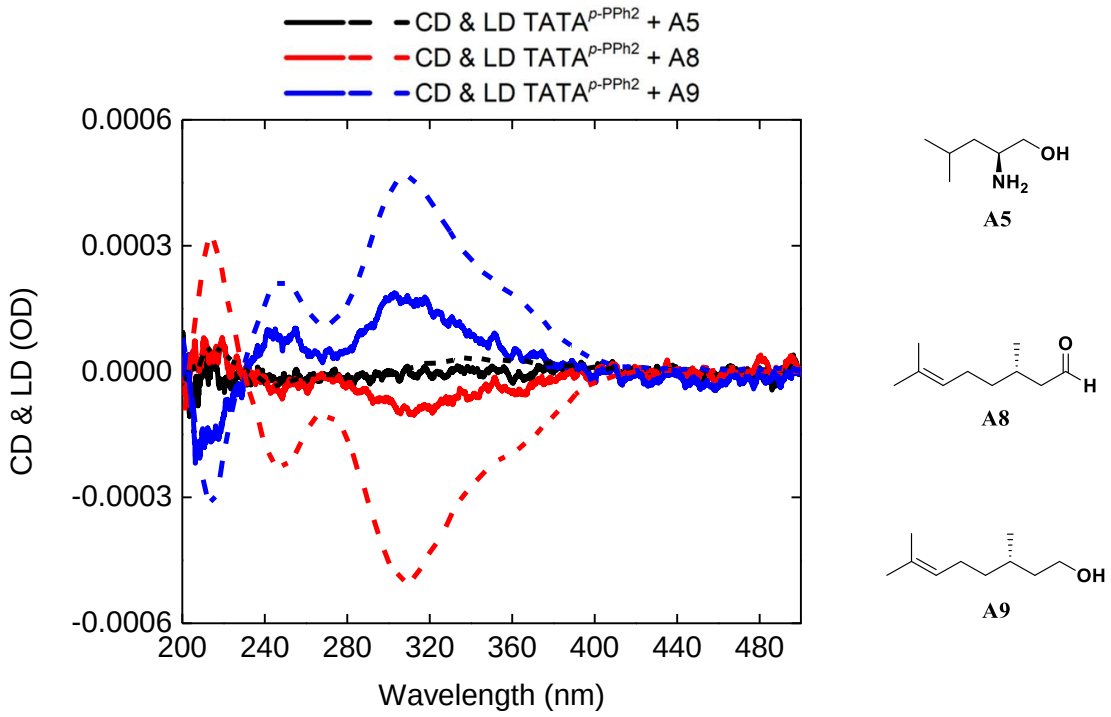

Figure V.11 CD (solid lines) + LD (dashed lines) analyses of mixtures of **TATA$^{p\text{–PPh2}}$** (1 mM) with **A5**, **A8** or **A9** (1 mM, 100 mol%, molecular structures on the right) in decalin (1 mM) at 20°C.

Mixtures with **A10** and **A11** exhibited more intriguing analyzes and are thus described separately below. The mixture with additive **A10** shows a weak CD signal which is inverted upon cooling from about 110°C to 20°C (**Figure V.12a**) in a repeatable way, while the evolution of corresponding LD signals is more erratic, sometimes positive, sometimes negative (**Figure V.12b**). Nevertheless, both CD spectra at 20°C and 106°C are largely affected upon sample flipping, suggesting that a large part of the signal is coming from LD. Again, the competitive nature of **A10** is reflected by the lower degree of aggregation between 20°C and 50°C than the ligand alone ($\alpha_{Agg} \approx 0.83$ *vs.* 0.93 for the mixture and pure ligand, respectively).

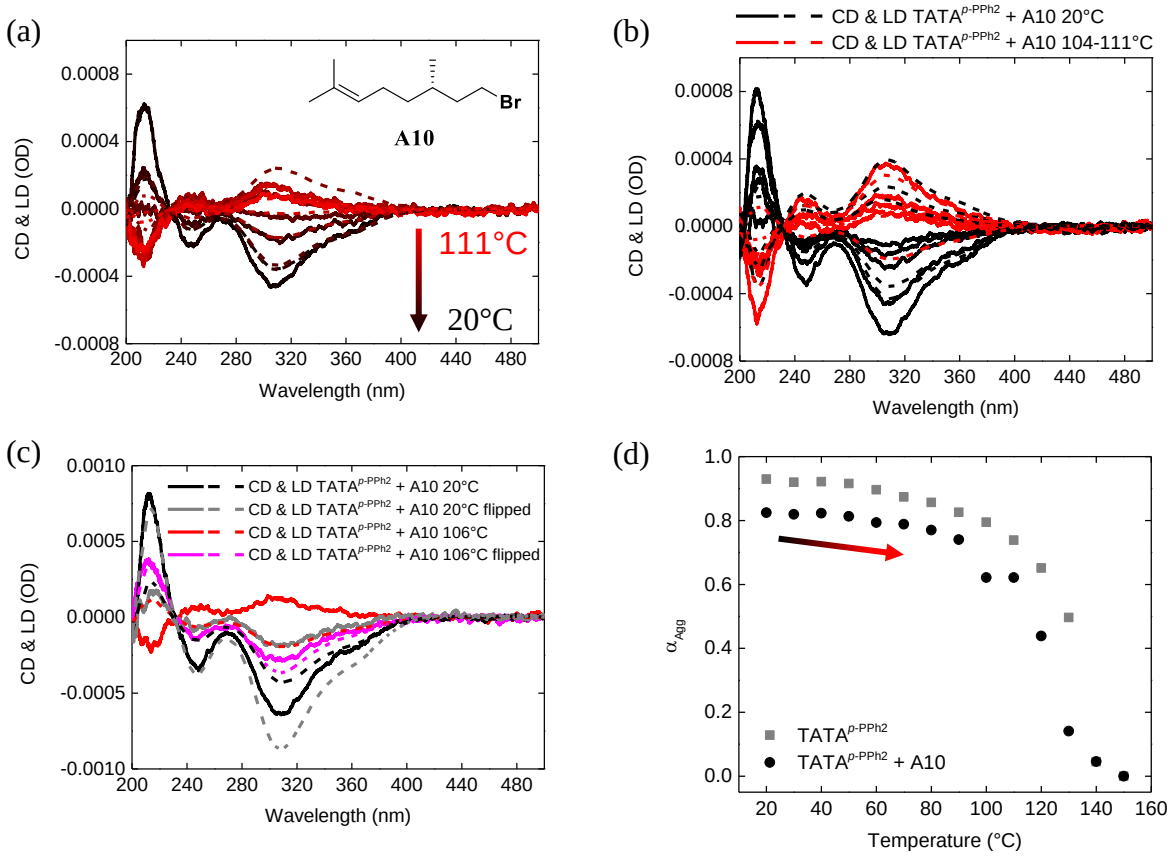

Figure V.12 (a) Temperature-dependent CD (solid lines) + LD (dashed lines) analyses of the mixture of **TATA$^{p\text{–PPh2}}$** (1 mM) with **A10** (1 mM, 100 mol%) in decalin. Spectra were recorded during a cooling process at 111°C, 100°C, 90°C, 80°C, 60°C, 40°C and 20°C. (b) Repeated CD (solid lines) + LD (dashed lines) at 20°C and high temperature (between 104°C and 111°C). (c) CD (solid lines) + LD (dashed lines) analyses of the same mixture, at 20°C and 106°C, before and after a 180°-rotation around the vertical axis ("flipped"). (d) Evolution of the degree of aggregation as a function of the temperature, as deduced from **Figure V.4** and **Figure SV.21**. The degree of aggregation (α_{Agg}) was calculated from the evolution of the free C=O stretching vibration absorption signal at 1706 cm^{-1}, as a function of the temperature.

Finally, the mixture with **A11** was analyzed by flipping and by rotating the CD cell (**Figure V.13**). The CD signal is inverted upon flipping. The rotation, was performed in such a

way that the digital integration time[XLIV] and the revolution of the sample are of the same magnitude. This induced saw-toothed CD signals but we can conclude that the CD is only the fruit of contributions coming from LD and to a lesser extent from spectrophotometric artefacts.

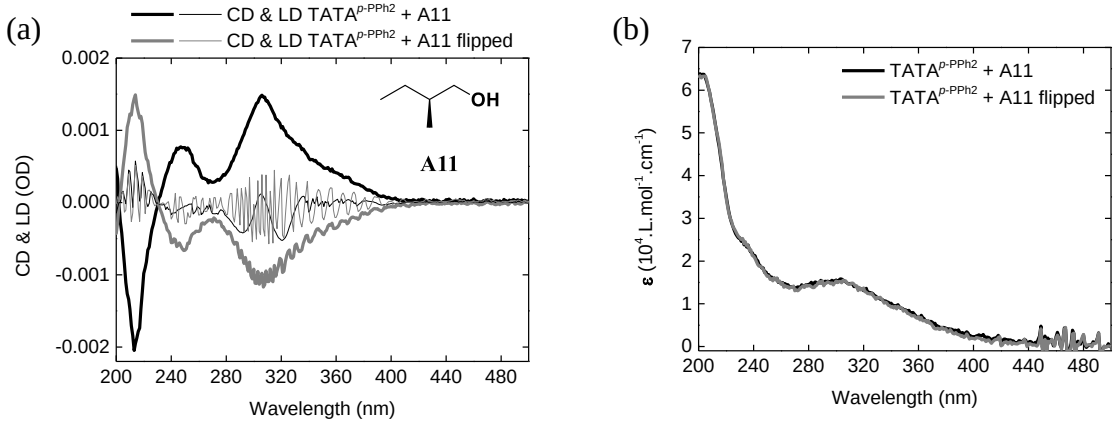

Figure V.13 (a) CD (solid lines) + LD (dashed lines) and (b) UV–Vis analyses of the mixture of **TATA$^{p\text{–PPh2}}$** (1 mM) with **A11** (1 mM, 100 mol%, molecular structure on the top right corner of (a)) in decalin (1 mM) at 20°C. The sample was analyzed, before and after a 180°-rotation around the vertical axis ("flipped"). Spectra were recorded in a cylindrical cell under rotation (330 rpm, one revolution each 0.18 s) with a digital integration time between 0.125 s and 0.25 s, controlled by the spectrophotometer.

In summary, addition of a stoichiometric amount of chiral additives to **TATA$^{p\text{–PPh2}}$** decalin solutions did not succeed to direct the handedness of assemblies, despite competing with the hydrogen-bonded stacks. CD signals, measured and interpreted by considering the contributions coming from LD and to a lesser extent from spectrophotometric artefacts, highlighted again that CD spectra must be interpreted cautiously, especially in strongly associated systems like gels.

[XLIV] The "digital integration time or D.I.T. is the amount of time that the data is integrated over or the length of time the detector collects photons before transferring the signal to the A/D converter for processing."[34] In this way, by optimizing the D.I.T. to collect the light passing through the sample during one complete rotation, it could nullify the contributions depending on the sample orientation, like the artefacts coming from the spectrophotometer[35]. Unfortunately, it was not possible here to adjust exactly the D.I.T. with the rotation of the cell, leading to sawtooth signals of which the rotation-dependent contributions are more or less cancelled.

IV. 4. In (−)-α-pinene and (*R*)-limonene

(−)-α-pinene and (*R*)-limonene were then used as solvent to test if their chirality could be transferred to the **TATA$^{p–PPh2}$** assemblies, as already observed for macromolecular[2,7–9] and supramolecular[13,14] polymers. Interestingly, these chiral solvents do not absorb in the UV range of the main absorption band of the **TATA$^{p–PPh2}$** molecule, nor in the N-H region in FT−IR. 1.8 mM solutions of **TATA$^{p–PPh2}$** in (−)-α-pinene and (*R*)-limonene were thus prepared, and analyzed by CD and LD (**Figure V.14a** and **b**) spectroscopy, as well as by VT–UV–Vis (**Figure V.14c** and **d**) and VT–FT–IR (**Figure V.15**) techniques.

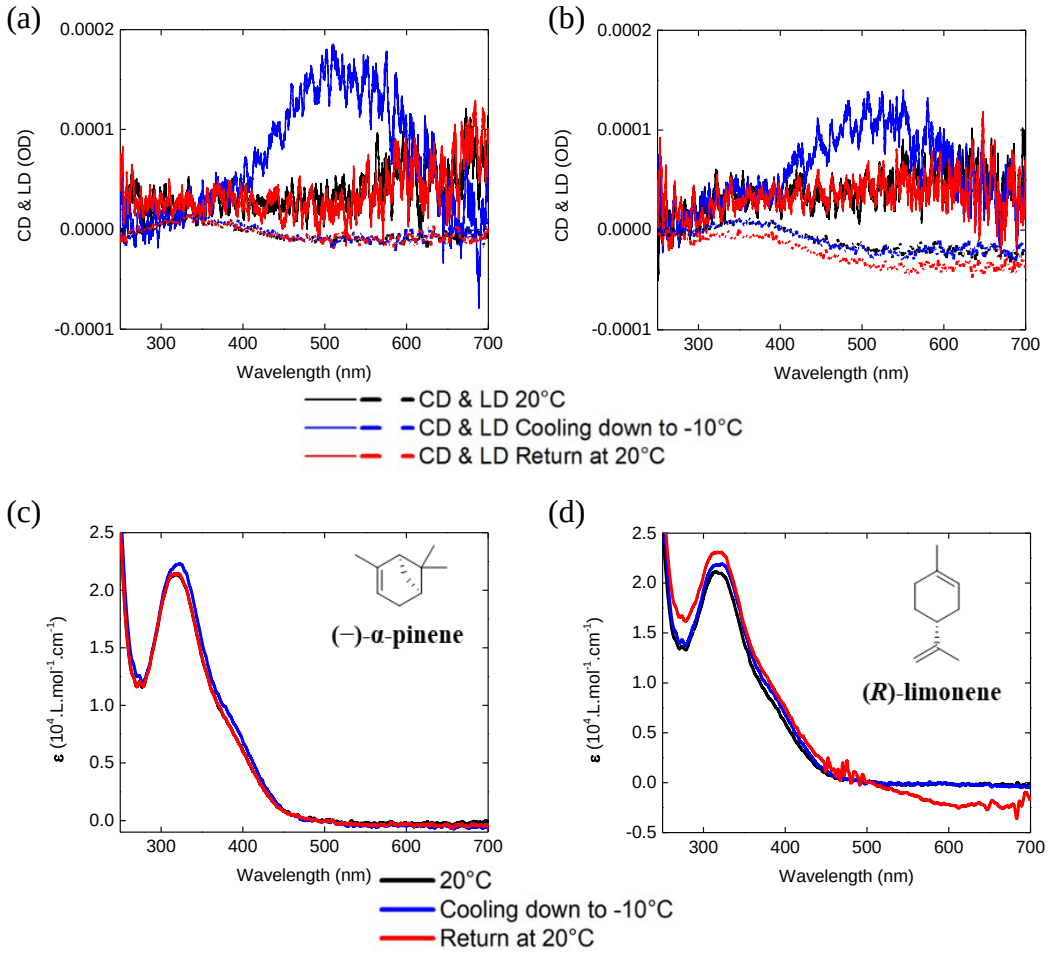

Figure V.14 (a–b) CD (thin solid lines) + LD (thick dashed lines) and (c–d) UV–Vis analyses of **TATA$^{p–PPh2}$** in (a and c) (−)-α-pinene or (b and d) in (*R*)-limonene (1.8 mM) at 20°C, at -10°C and at 20°C after the cooling process. (d) The baseline issue of the molar extinction coefficient between 500 and 700 nm is maybe due to the presence of limonene oxide.

No CD nor LD signals were observed for **TATA$^{p\text{–PPh2}}$** in (−)-α-pinene and (*R*)-limonene, but a weak CD signal devoid of LD contributions was measured at -10°C for both solutions. Nevertheless, this broad CD is outside from the absorption range of **TATA$^{p\text{–PPh2}}$** and cannot be in this way regarded as the manifestation of TATA assemblies with a biased handedness, but rather likely the sign of weak artifacts.

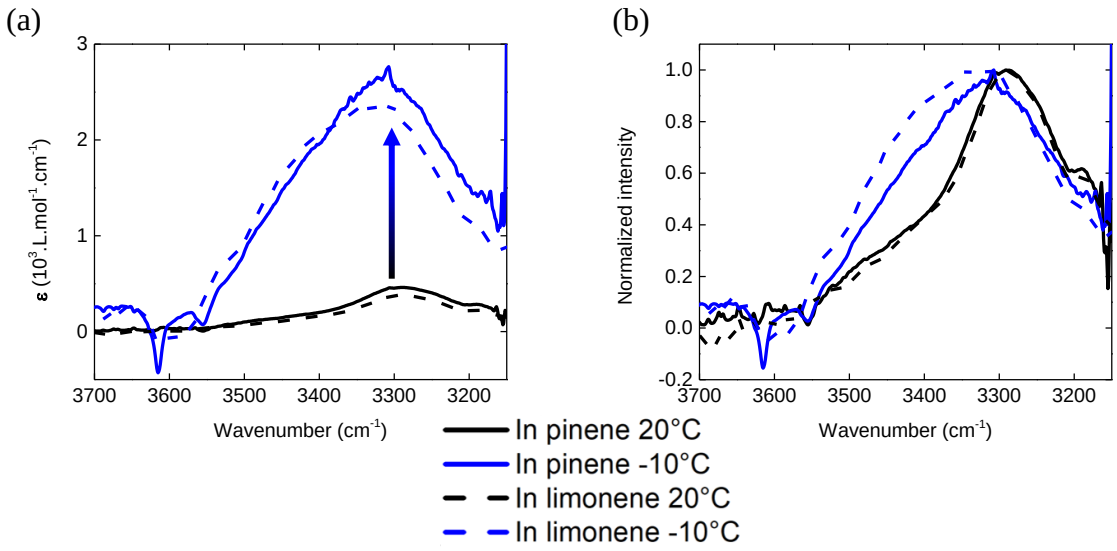

Figure V.15 FT–IR analyses of **TATA$^{p\text{–PPh2}}$** in (−)-α-pinene or (*R*)-limonene (1.8 mM) at 20°C and -10°C, in (a) molar extinction coefficient and (b) normalized intensity.

Regarding the VT–FT–IR results depicted in **Figure V.15**, both solutions in (−)-α-pinene and (*R*)-limonene showed a very broad signal centered on 3300 cm^{-1}, in the IR region corresponding to the stretching vibrations of hydrogen bonded N-H[30]. The intensity increases surprisingly upon cooling ($\Delta\varepsilon \approx 2 \times 10^3$ L.mol^{-1}.cm^{-1}), which is probably due to precipitation.

V. Conclusion

This chapter deals with the synthesis and characterization of designed TATA ligands, the characterization of their self-assemblies in different solvents and various attempts aimed at inducing a preferential handedness to their helical assemblies by means of chiral additives and solvents. These attempts belong to the second proposed strategy for absolute asymmetric catalysis, for which helically biased supramolecular polymers composed only of TATA ligands are engaged in asymmetric reactions.

More precisely, two TATA ligands, **TATA$^{p–PPh2}$** and **TATA$^{m–PPh2}$** featuring a PPh_2 unit connected to *meta* and *para* position of a phenylene linker, were synthesized for the first time thanks to a multi-step procedure. Solubility tests at 1 mM in solvents of various polarities evidenced that TATA ligands are soluble in a large range of solvents, including chlorinated solvents, and formed long assemblies in key solvents for catalytic applications such as toluene. The study of self-association properties of **TATA$^{p–PPh2}$** in toluene, dichloromethane and decalin, by VT–UV–Vis and FT–IR spectroscopy, showed the reversible formation of long hydrogen-bonded stacks. Next, a library of enantiopure small molecules (10 mol% or 100 mol%), covering a broad spectrum of functional groups, were added to **TATA$^{p–PPh2}$** in toluene, dichloromethane or decalin solutions. In summary, these chiral additives did not succeed to direct the handedness of assemblies, despite competing with the hydrogen-bonded functions of the stacks in a large number of cases. (−)-α-Pinene and (*R*)-limonene were then used as solvents for **TATA$^{p–PPh2}$**, but no strong CD accounting for biased **TATA$^{p–PPh2}$** aggregates was measured.

Along the same direction, new chiral additives including arene groups could be tested, expecting it will favor aromatic interactions, and maybe intercalations within **TATA$^{p–PPh2}$** assemblies. Derivatives of citronellol (e.g. **A8**, **A9** and **A10**) could also be tested as chiral solvents. In addition, CPL could be employed as chiral inducer either in chlorinated solvents (with the concomitant formation of radicals, similarly to what was attempted with **TATA-SDA** in Chapter IV) or in decalin, e.g. by irradiating a decalin solution heated up to reach the monomeric state and cooled to form hydrogen-bonded helical stacks.

VI. Supporting Information

VI. 1. Supplementary Figures

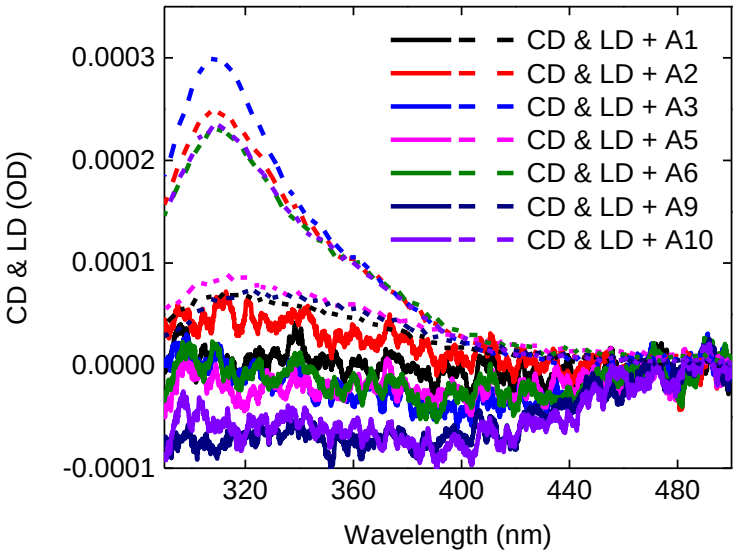

Figure SV.16 CD (solid lines) + LD (dashed lines) analyses of **TATA**$^{p\text{–PPh2}}$ in toluene (1.8 mM) at 20°C and of mixtures with **A1**, **A2**, **A3**, **A5**, **A6**, **A9** or **A10** at 10 mol%.

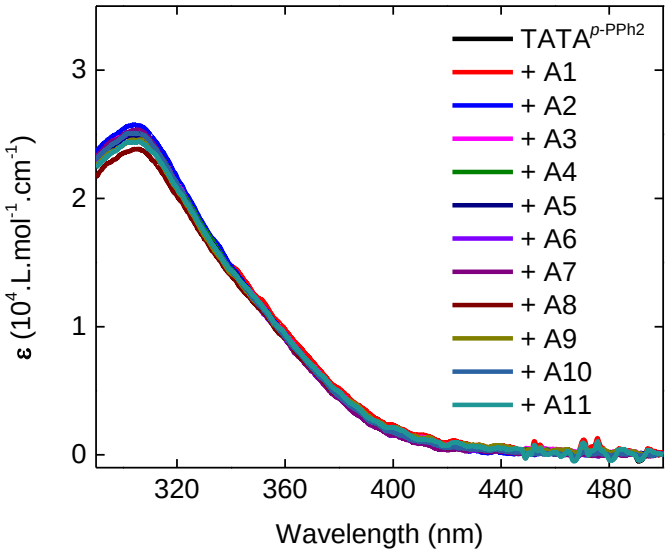

Figure SV.17 UV–Vis analyses of **TATA**$^{p\text{–PPh2}}$ in toluene (1.8 mM) at 20°C and of mixtures with **A1** to **A11** at 10 mol%.

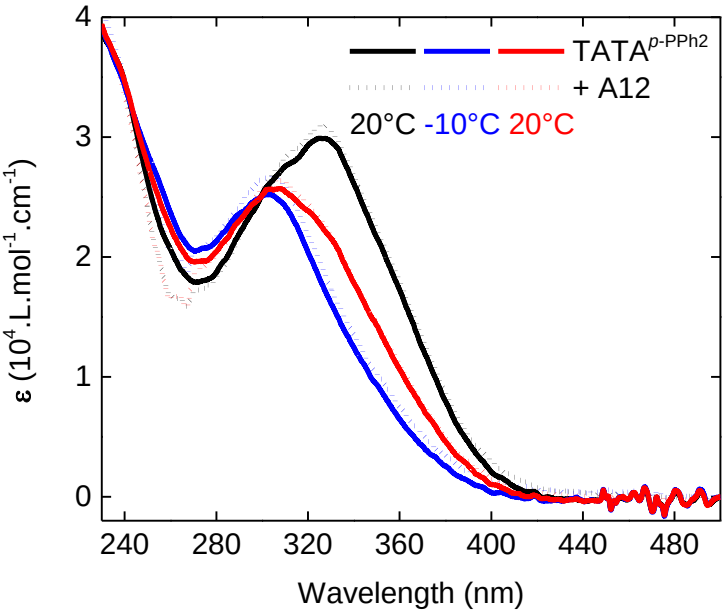

Figure SV.18 UV–Vis analyses of **TATA$^{p\text{–PPh2}}$** in dichloromethane (1.8 mM, solid lines) and of mixtures with **A12** at 10 mol% (short dots) at 20°C, at -10°C and at 20°C after the cooling process.

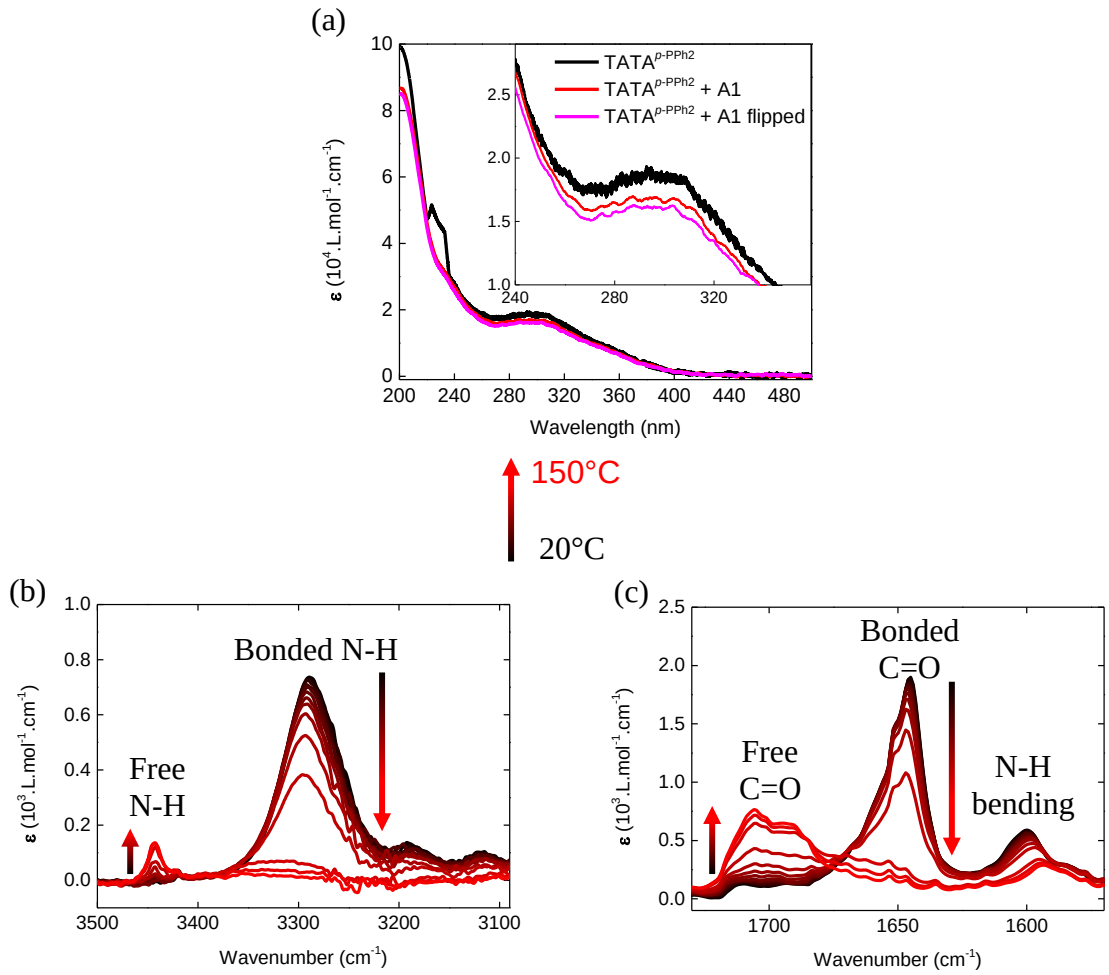

Figure SV.19 (a) UV–Vis analyses of **TATA$^{p\text{–}PPh2}$** in decalin (1 mM) at 20°C, and of mixtures with **A1** at 100 mol% before and after a 180°-rotation around the vertical axis ("flipped"). (b–c) FT–IR analyses of **TATA$^{p\text{–}PPh2}$** in decalin (1 mM) and of mixtures with **A1** at 100 mol%, with a zoom on the (b) N-H and (c) C=O regions. FT–IR spectra were recorded during a heating process between 20°C and 150°C for a rate of 0.7°C/min.

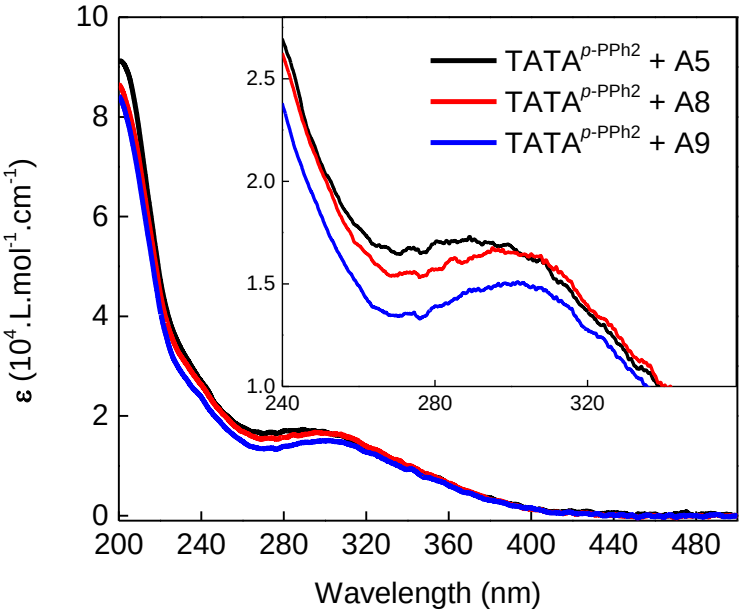

Figure SV.20 UV–Vis analyses of **TATA$^{p\text{–PPh2}}$** in decalin (1 mM) at 20°C and of mixtures with additives **A5**, **A8** or **A9** at 100 mol%.

The main UV signals appear to be also inconsistent compared with the ligand alone ($\varepsilon \approx 1.9 \times 10^4$ L.mol^{-1}.cm^{-1} and $\lambda = 295$ nm), either hypo- and batho-chromically shifted with the additive **A5** ($\varepsilon \approx 1.7 \times 10^4$ L.mol^{-1}.cm^{-1} and $\lambda = 289$ nm), or hypo- and hyper-chromically shifted with the additives **A8** and **A9** ($\varepsilon \approx 1.7 \times 10^4$ L.mol^{-1}.cm^{-1} / $\lambda = 296$ nm and $\varepsilon \approx 1.5 \times 10^4$ L.mol^{-1}.cm^{-1} / $\lambda = 302$ nm, respectively), impelling us to suspend our judgement on this set of results.

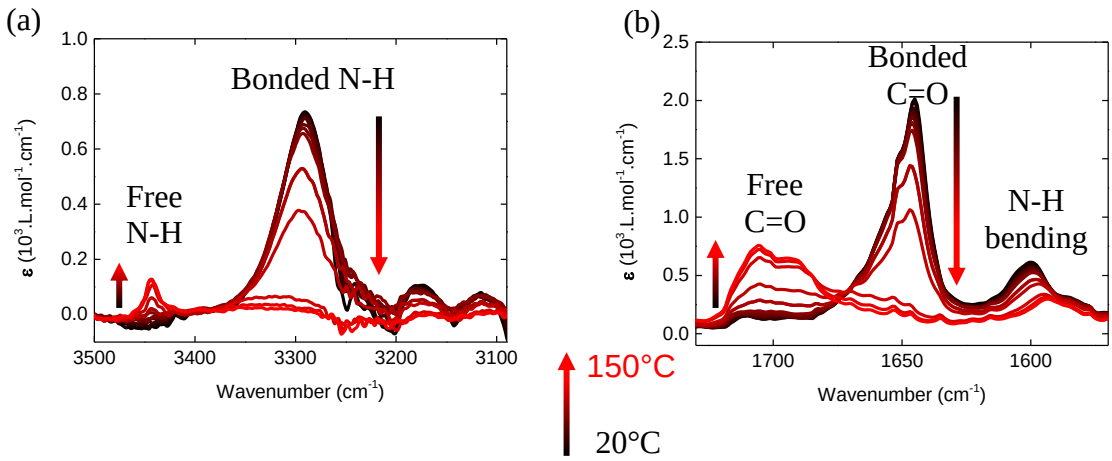

Figure SV.21 (a–b) FT–IR analyses of **TATA$^{p–PPh2}$** in decalin (1 mM) and of mixtures with **A10** at 100 mol%, with a zoom on the (a) N-H and (b) C=O regions. FT–IR spectra were recorded during a heating process between 20°C and 150°C for a rate of 0.7°C/min.

VI. 2. Experimental section

VI. 2. 1. Materials

A1: (*S*)-(+)-2-octanol (99%); **A2**: (*S*)-(+)-2-amino-3-methyl-1-butanol (96%); **A3**: L-methionine methyl ester (98%); **A4**: L-leucine methyl ester (98%); **A5**: (*S*)-(+)-leucinol (96%); **A6**: L-norleucine methyl ester (95%); **A7**: β-cyclohexyl-L-alanine methyl ester (95%); **A8**: (*S*)-(−)-citronellal (96%); **A9**: (*S*)-(−)-ß-Citronellol (≥97%); **A10**: (*S*)-(+)-citronellyl bromide (95%); **A11**: (*S*)-(−)-2-methylbutanol (99%); and **A12**: L-phenylalanine methyl ester (98%) were purchased from Sigma-Aldrich and Fluorochem, and used as received. Cs_2CO_3, RuPhos, $Pd(OAc)_2$, Hydrazine hydrate, Stearic acid, $SnCl_2$, 3-Fluorobenzoic acid, lithium hydroxide, Ph_2PK in THF, 4-(Diphenylphosphino)-benzoic acid, 4-bromonitrobenzene, *N*-methyl-2-pyrrolidone, acetic acid, phthalic anhydride, 4,4'-diaminodiphenylamine sulfate hydrate, *N*-(3-dimethylaminopropyl)-*N'*-ethylcarbodiimide hydrochloride (EDC·HCl), and 4-(Dimethylamino)pyridine (DMAP) were purchased from Acros, Alfa Aesar, Sigma-Aldrich, Fluorochem or TCI suppliers and used as received. Unless otherwise noted, chromatography-grade solvents were used as received. Dried toluene was obtained from a Solvent Purification System (SPS, IT-Inc). DMSO-d_6 and CD_2Cl_2 were bought from Eurisotop and used without further purification.

VI. 2. 2. Methods

NMR spectra were recorded on a Bruker Avance 400 or 300 spectrometer and calibrated to the residual solvent peak: DMSO-d_6 (^{1}H: 2.50 ppm; ^{13}C: 39.52 ppm), $CDCl_3$ (^{1}H: 7.26 ppm; ^{13}C: 77.16 ppm) or CD_2Cl_2 (^{1}H: 5.32 ppm; ^{13}C: 53.84 ppm). Peaks are reported with their corresponding multiplicity (s: singlet (br for broad); d: doublet, t: triplet; q: quartet; quint: quintuplet; hept: heptuplet; dd: doublet of doublets, dt: doublet of triplets; td: triplet of doublets), integration and J coupling constant given in Hertz.

Solubility tests were carried out inside screw cap vials with 2 mL of solvent.

Fourier-Transform Infrared (FT–IR) measurements were performed on a Nicolet iS10 spectrometer. Solution spectra were measured in CaF2 cells of various pathlength (1 and 2 mm, according to the concentration) and were corrected for air, solvent and cell absorption. Films were measured on KBr pellets and corrected for air and cell absorption.

UV–Vis absorption spectra were extracted from CD analyses and obtained after correction of the absorption of air, solvent, and cell contribution at the same temperature. Circular dichroism (CD) measurements were performed on a Jasco J-1500 spectrometer equipped with a Peltier thermostatted cell holder and Xe laser. Data were recorded with the following parameters: 50, 100 or 200 nm.min^{-1} sweep rate, 0.05, 0.5 or 1 nm data pitch, 1 or 2 nm bandwidth, and between 700 or 400 and 220 or 200 nm.

VI. 3. Syntheses of TATA$^{p\text{–}PPh2}$ and TATA$^{m\text{–}PPh2}$

VI. 3. 1. Synthesis of 1 (adapted from Sugawara *et al.*[36])

4,4'-diaminodiphenylamine sulfate hydrate (16.5 g, 55.49 mmol, 1 eq) and phthalic anhydride (18.1 g, 122.20 mmol, 2.2 eq) were dissolved into a mixture acetic acid (155 mL), *N*-methyl-2-pyrrolidone (78 mL) in a round-bottom flask equipped with a reflux condenser, then heated at 125°C. The reactive medium was stirred for 24 h then let to come back to room temperature. 66 mL of methanol were added, and the precipitate was isolated by filtration, washed with 80 mL of methanol, then suspended in 94 mL of *N*-methyl-2-pyrrolidone and heated to 100°C for dissolution. After cooling this solution to room temperature, 187 mL of

methanol were added and the precipitate was filtered off, prior to be washed with 87 mL of methanol and dried *in vacuo* to give the product **1** as a green solid (20.6 g, 81% yield). ^{1}H NMR (DMSO-d_6, 400 MHz, 300 K): δ (ppm) = 8.62 (s, 1H), 7.95 (dd, J = 6.1, 4.1 Hz, 4H), 7.91 (dd, J = 5.1, 2.1 Hz, 4H), 7.30 (d, J = 7.5 Hz, 4H), 7.26 (d, J = 7.5 Hz, 4H).

VI. 3. 2. Synthesis of 2

4-bromonitrobenzene (9.72 g, 48.12 mmol, 2.2 eq) was dissolved in 480 mL of THF in a round-bottom flask. **1** (10.03 g, 21.83 mmol, 1 eq), Cs_2CO_3 (14.19 g, 21.83 mmol, 2 eq), RuPhos (0.72 g, 1.53 mmol, 0.07 eq), and $Pd(OAc)_2$ (0.20 g, 0.87 mmol, 0.04 eq) were then added at room temperature and under argon. The reactive medium was stirred for 18 h under reflux (90°C) and followed by ^{1}H NMR. The solution was cooled down to room temperature, evaporated *in vacuo* and the resulting solid was washed successively with 150 mL of HCl (0.1 M), dichloromethane, ethyl acetate and methanol. The solid was dried in vacuo to give the product **2** as a yellow solid (8.86 g, 70% yield). ^{1}H NMR (DMSO-d_6, 400 MHz, 300 K): δ (ppm) = 8.17 (dd, J = 9.0, 4.8 Hz, 2H), 8.02 – 7.96 (m, 4H), 7.95 – 7.89 (m, 4H), 7.56 (dd, J = 9.2, 4.4 Hz, 4H), 7.44 (dd, J = 8.8, 5.2 Hz, 4H), 7.01 (dd, J = 9.4, 4.8 Hz, 2H).

VI. 3. 3. Synthesis of 3 (inspired from Leung *et al.*[22])

2 (11.55 g, 19.90 mmol) was dissolved in ethanol (900 mL) inside an oven-dried 2-necked round-bottom flask under stirring for 5 min at room temperature. Hydrazine hydrate (2.90 mL, 2.99 g, 59.7 mmol) was then added. The reactive medium was stirred for 3 h 30 under reflux (90°C). The solution was cooled down to room temperature, evaporated *in vacuo* and washed with dichloromethane on a Buchner filter. The red dichloromethane phase was evaporated to give the product **3** as a red solid (5.21 g, 82% yield). ^{1}H NMR (DMSO-d_6, 300 MHz, 300 K): δ (ppm) = 7.95 (dd, J = 9.2, 5.3 Hz, 2H), 6.95 (dd, J = 8.5, 4.5 Hz, 4H), 6.60 (dd, J = 9.1, 4.4 Hz, 4H), 6.53 (dd, J = 9.3, 5.6 Hz, 2H), 4.15 (s, 4H).

VI. 3. 4. Synthesis of 4

Stearic acid (2.7 g, 9.37 mmol, 3 equiv.), DMAP (1.2 g, 9.98 mmol, 3.2 equiv.) and EDC·HCl (1.8 g, 9.37 mmol, 3 equiv.) were dissolved under stirring in non-stabilized dry THF (240 mL) in an oven-dried round-bottom flask under argon during 10 min. Then, **3** (1.0 g, 3.12

mmol, 1 equiv.) was added as solid under argon. The reactive mixture was refluxed at 90°C for 3 days under argon. The solution was cooled down to room temperature, washed with HCl at 1M (300 mL) and extracted with 200 mL of dichloromethane. The organic phase was washed with 200 mL of saturated NaHCO3 and brine, dried over $MgSO_4$, filtered and evaporated under vacuum to yield the crude product. It was purified by flash column chromatography (dichloromethane:ethyl acetate, 9:1) on silica column to give the product **4** as a yellow solid (2.11 g, 79% yield). ^{1}H NMR ($CDCl_3$, 400 MHz, 300 K): δ (ppm) = 8.02 (d, J = 8.6 Hz, 2H), 7.52 (d, J = 7.9 Hz, 4H), 7.16 – 7.08 (m, 6H), 6.88 (d, J = 8.6 Hz, 2H), 2.36 (t, J = 7.2 Hz, 4H), 1.72 (q, J = 7.4 Hz, 4H), 1.45 – 1.20 (m, 56H), 0.88 (t, J = 5.3 Hz, 6H).

VI. 3. 5. Synthesis of 5 (inspired from Giuseppone *et al.*[23])

4 (400 mg, 0.47 mmol, 1 eq) was refluxed at 95°C for 17 h with $SnCl_2$ (1.2 g, 6.33 mmol, 13.5 eq) in a mixture of acetonitrile (6.5 mL) and ethanol (8 mL) under argon. The reactive mixture was then diluted with 100 mL of ethyl acetate, washed with 60 mL of NaOH (1 M) and 50 mL of brine, dried over $MgSO_4$, filtered and condensed *in vacuo* to give the product **5** as a beige solid (182 mg, 47%). ^{1}H NMR (CD_2Cl_2, 400 MHz, 300 K): δ (ppm) = 7.31 (d, J = 8.2 Hz, 4H), 7.10 (s, 2H), 6.93 (d, J = 8.1 Hz, 4H), 6.89 (dd, J = 7.8 Hz, 2H), 6.62 (d, J = 8.1 Hz, 2H), 3.65 (s, 2H), 2.29 (t, J = 7.4 Hz, 4H), 1.67 (q, J = 7.0 Hz, 4H), 1.45 – 1.19 (m, 56H), 0.88 (t, J = 6.7 Hz, 6H).

VI. 3. 6. Synthesis of 6 (inspired from Stelzer *et al.*[24])

3-Fluorobenzoic acid (2.101 g, 15 mmol, 1 eq) and lithium hydroxide (0.359 g ,15 mmol, 1 eq) were mixed in 200 mL of methanol with traces of water before evaporation *in vacuo*. The lithium salt of 3-fluorobenzoic acid (2.146 g, 14.7 mmol) was then added at ambient temperature to a THF solution (30 mL) of Ph_2PK (3.36 g, 15 mmol). The reactive mixture was refluxed (70°C) for 26 h. The solution was cooled down to room temperature and the solvent was removed under reduced pressure (1 mbar, 30°C). The remaining residues were dissolved in 150 mL of water and filtered through a funnel with fine porosity fritted disc. On acidification of the filtrate, a colorless solid precipitated, which was collected and further purified by recrystallization from a methanol/water mixture to give the product as needle crystals (2.1 g,

46% yield). ^{1}H NMR (DMSO-d_6, 400 MHz, 300 K): δ (ppm) = 13.05 (s, 2H[XLV]), 7.94 (d, J = 7.3 Hz, 2H), 7.79 (d, J = 7.0 Hz, 2H), 7.56 – 7.35 (m, 18H[I]), 7.30 – 7.20 (m, 9H[I]). ^{13}C{^{1}H} NMR (DMSO-d_6, 100 MHz, 300 K): δ (ppm) = 166.9 (s), 137.7 (d, J = 13.1 Hz), 137.3 (d, J = 20.0 Hz), 136.0 (d, J = 11.3 Hz), 133.6 (d, J = 19.2 Hz), 133.3 (d, J = 19.9 Hz), 131.1 (d, J = 7.2 Hz), 129.8 (s), 129.2 (s), 129.0 (d, J = 7.0 Hz), 128.9 (d, J = 7.3 Hz). ^{31}P{^{1}H} NMR (DMSO-d_6, 122 MHz, 300 K): δ (ppm) = -6.20 (with a little of phosphine oxide at 25.8 ppm). ^{13}C and ^{31}P NMR data are in agreement with that of Stelzer *et al.*[24].

VI. 3. 7. Synthesis of TATA^{m-PPh2}

6 (460 mg, 1.50 mmol, 3.1 eq) was dissolved in 280 mL of non-stabilized dry THF in an oven-dried round-bottom flask under argon. DMAP (202 mg, 1.65 mmol, 3.4 eq), EDC·HCl (286 mg, 1.50 mmol, 3.1 eq) and **5** (400 mg, 0.49 mmol, 1 eq) were added as solid and the reactive mixture was let under reflux (70°C) for 48 h under argon. After 48 h, the reactive mixture was washed with brine (200 mL), dried over $MgSO_4$ and condensed in a rotary evaporator, to yield the crude product. This crude product was purified by flash silica column chromatography with cyclohexane/AcOEt (1/1) to give **TATA^{m-PPh2}** as a yellowish solid (272 mg, 50% yield). ^{1}H NMR (CD_2Cl_2, 400 MHz, 300 K): δ (ppm) = 7.80 (m, 3H), 7.50 – 7.25 (m, 16H), 7.22 (s, 2H), 6.99 (m, 6H), 2.30 (t, J = 7.6 Hz, 4H), 1.68 (q, J = 7.0 Hz, 4H), 1.26 (m, 56H), 0.88 (t, J = 7.0 Hz, 6H). ^{31}P{^{1}H} NMR (CD_2Cl_2, 122 MHz, 300 K): δ (ppm) = -5.34 (with a little of phosphine oxide at 27.9 ppm).

VI. 3. 8. Synthesis of TATA^{p-PPh2}

4-(Diphenylphopshino)-benzoic acid (160 mg, 0.52 mmol, 3.1 eq) was dissolved in 100 mL of non-stabilized dry THF in an oven-dried round-bottom flask under argon. DMAP (70 mg, 0.57 mmol, 3.4 eq), EDC·HCl (100 mg, 0.52 mmol, 3.1 eq) and **5** (140 mg, 0.17 mmol, 1 eq) were added as solid and the reactive mixture was left under reflux for 48 h at 70°C under argon. After 48 h, the reactive mixture was washed with brine (100 mL), dried over $MgSO_4$ and condensed in a rotary evaporator, to yield the crude product. This crude product was purified

[XLV] Overestimated.

by flash silica column chromatography with cyclohexane/AcOEt (1/1) to give **TATA$^{p\text{–PPh2}}$** as a yellowish solid (75 mg, 40% yield). ^{1}H NMR (CD_2Cl_2, 400 MHz, 300 K): δ (ppm) = 7.87 (s, 1H), 7.80 (d, J = 7.7 Hz, 2H), 7.50 (m, 2H), 7.37 (m, 15 H), 7.20 (s, 2H), 7.01 (m, 5H), 2.30 (t, J = 7.5 Hz, 4H), 1.67 (q, J = 7.4 Hz, 4H), 1.45 – 1.19 (m, 56H), 0.88 (t, J = 7.0 Hz, 6H). ^{31}P{^{1}H} NMR (CD_2Cl_2, 122 MHz, 300 K): δ (ppm) = -5.42.

VI. 4. NMR spectra

1. ^{1}H NMR (DMSO-d_6, 400 MHz, 300 K)

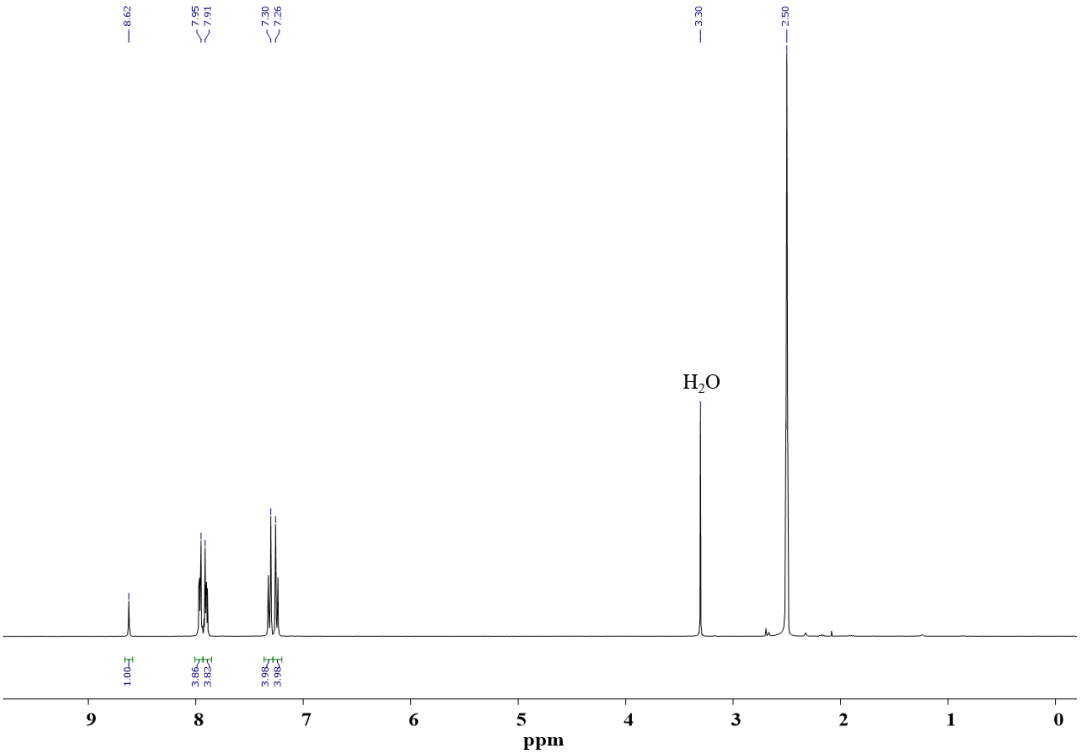

2. ^{1}H NMR (DMSO-d_6, 400 MHz, 300 K)

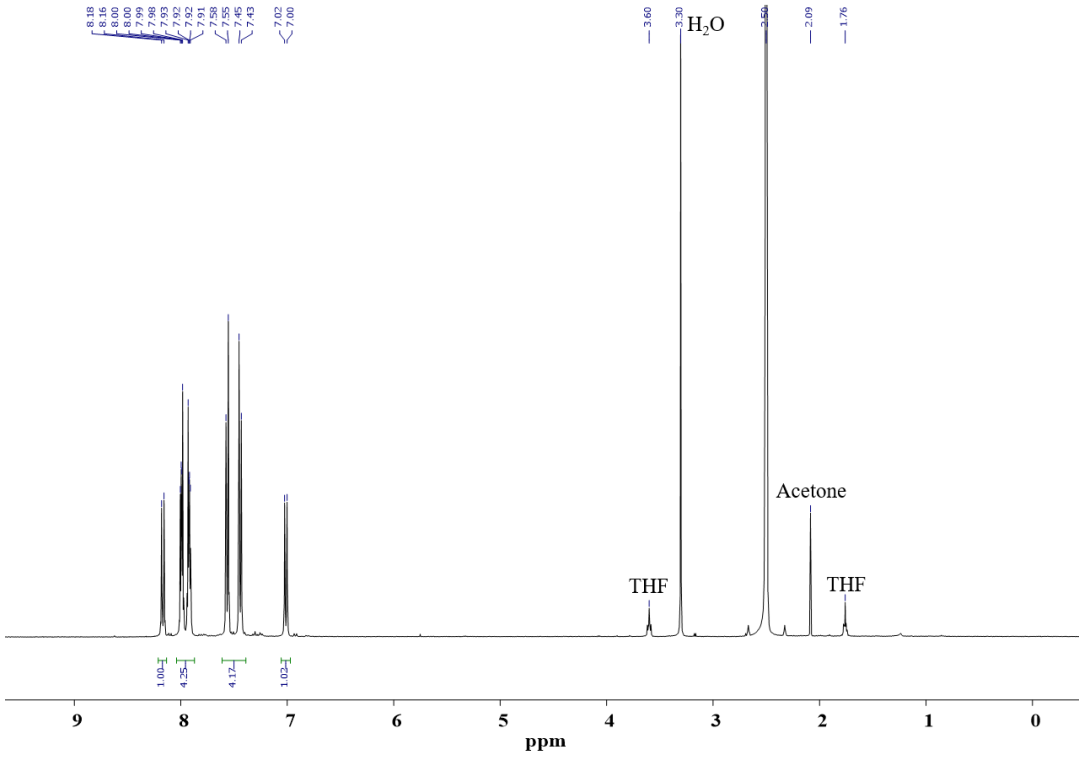

3. ^{1}H NMR (DMSO-d_6, 300 MHz, 300 K)

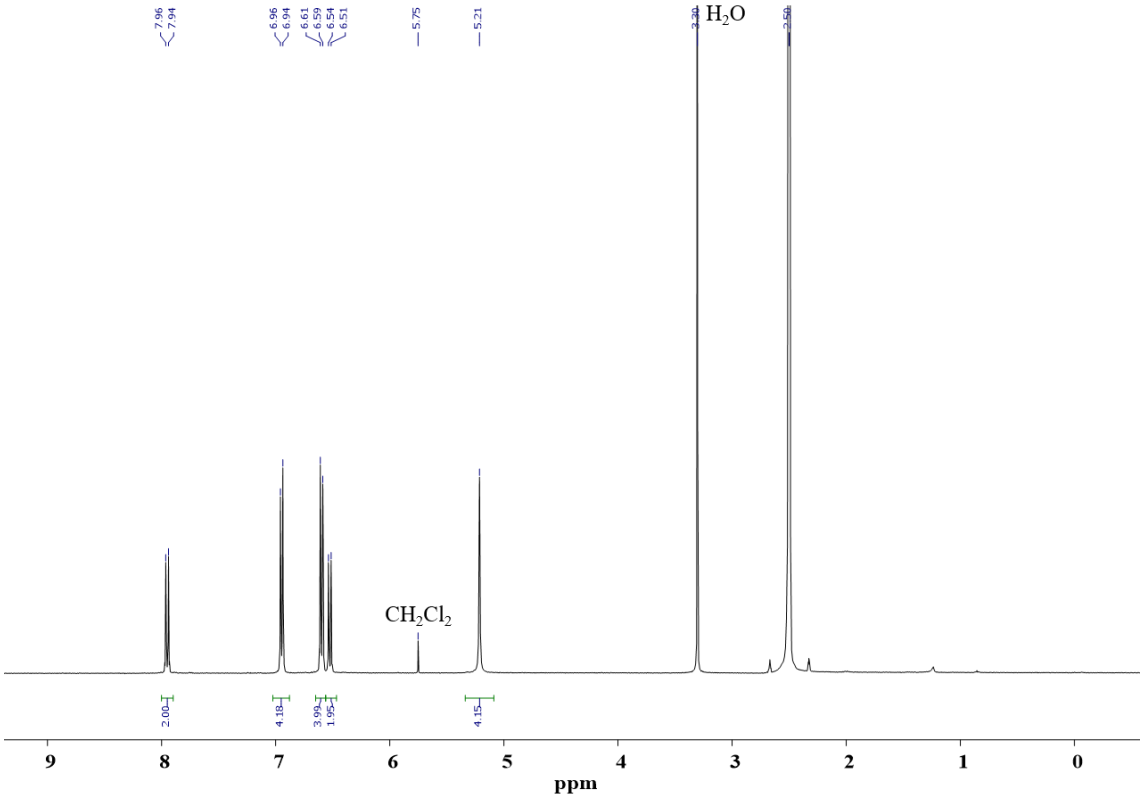

4. ^{1}H NMR ($CDCl_3$, 400 MHz, 300 K)

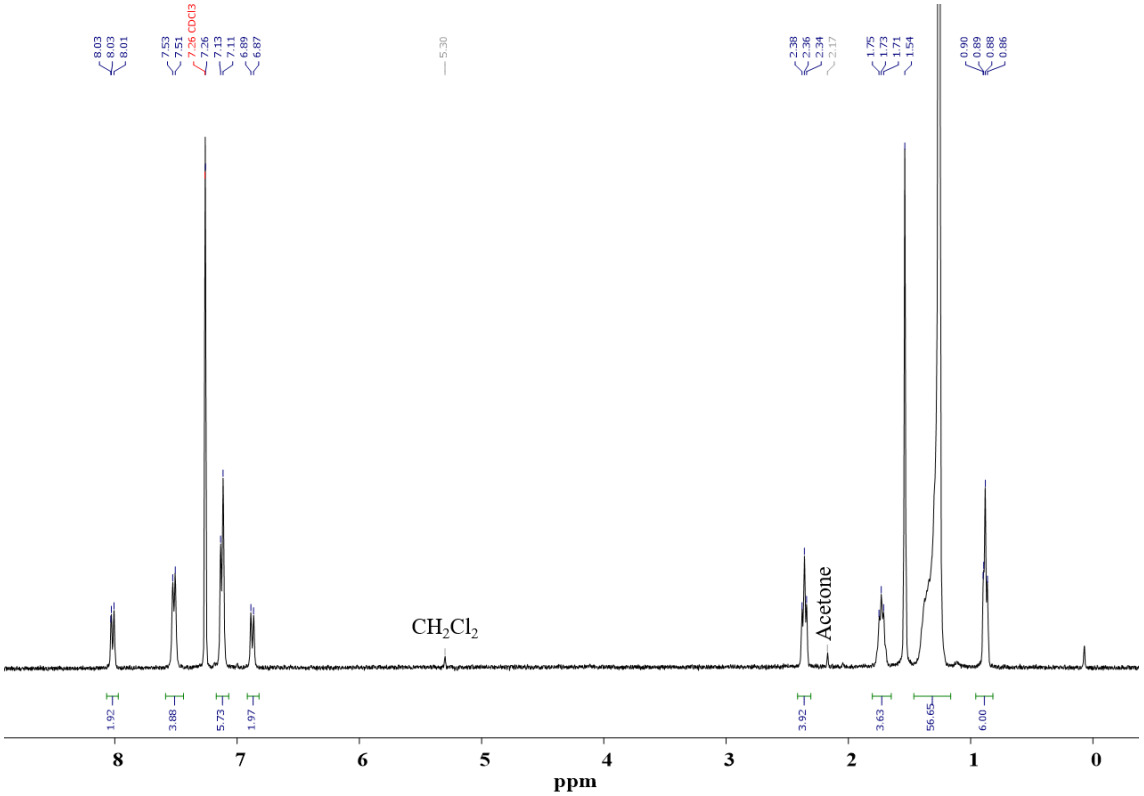

5. ^{1}H NMR (CD_2Cl_2, 400 MHz, 300 K)

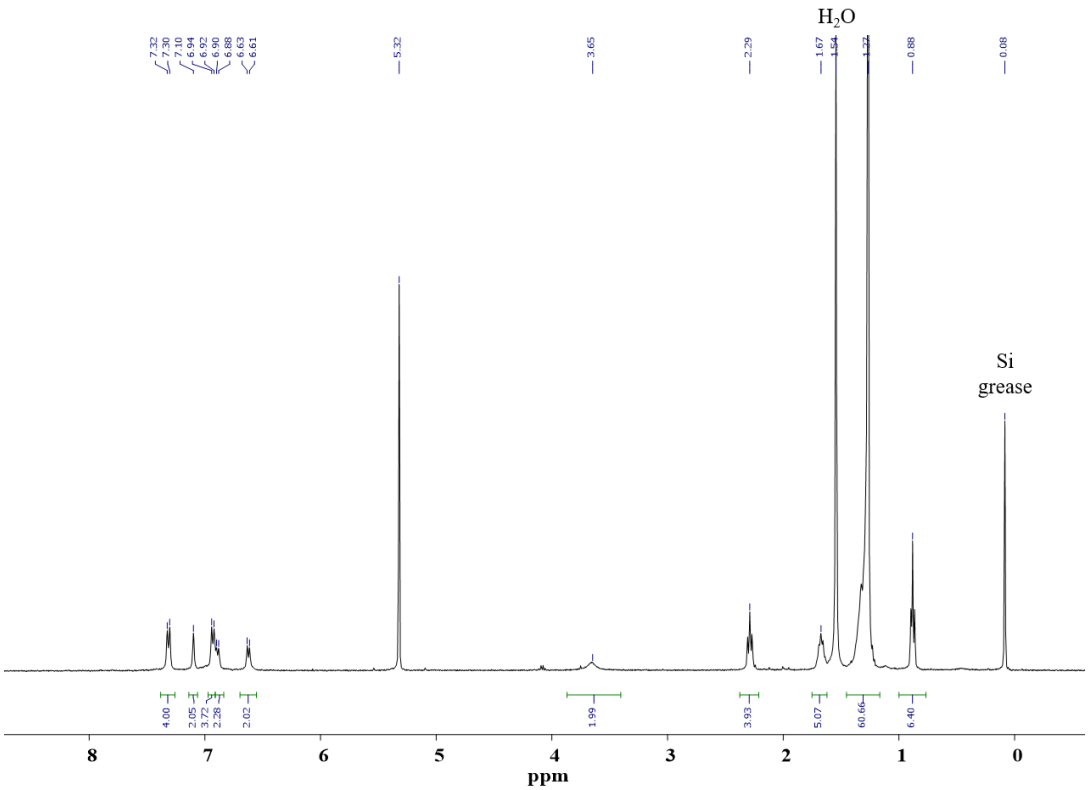

6. ^{1}H NMR (DMSO-d_6, 400 MHz, 300 K)

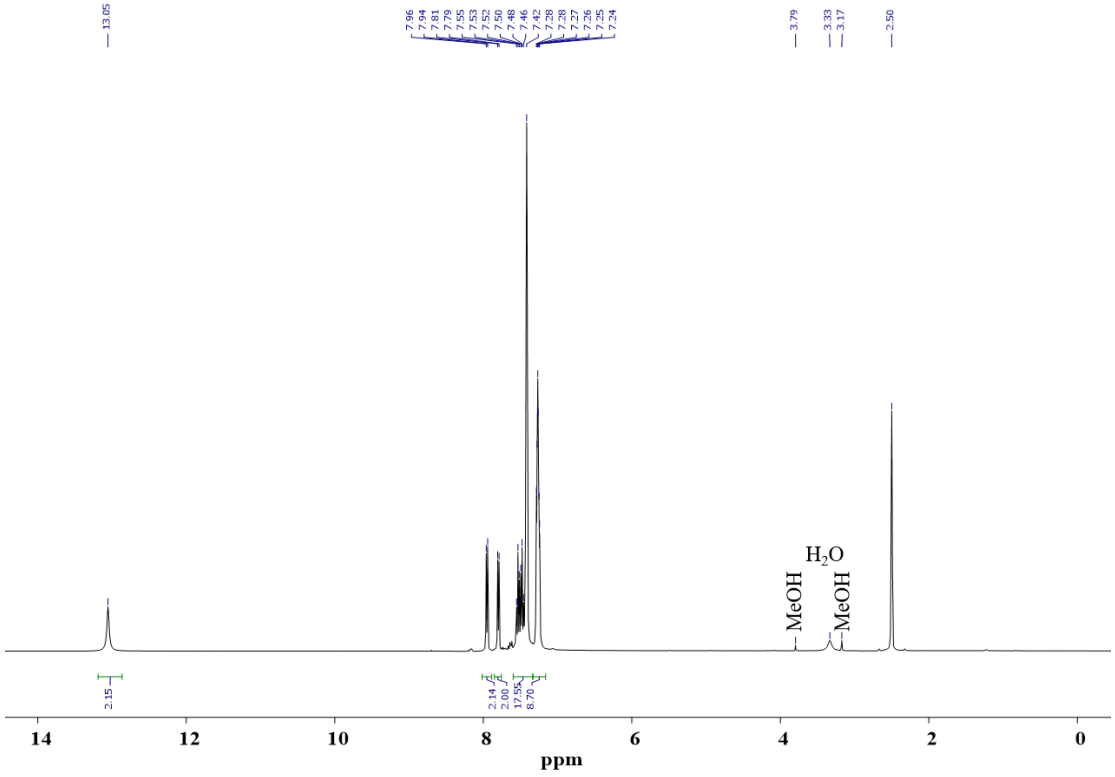

6. JMOD spectrum (DMSO-d_6, 100 MHz, 300 K)

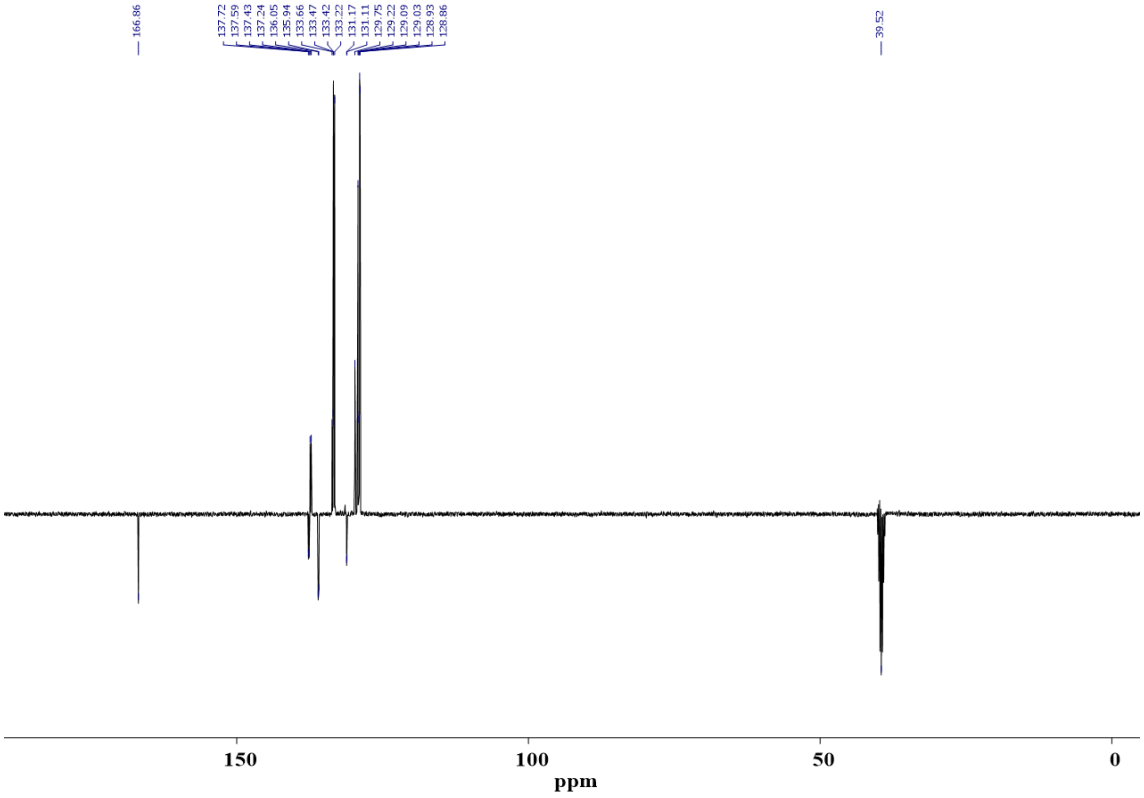

6. $^{31}P\{^{1}H\}$ NMR (DMSO-d_6, 122 MHz, 300 K)

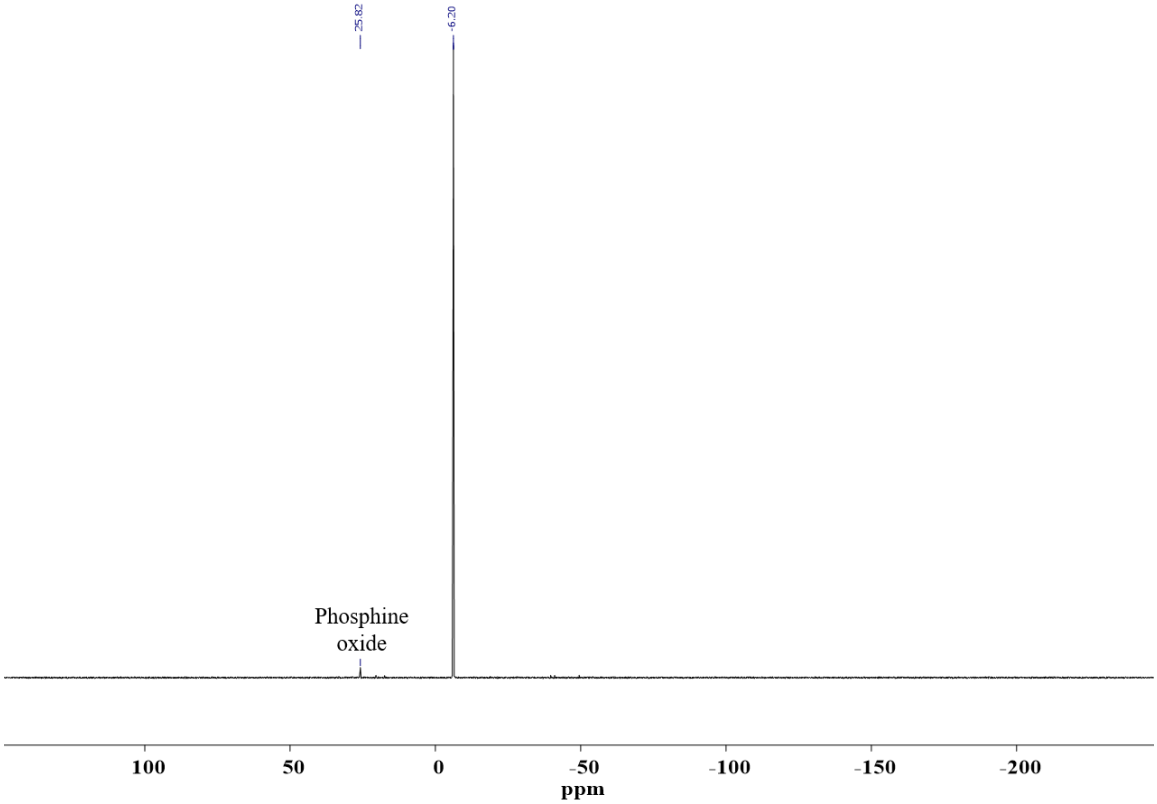

TATA*m*–PPh2. ^{1}H NMR (CD_2Cl_2, 400 MHz, 300 K)

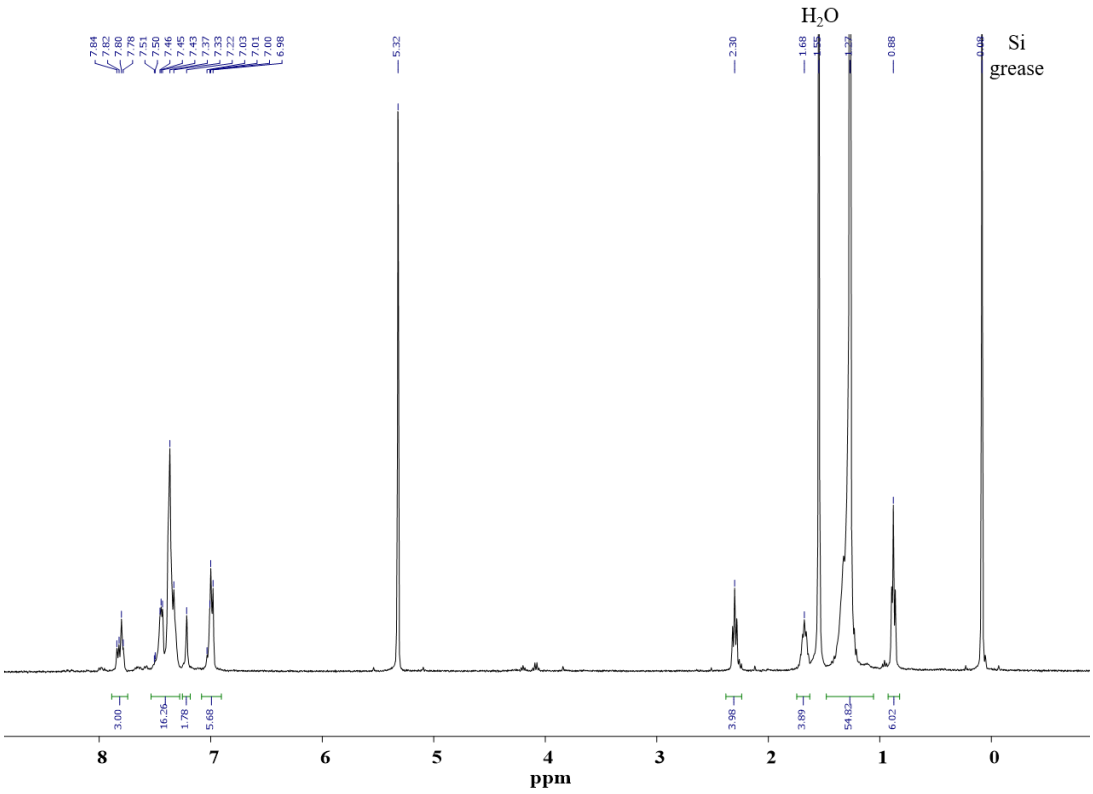

TATA*m*–PPh2. $^{31}P\{^{1}H\}$ NMR (CD_2Cl_2, 122 MHz, 300 K)

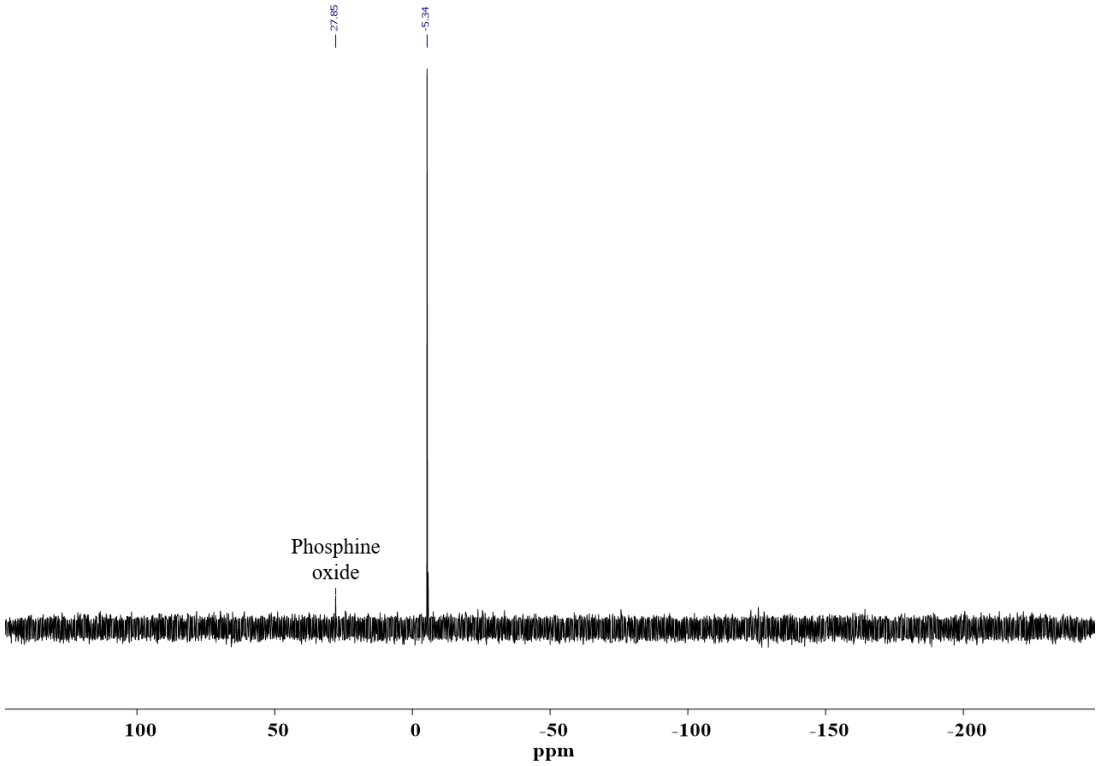

TATA*p*–PPh2. ^{1}H NMR (CD_2Cl_2, 400 MHz, 300 K)

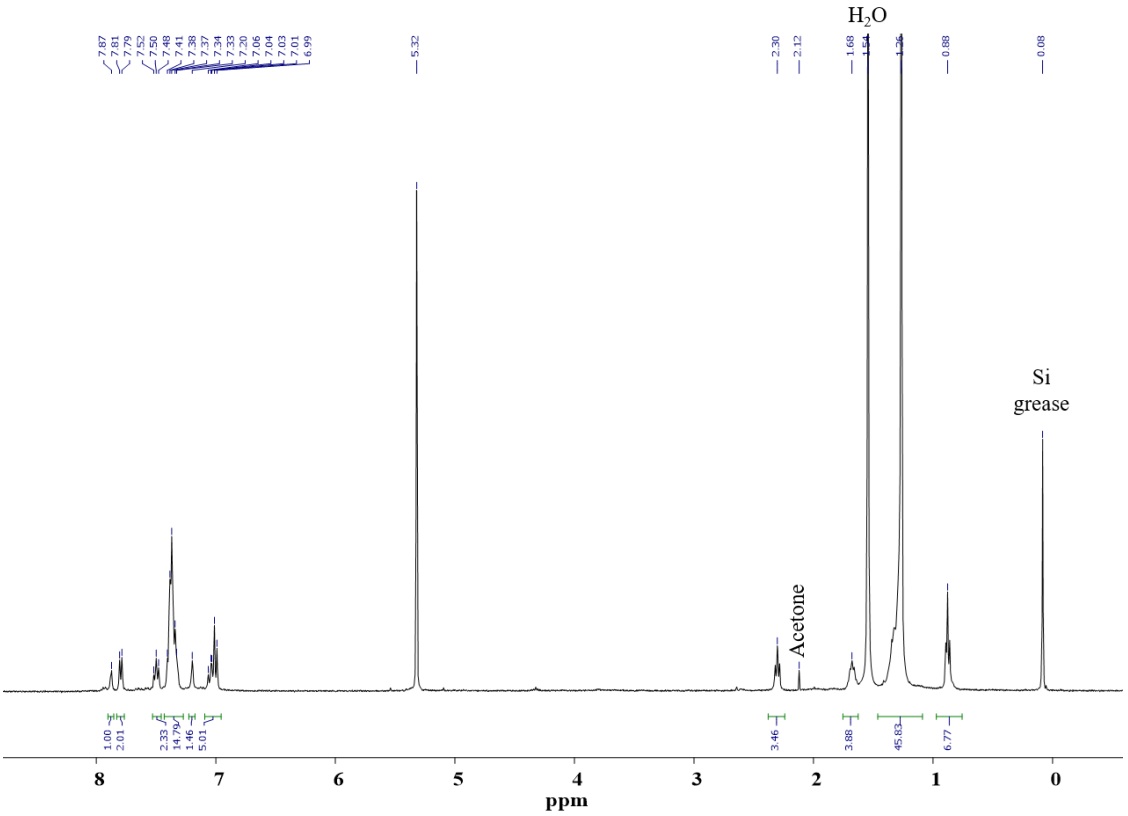

TATA$^{p\text{–PPh2}}$. $^{31}P\{^{1}H\}$ NMR (CD_2Cl_2, 122 MHz, 300 K)

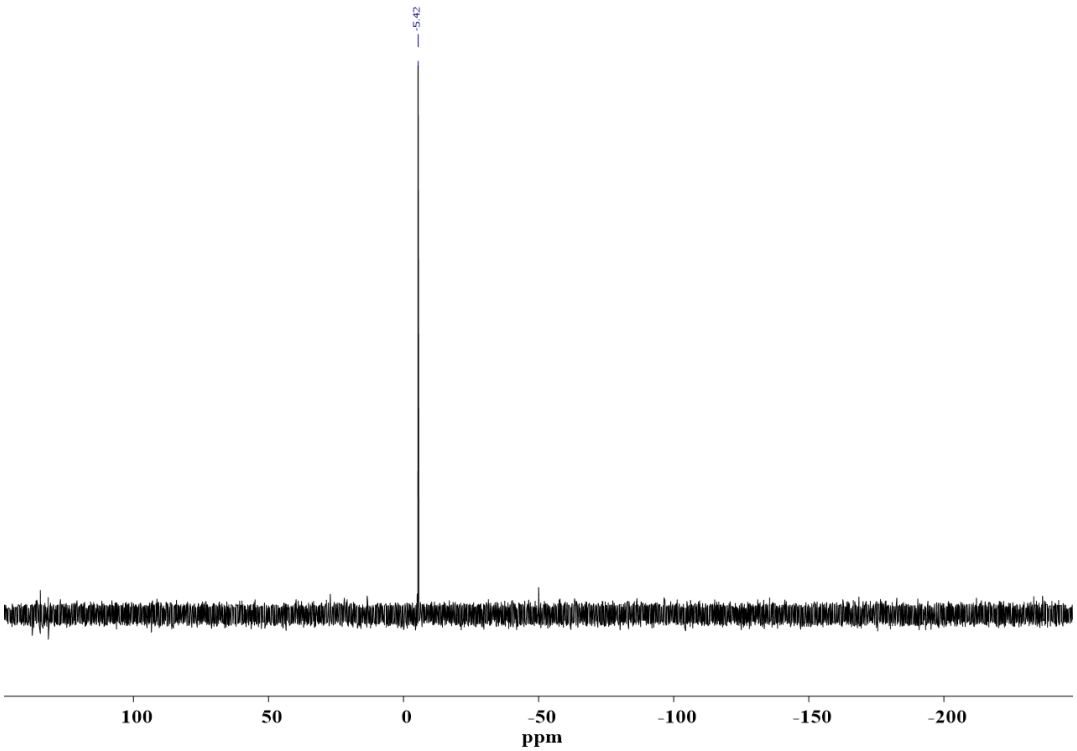

VII. References

1 M. Fujiki, *Symmetry*, 2014, **6**, 677–703.
2 Y. Nagata, R. Takeda and M. Suginome, *ACS Cent. Sci.*, 2019, **5**, 1235–1240.
3 M. M. Green, C. Khatri and N. C. Peterson, *J. Am. Chem. Soc.*, 1993, **115**, 4941–4942.
4 E. Yashima, T. Matsushima and Y. Okamoto, *J. Am. Chem. Soc.*, 1995, **117**, 11596–11597.
5 E. Yashima, K. Maeda and Y. Okamoto, *Nature*, 1999, **399**, 449–451.
6 H. Nakashima, J. R. Koe, K. Torimitsu and M. Fujiki, *J. Am. Chem. Soc.*, 2001, **123**, 4847–4848.
7 Y. Kawagoe, M. Fujiki and Y. Nakano, *New J. Chem.*, 2010, **34**, 637.
8 Y. Nakano, F. Ichiyanagi, M. Naito, Y. Yang and M. Fujiki, *Chem. Commun.*, 2012, **48**, 6636.
9 J. Liu, J. Zhang, S. Zhang, N. Suzuki, M. Fujiki, L. Wang, L. Li, W. Zhang, N. Zhou and X. Zhu, *Polym Chem*, 2014, **5**, 784–791.
10 A. R. A. Palmans, J. A. J. M. Vekemans, E. E. Havinga and E. W. Meijer, *Angew. Chem. Int. Ed. Engl.*, 1997, **36**, 2648–2651.
11 S. J. George, Ž. Tomović, M. M. J. Smulders, T. F. A. de Greef, P. E. L. G. Leclère, E. W. Meijer and A. P. H. J. Schenning, *Angew. Chem. Int. Ed.*, 2007, **46**, 8206–8211.
12 S. J. George, Ž. Tomović, A. P. H. J. Schenning and E. W. Meijer, *Chem. Commun.*, 2011, **47**, 3451–3453.

13 B. Isare, M. Linares, L. Zargarian, S. Fermandjian, M. Miura, S. Motohashi, N. Vanthuyne, R. Lazzaroni and L. Bouteiller, *Chem. - Eur. J.*, 2010, **16**, 173–177.
14 V. Stepanenko, X.-Q. Li, J. Gershberg and F. Würthner, *Chem. - Eur. J.*, 2013, **19**, 4176–4183.
15 T. Kim, T. Mori, T. Aida and D. Miyajima, *Chem Sci*, 2016, **7**, 6689–6694.
16 I. Różalska, P. Kułyk and I. Kulszewicz-Bajer, *New J. Chem.*, 2004, **28**, 1235–1243.
17 P. Ruiz-Castillo and S. L. Buchwald, *Chem. Rev.*, 2016, **116**, 12564–12649.
18 T. Yamamoto, M. Nishiyama and Y. Koie, *Tetrahedron Lett.*, 1998, **39**, 2367–2370.
19 D. S. Surry and S. L. Buchwald, *J. Am. Chem. Soc.*, 2007, **129**, 10354–10355.
20 D. S. Surry and S. L. Buchwald, *Chem Sci*, 2011, **2**, 27–50.
21 H. R. Ing and R. H. F. Manske, *J. Chem. Soc. Resumed*, 1926, **129**, 2348–2351.
22 M. Leung, Y.-S. Lin, C.-C. Lee, C.-C. Chang, Y.-X. Wang, C.-P. Kuo, N. Singh, K.-R. Lin, C.-W. Hu, C.-Y. Tseng and K.-C. Ho, *RSC Adv.*, 2013, **3**, 22219.
23 J. J. Armao, M. Maaloum, T. Ellis, G. Fuks, M. Rawiso, E. Moulin and N. Giuseppone, *J. Am. Chem. Soc.*, 2014, **136**, 11382–11388.
24 M. Hingst, M. Tepper and O. Stelzer, *Eur. J. Inorg. Chem.*, 1998, **1998**, 73–82.
25 M. Raynal, F. Portier, P. W. van Leeuwen and L. Bouteiller, *J. Am. Chem. Soc.*, 2013, **135**, 17687–17690.
26 A. Desmarchelier, X. Caumes, M. Raynal, A. Vidal-Ferran, P. W. N. M. van Leeuwen and L. Bouteiller, *J. Am. Chem. Soc.*, 2016, **138**, 4908–4916.
27 J. M. Zimbron, X. Caumes, Y. Li, C. M. Thomas, M. Raynal and L. Bouteiller, *Angew. Chem. Int. Ed.*, 2017, **56**, 14016–14019.
28 Y. Li, A. Hammoud, L. Bouteiller and M. Raynal, *J. Am. Chem. Soc.*, 2020, **142**, 5676–5688.
29 D. Lin-Vien, N. B. Colthup, W. G. Fateley and J. G. Grasselli, in *The Handbook of Infrared and Raman Characteristic Frequencies of Organic Molecules*, eds. D. Lin-Vien, N. B. Colthup, W. G. Fateley and J. G. Grasselli, Academic Press, San Diego, 1991, pp. 117–154.
30 D. Lin-Vien, N. B. Colthup, W. G. Fateley and J. G. Grasselli, in *The Handbook of Infrared and Raman Characteristic Frequencies of Organic Molecules*, eds. D. Lin-Vien, N. B. Colthup, W. G. Fateley and J. G. Grasselli, Academic Press, San Diego, 1991, pp. 155–178.
31 I. Nyrkova, E. Moulin, J. J. Armao, M. Maaloum, B. Heinrich, M. Rawiso, F. Niess, J.-J. Cid, N. Jouault, E. Buhler, A. N. Semenov and N. Giuseppone, *ACS Nano*, 2014, **8**, 10111–10124.
32 J. Kim, J. Lee, W. Y. Kim, H. Kim, S. Lee, H. C. Lee, Y. S. Lee, M. Seo and S. Y. Kim, *Nat. Commun.*, 2015, **6**, 6959.
33 M. Sumimoto, D. Yokogawa, M. Komeda, H. Yamamoto, K. Hori and H. Fujimoto, *Spectrochim. Acta. A. Mol. Biomol. Spectrosc.*, 2011, **81**, 653–660.
34 Circular Dichroism Spectroscopy | JASCO, https://jascoinc.com/learning-center/theory-of-spectroscopy/circular-dichroism-spectroscopy/, (accessed March 3, 2021).
35 G. Albano, G. Pescitelli and L. Di Bari, *Chem. Rev.*, 2020, **120**, 10145–10243.
36 M. Sugawara, S. Kiriki, K. Ejiri, WO/2018/159459, 2018.

General conclusion

The objectives of this thesis were to control the handedness of assemblies made of triarylamine trisamide (TATA) monomers, by means of circularly polarized light (CPL) or chiral additives, to pave the way towards absolute asymmetric catalysis. TATA derivatives form supramolecular helices which display an extremely high degree of chirality amplification, and recent progress even indicates that their supramolecular chirality can potentially be controlled by CPL irradiation. On the other hand, the supramolecular handedness of helical assemblies, made of disk-like molecules, was recently used as the chiral inducer in asymmetric organometallic reactions. However, prior to this work, no example of absolute asymmetric catalysis was reported at periphery of supramolecular helical polymers directed by CPL. In addition, the mechanisms at the origin of the CPL-controlled supramolecular helicity are overall badly understood and likely differ from one system to another.

In chapter III, the associative behaviour of simple TATA, bearing C11/C12 aliphatic side chains, was probed (**TATA-C12** and **TATA-C13**, respectively). The assembly properties have been scrutinized by multifarious techniques (SANS, EPR, NMR, UV–Vis–NIR and FT–IR) in order to gain as much information as possible on the nature and structure of the aggregates. We showed that neutral TATA molecules compete into different structures in solution, and that the nature of the dominant structure will determine the amount of $TATA^{\bullet+}$ species generated upon light irradiation and the nature of resulting structure of the co-assemblies formed between neutral and radical species. Two types of TATA assemblies have been unambiguously identified: non-specific one-dimensional aggregates and ribbons composed of hydrogen-bonded helical stacks. Thin films were also prepared and were found to consist mainly of long stacks of hydrogen-bonded TATAs. Upon light irradiation, radical and neutral species co-assemble into non-specific aggregates at intermediate concentration, without exhibiting significant change in the structure of assemblies. The delocalization of the unpaired electrons of $TATA^{\bullet+}$ species in these non-specific aggregates is slow as probed by ^{1}H NMR and EPR analyses. By decreasing the temperature, these non-specific aggregates transform into hydrogen-bonded stacks which likely incorporate a fraction of $TATA^{\bullet+}$ species. At higher concentration, generation of the $TATA^{\bullet+}$ species slightly shortens the ribbons composed of

hydrogen-bonded stacks present in the gel state, which further reveal the competitive nature of the co-assembly process. Only a part of the radical cationic species are found to be present into the hydrogen-bonded stacks under these conditions. The unpaired electrons of $TATA^{\bullet+}$ species in these hydrogen-bonded co-assemblies appear to be localized according to EPR analysis. We attribute this surprising observation to the possible disorder present upon stacking of neutral and radical TATA molecules in the gel. Finally, drop casting of light irradiated solutions of TATA yields films for which both radical cationic and neutral TATA molecules are co-assembled within hydrogen-bonded stacks. The amount of radicals in these stacks can be tuned more easily than the aforementioned gels but defects in the hydrogen bonds network are created upon co-assembly. However, the unpaired electrons of the triarylammonium radicals are fully delocalized within the stacks present in the films, as demonstrated by EPR measurements. These complex manifestations offered some guiding parameters that may lead to CPL-controlled supramolecular chirality: i) by irradiating TATA molecules present in the non-specific aggregates with CPL and subsequently triggering their incorporation into hydrogen-bonded helical stacks by cooling or evaporation; or ii) by irradiating TATA molecules already present in hydrogen-bonded helical stacks.

In chapter IV, we focused on reproducing the **TATA-SDA**-based system for which CPL-controlled supramolecular chirality has been reported, and on better understanding the mechanism behind this phenomenon. In toluene, **TATA-SDA** molecules stack into long one-dimensional hydrogen-bonded rod-like assemblies. In 1,2-dichloroethane and chloroform, **TATA-SDA** molecules form assemblies of similar structure than TATA bearing saturated side chains, *i.e.* either non-specific aggregates mainly devoid of H-bonding interactions and hydrogen-bonded stacks. Also, it was found that light irradiation has little influence on the nature of self-assemblies both present in solution and film, and that **TATA-SDA**$^{\bullet+}$ species co-assemble with neutral molecules following the same trend than **TATA-C12/-C13**. Nevertheless, we demonstrated that **TATA-SDA** is photo-oxidized with less efficiency in DCE, and that their assemblies composed of hydrogen-bonded stacks are more prone to precipitation. CD measurements were carried out in CPL-illuminated DCE solutions of **TATA-SDA** in order to track the possibility of generating **TATA-SDA** helical assemblies with a preferred handedness, dictated by the rotational direction of CPL. Our studies revealed CD-related issues accompanying this weakly soluble system, entailing anisotropies, through the formation of

macroscopically-orientated aggregates, which can couple with spectrophotometer artifacts. Even so, we can rule out the possibility of using CPL to direct the handedness of **TATA-SDA** assemblies in the conditions stated in the literature (2.3 mM in DCE). In fact, since radical cationic species have only disordered and/or weak interactions in most solute conditions, they can in this way hardly transfer a putative chirality. On the other hand, irradiation of 11.7 mM solution and conservation in the dark for allowing further aggregation led to a CD devoid of LD influence. Further experiment, such as irradiation by *r*-CPL and *l*-CPL are necessary to demonstrate the possibility of biasing the handedness of **TATA-SDA** helical assemblies under these conditions.

In chapter V, the synthesis and characterization of two TATA bearing coordinating groups, **TATA$^{p\text{–}PPh2}$** and **TATA$^{m\text{–}PPh2}$** featuring a PPh_2 unit connected to *meta* and *para* position of a phenylene linker, respectively, were synthesized for the first time thanks to a multi-step procedure. The study of self-association properties of **TATA$^{p\text{–}PPh2}$** in toluene, dichloromethane and decalin showed the reversible formation of long hydrogen-bonded stacks upon temperature change. Next, a library of enantiopure small molecules, covering a broad spectrum of functional groups, were added to **TATA$^{p\text{–}PPh2}$** in toluene, dichloromethane or decalin solutions at 10 mol% or 100 mol%. Despite competing with the hydrogen-bonded functions of the stacks in a large number of cases, these chiral additives did not succeed to direct the handedness of assemblies. (−)-α-Pinene and (*R*)-limonene were then used as solvent for **TATA$^{p\text{–}PPh2}$**, but no strong CD accounting for biased **TATA$^{p\text{–}PPh2}$** aggregates was measured.

In the future, a few possible outlooks towards the control of the handedness of TATA-based assemblies are offered:

1) Chiral additives embedding arene groups and derivatives of citronellol. The first may interact with TATA helical assemblies through directional aromatic interactions, the second one through hydrogen bonds between the alcohol function and the amide carbonyl.
2) Chiral co-monomers at very low concentrations or as the unique building block. The former could benefit from the extremely high amplifications properties of TATA, and the latter could exploit the pathway complexity that can exhibit the supramolecular

polymerization of TATA, leading in some cases to handedness inversion upon a change in temperature.

3) CPL could be further tested as a chirality inducer. The strategy based on the light irradiation of homoassemblies composed of TATA ligands appears now to be the most promising solution. The chiral induction could be mediated by neutral or radical cationic species. In the first case, CPL irradiation could be carried out while heating up to reach the monomeric state in decalin and cooling down to form hydrogen-bonded helical stacks. In chlorinated solvents, it could be envisaged to generate a few radicals under conditions for which the TATA ligand is not fully aggregated and then promote its assembly into hydrogen-bonded stacks in the dark upon time, cooling or evaporation. In the realm of catalysis in the homogenous phase, the first two approaches (time and cooling) would be more suitable. Alternatively, mixtures of apolar and chlorinated solvents can be envisaged to get the possibility to trigger the formation of radicals under conditions for which the hydrogen-bonded assemblies are strongly stabilized.
4) The multifarious techniques used in this study could be extended to fluorescence spectroscopy or microscopy analyses, density functional theory calculations and x-ray diffraction. It may give more insight on the underlying assembly and chirality induction mechanisms, by probing: the formation of aggregates in solution and the effect of delocalized radicals on them (fluorescence); the structure of assemblies in the solid state, thanks to the XRD of crystalline materials or by means of microscopy techniques such as AFM and SEM; the molecular origin of the Cotton effects of TATA with the help of DFT calculations. This characterization could give a rationale for the association and amplification properties of TATA molecules upon CPL irradiation, and may allow to use a similar strategy of supramolecular chirality control with other supramolecular polymers.

Résumé

Comment un excès énantiomérique émerge-t-il ? Cette question concerne aussi bien l'homochiralité biologique – acides aminés protéinogènes et sucres naturels respectivement de configuration absolue (*S*) et (*R*) –, signature de la vie dont l'origine reste un mystère, que l'une de ses conséquences : le défi de synthétiser des molécules bioactives énantiopures.

Alors que la séparation des énantiomères est onéreuse, et l'exploitation des molécules chirales naturelles restreinte, la catalyse asymétrique implique d'utiliser des composés déjà chiraux pour orienter la réaction catalytique vers l'énantiomère désiré. À rebours de ces méthodes nécessitant une chiralité préexistante, la synthèse asymétrique absolue permet la formation de produits énantiomériquement enrichis sans avoir recours à une espèce chimique chirale préexistante.

Les polymères supramoléculaires – chaînes réversibles de molécules liées par interactions non-covalentes – constituent à cet égard une opportunité. Leur caractère dynamique leur confère des propriétés d'amplification de chiralité permettant le transfert coopératif d'un biais chiral du niveau moléculaire à l'échelle de l'assemblage supra-macromoléculaire (effet sergents-et-soldats). La chiralité supramoléculaire de l'autoassemblage peut également être inversée et modulée par l'ajout de co-monomères énantiopurs de chiralité opposée (règle de la majorité).

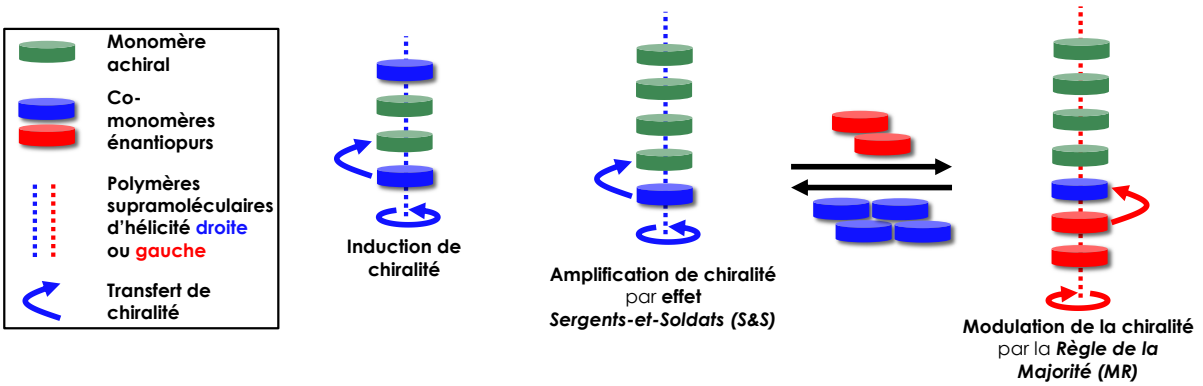

Figure 1 Représentation schématique des propriétés d'amplification de chiralité des polymères supramoléculaires.

Les propriétés d'amplification de chiralité des polymères supramoléculaires furent mises en œuvre avec succès en catalyses asymétrique. Des polymères supramoléculaires, composés d'un co-assemblage de monomères capables de former des complexes métalliques achiraux (centres catalytiques, soldats) et de co-monomères chiraux (sergents), ont déjà été développés dans cette optique au laboratoire. Il fut démontré que la chiralité supramoléculaire des autoassemblages de benzène-1,3,5-tricarboxamide (BTA) est induite aux centres métalliques se trouvant à leur périphérie, qui à leur tour orientent spécifiquement la réaction catalytique vers la formation préférentielle d'un énantiomère.

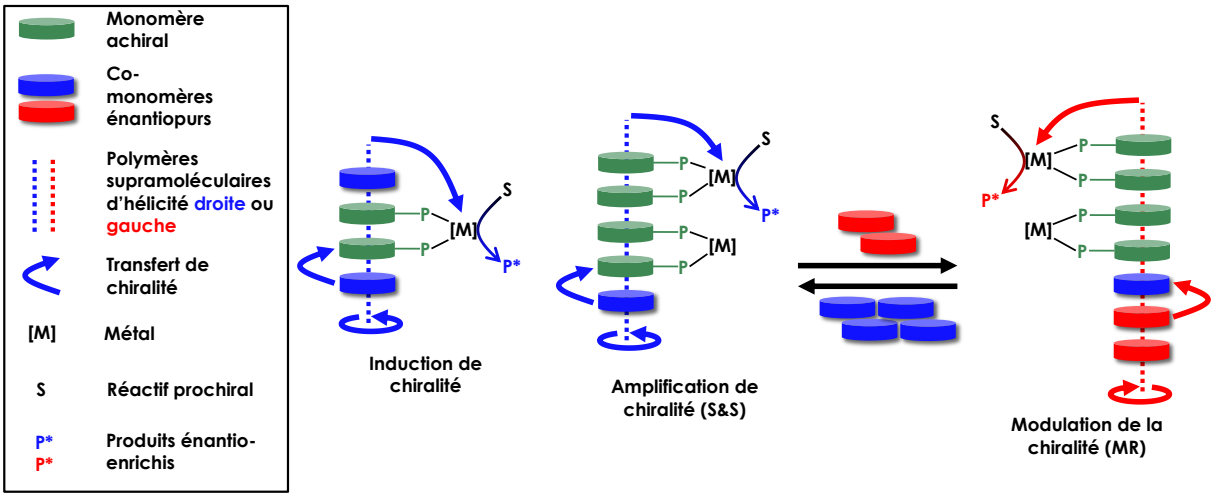

Figure 2 Représentation schématique de la catalyse asymétrique supra-macromoléculaire modulable développée précédemment au laboratoire.

En parallèle de ces travaux faisant le pont entre les polymères supramoléculaires et la catalyse asymétrique, des chercheurs coréens, sous la direction de Sang Youl Kim, ont récemment employé la lumière polarisée circulairement (LPC) pour contrôler la chiralité d'édifices supra-macromoléculaires. Ils montrèrent que des polymères supramoléculaires hélicoïdaux de triarylamine trisamide (TATA), générés sous l'influence de LPC, avaient une chiralité supramoléculaire induite et commutable (hélicité droite ou gauche) par la LPC en fonction de sa polarisation (droite ou gauche).

Fort de ces résultats émanant du laboratoire ou de la littérature, ce travail de thèse avait pour but d'établir les fondations d'une catalyse asymétrique absolue en réunissant ces deux concepts : la catalyse asymétrique supra-macromoléculaire et l'orientation de la chiralité

d'hélices supramoléculaires par la LPC. L'objectif était alors de « Contrôler la chiralité d'assemblages de triarylamine trisamide au moyen de la lumière polarisée circulairement ou d'additifs chiraux ».

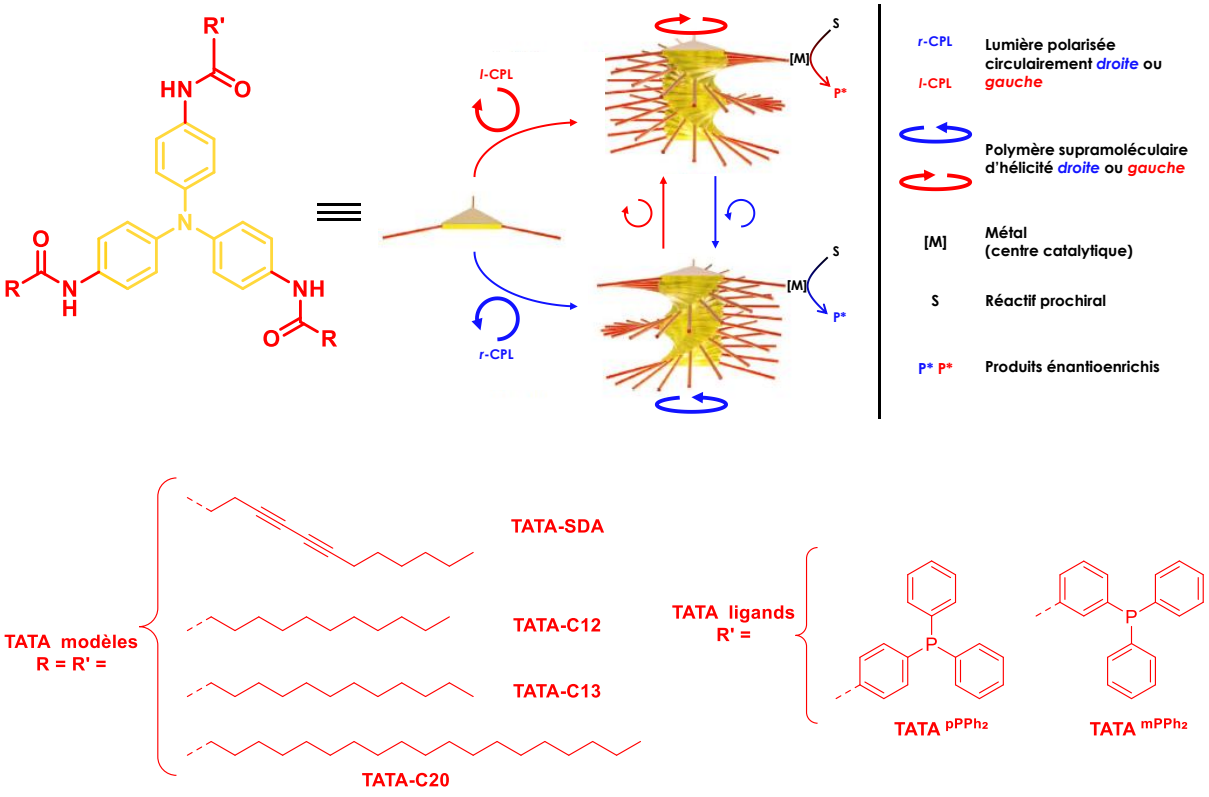

Figure 3 Représentation schématique de la catalyse asymétrique absolue supra-macromoléculaire, objectif final de ce travail de thèse. Molécules synthétisées lors de ce travail de thèse.

Dans un premier chapitre expérimental (Chapitre III), nous avons étudié les propriétés d'auto-association de TATA aux chaînes latérales saturées (analogues de la **TATA-SDA** employée par l'équipe coréenne) en mettant en évidence les conditions de son autoassemblage. Puis, nous avons pu sonder la structure des agrégats (par exemple leur forme, leur longueur et les interactions entre les molécules). L'effet de l'irradiation lumineuse, ainsi que des radicaux triarylammonium qui découlent de la photo-oxydation des TATA, a ensuite été examiné pour divers états d'association. Le co-assemblage entre les espèces radicalaires cationiques, fruit de l'irradiation lumineuse, et les molécules neutres, ainsi que le type d'interactions impliquées, furent investigués. Notamment, une attention particulière a été accordée aux liaisons

hydrogène, directionnelles par nature et probablement les liens directeurs de la chiralité supramoléculaire dans le cas de son contrôle par LPC.

Après la synthèse à l'échelle du gramme de TATA aux chaînes latérales à 11, 12 et 19 atomes de carbone (respectivement la **TATA-C12**, la **TATA-13** et la **TATA-C20**), leurs tests de solubilité ont permis de montrer la faible solubilité de la **TATA-C20** dans les solvants d'intérêt photochimique et catalytique, ce qui nous poussa à l'abandonner pour la suite. Une étude en concentration mêlant spectroscopie d'absorption dans l'UV, visible et proche infrarouge, ainsi que dans le moyen infrarouge, et la diffusion des neutrons aux petits angles, nous a permis d'identifier dans le chloroforme trois concentrations présentant des états d'association distincts :

1) à 0,1 mM, où les molécules de TATA ne sont pas assemblées par liaison H mais de structure non déterminée;
2) à 2,3 mM, où les molécules de TATA s'assemblent dans des agrégats non-spécifiques, où elles interagissent par interactions de Van der Waals et hydrogène mal définies, avant de s'auto-assembler sous l'effet du temps ou d'un refroidissement en longs édifices composés hélicoïdaux par liaisons hydrogène.
3) À 11,4 mM, où les molécules de TATA sont principalement impliquées dans des empilements monodimensionnels tenus par interactions hydrogène, regroupés en des rubans de grande taille à la frontière entre l'état soluble et à l'état solide.
4) Enfin, seul l'état solide au travers de couches minces présente des molécules exclusivement liées par interactions hydrogène.

Puis cette étude s'est intéressée à l'effet de la lumière sur les assemblages. Elle mit notamment en évidence :

1) à 0,1 mM, la formation lors de l'irradiation d'espèces radicalaires cationiques aux électrons non-appariés localisées. Nous avons pu démontrer que ces espèces ne déclenchent pas l'assemblage des TATA par interactions hydrogène, sans être capable néanmoins de rejeter définitivement la formation de co-agrégats non-spécifiques entre les espèces radicalaires cationiques et neutres.

2) À 2,3 mM, l'irradiation lumineuse favorise la formation entre les espèces radicalaires cationiques et neutres de co-agrégats non-spécifiques, constitués grâce à des interactions π et hydrogène mal définies. Ainsi, une étude par résonance paramagnétique électronique a montré que les électrons non appariés des triarylammoniums de ces agrégats se délocalisent lentement à cause du désordre. Une diminution de la température permet probablement d'incorporer certaines espèces radicalaires cationiques à l'intérieur d'assemblages hélicoïdaux.

3) À 11,4 mM, l'irradiation lumineuse produit des espèces radicalaires persistant plus d'une journée, et qui raccourcissent les superstructures composées de faisceaux de fibres monodimensionnelles constituées de liaisons hydrogène. Ce raccourcissement provient de la rupture d'interactions hydrogène pour rendre disponible des molécules neutres à la photo-oxydation. Ces interactions se forment de nouveau lors d'un vieillissement de plusieurs heures, entraînant la formation d'agrégats plus courts. Les espèces radicalaires cationiques sont pour une partie en contact avec les espèces neutres dans de longs assemblages hélicoïdaux formant le gel, mais la possible présence de défauts ne permet pas une délocalisation rapide de leur charge électronique.

4) Enfin, l'irradiation lumineuse d'une solution puis son évaporation engendre un film mince pour lequel les électrons non appariés des molécules radicalaires sont délocalisés de façon rapide entre les molécules liées par interactions hydrogène. La présence d'un nombre important de radicaux conduit à la formation de défauts par liaison H dans les empilements mais sans ralentir significativement la délocalisation.

Ces manifestations complexes offrent quelques conditions où le co-assemblage d'espèce radicalaires, ayant nécessairement interagi avec la lumière, avec des espèces neutres pourrait conduire à un contrôle de la chiralité supramoléculaire. Les films minces sont prometteurs, en incorporant directement des espèces radicalaires cationiques à l'intérieur d'empilements construits sur réseau de liaisons hydrogène. Si les triarylammoniums radicaux sont probablement peu biaisés par la LPC par photorésolution, d'autres espèces comme les agrégats courts, par exemple les nuclei, pourraient également interagir avec un rayonnement de LPC qui pourrait diriger leur conformation hélicoïdale naissante. À cet égard, la possibilité de former des radicaux dans des agrégats non spécifiques et d'induire la formation d'empilements

hélicoïdaux avec le temps, la température ou l'évaporation dans le noir offrent une perspective intéressante pour le contrôle de la chiralité supramoléculaire.

Ce chapitre portant sur l'étude de TATA aux chaînes latérales saturées a permis de se familiariser avec cette plateforme moléculaire et d'en examiner les propriétés en matière d'assemblage, en présence ou non de lumière.

Ensuite, le pont vers la catalyse passait par la reproduction et la compréhension du contrôle par LPC de la chiralité supramoléculaire des agrégats de **TATA-SDA** (Chapitre IV), reporté précédemment, mais sans avoir donné d'explication précise du mécanisme à l'œuvre. Dans ce but, la molécule de **TATA-SDA** a été synthétisée en trois étapes et entièrement caractérisée. Un premier examen de la **TATA-SDA** en solution a mis en évidence la présence de polydiacétylène, ainsi que la manière de l'éliminer (par filtration), et a démontré la solubilité de la **TATA-SDA** à 1 mM dans le toluène et les solvants chlorés, clefs pour la catalyse et la photo-oxydation.

Les propriétés d'auto-association ont ensuite été étudiées dans le toluène, le 1,2-dichloroéthane (DCE) et le chloroforme. Dans le toluène, le **TATA-SDA** forme de longs autoassemblages unidimensionnels, maintenus par des liaisons hydrogène bien définies entre les molécules. Dans le 1,2-dichloroéthane, les molécules de **TATA-SDA** ont été étudiées dans quatre conditions différentes :

1) à 2,3 mM et à température ambiante, la **TATA-SDA** est stable en solution, dont une fraction significative se compose d'agrégats non-spécifiques dépourvus de liaisons hydrogène.
2) Les analyses à basse température de la **TATA-SDA** dans le DCE à 2,3 mM ont mis en évidence un autoassemblage réversible en assemblage hélicoïdal.
3) À 11,7 mM, bien que les molécules de **TATA-SDA** soient autoassemblées en agrégats solubles dans le chloroforme, les solutions de 1,2-dichloroéthane ont révélé un système complexe dans lequel des agrégats composés d'empilements hélicoïdaux précipitent rapidement.
4) Enfin, une solution de **TATA-SDA** à 2,3 mM dans le DCE fut employée pour former des films minces, de structure proche de celle de la poudre, c'est-à-dire composés

d'assemblages hélicoïdaux. Le degré d'association était pratiquement total dans ces conditions, alors qu'il était seulement partiel à 2,3 mM et basse température ainsi qu'à 11,7 mM.

Dans le 1,2-dichloroéthane et le chloroforme, la production de **TATA-SDA**$^{\bullet+}$ induite par photo-oxydation fut démontrée par RMN, RPE, UV–Vis–NIR et FT–IR, tandis que leur impact sur les propriétés associatives de la **TATA-SDA** s'est avéré assez faible. Les mesures de dichroïsme circulaire (CD) ont été effectuées dans le DCE, solvant utilisé par l'équipe coréenne où **TATA-SDA** est moins soluble que dans le chloroforme, ce qui favorise la précipitation de ses assemblages. L'étude a été réalisée en gardant à l'esprit les difficultés de mesure du CD, tels que les artefacts du spectrophotomètre et l'anisotropie des échantillons contenant des agrégats macroscopiques orientés. Pour trouver les conditions d'émergence d'une chiralité supramoléculaire contrôlée par LPC, toutes les conditions précédemment étudiées ont été étudiées sous irradiation et de nombreux paramètres ont été modulés, tels que la puissance optique, le degré de polarisation circulaire, le temps d'irradiation et post-irradiation, ainsi que les températures d'irradiation, post-irradiation et de mesure. Contrairement à ce qu'a reporté l'équipe coréenne, à 2,3 mM, l'irradiation par LPC et la production de **TATA-SDA**$^{\bullet+}$ avant l'autoassemblage à basse température ou la formation de couches minces semblent inefficaces pour biaiser la chiralité des édifices supramoléculaires formés. Néanmoins, dans une expérience à haute concentration couplant irradiation en refroidissant et vieillissement à température ambiante, un CD dépourvu de LD ou d'artefacts a pu être mis en évidence.

Au global, cette étude indique que les espèces radicalaires cationiques ne sont probablement pas idoines pour un transfert de chiralité provenant de la LPC. En effet, la chiralité des monomères **TATA-SDA**$^{\bullet+}$ est vraisemblablement faible voire inexistante, en raison de leur conformation rendue quasi planaire par la délocalisation de leur charge électronique. De même, les agrégats non-spécifiques qu'ils peuvent former avec les espèces neutres, dépourvues d'interactions hydrogène directionnelles, ne semblent pas les sites pertinents pour un transfert de chiralité. En outre, même les monomères neutres, dont la barrière énergétique d'interconversion entre les deux conformation chirales miroirs s'approche certainement de 4.8 kcal/mol, ne peuvent probablement pas conserver une configuration chirale en excès après avoir interagi avec la LPC.

À l’aune de ces conclusions, l'une des conditions préalables à une chiralité supramoléculaire contrôlée par LPC est l’irradiation d’objets capables de conserver leur configuration chirale pendant l’autoassemblage. Dans le cas des TATA, les agrégats naissants, formés par un réseau de liaisons hydrogène, pourraient être la solution. L'irradiation lumineuse de molécules en cours d'autoassemblage pourrait orienter la conformation hélicoïdale de leur empilement, grâce à la stabilité relativement faible de ces objets non encore figé par leur allongement. Cette hypothèse est en adéquation avec la solution ayant montré du CD dans cette étude, à une concentration de 11,7 mM et irradiée lors de son assemblage puis laissée suffisamment longtemps au repos pour que les agrégats orientés par LPC s’allongent et induisent un dichroïsme circulaire mesurable.

Cette hypothèse est également en cohérence avec trois travaux récemment publiés. La même équipe coréenne que celle citée précédemment a révélé en 2020 la possibilité d’obtenir des couches minces d’hélices supramoléculaires à la chiralité biaisée par la LPC. Pour cela, ils ont irradié des molécules à cœur tris(stilbène)amine et chaînes latérales amido-diacétyléniques dans des solutions non-chlorées (dans le benzène) « lors de l'autoassemblage et de la formation d’un film mince ». Ils avancèrent qu'en l'absence de radicaux triarylammoniums, la force opto-mécanique de la LPC, à travers l'interaction de son moment angulaire avec le moment dipolaire des électrons π du noyau triarylamine, induit une conformation hélicoïdale préférentielle au cours de la photo-excitation des molécules, qui agissent ensuite en tant que sergents lors de l’agrégation. Le caractère négligeable d’artefacts du spectrophotomètre ou du LD fut vérifié par rotation et retournement de l'échantillon. Dans le même ordre d'idées, une équipe chinoise dirigée par Gang Zou a réussi à contrôler la chiralité supramoléculaire d’assemblages composés de dérivés de la porphyrine au moyen d'une irradiation par LPC pendant les premières étapes d'un processus de gélification. Ils ont affirmé que le biais chiral provient de la déformation de la structure plane du cœur porphyrinique sous l'influence de la LPC par photorésolution. Enfin, l’équipe espagnole de Luis Sánchez a démontré que l'irradiation par LPC de pérylènetétracarboxamides N-annulés à l'état monomère à haute température pouvait induire, lors du refroidissement, des agrégats hélicoïdaux énantioenrichis.

Pour les TATA, la clef semble résider en un ensemble de paramètres finement choisis pour tirer profit de l’agrégation au cours du vieillissement à une concentration élevée, en

refroidissant une solution à une concentration modérée, ou lors de la formation d'un film mince. La catalyse imposera de trouver un équilibre dans la durée d'irradiation par LPC pour induire une chiralité au maximum de molécules/agrégats pour permettre une chiralité supramoléculaire homogène. Un deuxième défi sera l'observation du CD, qui devra être systématiquement contrôlé par des procédures de retournement et de rotation de cellule et l'irradiation par les deux polarisations de la CPL en vue d'obtenir des spectres dichroïques miroir. Sa mesure par spectroscopie à matrice de Mueller, impliquant quatre modulateurs photoélastiques et capable d'isoler tous les dichroïsmes et biréfringences circulaires et linéaires d'un échantillon, pourrait être également très intéressante pour identifier les conditions fiables d'émergence et d'observation du dichroïsme circulaire.

Dans un cinquième et dernier chapitre expérimental (Chapitre V), la synthèse et la caractérisation des autoassemblages dans plusieurs solvants d'une TATA comportant un groupement complexant des centres métalliques furent réalisées. Plusieurs essais pour induire un biais dans la chiralité supramoléculaire de ces autoassemblages furent conduits, à l'aide d'additifs ou de solvants chiraux. Ces expériences relèvent d'une seconde stratégie relative au développement de la catalyse asymétrique absolue, au moyen d'assemblages composés uniquement de molécules ligands.

Deux TATA portant un groupement triphénylphosphine (**TATA$^{m\text{–PPh2}}$** et **TATA$^{p\text{–PPh2}}$**), en *méta* ou *para* d'un espaceur phénylène le reliant au cœur TATA, furent synthétisées pour la première fois en six étapes. Les propriétés associatives de la **TATA$^{p\text{–PPh2}}$** ont été sondées en l'absence de lumière par spectroscopie d'absorption UV–Vis–NIR et FT–IR. Ces analyses ont montré la formation thermoréversible de longs assemblages par liaisons hydrogène. Les solutions à 1,8 mM dans le toluène et à 1 mM dans la décaline sont hautement associées à 20°C (respectivement $\alpha_{Agg} \approx 0.75$ et 0.93,), tandis qu'à 1.8 mM dans le dichlorométhane, les molécules de **TATA$^{p\text{–PPh2}}$** sont presque exclusivement libres. À haute température (> 130°C), les assemblages dans la décaline se cassent, tandis qu'à -10°C, les molécules de **TATA$^{p\text{–PPh2}}$** dans le dichlorométhane sont hautement associées ($\alpha_{Agg} \approx 0.95$).

Ensuite, une série de douze molécules énantiopures, comprenant notamment des esters d'acides aminés et des dérivés de citronellol, fut employée pour tenter d'induire une chiralité

supramoléculaire prédominante aux assemblages de **TATA$^{p\text{–}PPh2}$**. Des ajouts dans le toluène, le dichlorométhane ou la décaline à 10% ou 100% molaire de ces additifs chiraux n'ont pas donné lieu à un signal de dichroïsme circulaire, signe d'une hélicité en excès, mais ont plutôt eu tendance à raccourcir les assemblages. Cela révéla des interactions entre certains additifs et les assemblages de **TATA$^{p\text{–}PPh2}$**, mais pas de nature à biaiser leur sens de rotation. La (–)-α-pinène et le (*R*)-limonène fut finalement employés comme solvants, pour tester si leur chiralité pouvait être transférée aux agrégats. Malgré la présence d'assemblage par liaison hydrogène de **TATA$^{p\text{–}PPh2}$**, aucun signal CD significatif ne fut détecté.

En perspective de ce chapitre, de nouveaux additifs chiraux comprenant des groupements aromatiques pourraient être testés, dans le but de favoriser les interactions π avec les molécules de **TATA$^{p\text{–}PPh2}$**, voire une intercalation au sein de leurs assemblages. Des dérivés liquides du citronellol, déjà utilisés en tant qu'additifs, pourraient également être employés en tant que solvants chiraux.

Titre : Contrôle de la chiralité supramoléculaire d'assemblages de triarylamine trisamide grâce à la lumière polarisée circulairement ou des additifs chiraux

Résumé :

Pour ouvrir la voie à la catalyse asymétrique absolue, des polymères supramoléculaires de triarylamine trisamide (TATA) ont été étudiés sous l'influence de la lumière polarisée circulairement (LPC) et d'additifs/solvants chiraux. Les propriétés associatives de TATA aux chaînes latérales saturées ou diacétyléniques furent sondées en présence ou non de LPC par SANS, UV–Vis–NIR, FT–IR, RMN et RPE. Les deux types d'autoassemblage formés par ces molécules, agrégats non-spécifiques et assemblages hélicoïdaux par liaisons hydrogène, sont en compétition et la nature de l'espèce majoritaire dépend des conditions. La lumière et les espèces radicalaires cationiques qui en découlent n'induisent pas de changement significatif dans leur structure, bien que le co-assemblage entre espèces neutres et radicalaires soit démontré. Dans ces co-assemblages, les électrons non-appariés sont soit lentement délocalisés en solution, soit rapidement délocalisés au sein de fibres alignées dans des films minces. Notre étude par dichroïsme circulaire écarte la possibilité d'utiliser la LPC pour orienter la chiralité des assemblages de TATA dans les conditions décrites dans la littérature. Enfin, des monomères TATA comportant une unité triphénylphosphine furent synthétisés. Leur étude dans le toluène, dichlorométhane et décaline a montré la formation d'assemblages par liaisons hydrogène thermoréversible. Une série d'additifs et de solvants énantiopurs fut employée sans succès afin d'en contrôler la chiralité supramoléculaire. La caractérisation fine des assemblages réalisée dans cette thèse ouvre la voie à un meilleur contrôle de la structure des assemblages hélicoïdaux fonctionnalisés.

Mots-clefs : polymères supramoléculaires ; triarylamine trisamide ; lumière polarisée circulairement ; catalyse asymétrique absolue.

Title: Controlling handedness of triarylamine trisamide assemblies by means of circularly polarized light or chiral additives

Abstract:

To pave the way for the absolute asymmetric catalysis, triarylamine trisamide (TATA) supramolecular helical polymers were investigated under the influence of circularly polarized light (CPL) and chiral additives/solvents. The association properties of TATA molecules with saturated or diacetylenic side chains were probed in presence and absence of CPL, by SANS, UV–Vis–NIR, FT–IR, NMR and EPR. The two types of self-assembly formed by these TATA molecules, non-specific aggregates and hydrogen-bonded helical stacks, are in competition and the majority assembly depends on conditions (concentration, temperature, solution/gel/solid). Light and the resulting radical cationic species do not strongly affect the structure of these assemblies, while the co-assembly between neutral and radical cationic species is demonstrated. In these co-assemblies, the unpaired electrons are either slowly delocalized in solution, because of the disorder in assemblies, or rapidly delocalized within long aligned fibers of thin films. Our CD study discards the possibility of using CPL to direct the handedness of TATA-SDA assemblies in the conditions stated in the literature. Finally, the synthesis of TATA ligands bearing a triphenylphosphine unit was achieved. Their study in toluene, dichloromethane and decalin showed the thermoreversible formation of long hydrogen-bonded stacks. Despite the use of a library of enantiopure small molecules as chiral additives or solvents, no biased supramolecular helices were detected. The in-depth characterization of assemblies carried out in this thesis paves the way towards a better control of the structure of functionalized helical assemblies.

Keywords: supramolecular polymers; triarylamine trisamide; circularly polarized light; absolute asymmetric catalysis.